Proceedings of the

1st International Conference on Mechanical and Manufacturing Engineering Research and Practice (iCMMERP-2019)

24-28 November 2019, Sydney, Australia

http://icmmerp.net.au/

978-0-6482681-8-5

Richard Yang, Leo Zhang, Ming Zhao, Gu Fang and Rafiqul Islam, Eds

Proceedings of the 1st International Conference on Mechanical and Manufacturing Engineering Research and Practice (iCMMERP-2019), 24 to 28 November 2019, Sydney, Australia

Published by Science, Technology and Management Crescent Australia Ltd
in association with
Global Circle for Scientific, Technological and Management Research, Sydney, Australia

Editors:

Prof Richard Yang

Dr Leo Zhang

Prof Gu Fang

Assoc Prof Ming Zhao

Dr Rafiqul Islam

Date published: 24 November 2019

Paper Peer Review Process:

All full-length papers included in the Proceedings of the 1st International Conference on Mechanical and Manufacturing Engineering Research and Practice (iCMMERP-2019), 24 to 28 November 2019 have been independently peer reviewed. The full papers were reviewed, and the review comments were sent to the authors to address the comments. The revised papers submitted by the authors were then checked by the Editors and accepted once the papers satisfied the requirements of the iCMMERP-2019.

SPONSORS

iCMMERP-2019 is proudly sponsored by:

Western Sydney University

LEAP AUSTRALIA PTY LTD

Festo PTY LTD

CNC Machinery Sales Australia

Emona Instruments Pty Ltd

Emona Instruments Pty Ltd

Welcome by Conference General Chair

The International Conference on Mechanical and Manufacturing Engineering Research (iCMMERP-2019), aims to provide an international platform for effective exchange of ideas, reaffirming the existing collegial contacts, provide opportunities of professional interaction amongst researchers, industrials and students, to present and share their latest research and practice and to showcase latest advancements, trends and future challenges in a broad range of disciplines related to Mechanical and Manufacturing Engineering.

As the General Chair of the 1st International Conference on Mechanical and Manufacturing Engineering Research and Practice (iCMMERP-2019), I would like to thank the Plenary Speakers, Keynote Speakers, Invited Speakers, Authors, Sponsors, Secretaries, IT Team Members, Conference Advisory Committee Members, Organising Committee Members, Technical Committee Members, Reviewers and Volunteers for making this conference successful.

I would also like to thank Professor Barney Glover, Vice-Chancellor and President, Western Sydney University for his kind support towards this congress. I would also like to thank Professor Simeon Simoff, Dean, School of Computing, Engineering and Mathematics, and Professor Yang Xiang, Interim Dean (Planning), School of Engineering for their kind support and encouragement to make this congress successful.

Professor Ataur Rahman, PhD, FIE Aust, MASCE, MAGU, MIWA
General Chair
1st International Conference on Mechanical and Manufacturing Engineering Research and Practice
(iCMMERP-2019)

Welcome from the Conference Chair of iCMMERP-2019

On behalf of the Organising Committee and Co-chairs of iCMMERP-2019, it is my pleasure to welcome you to Sydney and participate in the 1st International Conference on Mechanical and Manufacturing Engineering Research and Practice (iCMMERP-2019).

The iCMMERP-2019 is jointly organised by the School of Computing, Engineering and Mathematics (SCEM) at Western Sydney University (WSU), Sydney, Australia and Global Circle for Scientific, Technological and Management Research (GCSTMR) as part of its fifth World Congress. The main themes of iCMMERP-2019 include Additive Manufacturing, Advanced Manufacturing, Additive Manufacturing, Advanced Engineering Materials and Structures, Composite materials, Material Joining Technologies, Material Fabrication and Characterisation, Automation and Dynamic Control, Robotics, Biomechanics, Biomaterials and Biomedical Engineering, Fracture Mechanics, Fatigue and Damage Tolerance, Design and Optimisation, Nano and Micro Mechanics, Multi-scale Computational Modelling, Computational Fluid Dynamics, Thermal and Fluid Engineering, etc.

The iCMMERP-2019 conference intends to cover all aspects of scientific investigations and systems design in Mechanical and Manufacturing Engineering, and to showcase latest advancements, trends and future challenges in a broad range of disciplines related to Mechanical and Manufacturing Engineering.

On behalf of the organising committee, I would like to sincerely thank all authors for their papers and contributions to this Conference. I would like to sincerely thank Western Sydney University management for providing the facilities and infrastructure at Parramatta South Campus that made the organisation of this conference possible. I also would like to show our gratitude to the plenary/keynote speakers to share their wealth of experiences and knowledge in Mechanical and Manufacturing Engineering.

I would like to share with you our gratitude towards all members of the organising committee for their excellent efforts and dedication to the success of iCMMERP-2019.I offer thanks to all the Co-chairs for their excellent contributions, members of the international technical committee and other reviewers, who offered their time and technical expertise during the review process. Special thanks to all session chairs, School's HDR student volunteers and sponsors for their contributions to make iCMMERP-2019 a success altogether.

Last but not least, I would like to sincerely thank all speakers, participants and attendees of iCMMERP-2019, and we are looking forward to several days of stimulating presentations, enthusiastic debates, friendly interactions and thoughtful discussions which could greatly forward Mechanical and Manufacturing Engineering.

Professor Richard Yang, PhD
Chair
1st International Conference on Mechanical and Manufacturing Engineering Research and Practice
(iCMMERP-2019)

1st International Conference on Mechanical and Manufacturing Engineering Research and Practice (iCMMERP-2019)

Conference Committee

General Chair
Professor Ataur Rahman, Western Sydney University, Australia

Chair
Professor Richard Yang, Western Sydney University, Australia

Co-Chairs
Professor Gu Fang, Western Sydney University, Australia
Associate Professor Ming Zhao, Western Sydney University, Australia
Dr Rafiqul Islam, Solar-e-Technology, Australia

Conference Secretary
Dr Leo Zhang, Western Sydney University, Australia

Treasurer
Dr Hasan Rahman, GCSTMR, Australia

Conference Management Coordinator
Ms Jenis Islam

Members
Professor Chin Leo, Western Sydney University, Australia
Professor Vivian Tam, Western Sydney University, Australia
Professor Gu Fang, Western Sydney University, Australia
Associate Professor Fidelis Mashiri, Western Sydney University, Australia
Associate Professor Swapan Saha, Western Sydney University, Australia
Associate Professor Ming Zhao, Western Sydney University, Australia
Dr Vojislav Ilic, Western Sydney University, Australia
Dr Qinghua Zeng, Western Sydney University, Australia
Dr Abdul Alim, Western Sydney University, Australia
Dr Tosin Famakinwa, Western Sydney University, Australia
Dr Helen Wu, Western Sydney University, Australia
Dr Rafiqul Islam, Western Sydney University, Australia

Engr Mainul Hossain, Western Sydney University, Australia

Advisory Committee

Prof Bill McBride, The University of Newcastle, Australia
Prof Candace Lang, Macquarie University, Australia
Prof Dikai Liu, The University of Technology Sydney, Australia
Prof Firoz Alam, RMIT University, Australia
Prof Gangadhara Prusty, University of New South Wales, Australia
Prof Graeme E. Murch, The University of Newcastle, Australia
Prof Henry W. K. Kwan, ENTPE Universite De Lyon, France
Prof Lin Ye, University of Sydney, Australia
Prof Qing Li, University of Sydney, Australia
Prof Ranjit Perera, University of Moratuwa, Sri Lanka
Prof Shaokoon Cheng, Macquarie University, Australia
Prof Simeon Simoff, Western Sydney University, Australia
Prof Taha B. M. J. Ouarda, National Institute of Scientific Research, INRS, Canada
Prof Thomas Fiedler, The University of Newcastle, Australia
Prof Weihua Li, University of Wollongong, Australia
Prof Yang Xiang, Western Sydney University, Australia
Prof Zhen Luo, The University of Technology Sydney, Australia
Prof Zhengyi Jiang, University of Wollongong, Australia
Prof Xu Han, Hebei University of Technology, China
Prof Andrew Chan, University of Tasmania, Australia
Prof Xiaodong Yang, Beijing University of Technology, China
Prof Jing JI, Deputy Dean, South China University of Technology, China

Technical Committee

Baolin Wang, Western Sydney University, Australia
Dongfang Liang, Cambridge University, UK
Faisal Anwar, Curtin University, Australia
Haiping Zhu, Western Sydney University, Australia
Helen Wu, Western Sydney University, Australia
Hui Xie, Western Sydney University, Australia
Leigh Sheppard, Western Sydney University, Australia
Lin Lu, Dalian University of Technology, China
Neaz Sheikh, The University of Wollongong, Australia
Na Lv, Shanghai Jiaotong University
Omar Mubin, Western Sydney University, Australia
Sasha Alexander, Western Sydney University, Australia
Tawhidul Islam Khan, Saga University, Japan
Thinh Nguyen, Victoria University, Australia
Vojislav Ilic, Western Sydney University, Australia
Xiaolin Wang, University of Tasmania, Australia

Yanling Xu, Shanghai Jiao Tong University, China
Yanzhi Zhao, Yanshan University, China
Yingyan Zhang, Western Sydney University, Australia
Richard Wuhrer, Western Sydney University, Australia
Prof. Yuhong Cui, Tianjin University, China
Prof. Qingsheng Yang, Beijing University of Technology, China.
Associate Professor Jing LI, South China University of Technology, China
Dr. Xiaoshan Lin, RMIT, Australia

PLENARY SPEAKER

Professor Lin Ye, Centre for Advanced Materials Technology, School of Aerospace, Mechanical and Mechatronic Engineering, the University of Sydney, NSW 2006, Australia

Topic: Fusion Bonding and Consolidation of 3D Printed Continuous Carbon Fibre Reinforced Polyamide Composites

Biography: Lin Ye currently is a full professor at the School of Aerospace, Mechanical and Mechatronic Engineering (AMME) and the Director of the Centre for Advanced Materials Technology (CAMT) of The University of Sydney. He received his BEng degree from Harbin Engineering University in 1982, and MEng in 1984 and PhD in 1987 from Beihang University (formerly Beijing Institute of Aeronautics and Astronautics). Then, in early 1988, he was appointed Lecturer at Xi'an Jiaotong University. He joined University of Sydney in July 1992 after working as an Alexander von Humboldt Fellow at the Institute for Composite Materials (IVW GmbH), 1990 to 1992. He was Head of the School of AMME for a period of four years, 2004 to 2007. His research publications include 3 research monographs, 5 edited books, 10 book chapters and over 380 refereed scientific articles in leading journals as well as more than 30 plenary, keynote and invited lectures presented at major international conferences. Most of his research papers have been published in the top journals in his field including Composites Science & Technology, Composites Part A, etc. His major research interests are in the areas of composites science and technology, smart materials and structures, nano-materials and nano-composites, structural integrity and durability. He has supervised 28 PhD and 12 MPhil students, and over 30 postdoctoral research fellows/associates and visiting scholars in AMME, University of Sydney. He was elected a Fellow of the Australian Academy of Technology and Engineering (ATSE) in 2005.

KEYNOTE SPEAKER

Professor Zhengyi Jiang, School of Mechanical, Materials, Mechatronic and Biomedical Engineering, University of Wollongong, Australia

Topic: Current progress of advanced micro manufacturing of composites

Biography: Professor Zhengyi Jiang is currently Senior Professor and Leader of Advanced Micro Manufacturing Centre at the University of Wollongong (UOW). He has been carrying out research on rolling mechanics with significant expertise in rolling theory and technology, tribology in metal manufacturing, contact mechanics and computational mechanics in metal manufacturing, numerical simulation of metal manufacturing, advanced micro manufacturing, development of novel composites, and artificial intelligent applications in rolling process. He obtained his PhD from Northeastern University in 1996, and was promoted full professor at Northeastern University in 1998 and at UOW in 2010. He has over 620 publications (more than 430 journal articles) and 3 monographs in the area of advanced metal manufacturing. He has been awarded over 38 prizes and awards from Australia, Japan, Romania and China, including ARC Future Fellowship (FT3), Australian Research Fellowship (twice), Endeavour Australia Cheung Kong Research Fellowship and Japan Society for the Promotion of Science (JSPS) Invitation Fellowship.

KEYNOTE SPEAKER

Professor Lin Lu, Deputy director of the State Key Laboratory of Coastal and Offshore Engineering, and Director of the Center of Deep Water Engineering, Dalian University of Technology, China.

Topic: Nonlinear behaviors of wave-induced fluid oscillations in the gap between two fixed barges

Biography: Prof. Lin Lu is a professor of Dalian University of Technology, China. He is the deputy director of the State Key Laboratory of Coastal and Offshore Engineering, and director of the Center of Deep Water Engineering, Dalian University of Technology. He got his Bachelor and Master degrees from Ocean University of China in 1999 and 2002, and PhD. from Dalian University of Technology in 2006. He has been research fellow of the University of Western Australian 2007-2008 and senior visiting scholar of UWA 2018, and visiting scholar of Bureau Veritas France 2011-2012. Prof Lu's research areas cover water wave interaction with floating bodies, flow and structure interactions, sediment scour around subsea structures, and CFD and experimental modelling of ocean dynamics.

KEYNOTE SPEAKER

Associate Professor Tawhidul Islam Khan, Department Mechanical Engineering, Faculty of Science and Engineering, Saga University, 1 Honjo, Saga 840-8502, Japan

Topic: New devising in diagnosis of knee osteoarthritis based on acoustic emission imaging

Biography: Dr. T. I. Khan graduated from the Department of Mechanical Engineering, Khulna University of Engineering and Technology (KUET), Bangladesh in 1991. He completed his masters and doctorate degrees from Saga University, Japan in 1997 and 2003 respectively. After his PhD, he awarded the JSPS postdoctoral fellowship and continued his research at Saga University until September, 2007. Since October 2007 till to date he has been working as an Associate Professor in the Department of Mechanical Engineering of Saga University, Japan. He also worked as Lecturer and Assistant Professor in the Department of Mechanical Engineering of KUET, Bangladesh until February, 2005. His current research interests are Intelligent Machines, Acoustic Emission in NDE, Diagnostics, Biomedical Imaging, Moiré Topography, and so on. He is the author of more than 80 technical papers. He is an active member of SICE, ASJ, JSME, JSNDI, IIAV.

KEYNOTE SPEAKER

Professor Chunwei Zhang, School of Civil Engineering, Qingdao University of Technology, 266033, P.R. China

Topic: New Active Control Method to Improve the Dynamic Stability of High-speed Trains

Biography: Professor Chunwei Zhang is the Chair Professor and discipline leader of Civil Engineering at Qingdao University of Technology, China. He is the Founding Director of Structural Vibration Control research group. He is the Director of Qingdao Municipal Engineering Research Center for Protective Structures, and the Director of Qingdao International Science and Technology Collaboration Center for Infrastructure Engineering. His research interests include structural dynamics, vibration control, structural health monitoring, anti-blast, anti-impact and protective structures.

KEYNOTE SPEAKER

Professor Li Sun, School of Civil Engineering, Shenyang Jianzhu University, Shenyang 110168, P.R. China

Topic: Development and application of Fiber Bragg Grating strain sensors using Additive Manufacturing Technology

Biography: Professor Li Sun is China national Million Talents "Hundreds Level", Endeavour Fellowship of Australia, Distinguished Professor of Liaoning Province, Director of Provincial Centre for Structural Safety and Damage Control, outstanding teacher of Liaoning Province. No.1 awardee of three second grade prizes for scientific and technological progress or innovation of Liaoning Province government. Her research interests are structural health monitoring, damage identification and control, composite materials and structures, applications of intelligent materials in civil engineering.

Table of Contents

Engineering Design and Optimisation

Deep Learning and Big Data

Abstracts/Extended Abstracts

Recent Progress in Shape Memory Polymers in Biomedical Applications

Lama Hewage Janitha Jeewantha
Centre for Future Materials &
School of Mechanical and Electrical Engineering, Faculty of Health, Engineering and Sciences
University of Southern Queensland
Toowoomba, Australia
Janitha.Jeewantha@usq.edu.au

Md Mainul Islam
Centre for Future Materials &
School of Mechanical and Electrical Engineering, Faculty of Health, Engineering and Sciences
University of Southern Queensland
Toowoomba, Australia
Mainul.Islam@usq.edu.au

Jayantha Ananda Epaarachchi
Centre for Future Materials &
School of Mechanical and Electrical Engineering, Faculty of Health, Engineering and Sciences
University of Southern Queensland
Toowoomba, Australia
Jayantha.Epaarachchi@usq.edu.au

***Abstract*—The rapid progress and innovation of modern materials in engineering sciences are enabling us to overcome many limitations due to traditional materials used in various engineering and biomedical fields. Additionally, it is helping us to develop new products. Intelligent materials such as shape memory polymers (SMPs) have played a vital role in this field. They have unique ability to recover their original shape upon external stimuli such that temperature, light, electricity, water, pH, magnetism and specific ions. The SMPs are currently used in wider range of engineering disciplines due to their exceptional structural properties like good manufacturability, high shape deformability and recoverability. Additionally SMPs have shown a good prospective development in the biomedical applications due to their special characteristics such as biocompatibility, biodegradability, low rejection by host, low density and fairly good glass transition temperature (T_g). Recently developed SMPs are used in self-tightening sutures, controlled drug delivery systems, self-retractable and removable stents, fasteners and scaffolds for tissue engineering, endovascular clot removal, orthodontic appliances, etc. In this article recent advancement of the SMP materials and their applications are discussed.**

Keywords— Shape memory polymer, Shape memory effect, Biomedical, potential applications

I. INTRODUCTION

SMP materials are being used in a wider range of applications in engineering. Recent development and continuous progression enhanced the SMP material properties dramatically. SMP materials can be classified in to physically cross-linked or chemically cross-linked and based on the stimulus techniques as well. The traditional SMPs have two shapes only but presently triple and quadruple or multiple SMPs have been developed by the scientists. Moreover some SPMs can respond to multi stimulus as well [1].

The applications of SMPs can be seen in textile, aerospace and most interestingly in biomedical fields. In this article recent developments and applications related to biomedical fields are discussed.

II. APPLICATIONS IN BIOMEDICAL FIELDS

In addition to biodegradability and biocompatibility, low toxicity is another important property of SMPs. Due to this reason most of the parts of implants being manufactured using SMP materials. Furthermore, SMPs are found in stents, sutures, tissue engineering and drug delivery systems. Some of the recent developments are discussed below.

A. Maintaining SMP-based Stents

Surgical procedures have been simplified with the development of SMP based equipment. The stents can be inserted into the body without creating conventional openings, since the full shape can be achieved through external triggering once it has reached the required location. In 2002 the first successful microvascular device was made with SMP to remove blood clots in stroke patients. This development of new treatment modality has had significant benefits to stroke patients [2]. The development of stents have given the most attention in the SMP because, Venkatraman et al. [3] successfully tested bi-layered biodegradable stent by using the concept of SMP. Recently Zheng et al. [4] developed self-expandable stent by using poly (propylene carbonate) (PPC) and polycaprolactone (PCL). First they dried two compounds up to 40ºC in a vacuumed oven and before it melted, they blended in different volume fractions of PCL through a twin-screw extruder. After that pellets were hot pressed into the matrix at 130°C for 5 min under 10 MPa to achieve shape memory effect. The shape memory performance of the material was depended on added PCL content. The optimal shape recovery (R_r) and shape fixity (R_f) achieved 25% volume percentage of PCL. They specified new material as PL-25 which most importantly has its glass transition temperature (T_g) near body temperature which led to the invention of biomedical stent. Moreover blood compatibility, in vitro degradation, and drug release behaviour were tested and results were really inspiring. Further they pointed out that this material could have good blood compatibility in vitro degradation and drug release abilities. Ansari et al. [5] further investigated thermoplastic polyurethane (TPU) and PCL shape memory polymers experimentally. With contrast to Zheng, Ansari's group mixed and blended the compounds. In-depth experimental data analysis revealed that blend mixing method had higher storage modulus and loss modulus compared to melt mixing techniques. The material was torsion and stretched prior to the procedure to obtain better usage. Further they concluded that angle recovery was affected by high pre-stretch and normal strain recovery was affected by high pre-torsion. Hence by adjusting pre-stretch and deformation start temperature, we can control recovery start temperature and maximum recovery in the strip. They concluded that the setting up deformation temperature (T_d) around 40°C can be used to enhance the existing applications in biomedical engineering especially in stents.

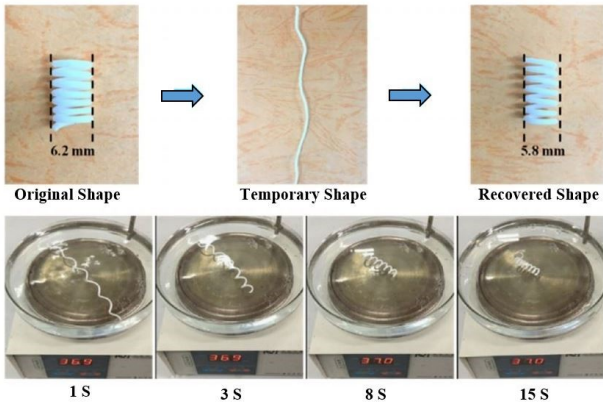

Fig. 1. Images of the shape memory cycle of the PL-25 stent recorded by a digital camera

B. *SMP-based Wound Closure Materials*

Most of surgeries such as endoscopies, closing of the wound lips without affecting to surrounding muscles was quite challenging. Centuries before, biodegradable surgical threads were not available. Hence the success of the surgery totally depended on the skills of the surgeon, and continuous consultation was required. Moreover removing surgical sutures after certain number of days was quite painful. But the development of biodegradable shape memory polymer (BSMP) materials solved this issue quite remarkably [6]. Langer et al. [7] tested first SMP based suture material to seal wound and they were the pioneers in this research field. The main aim was applying sutures loosely and then to provide external stimulus to recover the permanent shape. Baia et al. [8] proposed new SMP for surgical sutures which consisted of highly biodegradable ethyl cellulose (EC) and PCL. They achieved 621% elongation and most importantly switching temperature was 37.2^{o}C, which was closer to body temperature. To adjust switching temperature they tailored the graft length of PCL in polymer network. Before Zheng, Jing et al. [9] has conducted a same kind of extrusion to obtain two biocompatible TPU and PCL. The best shape memory properties, 98% R_r and 90% R_f have been achieved with configuration of 25% TPU and 75% PCL. They identified two regions in TPU 25% domain. The crystalline region maintained the shape temporarily when it elongated and rubbery region helped to reconfigure it into original shape upon heat. Jing prepared 50x1x1 mm specimen by stretching up to 1000% of its initial length in room conditions. Sample string was put in to a 60^{o}C hot water bath to prove suturing capability, and within 2 seconds it was knotted automatically. Further Jing stated that exposing human skin cells to 60^{o}C hot air will be safer for few seconds, which will need further investigation and certification before putting into clinical practice.

C. *SMP Materials in Tissue Engineering*

The main objective of the tissue engineering is to construct, restore and maintain or improve the damaged tissues in human body. However researchers mostly focused on bone tissue regeneration [6]. Nowadays there are few highly technical methods available to fabricate these body parts. For example casting, 3D/4D printing and electrospinning [10-13]. Bao et al. [11] fabricated new SMP using electrospinning technique. The main biodegradable compound was poly (D,L-lactide-co-trimethylene carbonate) known as PDLLA-co-TMC. They were able to vary fibre fineness, T_g, and SMP mechanical properties up to great extent by changing the composition of DLLA and MTC in the copolymer. Both 2D and 3D forms given excellent R_r (>94%) and R_f (>98%) within 10 seconds and less than 39^{o}C. Further they discovered bone forming ability by observing bio-mineralization-relevant alkaline phosphatase expression and mineral deposition on the bone. As an enhancement in same stream SMP polydopamine coated self-fitting biodegradable shape memory scaffold was developed by Zhang et al. [10]. The scaffold was prepared with PCL diacrylate using a SCPL method. As a thermo-responsive scaffold was fitted into the irregular defect and stimulated. The regenerated shape was withstand while cooling. Experiment team confirmed that outer polydopamine coat did not affect core features of the SMP. After soaking 7 and 14 days they have detected mineralization on the component. It was an indication of bioactivity and potential to bond to adjacent bone. Finally they concluded that prepared self-fitting scaffold is capable to treat carnio-maxillofacial (CMF) bone defects. Some researchers are interested on electroactive shape memory polymers (ESMPs). The ESMPs mainly consist of PLA and aniline trimer (AT). The specimen underwent various tests and it gave higher mechanical properties. Especially modulus of the material was in gigapascal range besides that short recovery time, higher R_r (< 94%) and higher R_f (~100%) were really encouraging. Hence Xie et al. [14] strongly recommended this material for bone regeneration applications.

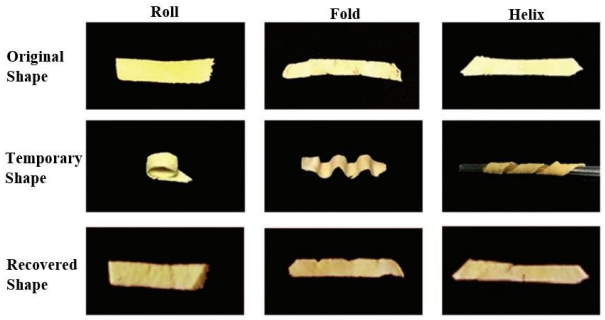

Fig. 2. Water-responsive shape-memory effect of PBF scaffolds from various temporary shapes.
(Reproduced from [15] Copyright 2019. The Royal Society of Chemistry)

Guo [15] and his team developed new class of shape memory materials which were responsive to water. Those were really limited and relatively complicated compared to other SMPs. To prepare butanetetrol fumarate (PBF) thermal curing and salt leaching methods have been used. It has shown higher shape recovery and R_f (> 95%) rates. Further their results showed that scaffold has good elasticity property, which is more favourable for implementation on dynamic environments.

D. SMP Materials in Embolization

Embolization is a medical technique currently used to block the blood flow to a particular area in the body. It helps to prevent internal massive bleedings, control the blood flow, block the blood flow to tumours and eliminate abnormal connection to veins. Continuous development in SMP has facilitated in the progress of embolization techniques. With combination of shape memory effect (SME) with elastic recovery will be a useful property to address embolization challenges [6]. In the recent past, coil type embolization was most commonly used. However Redriguez et al. [16] tested filling type embolization and used polyurethane-based as a filler material. They planned to achieve two goals, firstly to check the biocompatibility of polyurethane-based SMP, and secondly to practically implant in aneurysm. For the practical evaluation swine around 3 to 4 months old were used and their weights were approximately 30 to 40 kg. Pathological results indicated the validity of their model to use in clinical applications. They made this conclusion after evaluating the devises in three different time periods 0, 30 and 90 days. In later year Redriguez et al. [17] tested foam type SMP for vascular applications. The main objective was to develop non-destructive grid to process the foam between pore cells.

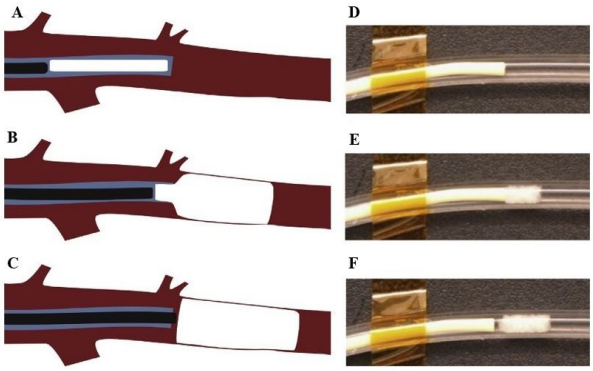

Fig. 3. Schematic diagram of endovascular deployment of the SMP foam VOD: (A) the device is pushed near the catheter tip by the guidewire, (B) the guidewire pushes the self-actuating device out of the catheter, and (C) deployed device fills the vessel lumen. (D–F) In vitro demonstration of developed occlusion device in 37 °C (body temperature).

Landsman et al. [18] conducted a study related to foam based SMP. In that investigation they focused more on SMP material properties, safety and effectiveness which can especially be used in peripheral embolization devices (PED). They studied T_g of the material and required time to deploy it in to the correct place without forming. The efficiency of the device was verified by performing blood flow studies. Further his team investigated the volume-filling ability of the SMP and swelling capacity of hydrogels used to prevent haemorrhages. Landsman discussed advantages in each materials and their combined composites as well. Maintaining the expansion pressure during the process was critical because high pressure may damage more tissues and internal organs. The experiment was conducted in 37^{o}C water and during the test expansion force did not exceed 0.6 N and tissue damage was unlikely to occur [19]. But their findings need to be verified with more practical tests including animal models before it is applied in humans. Nathan et al. [20] were interested on SMP foams. They mainly focused on particulate number and the size of the form. In conclusion they stated that without damaging tissues and cells, SMP foams can be used as a vascular blockage device. By closely monitoring recent research finding and trends in SMP, we believe SMP foam materials have more potential in embolization devices.

E. SMP Materials in Drug Release

According to Ruiz-Rubio [6], limited number of researchers conducted experiments in this field. However material properties of SMP are encouraging to use them in this field. Diffusion coefficient is the most important parameter if SMPs are used as a drug release agent, because low diffusion coefficient can release drugs at a very slow phase to the body fluid environment. Therefore immense potential is recognized with SMP in drug delivery. Kashif et al. [21] blended PCL and trisilanolphenyl polyhedral oligomeric silsequioxane (TspPOSS) nanocomposite with drugs. They stated that PCL/TspPOSS nanocomposite (90 wt/10 wt) with drug 10 wt% has given good thermal triggering to the SMP. According to them TspPOSS improved deration rate of the PCL matrix delayed the drug delivery rate. Most of the SMPs thermally triggered but Chen et al. [22] successfully tested SMP drug release agent triggered by the variation of pH. Zheng's group [4] blended Metoprolol tartrate (MPT) drug through twin-screw mini-extruder. The drug percentage was 5% of the total weight of the PL-25. They made tablets which had thickness 0.8 mm and diameter 10 mm. Linear drug diffusion was observed over a period of two months. During that period approximately 60% MPT was released. Further they stated that PL-25 can build drug loaded stent which can deliver drug long period of time.

III. CONCLUSIONS

SMP based various applications can be seen in biomedical fields. Recently developed SMP materials for self-tightening sutures, stents, endovascular clot removal, scaffolds, and controlled drug delivery were discussed in this paper. Many of the experiment outcomes are yet to be verified and validated with existing models before applying to clinical practices. The development of SMP dramatically stepped up existing surgical procedures and techniques. Most importantly some of the critical surgeries can be done through a small cut. In addition to that, implanted parts are not necessary to be removed and will degrade with the time. This is helping us to reduce hospital wastage in another way to protect our environment. We believe that further development in this field is required as it is immensely useful to the humankind.

REFERENCES

[1] K. M. Herbert, S. Schrettl, S. J. Rowan, and C. Weder, "50th anniversary perspective: Solid-state multistimuli, multiresponsive polymeric materials," Macromolecules, vol. 50, no. 22, pp. 8845-8870, 2017.

[2] M. F. Metzger, T. S. Wilson, D. Schumann, D. L. Matthews, and D. J. Maitland, "Mechanical properties of mechanical actuator for treating ischemic stroke," Biomedical Microdevices, vol. 4, no. 2, pp. 89-96, 2002.

[3] S. S. Venkatraman, L. P. Tan, J. F. D. Joso, Y. C. F. Boey, and X. Wang, "Biodegradable stents with elastic memory," Biomaterials, vol. 27, no. 8, pp. 1573-1578, 2006.

[4] Y. Zheng, Y. Li, X. Hu, J. Shen, and S. Guo, "Biocompatible shape memory blend for self-expandable stents with potential biomedical

applications," ACS applied materials & interfaces, vol. 9, no. 16, pp. 13988-13998, 2017.

[5] M. Ansari, M. Golzar, M. Baghani, and M. Soleimani, "Shape memory characterization of poly (ε-caprolactone)(PCL)/polyurethane (PU) in combined torsion-tension loading with potential applications in cardiovascular stent," Polymer Testing, vol. 68, pp. 424-432, 2018.

[6] L. Ruiz-Rubio, L. Pérez-Álvarez, and J. L. Vilas-Vilela, "Biodegradable Shape-Memory Polymers," Shape Memory Polymers, Blends and Composites, pp. 219-236: Springer, 2020.

[7] A. Lendlein, and R. Langer, "Biodegradable, elastic shape-memory polymers for potential biomedical applications," Science, vol. 296, no. 5573, pp. 1673-1676, 2002.

[8] Y. Bai, C. Jiang, Q. Wang, and T. Wang, "A novel high mechanical strength shape memory polymer based on ethyl cellulose and polycaprolactone," Carbohydrate polymers, vol. 96, no. 2, pp. 522-527, 2013

[9] X. Jing, H.-Y. Mi, H.-X. Huang, and L.-S. Turng, "Shape memory thermoplastic polyurethane (TPU)/poly (ε-caprolactone)(PCL) blends as self-knotting sutures," journal of the mechanical behavior of biomedical materials, vol. 64, pp. 94-103, 2016.

[10] D. Zhang, O. J. George, K. M. Petersen, A. C. Jimenez-Vergara, M. S. Hahn, and M. A. Grunlan, "A bioactive "self-fitting" shape memory polymer scaffold with potential to treat cranio-maxillo facial bone defects," Acta biomaterialia, vol. 10, no. 11, pp. 4597-4605, 2014.

[11] M. Bao, X. Lou, Q. Zhou, W. Dong, H. Yuan, and Y. Zhang, "Electrospun biomimetic fibrous scaffold from shape memory polymer of PDLLA-co-TMC for bone tissue engineering," ACS applied materials & interfaces, vol. 6, no. 4, pp. 2611-2621, 2014.

[12] F. S. Senatov, K. V. Niaza, M. Y. Zadorozhnyy, A. Maksimkin, S. Kaloshkin, and Y. Estrin, "Mechanical properties and shape memory effect of 3D-printed PLA-based porous scaffolds," Journal of the mechanical behavior of biomedical materials, vol. 57, pp. 139-148, 2016.

[13] F. Senatov, M. Y. Zadorozhnyy, K. Niaza, V. Medvedev, S. Kaloshkin, N. Y. Anisimova, M. Kiselevskiy, and K.-C. Yang, "Shape memory effect in 3D-printed scaffolds for self-fitting implants," European Polymer Journal, vol. 93, pp. 222-231, 2017.

[14] M. Xie, L. Wang, J. Ge, B. Guo, and P. X. Ma, "Strong electroactive biodegradable shape memory polymer networks based on star-shaped polylactide and aniline trimer for bone tissue engineering," ACS applied materials & interfaces, vol. 7, no. 12, pp. 6772-6781, 2015.

[15] Y. Guo, Z. Lv, Y. Huo, L. Sun, S. Chen, Z. Liu, C. He, X. Bi, X. Fan, and Z. You, "A biodegradable functional water-responsive shape memory polymer for biomedical applications," Journal of Materials Chemistry B, vol. 7, no. 1, pp. 123-132, 2019.

[16] J. N. Rodriguez, F. J. Clubb, T. S. Wilson, M. W. Miller, T. W. Fossum, J. Hartman, E. Tuzun, P. Singhal, and D. J. Maitland, "In vivo response to an implanted shape memory polyurethane foam in a porcine aneurysm model," Journal of Biomedical Materials Research Part A, vol. 102, no. 5, pp. 1231-1242, 2014.

[17] J. N. Rodriguez, M. W. Miller, A. Boyle, J. Horn, C.-K. Yang, T. S. Wilson, J. M. Ortega, W. Small, L. Nash, and H. Skoog, "Reticulation of low density shape memory polymer foam with an in vivo demonstration of vascular occlusion," Journal of the mechanical behavior of biomedical materials, vol. 40, pp. 102-114, 2014.

[18] T. L. Landsman, R. L. Bush, A. Glowczwski, J. Horn, S. L. Jessen, E. Ungchusri, K. Diguette, H. R. Smith, S. M. Hasan, and D. Nash, "Design and verification of a shape memory polymer peripheral occlusion device," Journal of the mechanical behavior of biomedical materials, vol. 63, pp. 195-206, 2016.

[19] T. Landsman, T. Touchet, S. Hasan, C. Smith, B. Russell, J. Rivera, D. Maitland, and E. Cosgriff-Hernandez, "A shape memory foam composite with enhanced fluid uptake and bactericidal properties as a hemostatic agent," Acta biomaterialia, vol. 47, pp. 91-99, 2017.

[20] A. L. Nathan, G. K. Fletcher, M. B. B. Monroe, W. Hwang, S. M. Herting, S. M. Hasan, B. K. Keller, and D. J. Maitland, "Particulate Release From Nanoparticle-Loaded Shape Memory Polymer Foams," Journal of medical devices, vol. 11, no. 1, pp. 011009, 2017.

[21] M. Kashif, B.-m. Yun, K.-S. Lee, and Y.-W. Chang, "Biodegradable shape-memory poly (ε-caprolactone)/polyhedral oligomeric silsequioxane nanocomposites: Sustained drug release and hydrolytic degradation," Materials Letters, vol. 166, pp. 125-128, 2016.

[22] H. Chen, Y. Li, Y. Liu, T. Gong, L. Wang, and S. Zhou, "Highly pH-sensitive polyurethane exhibiting shape memory and drug release," Polymer Chemistry, vol. 5, no. 17, pp. 5168-5174, 2014

Airflow dynamics and aerosol particle transport in a human lung

Md. M Rahman
School of Computing, Engineering, and Mathematics
Western Sydney University
Penrith, NSW, 2751, Australia
19615253@student.westernsydney.edu.au

Ming Zhao*
School of Computing, Engineering, and Mathematics
Western Sydney University
Penrith, NSW, 2751, Australia
M.Zhao@westernsydney.edu.au

Mohammad S Islam
School of Mechanical and Mechatronic Engineering
University of Technology Sydney
Ultimo, NSW 2007, Australia
mohammadsaidul.islam@uts.edu.au

Kejun Dong
Center for Infrastructure Engineering,
Western Sydney University, 2751 Penrith, NSW, Australia
kejun.dong@westernsydney.edu.au

Suvash C Saha
School of Mechanical and Mechatronic Engineering
University of Technology Sydney
Ultimo, NSW 2007, Australia
suvash.saha@uts.edu.au

***Abstract*—The knowledge of the aerosol particle transport and deposition (TD) is essential for the health risk assessment and the targeted drug delivery in a respiratory tract. Many studies have been performed for the airflow characterization at the mouth-throat and oral airways. The precise understanding of the airflow and particle dynamics at the upper lung airways could improve the TD. Therefore, an advanced numerical framework is developed for the particle TD into the human lung airway grounded upon Weibel's lung model. Primarily this study intends to examine the particle TD based on inhalation condition in the human lung by using the ANSYS Fluent software. Particle deposition efficiency is calculated based on the Euler-Lagrange (E-L) approach. Also, the different particle diameter** ($1\ \mu m \leq dp \leq 10\mu m$) **factor for deposition is discussed. The preliminary results suggest that the particle deposition efficiency increases with the increase of the Reynolds number and the particle diameter in the lung airways.**

Keywords— Tracheobronchial airways; Inhalation; Drug delivery; Respiratory health risk assessment; Aerosol particle transport and deposition (TD).

I. INTRODUCTION

The study of airflow and particle transport and deposition (TD) in human lungs is receiving considerable attention from many researchers because of its practical importance of science and engineering. However, the numerical modelling of the human using Computational Fluid Dynamics (CFD) lung is still a challenge because of the complexity of the geometry of the respiratory system. Therefore, to understand the particle TD in a lung, correctly predicting airflow in the lune is the main stage to prevent respiratory diseases in the human lung. Hence, the particle TD as a propounding impact over the respiratory airways while the particles were suspended in the atmosphere air [1].

There are different particle deposition mechanisms in the human lung, including gravitational sedimentation, initial impaction, and Brownian diffusion [2, 3]. The extrathoracic airways like a mouth-throat model are the primary entrance of the aerosol particle TD to the human lung airways. The overall airflow pattern and aerosol particle TD is affected by the Reynolds number for an idealized mouth-throat model [4]. Few studies have investigated radioactive aerosol particles TD for the mouth-throat model [5-6]. Helium-oxygen mixture for an aerosol particle TD in the human lung has been studied by image processing data analysis [7]. Due to the effect of pressure losses, a less deposition of aerosol particle TD was found at the upper airways for helium-oxygen gas mixture compare to the air. [8-9].

Moreover, different types of model, like in-vivo and in-silico, has been designed and examined for aerosol particle TD in the human respiratory airways [10-11]. Many researchers [12-17] have developed different types of and non-realistic lung geometries which are either symmetric or asymmetric, and analyses the airflow pattern. Realistic lung model is also developed using CT-scan data by several researchers [18-24].

The understanding of the particle TD in the well-known symmetric Lung Model is vital for targeted drug delivery systems. Therefore, this study intends to build up a Weibel's based model on flow characteristics of particle TD into the human lung.

II. FINITE ELEMENT MODELLING

A. THE GEOMETRY OF DOUBLE BIFURCATION

A Three-dimensional (3D) anatomical model is generated based on Weibel's model, where the symmetrical examined data are outlined in TABLE 1. The SolidWorks software is used to modify the final 3-D anatomical model. The Finite Volume-based ANSYS FLUENT solver is used for the computational purpose and Fluent User Defined Function is used for advanced modelling. Tecplot software is used for post-processing purposes.

B. NUMERICAL METHODS

The following governing equations are solved using the ANSYS FLUENT 19.2 with considering the proper boundary conditions. The equations for continuity and momentum are:

$$\frac{\partial u_i}{\partial x_i} = 0 \tag{2.1}$$

$$\frac{\partial u_i}{\partial t} + u_j \frac{\partial u_i}{\partial x_j} = -\frac{1}{\rho}\frac{\partial p}{\partial x_i} + \frac{\partial}{\partial x_j}\left[(\nu + \nu_T)\left(\frac{\partial u_i}{\partial x_j} + \frac{\partial u_j}{\partial x_i}\right)\right] \tag{2.2}$$

where u_i and u_j, {i, j = 1, 2, 3, ….} represents the velocity components along *x*-, *y*- and *z*- directions. ν_T represents the kinematic turbulent viscosity, ν, represents the kinematic fluid viscosity, ρ represents the fluid density, and p represents the pressure, respectively.

The flow equations are solved by the upwind second order numerical scheme. While the coupling algorithm is used to simulate the pressure-velocity coupling.

The standard *k–ω* model is used to simulate the effect of turbulence inside the lung airways. The Lagrangian particle tracking approach and discrete phase model (DPM) are applied to simulate the particle trajectories in human lung airways. Therefore, the force balance equation is represented as:

$$\frac{d\overrightarrow{u_p}}{dt} = \overrightarrow{F_D}\left(\vec{u} - \overrightarrow{u_p}\right) + \frac{\vec{g}}{\rho_p}\left(\rho_p - \rho\right) + \overrightarrow{F} \tag{2.3}$$

where $\vec{g}$ is the gravity, $\vec{u}$, is the fluid velocity, $\overrightarrow{u_p}$, is the particle velocity, $\overrightarrow{F}$ is the additional acceleration force term which is considered zero ($\overrightarrow{F} = 0$), and $\overrightarrow{F_D}\left(\vec{u} - \overrightarrow{u_p}\right)$ is the drag force. The drag force that plays the key role is calculated as:

$$\overrightarrow{F_D} = \frac{18\mu}{\rho_p d_p^2} C_D \frac{Re_P}{24} \tag{2.4}$$

where C_D is the drag coefficient, Re_P is the particle Reynolds number defined as $Re_P \equiv \frac{\rho d_P |\overrightarrow{u_p} - \vec{u}|}{\mu}$. d_P ρ_P and μ are, the particle diameter, the particle density and fluid viscosity, respectively.

The pressure outlet and velocity inlet boundary conditions are considered in the upper lung airway model. A zero-pressure conditions were used all the outlets of the lung model. The different sizes of spherical aerosol particles were randomly injected from the inlet surface. A total number of 1800 particles were injected at once from the inlet. The particle density is considered as 1100 kg/m^3. The polydisperse particles are introduced by the Rossin-Rammler diameter distribution technique into the present model. The airway wall was considered stationary and the wall surface was considered as 'no-slip'. For the particle's deposition purpose, a 'trap' condition was used in the trachea wall. When the particles are touching the airway wall surface, then it would be deposited because of the trap condition.

C. MESH GENERATION ANALYSIS

A double bifurcation symmetric model based on Weibel's model is constructed. Smooth inflation with ten-layer size mesh near the wall is created to determine the flow characteristics in a complex lung airway. Also, a dense tetrahedral mesh is used to investigate better fluid flow inside near the wall.

A grid refinement test is essential for every CFD simulation. The velocity, or pressure can be used as a function of grid number during the grid refinement test. Therefore, we considered a suitable grid refinement test during the simulation. It is mentioned that when the number of element is 2.61 million, the dynamic pressure showed as a steady state. Therefore, we considered the 2.61 million cells for the numerical simulations. Moreover, the model contains 51.29 million triangular interior faces.

D. DEPOSITION EFFICIENCY

Deposition efficiency (DE) is the percentages of the particle absorption in the trachea wall. Hence, the micro particles regional deposition in the trachea wall may be measured in relations of DE which may be illustrated as:

$$\text{DE} = \frac{\text{Specific number of particles are trapped in a lung airways}}{\text{Total number of particles are trapped in the lung airways}}$$

III. RESULT AND DISCUSSION

The model is validated against several published data. For brevity results are not presented here. The lung model geometry parameters as well as fluid parameters are outlined in Table 1 and Table 2. In the present study, a double bifurcation symmetric Weibel's lung model geometry was shown in Fig. 1a. Fig. 1 (b) shows the ten-layer inflation mesh at the 3-generation (G3-G5).

TABLE 1

Double bifurcation Geometric parameters (Dimensions represents in centimetre)

	Model of bifurcation					
	First		**Second**		**Third**	
Diameter	D1	0.56	D2	0.45	D3	0.35
Length	L1	0.76	L2	1.27	L3	1.07

TABLE 2. **Fluid Parameters**

Fluid density	1.225 (kg/m^3)			
Viscosity of fluid	1.7894e-05 (kg/m-s)			
Reynolds number	R1=500	R1=1000	R1=1500	R1=2000
Fluid Velocity (m/s)	V1=1.3	V2=2.62	V3=3.93	V4=5.24

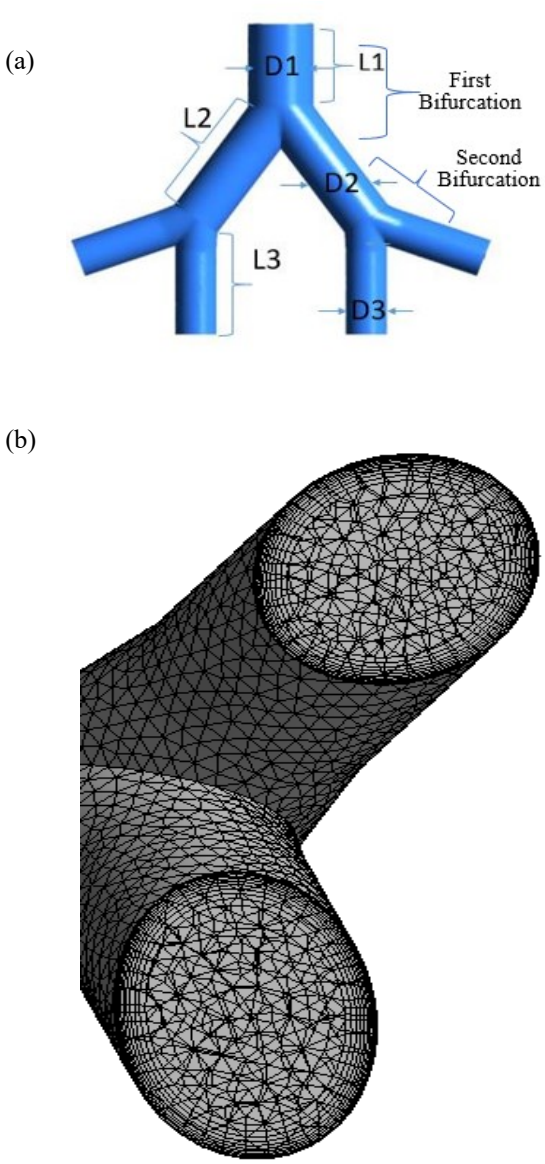

Fig. 1. An overview generated model (a) Double bifurcation symmetric Weibel's lung, (b) Inflation layer mesh

A wide-range of particle TD has presented considering several Reynold numbers such as 500, 1000, 1500, and 2000. The velocity contours at three selected planes for Re=500, and dp=1µm are shown as Fig. 2. The non-realistic symmetric model shows that velocity is changing in a different plane due to the effect of turbulent.

The wall shear is calculated by considering the Reynolds number 500 with particle diameter is 1µm (Fig. 3). The maximum wall shear value is 0.1 *pa,* which is found at different positions.

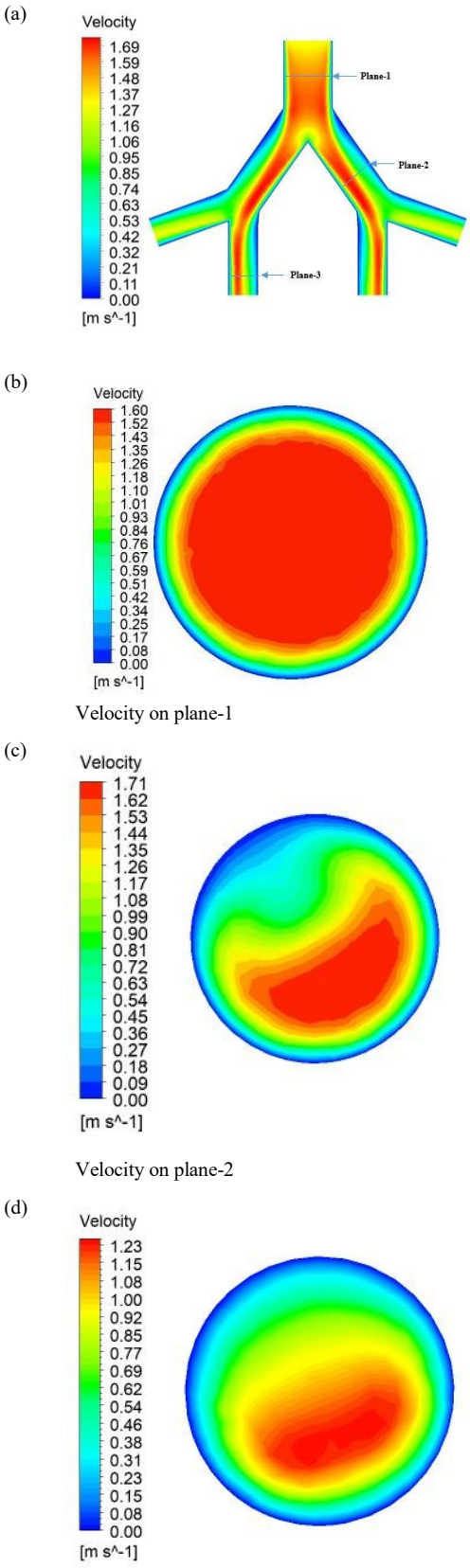

Fig. 2. Velocity contours for the selected three planes for Re=500.

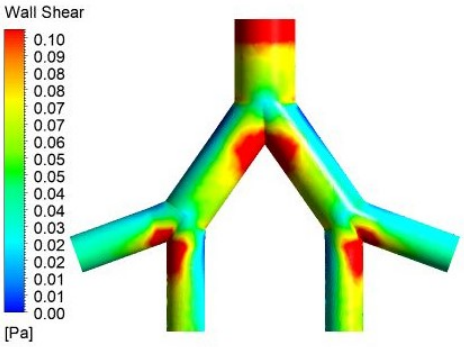

Fig. 3. Wall shear effect based on Weibel's lung model at Re=500

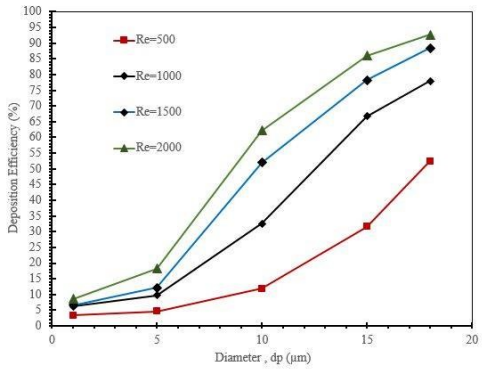

Fig. 4. Polydisperse particle DE of the symmetric lung model at different Reynolds numbers.

The total deposition efficiency (DE) as a function of different micrometer particles has shown in Fig. 4. At Re=2000, 92.6% of the particles were absorbed at the lung wall. On the other hand, 88.3%, 78%, and 52.4% of particles were absorbed at the lung wall, when Reynolds number is 1500, 1000, and 500, respectively. The particles usually flow the fluid streamline. However, due to increasing the fluid velocity rate, the particles did not flow the streamline. Therefore, the particles are quickly hit the tracheal wall; as a result, particles deposited. Hence, the particle DE has increased with increasing Reynold number due to the effect of inertial impaction mechanism.

IV. CONCLUSION

The micro-particle TD in the upper lung airways model is simulated numerically. The well-known Weibel's lung model is considered for the overall numerical investigation. The numerical results report the following observations:

The particle sizes and the flow rates are the most crucial element for particle deposition. The deposition information in terms of stokes correlation is essential in human epidemiological studies. Hence, the deposition efficiency for a non-realistic symmetric Weibel's lung increased with increases flow rate. Wall shear at the bifurcating region is found maximum.

The results will eventually help to understand the deposition efficiency of the targeted drug delivery in a human lung. Moreover, the authors will incorporate a more generation in a whole lung model to examine and forecast the particle TD in future studies.

REFERENCES

[1]. Schulz, H., Brand, P., & Heyder, J. (2000). Particle deposition in the respiratory tract. *Lung biology in health and disease*, *143*, 229-277.

[2] Choi, J. I., & Kim, C. S. (2007). Mathematical analysis of particle deposition in human lungs: an improved single path transport model. *Inhalation toxicology*, *19*(11), 925-939.

[3]. Everard, M. L. (2001). Guidelines for devices and choices.*Journal of Aerosol Medicine*, *14*(1, Supplement 1), 59-64.

4. Grgic, B., Finlay, W. H., & Heenan, A. F. (2004). Regional aerosol deposition and flow measurements in an idealized mouth and throat. *Journal of Aerosol Science*, *35*(1), 21-32.

[5]. CHAN, T. L., & LIPPMANN, M. (1980). Experimental measurements and empirical modelling of the regional deposition of inhaled particles in humans. *American Industrial Hygiene Association Journal*, *41*(6), 399-409.

[6]. Stahlhofen, W., Gebhart, J., & Heyder, J. (1980). Experimental determination of the regional deposition of aerosol particles in the human respiratory tract. *American Industrial Hygiene Association Journal*, *41*(6), 385-398a.

[7]. Greenblatt, E. E., Winkler, T., Harris, R. S., Kelly, V. J., Kone, M., Katz, I., ... & Venegas, J. G. (2016). Regional ventilation and aerosol deposition with helium-oxygen in bronchoconstricted asthmatic lungs. *Journal of aerosol medicine and pulmonary drug delivery*, *29*(3), 260-272.

[8]. Sandeau, J., Katz, I., Fodil, R., Louis, B., Apiou-Sbirlea, G., Caillibotte, G., & Isabey, D. (2010). CFD simulation of particle deposition in a reconstructed human oral extrathoracic airway for air and helium–oxygen mixtures. *Journal of aerosol science*, *41*(3), 281-294.

[9]. Darquenne, C., & Prisk, G. K. (2004). Aerosol deposition in the human respiratory tract breathing air and 80: 20 heliox.*Journal of aerosol medicine*, *17*(3), 278-285.

[10]. Rahimi-Gorji, M., Gorji, T. B., & Gorji-Bandpy, M. (2016). Details of regional particle deposition and airflow structures in a realistic 6tmodel of human tracheobronchial airways: two-phase flow simulation. *Computers in biology and medicine*,*74*, 1-17.

[11]. Farkas, Á., Balásházy, I., & Szőcs, K. (2006). Characterization of regional and local deposition of inhaled aerosol drugs in the respiratory system by computational fluid and particle dynamics methods. *Journal of Aerosol Medicine*,*19*(3), 329-343.

[12]. Russo, J., Robinson, R., & Oldham, M. J. (2008). Effects of cartilage rings on airflow and particle deposition in the trachea and main bronchi. *Medical engineering & physics*, *30*(5), 581-589.

[13]. Horsfield, K., & Cumming, G. (1968). Morphology of the bronchial tree in man. *Journal of applied physiology*, *24*(3), 373-383.

[14]. Kleinstreuer, C., Zhang, Z., & Li, Z. (2008). Modeling airflow and particle transport/deposition in pulmonary airways. *Respiratory physiology & neurobiology*, *163*(1-3), 128-138.

[15]. Liu, Y., So, R. M. C., & Zhang, C. H. (2003). Modeling the bifurcating flow in an asymmetric human lung airway. *Journal of biomechanics*, *36*(7), 951-959.

[16]. Comer, J. K., Kleinstreuer, C., Hyun, S., & Kim, C. S. (1999). Aerosol transport and deposition in sequentially bifurcating airways. *J. Biomech. Eng.*, *122*(2), 152-158.

[17]. Kim, C. S., & Fisher, D. M. (1999). Deposition characteristics of aerosol particles in sequentially bifurcating airway models. *Aerosol Science & Technology*, *31*(2-3), 198-220.

[18]. Islam, M. S., Saha, S. C., Sauret, E., Gu, Y. T., & Molla, M. M. (2017, June). Numerical investigation of diesel exhaust particle transport and

deposition in the CT-scan based lung airway. In *AIP Conference Proceedings* (Vol. 1851, No. 1, p. 020092). AIP Publishing.

[19]. Islam, M. S., Saha, S. C., Sauret, E., Gemci, T., Yang, I. A., & Gu, Y. T. (2017). Ultrafine particle transport and deposition in a large scale 17-generation lung model. *Journal of biomechanics*, *64*, 16-25.

[20]. Islam, M. S., Saha, S. C., Gemci, T., Yang, I. A., Sauret, E., & Gu, Y. T. (2018). Polydisperse microparticle transport and deposition to the terminal bronchioles in a heterogeneous vasculature tree. *Scientific reports*, *8*(1), 16387.

[21]. Islam, M. S., Saha, S. C., Gemci, T., Yang, I. A., Sauret, E., Ristovski, Z., & Gu, Y. T. (2019). euler-Lagrange prediction of Diesel-exhaust polydisperse particle transport and Deposition in Lung: Anatomy and turbulence Effects. *Scientific reports*, *9*(1), 1-16.

[22]. Islam, M. S., Saha, S. C., Sauret, E., Gu, Y. T., & Molla, M. M. (2017, June). Numerical investigation of diesel exhaust particle transport and deposition in the CT-scan based lung airway. In *AIP Conference Proceedings* (Vol. 1851, No. 1, p. 020092). AIP Publishing.

[23]. Islam, M. S., Saha, S. C., Sauret, E., Gemci, T., & Gu, Y. (2017). Pulmonary aerosol transport and deposition analysis in upper 17 generations of the human respiratory tract. *Journal of Aerosol Science*, *108*, 29-43.

[24]. Islam, M. S., Saha, S. C., Sauret, E., Gu, Y., & Ristovski, Z. (2015, July). Numerical investigation of aerosol particle transport and deposition in realistic lung airway. In *Proceedings of the International Conference on Computational Methods* (Vol. 2). Scientech Publisher llc, USA.

Fatigue Life Analysis of Coronary Stents

Joseph A. Iaconis *
School of Computing, Engineering, and Mathematics
Western Sydney University
Penrith, NSW, 2751, Australia
17725819@student.westernsydney.edu.au

Nai Chun Liu
School of Aerospace, Mechanical and Mechatronic Engineering
The University of Sydney, Sydney,
NSW 2006, Australia
nliu2523@uni.sydney.edu.au

Zhongpu Zhang
School of Computing, Engineering, and Mathematics
Western Sydney University
Penrith, NSW, 2751, Australia
leo.zhang@westernsydney.edu.au

***Abstract*—Cardiovascular diseases are a leading cause of death in developed countries due to lifestyle factors and an ageing population. Cardiovascular stents are commonly used for unblocking coronary arteries occluded by the presence of plaque. Despite their immediate success, the ongoing biomechanical performance of stents is a major concern, and the chance of restenosis remains high due to numerous factors such as stent material selection, plaque geometry, stent placement, and many more. In this project, finite element analysis will be used to analyse the peak stress of stent structures and evaluate fatigue life according to the Goodman criteria. A series of design variables are considered here by including stent geometrical parameters, changes in stent material properties during manufacturing, and variations in both geometries and constituents for atherosclerotic plaque. The optimal stent structure would be manufactured by using a metal-based additive manufacturing technology system.**

Keywords—coronary stents, cardiovascular disease, finite element analysis

I. Introduction

Coronary Heart Disease

Coronary heart disease is the most common cause of death in the modern world, causing approximately 9 million deaths and 16% of all deaths in 2017. It is caused by chronic internal build-up of plaque in blood vessels, a condition called atherosclerosis. This results in narrowed vessels, which is called stenosis. Eventually, vessels can block, causing heart attacks and death. There is a non-surgical option to reduce the risk of heart attacks, called percutaneous coronary intervention. This involves inserting a balloon catheter with a stent crimped around it into the blocked vessel and expanding it by inflating the balloon. The balloon is removed, and the stent stays inside the vessel.

Stenting and Restenosis

Stenting was widely accepted in medicine in the 1990s, and the use of stents in interventional medical procedures increased from just 10% in 1994 to more than 80% in 2008 (Lim et al. 2008). Clinical success of the procedure is generally high; however, 20-30% of patients experience restenosis over 6-12 months following implantation (O'Brien and Carroll 2009). Restenosis is the regrowth of vessel tissue in the stent area due to tissue inflammation and mechanical fatigue or failure of the stent. An example of this is seen in Figure 1, where stent factures are present three months after implantation (Schievano et al. 2010). Variables influencing stent performance include geometry, placement, balloon folding, plaque geometry and topography of the vessel (Lim et al. 2008).

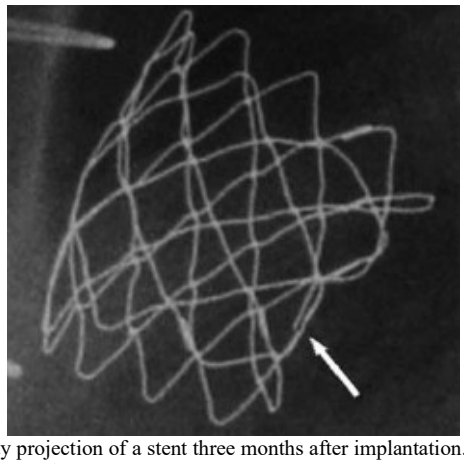

Fig. 1. X-ray projection of a stent three months after implantation. Arrow points to fracture location.

Other mechanical faults leading to restenosis are recoiling, foreshortening and dogboning. Recoiling is when the stent does not stay fully expanded after balloon deflation, foreshortening is a reduction in length of the stent during expansion and dogboning is the overexpansion of stent ends relative to the middle.

After implantation, stents undergo cyclic loading and are thus subject to fatigue stress. There is the tensile stress of expansion as well as the compressive and tensile stresses of vessels and blood flow. This repeated load could lead to fatigue fractures, so using design principles for cyclic loading would be intuitive for optimising stent performance. The recommended failure prediction method for ductile materials undergoing fluctuating stress is the Goodman method, and for ductile materials under dynamic loading with some uncertainty about loads, environment or material properties, the recommended design factor N is 2.5 to 4.0 (Mott 2004).

Computational Methods

Recent decades have seen the development of computational methods such as finite element analysis (FEA), capable of modelling vascular and stent geometry to further understand the factors influencing stent performance and how to improve it. Using FEA, stresses experienced by stents can be located and quantified, meaning stents can be compared quickly and easily without patient participation. This allows researchers to determine how stents can be made to last longer without the need for further treatment. Figure 2 shows an example of this.

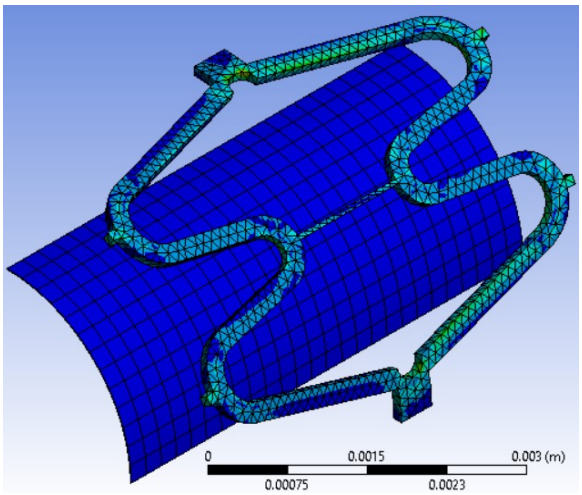

Fig. 2. FEA on a stent using ANSYS Workbench.

Stent Materials and Geometry

The stent material must have favourable mechanical properties, haemocompatibility, biocompatibility and drug-delivery ability (Mani et al. 2007). Early stents were made from bare metal, usually stainless steel, which tended to cause thrombosis or hyperplasia (Jorge and Dubois 2015). In more recent years, cobalt-chromium and platinum-chromium stents have outperformed steel by matching or exceeding its strength with thinner struts allowing for higher flexibility (Marrey et al. 2006, Jorge and Dubois 2015). To reduce restenosis, drug-eluting stents (DES) were introduced in the early 2000s, which release anti-proliferative drugs to inhibit hyperplasia. To facilitate gradual release of drugs, they have a polymer coating; however, stent thrombosis was still observed in patients after several years. This was attributed to inflammation induced by those polymers. Since then, DES have been revised constantly to prevent thrombosis by testing different drugs and more biocompatible polymers. Despite marked improvements, there is a research gap in this area, as stent thrombosis is yet to be eliminated.

Geometry can also influence performance and restenosis. Lim et al. (2008) created FE models of seven commercially available stents as well as a balloon. Their results showed differences of approximately 13% in foreshortening and 45% in dogboning. However, there were limitations to this study as plaque geometry, vessel topography and blood flow were not considered. This presents a research gap, as simulations involving vessel topography and blood flow are highly complex and not well-documented.

Roy and Chanda (2014) also modelled several commercially available stents, testing for optimal geometry and eight materials. They performed simulations focusing on strut connectors of each stent as that is the most highly stressed area. They concluded that all tested stents and materials were within the performance requirements, so further testing and analysis would be required to find the optimal material or design. However, there exists a limitation in this study as only a small section of each stent was evaluated.

The Arterial Layer

Numerous authors added an arterial layer to simulations (Owen et al. 2018, Gervaso et al. 2008, Holzapfel, Gasser and Stadler 2002). Many authors estimated or assumed arterial material properties and used hyperelastic material models such as Neo-Hookean, Mooney-Rivlin and Yeoh. Hyperelastic materials are classed as perfectly elastic for defined deformations, and their behaviour can be represented by a strain energy density function (Muhr 2005). Their behaviour is classed as anisotropic, as their stress-strain characteristics are non-linear in the elastic region. The presence of plaque decreases blood supply to the lumen, which is the interior of the vessel, resulting in thickening and stiffening of the vessel wall (Karimi et al. 2013, Claridge et al. 2009, David Chua et al. 2004, Chatzizisis and Giannoglou 2007). This changes the material properties of the arterial wall, as well as blood flow characteristics, both of which may influence stent performance (Karimi et al. 2013). Karimi et al. (2013) also found that healthy arteries have physiological and maximum elastic moduli 2.53 and 2.91 times higher than atherosclerotic arteries respectively, but age of the artery has no effect. There is a research gap in this area, as to the author's knowledge, there is no complete study showing true mechanical properties of human coronary arterial tissue.

II. Materials and Methods (Preliminary)

Stent Model

The author was given a stent model by their institution which was used in the preliminary study. It was created in SolidWorks and imported into ANSYS 19.1 for FEA. The material selected was structural steel. The model is shown in Figure 3.

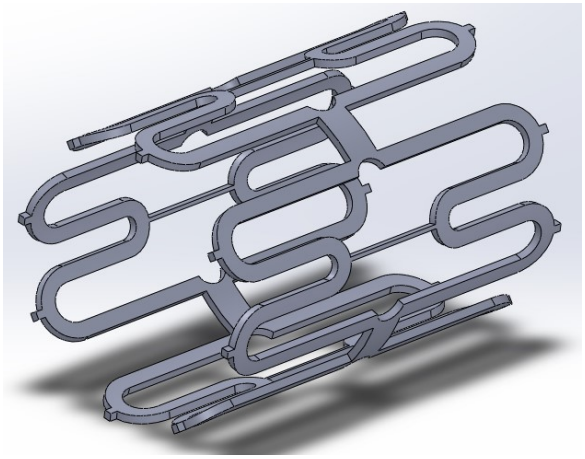
Fig. 3: Stent finite element model.

Table 1 shows a summary of the material properties for the stent in this study. To reduce computational time, a quarter-model was used.

Table 1: Material properties for structural steel.

Material	Young's Modulus (GPa)	Poisson's Ratio
Structural steel	200	0.3

Balloon Model

The balloon model was modelled as a cylinder made from an isotropic elastic material with a wall thickness of 0.01mm. Details are shown in Table 2.

Table 2: Material properties for balloon model.

Material	Young's Modulus (GPa)	Poisson's' Ratio
Balloon	0.9	0.3

Arterial/Plaque Layer Models

The arterial layer was considered to maximise realism of the study. Linear elasticity would be the simplest and easiest way to model the tissue, however it would only be accurate for very small strains (Owen et al. 2018). Human arterial tissue is anisotropic, so Young's Modulus cannot apply for the purposes of this study (Hug et al. 2015, Owen et al. 2018). Despite it being anisotropic, the literature shows that human arterial tissue is generally modelled as an isotropic, hyperelastic, incompressible material (Owen et al. 2018, Gervaso et al. 2008, Holzapfel, Gasser and Stadler 2002). This is to simplify studies, as stent performance is the focus (Owen et al. 2018). Unfortunately, the author was unable to replicate parameters used in those studies due to software limitations. Several trials were conducted using a sample hyperelastic material in the ANSYS material database, but the author was unable to complete a simulation including an arterial layer. Thus, in the interest of time, the arterial and plaque models were omitted from the study.

III. Preliminary Results

Parametric Analysis

There were four parameters in the stent model which could be altered, shown in Figure 4. Upper and lower limits of each parameter are shown in Table 3. Each permutation was numbered from 01 to 16 and the parameters of each are shown in Table 4.

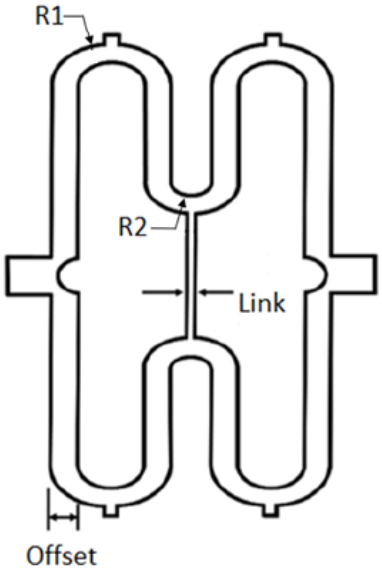

Fig. 4. Diagram of quarter-stent showing locations of each parameter.

Table 3: Upper and lower limits for each parameter.

Parameter	Lower Limit (mm)	Upper Limit (mm)
R1	0.4	0.5
R2	0.1125	0.15
Link	0.05	0.15
Offset	0.05	0.2

Table 4: Parameters used for each preliminary simulation.

	R1 (mm)	R2 (mm)	Link (mm)	Offset (mm)
01	0.4	0.1125	0.05	0.05
02	0.4	0.1125	0.05	0.2
03	0.4	0.1125	0.15	0.05
04	0.4	0.1125	0.15	0.2
05	0.4	0.15	0.05	0.05
06	0.4	0.15	0.05	0.2
07	0.4	0.15	0.15	0.05
08	0.4	0.15	0.15	0.2
09	0.5	0.1125	0.05	0.05
10	0.5	0.1125	0.05	0.2
11	0.5	0.1125	0.15	0.05
12	0.5	0.1125	0.15	0.2
13	0.5	0.15	0.05	0.05
14	0.5	0.15	0.05	0.2
15	0.5	0.15	0.15	0.05
16	0.5	0.15	0.15	0.2

Results from simulations were tabulated and graphed (Table 5 and Figure 5 respectively), and the performance of each was assessed on its maximum stress. In reality, the stent would have to withstand the stress of expansion, as well as the cyclic loading of blood flow. The average person's heart beats approximately 75 times per minute (Marieb, Mallatt and Wilhelm 2010), which is 108,000 beats per day. Over ten years, that equates to approximately $4_{x10}{}^{8}$ loading cycles. As a result, the stent design with the lowest maximum stress would be favourable. The ultimate tensile stress of structural steel in ANSYS is 515 MPa, so each stent was assessed on a pass/fail criterion based on the maximum stress it experienced. Since all sixteen iterations were under the required stress value of 515 MPa, the author decided to assess these simulations based on a design factor N of 3.25, which is in the middle of the suggested range for ductile materials subject to dynamic loads mentioned earlier (Mott 2004). Therefore, based on the following equation:

$$\sigma_a = \frac{\sigma_u}{N}$$

Where σ_a is the allowable stress in the material, σ_u is the ultimate stress of the material, and N is the design factor, the allowable stress for each stent was calculated as 158.46 MPa. Therefore, each iteration was given a pass/fail rating based on this value.

Using this criterion, eight simulations passed. The lowest stress was experienced in trial 13 (101.55 MPa), and the highest stress was experienced in trial 3 (273.46 MPa). This is a difference of approximately 270%.

Table 5: Maximum stress and pass/fail result in the preliminary study.

Trial	Max. stress (MPa)	Pass/Fail
01	237.79	Fail
02	160.66	Fail
03	273.46	Fail
04	195.57	Fail
05	111.67	Pass
06	163.72	Fail
07	126.82	Pass
08	145.12	Pass
09	115.84	Pass
10	164.05	Fail
11	115.24	Pass
12	166.57	Fail
13	101.55	Pass
14	163.18	Fail
15	121.05	Pass
16	153.12	Pass

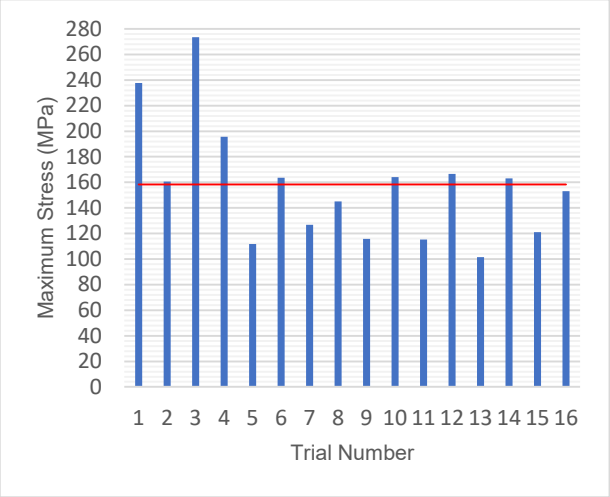

Fig. 5. Graphed results of preliminary study with critical stress value shown in red.

IV. Preliminary Discussion

Trial 13 showed the lowest maximum stress, but several other trials fell well below σ_a (5, 7, 9, 11 and 15). These trials shared an offset value of 0.05mm, meaning the struts were significantly thinner than stents with an offset of 0.15mm. There were two large outliers in the study, namely trials 1 and 3. Both had an offset of 0.05mm as with the well performing trial 13. However, they showed the second highest and highest maximum stresses with values of 237.79 MPa and 273.46 MPa respectively. Between each section of the stent is a scalloped connecting portion shown in Figure 6. The rounded part of the connecting portion is quite shallow in trial 13, whereas in trials 1 and 3, it was much more pronounced. This caused stents 1 and 3 to have extremely thin connecting portions which resulted in high stress concentrations in this area.

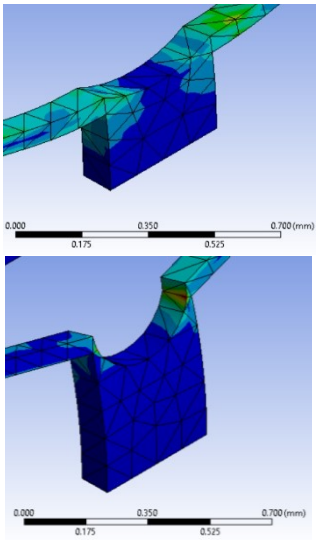

Fig. 6. Connecting portions and stress concentrations of trials 13 (top) and 3 (bottom).

The maximum stress in this area for trial 13 was approximately 60 MPa, a value more than four times smaller than that of trial 3. The location of maximum stress in trial 13 was at the centre of each section of the stent where the link joins to the main body. This was also true for the other well performing stents. The reason for the large depth of the rounded area in the connecting portions of trials 1 and 3 may have been because minimum vales for R1 and R2 parameters were used in these trials, whereas in all of the well performing stents, one or both of those parameters were set at the maximum value. Thus, it is likely that minimum values for both R1 and R2 combined with the 0.05mm offset parameter caused the rounded section to increase in depth. It was somewhat difficult to compare the locations of maximum stress with the literature, as to the author's knowledge, the stent used in this study is not a commercial stent, nevertheless, there were some similarities. The stents in this study experienced maximum stress at the intersection of different segments or the intersection between the thin link and the main body of each segment. Similarly, other authors found the locations of high stress to be at intersections between segments or sharp corners. As mentioned in earlier sections, stents with thinner geometry often perform better than those with relatively thicker struts as they allow for more flexibility (Marrey et al. 2006, Jorge and Dubois 2015). This is consistent with the results from this study. Based on results from this study and from the literature, it seems that thinner elements and smooth corners work well in reducing stress concentration. Trials where the offset was set as 0.2mm did not generally perform as well as those where 0.05mm was used. These stents all had wider struts, meaning a larger force was required to expand them, which is the likely reason a higher maximum stress was experienced in each. Of these trials where a 0.2mm offset was used, trial 4 was an outlier with a maximum stress of 195.57 MPa, an increase of approximately 23% over the average from the other trials using the 0.2mm offset of 159.49 MPa. Similar to the situation above, trial 4 was the only one of the 0.2mm offset trials having minimum values for both R1 and R2, whereas the other trials had one or both of these parameters at the maximum value. Besides trial 4, the other trials with the 0.2mm offset showed no significant difference between one another.

Unfortunately, there were several limitations to the preliminary study. Time and lack of knowledge in FEA software were the two largest contributors, but others included the fact that only one stent geometry and material were used in all simulations. Also, the fact that the balloon expansion was displacement driven rather than pressure driven prevented simulation of real-life phenomena such as dogboning. The student version of ANSYS was used, meaning full functionality was not available and a full model could not be used. Lastly, the Goodman method was not used to find the required safety factor in the interest of time. Before the end of the teaching session, the author will attempt to fin the maximum and minimum alternating stresses so the Goodman equation can be satisfied.

V. Materials and Methods (Secondary)

The secondary part of this study tests the effect of geometry on stent performance. Ten geometries were created in Solidworks and the same simulation with the same conditions as above was performed. The same pass/fail criterion was also used to assess each. The stents were named G1-G10 and their CAD models are shown in Figure 7.

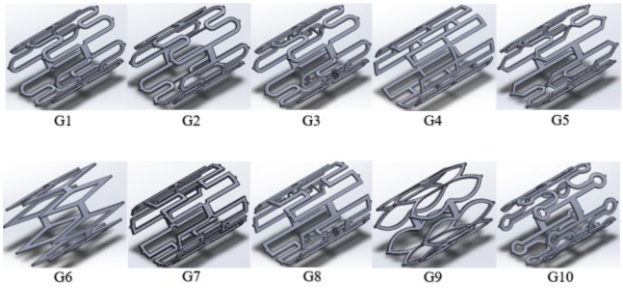

Fig. 7. Stents G1-G10 used in secondary study.

VI. Secondary Results

Results are shown in Table 6 and Figure 8.

Table 6: Maximum stress and pass/fail result in secondary study.

Trial	Max. stress (MPa)	Pass/Fail
G1	142.74	Pass
G2	156.5	Pass
G3	226.26	Fail
G4	244.60	Fail
G5	169.18	Fail
G6	243.22	Fail
G7	197.44	Fail
G8	150.72	Pass
G9	180.54	Fail
G10	139.62	Pass

Stents G1, G2, G8 and G10 achieved a pass and all other stents failed.

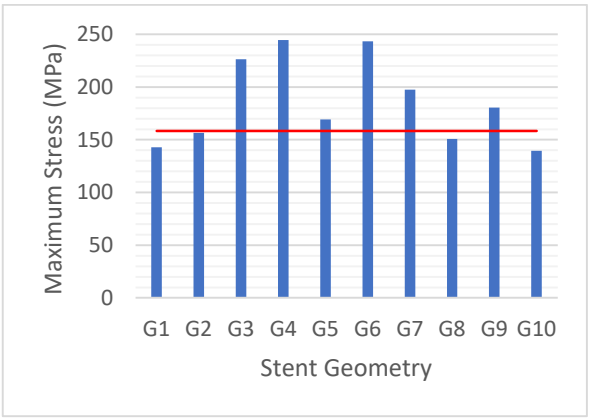

Fig. 8. Graphed results of secondary study with critical stress shown in red.

VII. Secondary Discussion

G1 was the model originally given to the author with no modifications. It passed with a maximum stress of 142.74 MPa. G2 and G3 were altered versions of G1and in both cases, performance was reduced. They achieved results of 156.5 MPa (pass) and 226.26 MPa (fail) respectively. The small difference between G1 and G2 was the removal of the rounded area shown in Figure 6 above. This resulted in an increase of approximately 10% in maximum stress, most likely due to the resulting wider connecting portion needing greater force for expansion. The small difference in G3 was the small link in the centre of the stent. It was changed from a straight linkage to one resembling a sine wave. This comparison is shown in Figure 9.

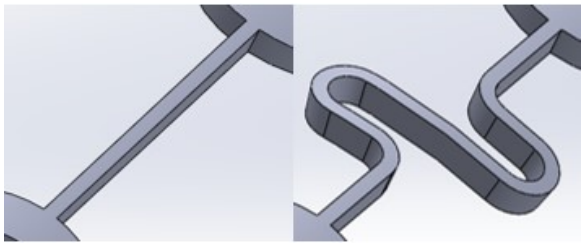
Fig. 9. Comparison of links in G1 (left) and G3 (right).

G3 failed drastically, with an increase of approximately 43% from the allowable stress of 158.46 MPa. The ANSYS results file makes it clear why this was the case. Shown in Figure 10, upon expansion the stent moved inwards, causing the link to fold on itself.

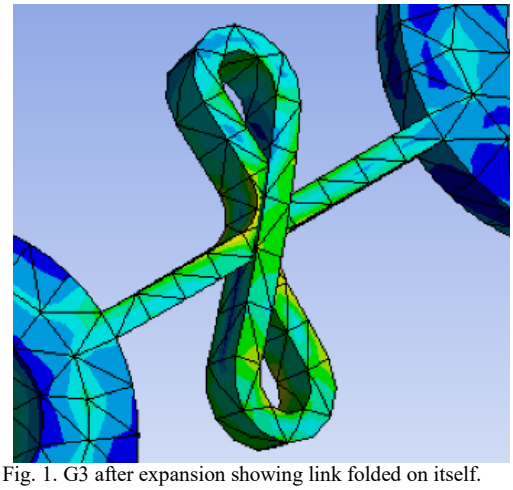
Fig. 1. G3 after expansion showing link folded on itself.

A similar situation was evident for G4, where the free ends of the stent collided (Figure 11), and its result of 244.6 MPa was approximately 54% above the critical stress value.

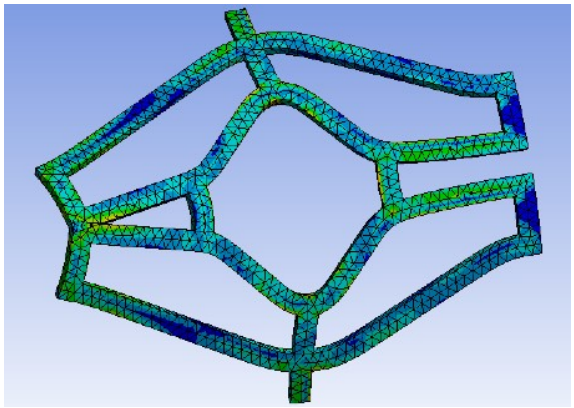
Fig. 2. G4 after expansion, showing free ends colliding.

When each simulation was set up in ANSYS, frictionless supports were placed on either side and one end of each stent (Figure 12) to represent all four quarters as well as extended length, while one end was left free as it would be in reality.

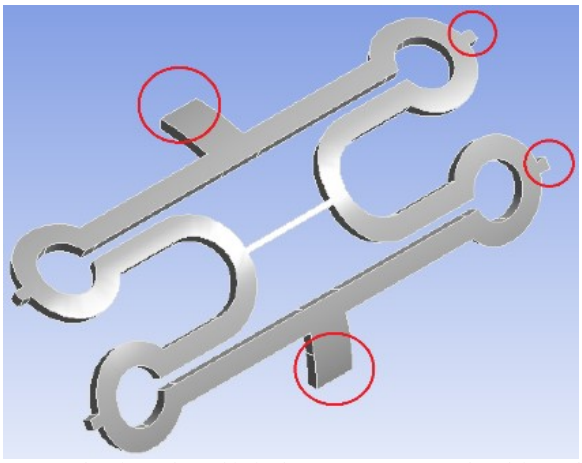

Fig. 3. G10 showing where frictionless supports were placed in each model.

As mentioned earlier, expansion was displacement driven rather than pressure driven, so this may have also contributed to these results, as a real stent has the middle expanded before the ends, which would prevent the above situations. Design flaws could also be a reason for the above results, as some designs performed quite well in comparison. If the author had more time and expertise with CAD software, commercial designs could have been replicated and tested, however novel designs were used to save time and gain a basic understanding of how geometry affects performance. G6, G7 and G9 also failed, showing similar results to G3 and G4 above.

G8 and G10 also received passes, falling approximately 5% and 12% below critical stress respectively. G8 was a combination of the designs in G7 and G3, both of which failed severely, but when combined they performed relatively well. This was somewhat of an anomaly, as G8 had none of the curved edges which allowed other stents to perform well. G10 was a novel design by the author, keeping in mind that curved geometries generally perform better. As the best performing geometry, it will be used by the author for future studies where different materials or another parametric analysis is performed. The author strongly believes a parametric study would yield yet more positive results based on the improvements seen in the preliminary study. If time permits before the close of the teaching session, another parametric study with G10 will be performed, as well as a comparison of different materials.

The major limitation in the secondary study was again time, as some simulations needed to be done on computers from the author's institution to utilise full functionality of ANSYS, and on those computers, simulations took up to one hour. This combined with other commitments meant there was less time than ideal to complete simulations. Even so, the author is pleased with their progress. With extra time and expertise, the author would perform the secondary study and a parametric analysis with commercial stents to optimise them, as well as test different materials.

VIII. Conclusions

In this study, a parametric analysis and geometric comparisons were performed on a stent model given to the author and several novel designs, and a critical stress value of 158.46 MPa was calculated to assess whether stents would likely perform well inside a real patient. Results from the preliminary parametric study showed stent performance can be greatly altered by changing strut thickness without changing overall geometry. It was found that thinner struts generally yielded lower stress values. Results from the secondary study showed stent performance could be greatly altered by changing geometry. It was found that stents with curved geometries and smooth corners generally performed better. With more time, the author would perform a third study investigating the effects of changing stent materials, as well as using the Goodman method to assess stent performance.

References

Chatzizisis, YS & Giannoglou, GD 2007, 'Coronary hemodynamics and atherosclerotic wall stiffness: A vicious cycle', Medical Hypotheses, vol. 69, no. 2, pp. 349-55, viewed 17 May 2019, Elsevier, DOI 10.1016/j.mehy.2006.11.053.

Claridge, MW, Bate, GR, Hoskins, PR, Adam, DJ, Bradbury, AW & Wilmink, AB 2009, 'Measurement of arterial stiffness in subjects with vascular disease: Are vessel wall changes more sensitive than increase in intima-media thickness?', Atherosclerosis, vol. 205, no. 2, pp. 477-80, viewed 17 May 2019, Elsevier, DOI 10.1016/j.atherosclerosis.2008.12.030.

David Chua, SN, MacDonald, BJ & Hashimi, MSJ 2004, 'Finite element simulation of slotted tube (stent) with the presence of plaque and artery by balloon expansion', Journal of Materials Processing Technology, vol. 155-56, Proceedings of the International Conference on Advances in Materials and Processing Technologies: Part 2, viewed 17 May 2019, Elsevier, DOI 10.1016/j.jmatprotec.2004.04.396.

Gervaso, F, Capelli, C, Petrini, L, Lattanzio, S, Di Virgilio, L & Migliavacca, F 2008, 'On the effects of different strategies in modelling balloon-expandable stenting by means of finite element method, Journal of Biomechanics, vol. 41, no. 6, pp. 1206-12, viewed 19 April 2019, Elsevier, DOI 10.1016/j.jbiomech.2008.01.027.\

Holzapfel, GA, Gasser, TC & Stadler, M 2002, 'A structural model for the viscoelastic behaviour of arterial walls: Continuum formation and finite element analysis', European Journal of Mechanics A/Solids, vol. 21, no. 3, pp. 441-63, viewed 19 April 2019, Elsevier, DOI 10.1016/S0997-7538(01)01206-2.

Hug, F, Tucker, K, Gennisson, J, Tanter, M & Nordez, A 2015, 'Elastography for muscle biomechanics: Toward the estimation of individual muscle force', Exercise and Sport Sciences Reviews, vol. 43, no. 3, pp. 125-33, viewed 13 September 2018, Ovid, DOI 10.1249/JES.0000000000000049.

Jorge, C & Dubois, C 2015, 'Clinical utility of platinum chromium bare-metal stents in coronary heart disease', Medical Devices – Evidence and Research, vol. 8, pp. 359-67, viewed 30 March 2019, Pubmed, DOI 10.2147/MDER.S69415.

Karimi, A, Navidbakhsh, M, Shojaei, A & Faghihi, S 2013, 'Measurement of the uniaxial mechanical properties of healthy and atherosclerotic human coronary arteries', Materials Science & Engineering C – Materials for Biological Applications, vol. 33, no. 5, pp. 2550-54, viewed 9 May 2019, Elsevier, DOI 10.1016/j.msec.2013.02.016.

Lim, DY, Cho, SK, Park, WP, Kristensson, A, Ko, JY, Al-Hassani, STS & Kim, HS 2008, 'Suggestion of potential stent design parameters to reduce restenosis risk driven by foreshortening or dogboning due to non-uniform balloon-stent expansion', Annals of Biomedical Engineering, vol. 36, no. 7, pp. 1118-29, viewed 26 March 2019, Biomedical Engineering Society, DOI 10.1007/s10439-008-9504-1.

Mani, G, Feldman, MD, Patel, D & Agrawal, CM 2007, 'Coronary stents: A materials perspective', Biomaterials, vol. 28, no. 9, pp. 1689-1710, viewed 26 March 2019, Elsevier, DOI 10.1016/j.biomaterials.2006.11.042.

Marrey, RV, Burgermeister, R, Grishaber, RB & Ritchie, RO 2006, 'Fatigue and life prediction for cobalt-chromium stents: A fracture mechanics analysis', Biomaterials, vol. 27, no. 9, pp. 1988-2000, viewed 23 March 2019, Elsevier, DOI 10.1016/j.biomaterials.2005.10.012.

Mott, RL 2004, Machine Elements in Mechanical Design, 4th edn, Prentice Hall.

Muhr, AH 2005, 'Modelling the stress-strain behaviour of rubber, Rubber Chemistry and Technology, vol. 78, no. 3, pp. 391-425, viewed 9 May 2019, ProQuest, DOI 10.5254/1.3547890.

O'Brien, B & Carroll, W 2009, 'The evolution of cardiovascular stent materials and surfaces in response to clinical drivers: A review', Acta Biomaterialia, vol. 5, no. 4, pp. 945-58, viewed 25 March 2019, Elsevier, DOI 10.1016/j.actbio.2008.11.012.

Owen, B, Bojdo, N, Jivkov, A, Keavney, B & Revell, A 2018, 'Structural modelling of the cardiovascular system', Biomechanics and Modelling in Mechanobiology, vol. 17, no. 5, pp. 1217-42, viewed 19 April 2019, Springer, DOI 10.1007/s10237-018-1024-9.

Schievano, S, Taylor, AM, Capelli, C, Lurz, P, Nordmeyer, J, Migliavacca, F & Bonhoeffer, P 2010, 'Patient specific finite element analysis results in more accurate prediction of stent fractures: Application to percutaneous pulmonary valve implantation', Journal of Biomechanics, vol. 43, no. 4, pp. 687-93, viewed 23 March 2019, Elsevier, DOI 10.1016/j.jbiomech.2009.10.024.

Structural Optimisation of Porous Bone Tissue Scaffolds for Femur Fracture Treatment

Puchen Li
School of Computing, Engineering and Mathematics, Western Sydney University, Penrith, NSW 2751, Australia
19923765@student.westernsydney.edu.au

Zhongpu Zhang
School of Computing, Engineering and Mathematics, Western Sydney University, Penrith, NSW 2751, Australia
leo.zhang@westernsydney.edu.au

Chunhui Yang
School of Computing, Engineering and Mathematics, Western Sydney University, Penrith, NSW 2751, Australia
r.yang@westernsydney.edu.au

***Abstract* - With the advances of tissue engineering techniques, bone tissue scaffolds become one of primary projects in today's medical systems. Currently, the fixation plate for the bone tissue scaffolding treatment is one of the essential parts for femur treatments used for several femur diseases, such as femur fracture, arthritis, osteoporosis, infections, and cancer. According to literature, there are many scaffolds designed by using different structures and variant porosities. Thus these scaffolds have quite different mechanical performances.**

This research aims to numerically conduct an optimal design process to obtain a specific type of structure and porosity for the bone tissue scaffolds with expected mechanical performance. In this CAD, FEA and CFD-based optimisation process, main design parameters of the bone tissue scaffold including the porosity are set as design variables and its effective Young's modulus and permeability are set as design objectives, as part of its mechanical performance. CAD models of the scaffold are firstly built by using SolidWorks, and finite element analyses (FEA) are performed for determining the effective Young's modulus. Then the Computational Fluid Dynamics (CFD) analysis is devised to simulate fluid flow field and determine the permeability of the scaffold. Based on these numerical results, multi-objective optimisation processes are conducted to extract optimal values. For validation, the assembly of a femur fixation plate and a porous bone tissue scaffold with a porosity of 52% in a square structure is analysed by using FEA to evaluate its mechanical performance.

Keywords – Bone tissue scaffold; Porosity, Effective Young's modulus; Permeability; Multi-objective optimisation; Finite element analysis

I. INTRODUCTION

In orthopaedics, there are around 206-208 individual bones in adults. The femur bone is the most important bone in the human body. The protection and support of body organs are the central role of bones and are widely studied in ontology research [1]. However, due to unhealthy eating habits and their causes, patients with bone injuries increase exponentially, especially in the case of femoral fractures. When a femoral fracture occurs, the lower extremity cannot move. Furthermore, the division is characterised by severe swelling and pain, as well as distortion or angle, sometimes shortening the length of the lower limbs. Because the femur is the most prominent bone in the body, if it is not treated in time, it can lead to much severe complications such as bleeding and nerve damage [2]. Therefore, the appropriate selection of treatment methods is of great significance.

In recent decades, bone tissue scaffolds attracted a lot of attention in medical research fields, especially in orthopaedic surgery. According to the development of tissue engineering, bone scaffolds can be used as an assistant in the rehabilitation process [3]. Due to the structural and mechanical properties of the scaffold, it is critical to determine the structure, size, and morphology of regenerated tissues, which serve as a framework for joining cells and tissues to guide the increase of the fabrics into a particular morphology. Moreover, as a carrier signal molecule, it is transported to the defect site, and as a slow release inducing factor provides a space for the slow functioning of the engineered tissues to guide the whole group, including nerve, bone, for the angiogenesis and growth. Also, it contains nutrients for cell growth and eliminates wastes due to tissue propagation, differentiation, and metabolism [4].

Besides, the specific location on the scaffolds faces a particular response to the tissues, identifying and selecting adhesion to different cell types. Furthermore, as a mechanical support, they resist external pressure and maintain the original shape and tissue integrity of the tissue. The scaffold material can be used as a conveyor with active factors, which can be used to carry some biologically active substances. As a growth factor, it provides nutrition for cell growth, differentiation, and proliferation. According to the characteristics of tissue engineering, the biodegradation and non-toxicity of bone scaffolds must be considered. Also, due to the nature of the bone, which can support and protect the internal properties of the organ, the mechanical and physical properties of the scaffolds are further considered. Moreover, the surface roughness is also an important factor affecting the growth reactor during tissue culture [5]. Therefore, data obtained through numerical modelling and simulations can help researchers conduct an optimisation on scaffold structure, which is becoming a commonly-used practice in the field of tissue engineering.

This present study focuses on the optimal design of femur scaffolds to evaluate the most suitable design structure with a particular material used. A systematic

optimal design approach is developed, which combines CAD, FEA, CFD and multi-objective optimisation altogether. The proposed optimal design procedure can be divided into several design phases step by step to determine the most suitable scaffold structure, identify the most suitable scaffold porosity, and develop the finite element analysis for the assembly of the femur scaffold and the femur fixation plate, respectively. As a study case, the porous bone tissue scaffold is optimally designed. Its effective Young's modulus and permeability are set as two main design variables. The effects of porous structure and porosity of the bone tissue scaffold on the effective Young's modulus and permeability are evaluated. The results prove that the structure and the porosity significantly affect the overall performance of the bone tissue scaffolds.

II. RESEARCH METHODOLOGY AND PROCEDURE

According to the proposed optimal design procedure, the research included three main components by using the porous bone tissue scaffold as the study case: a) identification of The research procedure will be introduced with three major parts, including determining the most suitable scaffold structure; b) determination of the most suitable porosity for the proposed bone tissue scaffold; and c) evaluation of the mechanical performance of the assembly of the proposed scaffold and femur fixation plate.

To achieve the modelling of the femur bone, ScanIP was used as the CAD tool to get the original model, and then it was modified and used to construct a femur fixation plate model by using the powerful CAD software package – SolidWorks. SolidWorks was also used to build the scaffold models and their inverse models, which were used for determining the effective Young's modulus of the designed scaffold by using the FEA package – Abaqus/CAE. Then these models were further employed to determine the permeability of the scaffold by using CFD via the engineering analysis package – ANSYS/Workbench CFX. In addition, Matlab and Excel were both utilised as the means to conduction the multi-objective optimisation to extract the optimised design parameters.

A. CAD Modelling and Design of Femur Scaffold

The CAD modelling of the femur scaffold was divided into two processes in sequence: a) the scanning and imaging process and b) the model design process, respectively. Firstly, the scanning and image process constructed the raw model of the femur bone according to the CT scans via using ScanIP, as shown in Fig. I. This femur model constructed in ScanIP was further imported into the SolidWorks to obtain the solid model.

Figure I. Femur bone model constructed by using ScanIP

This solid model contributed to design the models for the fixation plate and porous bone tissue scaffold. To develop the femur bone model. In order to properly place the scaffold into the femur, the femur bone model was cut in its middle part with a length of 50 mm, which is identical to the proposed porous bone tissue scaffold. The scaffold was designed to have a cylindrical shape with a diameter of 28 mm and a length of 50 mm too. The figure below shows the assembly of the scaffold model and the femur bone model.

As bone tissue scaffolds cooperate with the femur fixation plate, the fixation plate model was constructed on the modified femur bone model. The fixation plate model has seven components, including one cuboid plate with ten fixation holes and five screws, fixed on the side of the femur bone show as the figure below. There are six holes drilled on the femur bone model, one of them is used for the adjustment.

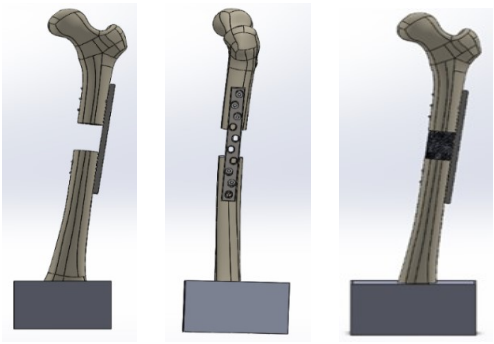

(a) Fixation plate model (b) Assembly model

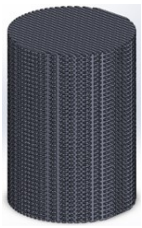

(c) Porous bone tissue scaffold model

Figure II CAD models of femur fixation plate, porous bone tissue scaffold and their assembly

The design of porous bone tissue scaffold is the most critical part which was divided into two section. Firstly, the bone tissue scaffolds were designed by considering three different internal structures with square, hexagon, and pore

shapes, respectively, as depicted in Figure III. Each type of the structure has three different bone tissue scaffold models with the same variations of the porosity, for example, 60%, 70%, and 80%, respectively, as shown in Figure IV. The designed bone tissue scaffolds were used to determine which one are the most suitable porous structure for the bone tissue scaffold.

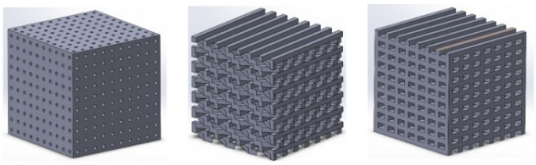

Figure III Different structures of the porous bone tissue scaffolds

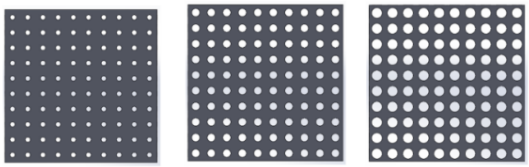

Figure IV Pore structure scaffolds with different porosities

Secondly the selected scaffold structure for the designed bone tissue scaffold was employed to determine the most suitable porosity by varying the porosity from 10%, 15%, 20% up to 90%. In total 17 models were run and tested. Finite element analyses were conducted to determine the effective Young's modulus by conducting a compression test digitally with Abaqus/CAE as shown in Fig. V.

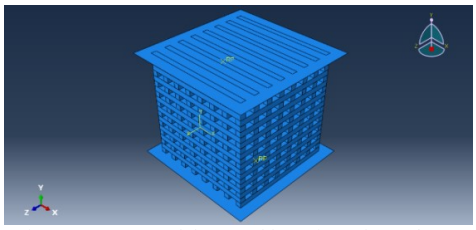

Figure V FEA Model created by using Abaqus/CAE

In order to determine the permeability of the porous bone tissue scaffold, its inverse models were created with additional channels for facilitating directional flows and CFD analyses were conducted by using ANSYS/Workbench CFX module

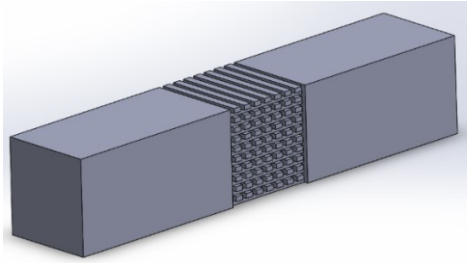

Figure VI Inverse model used for CFD with ANSYS/Workbench CFX.

Based on the numerical results obtained from FEA and CFD as well as conducting a multi-objective optimisation process, the porous bone tissue scaffold can be optimally designed as the final outcome.

B. FEA and CFD Simulations of Porous Bone Tissue Scaffold

The simulation section is the most critical section in this research which can be divided into three partsFEA and CFD simulations were used for determining the most suitable internal structure and the most suitable porosity for the proposed bone tissue scaffold. Also FEA of the standard compression test was employed to analyse the overall performance of the assembly of the designed scaffold and a femur fixation plate model. In order to determine the most suitable structure for the bone tissue scaffold, the effective Young's modulus and the permeability of the scaffold models were chosen as the design objectives, which can be determined by using FEA and CFD, respectively.

In FEA, the effective Young's modulus can be determined with Eq. (1).

$$E = \frac{Stress}{Strain} = \frac{\frac{Force}{Contacted\ Area}}{\frac{Displacement}{Original\ Leight}} \quad (1)$$

In the compression simulations, the two rigid plates contribute to the settings of the boundary conditions and help evaluate the displacements for the scaffold models.

In CFD, the permeability of the bone tissue scaffold can be determined with Eq. (2):

$$k = \frac{\mu L Q}{A \Delta P} \quad (2)$$

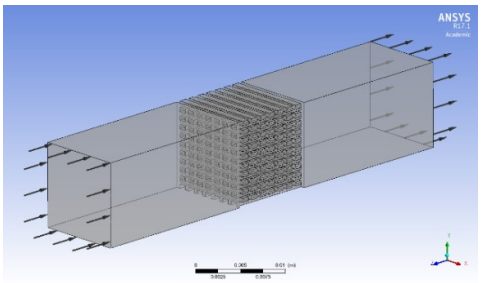

Figure VII Models in ANSYS/Workbench CFX

After obtaining the values of the effective Young's modulus and the permeability of the bone tissue scaffolds, the most suitable scaffold structure can be determined. The target is to obtain a highest value of the effective Young's modulus and a highest value of the permeability as well, which stands for this specific type of scaffold structure have a good mechanical performance and a better ability to accelerate the healing process after the porous bone tissue scaffold is implemented.

C. Multi-objective Optimisation of Porous Bone Tissue Scaffold

On top of the FEA and CFD analyses, the identification of the most suitable porosity of the bone tissue scaffold was conducted by developing the multi-objective optimisation

process. The effective Young's modulus and the permeability are the two design variables. MS EXCEL Spreadsheet was used to establish the regression equations with the data analysis function available. After obtaining the regression equations, the multi-objective optimisation can be constructed by using Matlab with its optimisation tool function, with varying the porosity from 0.1 to 0.9. From the results of the design points generated in the multi-objective optimization procedure, the knee point is determined, and the distance from each design point to the knee point is calculated with the equation shown below.

$$d = \sqrt{(x_1 - x_2)^2 + (y_1 - y_2)^2} \qquad (3)$$

In the resulting diagram, the distance from every design point to the knee point was calculated, which has the smallest values for both design objectives. The point has the smallest distance value is the result design point. Therefore, the most suitable porosity of the bone tissue scaffolds can be determined.

D. Assembly Analysis of Femur Fixation Plate and Porous Bone Tissue Scaffold

The porous bone tissue bone scaffold was re-constructed by using the specific internal structure and the optimal porosity in SolidWorks. Then it was assembled with the femur fixation plate and then the assembly model was imported into ANSYS/Workbench for FEA, as shown in Fig. VIII.

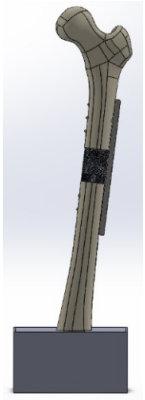

Figure VIII Assembly of the Designed Scaffold and the Fixation Plate

The Nickle-Titanium alloy was selected as the scaffold material due to its excellent mechanical properties and bio-compatibility, as well as the similar super-elastic behaviour compared with those of the human bones, as shown in Table I.

Table I Mechanical Properties

Materials	Young's Modulus (GPa)	Poisson's Ratio
NiTi Alloy	40	0.3
Stainless Steel	180	0.3
Cortical Bone	18	0.3
Cancellous Bone	0.05	0.3

The boundary conditions are shown in Fig. IX, including a 500-N force applied on the femur head area and a fixture on the bottom of the support box.

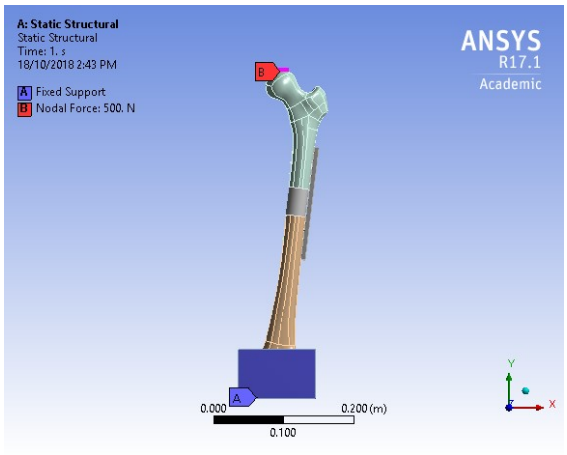

Figure IX Boundary conditions for the assembly analysis

The outcomes of the FEA include stresses and total deformations of the designed porous bone tissue scaffold, the femur bone parts, and the fixation plate. The obtained results were used to evaluate the mechanical performance of the porous bone tissue scaffold and the femur fixation plate.

III. RESULTS AND DISCUSSION

A. Internal Structure Selection

Table II shows the microstructure and the scaffold element samples.

Table II Scaffold Structures

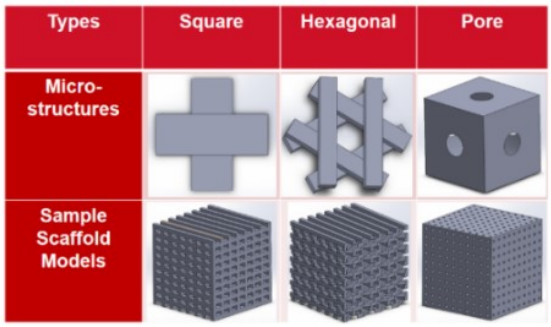

Three sets of scaffold samples with different porosities for each type of scaffold structure were designed. Based on these nine different bone tissue scaffolds, the most suitable scaffold structure was determined. Fig. X show the von Mises contour plot of the porous bone tissue scaffold model with a square structure and a porosity of 60% for a showcase.

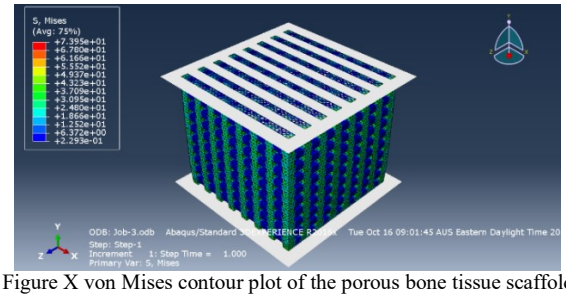

Figure X von Mises contour plot of the porous bone tissue scaffold model with a square structure and a porosity of 60%

The results for the effective Young's modulus and the permeability of the nine scaffold models were calculated by using Eqs. (1) and (2), which are shown in Table III and the results are shown in the table below.

Table III Scaffold Structure Selection

Model	Porosity	Effective Young's Modulus (GPa)	Permeability
Square	0.6	19.8	1.6457E-05
	0.7	14.6	3.18028E-05
	0.8	9.52	6.17459E-05
Hexagonal	0.6	8.3	2.53766E-05
	0.7	2	5.36772E-05
	0.8	0.182	9.50787E-05
Pore	0.6	11.1	9.31784E-07
	0.7	8.22	4.98803E-06
	0.8	5.55	1.25579E-05

Further these results were plotted in a diagram to evaluate the most suitable internal structure of the bone tissue scaffolds as shown in Fig. XI.

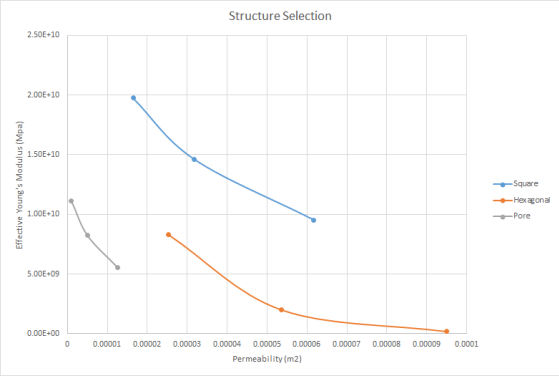

Figure XI Comparisons of Scaffold Structures

The design target is to select a specific scaffold structure, which could obtain good effective Young's modulus and permeability at the same time. It can be found that the pore structure could provide an excellent effective Young's modulus, but the permeability value for the pore structure is relatively low. The hexagon structure, on the other hand, has a good permeability, which can speed up the healing procedure, but its effective Young's modulus is much lower than the other two structures'. It is clear that, among these three types of structures, the square structure can provide wonderful effective Young's modulus and permeability at the same time. Therefore, the square structure was found as the most suitable structure for the porous bone tissue scaffold.

B. Permeability and Porosity

For CFD analyses of the 17 inverse models, the viscosity of the fluid flow was set as 0.001 $Pa{\cdot}s$, while the mass flow rate at the inlet of the model was set as 0.001 m^3/s. The typical outputs of the pressure were shown in Figure XII. The average pressure can be obtained to use for the permeability by employing Eq. (2).

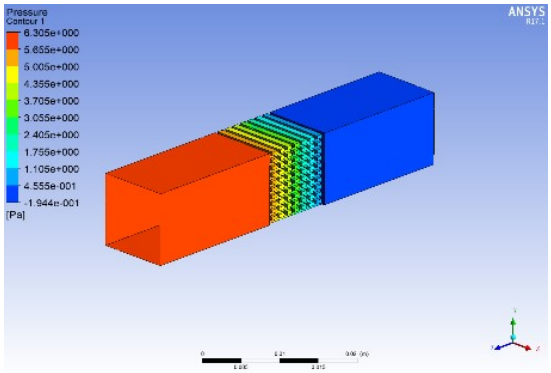

Figure XII Typical outputs of the pressure from ANSYS /Workbench CFX

Table IV shows the results of the effective Young's modulus and the permeability of the 17 models.

Table IV Scaffold porosity effects

porosity	Effective Young's modulus (GPa)	permeability (m2)
0.1	41.06	9.26269E-08
0.15	40.22	2.44694E-07
0.2	38.96	5.60626E-07
0.25	37.53	1.01538E-06
0.3	35.62	1.54799E-06
0.35	33.47	2.68902E-06
0.4	31.18	3.89813E-06
0.45	28.10	5.82042E-06
0.5	25.17	8.64768E-06
0.55	22.68	1.12115E-05
0.6	19.82	1.60041E-05
0.65	17.18	2.40339E-05
0.7	14.62	3.04473E-05
0.75	12.10	4.20762E-05
0.8	9.53	6.07936E-05
0.85	6.99	8.96588E-05
0.9	4.46	0.000137681

After this process, the regression equations were generated with the data analysis function in Excel as mentioned. The regression equations coefficients are shown in Table V.

Table V Regression equation coefficients

Parameter	X Variable 3	X Variable 2	X Variable 1	Intercept
Effective Young's Modulus	5650402904	-1.04421E+11	58581224430	41578752564
Permeability	0.000289666	-0.000863923	0.000812747	-2.60855E-05

After the regression equations determined, the regression equations were input into Matlab as a function, and the optimisation tool was used for conducting the multi-objective optimisation. Its results are shown in Fig. XIII.

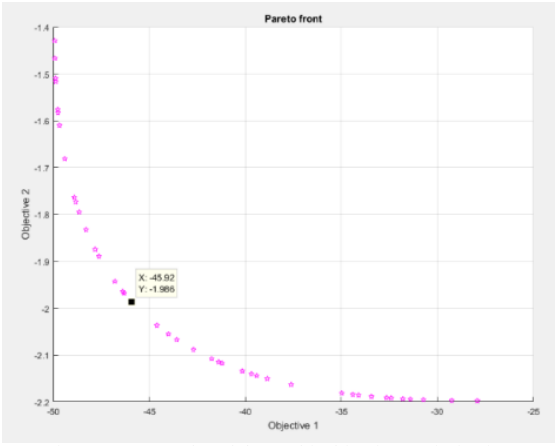

Figure XIII Results of the multi-objective optimisation

By using Eq. (3), the point with the closest distance to the knee point is determined, marked in the figure shown above. That point stands for the porosity of 52%.

C. FEA for the Assembly

The porous bone tissue square scaffold with a square structure and a 52% porosity was constructed in SolidWorks. In this case, the calculated effective Young's modulus with a value of 25.17 GPa was used to define the material model for the porous bone tissue scaffold which was treated as a solid body for saving computational time. The scaffold model was further assembled with the fixation plate and support box and it was employed for the assembly analysis. Figs. XIV and XV show the output results on stress and total deformation, respectively.

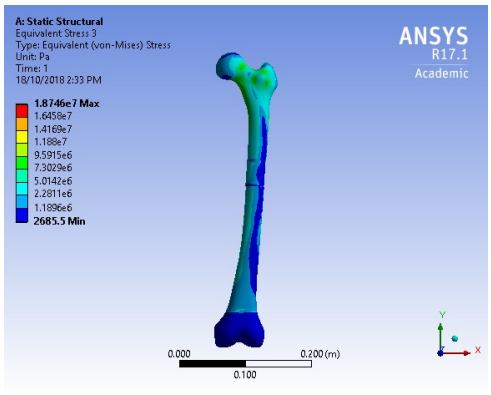

Figure XIV Stress Distribution Result

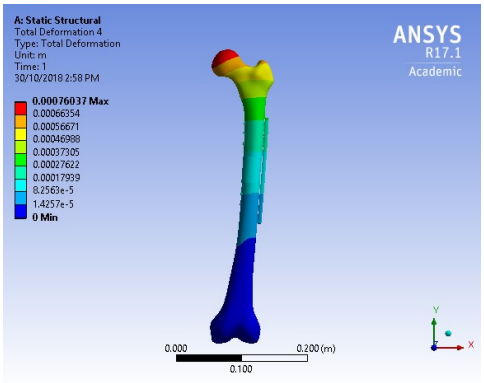

Figure XV Total Deformation Distribution Result

It is clear to find that the stress and total deformation distributions for the bone tissue scaffold part share the same trend with the other parts of the assembly, which means that the optimally-designed bone tissue scaffold has good mechanical behaviours, and it works well with the femur fixation plate.

IV. CONCLUDING REMARKS

This study has developed a systematic optimal design approach of the porous bone tissue scaffold for the femur fracture treatment, which combined the strengths and merits of CAD, FEA, CFD and multi-objective optimisation all together. According to the numerical results obtained, the following conclusions can be drawn:

- During the optimal design of porous bone tissue scaffold, three key material properties – the effective Young's modulus, permeability and porosity should be considered.
- In this optimal design approach, FEA could extract the effective Young's modulus while CFD can help get the permeability and the multi-objective optimisation determines the optimal porosity.
- Among three types of scaffold structures – square, hexagon, and pore, the square one provide the best mechanical performance in balance regarding the three key material properties – the effective Young's modulus, permeability and porosity of the proposed scaffolds.
- The optimally-designed porous bone tissue scaffold with the fixation plate and bones very well avoiding the stress shielding successfully.

As the current work is purely numerical, there are several limitations. One of them may be generated from the geometry of scaffold models as in clinical practices, the shape of the scaffold was determined is based on actual femur bones from patients, not universal. The support box designed and used for the assembly model may not be ideal which has a size issue too. Some future work could be conduct to minimise these. Firstly, the fixation plate model used can be evaluated with some variables, including the geometry of the fixation plate, the material used for the plate and screws, and the way of the screws fixed. Secondly if a clinic practice using this optimal design approach for solving the real-wold problem to validate this one.

ACKNOWLEDGEMENT

The authors would like to express their deep appreciation to Western Sydney University for financial and equipment supports for this research.

REFERENCES

[1] Rho, J. Y., Kuhn-Spearing, L., & Zioupos, P. (1998). Mechanical properties and the hierarchical structure of bone. Medical engineering & physics, 20(2), 92-102.

[2] Martin, R. B., Burr, D. B., Sharkey, N. A., & Fyhrie, D. P. (2015). Mechanical properties of bone. In Skeletal tissue mechanics (pp. 355-422). Springer, New York, NY.

[3] Rezwan, K., Chen, Q. Z., Blaker, J. J., & Boccaccini, A. R. (2006). Biodegradable and bioactive porous polymer/inorganic composite scaffolds for bone tissue engineering. Biomaterials, 27(18), 3413-3431.

[4] Yoshimoto, H., Shin, Y. M., Terai, H., & Vacanti, J. P. (2003). A biodegradable nanofiber scaffold by electrospinning and its potential for bone tissue engineering. Biomaterials, 24(12), 2077-2082.

[5] Liu, X., & Ma, P. X. (2004). Polymeric scaffolds for bone tissue.

Investigation on mechanical anisotropy of high impact polystyrene fabricated via fused deposition modelling

Nima Zohdi
School of Computing, Engineering and Mathematics
Western Sydney University
Kingswood 2747, NSW, Australia
N.Zohdi@westernsydney.edu.au

Saif Tareq
School of Computing, Engineering and Mathematics
Western Sydney University
Kingswood 2747, NSW, Australia
S.Tareq@westernsydney.edu.au

ChunhuiYang
School of Computing, Engineering and Mathematics
Western Sydney University
Kingswood 2747, NSW, Australia
R.Yang@westernsydney.edu.au

Abstract — **Mechanical anisotropy is considered as one of the major drawbacks for materials 3D printed by fused deposition modelling (FDM) technique. The mechanical anisotropy of a variety of 3D printed thermoplastic polymers was investigated before, however, anisotropic characteristics of high impact polystyrene (HIPS) still remained unknown. HIPS is impact-resistant, eco-friendly, cost-effective and most importantly, safe material to use in industry, especially in toys and foods industries. In this study, the HIPS polymer is firstly extruded as filament materials and then 3D printed via the FDM technique for additive manufacturing. Mechanical properties of HIPS samples are measured in different building orientations to study its mechanical anisotropy behaviours. Mechanical properties of 3D printed HIPS are compared with mould injected HIPS as well as 3D-printed acrylonitrile butadiene styrene (ABS) materials. Scanning electron microscopy (SEM), thermogravimetric analysis (TGA) and differential scanning calorimetry (DSC) are used to investigate influences of morphology and thermal properties on anisotropic behaviour of 3D printed materials.**

Mechanical strength results show that the HIPS samples provide similar mechanical properties when produced with mould injection machine or 3D printed in transversal and longitudinal building orientations. This suggests that there is minimal anisotropy in mechanical properties for this material under different build orientations. On the other hand, the lower mechanical strength of ABS in the transversal orientation compared to longitudinal direction indicates the anisotropy of mechanical properties in different orientations. Also, comparing mechanical strengths of these two polymers shows that ultimate strengths of HIPS sample built at the transversal orientation is 34.37% higher than ABS sample which was extruded from polymer pellets and then printed with the same conditions and in the same orientation. The results of this study unfold the potentials of the 3D printed HIPS polymer with providing much-unified properties in the 3D printing industry.

Keywords*— *fused deposition modelling (FDM), additive manufacturing, high impact polystyrene (HIPS), tensile test, Scanning Electron Microscopy (SEM), mechanical anisotropy.

I. INTRODUCTION

One of the most important challenges in producing polymer parts by fused deposition modelling (FDM) is anisotropy which results in un-unified properties in different printing orientations [1]. During the FDM printing process, a thermoplastic filament is fed through a heating chamber and is extruded through the printing nozzle upon its melting temperature. The filaments then deposit layer by layer on top of each other on the platform. Although the deposition lines can be integrated into adjacent deposition lines, inter and intra-layer deformation occurs in the form of cracks between the cylindrical lines. The extruded material cools quickly from melting to printer chamber temperature, resulting in the development of inner stresses responsible for the weak bond between two adjacent deposited lines. This causes delamination or part fabrication failure [2-4]. The structure inhomogeneity results in impaired mechanical strength in part produce via FDM. Mechanical anisotropy in parts printed by the FDM method is defined as the unequal and low tensile strength properties when the part is being printed in orientations perpendicular to the build orientation [5]. Anisotropy can also be referred to the low electrical and thermal properties in parts printed in orientations perpendicular to the orientation of the applied electrical or thermal force (Z-axis). These differences were confirmed and studied previously for polymer parts printed with the FDM method [5, 6]. The mechanical anisotropy in parts produced by FDM could go as high as 50% depending on the layer dimension (thickness, width or diameter) [4, 7-9].

One significant factor causing the anisotropy is the insufficient interlayer bonding adhesion between adjacent rasters which is a consequence of incomplete diffusion and neck growth between layers [10]. The other factor leading to anisotropy is the air voids that form between adjacent cylindrical lines while printing [11]. Although these air voids can be reduced in size by changing the printing parameters like air gap, the negative effect and the presence of these voids cannot be removed fully and still remains a challenge [11]. The intensity of anisotropy for polymer materials produced via FDM could vary by changing the machine factors, the process of production and by changing the polymer type.

High impact polystyrene (HIPS) is a synthetic copolymer consists of polystyrene and polybutadiene rubber which benefits the hardness of polystyrene and the elasticity of polybutadiene. To investigate the effect of polymer type, many publications have investigated conventional thermoplastics such as acrylonitrile butadiene styrene (ABS), and polylactic acid (PLA) but HIPS as a durable, cheap, non-toxic and recyclable thermoplastic polymer has not been investigated extensively.

The focus of this paper is to specifically investigate the mechanical anisotropy behaviour of high impact polystyrene (HIPS) and compare it with anisotropy behaviours of ABS to understand the differences in mechanical anisotropy for different 3D printed polymers. Throughout this study, for all

samples, the machine factors such as air gap, raster angle, etc. were kept constant except the build orientations, which involves a sensitivity study.

II. MATERIALS AND METHODS

All the material fabrication and testings were conducted at the labs in WSU Advanced Manufacturing Precinct at Building Z, Penrith (Kingswood) campus, WSU. The material characterisation was conducted at Advanced Materials Characterisation Facilities at Building EHa, Parramatta South Campus, WSU.

The whole fabrication process of material samples was designed to have the two stages: a) Stage I – Fabrication of filament materials using extrusion: the filament extruder was used from the HIPS and ABS pellets to create the filament materials, which can be used for the 3D printing of coupon samples for tensile testing; and b) Stage II – Fabrication of coupon samples: the coupon samples were 3D printed by using the created filament materials, which are ready for the standard tensile tests for their material properties and microstructural analysis for their morphologies, respectively.

In Stage I, the pellets of two different polymers of HIPS and ABS were used to prepare the filaments. Pellets of HIPS (C8H8) n was purchased from Trinseo (Berwyn, Pennsylvania, U.S.). Pellets of ABS grade PA747 (C8H8·C4H6·C3H3N) n suitable for 3D printing was purchased from ChiMei corporation, (ChiMei, Taiwan). Conventional premium transparent filaments of ABS polymer with 1.75 mm of diameter were purchased from Inkstation (Inkstation, Australia) to be used for the purpose of comparison of properties with the extruded polymers.

As for the pre-processing of the raw material pellets, the as-received polymer pellets were dried overnight in an oven at 65 °C before extruding. A single screw extruder – Noztek Xcalibur from Noztek, London, UK, with a 2.5 mm die orifice was used to extrude the polymer filament at a temperature range of 180 °C to 200 °C. To keep the diameter of the produced polymer in an acceptable range of at 1.75 mm (± 0.1mm), a filament winder – Noztek winder 2.0 also from Noztek was employed. Extruding and winding parameters are shown in Table I, which were used in the fabrication process consistency to get stable results.

Table I. Extruding parameters for fabrication of filament materials

Parameters	*Values*
Extruder bore diameter	2.5 mm, blank
Temperature	ABS: 240 °C HIPS: 240 °C
Extrusion speed	15 rpm
Winding speed	14 rpm
Extruded filament diameter	1.75 mm (±0.1mm)

In Stage II, the coupons for tensile tests and morphology analysis were first designed in Solidworks software and were produced using an Up Plus 3D printer (Tiretime, Beijing) and Up Studio software. Coupons were printed out based on ASTM D638 type V standard (63.5 mm x 9.53 mm x 3.18 mm) with different build orientations, either in transversal direction or longitudinal direction.

Figure 1 shows the shape and detailed dimensions of the tensile test coupons which were designed according to the ASTM standards strictly and fabricated by using 3D printing.

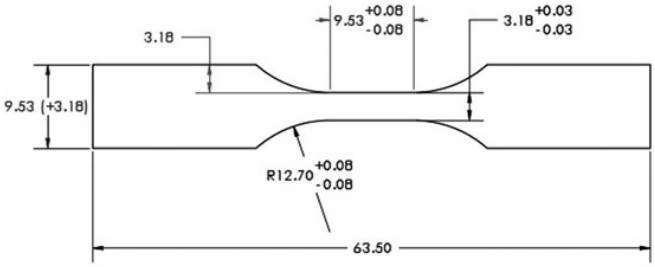

Figure 1. ASTM D638 samples geometries

The machine factors for 3D printing of the polymer parts are shown in Table II. For all the materials a temperature of 240 °C was maintained and there were no infill structures employed as the solid material samples were created. A layer thickness of 0.2 mm was employed constantly.

Table II. Printing parameters for fabrication of 3D printed coupon samples

Machine factor	***Value***
Printing temperature	As received ABS filaments: 240 °C ABS: 240 °C HIPS: 240 °C
Bed temperature	Room temperature
Raster angle	± 45°
Infill density	99%
Fill pattern	Line
Air gap	0
Feed rate	8.0 mm^3/S
Layer thickness	0.2 mm
Raster width	0.5 mm
Nozzle diameter	0.4 mm

For a comparison purpose, HIPS samples were also fabricated by using the traditional moulding injection process. To prepare those mould injected samples, a Fanuc Alpha 15C injection moulding machine was employed. Samples were moulded in a rectangular box by a two gated mould at 235 °C and with a back pressure of 100 kPa and 90.3 cm^3/s injection rate. The holding time was counted as 10 seconds with a 300 kPa packing pressure and a cooling time of 15 seconds. It is worth mentioning that for each set of the material samples, at least 5 replicates for mechanical testing were prepared.

To measure the tensile strength of samples, Instron 3365 with a 5 kN load cell was employed for the tensile tests. The test was conducted according to the standard process regulated in ASTM D638. As for the morphological analysis, Scanning Electron Microscopy (SEM) was carried out using a FlexSEM 1000 II. The Ultra-Variable-Pressure Detector (UVD) feature was used to record images at low-accelerating-voltages and low-vacuum conditions. SEM was used to investigate the morphology of printed parts, the void formation and the interface of printed layers. Thermogravimetric and differential scanning measurements were performed using STA 449 F3 Jupiter TGA-DSC analyser (NETZSCH, Gebrüder, Germany) using closed aluminium pans. The weights of samples were tried to be kept almost constant at around 8 mg ± 0.5 mg (balance accuracy 0.0001). Specimens were heated from 30 °C to 590 °C at a rate of 10 K under a constant flow of Nitrogen gas (25 ml/min, a purity of >99%).

III. RESULTS AND DISCUSSION

From the TGA results, HIPS degradation onset temperature is the highest (415 °C) followed by ABS filaments extruded from polymer pellets (408 °C) and finally as received ABS filaments (387 °C). This means that the HIPS polymer needs a higher temperature to degrade than other two ABS polymers. Having considered the abovementioned comparisons, the temperature range required for 3D printing is well below these numbers (240 °C) which means no significant changes in polymer behaviours would occur during the 3D printing process. Based on the DSC results, the glass-transition temperature (Tg) related to all three samples are in the range of 100 °C-102 °C, which indicates that the pre-selected 240 °C printing temperature is well above the glass temperature and can guarantee a good flow of the polymers in extruding as well as 3D printing.

Tensile tests for different polymers at different build orientations were performed for a sensitivity study. Also, to understand the observed mechanical strength differences in 3D printed samples, microstructural analyses using Scanning Electron Microscopy (SEM) were performed to determine the morphologies fo the tested materials. Results of mechanical testing and microstructural analysis for different samples are shown in Figures 2 and 3, respectively.

Table III shows the detailed average results obtained from tensile test investigation for all samples. The mould injected HIP samples have the highest strength and elongation and thus they were used as the benchmarking.

Table III. Material Properties of ABS and HIPS coupon samples

Average strength and elongation results			
Sample	*Values*		
		Strength (MPa)	*Elongation (%)*
As received ABS filament	Longitudinal	9.74	1.21
	Transversal	3.05	0.44
Extruded ABS	Longitudinal	22.26	6.89
	Transversal	14.55	4.98
Extruded HIPS	Longitudinal	22.06	6.05
	Transversal	22.17	6.09
Mould injected HIPS		26.25	11.16

From Figures 2 (a) and (b) and also Table III, the ultimate tensile strengths of HIPS sample built at the transversal orientation is 86.24% higher than as received ABS filaments and 34.37% higher than parts printed from ABS samples extruded from polymer pellets. Also, HIPS samples printed in longitudinal and transversal build orientations show less than 0.5% difference while both types of ABS samples showed 68.75% and 34.63% difference when printed in transversal orientation compared to the samples printed in the longitudinal direction. This indicates that the mechanical anisotropy behaviour was not observed greatly for HIPS compared to those in ABS.

SEM images are also in good agreement with these findings. From the cross-section SEM image of HIPS printed in the transversal orientation shown in Figure 3(f), a visible interlayer gap cannot be detected. This shows that the diffusion of layers was performed well. That might be the reason for having good mechanical properties close to mould-injected HIPS samples. Also, the rough fracture surface which was formed for HIPS in Figure 3 (f) implies that fracture did not occur at the interlayer surfaces due to the high interlayer adhesion.

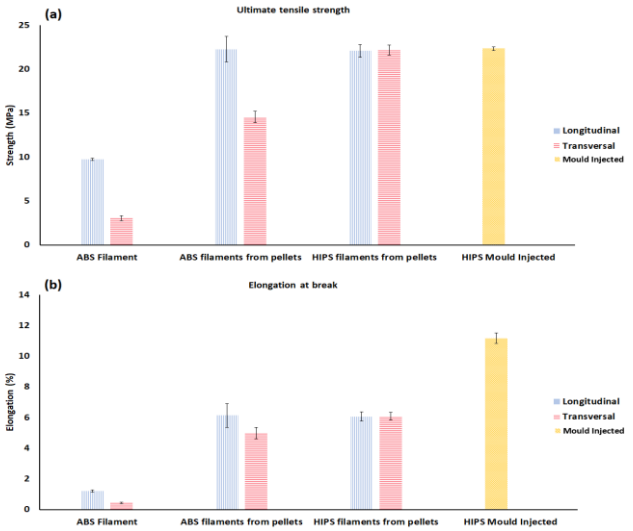

Figure 2. Tensile test results (a) Ultimate tensile strength, (b) Elongation at the break. The error bars represent the standard deviation of the samples.

On the other hand, the difference in mechanical properties of ABS samples printed in two different build orientations is an indication of the mechanical anisotropy of ABS samples. The visible interlayer gaps and the visible smooth fracture surfaces of the ABS samples printed in transversal orientation as shown in Figures 3(b) and (d) justifies the obtained low mechanical properties results and poor interlayer adhesion.

Also, from the SEM images, distinct layer delamination can be traced for the extruded ABS samples, which are marked as red circles in Figures 3(c) and (d). This also could justify the lower mechanical properties of the ABS samples compared to the HIPS samples.

The results indicate that the samples made of as received ABS filaments had the lowest tensile strength and elongation at break as shown in Figures 3 (a) and (b) in every build orientation amongst all the samples. From the SEM images as shown in Figure 3(a), it can be perceived that for the as-received ABS filament in longitudinal built orientation, greater number of pores on the fracture surface can be attributed to the low mechanical properties found. Also, from Figure 3(b), the transversal built orientation of this sample shows a very smooth fracture surface with big interlayer gaps, which confirms the low interlayer adhesion.

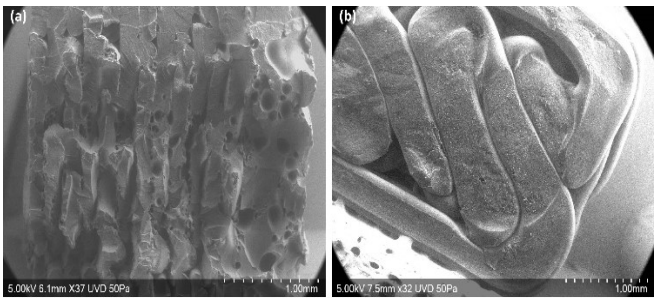

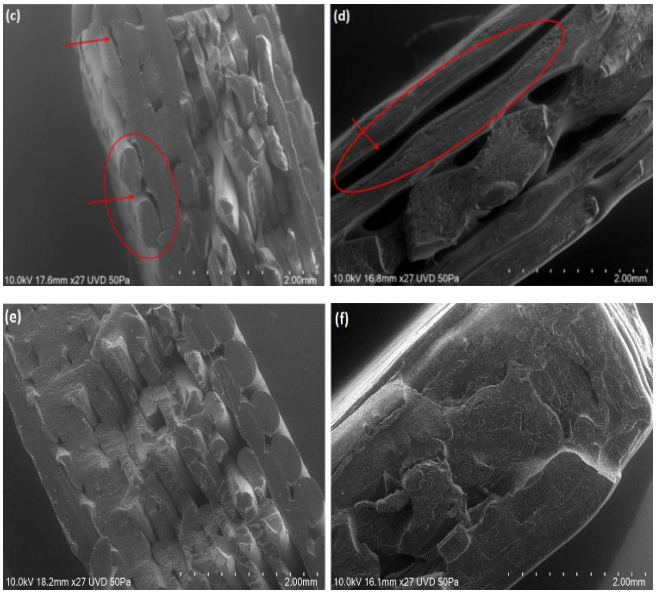

Figure 3. SEM images from the cross-section of ABS filament printed (a) longitudinal, (b) transversal; of ABS pellets printed (c) longitudinal, (d) transversal; and HIPS pellets printed (e) longitudinal, (f) transversal.

Figure 4 shows fractured samples printed in two build orientations of (a) longitudinal and (b) transversal, respectively. The samples printed in the longitudinal orientation showed rough fractured surfaces caused by shearing as a ductile material. On the other hand, the samples printed in the transversal orientation showed smoother fractured surfaces like a brittle material.

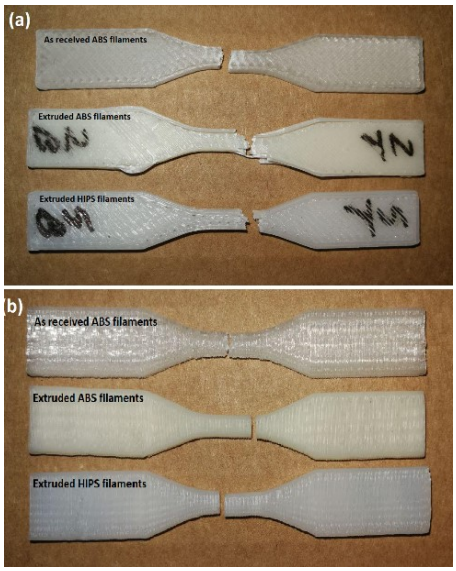

Figure 4. Fractured 3D printed samples in different build orientations: (a) Longitudinal (b) Transversal.

These observed behaviours also support that the weak interlayer adhesion of the samples when 3D printed in the transversal direction.

IV. Conclusion

Mechanical anisotropy of 3D printed HIPS was investigated and compared with the behaviour of ABS as well as mould injected HIPS samples. Based on the tensile measurements and SEM images, HIPS samples (unlike ABS samples) did not show a great deal of anisotropy. This finding suggests that different polymers behave differently in terms of mechanical anisotropy. Moreover, the tensile strength results for 3D printed HIPS were close to values for the mould injected samples of this polymer. HIPS also had greater mechanical strength when compared to ABS samples. Future works towards understanding the fundamentals of observed behaviours can help to improve the properties of 3D printed polymers with low mechanical properties in the transversal direction. The results also showed the capability of SEM analysis in characterising the morphological aspects such as interlayer adhesion and interlayer gap and their effects on the observed mechanical behaviour of 3D printed samples.

The research is on-going and future studies will also focus on understanding the other types of anisotropy such as thermal and electrical properties in polymer composites printed by the additive manufacturing method.

Acknowledgment

The first author would like to show his gratitude to the financial support from Western Sydney University through the Postgraduate Scholarship Award. The authors would like to thank Raju Majji for his assistance in providing technical supports. Also, the authors sincerely acknowledge the great support from Drs Richard Wuhrer and Laurel George from Advanced Materials Characterisation Facility at Western Sydney University for their assistance with microscopy imaging.

References

1. Roberson, D., et al., *Expanding the applicability of FDM-type technologies through materials development.* Rapid Prototyping Journal, 2015. **21**(2): p. 137-143.
2. Dizon, J.R.C., et al., *Mechanical characterization of 3D-printed polymers.* Additive Manufacturing, 2018. **20**: p. 44-67.
3. Ngo, T.D., et al., *Additive manufacturing (3D printing): A review of materials, methods, applications and challenges.* Composites Part B: Engineering, 2018. **143**: p. 172-196.
4. Shih, C.-C., et al., *Effects of cold plasma treatment on interlayer bonding strength in FFF process.* Additive Manufacturing, 2019. **25**: p. 104-111.
5. Mohan, N., et al., *A review on composite materials and process parameters optimisation for the fused deposition modelling process.* Virtual and Physical Prototyping, 2017. **12**(1): p. 47-59.
6. Türk, D.-A., et al., *Mechanical characterization of 3D printed polymers for fiber reinforced polymers processing.* Materials & Design, 2017. **118**: p. 256-265.
7. Gnanasekaran, K., et al., *3D printing of CNT- and graphene-based conductive polymer nanocomposites by fused deposition modeling.* Applied Materials Today, 2017. **9**: p. 21-28.
8. Shemelya, C., et al., *Anisotropy of thermal conductivity in 3D printed polymer matrix composites for space based cube satellites.* Additive Manufacturing, 2017. **16**: p. 186-196.
9. Prajapati, H., et al., *Measurement of anisotropic thermal conductivity and inter-layer thermal contact resistance in polymer fused deposition modeling (FDM).* Additive Manufacturing, 2018.

21: p. 84-90.
10. Aliheidari, N., et al., *Interlayer adhesion and fracture resistance of polymers printed through melt extrusion additive manufacturing process.* Materials & Design, 2018. **156**: p. 351-361.
11. Ziemian, C., M. Sharma, and S. Ziemi, *Anisotropic Mechanical Properties of ABS Parts Fabricated by Fused Deposition Modelling*, in *Mechanical Engineering*. 2012, ISBN: 978-953-51-0505-3, InTech.

A Case Study on 3D Printing of 17-4PH Stainless Steel

Laurence Wong
School of Computing, Engineering and Mathematics, Western Sydney University, Penrith, NSW 2751, Australia
18643334@student.westernsydney.edu.au

Raju Majji
School of Computing, Engineering and Mathematics, Western Sydney University, Penrith, NSW 2751, Australia
r.majji@westernsydney.edu.au

Chunhui Yang
School of Computing, Engineering and Mathematics, Western Sydney University, Penrith, NSW 2751, Australia
r.yang@westernsydney.edu.au

Noel Hosking
Colmar Engineering Pty Ltd, St Marys NSW 2760, Australia
noel@colmar.net.au

Kim Hosking
Colmar Engineering Pty Ltd, St Marys NSW 2760, Australia
kim@colmar.net.au

***Abstract*—Additive manufacturing is a category of fabrication techniques that synthesise objects using CAD models as three-dimensional blueprints. As a new advanced manufacturing technology, further researches are urgently needed to explore the printing process to get expected mechanical properties of 3D printed materials. In this study, as a research case, the design, fabrication, and characterisation of selective laser melted 17-4PH stainless steel is experimentally conducted and tensile tests of the specimens are carried out to determine its material properties and mechanical behaviours. These experimental data are used as a base for comparing the mechanical properties of material samples by using various additive manufacturing processes. The tensile testing of the heat-treated specimens yielded mechanical properties that are found between those expected of as-built and heat-treated samples of 17-4PH stainless steel. Additionally, the mechanical properties collected from the experimental data are used to numerically analyse the structural integrity of a component for high-pressure fluid applications. While the 17-4PH material from this study has average valued material properties compared to those of other studies, the numerical analyses still show reasonable results within safety limits designed for the component in industrial settings.**

Keywords—selective laser melting, additive manufacturing, heat treatment, 17-4PH stainless steel, finite element analysis

I. Introduction

Additive manufacturing is a novel advanced manufacturing technology that is steadily being introduced and implemented in industry. However, even with the flexibility of fabricating intricate geometries with little to no waste material, it does not come automatically without faults. Suboptimal printing parameters result in flawed components that fail earlier and have inferior mechanical properties when compared to those made from traditional processes. Experimental and theoretical analyses aim to optimise additive manufacturing processes so to expedite the incorporation of this technology into industry.

In the presence of the most corrosive environments, stainless steel is typically the most economical and practical selection. Martensitic stainless steels exhibit incredible mechanical and chemical properties. Martensitic grades can also be heat-treated for hardness and strength. ASTM A564/A564M (2010) standards claim that 17-4PH stainless steel is typically heat treated in the H900 condition. Schaller et al. (2017) stated that the H900 precipitation hardening process transforms the original austenite into martensite as it cools. Beyond just enhancing the alloy's strength and hardness, Carter et al. (1971) claimed that aging the alloy beyond its peak strength condition can also improve its resistance against stress corrosion cracking; something that martensitic steels tend to suffer from.

There are numerous printing parameters that can drastically influence material properties and performance of an additively manufactured component. DebRoy et al. (2018) suggested that defects, such as the loss of alloying elements, porosity, surface roughness, residual stress, and distortion are all consequences due to suboptimal process parameters and printing conditions. Liu et al. (2016) stated that during selective laser melting, compressive stresses can be generated at the bottom of the component while tensile stresses are generated at the top, leading to a loss of geometric tolerance. Mukherjee et al. (2016) claimed that an extremely high laser energy density coupled with an alloy element with a relatively low boiling point results in the vaporisation of certain elements which can degrade an alloy's properties. Islam et al. (2013) stated that balling occurs due to the improper and insufficient melting of the metallic powder. Additionally, Li et al. (2011) asserted that existing balls could increase the surface roughness, decreasing the dimensional accuracy and resulting in further metalworking. Porosity is another common defect that can be a result of high power densities, atmospheric or residual gases, or the development of voids due to insufficient fusion. Jeon et al. (2018) studied these factors by conducting several prints using powders of various sizes and morphologies. With powders ranging from 20 µm to 60 µm, Jeon et al. (2018) found that using powders of only 20 µm yielded the lowest porosity and it indicates fine powders should be used.

The additive manufacturing of 17-4PH stainless steel was previously tested but it is difficult to conclusively present printing parameters that optimise the alloy's mechanical properties. This is due to the variations between different metal 3D printers and the intermingled influences that the printing parameters have on one another. Auguste et al. (2018) studied not only different build orientations and patterns, but also various heat-treatment procedures. With the printing parameters provided in Table I, Auguste et al. (2018) constructed test specimens in both the XY axes and the Z axis for the build orientations by using a cross-hatching pattern. Furthermore, the applied heat-treatments and their abbreviations are listed in Table II, which was used to reduce the residual stress effects and control the unwanted deformation and distortion of the fabricated components.

Table I. Printing parameters used by Auguste et al. (2018)

Layer Thickness (µm)	50
Power (W)	275
Speed (mm/s)	760
Hatching (µm)	120
Substrate Temperature (°C)	200
Base Plate Material	AISI 310S
Gas Atmosphere (min. 99.99%)	Argon

Table II. Heat-treatments used by Auguste et al. (2018)

Heat-Treatment	Abbreviation
None (As-Built)	AsB
Tempering (480°C, 1 hr)	T480
Tempering (550°C, 4 hr)	T550
Tempering (620°C, 4 hr)	T620
Tempering (760°C, 2 hr) + Tempering (620°C, 4 hr)	T760
Solution Heat Treatment (1040°C, 1.5 hr) + Quenching + Tempering (480°C, 1 hr)	SHT-T480
Homogenisation (1190°C, 2 hr) + Solution Heat Treatment (1040°C, 1.5 hr) + Quenching + Tempering (480°C, 1 hr)	H-SHT-T480

Mower and Long (2016) utilised direct metal laser sintering to fabricate 17-4PH test specimens. The study involved testing and comparing additively manufactured specimens built horizontally and at a 45° incline with those produced by using conventional methods. Table III contains the printing parameters that were used by Mower and Long (2016) in their research.

Table III. Printing parameters used by Mower and Long (2018)

Laser Power (W)	195
Spot Size (µm)	100
Scanning Speed (mm/s)	750
Substrate Temperature (°C)	82
Layer Thickness (µm)	20
Gas Atmosphere	Nitrogen

This study attempts to experimentally investigate the mechanical properties of 17-4PH stainless steel printed by using selective laser melting method in accordance to 3D metal printer supplier's suggestions. In the subsequent section – Section II, tensile test specimens are designed and fabricated for conducting standard tensile tests to determine the alloy's mechanical properties. Section III shows a case study on the mechanical performance of an industrial component by using the 3D printed material via finite element modelling and simulations. Finally, the results acquired in this study were validated by comparing the available data from literature. The detailed result comparisons of mechanical properties extracted from current study with others are shown in Section IV.

II. Experimental Analysis of Selective Laser Melted 17-4PH Stainless Steel

A. Design of Tensile Test Specimens

Tensile test specimens were designed in accordance to the ASTM E8/E8M-16a (2016) standards for sheet-type specimens as shown in Table IV. Fig. 1 illustrates the dimensioned CAD model of the specimens.

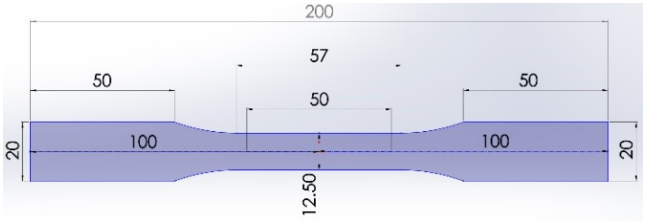

Figure 1. CAD model of the tensile test specimen

Table IV. Sheet-type dimensions by ASTM E8/E8-16a (2016)

Gauge Length (mm)	50.0 ± 0.1
Width (mm)	12.5 ± 0.2
Thickness (mm)	-
Radius of fillet, min (mm)	12.5
Overall Length, min (mm)	200
Length of Reduced Parallel Section, min (mm)	57
Length of Grip Section (mm)	50
Width of Grip Section, approximate (mm)	20

B. Fabrication of Tensile Test Specimens

The 17-4PH stainless steel powder, under the name of LaserForm 17-4PH (B), was supplied by 3D Systems. Table V details the chemical composition of their 17-4PH powder with ASTM A564/A564M (2010) standards. As shown in Table V, when compared to ASTM A564/A564M (2010), the chemical composition of the powder supplied by 3D Systems lacked certain elements, namely carbon, phosphorus, tantalum, and sulfur. However, the main alloy elements have a good match with those from the standards and the percentages do not deviate noticeably. Due to a combination of various defects, such as residual thermal stress and distortion, the dimensions of the printed specimens slightly deviated from desired dimensions.

Table V. Chemical composition of 17-4PH by 3D Systems

	Composition (%)			
	Mn	Si	Cr	Ni
3DS	<1.0	<1.0	15.0-17.5	3.0-5.0
ASTM	1.0	1.0	15.0-17.0	3.0-5.0
	Cu	Nb	Ta	C
3DS	3.0-5.0	0.15-0.45	-	-
ASTM	3.0-5.0	0.15-0.45		0.07
	P	S	Fe	
3DS	-	-	Bal.	
ASTM	0.04	0.03	Bal.	

The selective laser melting took place in a 3D metal printer - 3D Systems ProX DMP 300 available at Advanced Manufacturing Precinct, Kingswood campus, WSU. This 3D

metal printer is equipped with a 500-W fibre laser that had a wavelength of 1070 nm. Table VI lists the printing parameters that were used to conduct the selective laser melting of the five tensile test specimens. After the printing process was completed, wire electric discharge machining was implemented to remove the tensile test specimens from the printer's substrate.

Table VI. Printing parameters used in this study

Style					
Style	Back and Forth	Non-collinear	Radius (µm)	Overlap (µm)	Progress
Hexagons	True	True	25000	100	True
Laser					
Mark Speed (mm/s)	Jump Speed (mm/s)	Laser Power (%)	Defocusing (mm/10)	Spacing (µm)	Gas Atmosphere
1200	5000	30	0	50	Nitrogen
Compensations					
Collinear Start (µm)		Collinear Stop (µm)	Non-collinear Start (µm)		Non-collinear Stop (µm)
340		370	340		370
Delays					
Laser ON		Laser OFF	Mark Delay (µs)		Jump Delay (µs)
600		20	15		30

The specimens were then sent to undergo solution annealing and age hardening in a nitrogen atmosphere to enhance its mechanical properties and to relieve their residual thermal stresses. The solution annealing started at a vacuum of 133.332 Pa and a starting heat rate of approximately 16.667°C per minute. Once it reached a holding temperature of 1037.778 ± 889°C, conditions were kept constant for 1 ± 0.25 hours. The nitrogen quenching was at a pressure of 2 kPa and a temperature of less than 65.556°C. The tensile test specimens were then air cooled to less than 32.222°C. The age hardening process commenced after the solution annealing was completed. Like the solution annealing, the process started at a vacuum of 133.332 Pa and a starting heat rate of 16.667°C per minute. Once it reached a holding temperature of 482.222 ± 12.222°C, conditions were kept constant for 1 ± 0.25 hours. The nitrogen quenching was at a pressure of -16931.945 Pa and a temperature of less than 32.222°C. Finally, the specimens were air cooled to room temperature, which are ready for the tensile tests.

C. Characterisation of Tensile Test Specimens

Before the tensile test, all the five tensile specimens were measured carefully to make sure that their dimensions falling into right ranges, not influencing the experimental results significantly.

The mechanical properties of the of the five tensile test specimens were characterised using the Instron 6027 tensile testing machine. The specimens were loaded into the testing apparatus and clip-on extensometers were connected to both sides of the specimens. The tensile tests were conducted by using a test rate of 2 mm/minute to maintain static loading status until the specimens failed. The data on load, displacement, stress and strain were then obtained.

III. Numerical Analysis of Industrial Component Made of Selective Laser Melted 17-4PH Stainless Steel

The industrial component was designed to have a hollow structure with holes where high-pressured fluid could enter and be redirected through. Considering the symmetric features of the components, only quarter of it was modelled to save the computational costs in a static structural analysis by using ANSYS Workbench Version 19.0. Its CAD model is shown in Fig. 2.

Since the component was to be tested under high-pressure conditions, a ramped pressure of 10 bar (1 MPa) was applied to the interior. Fixtures were placed on the surfaces of the inlets and outlets since deformation should not occur at a location without normal contact from the fluid. Fig. 2 also depicts the application of the pressure and fixed supports for this static structural analysis.

The averaged mechanical properties collected from the five tensile test specimens in this study were used to define the 3D printed material model of 17-4PH stainless steel, which can be found in Table VIII, which will be further discussed in Section IV.

Lastly, to obtain the reliable results, convergence tests were conducted for all three numerical results – total deformation, equivalent stress, and equivalent elastic strain with an allowable variation of 5%. All the tests consistently concluded with final changes of less than 1% between the nth and n-1th iterations, which are suggesting very successful convergences were achieved.

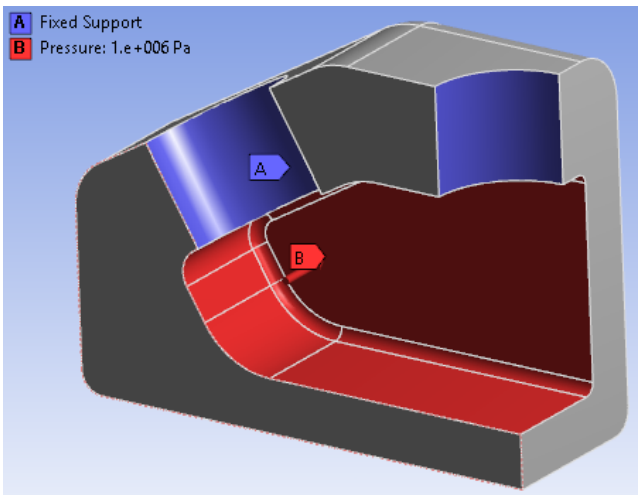

Figure 2. Boundary conditions used for the static structural analysis

IV. Results and Discussion

A. Characterisation of Fractured Tensile Specimens

It is worth noting that from the tensile testing of the five specimens, the first broke below the gauge length, the fifth broke above the gauge length, and the other three perfectly fractured within the gauge length.

Table VII provides the dimensions and cross-sectional areas at the fracture point of the specimens. These measurements were taken for reference only since only the part within the gauge length is of interest, at the middle of the specimens, where the dimensions are presumably at their thinnest.

Table VII. Dimensions at fracture points

Samples	Thickness (mm)	Width (mm)	Area (mm^2)
#1 (Before)	5.1	12.3	62.73
#1 (After)	5.08	12.39	62.9412
#2 (Before)	5.1	12.4	63.24
#2 (After)	4.95	12.25	60.6375
#3 (Before)	5.2	12.3	63.96
#3 (After)	5.17	12.31	63.6427
#4 (Before)	5.0	12.3	61.5
#4 (After)	5.14	12.30	63.222
#5 (Before)	5.1	12.3	62.73
#5 (After)	5.01	12.29	61.5729

The tensile testing extracted five sets of parameters, namely the extensions, loads, tensile stresses, and tensile strains per increment of 0.1 seconds. Fig. 3 illustrates the stress-strain curves of the five specimens plotted onto a single graph. Fig. 4 represents the load versus extension of the five tensile specimens during the tensile testing. Table VIII contains the comparison of the mechanical properties of 17-4PH stainless steel gathered from various sources. The test results from the five test specimens have been averaged into one.

By comparing the yield strength and ultimate tensile strength from this study to those from 3D Systems' as-built values, it is evident that a heat-treatment process is very important to the suboptimal mechanical properties of the 3D printed metals. Furthermore, considering the mechanical properties provided by Auguste et al. (2018), heat-treatments greatly influence the component's mechanical properties with homogenisation, quenching, tempering, etc., to produce the expected properties . From the data, it is seen that 3D printed specimens in the XY direction consistently produce superior mechanical properties when compared to those built in the Z direction. For the specimens built in the Z direction, the tensile force acts perpendicular to the layers, resulting in poorer performance which may be caused by weak interlayer bonding among 3D printed layers.

B. Material Properties of 17-4PH Stainless Steel

Figs. 3 and 4 provide the mechanical behaviours of the five 3D printed tensile specimens and based on these experimental data, the results were extracted for those material properties, including Young's modulus, E, Yielding Strength, YS, Ultimate Tensile Strength, UTS, etc. The five specimens show the results discrepancies though they were printed at one shot in the same base.

Table VIII lists these above-mentioned results along with other 12 sets of mechanical properties for stainless steels. For comparison, the results of heat treated 17-4PH Stainless Steel from 3D Systems were used as a benchmarking example (highlighted in yellow). It has a yielding strength of 1100 ± 50 MPa, and a ultimate tensile strength of 1300 ± 50 MPa, compared to the one without heat treatment with a YS of 620 ± 50 MPa, and a UTS of 1100 ± 50 MPa. The current study extracted the values at 658.25 ± 75 and 966.38 ± 89 MPa, respectively (highlighted in orange). These average values did not reach the data from 3D Systems for the material sample after heat treatment but still higher than the one without heat treatment. However, if only looking at the best sample, the Young's modulus, yielding strength and ultimate tensile strength can reach to 160 GPa, 900 and 1000 MPa, respectively, referring to Fig. 3.

The error percentages were calculated for highlighting the discrepancies of all materials available from literatures. The comparisons indicate that the 3D printing process and heat treatment post-processing of stainless steels need to be optimised to get controllable material properties and quality performance, such as high strength-to-weight ratio. A review on the heat treatment process was conducted and a new one was proposed to further improve the material properties of 3D printed stainless steel.

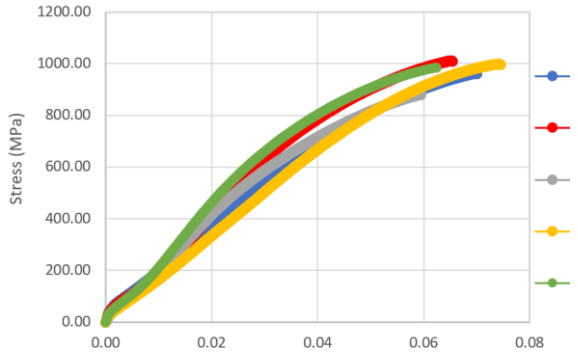

Figure 3. Stress-strain curves of the five tensile test specimens

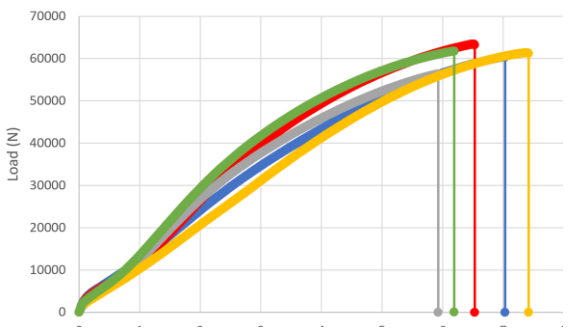

Figure 4. Load versus extension curves of the five tensile test specimens

Table VIII. Comparison on mechanical properties of stainless steels fabricated by using different methods

(Highlighted properties were used in the numerical study)

Condition	Source	YS (MPa)	ΔYS (%)	UTS (MPa)	ΔUTS (%)	E (GPa)	Elongation at Break (%)	Hardness (HVs)
AsB (Z)	Auguste et al. (2018)	500	-54.5455	1075	-17.3077	-	7	330
AsB (XY)	Auguste et al. (2018)	520	-52.7273	1075	-17.3077	-	10.5	330
Horizontal	Mower and Long (2016)	610	-44.5455	1072	-17.5385	172.2	7.2	-
AsB	3D Systems	620 ± 50	-43.6364	1100 ± 50	-15.3846	-	16 ± 2	300 ± 20
Heat-treated	Current study (averaged)	658.25 ± 75	-40.1591	966.38 ± 89	-25.6631	102.26 ± 9.5	-	-
45° Incline	Mower and Long (2016)	737	-33	914	-2923	192.9	-	-
SHT-T480 (XY)	Auguste et al. (2018)	770	-30	970	-25.3846	-	4.5	305
T480 (Z)	Auguste et al. (2018)	800	-27.2727	1050	-19.2308	-	5	370
Wrought	Mower and Long (2016)	898	-18.3636	1085	-16.5385	193.9	6.5	-
T480 (XY)	Auguste et al. (2018)	980	-10.9091	1150	-11.5385	-	6	370
Heat-treated	3D Systems	1100 ± 50	0	1300 ± 50	0	-	10 ± 2	400 ± 20
H-SHT-T480 (Z)	Auguste et al. (2018)	1250	13.63636	1300	0	-	1	480
H-SHT-T480 (XY)	Auguste et al. (2018)	1300	18.18182	1400	7.692308	-	3.5	480

C. Structural Static Analyses on Industrial Component of 17-4PH Stainless Steel

The seven sets of mechanical properties for stainless steels (highlighted in Table VIII) were applied to the component to define the material models for comparisons. The static structural analyses were used to quantify and assess how much deformation, equivalent stress, and equivalent elastic strain will be inflicted into each variant of 17-4PH. Fig. 5 illustrates the contours of the deformation, stress, and strain, respectively, of the component assigned with the averaged mechanical properties extracted in this study as a set of typical results. It is evident that there exists strain/stress concentrations along the 2 mm fillet. This suggests that if the component be subjected to a much greater pressure; it may fail at the fillet due to the local strain/stress concentrations.

Table IX lists the maximum deformation, stress, and strain based on the mechanical properties from different authors and sources for comparisons. From the information shown in Table IX, the selective laser melted 17-4PH stainless steel by Auguste et al. (2018) is superior to the other methods showcased in this comparative study. The noticeably larger deformation for the 17-4PH stainless steel of this study was a result of the inferior elastic modulus.

Table IX. Maximum deformation, stress, and strain from static structural analyses using various mechanical properties

Source	Deformation (m)	Equivalent Stress (MPa)	Equivalent Strain (m/m)
Auguste et al. (2018) AsB (XY)	1.5726e-6	22.087	0.00011043
Mower and Long (2016) Horizontal	1.9061e-6	22.087	0.00013386
3D Systems AsB	1.5726e-6	22.087	0.00011043
Current study (averaged) Heat-treated	3.0755e-6	22.087	0.00021598
Mower and Long (2016) Wrought	1.6909e-6	22.087	0.00011875
3D Systems Heat-treated	1.5712e-6	22.081	0.00011041
Auguste et al. (2018) H-SHT-T480 (XY)	1.5726e-6	22.087	0.00011043

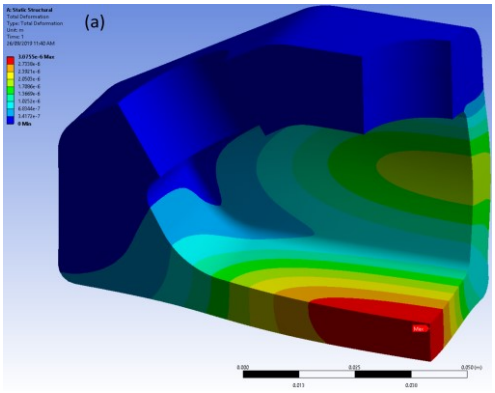

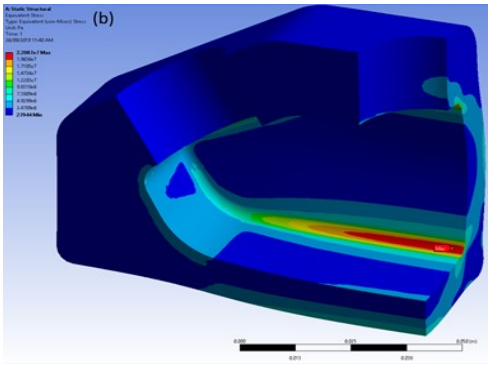

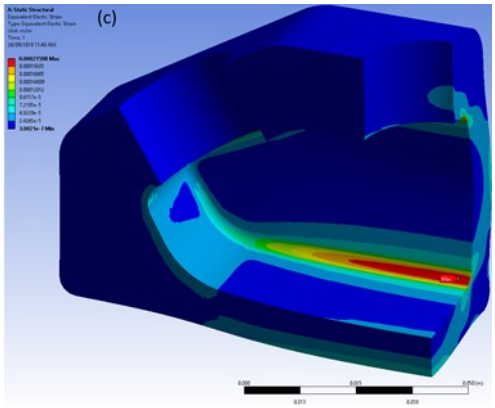

Figure 5. Numerical results of the high fluid pressure part: (a) total deformation, (b) equivalent stress, and (c) equivalent elastic strain with this study's averaged mechanical properties

V. Conclusions and Recommendations

This initial study examined the design, fabrication, and characterisation of selective laser melted 17-4PH stainless steel by experimentally creating and testing tensile test specimens to extract the alloy's mechanical properties. These experimental data provide insights into how printing parameters and heat-treatments influence a 3D printed component's mechanical properties. By comparing the resultant properties with those from other publications and sources, changes can be made to optimise the selective laser melting process and its post-processing – heat treatment.

Beyond optimising printing parameters, it is important to consider the ideal heat-treatment process to further enhance the material properties of 17-4PH stainless steel. Compared to the properties provided by 3D Systems, this study's heat-treated mechanical properties ranked slightly higher than their as-built properties but lower than their heat-treated properties. This suggests that the heat-treatment process conducted for this study did not impart the desired effects. Additionally, the findings in this study show that a combination of homogenisation, solution heat-treatment, quenching, and tempering provides a lot of improvements on yield strength, ultimate tensile strength, and hardness. Furthermore, components should be oriented so that the layers are parallel to the proposed loads to maximise integrity of the layers.

Utilising finite element analysis to evaluate how printed material behaves is useful for assessing the practicality and feasibility behind adopting a fabrication technology and its materials. In the application of a hollow vessel that is subjected to high-pressure fluids, the 17-4PH stainless steel produced in this study fares quite well despite the suboptimal mechanical properties.

As for the future work, an on-going research is being conducted currently to focus on the redesign of this high pressure vessel by using the rules of Design for 3D Printing and principles of optimisation design to optimally control the 3D printing process and extract a light but still reliable component. Meanwhile the post-processing of the 3D printed component is further investigated to improve its overall mechanical performance strictly aligning with industrial standards.

Aknowlegement

The authors would like to show their gratitude to the LaunchPad, Western Sydney University and the Department of Industry, NSW State Government for their financial supports through the TechVouchers NSW Funding Program.

References

American Society for Testing and Materials 2010, *Specification for Hot-Rolled and Cold-Finished Age-Hardening Stainless Steel Bars and Shapes*, ASTM A564/A564M, ASTM International, DOI 10.1520/A0564_A0564M-13E01

American Society for Testing and Materials 2016, *Standard Test Methods for Tension Testing of Metallic Materials*, ASTM E8/E8M-16a, ASTM International, DOI 10.1520/E0008_E0008M-16A

Auguste, P, Mauduit, A, Fouquet, L, Pillot, S 2018, 'Study on 17-4 PH stainless steel produced by selective laser melting', *UPB Scientific Bulletin, Series B: Chemistry and Materials Science*, vol. 80, no. 4, pp. 197-210, Retrieved from <https://researchgate.net>

Carter, CS, Farwick, DG, Ross, AM, Uchida, JM 1971, 'Stress corrosion properties of high-strength precipitation-hardening stainless steels in 3.5% aqueous sodium chloride solution', *Corrosion*, vol. 27, no. 5, pp. 190-197, NACE International, DOI 10.5006/0010-9312-27.5.190

DebRoy, T, Wei, HL, Zuback, JS, Mukherjee, T, Elmer, JW, Milewski, JO, Beese, AM, Wilson-Heid, A, De, A, Zhang, W 2018, 'Additive manufacturing of metallic components – Process, structure and properties', *Progress in Materials Science*, vol. 92, pp. 112-224, Elsevier BV, DOI 10.1016/j.pmatsci.2017.10.001

Islam, M, Purtonen, T, Piili, H, Salminen, A, Nyrhilä, O 2013, 'Temperature profile and imaging analysis of laser additive manufacturing of stainless steel', *Physics Procedia*, vol. 41, pp. 835-842, Elsevier BV, DOI 10.1016/j.phpro.2013.03.156

Jeon, T, Hwang, T, Yun, H, VanTyne, C, Moon, Y 2018, 'Control of porosity in parts produced by a direct laser melting process', *Applied Sciences*, vol. 8, no. 12, pp. 2573, MDPI AG, DOI 10.3390/app8122573

Li, R, Liu, J, Shi, Y, Wang, L, Jiang, W 2011, 'Balling behavior of stainless steel and nickel powder during selective laser melting process', *The International Journal of Advanced Manufacturing Technology*, vol. 59, no. 9-12, pp. 1025-1035, Springer Science and Business Media LLC, DOI 10.1007/s00170-011-3566-1

Liu, Y, Yang, Y, Wang, D 2016, 'A study on the residual stress during selective laser melting (SLM) of metallic powder', *The International Journal of Advanced Manufacturing Technology*, vol. 87, no. 1-4, pp. 647-656, Springer Science and Business Media LLC, DOI 10.1007/s00170-016-8466-y

Mower, TM, Long, MJ 2016, 'Mechanical behavior of additive manufactured, powder-bed laser-fused materials', *Materials Science and Engineering: A*, vol. 651, pp. 198-213, Elsevier BV, DOI 10.1016/j.msea.2015.10.068

Mukherjee, T, Zuback, JS, De, A, DebRoy, T 2016, 'Printability of alloys for additive manufacturing', *Scientific Reports*, vol. 6, no. 1, Springer Science and Business Media LLC, DOI 10.1038/srep19717

Schaller, RF, Taylor, JM, Rodelas, J, Schindelholz, EJ 2017, 'Corrosion properties of powder bed fusion additively manufactured 17-4 PH stainless steel', *Corrosion*, vol. 73, no. 7, pp. 786-807, NACE International, DOI 10.5006/2365

Numerical investigation of flow past a spinning sphere at a Reynolds number of 4000 within the sub-critical flow reigme

Benjamin Curtis
School of Computing, Engineering and Mathematics
Western Sydney University
Kingswood 2747, NSW, Australia

Ming Zhao
School of Computing, Engineering and Mathematics
Western Sydney University
Kingswood 2747, NSW, Australia

Michael Fernandez
School of Computing, Engineering and Mathematics
Western Sydney University
Kingswood 2747, NSW, Australia

***Abstract*— The influence of the non-dimensional spin parameter on the force coefficients is numerically investigated for fluid flowing past a rotating sphere using Direct Numerical Simulations. Spin parameters in the range between 0 and 2 are tested at a Reynolds number of 4000. Results showed that both the lift and drag coefficients increased until a critical spin parameter of 1 as a result of a strong pressure difference between the upper and lower hemispheres of the sphere. Beyond the critical spin parameter, the pressure difference decreased and the wake region behind the sphere was found to shrink and as a result, the lift and drag coefficients reduced in magnitude.**

Keywords*— *Magnus Effect, Spin, Rotation, Sphere, Sub-critical Flow.

I. INTRODUCTION

Isaac Newton first wrote about the motion of a spinning ball through the air in a letter to The Royal Society of London in 1671, where he described how tennis balls, herein after referred to as spheres, move in curved paths as a result of rotational motions imparted by tennis rackets [1]. Little did Newton know that the phenomenon that he had just written about wouldn't be explained in detail until the late 1800's and would continue to be an area of extensive research some 350 years later, where it would have applications in various fields including the modelling of blood cells through the human body in the medical industry [2]. The additional forces that cause a rotating sphere to curve, unlike that of spheres with no rotation, are a result of the Magnus Effect, which was named after Gustav Magnus, a Physics Professor at the University of Berlin between the years of 1834 and 1869 [3].

The Magnus Effect is best explained by considering the fluid flowing past the 'upwind' and 'downwind' surfaces of the sphere. Fluid flow on the downwind side of the sphere is travelling in the same direction as the rotational motion, where additional momentum is transferred to the fluid [4]. The result is that the fluid is travelling faster in the streamwise direction which forms a pressure gradient between the upper and lower surfaces of the sphere as shown in Fig. 1, and thus a cross force is created which is commonly known as the Magnus force, or Lift force hereafter.

Methods for researching the Magnus Effect have changed as more advanced technologies have been developed. Fundamental studies by Briggs [5] and Thomson [6] used simple apparatus' in wind tunnels to observe the effects of fluid flowing past rotating spheres, where the instantaneous fluid flow was captured using high speed film cameras. Advancements in modern technology have enabled the use of high speed, modern computers to conduct numerical investigations in place of the experimental methods used in years gone by [7-9]. The flow investigations in literature have focused on two cases, the first case having a non-rotating sphere and the second having a rotating sphere, both of which have different fluid flow characteristics.

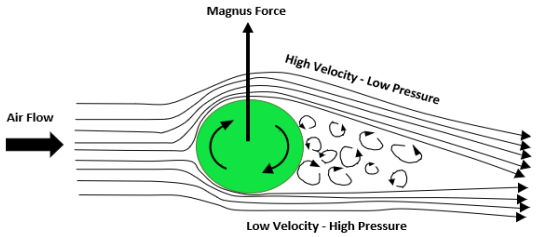

Fig. 1. A sketch of fluid flow past a rotating sphere

A. Flow past non-rotating sphere

Flow passing over non-rotating spheres in the sub-critical flow regime has been outlined in detail in [4; 10-14]. Arguably one of the most referenced papers in this area is [10] who proved that the drag coefficient during the sub-critical regime, when $5\times10^4 < Re < 3.4\times10^5$, is independent of Reynolds number and maintains a constant value of approximately $C_D \approx 0.5$. The definition for both the lift and drag forces on sphere can be given by:

$$C_D = \frac{F_D}{\frac{1}{2}\rho A U^2} \quad (1)$$

$$C_L = \frac{F_L}{\frac{1}{2}\rho A U^2} \quad (2)$$

where F_D and F_L are the drag and lift force on the sphere, ρ is the fluid density, A is the projecting area, and U is the incoming flow velocity.

Taneda [12] continued the research by Achenbach [10] by focusing on the flow visualization of the fluid passing over a sphere and found results that agreed with those in [10]. Additional studies have shown that the drag coefficient in the subcritical regime continues to remain constant down to Re = 3000 [15-18]. An in-depth regime mapping study was conducted recently which discovered that Reynolds number during the sub-critical flow regime spans from $3000 < Re < 3.4\times10^5$ [17]. Studies in [10; 12; 19] found that Strouhal's number varied depending on the fluid flow regime.

It was identified that during the sub-critical flow regime, when Reynolds number was between $3\times10^3 < Re < 6\times10^4$ two Strouhal numbers exist, namely, the high-mode and low-mode Strouhal number.

Numerical investigation has proven to be an accurate method of analysis in the fluid mechanics domain. Multiple numerical investigations proved that the drag coefficient and Strouhal number on a non-rotating sphere can be replicated with high accuracy using numerical analysis [8; 9; 13; 17; 20]. In all the previously mentioned cases, both experimental and numerical, the lift and side forces have been approximately equal to zero.

B. Flow past a rotating sphere

Analysis of non-rotating spheres is considerably simpler since the Magnus Effect is not present, however, once a rotational motion is added to the sphere, the Magnus Effect is quite pronounced. Early investigations found that the drag coefficient remained mostly constant for varying spin parameters, SP, and was equal to $C_D \approx 0.44$ [21; 22]. The spin parameter, SP, is given by Eq. (3). The lift force created by the Magnus Effect was empirically modelled by [23] and [22] where it could be expressed by (4) and (5), respectively, when Reynolds number was within the sub-critical flow regime.

$$SP = \frac{\omega' D}{2U} \tag{3}$$

$$C_L = \frac{1}{2.202 + 0.981\left(\frac{U}{\omega'}\right)} \tag{4}$$

$$C_L = 3.19 \times 10^{-1}[1 - \exp(-2.48 \times 10^{-3}\omega')] \tag{5}$$

where C_L is the lift coefficient, U is linear velocity of the incoming flow, and ω' is the angular velocity of the spinning sphere in rad/s.

Equations (4) and (5) were calculated for small spin parameters, where $SP < 0.5$ or $\omega < 1000$. Experiments in [23] and [22] were focused on the higher sub-critical flow regime where $5\times10^4 < Re < 3.4\times10^5$. Few studies have investigated the lower spectrum of the sub-critical flow regime however, a recent study by [9] experimentally investigated the effect of rotation on drag and lift forces in the intermediate Reynolds number range, where $10^3 < Re < 10^4$ and $SP \leq 5$. They concluded that there was a sudden drop in force coefficients at a critical spin ratio which varied depending on Reynolds number. Flow visualization was used to aid in their investigation, where they hypothesized that the reason for the significant reduction in force coefficients was due to the upwind side undergoing a transition to turbulent flow before that of the downwind side.

The literature has shown that limited numerical investigations have been conducted on rotating sphere's at intermediate Reynolds numbers. Therefore, this paper will investigate the flow of fluid past a non-rotating and rotating sphere within the sub-critical flow regime, where $10^3 < Re < 10^4$, using numerical analysis. The rotational direction of the sphere is perpendicular to the direction of the flow for all rotational cases to replicate forward and backward spin. The influence of the spin parameter is analyzed to understand how the force coefficients and fluid flow changes as SP is varied from 0 to 2, in increments of 0.5. A Reynolds number of 4000 was chosen as it was large enough to be within the sub-critical flow regime but would allow for direct simulation of the Navier-Stokes equations without significant computational costs.

The remainder of this paper is organized in the following order. The numerical method is provided in Section 2. The results and discussion are presented in Section 3. Finally, the conclusion is provided in Section 4.

II. Numerical Method

Direct numerical simulations were conducted using the numerical method developed by [24], where the Petrov-Galerkin finite element method was employed to solve the three-dimensional (3-D) Navier-Stokes equations.

A. Governing equations

The non-dimensional variables in this study are given by $u = u'/U$, $v = v'/U$, $w = w'/U$, $\omega = \omega' D/2U$ which is equal to the spin parameter, SP, and $t = t' D/U$, where u, v, w are the non-dimensional velocities, ω is the non-dimensional angular velocity, U is the incoming flow velocity, D is the diameter of the sphere, and t is the dimensional time. The variables with and without a prime stand for non-dimensional and dimensional values, respectively. The non-dimensional Navier-Stokes equations, along with the continuity equation are

$$u_{i,t} + u_j u_{i,j} + p_{,i} - \frac{1}{Re} u_{i,jj} = 0 \tag{6}$$

$$u_{i,j} = 0 \tag{7}$$

where x_1=x, x_2=y and x_3=z, u_i is the velocity in the x_i-direction, the subscripts in $f_{,t}$ and $f_{,i}$ represent the derivatives of f with respect to time t and x_i, respectively, and p is the pressure [24]. The Reynolds number is defined as Re=UD/v, where v is the kinematic viscosity of the fluid.

B. Computaitonal domain and boundary conditions

A Cartesian coordinate system was defined with its x-direction being the same as the flow direction and a rectangular computational domain as shown in Fig. 2 is used with the sphere located at the center of the yz-plane.

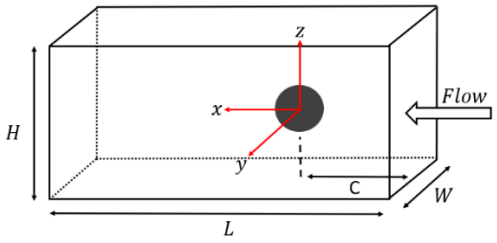

Fig. 2. Numerical Domain

The non-dimensional length, width and height of the domain were 45, 25 and 25, respectively. The sphere was positioned at the origin of the coordinate system, which has a non-dimensional distance of 15 from the inlet boundary, leaving a distance of 30 behind the sphere, which was deemed an acceptable amount of space to capture the wake flow for this study. The inlet boundary on the right side of the domain in Fig. 2 had a non-dimensional velocity of 1. At the outlet boundary, both the pressure and velocity gradients in the x-direction were equal to 0. Symmetrical boundary conditions were added to the remaining 4 domain boundaries so that the

pressure and velocity normal to the boundary were 0. A non-slip boundary condition was added to the surface of the sphere. The velocity on the surface of the sphere was equal to 0 for the non-rotational cases. The velocity at the surface of the rotating sphere was using $U_T = \omega D/2$, where U_T is the tangential velocity on the sphere surface. An example of the rotational case can be seen in Fig. 3 and the equations for the velocity component in the *x*- and *z*-directions on the surface of the sphere can be seen in (8) and (9).

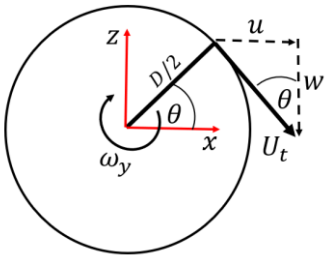

Fig. 3. Velocity at the surface of the rotating sphere

$$u = U_t \sin(\theta) \times \frac{2z}{D} \quad (8)$$

$$w = -U_t \cos(\theta) \times \frac{2x}{D} \quad (9)$$

where, θ is the angular position along the surface of the sphere. A computational time step of 0.0015 was used for each simulation.

C. Mesh

Structured hexahedron finite elements were used for this study with a total node number of 363,000. The thickness of the first layer elements is 0.002. An example of the 3D mesh can be seen in Fig. 4.

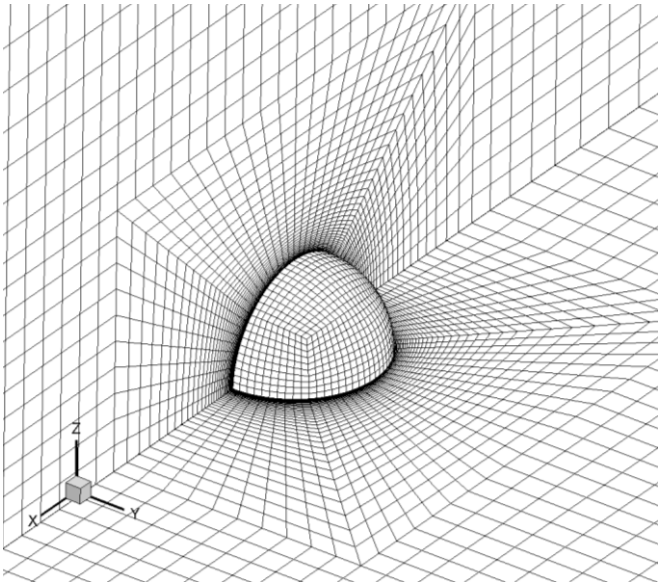

Fig. 4. Three-dimensional isometric view of the structured mesh near the sphere

III. Results and Discussion

A. Validation Study

A validation study was conducted to confirm that the numerical model was accurate in determining drag coefficient for non-rotating cases. Initially, four different Reynolds numbers were tested, two of which were within the intermediate subcritical flow regime. Simulations for *Re* = 1000, 2000, 4000, and 10000 were conducted and the time histories for these simulations can be seen in Fig. 5. The drag coefficient are seen to oscillate because of the turbulent wake flow. The averaged drag coefficients for the four Reynolds number were found to be very close to each other. The results showed that the averaged drag coefficients for *Re* = 1000, 2000, 4000, and 10000 were C_D = 0.484, 0.456, 0.454, and 0.448, respectively, which are in agreement with the published values in 0. The flow visualization in Fig. 6 (a) shows that the flow separation angle is approximately $\emptyset_s = 81°$, which agrees with the published results from [12] and [25], who observed the flow separation point to be $\emptyset_s = 80°$ and $\emptyset_s = 82.5°$, respectively.

The pressure distribution over the surface of the non-rotating sphere can be seen in Fig. 6 (a), where there are symmetrical pressure contours on the upper and lower hemispheres. The symmetrical nature of the low-pressure region around the surface of the sphere is evident in the time histories of the lift and side force coefficients, which had a mean value of zero.

The results from the validation study have been summarized in 0, along with a comparison between published data and that obtained in this study. It is interesting to note the range of results that have been obtained, both experimentally and numerically. The results show that the drag coefficient within the sub-critical flow regime ranges from 0.410 up to 0.505.

Comparison of drag and lift coefficient for flow past a non-rotating sphere with Re = 4000

Re = 4000	**Results**		
	C_D	C_L	$\emptyset_s$ (°)
Present Study	0.454	0.0042	81
Reference [9]	0.505	0.00	-
Reference [15]	0.468	-	-
Reference [25]	0.410	-	82.5
Reference [26]	0.440	-	-

B. Numerical Analysis of flow past a rotating sphere

Numerical analyses were conducted on four different spin parameters *SP* = 0.5, 1, 1.5, 2 and a constant Reynolds number of *Re* = 4000. Spin parameters greater than 2 were not covered in this study as they would require significant refinement of the mesh which would result in larger computational costs. A summary on the numerical simulations can be seen in 0

The results for all the cases outlined in 0 can be seen in Fig. 6 through to 10, where the pressure distribution on the surface of the sphere and streamlines are shown

in (a) and the vorticity in the x-direction is shown in (b). Fig. 6 has been added for reference, where the spin parameter is equal to zero. Observations of Fig. 6 (a) show a symmetrical pressure distribution on the upper and lower hemispheres with somewhat symmetrical vortices forming behind the sphere.

Time histories of the lift and drag coefficients show a cyclic nature as the vortices are shed from the sphere. In Fig. 6 (a) the lower vortex is being shed from the sphere as the upper vortex is forming. It should be noted that the streamlines in Fig. 6 through to 10 have been projected onto the *zx*-plane and are three-dimensional in nature. The vorticity contour plot in Fig. 6 (b) shows the vortices being shed downstream of the sphere in a straight path. This means that the force acting on the sphere as the vortices are shed should have a mean value of zero, since the positive or negative force from a shed vortex would cancel the other out. This was confirmed using the time history plots for forces in the *z*-direction which showed a mean lift coefficient of zero, as can be seen in Fig. 11.

SIMULATION CASES WITH VARIABLE SPIN PARAMETERS

Case	Parameters		
	Re	***SP***	***ω***
1	4000	0.5	0.5
2	4000	1	1
3	4000	1.5	1.5
4	4000	2	2

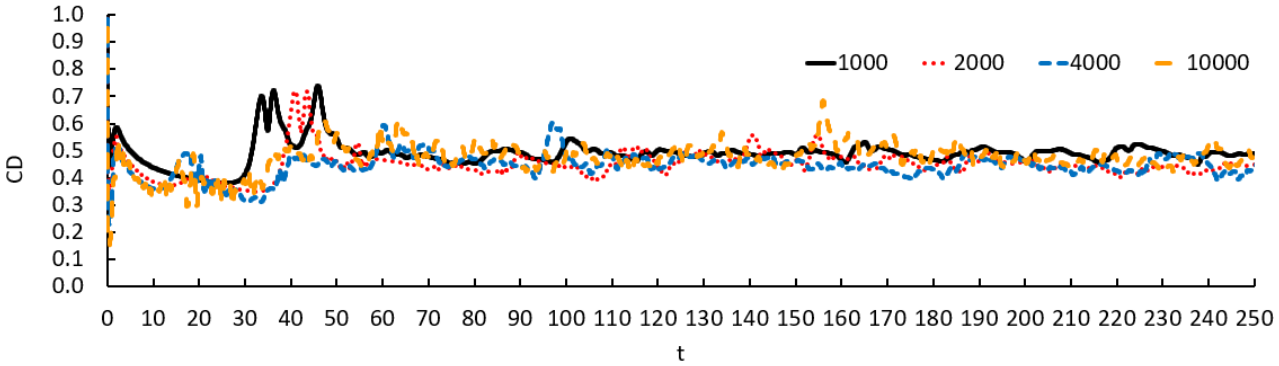

Fig. 5. Time histories of the drag coefficient, C_D, for flow past a stationary sphere for varying Reynolds numbers

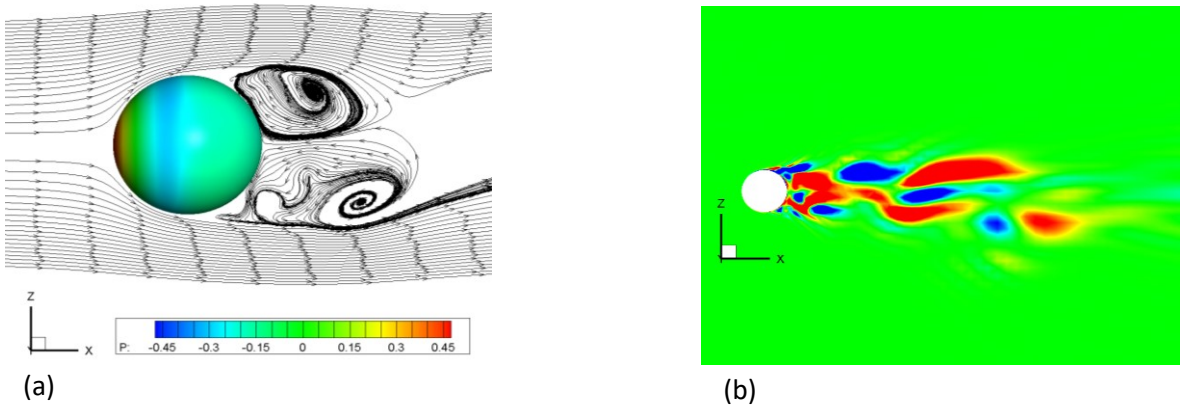

Fig. 6. (a) Surface pressure distribution and streamlines (b) vorticity contour for SP = 0

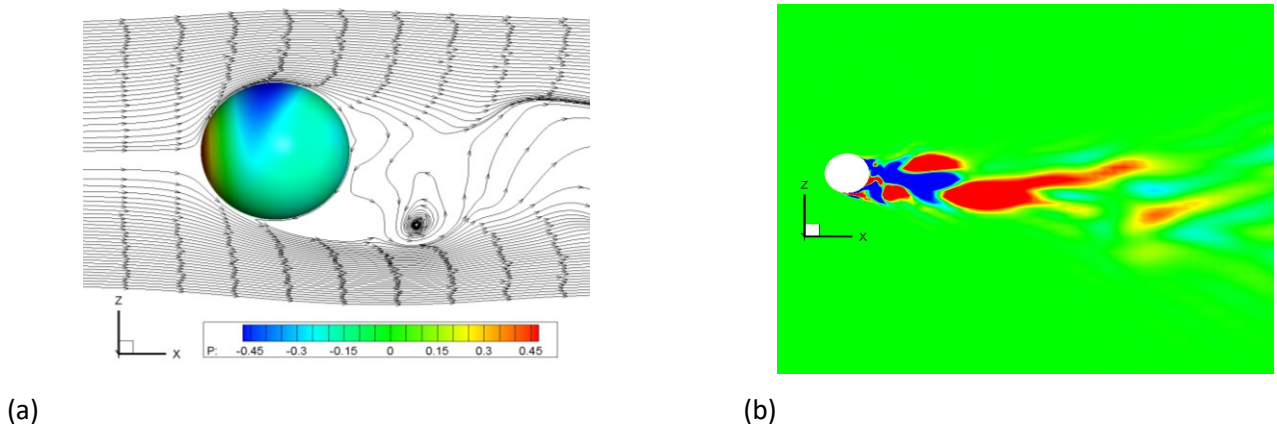

Fig. 7. (a) Surface pressure distribution and streamlines (b) vorticity contour for SP = 0.5

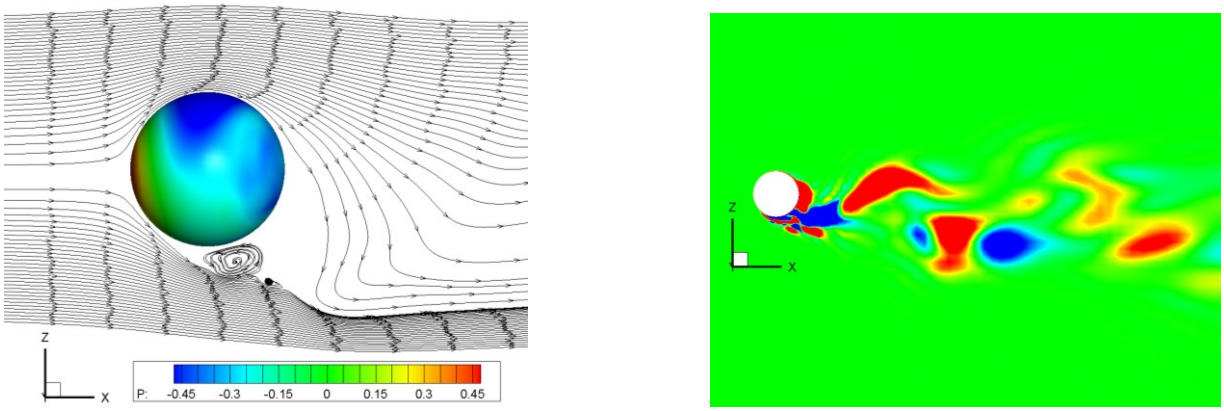

(a) (b)

Fig. 8. (a) Surface pressure distribution and streamlines (b) vorticity contour for SP = 1

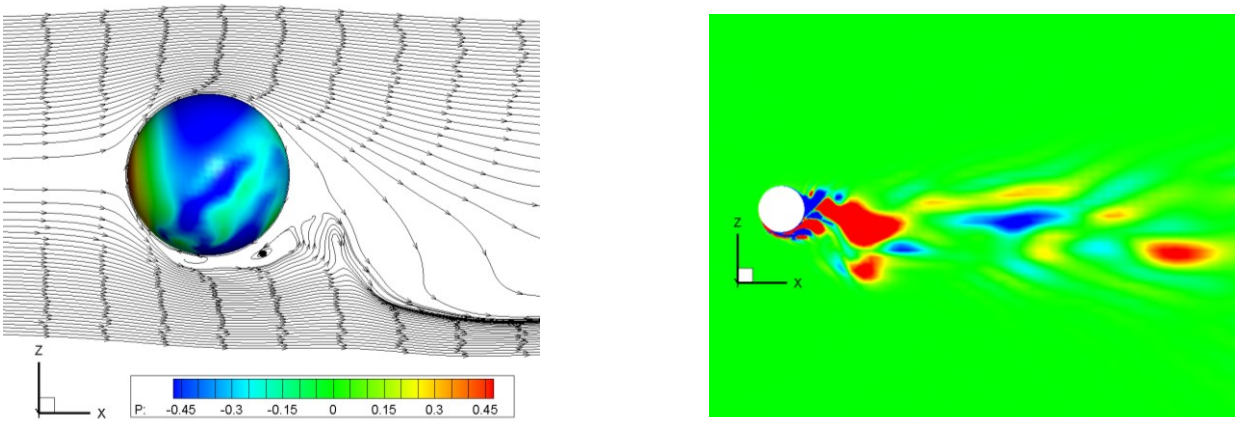

(a) (b)

Fig. 9. (a) Surface pressure distribution and streamlines (b) vorticity contour for SP = 1.5

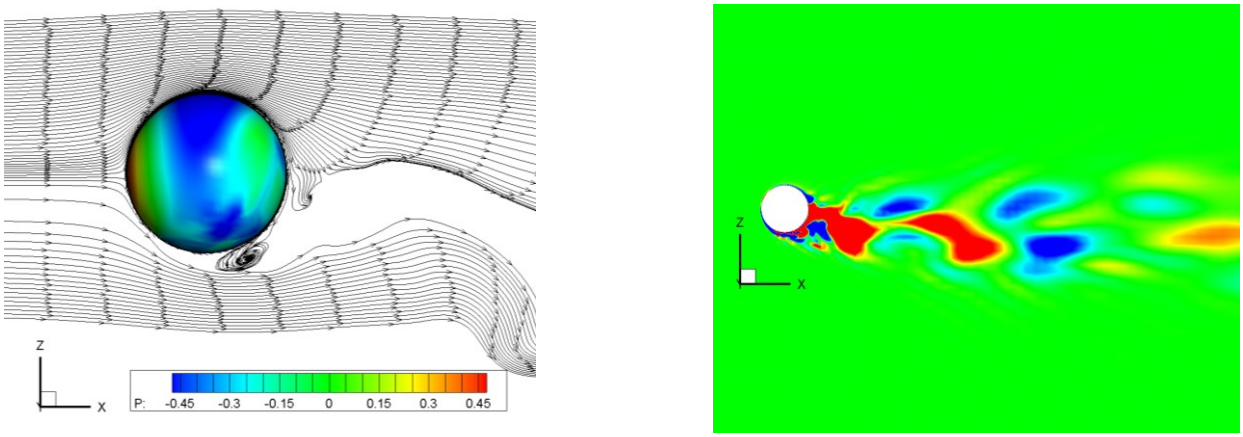

(a) (b)

Fig. 10. (a) Surface pressure distribution and streamlines (b) vorticity contour for SP = 2

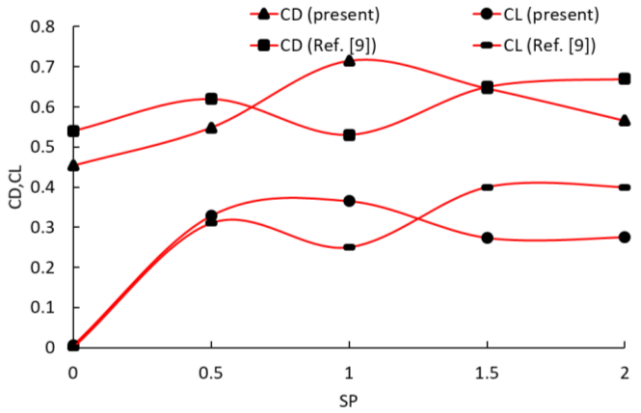

Fig. 11. CD,CL vs SP at Re = 4000 (current) and Re = 25000 (Ref. [9])

The results for a spin parameter of 0.5 can be seen in Fig. 7. Observations of the pressure distribution and the streamlines in Fig. 7 (a) show that the rotational motion significantly alters the fluid past the sphere. In this case, the fluid velocity is accelerated over the top of the sphere, where a lower pressure region is formed on the upper hemisphere of the sphere's surface. The wake flow is no longer symmetrical, but instead it is observed to trend in a negative *z*-direction, which is also confirmed by the vorticity contours in Fig 7 (b). Similar observations are made on Fig. 8 except that the low-pressure region on the upper hemisphere appears to be larger as a result of an increased rotational speed associated with the increased spin parameter. The lift and drag coefficients in Fig. 11 continue to increase up until $SP = 1$, where they then begin to decrease. The critical spin parameter in this study, where $Re = 4000$ is observed to occur at $SP = 1$. A comparison with the results from [9], show that the critical spin parameter was higher for this study when compared to theirs, which used a Reynolds number of 25000. This is in good agreement with the study from [27] which concluded that the critical spin parameter increases with a decrease in Reynolds number.

The reason for the decrease in lift and drag coefficients beyond the critical spin parameter is apparent when looking at Fig. 9 and 10. The streamline and pressure contour plots show that the low-pressure region is now distributed across both the upper and lower hemispheres. The pressure differential between the upper and lower hemispheres that were previously seen in Fig. 6 and 7 is no longer observed to be a strong and hence the cross force is reduced. Observations of the differences between the wake behind the sphere in Fig. 7 and 10 show that the region of turbulence is significantly reduced. A reduction in the wake behind the sphere is seen to significantly reduce the overall drag forces. This is easily explained when considering the reduction in pressure gradients between the front and rear of sphere.

The results from each of the cases have been summarized in 0

SUMMARY OF RESULTS FOR A ROTATING SPHERE

Case	Variables		
	SP	**Mean *CD***	**Mean *CL***
1	0.5	0.512	0.301
2	1	0.706	0.384
3	1.5	0.625	0.296
4	2	0.588	0.298

IV. Conclusion

The flow past a sphere at a Reynolds number of 4000, with a spin parameter ranging from 0 to 2 has been investigated numerically. The three-dimensional Navier-Stokes equations have been solved directly using the Petrov-Galerkin finite element method developed by [24]. The results from this study have shown the following:

(1) The numerical method used for this experiment was validated and able to replicate the published results that have been obtained both experimentally and numerically.

(2) The lift and drag coefficients increased at a linear rate up until a critical spin parameter of 1, where the force coefficients are maximum. The rotational motion from the sphere is seen to accelerate the flow on the upper hemisphere which generates a pressure differential between the upper and lower hemispheres and hence a cross force is created (lift).

(3) Beyond the critical spin parameter of 1, for a Reynolds number of 4000, the wake region behind the sphere is observed to shrink which results in a reduction in drag. The pressure difference between the two hemispheres is observed to reduce and as a result, the lift force is reduced.

Further study in this area is recommend to determine how the flow changes as the spin parameter is increased beyond 2. The hypotheses outlined in this report from [9] would suggest that increasing the spin parameter beyond 2 may result in both the upwind and downwind sides transitioning to turbulent flow. If both sides were to transition to turbulent flow, then there may be changes to the force coefficients too.

Acknowledgment

The authors would like to acknowledge the support from the HPC supercomputer team in Western Sydney University for their assistance in accessing the HPC supercomputer for the numerical simulations.

REFERENCES

[1] Newton, I 1672, *New theory about light and colors*, vol. 61.

[2] Geislinger, TM & Franke, T 2014, 'Hydrodynamic lift of vesicles and red blood cells in flow — from Fåhræus & Lindqvist to microfluidic cell sorting', *Advances in Colloid and Interface Science*, vol. 208, pp. 161-76.

[3] Swanson, WM 1961, *The Magnus Effect: A Summary of Investigations to Date*, vol. 83.

[4] Kray, T, Franke, J & Frank, W 2012, 'Magnus effect on a rotating sphere at high Reynolds numbers', *Journal of Wind Engineering and Industrial Aerodynamics*, vol. 110, pp. 1-9.

[5] Briggs, LJ 1959, 'Effect of Spin and Speed on the Lateral Deflection (Curve) of a Baseball; and the Magnus Effect for Smooth Spheres', *American Journal of Physics*, vol. 27, no. 8, pp. 589-96.

[6] Thomson, R 1966, 'A ball in flight', Education + Training, vol. 8, no. 9, pp. 410-2.

[7] Bordogna, G, Muggiasca, S, Giappino, S, Belloli, M, Keuning, JA, Huijsmans, RHM & van 't Veer, AP 2019, 'Experiments on a Flettner rotor at critical and supercritical Reynolds numbers', *Journal of Wind Engineering and Industrial Aerodynamics*, vol. 188, pp. 19-29.

[8] Li, J, Tsubokura, M & Tsunoda, M 2017, 'Numerical Investigation of the Flow Past a Rotating Golf Ball and Its Comparison with a Rotating Smooth Sphere', *Flow, Turbulence and Combustion*, vol. 99, no. 3, pp. 837-64.

[9] Sareen, A, Zhao, J, Sheridan, J, Hourigan, K, Thompson, M & Lo, D 2019, *FLOW PAST A TRANSVERSELY ROTATING SPHERE*.

[10] Achenbach , E 1972, *Experiments on the flow past spheres at very high Reynolds numbers*, vol. 54.

[11] Jang, YI & Lee, SJ 2007, 'Visualization of turbulent flow around a sphere at subcritical reynolds numbers', *Journal of Visualization*, vol. 10, no. 4, pp. 359-66.

[12] Taneda, S 1978, 'Visual observations of the flow past a sphere at Reynolds numbers between 104 and 106', *Journal of Fluid Mechanics*, vol. 85, no. 1, pp. 187-92.

[13] Yen, C, J Hui, U, Y We, Y, Sadikin, A, Nordin, N, Taib, I, Abdullah, K, Mohammed, AN, Sapit, A & A Razali, M 2017, *Numerical study of flow past a solid sphere at high Reynolds number*, vol. 243.

[14] Yun, G, Kim, D & Choi, H 2006, 'Vortical structures behind a sphere at subcritical Reynolds numbers', *Physics of Fluids*, vol. 18, no. 1, p. 015102.

[15] Hassanzadeh, R, Sahin, B & Ozgoren, M 2011, 'Numerical investigation of flow structures around a sphere', *International Journal of Computational Fluid Dynamics*, vol. 25, no. 10, pp. 535-45.

[16] Seidl, V, Muzaferija, S & Perić, M 1997, 'Parallel DNS with Local Grid Refinement', *Applied Scientific Research*, vol. 59, no. 4, pp. 379-94.

[17] Tiwari, SS, Pal, E, Bale, S, Minocha, N, Patwardhan, AW, Nandakumar, K & Joshi, JB 2019, 'Flow past a single stationary sphere, 2. Regime mapping and effect of external disturbances', *Powder Technology*.

[18] White, FM 2011, *Fluid Mechanics*, McGraw Hill.

[19] Sakamoto, H & Haniu, H 1990, 'A Study on Vortex Shedding From Spheres in a Uniform Flow', *Journal of Fluids Engineering*, vol. 112, no. 4, pp. 386-92.

[20] Liu, L, Yang, J, Lu, H, Tian, X & Lu, W 2019, 'Numerical simulations on the motion of a heavy sphere in upward Poiseuille flow', *Ocean Engineering*, vol. 172, pp. 245-56.

[21] Davies, JM 1949, 'The Aerodynamics of Golf Balls', *Journal of Applied Physics*, vol. 20, no. 9, pp. 821-8.

[22] Štěpánek, An 1988, *The aerodynamics of tennis balls-The topspin lob*, vol. 56.

[23] Robinson, G & Robinson, I 2013, 'The motion of an arbitrarily rotating spherical projectile and its application to ball games', *Physica Scripta*, vol. 88, no. 1, p. 018101.

[24] Zhao, M, Cheng, L & Zhou, T 2009, 'Direct numerical simulation of three-dimensional flow past a yawed circular cylinder of infinite length', *Journal of Fluids and Structures*, vol. 25, no. 5, pp. 831-47.

[25] Achenbach, E 1974, 'Vortex shedding from spheres', *Journal of Fluid Mechanics*, vol. 62, no. 2, pp. 209-21.

[26] Constantinescu, GS & Squires, KD 2003, 'LES and DES Investigations of Turbulent Flow over a Sphere at Re = 10,000', *Flow, Turbulence and Combustion*, vol. 70, no. 1, pp. 267-98.

[27] Kim, J, Choi, H, Park, H & Yoo, JY 2014, 'Inverse Magnus effect on a rotating sphere: when and why', *Journal of Fluid Mechanics*, vol. 754, p. R2.

Flow control using a rotating control rod to delay airfoil stall

Michael Fernandez *
School of Computing, Engineering, and Mathematics
Western Sydney University
Kingswood 2747, Australia

Ming Zhao
School of Computing, Engineering, and Mathematics
Western Sydney University
Kingswood 2747, Australia

Benjamin Curtis
School of Computing, Engineering, and Mathematics
Western Sydney University
Kingswood 2747, Australia

***Abstract*— The effectiveness of flow control on the aerodynamic performance of an S809 wind turbine airfoil using a rotating control rod is numerically investigated for a constant Reynolds number of 1×10^6. The effectiveness of non-rotating and rotating control rods in delaying flow separation and improving the lift coefficient of the airfoil is compared. The numerical results showed that passive flow control using a non-rotating rod effectively improved the aerodynamic performance of the airfoil for attack angles between 12° and 19.5°, with the maximum increase in lift found at an attack angle of β=15°. Through further numerical analyses of flow past an airfoil with a rotating rod with a non-dimensional rotation speed of 3, it was concluded that the clockwise-rotating rod effectively suppressed flow separation for attack angles between 0° and 25.5°. The maximum lift coefficient of 2.055 was found at an attack angle of β=15°, and the greatest increase of 109% at β=24°, from 0.872 to 1.825.**

Keywords — Airfoil, Stalling, Flow Control, Flow separation

I. INTRODUCTION

The study of the relative motion between air flow and stationary or moving objects, and the associated forces is a referred to as aerodynamics [1]. This branch of fluid mechanics has long been utilised in the aeronautical industry, wind energy generation, and car racing to name a few. Each industrial application of aerodynamics involves the use of one or more airfoils to produce force in the perpendicular direction to fluid flow, known as lift force. In the aeronautical industry, aircrafts make use of multiple airfoils in succession to improve the lift capabilities of the aircraft's wings; in contrast to race car wings to produce a downward lift force known as downforce. Additionally, the ability of wind turbines to efficiently absorb power from the forces generated by its blades is significantly influenced by the underlying aerodynamic performance of the wind turbine blade airfoils [2].

An airfoil's performance is measured by its ability to produce high lift forces without a significant increase in drag force. An airfoil's attack angle – its chord inclination with respect to incoming flow – is often altered to produce varying lift and drag forces [3]. As the attack angle is increased beyond a certain inclination, a phenomenon known as airfoil stalling occurs, resulting in significant reductions in lift forces and subsequent increases in drag, as well as wildly unpredictable aerodynamic performance, rendering the airfoil somewhat useless.

In a 2017 report by the Aircraft Owners and Pilots Association, it was identified that 10% of all non-commercial aircraft accidents between 2000 and 2014 resulted from unintended stall, which also accounted for almost 24% of all fatal accidents in the same period [4]. Stalling of wind turbine blade airfoils significantly reduces the lift forces generated and thus a loss in power generation results. Current and previous research in the field of aerodynamics therefore focuses heavily on methods of preventing airfoil stall for a variety of industrial applications

The detachment of fluid particles from the airfoil surface, known as flow separation, is a primary cause of stalling, due to an intense adverse pressure gradient causing the velocity of air in the boundary layer to reduce to zero [5-7]. Increasing the attack angle further results in the velocity of these boundary layer particles changing direction, generating a separation bubble, and inciting the development of vortices downstream of the point of flow separation.

As these vortices continue to develop and detach they impose an oscillating force on the airfoil, potentially causing excessive vibrations and noise, ultimately reducing its ability to generate lift [8]. Numerous authors have studied airfoil performance under stall conditions finding unpredictable and unstable results where lift and drag forces follow a non-linear and stochastic process [9; 10].

The study of flow control devices (FCDs) for airfoils has become particularly important of late. The common operating principle amongst both active and passive FCDs is their reliance on disturbing the fluid velocity in the boundary layer to increase turbulence, ultimately reducing the flow separation caused by the adverse pressure gradient [11; 12]. An extensive amount of literature exists regarding the use of static control rods as passive flow control devices to delay flow separation and increase the critical stall angle of airfoils. Shi et al. [2] found a static microcylinder placed close to an airfoil's leading edge effectively suppressed flow separation and delayed the critical stall angle, up to 22°. Luo, Huang and Sun [13] conducted a similar analysis and determined that a control rod with a diameter of 10% of the airfoil chord length effectively suppressed flow separation to improve airfoil performance. Burnazzi and Radespiel [14] concluded that the use of passive FCDs such as leading-edge slats significantly improved the pressure distribution over the airfoil surface and enhanced both the maximum lift coefficient and stall angle. These passive devices tend to increase boundary layer turbulence and velocity, opposing the effects of the adverse pressure gradient along the surface of the airfoil. These combined affects assist in maintaining flow attachment and thus improve airfoil aerodynamic performance.

The aforementioned studies focused heavily on passive flow control, rather than active devices. However, active flow control devices in the form of rotating cylinders have been extensively studied regarding their effectiveness in reducing flow induced vibration (FIV) on larger cylinders for applications such as sub-sea pipelines [15]. Of particular

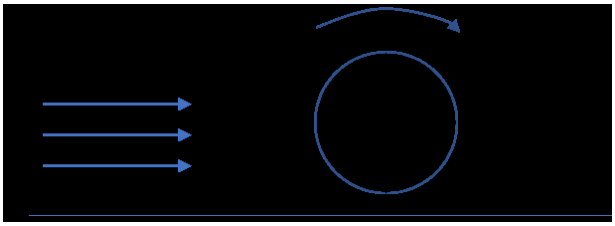

interest to this study is the use of moving boundaries and rotating circular cylinders to reduce or prevent a specific type of FIV, namely Vortex-induced Vibration (VIV). As fluid passes over a bluff body such as a circular cylinder or an airfoil at high attack angles, flow separation induces vortices in the wake of the object. As the fluid continues to flow, new vortices form, and the previous ones shed from the body's surface in an oscillatory fashion forming what is known as the Karmen Vortex Street [16-19].

Rotating cylinders have been analysed as a method of flow control using a moving boundary in close proximity to a larger object to suppress the vibrations produced by the shedding of vortices downstream of that object. Wang, Xu and Tian [18] found that this moving boundary had the influence of providing additional momentum into the region of flow separation, assisting the fluid particles in the boundary layer in travelling in the forward direction, thus counteracting the effects of the adverse pressure gradient. Rao et al. [20] found that vortex shedding can be suppressed when a control cylinder near a stationary wall is rotating in the same direction as the fluid flow as depicted in Fig. 1, up to a speed of $\alpha = 3$. The non-dimensional rotation speed is defined as:

$$\alpha = \frac{\omega D}{2U} \tag{1}$$

and ω, D and U refer to the angular velocity of the cylinder, the cylinder's diameter, and the incoming fluid velocity respectively.

Mittal and Kumar [16] used the same dimensionless rotational velocity shown in (1) and successfully suppressed vortex shedding in the range $1.91 \leq \alpha \leq 4.34$. The suppression of vortex shedding in each of these studies also resulted in a reduction in the total drag force of the larger cylinder, and in some cases provided additional lift [18].

It is evident that current studies in the realm of flow control around airfoils lack investigation into the effects of active FCDs in the form of rotating control rods in delaying or preventing flow separation and increasing the critical stall angle. Consequently, there is little understanding of the influence a moving boundary in close proximity to the leading edge of an airfoil on its aerodynamic performance at large attack angles. This study aims to incorporate findings from passive flow control around airfoils, and the use of rotating cylinders to suppress vortex induced vibrations, to analyse the effectiveness of rotating control rods for stalled airfoils. This study will focus on furthering the findings from Shi et al. [2] by analysing the performance of an S809 wind turbine blade airfoil with active flow control, to determine if a greater stall angle and maximum lift coefficient can be achieved when compared to the use of a static control rod for the same airfoil.

II. NUMERICAL METHOD

A. Problem Defintion

The aerodynamic performance of an S809 wind turbine airfoil is numerically analysed with passive and active flow control, in the form of a static or rotating microcylinder placed in close proximity to the airfoil's leading edge. A range of attack angles are analysed from 0° to 27°. In the following discussion, the attack angle is defined as β. A non-dimensional chord length of 1 is used for airflow at a Reynolds number of 1×10^6, where:

$$Re = \frac{\rho U c}{\mu}$$

and ρ, U, and μ represent the air density, velocity, and dynamic viscosity respectively, and c represents the airfoil chord length. A control rod of diameter 1.8% of the airfoil chord length is placed upstream and above the airfoil leading edge by $0.02c$ in the x-direction, and $0.04c$ in the y-direction. Previous studies have determined these sizes and spacings for a static control rod provide the optimal improvements in airfoil performance [2; 13]. The airfoil performance is evaluated through the analysis and comparison of lift and drag coefficients with existing experimental data for the S809 airfoil available from Hand et al. [21].

B. Governing Equations and Numerical Model

The unsteady Reynolds-Averaged Navier-Stokes (RANS) equations are solved for simulating the flow. For the purposes of this study, modelling fluid flow past an S809 wind turbine blade airfoil is simplified to ignore thermal energy transfer and thus the flow is considered to be incompressible and this turbulence model is suitable. The flow is assumed to be low speed incompressible flow. The non-dimensional variables in this study are given by $x = x'/c$, $y = y'/c$, $u = u'/U$, $v = v'/U$, $t = t'c/U$, where x and y are coordinates in the streamwise and cross-flow directions, respectively, u and v are the non-dimensional velocities in the x and y-directions, respectively, U is the incoming flow velocity, and t is the time. The variables with and without a prime stand for non-dimensional and dimensional values, respectively. The non-dimensional Navier-Stokes equations, along with the continuity equation are:

$$\frac{\partial u_i}{\partial t} + u_j \frac{\partial u_i}{\partial x_j} = -\frac{\partial}{\partial x_i}\left(p + \frac{2}{3}k\right) + \frac{\partial}{\partial x_i}\left(\frac{1}{\mathrm{Re}}\frac{\partial u_i}{\partial x_j} + 2\nu_t S_{ij}\right) \tag{2}$$

$$\frac{\partial u_i}{\partial x_i} = 0 \tag{3}$$

where x_1=x, x_2=y, u_i is the velocity in the x_i-direction, S_{ij} is the mean strain rate tensor, ν_t is the turbulent viscosity and k is the turbulent energy

There has been an overwhelming response in previous studies to the use of the unsteady Reynolds-averaged Navier-Stokes solving method in conjunction with the k-ω SST turbulence model in obtaining the most accurate solution to 2D simulations of airfoil performance [22-24; 2]. In their 2010 study, Wang et al. [24] concluded the shear stress transport (SST) k-ω model was the preferred turbulence model for studying stalling conditions of the NACA 0012 airfoil. Therefore, the shear-stress transport (SST) k-ω

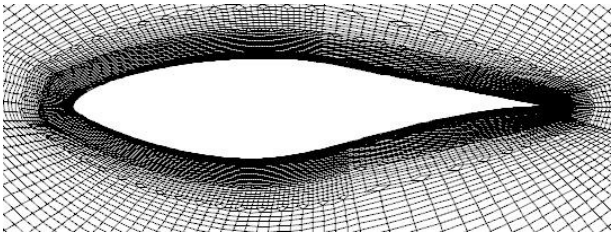

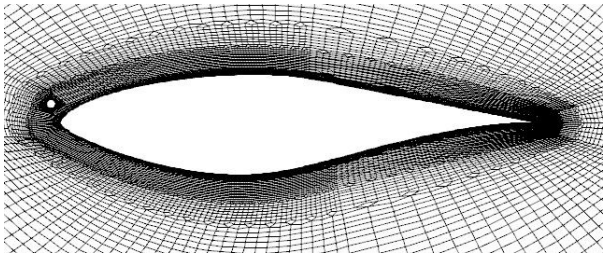

turbulence model was used with a structured mesh in this study.

C. *Boundary Conditions*

A rectangular fluid domain is used and its non-dimensional lengths in the flow and cross-flow directions are 60 and 40 respectively. The inlet is 20*c* upstream of the leading edge of the airfoil. Wang et al. [24] reported that a fluid domain with at least 20*c* upstream of the airfoil leading edge, as well as above and below, and at least 40*c* downstream is necessary. The domain size used in this study meets the above requirement. Non-slip boundary conditions are applied to the airfoil and control rod surfaces, and free-slip conditions applied to the top and bottom edges of the fluid domain, and the non-dimensional inlet velocity is 1. At the outlet boundary, the pressure is zero.

D. *Validation Study*

The Reynolds-Averaged Navier-Stokes equations are solved using a finite element method (FEM) code developed by the second author of this paper [25]. Fig. 2 shows the computational mesh near the airfoil and the control rod.

The computational model is extensively detailed and validated by Zhao et al. [25] for the analysis of the hydrodynamic forces on two cylinders of different diameters. To further validate the, flow past an S809 airfoil at $Re = 10^6$ was simulated with no form of flow control, at a range of attack angles. The obtained numerical results are compared to experimental results documented by Hand et al. [21]. The results show positive alignment between existing experimental data and the present numerical results. The model is therefore suitable for this study.

III. Results and Discussion

A. *Non-rotating control rod*

The aerodynamic performance of an S809 airfoil was examined with and without the use of a static control rod flow

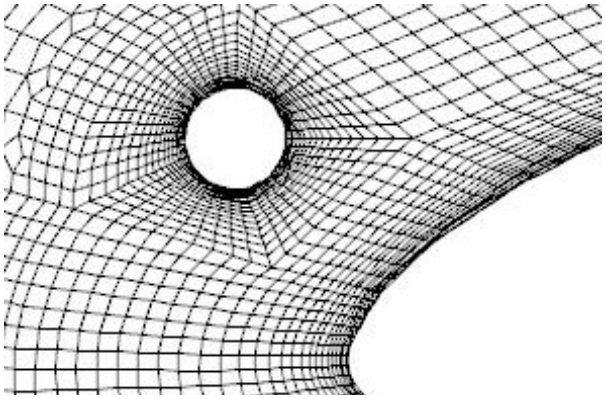

control device. The numerical results presented in the *Validation Study* section of this paper served as the lift and drag coefficient benchmarks to which the airfoil's performance with a passive FCD could be compared against. The meshes used for these benchmark simulations were modified to include the control rod as shown in Fig. 3.

Inflation layers were applied to the cylinder boundary and the mesh refined between the two bodies to accurately capture the flow behaviour in this region.

For the range of attack angles analysed, the use of a static control rod resulted in higher lift coefficients for angles between 12° and 19.5°, with the maximum increase seen at 15°. In all cases, the presence of the control rod near the airfoil leading edge also returned higher drag coefficients, simply due to the additional body in the path of fluid flow. Fig. 5 details the results of the comparative analysis between the S809 airfoil with and without a passive FCD.

It can be seen that the control rod provided little to no benefit at angles below 10°. However, beyond this it enabled the airfoil to achieve higher lift coefficients where it would otherwise begin to reduce as it approaches stalling. Further

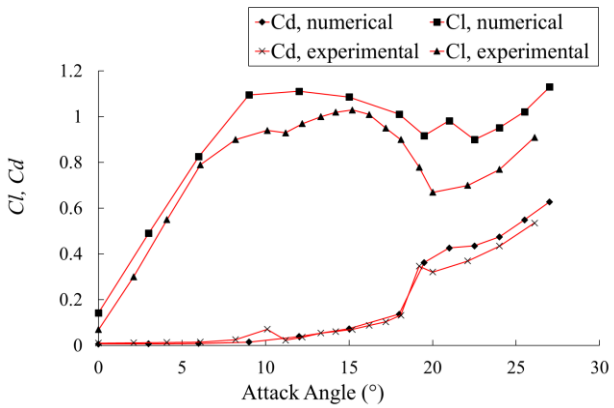

Fig. 5 Comparison of numerically obtained lift and drag

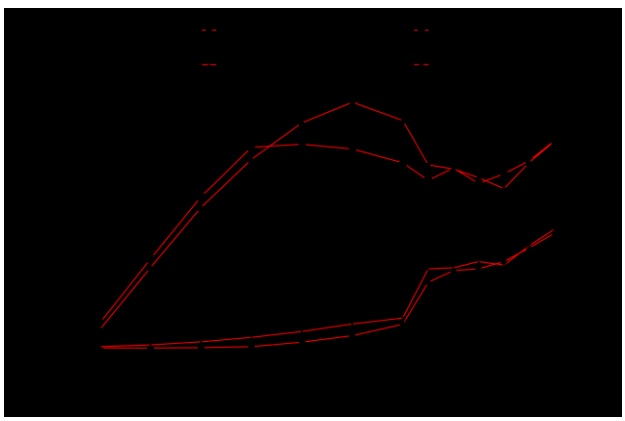

Fig. 4 Lift and drag coefficients with and without a stationary

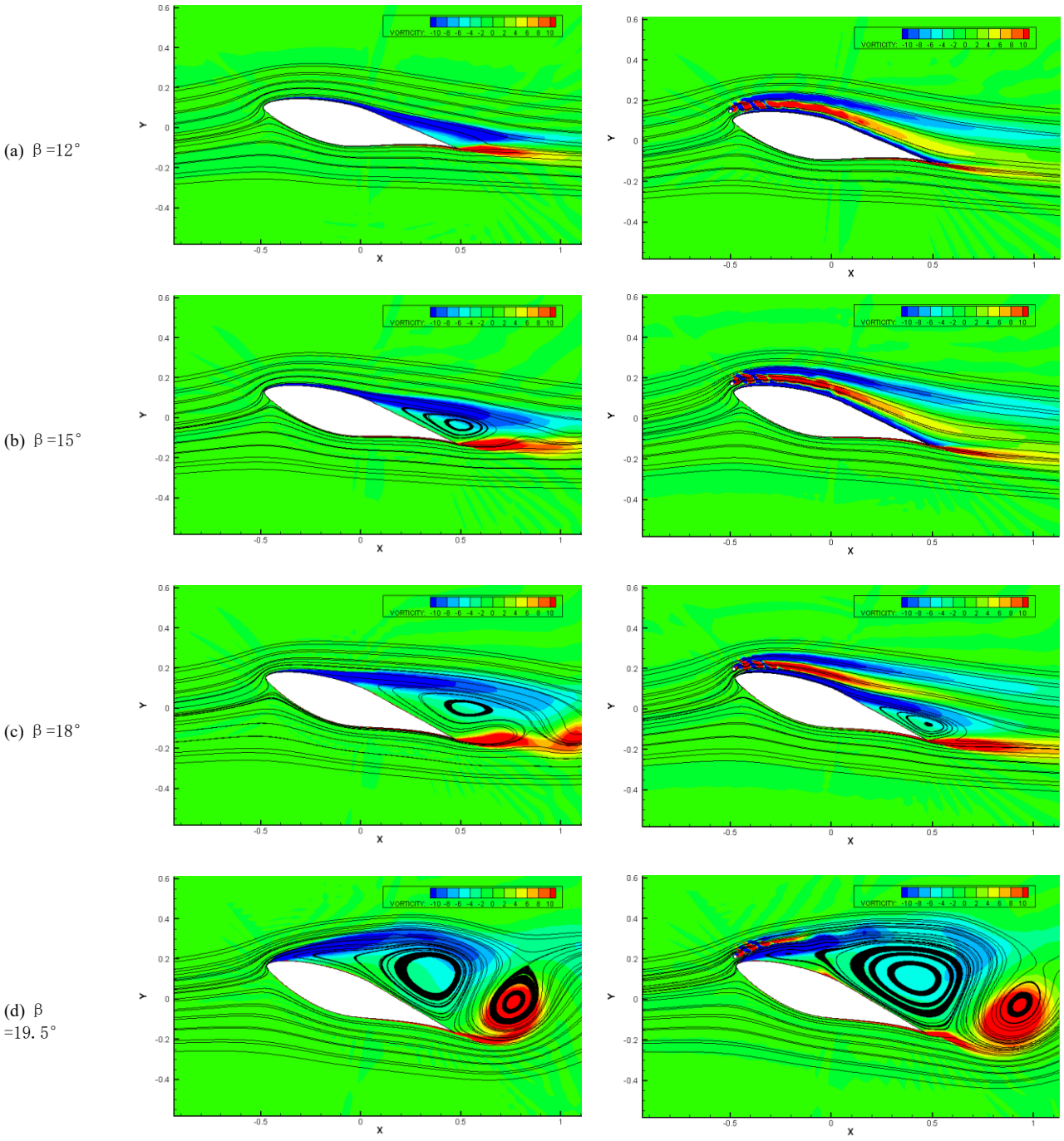

Fig. 6 Velocity streamlines and vorticity for flow past an airfoil with and without a non-rotating control rod for β =12° to 19. 5°

inclination beyond 19.5° shows the airfoil to begin to stall resulting in a sudden increase in drag and subsequent decreases in lift. This phenomenon is well reflected by the streamlines of velocity as well as vorticity for attack angles 12°, 15°, 18° and 19.5°. Minimal flow separation is seen at 12° and 15° in Fig. 6 (a) and (b). In Fig. 6 (c) greater flow separation can be seen when the airfoil reaches 18°. Lastly, the greatest separation is seen at 19.5° in Fig. 6 (d) where stalling is evident. In each of these cases however, the control rod has a significant influence on the degree to which the airflow is able to detach from the suction surface of the airfoil.

Flow separation is greatly reduced in the first three configurations when the control rod is introduced, as well as a significant improvement in flow vorticity. At attack angles lower than 19.5° the control rod has the effect of disturbing the incoming air flow near the airfoil leading edge by increasing its velocity in the airfoil's boundary layer as it passes between the two solid bodies. As previously mentioned, this increased velocity opposes the adverse pressure gradient. Consequently, the point of flow separation in each configuration below 19.5° is seen to move toward the trailing edge of the airfoil. This reduction in flow separation is the primary cause for an increase in lift found when a control rod is used. Although there is also a slight increase in drag due to the presence of the control rod and the vortex shedding caused by its vibration in the air flow, this drag increase is relatively minor in comparison to the gains in lift.

Ultimately, the control rod was found to improve the airfoil's lift to drag ratios for attack angles between 12° and 19.5°. The highest lift coefficient of 1.34 was obtained at 15° with the control rod, as opposed to 1.09 without any flow control.

The effects of the static control rod diminish however when the airfoil reaches an attack angle of 19.5°, also evident in the lift and drag coefficients depicted in Fig. 4. As the airfoil's inclination is increased further resulting in greater stalling, the point of flow separation moves too close to the airfoil leading edge for the control rod to remain effective. The stationary boundary of the cylinder is unable to adequately disturb the boundary layer flow and provide a large enough increase in fluid velocity in this region to overcome the adverse pressure gradient and maintain flow attachment. As shown in Fig. 4, there is almost no gain in lift in this configuration, although there is a significant increase in drag due to the presence of an additional body as well as the effects of cylinder vibration and airfoil stalling.

B. Rotating control rod

To analyse the effectiveness of the rotation of the control rod on improving aerodynamic performance of the S809 airfoil, the control rod was given a non-dimensional rotational speed of α=3. As previously mentioned, Mittal and Kumar [16] successfully suppressed vortex shedding behind a rotating cylinder for $1.91 \leq \alpha \leq 4.34$. A preliminary analysis at an attack angle of 18° concluded that clockwise rotation of the control rod proved to be beneficial to the airfoil performance and effectively suppressed flow separation. In contrast, counter-clockwise rotation had a negative effect on the airfoil performance as it significantly increased the vibration of the control rod. These vibrations resulted in the development of additional vortices behind the cylinder, and a large increase in flow separation from the airfoil suction surface. The lift and drag coefficients of the airfoil in this configuration were wildly unpredictable and a stable solution was unable to be obtained. The resultant velocity streamlines and vorticity for counter-clockwise and clockwise rotation at 18° attack angle are shown in Fig. 8 and **Fig. 7** respectively.

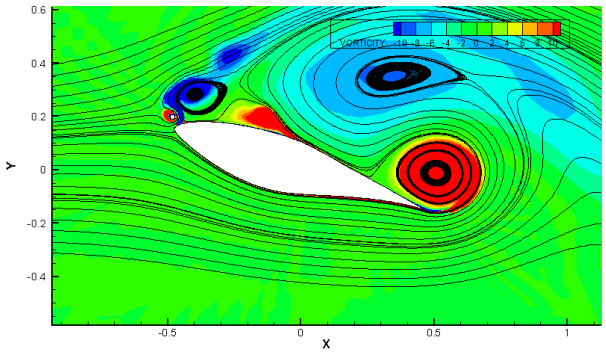

Fig. 8 Velocity streamlines and vorticity at β=18° with a

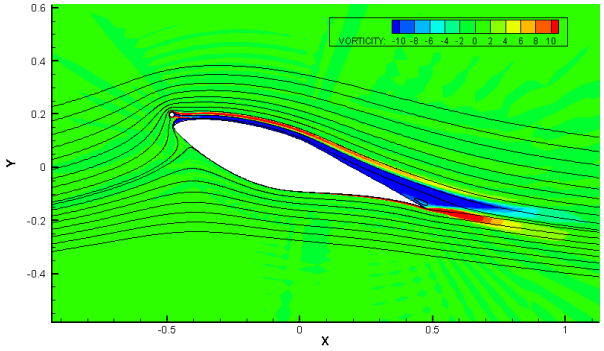

Fig. 7 Velocity streamlines and vorticity at β=18° with a clockwise rotating control rod at α = 3

The clockwise rotation of the control rod however was shown to significantly improve the flow over the airfoil, and almost no flow separation is evident as shown in **Fig. 7**. The streamlines of velocity also remain smooth over the entire suction surface of the airfoil, particularly so when this configuration is compared to the use of a static control rod at 18° as shown in Fig. 6 (c) and Fig. 11 (b). In addition to improvements in flow attachment and the smoothness of the velocity streamlines, the clockwise rotation also resulted in a significant reduction in vortex shedding behind the cylinder. With the control rod rotating in the clockwise direction, the boundary nearest to the airfoil opposed the fluid velocity and had the effect of slowing these particles and pushing them toward the airfoil surface. Ultimately this ensured the flow remained attached to the airfoil, and an increased lift coefficient of 2.06 was found in this configuration. Additionally, the coefficient of drag was reduced from 0.14 for the static control rod, to 0.01 for clockwise rotation.

A clockwise-rotating control rod was analysed for attack angles in the range of β=0° to 25.5° to determine if these effects could be further replicated and delay stalling of the airfoil. In each case, the control rod consistently decreased the total drag coefficient, and a subsequent increase in lift was found as shown in Fig. 9. For attack angles between 0° and 9°, a small yet consistent lift increase is evident. Beyond 9° however, a significantly higher coefficient of lift is obtained compared to a non-rotating rod. This, combined with a reduction in drag for all angles, resulted in an increased lift to drag ratio for each case where a clockwise rotating control rod is present. The greatest increases in lift were found at attack angles of 22.5° and 24°, increasing by 99% from 0.932 to 1.856 for 22.5°, and 109% from 0.872 to 1.825 for 24°. The resultant velocity streamlines and vorticity for each angle tested are presented in Fig. 10 and Fig. 11 in the following pages, illustrating the effectiveness of a non-rotating and rotating control rod in suppressing flow separation and delaying stalling .

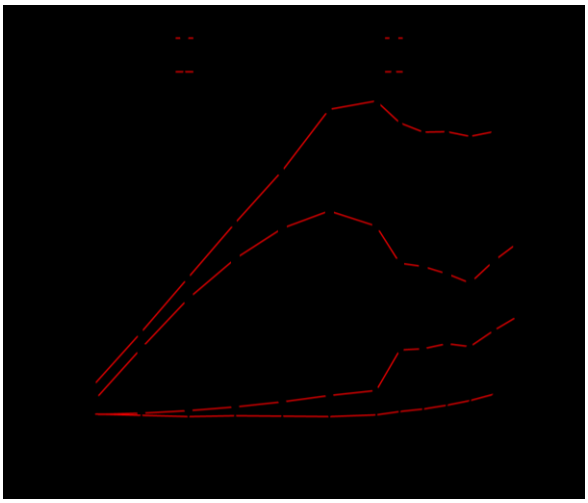

Fig. 9 Lift and drag coefficients with a non-rotating and rotating

(a) β=3°

(b) β=6°

(c) β=9°

(d) β=12°

(e) β=15°

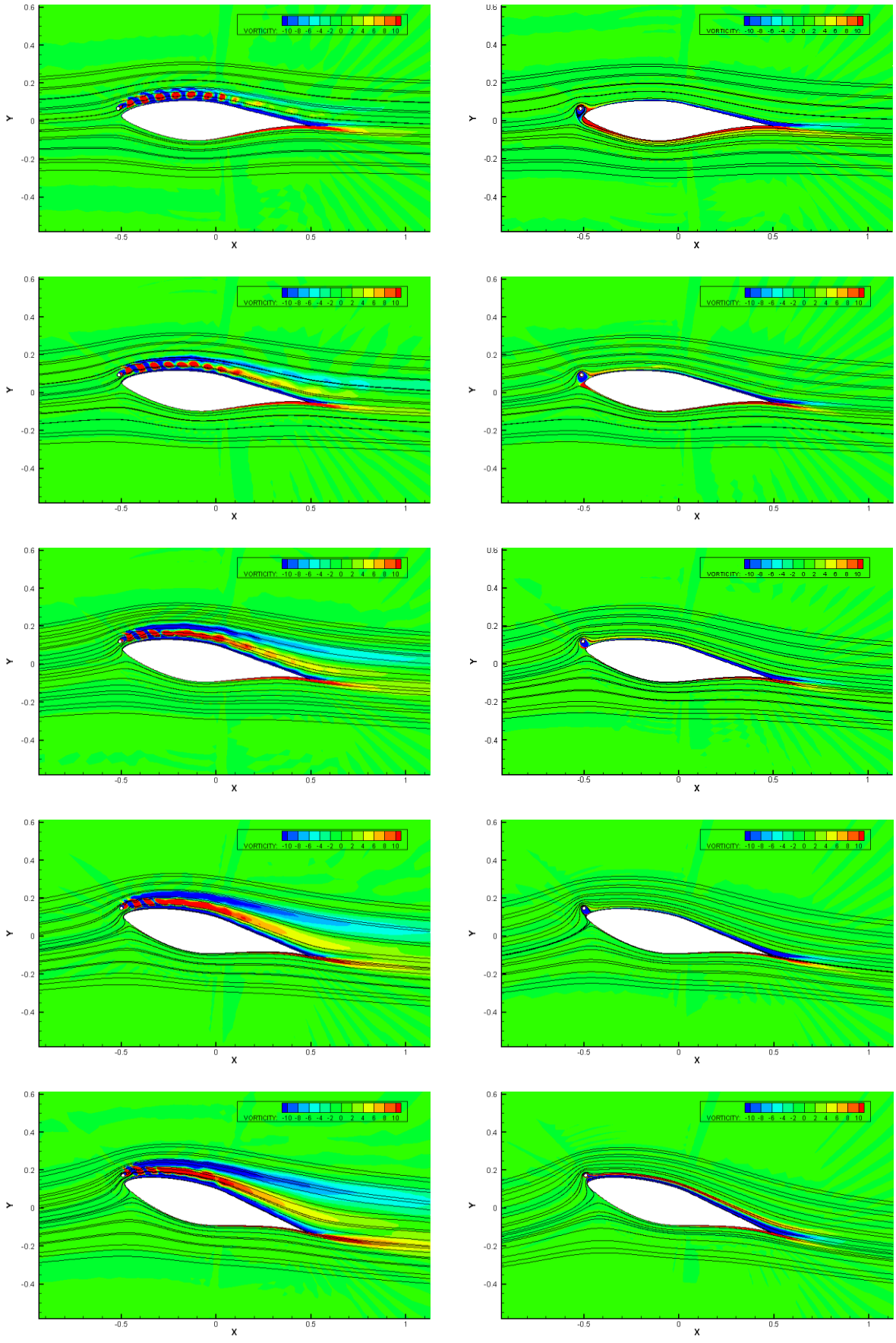

Fig. 10 Velocity streamlines and vorticity for flow past an airfoil with a non-rotating control rod and with a rotating control rod for β=3° to 15°

(a) β=18°

(b) β=21°

(c) β=22.5°

(d) β=24°

(e) β=25.5°

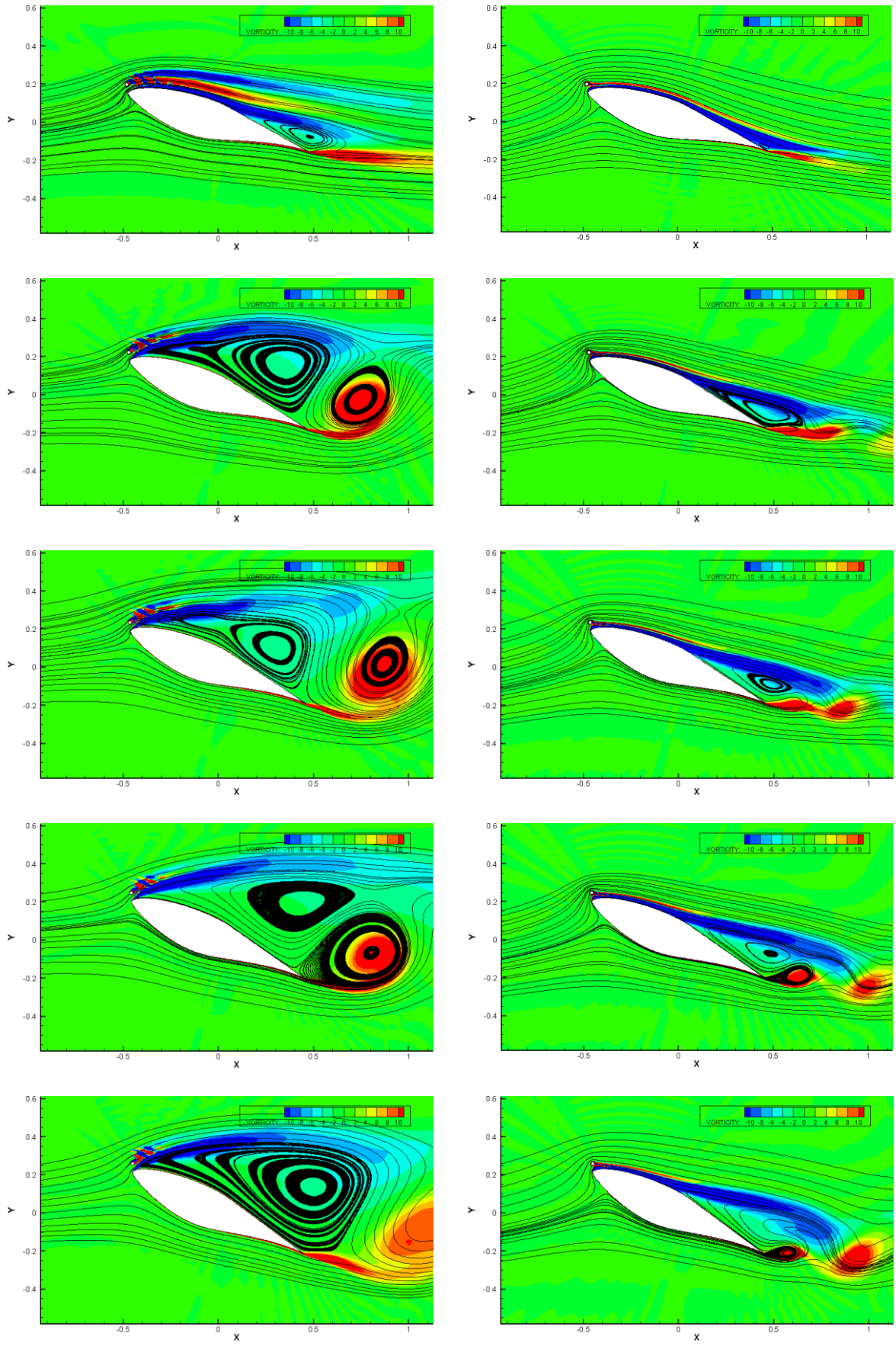

Fig. 11 Velocity streamlines and vorticity for flow past an airfoil with a non-rotating control rod and with a rotating control rod for β=18° to 25.5°

With a non-rotating control rod at attack angles of 18° and 21° as shown in Fig. 11 (a) and (b) the airfoil is seen to begin to stall, and large flow separation bubbles are evident. The use of a rotating control rod at these same angles sees the point of flow separation move toward the airfoil trailing edge and thus the streamlines remain attached to the airfoil upper surface for a longer period of time before detaching. As the airfoil is inclined past 21° the rotating rod continues to suppress flow separation, although its effectiveness is gradually reduced at higher attack angles. This is well reflected in Fig. 9 where the lift coefficient with the rotating rod decreases slower with increasing attack angles, than it does with the use of a non-rotating rod. However, in all cases the rotation of the control rod successfully suppressed the generation of vortices behind the cylinder, contributing the the reduced drag coefficient in each case. The flow therefore remains attached to the airfoil for longer in each configuration, producing higher lift coefficients and therefore lift to drag ratios.

IV. Conclusion

An S809 wind turbine airfoil was investigated at a range of attack angles, with and without passive and active flow control for a Reynolds Number of 10^6. A static circular cylinder placed in close proximity to the airfoil leading edge was used as a form of passive control, and a non-dimensional rotation of $\alpha = 3$ applied to the cylinder to represent an active flow control rod. A static control rod was shown to improve the aerodynamic performance of the airfoil for attack angles between 12° and 19.5°, with the greatest improvement in lift to drag ratio found at 15°. Beyond an attack angle of 19.5° the airfoil stalling became too great for the control rod to overcome and was no longer effective in reducing the size of the flow separation bubble. Beyond this inclination the static control rod made little to no improvement on the airfoil's aerodynamic performance.

Counter-clockwise rotation of the control rod was found to be detrimental to the lift capabilities of the airfoil in this configuration. Additional vortices were developed in the wake of the cylinder due to its increased vibration, imposing greater oscillating forces on the airfoil resulting in unpredictable lift and drag properties. However, with the control rod rotating in the clockwise direction, flow separation was almost suppressed entirely for an attack angle of 18° and streamlines of velocity were completely smooth along the length of the airfoil.

A clockwise-rotating control rod at α=3 was therefore analysed for attack angles from 0° to 25.5°. In all configurations the control rod rotating in this fashion reduced its vibration and thus vortex shedding in the wake of the cylinder was significantly reduced. The moving boundary of the control rod had the effect of slowing the fluid particles between the rod and the airfoil as they were about to detach from the suction surface. Flow separation was effectively suppressed in all configurations analysed and the velocity streamlines remained smooth and attached to the airfoil for angles up to and including 18°. Beyond 18°, the rotating control rod continued to remain effective in enhancing flow attachment and had the effect of moving the point of flow separation toward the trailing edge of the airfoil. Reduced drag coefficients were found at all attack angles, as well as greater lift coefficients when compared to the non-rotating control rod. The maximum lift coefficient of 2.055 was found at an attack angle of 18°, as opposed to the maximum of 1.341 at 15° with a non-rotating rod. The greatest lift increase with a clockwise-rotating rod was by 109% at 24°. The clockwise rotating cylinder therefore provided the greatest improvement to the aerodynamic performance of the S809 airfoil.

The results of this study well reflected the literature regarding the use of a static flow control device to improve the lift capabilities of an S809 airfoil. Additionally, the suppression of vortex shedding behind a rotating cylinder was effectively replicated when using a moving boundary for active flow control purposes. This study was limited in the analysis of active flow control to a single non-dimensional rotational speed of α=3. Further studies should be conducted to analyse the influence of active flow control for a wider range rotational speeds to ultimately determine if the effectiveness of a rotating control rod can be further improved.

Acknowledgment

The authors would like to acknowledge the support from the HPC supercomputer team in Western Sydney University for their assistance in accessing the HPC supercomputer for the numerical simulations.

References

[1] Watkinson, J 2016, *Aerodynamics*, American Institute of Aeronautics and Astronautics.

[2] Shi, X, Xu, S, Ding, L & Huang, D 2019, 'Passive flow control of a stalled airfoil using an oscillating micro-cylinder', *Computers & Fluids*, vol. 178, pp. 152-65.

[3] Fearn, R 2008, 'Airfoil Aerodynamics Using Panel Methods', *TMJ*, vol. 10, no. 4.

[4] Kenny, DJ 2017, *Stall and Spin Accidents*, Frederick, MD.

[5] Greenblatt, D & Wygnanski, IJ 2000, 'The control of flow separation by periodic excitation', *Progress in aerospace Sciences*, vol. 36, no. 7, pp. 487-545.

[6] Simpson, RL 1989, 'Turbulent Boundary-Layer Separation', *Annual Review of Fluid Mechanics*, vol. 21, no. 1, pp. 205-32.

[7] Yarusevych, S, Sullivan, PE & Kawall, JG 2006, 'Coherent structures in an airfoil boundary layer and wake at low Reynolds numbers', *Phys. Fluids*, vol. 18, no. 4.

[8] Buchner, AJ, Lohry, MW, Martinelli, L, Soria, J & Smits, AJ 2015, 'Dynamic stall in vertical axis wind turbines: Comparing experiments and computations', *Journal of Wind Engineering & Industrial Aerodynamics*, vol. 146, pp. 163-71.

[9] Bertagnolio, F, Rasmussen, F, Sørensen, NN, Johansen, J & Madsen, HA 2010, 'A stochastic model for the simulation of wind turbine blades in static stall', *Wind Energy*, vol. 13, no. 4, pp. 323-38.

[10] Broeren, A & Bragg, M 1998, *Low-frequency flowfield unsteadiness during airfoil stall and the influence of stall type*, American Institute of Aeronautics and Astronautics, Reston.

[11] Menon, M 2016, *On the aerodynamic properties of slotted-flap flow-control devices for wind turbine applications*, ProQuest Dissertations Publishing.

[12] Shuang, L, Lei, Z, Ke, Y, Jin, X & Xue, L 2018, 'Aerodynamic Performance of Wind Turbine Airfoil DU 91-W2-250 under Dynamic Stall', *Applied Sciences*, vol. 8, no. 7, p. 1111.

[13] Luo, D, Huang, D & Sun, X 2017, 'Passive flow control of a stalled airfoil using a microcylinder', *Journal of Wind Engineering & Industrial Aerodynamics*, vol. 170, pp. 256-73.

[14] Burnazzi, M & Radespiel, R 2014, 'Assessment of leading-edge devices for stall delay on an airfoil with active circulation control', *CEAS Aeronautical Journal*, vol. 5, no. 4, pp. 359-85.

[15] Zhao, M & Cheng, L 2012, 'Numerical simulation of vortex-induced vibration of four circular cylinders in a square configuration', *Journal of Fluids and Structures*, vol. 31, pp. 125-40.

[16] Mittal, S & Kumar, B 2003, 'Flow past a rotating cylinder', *Journal of Fluid Mechanics*, vol. 476, no. 476, pp. 303-34.
[17] Homescu, C, Navon, IM & Li, Z 2002, 'Suppression of vortex shedding for flow around a circular cylinder using optimal control', *International Journal for Numerical Methods in Fluids*, vol. 38, no. 1, pp. 43-69.
[18] Wang, J, Xu, Y & Tian, Y 2013, 'Active control of circular cylinder flow by affiliated rotating cylinders', *Science China Technological Sciences*, vol. 56, no. 5, pp. 1186-97.
[19] Zhao, M, Cheng, L & Lu, L 2014, 'Vortex induced vibrations of a rotating circular cylinder at low Reynolds number', *Phys. Fluids*, vol. 26, no. 7.
[20] Rao, A, Stewart, BE, Thompson, MC, Leweke, T & Hourigan, K 2011, 'Flows past rotating cylinders next to a wall', *Journal of Fluids and Structures*, vol. 27, no. 5, pp. 668-79.
[21] Hand, M, Simms, D, Fingersh, L, Jager, D & Cotrell, J 2002, 'Unsteady aerodynamics experiment, phase VI, wind tunnel test configurations and available data campaigns', *STAR*, vol. 40.
[22] Bogos, S, Dumitrache, A & Frunzulica, F 2015, *Turbulence models in CFD simulation of low-Reynolds number airfoils flow*, 0094-243X.
[23] Liu, D & Nishino, T 2018, 'Numerical analysis on the oscillation of stall cells over a NACA 0012 aerofoil', *Computers & Fluids*, vol. 175, pp. 246-59.
[24] Wang, S, Ingham, DB, Ma, L, Pourkashanian, M & Tao, Z 2010, 'Numerical investigations on dynamic stall of low Reynolds number flow around oscillating airfoils', *Computers and Fluids*, vol. 39, no. 9, pp. 1529-41.
[25] Zhao, M, Cheng, L, Teng, B & Dong, G 2007, 'Hydrodynamic forces on dual cylinders of different diameters in steady currents', *Journal of Fluids and Structures*, vol. 23, no. 1, pp. 59-83.

Nonlinear Behaviors of Wave-Induced Fluid Oscillations in a Single Gap Between Two Fixed Barges

Zhiwei Song
State Key Laboratory of Coastal and Offshore Engineering, Dalian University of Technology, Dalian, 116024, China.
zhiwei_song@mail.dlut.edu.cn

Lin Lu *
State Key Laboratory of Coastal and Offshore Engineering, Dalian University of Technology, Dalian, 116024, China.
* Lulin@dlut.edu.cn

***Abstract* — Wave-induced fluid resonance in a single gap between two fixed barges is numerically investigated based on finite element linear and fully nonlinear potential flow models in time domain. Established two numerical models are first validated with available experimental and numerical results, and then, amplitude-frequency responses of fluid oscillations, induced by incident wave with frequency $\omega/\omega_R \in [0.29, 1.48]$ where ω_R is resonant frequency, are demonstrated to study the nonlinear behaviors by comparing linear and fully nonlinear results, and then nonlinear effects at resonant points are further manifested with amplitude spectrum and phase portraits. Further, harmonic analysis on the response time histories reveals each order amplitude-frequency response, and provides the relationship of each order components. Finally, super-harmonic resonance, namely, second order resonance, third order resonance and combined harmonic resonance, is provided based on fully nonlinear potential model.**

I. INTRODUCTION

Fluid resonance in narrow gaps, or gap resonance, has been received wide attentions on account of extremely large response amplitudes in gaps may be excited [1-5]. With regard to response amplitudes, damping [3, 4] and nonlinearity [4, 5] are mainly two factors. Previous investigations [4, 5] on the nonlinearity are mainly focused on the response around first-order resonant frequencies ω_R, and give conclusion that nonlinearity played a minor role in the resonance response. However, as discussed in [6], second order resonance is demonstrated at half of resonant frequencies $\omega_R/2$ in a gap between two barges, where resonance is mainly depending on second-order effects, indicating that nonlinearity plays a main role in the response around half of resonant frequencies. From author knowledge, investigations on the amplitude-frequency response of wave-induced fluid oscillation in a gap within a wide range of frequencies, containing half and one third of resonant frequency, are limited, and nonlinear effects on the response amplitude at the low frequencies are not revealed. Hence, present paper mainly investigates nonlinear behaviors of wave-induced fluid oscillations in a single gap for a wide range of incident wave frequency [$0.29\omega_R$, $1.48\omega_R$], and gives an overall understanding of nonlinear effects on the wave response.

II. NUMERICAL WAVE FLUME

Wave induced fluid oscillations in a single gap between two fixed barges are investigated in time domain within potential flow theory, and corresponding schematic diagram of numerical setup is presented in Fig. 1, where the origin of a Cartesian coordinate system *O-xy* is placed at the mean water free surface with *x* positive in the propagation direction of incident waves and *y* directed vertically upwards. As shown in Fig.1, numerical setups of present paper are: barge breadth $B_1 = B_2 = 0.50$m, barge draft $d_1 = d_2 = 0.25$m, and gap width $B_g = 0.05$m. All the numerical investigations of this work will be conducted in the wave flume with a length $L = 40.0$m and a water depth $h = 0.50$m for the incident wave with frequency ω varying from 1.57rad/s to 7.85rad/s, which contains the ω_R, $\omega_R/2$, and $\omega_R/3$, where ω_R is the resonant frequency of above-mentioned numerical-setup system.

A. Mathematical Formulations

The fluid is assumed to be incompressible, and the flow is ir-rotational. Hence, the velocity potential $\phi(x, y, t)$ exists and satisfies the Laplace's equation in the whole fluid domain:

$$\nabla^2\phi(x, y, t) = \frac{\partial^2\phi}{\partial x^2} + \frac{\partial^2\phi}{\partial y^2} = 0 \tag{1}$$

The kinematic and dynamic boundary conditions are satisfied on the instantaneous free surface S_F

$$\frac{\partial\eta}{\partial t} - \frac{\partial\phi}{\partial y} + \frac{\partial\phi}{\partial x}\frac{\partial\eta}{\partial x} = 0, \quad g\eta + \frac{\partial\phi}{\partial t} + \frac{1}{2}\nabla\phi\cdot\nabla\phi = 0 \tag{2}$$

where g is the gravity acceleration, η is the free surface elevation and t is time.

As for the boundary condition on the solid wall, the impermeable boundary condition is given.

$$\frac{\partial\phi}{\partial\mathbf{n}} = \mathbf{V} \tag{3}$$

where $\mathbf{V}$ is the normal velocity vector of the body, which is zero on the wave flume bottom S_D, the end wall of wave flume S_E and the fixed body S_B, and $\mathbf{n}$ is the unit normal vector of the free surface directed outwards from the fluid domain. At the inlet boundary S_I, velocity potential is specified according to the analytical solutions. In addition to the above boundary conditions, the initial calm water condition is applied, namely:

$$\phi(x, y, t = 0) = 0; \qquad \eta(x, t = 0) = 0 \tag{4}$$

Here, wave-induced fluid oscillations in the narrow gap are investigated based on two numerical models, that is, finite element linear potential flow model (FEL) and finite element fully nonlinear potential flow model (FENL). Under the condition of fixed bodies, the main difference between above two numerical models is that the treatment of the boundary conditions on the free surface S_F.

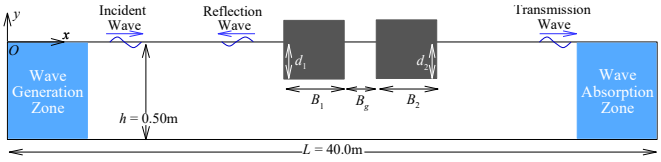

Figure 1. Schematic diagram of wave-induced fluid oscillations in a single gap between two barges

Finite Element Fully Nonlinear Potential Flow Model (FENL)

To satisfy the fully nonlinear free surface boundary conditions Eq. (2), the instantaneous free surface should be tracked at each time step. Here, fully nonlinear kinematic and dynamic boundary conditions at the free surface S_F are formulated in the Arbitrary-Lagrangian-Eulerian (ALE) frame [7]:

$$\frac{\delta\eta}{\delta t}-\frac{\partial\phi}{\partial y}-\left(u_{mx}-\frac{\partial\phi}{\partial x}\right)\frac{\partial\eta}{\partial x}=0\ ,\ g\eta+\frac{\delta\phi}{\delta t}+\left(\frac{1}{2}\nabla\phi-\mathbf{u}_{\mathrm{m}}\right)\cdot\nabla\phi=0 \tag{5}$$

where $\mathbf{u_m} = (u_{mx}, u_{my})$ denotes the velocity vector of the moving computational grid. Through further collaboration with a moving grid strategy, above Eq. (5) can be used to track the instantaneous free surface position and update the free surface potential, respectively, resulting the fluid domain is updated at each time steps. Further, Fenton's [8] fifth-order Stokes wave potential is imposed at the inlet boundary S_I to keep consistent with the nonlinear boundary conditions.

Finite Element Linear Potential Flow Model (FEL)

Compared with FENL, fully nonlinear free surface boundary conditions are linearized by using perturbation method [9] on its mean free surface $S_F^{(0)}$, where the fluid domain is time-independent. Based on Stokes expansion procedure, mathematical formulations, namely, governing equation and boundary conditions, about the first order are written as:

$$\nabla^2\phi^{(1)}=0 \tag{6}$$

$$\text{and}\ \ \frac{\partial\eta}{\partial t}-\frac{\partial\phi}{\partial y}=0\ ,\ \frac{\partial\phi}{\partial t}+g\eta=0\ \ \text{on}\ S_F^{(0)} \tag{7}$$

$$\frac{\partial\phi}{\partial\mathbf{n}}=0\ \ \text{on}\ S_B^{(0)},\ S_D^{(0)}\ \text{and}\ S_E^{(0)} \tag{8}$$

where $S_F^{(0)}$ is the still water surface, $S_B^{(0)}$ is the surface of fixed body, $S_D^{(0)}$ is the bottom and $S_E^{(0)}$ is the end wall of wave flume, and superscripts (1) indicates components at the first-order based on perturbation method. To keep consistency of linear boundary condition on the free surface, the velocity potential at the inlet boundary is given based on the linear wave, namely, airy wave.

B. Numerical Implementation

The above-mentioned mixed boundary value problems at each time step are solved by using the finite element method (FEM). The whole fluid domain is discretized into finite computational elements, and the velocity potential is expressed in terms of bilinear shape functions, $N_j(x, y)$:

$$\phi=\sum_{j=1}^{m}\phi_j N_j\left(x,y\right) \tag{9}$$

where ϕ_j denotes the value of velocity potential at node j, and m is total number of nodes. Using the standard Galerkin method, the governing equation and boundary conditions can be written as follows:

$$\int_\Omega\nabla N_i\cdot\sum_{j=1}^{m}\phi_j\nabla N_j d\Omega\Big|_{j\notin S_1}=\circ\ -\ dS-\int_\Omega\nabla N_i\cdot\sum_{j=1}^{m}\phi_j\nabla N_j d\Omega\Big|_{j\in S_1} \tag{10}$$

where Ω denotes the entire fluid domain, S_1 corresponds to the Dirichlet boundary on which the velocity potential is known, and S_2 indicates the Neumann boundary where the normal derivative of the velocity potential (f_n) is known. Eq. (10) can be further written in a matrix form.

$$\left[A\right]\left\{\phi\right\}=\left\{B\right\} \tag{11}$$

where

$$\left\{\phi\right\}=\left[\phi_1,\phi_2,\phi_3,...,\phi_i,...\right]^T\ \ \left(i\notin S_1\right),$$

$$A_{ij}=\int_\Omega\nabla N_i\cdot\nabla N_j d\Omega\ \ \left(i\notin S_1, j\notin S_1\right),\ \text{and}$$

$$B_i=\circ\ -\ dS-\int_\Omega\nabla N_i\cdot\sum_{\substack{j=1\\ j\in S_1}}^{m}\phi_j\nabla N_j d\Omega\ \ \left(i\notin S_1\right)$$

The solution of above linear system is obtained by using the popular conjugate gradient method. It is noted that the coefficient matrix A_{ij} in FEL keeps unchanged because fluid domain is time-independent, while A_{ij} in FENL should be updated at each time step. At the beginning of simulation, a ramp function is applied to prevent the impulse-like solution and to reduce the transient waves. Relaxation zone method developed by Jacobsen et al. [10] is employed to eliminate wave reflection. The 4th-order Runge–Kutta scheme is adopted to update free surface boundary conditions, and a Chebyshev 5-point smoothing scheme is employed in FENL to eliminate the saw-tooth numerical instabilities.

C. Numerical Validation

Established numerical models, FEL and FENL, are validated by available experimental and numerical results of wave-induced fluid resonance in a single gap, which is provided by Liu et al. [11]. Numerical setups are in accordance with the experimental setups reported in Liu et al. [11], that is, B_1 = 0.20m, B_2 = 1.00m, $d_1 = d_2$ = 0.25m, B_g = 0.05m, h = 0.50m, H = 0.03m and $\omega\in$[3.14rad/s, 7.85rad/s], where H denotes the incident wave height. Comparisons on the variations of non-dimensional average wave response height H_1/H, where H_1 is wave response height in gap, with respect to non-dimension incident wave frequency $\omega/(g/h)^{0.50}$ are demonstrated in Fig. 2. It is pointed out that the computation of FENL is collapsed around the resonant frequency ω_R because of mesh over-distortions induced by the extremely large amplitude of response in gap. Firstly, compared with the boundary element linear potential results provided by Liu et al. [11], it can be seen that both present finite element linear and fully nonlinear models can give satisfied agreements. Compared with the experimental results, potential flow model is able to accurately predict variation trend of response with frequency and the resonant frequency, although it over-predicts the resonant amplitude inside the gap around the resonant frequency because of neglecting energy dissipation. Further, it can be observed that non-dimensional fully nonlinear response amplitude H_1/H is relatively smaller than that of linear potential results when the incident wave

frequency ω approaches the resonant frequency ω_R, and nonlinear results are closer to experimental results. The difference value between them is $\Delta = 2.54$ at a specific incident wave frequency $\omega = 0.97\omega_R$, meaning that the transfer of energy to higher modes owing to nonlinearities associated with the free surface plays a certain role in the wave response. Moreover, due to the nonlinear effects, dumping phenomenon is observed in the fully nonlinear potential flow results, as denoted in blue arrow line, while linear results, represented by black arrow line, demonstrate a vertical variation trend with incident wave frequency approaching to resonant frequency.

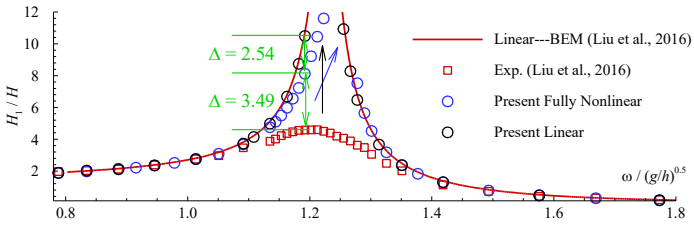

Figure 2. Comparisons of present numerical results with available experimental and numerical results about wave-induced fluid resonance in a single gap formed by two barges. In figure, $\Delta = 2.54$ and $\Delta = 3.49$ denote the difference values between linear results and fully nonlinear results, between fully nonlinear results and experimental results, respectively, at a specific incident wave frequency $\omega = 0.97\omega_R$. Arrow line in black ↑ represents the trend of linear response around the resonant frequency, and blue arrow line ↗ denotes the fully nonlinear response tendency.

III. RESULTS AND DISCUSSIONS

A. *Amplitude-Frequency Responses*

Employing above-validated finite element fully nonlinear and linear potential flow models, amplitude-frequency response of wave-induced fluid oscillations in a single gap between two fixed barges are firstly studied for the incident wave frequency $\omega \in [1.57\text{rad/s}, 7.85\text{rad/s}]$ with a constant wave height $H = 0.04$m. Firstly, nonlinear and linear amplitude-frequency response curves are demonstrated in Fig. 3, where response height H_1 is obtained by averaging the difference values between maximum and minimum in each periods during serial twenty steady periods, as shown in the insert diagram of Fig. 3. Results demonstrate that one peak response amplitude is observed at $\omega = \omega_R = 5.32$rad/s in the linear model, both boundary element model [3] and present finite element model, while there are other two local extreme points at $\omega = \omega_R/2$ and $\omega = \omega_R/3$ in fully nonlinear potential flow results, as shown in the points **A** ● and **B** ● of Fig. 3. Existence of local extreme response amplitudes at $\omega = \omega_R/2$ and $\omega = \omega_R/3$, namely, super-harmonic resonance, is mainly induced by nonlinear effects, which will be discussed in detail later. Compared with the linear response, except for super-harmonic resonance at $\omega = \omega_R/2$ and $\omega = \omega_R/3$, it also can be seen that fully nonlinear response amplitudes are not equal to those in linear response with the incident wave frequency approaching to above three extreme points, as demonstrated in the grey zone **I, II** and **III** plotted in Fig. 3. As for the incident wave frequency ω belongs to Zone **I**, fully nonlinear response amplitude is smaller than linear response amplitude, and the closer to resonant frequency ω_R, the bigger relative difference values Δ are, as demonstrated by $\Delta = 0.99$ at $\omega = 0.96\omega_R$ and $\Delta = 3.25$ at $\omega = 0.98\omega_R$ in Fig. 3. For ω is confined in the Zone **II** and **III**, fully nonlinear response amplitudes are larger than linear results because higher order harmonic responses are excited, unveiled by fully nonlinear potential flow model. For incident wave frequencies ω in other zone, fully nonlinear response amplitudes are almost equal to linear response amplitudes, indicating that the nonlinear effects are negligible.

To give a further understanding of nonlinear behaviors at above demonstrated extreme points, time histories of wave response in gap at $\omega = 0.99\omega_R$, $\omega = \omega_R/2$, and $\omega = \omega_R/3$, and corresponding amplitude spectrums and phase portraits on the plane $(d\eta/dt, \eta)$, are presented in Fig. 4. Firstly, comparisons in the time series, depicted in first column, indicate that the free surface nonlinear factor affects not only on the response amplitude, but also on the wave form, which mainly manifest two wave crests at $\omega_R/2$ and three crests at $\omega_R/3$ in a period, indicating the higher order harmonics are motivated and play the main role in the response amplitude. Above discussions can further be confirmed in the amplitude spectrum. As shown in the second column, second order response amplitude at $\omega_R/2$ is excited and is bigger than first order response amplitude, and third order response amplitude at $\omega_R/3$ is motivated and is almost equal to the first order response amplitude. Meanwhile, phase portrait in third column demonstrates that periodic doubling motion exists in the response at $\omega = \omega_R/2$, and $\omega = \omega_R/3$.

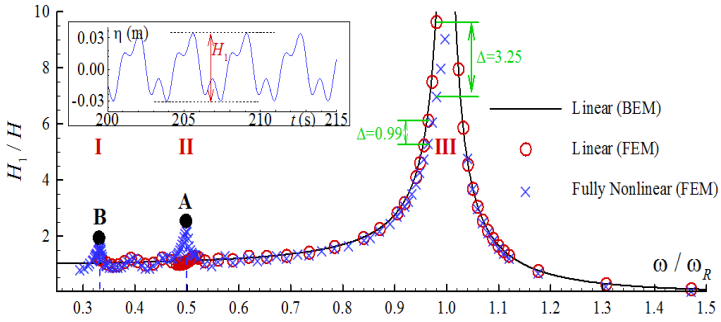

Figure 3. Variations of non-dimension wave response amplitude H_1/H, obtained by linear and fully nonlinear models, with respect to non-dimensional incident wave frequency ω/ω_R. In figure, Grey Color Zone (**I, II and III**): Meaning the fully nonlinear results are not identical to the corresponding linear response when ω is confined in the grey zone, and the difference value between them is denoted by Δ at any two points. **A** and **B** points ● are the half of and one third of the resonant frequency ω_R, respectively, correspond to local extreme response. The insert show how the average response height H_1 is defined.

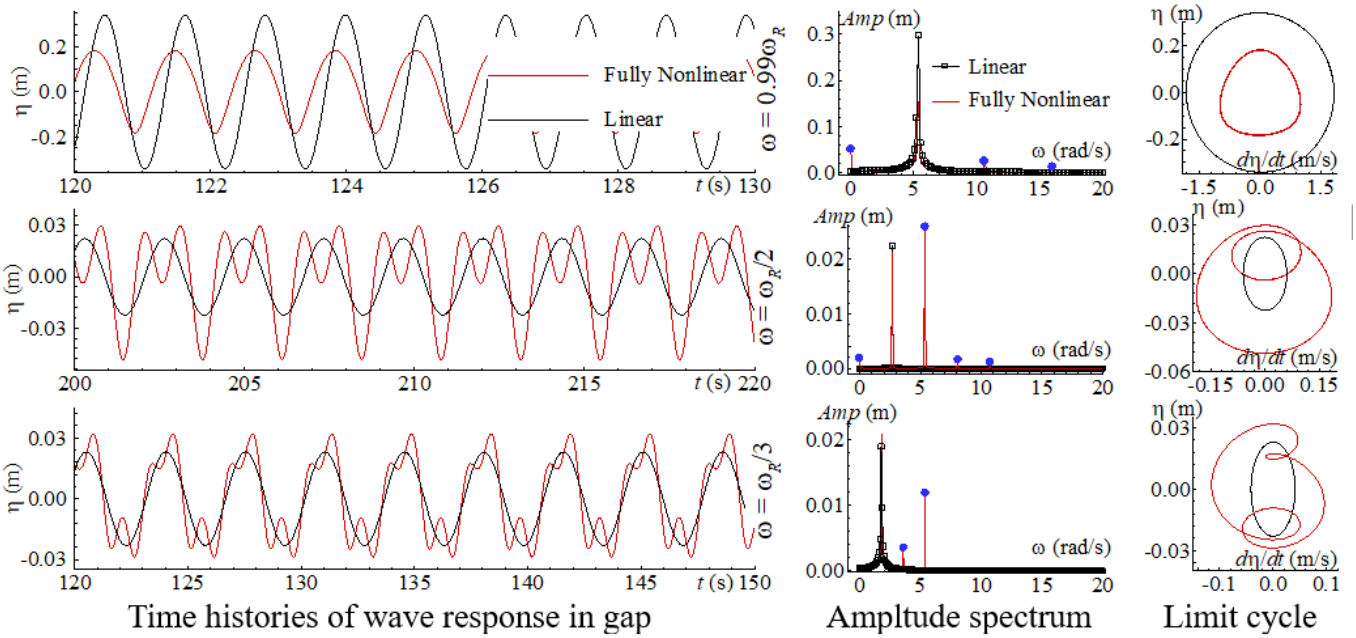

Figure 4. Time histories of wave response in the gap, obtained by linear model (represented in black color) and fully nonlinear model (expressed in red color), in first column, amplitude spectrum in second column and corresponding phase portrait on the plane ($d\eta/dt$, η) in third column at incident wave frequencies $\omega = 0.99\omega_R$, $\omega = \omega_R/2$, and $\omega = \omega_R/3$. In the second column, ● represents the extra higher order components in fully nonlinear results compared with the linear response.

B. Harmonic Analysis and Super-Harmonic Resonance

Harmonic analysis on the response time histories is further conducted based on the Fourier transformation for all the considered incident wave frequencies $\omega \in [1.57\text{rad/s}, 7.85\text{rad/s}]$. Variations of non-dimension each order harmonic wave response amplitudes $H_1^{(n)}/H$ ($n = 0$, 1, 2, and 3), analyzed based on fully nonlinear results, with respect to non-dimensional incident wave frequency ω/ω_R are demonstrated in Fig. 5, where, n = 0, namely, zero order component, represents the mean wave level (MWL), n =1, 2 and 3 denote the nth order components based on Fourier transformation and are different from that in perturbation method, and total response is also depicted for convenient comparisons. Results demonstrate that the maximum values of first order response amplitude and MWL are found around the resonant frequency ω_R, second order response amplitude reaches its maximum value at $\omega = \omega_R/2$, and third order response amplitude obtains its maximum values at $\omega = \omega_R/3$, which reveal that super-harmonic resonance may be observed in the response if nonlinear effects are strong enough, and will be discussed in the last part of the paper. Next, it can be observed that the total response amplitudes H_1 are almost equal to first order response amplitudes $H_1^{(1)}$ for most of the considered incident wave frequencies, except the incident frequency ω located in Zone 𝔸 with grey color, around the $\omega = \omega_R/2$, and $\omega = \omega_R/3$. As the incident wave frequency is not confined in the Zone 𝔹 with blue color, second order response amplitudes $H_1^{(2)}$ are almost equal to mean water level $H_1^{(0)}$, which indicates that the change of mean water level is mainly induced by second order effects. Finally, when the incident wave frequency ω is located in Zone ℂ with carmine color, near the $\omega_R/2$, second order response amplitudes $H_1^{(2)}$ are larger than first order response amplitudes $H_1^{(1)}$, meaning that super-harmonic components play the main role in the response.

Above parts have revealed the possibility of super-harmonic resonance, big response amplitudes when forcing frequency $\omega = \omega_n / N$, where ω_n is natural frequency of vibration system and N is an arbitrary integer, and mainly demonstrates multiple peaks due to nonlinearity even though it is a single DOF system, as shown in Fig. 3, and the increase of harmonic response amplitude at ω_n components with time. It is noted that the natural frequency ω_n is considered to be equal to resonant frequency ω_R in paper. To give a clearly demonstration of super-harmonic resonance, fluid oscillations in a single gap induced by monochromatic wave with $\omega = \omega_R/2$, and $\omega = \omega_R/3$ in a constant wave height H = 0.08m, and by bi-chromatic waves with $\omega_I = \omega_R/4$, $\omega_{II} = 3\omega_R/4$, H_I = 0.04m and H_{II} = 0.04m, are simulated by present fully nonlinear and linear potential flow models, where bi-chromatic waves in FENL are generated based on second order nonlinear wave with wave frequencies ω_I, ω_{II} and wave heights H_I, H_{II}. Obtained response results in gap are presented in Fig.5, where time series in (*a*) and (*b*) are monochromatic wave with $\omega = \omega_R/2$, and $\omega = \omega_R/3$, respectively, and (*c*) is bi-chromatic wave, corresponding amplitude spectrums during different time intervals are plotted in the second column. Firstly, linear results, in black color in Fig. 5, indicate that the fluid in gap vibrates with the frequency identical to incident wave frequency, either monochromatic or bi-chromatic waves, and the response amplitude reaches a small value within a short time and keeps unchanged with time. However, fully nonlinear response, in red color in Fig. 5, manifests different phenomena. Induced by monochromatic wave with $\omega = \omega_R/2$, it can be seen that response amplitude in time series grows with time processing, and the amplitude spectrums at different time intervals, $t \in$ [10s, 50s] and $t \in$ [50s, 100s], demonstrate the increase of second order response amplitude, namely, at double incident wave frequency $2\omega = \omega_R$, leads to the total response amplitude increasing, that is,

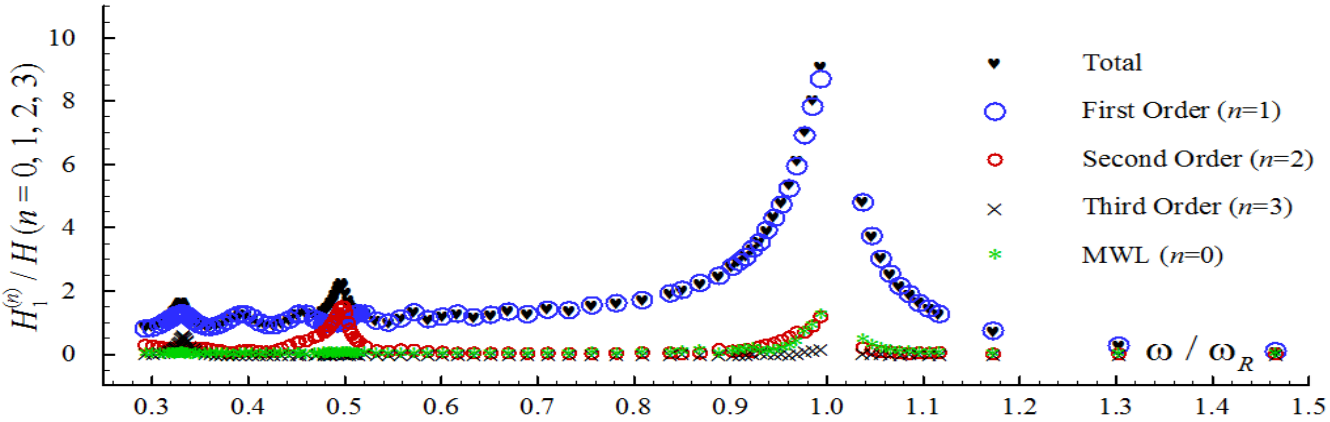

Figure 5. Variations of non-dimension each order harmonic wave response amplitudes $H_1^{(n)}/H$ (n = 0, 1, 2, and 3), obtained by fully nonlinear models, with respect to non-dimensional incident wave frequency ω/ω_R. In figure, as for ω/ω_R confined in Zone **A** with grey color, first order response amplitude ○ is not equal to total response amplitude ♥; and for ω/ω_R confined in Zone **B** with blue color, second order response amplitude ○ is not equal to amplitude of MWL *; and for ω/ω_R confined in Zone **C** with carmine color, second order response amplitude ○ is larger than first order response amplitude ○.

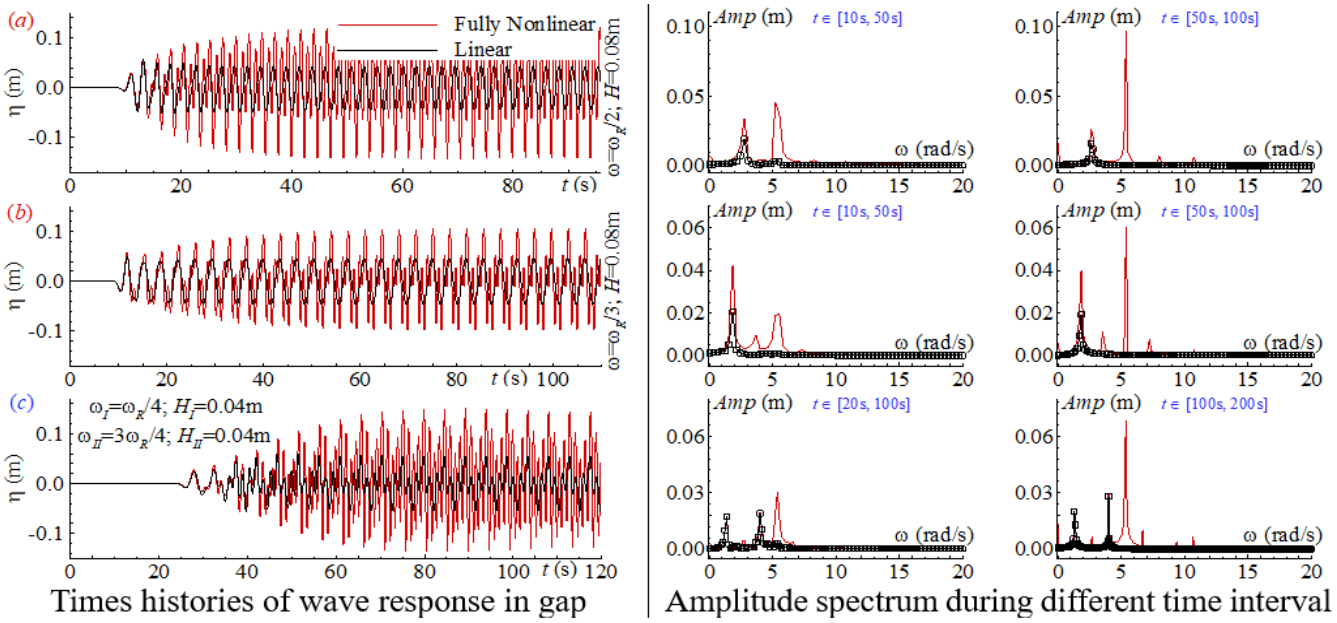

Figure 6. Times histories of wave response in the single gap, (*a*) and (*b*) induced by monochromatic wave with $\omega = \omega_R/2$, and $\omega = \omega_R/3$, respectively, and (*c*) induced by bi-chromatic waves with $\omega_I = \omega_R/4$, and $\omega_{II} = 3\omega_R/4$, are presented in the first column, corresponding amplitude spectrums during different time intervals are demonstrated in the second column.

second order resonance. Similarly, results at monochromatic wave $\omega = \omega_R/3$, indicate that the third order response amplitude at $3\omega = \omega_R$ grows with time, and resulting the total response amplitude increasing, namely, third order resonance. As for the bi-chromatic wave-induced response in gap, response amplitude at their sum-frequency, $\omega_I + \omega_{II} = \omega_R$, increases with time processing, which is combined harmonic resonance. More important, it can be observed that response amplitudes of the second order components at monochromatic wave with $\omega = \omega_R/2$, of third order at monochromatic wave with $\omega = \omega_R/3$, and of sum-frequency at bi-chromatic, are all higher than that at the first order frequency, demonstrating that super-harmonics play the main role in the response.

IV. Conclusions

Linear amplitude-frequency response demonstrates a single peak of response at resonant frequency ω_R, while nonlinear amplitude-frequency response manifests three local extreme maximum points at ω_R, $\omega_R/2$ and $\omega_R/3$, which embodies a popular nonlinear features, namely, super-harmonic response. And demonstrations show that linear response amplitude is almost equal to nonlinear response amplitude except the frequencies around above-mentioned three extreme points. Then, harmonic analysis of response indicates that the zero order (MWL) and first order response amplitude reach their peaks at resonant frequency ω_R, second order response amplitude obtains its maximum at $\omega_R/2$ and amplitude of third order harmonic reaches its crest at $\omega_R/3$. Each order harmonic amplitude-frequency responses

demonstrate that total response amplitude is almost equal to first order response amplitude except frequencies around $\omega_R/2$ and $\omega_R/3$, that second order response amplitude is nearly identical to zero order response amplitude (MWL) for ω is larger than $\omega_R/2$, that second order response amplitudes are larger than first order response amplitudes around $\omega_R/2$ at incident wave height H = 0.04m. Finally, considering the higher order harmonic response amplitudes increase with time, and are larger than first order response amplitudes, super-harmonic resonance are provided by monochromatic wave with $\omega = \omega_R/2$, and $\omega = \omega_R/3$ at H = 0.08m, and by bi-chromatic waves with $\omega_I = \omega_R/4$, $\omega_{II} = 3\omega_R/4$, H_I = 0.04m and H_{II} = 0.04m. However, it is pointed out that the present work is based on the potential flow theory without considering the fluid viscosity and energy dissipations.

ACKNOWLEDGMENT

This work is supported by the National Natural Science Foundation of China with grant No. 51490673 and National Key R&D Program of China with grant No. 2016YFE0200100.

REFERENCE

[1] Molin B. On the piston and sloshing modes in moonpools [J]. Journal of Fluid Mechanics, 2001, 430: 27-50.

[2] Lu L, Teng B, Sun L, et al. Modelling of multi-bodies in close proximity under water waves—Fluid forces on floating bodies [J]. Ocean Engineering, 2011, 38(13): 1403-1416.

[3] Lu L, Cheng L, Teng B, et al. Numerical investigation of fluid resonance in two narrow gaps of three identical rectangular structures [J]. Applied Ocean Research, 2010, 32(2): 177-190.

[4] Kristiansen T, Faltinsen O M. Application of a vortex tracking method to the piston-like behaviour in a semi-entrained vertical gap [J]. Applied Ocean Research, 2008, 30(1): 1-16.

[5] Feng X, Bai W. Wave resonances in a narrow gap between two barges using fully nonlinear numerical simulation [J]. Applied Ocean Research, 2015, 50: 119-129.

[6] Li Y. Fully nonlinear analysis of second-order gap resonance between two floating barges [J]. Engineering Analysis with Boundary Elements, 2019, 106: 1-19.

[7] Donea J, Giuliani S, Halleux J P. An arbitrary Lagrangian-Eulerian finite element method for transient dynamic fluid-structure interactions [J]. Computer Methods in Applied Mechanics and Engineering, 1982, 33(1-3): 689-723.

[8] Fenton J D. A fifth-order Stokes theory for steady waves [J]. Journal of Waterway, Port, Coastal, and Ocean Engineering, 1985, 111(2): 216-234.

[9] Isaacson M, Ng J Y. Time-domain second-order wave radiation in two-dimensions [J]. Journal of Ship Research, 1993, 37: 25-33.

[10] Jacobsen N G, Fuhrman D R, Fredsøe J. A wave generation toolbarge for the open-source CFD library: OpenFoam® [J]. International Journal for Numerical Methods in Fluids, 2012, 70(9): 1073-1088.

[11] Liu C, Lu L, Tan L, et al. Experimental and numerical investigations of wave resonance in gap between two floating barges with various breadths [C]// Proceeding of the 8th Chinese-German Joint Symposium On Hydraulic and Ocean Engineering, Qingdao, China. 2016.

Numerical Study on End Effect of A Near-wall Cylinder with A Perpendicular Wall

F.Yang[1], L. Lu[1*], G. Tang[1], X. Lou[1] and Z. Zhou[1]
[1]*State Key Laboratory of Coastal and Offshore Engineering*
Dalian University of Technology
Dalian, China
[*]*lulin@dlut.edu.cn*

***Abstract*—End Effect of a near-wall circular cylinder in turbulent flow has been analyzed in the present work numerically. The scenario of the cylinder in the present study is mounted on a vertical side wall. The aim of the study is to investigate the effects of gap to diameter ratio (G/D = ∞, 0.5 & 0.2), Reynolds number (Re_D = 1250, 2500 & 5000) and the length to diameter (aspect) ratio (L/D = 10, 20 & 40) on the End Effect. The flow structures and hydrodynamic characteristics have been explored. It is found that the three-dimensional flow structures formed in the junction area between the vertical wall and the cylinder are strongly affected by the gap ratio. The End Effect induced by the vertical wall is limited within 0.7D in the spanwise direction, 0.5D upstream and 3D downstream of the cylinder. The extent of the End Effect is not sensitive to the gap ratio, Reynolds number or the aspect ratio.**

Keywords—Horseshoe vortex, LES, End Effect, Gap ratio, 3D

I. INTRODUCTION

Steady flow around a horizontal cylinder mounted perpendicularly to side walls at two ends with a parallel plane boundary in proximity is often encountered in physical model testing (in water flumes or wind tunnels) of flow around a near wall cylinder for simulating local scour around subsea pipelines (Cheng et al., 2009) and related hydrodynamic forces (Yang et al. 2018). A schematic illustration of the configuration is shown in Fig. 1. The flow is highly three-dimensional (3-D) near the junction area between the cylinder and two plane boundaries. In some situations, the highly 3-D flow is unwanted and creates difficulty in interpreting the test results, as it is very different from the flow over the majority part of the cylinder. This is often referred to as "End Effect" in the literature. The highly 3-D flow is expected to exhibit the flow characteristics of the following two flows that are widely studied: (1) flow around junction area of a cylinder mounted on a perpendicular plane and (2) flow around a cylinder above a parallel plane. The existing work on those two flows in the literature will be briefly reviewed below.

Junction flow around a circular cylinder attached to a plane boundary has attracted substantial research interests over the past decades for its importance to engineering applications in the fields of aerodynamics, heat transfer and offshore hydrodynamics. Junction flow is generally a complex three-dimensional phenomenon, involving three-dimensional boundary layer separations, formation of coherent flow structures and vortex shedding. When a cylinder is mounted on a plane boundary, the adverse pressure gradient in front of the cylinder near the plane boundary leads to the boundary layer to separate and forms a series of vortex tubes to wrap around the junction of the cylinder. The vortex tubes formed around the base of the cylinder are often referred to as horseshoe vortices (HV) in the literature (Baker, 1985).

The HV is a genuine feature of the junction flow and has a side effect on model testing results in wind tunnels or water flumes. Flow boundary layer will naturally form on the solid walls (side, top and bottom) of the wind tunnel or water flume. When a two-dimensional slender model is mounted against the channel walls, a HV system will be formed at each end of the model. This HV represents an undesired three-dimensional disturbance to the flow field. For example, when the hydrodynamics/aerodynamics of a uniform cylinder is tested, the two ends of the cylinder are normally mounted with two end plates to avoid the three-dimensional effect from the free ends (Stansby, 1974). The diameter of the end plates is normally just slightly larger than the cylinder diameter, to limit the development of a thick boundary layer on the end plates (Gerich and Eckelmann, 1982). In this way, the End Effect due to HV can be managed to some extent. However, some model tests in a flume are not suitable for adding end plates to the cylinder. For example, when local scour below a cylinder is investigated in a water channel, normally the ends of the cylinder are set against the side walls of test section directly without end plates attached. This is because the end plates could cause extra scour. Sumer et al. (2001) mentioned a half HV around the end of a cylinder partially buried on the sand bed. The End Effect due to HV will lead to different shear stress distribution on the sand bed near the ends of the model cylinder. Consequently, it leads to different sediment transport rate which affects the time scale of the scour process. The HV formed at the ends will also affect the pressure distribution on the cylinder. Therefore, it is important to quantify the End Effect due to HV in similar testing setup.

The effect of a plane parallel to the cylinder on the flow around circular cylinder also attracted substantial research interests in the past a few decades. The flow structures and hydrodynamic forces of the cylinder are affected by the gap to diameter ratio (G/D), wall boundary layer thickness to diameter ratio (δ/D) as well as the turbulence intensity in the boundary layer. Bearman and Zdravkovich (1978) visualized flow around a circular cylinder near a plane boundary and measured pressure distribution on the cylinder surface and on the plane boundary at $Re_D = 4.5 \times 10^4$. It was found the vortex shedding was suppressed for all gaps less than 0.3D.

The influence of the blockage ratio and aspect ratio has been revealed by West and Apelt (1982). It was found that the blockage ratio affects pressure distributions, force coefficients and vortex shedding frequency. Lei et al. (2001) suggested

[1] State Key Laboratory of Coastal and Offshore Engineering, Dalian University of Technology, Dalian 116024, China

that the aspect ratio of cylinder must be larger than 4D in order to simulate the three-dimensional wake flow accurately. Sumner and Heseltine (2008) reported the junction flow around the circular cylinder with small aspect ratio. It was found that HV systems was weak, and as the aspect ratio increased, the strength of the system as well as the number of vortices increased.

A series of numerical simulations has been carried out using LES turbulence model to understand End Effect on a near-wall cylinder with a perpendicular plane boundary. Parts of the governing equations and the mesh dependency and the validation are not included in the current paper due to the limitations of space. The simulation results, followed by conclusions has been presented below.

II. Numerical Results

The numerical results are reported in this section. The main focus of the discussions will be on three-dimensional flow structures in the junction area between the cylinder and the plane walls and their influences on other physical quantities such as pressure, boundary layer separation on the cylinder surface, the shear stress on the wall parallel to the cylinder at different G/D conditions.

A. Influence of Gap Ratio

The influence of G/D on the three-dimensional flow feature is examined by analyzing the simulation results of Case 1, 2, and 3 with $G/D = \infty$, 0.5, and 0.2, respectively, at $Re_D = 2500$. It has been known that the vortex shedding from the cylinder will be suppressed for a cylinder near a plane boundary with $G/D < 0.3$ (Bearman and Zdravkovich, 1978). The cases with $G/D = 0.5$ and $G/D = 0.2$ are chosen to represent the flow regimes with and without vortex shedding, respectively, under the influence of the parallel wall. The hydrodynamic forces for the three gap ratios are presented in Table 1. The mean drag coefficient ($\overline{C}_D$) increases from 1.08 at $G/D = \infty$ to 1.18 at G/D=0.5 and then reduces to 1.09 at $G/D = 0.2$. The mean lift coefficient ($\overline{C}_L$) increases from 0.0 to 0.15 and 0.27 as G/D is reduced from ∞ to 0.5 and 0.2 correspondingly. The root-mean-square value of the lift, which is normally used as a measure of strength of vortex shedding, reaches a value of 0.177 at $G/D = 0.5$ and reduces to a very small value of 0.011 at $G/D = 0.2$, suggesting the suppression of vortex shedding at $G/D = 0.2$. The St increases slightly as G/D is reduced from ∞ to 0.5 and disappears at $G/D = 0.2$. The above results agree well with the experimental data in the subcritical flow regime reported by Jensen et al. (1990).

In order to examine the general 3-D vortex structure around the cylinder, the λ_2 criteria (Jeong and Hussain, 1995) is used to visualize the flow structure around the cylinder. Fig. 2 presents two selected 3-D views of time-averaged iso-surfaces of λ_2=1 for $G/D = \infty$, 0.5, and 0.2. The right column of Fig. 2 shows an overall view of the 3-D flow structures with the side wall (perpendicular to the cylinder) at the bottom and the parallel wall on the right, and the left column presents a projected view of that shown in the right column in the opposite direction to the z-axis with the parallel wall on the bottom side. It is seen from Fig. 2 that HV tubes are developed at the junction of the cylinder with the side wall and wrap around the cylinder surface facing the flow at a certain distance. For $G/D=\infty$ shown in Fig. 2 (a), four vortex tubes are observed in the junction area with the side wall. Three of the four vortex tubes are actually the horseshoe vortices (HVs) and one of them is the bottom attached vortex (BAV).

The length of the circulation bubble in the behind the cylinder in the averaged flow field is defined as W_L in this work. W_L and the locations of separation points on the cylinder surface are presented in Fig. 3 and Fig. 4. For $G/D = \infty$, WL drops dramatically as $z/D < 0.2$ and gradually stabilizes at $z/D > 0.35$. As z/D increases to around 1.5, W_L almost has no change, which agrees well with the results of Huang et al. (2014). Huang et al. (2014) examined the flow structures at different z/D slices and found the pattern of the recirculation bubble stabilized at $z/D > 1.6$. The variations of separation points on the top (S_{p1}) and bottom (S_{p2}) sides show the same influence of End Effect in the junction. The increases of S_{p1} and decreases of S_{p2} as z/D is moving towards the junction represents the separated boundary layer moves toward the downstream side under the influence of End Effect.

The extent of End Effect is further investigated by examining the sectional pressure distributions on the cylinder and the shear stress distributions on the parallel wall. Fig. 5 shows the distributions of mean pressure coefficient C_p along different cross sections for $G/D = \infty$, 0.5 and 0.2. It is seen that C_p values experience large variations for $z/D<0.3$ and rarely change for $z/D> 0.3$, especially near the peaks at $\theta = 80^o$ and 290^o. To further quantify this, the variation of $\Phi = C_{pb}$-$C_{p\text{-}min\text{-}gap}$ with z/D is plotted in Fig. 6, where C_{pb} is the base pressure and defined as the average of the pressure on the cylinder surface between θ= 120^o and 260^o , $C_{p\text{-}min\text{-}gap}$ is the minimum pressure at around $\theta = 290^o$ for all three gap ratios. It is seen that the influence of End Effect is limited at $z/D<$ 0.35 for $G/D = \infty$ and 0.5, and $z/D< 0.5$ for $G/D = 0.2$.

Shear stress distributions on the parallel wall are relevant to understanding local scour below the cylinder. When a cylinder is placed above an erodible boundary with a small gap, local scour will happen when the flow-induced shear stress exceeds the critical shear stress for sediment transport. To quantify the influence of side wall on the shear stress, the amplification factor of the shear stress, σ_0, is checked, where σ_0 is defined as $\sigma_0 = \tau_0/\tau_{ref}$, in which τ_0 is the magnitude of the shear stress, and τ_{ref} is the magnitude of reference shear stress in an area far away from the sidewall plane boundary and the cylinder. Shear stress τ_0 is defined as $\tau_0=\sqrt{\tau_x^2+\tau_z^2}$ in which $\tau_x=\mu(\partial u/\partial y)$ and $\tau_z=\mu(\partial w/\partial y)$ are the mean shear stress in the x- and z- directions respectively, and μ is the dynamic viscosity. Fig. 7 shows the contours of σ_0 as well as the streamlines on the parallel wall for G/D= 0.5 and 0.2. For $G/D = 0.5$ in Fig. 7(a), σ_0 underneath the cylinder is obviously higher than the other area. This is mainly due to the blockage effect of the cylinder. The variation of shear stress in the spanwise direction under the cylinder is clearly due to the existence of HVs at the junction. The area influenced by the side wall is roughly about $-0.5 < x/D < 1.7$ and $z/D < 0.5$. Similar to the results of G/D= 0.5, strong shear stress is also observed underneath the cylinder for G/D= 0.2. The range of End Effect is roughly at $-0.5 < x/D < 3$ and $z/D < 0.7$ in Fig. 7(b). To quantify the influence of the side wall, the shear stress distributions along a few lines with constant x/D values underneath the cylinder are extracted in Fig. 8. The range of End Effect on σ_0 is limited to $z/D < 0.4$ for $G/D = 0.5$ in Fig. 8(a) and the highest σ_0 is observed at around z/D=0.12 which

is due to horseshoe vortexes in the junction. As for G/D= 0.2, the range of End Effect on σ_0 is limited to z/D < 0.7. The fluctuations of σ_0 observed between z/D= 0.3 ~ 0.6 are good indications of the complex three-dimensionality in the junction area.

B. *Influence of Reynolds Number*

In the present work, the influence of Re_D on the flow and the End Effect is investigated at Re_D = 1250, 2500 and 5000 with G/D= 0.5. Due to the limitation of computational resources, relatively small Re_D values are employed.

The variation of the hydrodynamic forces with Re_D has been summarized in Table 3. $\bar{C}_D$, $\bar{C}_L$ and St are not very sensitive to Re_D within the range of Re_D investigated. The averaged positions of HVs at the plane of y= 0 have been given in Table 4 variation of force coefficients and Strouhal number with L/D. Two pairs of HVs have been observed for Re_D = 1250, and have almost exact the same positions as HV1 and HV2 of Re_D = 2500. As Re_D increases to 5000, only one pair of averaged HVs is reported. It is found that the locations of HVs are stationary at Re_D =1250 but become dynamic at Re_D = 2500 and 5000, although no instantaneous flow structures will be shown in this study.

The influence of Re_D on the extent of End Effect is quantified through the variation of Φ with z/D in Fig. 9 and the amplification factor of shear stress σ_0 in Fig. 10. The extent of the End Effect decreases with Re_D and is limited at z/D = 0.4, 0.35 and 0.25 for Re_D = 1250, 2500 and 5000 correspondingly.

C. *Influence of The Aspect Ratio*

The influence of the aspect ratio, L/D on the flow and the End Effect is examined in this study. Many studies have been carried out to investigate the influence of L/D on HV systems for a single cylinder without the parallel wall (Sumner and Heseltine, 2008, Rodríguez y Domínguez et al., 2006, Pattenden et al., 2005, Sumner et al., 2004). The largest L/D that has been previously studied was L/D= 6 (Sahin et al. (2007) and Sahin and Ozturk (2009)). In the present work, three different L/D, which are 10, 20 and 40, are employed for the case with G/D = 0.5. The hydrodynamic forces as well as the averaged positions of HVs in the plane of y= 0 are presented in Table 5, and variations of vortex center locations with L/D is presented in Table 6. It is seen that they are not sensitive to L/D, possibly because the minimum L/D investigated is too large. This is further confirmed by the variation of Φ with L/D in Fig. 7. The sectional drag, $C_{D\text{-}S}$ and lift $C_{L\text{-}S}$ coefficient are plotted in Fig. 12. The influence range of End Effect is limited at z/D = 0.5 for all three aspect ratios.

III. CONCLUSION

In the present work, the flow around a circular cylinder in a water channel is simulated through three-dimensional large eddy simulations. The influence of the side wall on the flow structure is investigated at three gap ratios (G/D = ∞, 0.5 and 0.2), three Reynolds numbers (Re_D = 1250, 2500 and 5000) and three aspect ratios (L/D = 10, 20 and 40). The main conclusions from the present work are summarized as follows:

1. The 3-D horseshoe vortex structures formed in the junction area between the cylinder and the side wall are strongly affected by the proximity of the parallel wall. The vortex tubes on the gap side between the cylinder and the parallel wall are squeezed, merged and weakened due to their interactions with the boundary layer above the parallel wall and the shear layer developed on the gap side of the cylinder surface. The vortex tubes move closer to the cylinder as G/D is reduced and a Luff vortex tube is formed along the spanwise direction.
2. The extent of the End Effect is examined by a number of quantities such as pressure distribution on the cylinder surface and shear stress on the parallel wall. It is found that the extent of the End Effect is not sensitive to gap ratio, Reynolds number and the aspect ratio within the parameter ranges studied. The End Effect is largely contained within 0.7D from the side wall.

ACKNOWLEDGMENT

The authors would like to acknowledge the support from the National Key R&D Program of China (Project ID: 2016YFE0200100 and 2017YFC1404202) and Fundamental Research Funds for the Central Universities (Grant No. DUT19RC(3)015). The simulations were conducted using the computational resources provided by the Pawsey Supercomputing Centre funded by the Australian Government and the Government of Western Australia.

REFERENCES

[1] BEARMAN, P. W. & ZDRAVKOVICH, M. M. 1978. Flow around a circular cylinder near a plane boundary. Journal of Fluid Mechanics, 89, 33-47.

[2] BAKER, C. J. 1985. The position of points of maximum and minimum shear stress upstream of cylinders mounted normal to flat plates. Journal of wind engineering and industrial aerodynamics, 18, 263-274.

[3] CHENG, L., YEOW, K., ZHANG, Z. & TENG, B. 2009. Three-dimensional scour below offshore pipelines in steady currents. Coastal Engineering, 56, 577-590.

[4] GERICH, D. & ECKELMANN, H. 1982. Influence of end plates and free ends on the shedding frequency of circular cylinders. Journal of Fluid Mechanics, 122, 109-121.

[5] HUANG, R. F., HSU, C. M. & LIN, W. C. 2014. Flow characteristics around juncture of a circular cylinder mounted normal to a flat plate. Experimental Thermal and Fluid Science, 55, 187-199.

[6] JENSEN, B. L., SUMER, B. M., JENSEN, H. R. & FREDSOE, J. 1990. Flow around and forces on a pipeline near a scoured bed in steady current. Journal of Offshore Mechanics and Arctic Engineering, 112, 206-213.

[7] JEONG, J. & HUSSAIN, F. 1995. On the identification of a vortex. Journal of fluid mechanics, 285, 69-94.

[8] LEI, C., CHENG, L. & KAVANAGH, K. 2001. Spanwise length effects on three-dimensional modelling of flow over a circular cylinder. Computer methods in applied mechanics and engineering, 190, 2909-2923.

[9] PATTENDEN, R. J., TURNOCK, S. R. & ZHANG, X. 2005. Measurements of the flow over a low-aspect-ratio cylinder mounted on a ground plane. Experiments in Fluids, 39, 10-21.

[10] RODRíGUEZ Y DOMíNGUEZ, M., ROMERO-MéNDEZ, R., RAMOS-PALáU, M. & PéREZ-GUTIéRREZ, F. G. 2006. The laminar horseshoe vortex upstream of a short-cylinder confined in a channel formed by a pair of parallel plates. Journal of visualization, 9, 309-318.

[11] STANSBY, P. K. 1974. The effects of end plates on the base pressure coefficient of a circular cylinder. The Aeronautical Journal (1968), 78, 36-37.

[12] SUMER, B. M., TRUELSEN, C., SICHMANN, T. & FREDSøE, J. 2001. Onset of scour below pipelines and self-burial. Coastal engineering, 42, 313-335.

[13] SUMNER, D. & HESELTINE, J. L. 2008. Tip vortex structure for a circular cylinder with a free end. Journal of Wind Engineering and Industrial Aerodynamics, 96, 1185-1196.

[14] SUMNER, D., HESELTINE, J. L. & DANSEREAU, O. J. P. 2004. Wake structure of a finite circular cylinder of small aspect ratio. Experiments in Fluids, 37, 720-730.

[15] WEST, G. S. & APELT, C. J. 1982. The effects of tunnel blockage and aspect ratio on the mean flow past a circular cylinder with Reynolds numbers between 10 4 and 10 5. Journal of Fluid Mechanics, 114, 361-377.

TABLES

Case $No.$	G/D	Re_D	L/D	$\overline{C_D}$	$\overline{C_L}$	St	C_L'
1	∞	2500	5	1.08	0	0.217	0.143
2	0.5	2500	5	1.18	0.15	0.253	0.177
3	0.2	2500	5	1.09	0.27	N/A	0.011

Table 1 Variation of force coefficients and Strouhal number with gap ratio.

Case $No.$	Vortex Centre position $(x/D, z/D)$		
	HV1	HV2	HV3
1	(-0.92, 0.06)	(-1.10, 0.06)	(-1.28, 0.05)
2	(-0.91, 0.06)	(-1.08, 0.06)	(-1.26, 0.05)
3	(-0.83, 0.06)	(-1.00, 0.05)	

Table 2 Variation of vortex centre locations with gap ratio.

Case $No.$	G/D	Re_D	L/D	$\overline{C_D}$	$\overline{C_L}$	St	C_L'
1	0.5	1250	5	1.19	0.13	0.258	0.131
2	0.5	2500	5	1.18	0.15	0.253	0.177
3	0.5	5000	5	1.21	0.15	0.255	0.243

Table 3 Variation of force coefficients and Strouhal number with *Re*.

Case $No.$	Vortex Centre position $(x/D, z/D)$		
	HV1	HV2	HV3
1	(-0.92, 0.08)	(-1.14, 0.07)	
2	(-0.91, 0.06)	(-1.08, 0.06)	(-1.26, 0.05)
3	(-1.20, 0.05)		

Table 4 Variation of vortex centre locations with *Re*.

Case $No.$	G/D	Re_D	L/D	$\overline{C_D}$	$\overline{C_L}$	St	C_L'
1	0.5	2500	10	1.18	0.15	0.253	0.177
2	0.5	2500	20	1.17	0.14	0.255	0.179
3	0.5	2500	40	1.18	0.15	0.256	0.179

Table 5 Variation of force coefficients and Strouhal number with *L/D*.

Case $No.$	Vortex Centre position $(x/D, z/D)$		
	HV1	HV2	HV3
1	(-0.91, 0.06)	(-1.08, 0.06)	(-1.26, 0.05)
2	(-0.94, 0.06)	(-1.13, 0.06)	(-1.3, 0.04)
3	(-0.91, 0.07)	(-1.13, 0.05)	(-1.26, 0.05)

Table 6 Variation of vortex center locations with *L/D* .

FIGURES

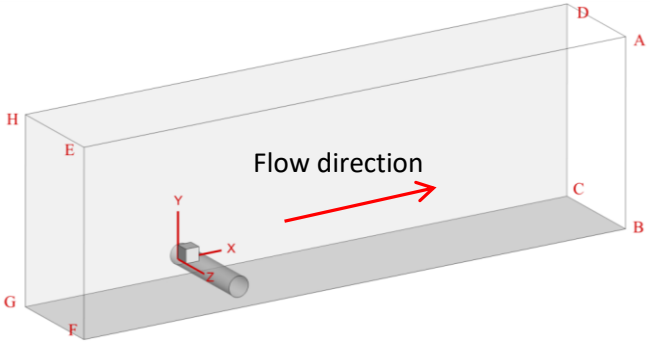

Figure 4 A sketch of computational domain with a side wall GHCD and a parallel plane GFCB below the cylinder.

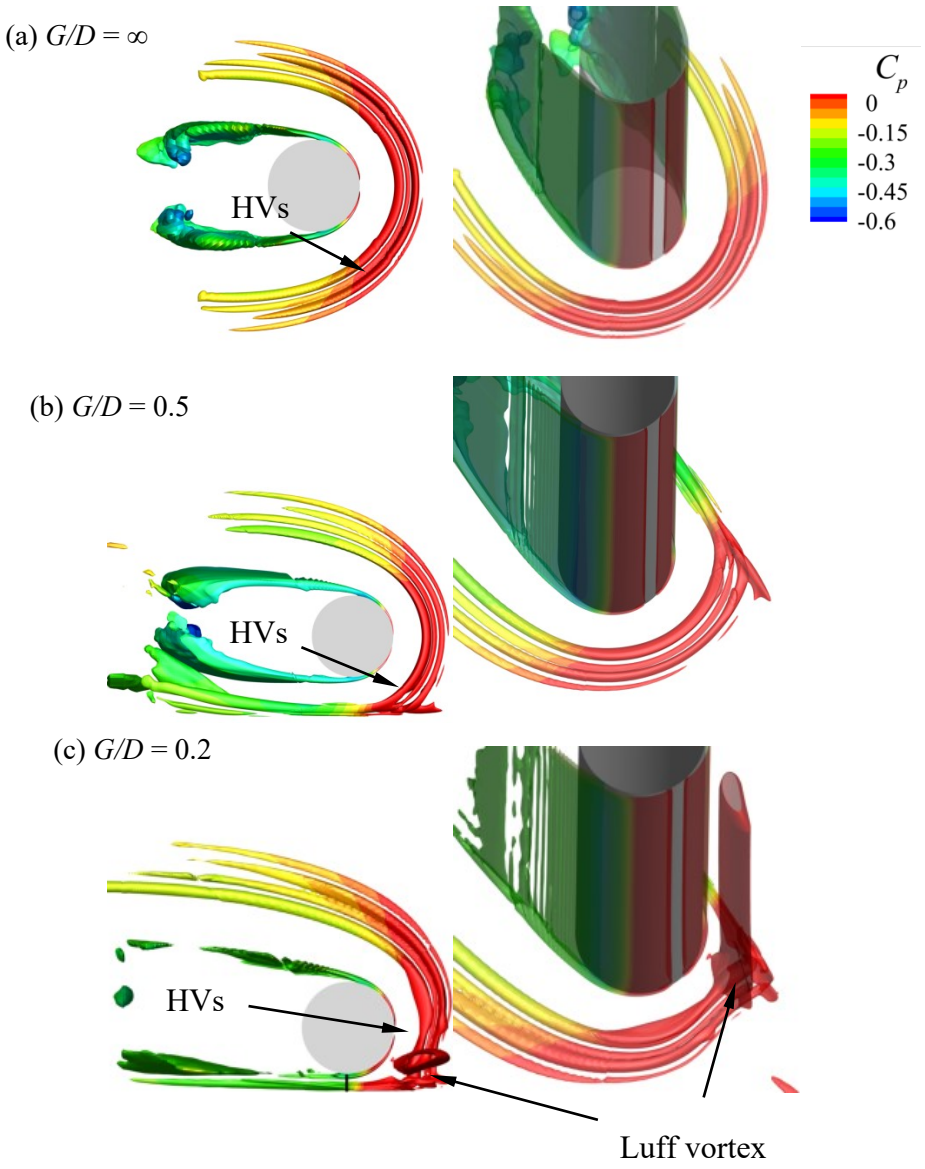

Figure 2 Snapshots of time-averaged iso-surfaces of λ for $G/D = \infty$ (a), 0.5 (b) and 0.2(c).

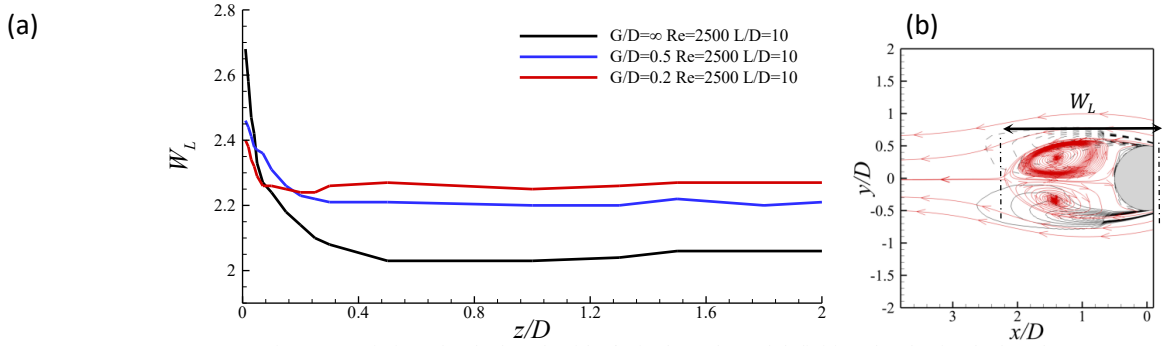

Figure 3 Variation of wake length with z/D in the wake and definition sketch of wake length.

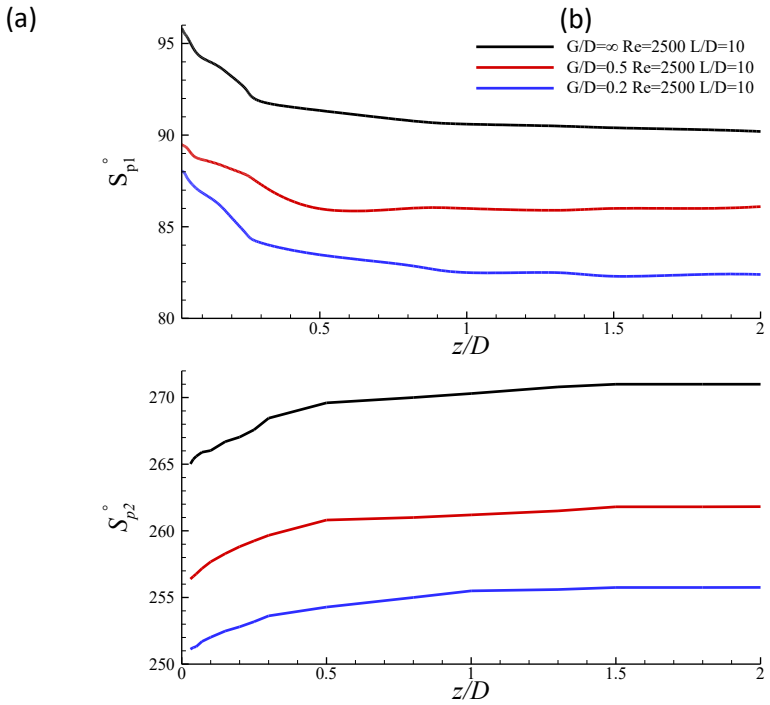

Figure 4 Variation of separation points on the cylinder surface with *z/D*. (a) separation points on the up side, S_{p1}, and (b) separation points on the gap side, S_{p2}.

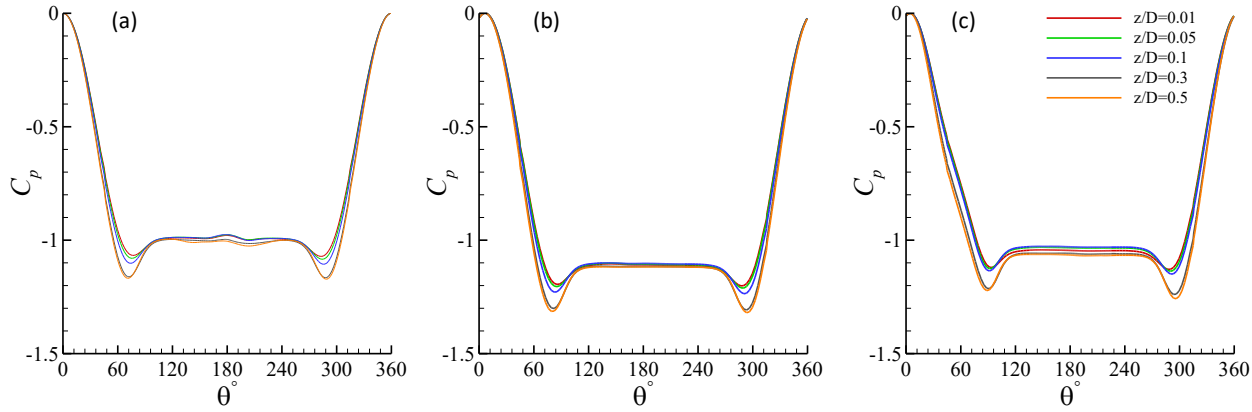

Figure 5 Sectional pressure distributions of the cylinder for (a) $G/D = \infty$, (b) for $G/D = 0.5$ and (c) for $G/D = 0.2$.

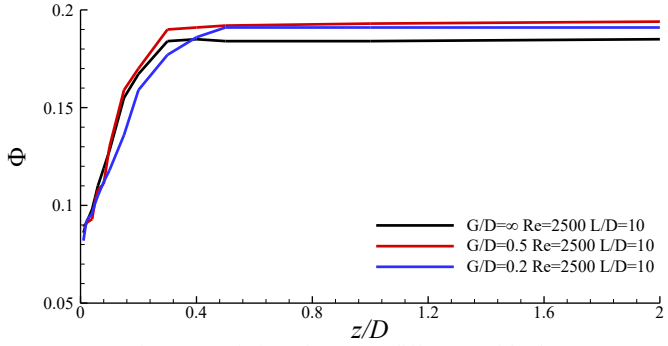

Figure 6 Variation of pressure difference with z/D.

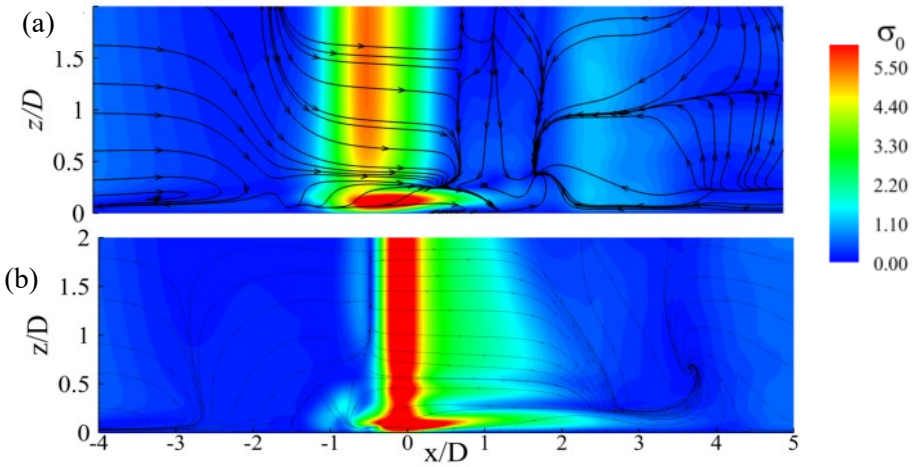

Figure 7 Magnitude of the wall shear stress on the seabed plane boundary for (a) G/D = 0.5 and (b) for G/D = 0.2.

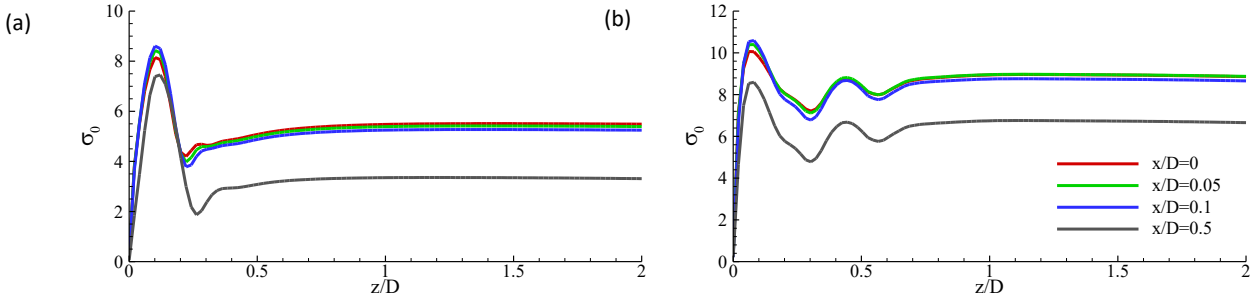

Figure 8 Comparison of amplification factor of the shear stress at x = 0. (a) G/D = 0.5, and (b) G/D = 0.2.

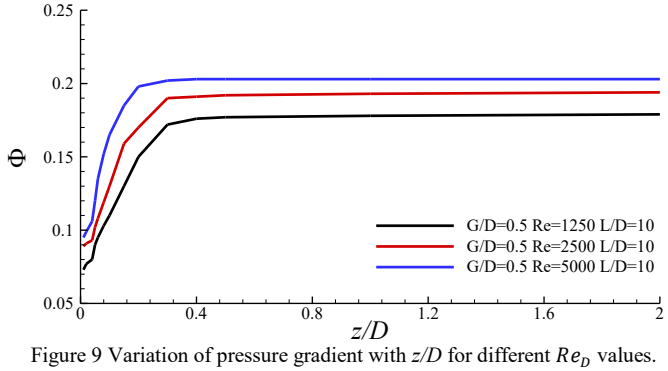

Figure 9 Variation of pressure gradient with z/D for different Re_D values.

(a) (b)

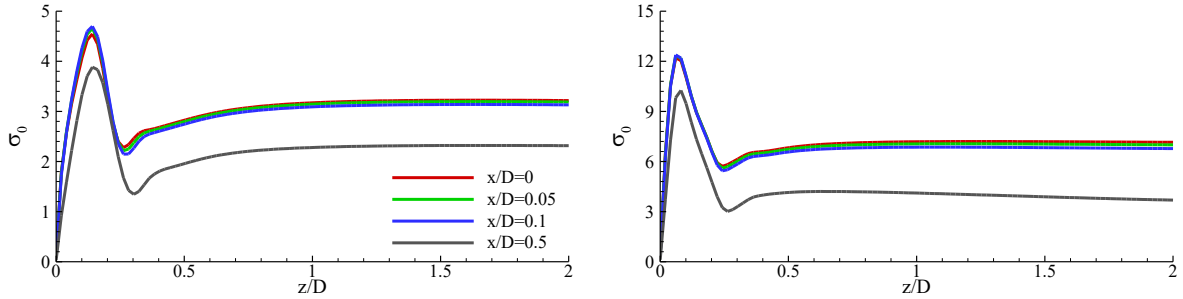

Figure 10 Comparison of amplification factor of the shear stress at $x = 0$. (a) Re_D = 1250. And (b) Re_D = 5000.

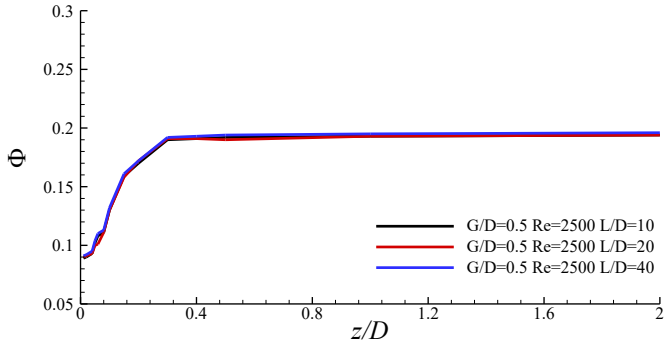

Figure 5 Variation of pressure gradient with z/D for different L/D.

(a)

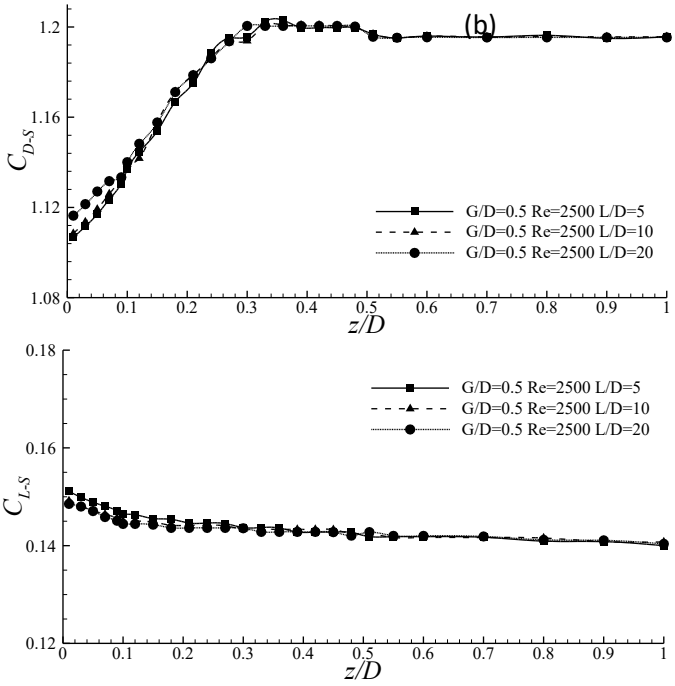

Figure 12 Variation of sectional drag (a) and lift (b) coefficients with z/D for different L/D values. (a) Sectional drag coefficient and (b) sectional lift coefficient.

CFD-based Modelling and Simulations of Flow Fields for a Shell-and-tube Heat Exchanger

Zhi Zhu
School of Computing, Engineering and Mathematics, Western Sydney University, Penrith, NSW 2751, Australia
30050832@westernsydney.edu.au

Chunhui Yang
School of Computing, Engineering and Mathematics, Western Sydney University, Penrith, NSW 2751, Australia
r.yang@westernsydney.edu.au

L&A Pressure Welding Pty Ltd, 77A Carrington St, Revesby, NSW 2212, Australia
raaid@la.services

Norman Chouaifaity
L&A Pressure Welding Pty Ltd, 77A Carrington St, Revesby, NSW 2212, Australia
norman@la.services

David Fox
L&A Pressure Welding Pty Ltd, 77A Carrington St, Revesby, NSW 2212, Australia
david@la.services

Abstract—**In this research, the full Computational Fluid Dynamics (CFD) model of a shell-and-tube heat exchanger yielded visualised results; A shell-and-tube heat exchanger with two baffles was modelled in SolidWorks and then numerically solved using ANSYS fluent 6.3, followed by analyses of a transient CFD simulation. The flow field, temperature and pressure distribution in the heat exchanger were investigated from the visualisation of CFD simulation. Both tube side and shell side fluids are resolved into computational elements in ANSYS mesh, a standard k−ω turbulence model was employed with enhanced wall boundary conditions in the simulations. Simulation results indicate two-baffle design in the shell side may be inefficient for such a heat exchanger due to majority of shell side fluid bypassing the tubes after the first baffle. Based on these findings, several improvements of the design of double-baffled shell-and-tube heat exchanger could be proposed. A transient CFD simulation is also conducted over the same heat exchanger model to obtain flow field changing pattern, temperature and pressure distribution by timestep.**

Keywords: Shell-and-Tube Heat Exchanger, heat exchange, CFD Simulation, temperature, pressure; flow velocity

I. INTRODUCTION

In today's process industries heat exchangers are widely used for energy interchange in many purposes, of which, shell-and-tube heat exchangers (STHEs) are the most commonly-used type due to their manufacturability and flexibility to different applications. A heat exchanger does the work of transferring heat from one fluid to another mainly via convection and conduction through its walls [1]. A STHe comprises of tubes in bundles encompassed by cylindrical shell in which two fluid flows between shell and tubes and trough tubes respectively. They are popular in many industries by their easiness of maintaining and parts replacement, and they are operational under harsh conditions owing to high tolerance of pressure and temperature.

The design and optimisation of STHEs usually concerns thermodynamic and fluid dynamic design, cost estimation and optimisation, largely involves empirical interdisciplinary knowledges and design rules, which makes it a highly complex process [2, 3]. The Kern method is usually employed in conjunction with the Bell-Delaware method to underpin the design of STHes [4, 5]. Kern method is restricted to evaluating shell-side pressure drop and heat transfer coefficient and is only applicable in cases where shell-side Reynolds number higher than 2000 and flow field is non-laminar [4]. Bell-Delaware method can make predictions on pressure drop and heat transfer coefficient with relatively better accuracy, however, it is unable to locate design weaknesses whilst determining whether design weaknesses exist [5]. With the assistance of Computational Fluid Dynamics (CFD), it is now possible to visualise the flow fields as well as temperature fields, simplifying the evaluation of design weaknesses. CFD discretise the model into tiny regular cells and solve governing equations to obtain numerical results of pressure distribution and temperature gradients [6]. This enables people to better understand the flow and temperature phenomenon within the STHes, allowing people to grasp the sources of design weaknesses and thus to further improve the design.

There were a lot of studies conducted for the purpose with various approaches, including both theoretical experimental. However, the past researches mainly focused on specific aspects of STHes without having a global perspective, which leaves a research gap for this research attempting to fill. Amongst them, Thirumarimurugan et.al [1] researched a Shell-and-Tube heat exchanger on its heat transfer characteristics. Zhang, et.al [7] adopted Bell-Delaware method combined with public literatures to establish such a method for design and evaluation of helically baffled STHes. Bhutta, et.al [6] tested the application of different turbulent models in Computational Fluid Dynamics (CFD) in terms of fluid flow mal-distribution, fouling, pressure drop and thermal analysis in the design of a heat exchanger. Li and Kottke [8, 9] studied the impacts of tube arrangement on local heat transfer coefficients of heat exchangers and have visualised the results. In addition, Karno and Ajib [10] further revealed the effect on heat transfer of heat exchangers of tube pitch. As compared to flow field tube side, shell side flow field is much more complex because numerous leakage paths and bypass streams among flow zones [11]. Gay and Mackley [12] and Gaddis investigated shell-side heat transfer and pressure drop using electrochemical mass transfer modelling technique and CFD respectively. CFD offers a cost effectiveness speedy solution to the development of this heat

exchanger by comparing conventional methods. The alternative CFD provides has eliminated the need of prototyping and has become an integral part of the heat exchanger development process [14]. However, large amounts of computational cost are inevitable for a complete CFD simulation over a delicate heat exchanger as the geometrical complexity will result in vast number of elements from discretisation. Prithiviraj and Andrews [15] estimated the number of elements an industrial STHes without simplification would be resolved into, which has necessitated the simplifications of heat exchangers. Several widely used simplification methods including porous medium model and the distributed resistance approach were employed and tested by Prithiviraj and Andrews [15], Sha, et al. [16] and He, et al. [17].

In this study, CFD-based numerical modelling and simulations of thermal-fluid fields in a miniature STHes designed by L&A at its shell side and tube side are carried out and the CFD model is devised by defeaturing negligible external features including handles, mountings and flanges to minimise geometrical complexity, which are not contributing to the internal CFD simulations. The flow, temperature and pressure fields of the STHes are determined as the main outcomes of the CFD simulations.

II. CFD MODELLING AND ANALYSIS

As shown in Figs. 1(a) and (b), the L&A's shell-and-tube heat exchanger consists of two tube bundles containing 5 tubes each, and 2 sets of inlet and outlet at each shell side and tube side, respectively. There are two windows designed for good observations and monitoring of two flow fields for both shell side and tube side within the heat exchanger. In the shell side, this STHes only has two baffles. The design parameters are presented in Table I. The geometric model of this STHes and the model after simplification are shown in Figs. 1(b) and (c), respectively. The latter one was created by defeaturing the minor features as mentioned above.

Table I. Design parameters of the heat exchanger

Shell size, D_s	154.06 mm
Tube size, T_s	11.84 mm
Outlet and inlet diameters, d_o and d_i	20.64 mm
Tube bundle geometry and pitch triangular	40.43 mm
Number of tubes, N_t	10
Length of the heat exchanger, L	1152.2 mm
Number of baffles, N_b	2
Baffle cut, B_c	24%

Based on Fig. 1(c), the CAD model of this STHes was created by using SolidWorks 2017, followed by being converted into parasolid format and further imported to ANSYS Workbench/Deisngmodeler, in which fluid domains and solid domain were identified, and media were assigned to them, respectively. The working fluid of both shell side and tube side was water, and stainless steel was selected to be the material of the heat exchanger. Then, ANSYS Fluent Version 6.3 was used to conduct a series of CFD simulations. Appropriate discretisation scheme and meshing were selected with using the k-ε turbulence model. CFD simulations yielded visualised results, which were later used in comparison with the results obtained by using the Bell-Delaware method.

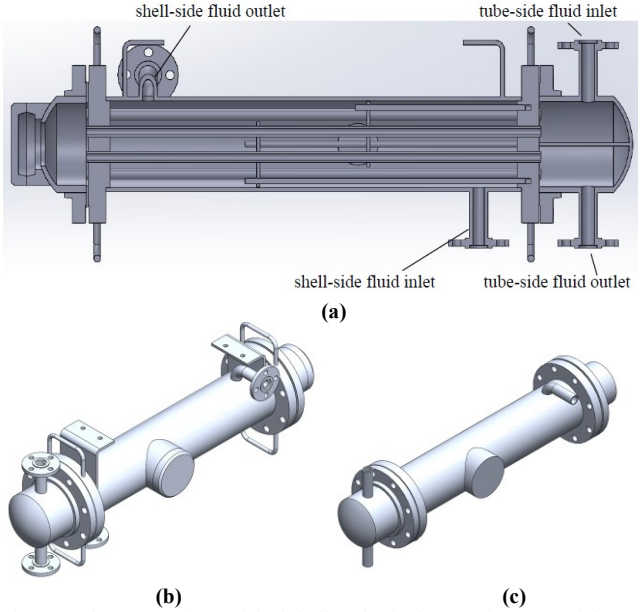

Figure 1 The geometric model of shell-and-tube heat exchanger and the simplified model: (a) section view of the heat exchanger, (b) isometric view of the heat exchanger, (c) isometric view of the simplified heat exchanger.

A. Boundary conditions

A constant 0.0861 kg/s mass flow rate was set to both the inlet of shell side and tube side, while a temperature of 373.15 K was assigned to tube side fluid at inlet and a room temperature of 298.15 K was assigned to shell side fluid at inlet constantly. Moreover, both the initial temperatures of shell side fluid and tube side fluid were set to be consistent with their respective input fluid temperatures. Zero gauge pressure is selected at outlet nozzles of both shell side and tube side. Gravitational acceleration was counted to be 9.8 m/s^2. In order to avoid sharp heat exchanging the walls were initially set to be at 318.15 K. Table 2 summarises those boundary conditions used in the CFD simulations.

Table II. Boundary conditions used in CFD models

Domain	Inlet flowrate (kg/s)	Inlet temp (K)	Initial temp (K)	Media
Wall	0	-	318.15	Steel
Shell side fluid	0.0861	298.15	298.15	Water
Tube side fluid	0.0861	373.15	373.15	Water

B. Mesh Convergence

Mesh generation was performed in ANSYS Mesh. The size function was selected to be curvature to attain more regular computational elements when dealing with sharp corners. Whereas, the mesh with a reasonably good mesh size was employed in this case with such a complexity. Proper constraints were applied to edges at key locations to better control the mesh for local refinement. Eventually approximately 4.4 million elements were used for model the heat exchanger was resolved into, which is sufficient enough

to yield a fine and accurate CFD simulation. The meshes of fluid domains for both tube side and shell side are shown in Fig. 2. The residual convergence criterions were set at 10^{-5}.

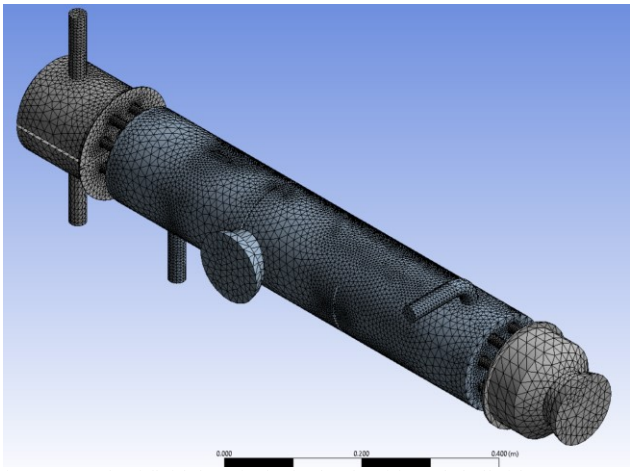

Figure 2 Mesh of fluid domain for both tube side and shell side.

C. Turbulence model

As a direct result of the instability of the flow turbulences can hardly be eliminated in industrial heat exchanger flow fields, and thus the flow turbulences should be taken into account in CFD simulations. Turbulent flows are usually accompanied by irregular and chaotic movements of fluid which differ them from laminar flows [18]. Because the turbulences involve a whole range of length, velocity and time scales, it is extremely laborious and nearly insolvable in the CFD simulations. A set of turbulence models using approximation or simplified approaches with different resolutions were thus developed to solve the turbulence problems. These approaches can make CFD simulation realisable to simulate turbulent flows. In commercial CFD packages, several turbulence models including Large Eddy Simulation (LES) and Reynolds Average Navirer-Stokes (RANS) are integrated and available for use. Specifically, under the RANS model there are several different types of models dealing with different characteristic of flows, of which, the standard *k-ε* model is the one was used in this study.

D. Standard k- ε model

The standard *k-ε* model was implemented in the current CFD model according to ANSYS FLUENT V6.3 User Manual [19], referencing a typical approach demonstrated by Launder and Spalding [20] in their study of mathematical models of turbulence. The standard *k-ε* model based on the usage of two transported variables to close the series of equations was proved to be able to achieve great dependability in terms of industrial use [21]. Turbulent kinetic energy, *k* and turbulent dissipation *ε* are the first and second transport variables, respectively, in this case. The modelled transport governing equations for two variables in this case can be described mathematically using the equations as follow,

For k,

$$\frac{\partial k}{\partial t} + \langle U_j \rangle \frac{\partial k}{\partial x_j} = \nu_T \left[\left(\frac{\partial \langle U_i \rangle}{\partial x_j} + \frac{\partial \langle U_j \rangle}{\partial x_i} \right) \frac{\partial \langle U_i \rangle}{\partial x_j} \right] - \varepsilon + \frac{\partial}{\partial x_j} \left[\left(\nu + \frac{\nu_T}{\partial k} \right) \frac{\partial k}{\partial x_j} \right] \quad (1)$$

For ε,

$$\frac{\partial \varepsilon}{\partial t} + \langle U_j \rangle \frac{\partial \varepsilon}{\partial x_j} = C_{\varepsilon 1} \nu_T \frac{\varepsilon}{k} \left[\left(\frac{\partial \langle U_i \rangle}{\partial x_j} + \frac{\partial \langle U_j \rangle}{\partial x_i} \right) \frac{\partial \langle U_i \rangle}{\partial x_j} \right] + C_{\varepsilon 2} \frac{\varepsilon^2}{k^2} + \frac{\partial}{\partial x_j} \left[\left(\nu + \frac{\nu_T}{\partial \varepsilon} \right) \frac{\partial \varepsilon}{\partial x_j} \right] \quad (2)$$

$$U_i = \langle U_i \rangle + u_i \quad (3)$$

$$\langle U_i \rangle = \frac{1}{2T} \int_{-T}^{T} U_i \, dt \quad (4)$$

The turbulent kinetic energy and dissipation rate were used to calculate turbulence time constant.

$$\tau = \frac{k}{\varepsilon} \quad (5)$$

In the use of k-*ε* model turbulent viscosity needs to be computed in order to close the equation.

$$\nu_T = C_\mu \frac{k^2}{\varepsilon} \quad (6)$$

Based on experiments of several basic types turbulent shear flows of air and water the k-*ε* model constants were thus determined empirically and generally considered to be consistent to all flows, despite that they deviate slightly in different flows [18]. Their default value is given in Table III below.

Table III. Standard *k- ε* model constants

Constants	Values
C_μ	0.09
$C_{\varepsilon 1}$	1.44
$C_{\varepsilon 2}$	1.92
σ_ε	1.3
σ_k	1.0

E. Near wall treatment

To relate different variables including velocity, temperature and pressure near the turbulence boundary layers, a set of formulas were developed and commonly accepted as wall functions. By applying the law of wall to formulate turbulence variables, wall functions are able to calculate the boundary conditions deviating from the wall. Based on different turbulence models, several types of wall functions are commonly used [5].

- Standard Wall Functions
- Non-Equilibrium Wall Functions
- Enhanced Wall Functions

In this study, enhanced wall functions were selected due to the improvement of predictions of wall shear stress and wall heat transfer. Nonetheless, enhanced wall functions required a finer mesh to provide higher near wall grid resolution, resulting in larger computational power cost by comparing to other wall functions consequently [22].

III. Results and Discussion

In a former study done by Ozden E [23], the results of a complete CFD model of a laminar flow heat exchanger were compared with experimental data gathered in a tiny teaching heat exchanger with only two baffles. Additionally, Ozden E

and Tari L [11] have investigated the simulation results sensitivity to the selection of turbulence model and discretization scheme using different inputting mass flow rate at shell side of a heat exchanger. Khaled C et al. [24] compared DNS data and the predicted streamwise simulation results at four locations in a previous study of CFD application on wavy surfaces. In the present study, overall heat transfer coefficients are calculated by following equations:

$$Q_h = m_h C_p(\Delta T_1 - T_{h,o}) \quad (7)$$

$$Q_c = m_c C_p(T_{c,i} - T_{c,o}) \quad (8)$$

$$Q = UA\Delta T_{LM} \quad (9)$$

where, Q is the heat transfer rate (W), A is the heat transfer area (m^2), U is the overall heat transfer coefficient ($W/m^2.K$), ΔT_{LM} is logarithmic mean temperature difference (K).

$$\Delta T_{LM} = \frac{\Delta T_2 - \Delta T_1}{ln\frac{\Delta T_2}{\Delta T_1}} \quad (10)$$

where,

$$\Delta T_1 = \Delta T_{h,i} - \Delta T_{c,o} \quad (11)$$

$$\Delta T_2 = \Delta T_{h,o} - \Delta T_{c,i} \quad (12)$$

A. Transient CFD simulation findings

Arendt and Krzaczek [25] developed a strategy using transient CFD model of indoor air and thermal envelop to fully simulate transient numerical model of heat transfer in building. Although transient CFD simulation demands way larger computational power and computing time, it allows the continuous observation on the instantaneous phenomenon of flow, which exists extensively in heat exchanger, making a more comprehensive study of turbulence flow and energy dissipation possible. In this study, we selected 12 locations to intermittently gather instant flow data with 2 seconds interval. Table VI and Fig. 3 show their locations in detail.

Table VI. Locations of sensors

Location	X (m)	Y (m)	Z (m)
Sensor 1	2.776e-01	6.771e-02	0.000e+00
Sensor 2	1.012e-01	-6.845e-02	0.000e+00
Sensor 3	2.329e-01	-6.918e-02	0.000e+00
Sensor 4	3.670e-01	-7.176e-02	0.000e+00
Sensor 5	3.670e-01	-1.111e-01	8.012e-02
Sensor 6	4.764e-01	-5.962e-02	4.206e-02
Sensor 7	6.011e-01	6.992e-02	0.000e+00
Sensor 8	8.623e-01	5.888e-02	4.604e-02
Sensor 9	8.623e-01	1.189e-01	0.000e+00
Sensor10	1.078e+00	1.248e-01	0.000e+00
Sensor11	1.078e+00	-5.888e-02	4.263e-02
Sensor12	1.078e+00	-1.152e-01	0.000e+00

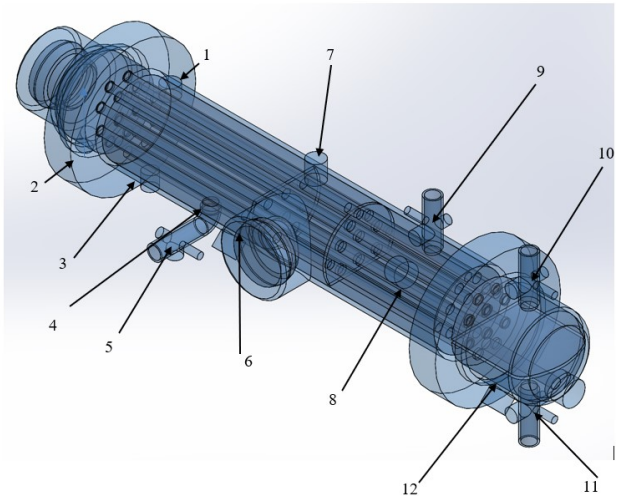

Figure 3 Locations of sensors

The historic data on temperature, pressure and velocity at these 12 sensors are shown in Fig. 4 for reference. At each location, temperature, pressure and velocity was monitored throughout 30 seconds time span which was segmented into 15 breakpoints.

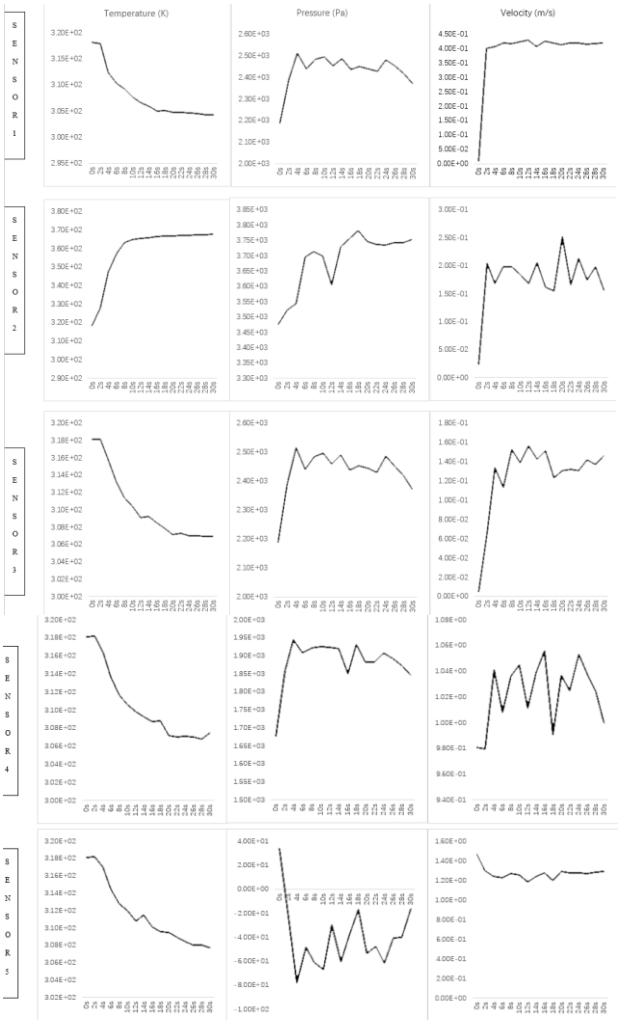

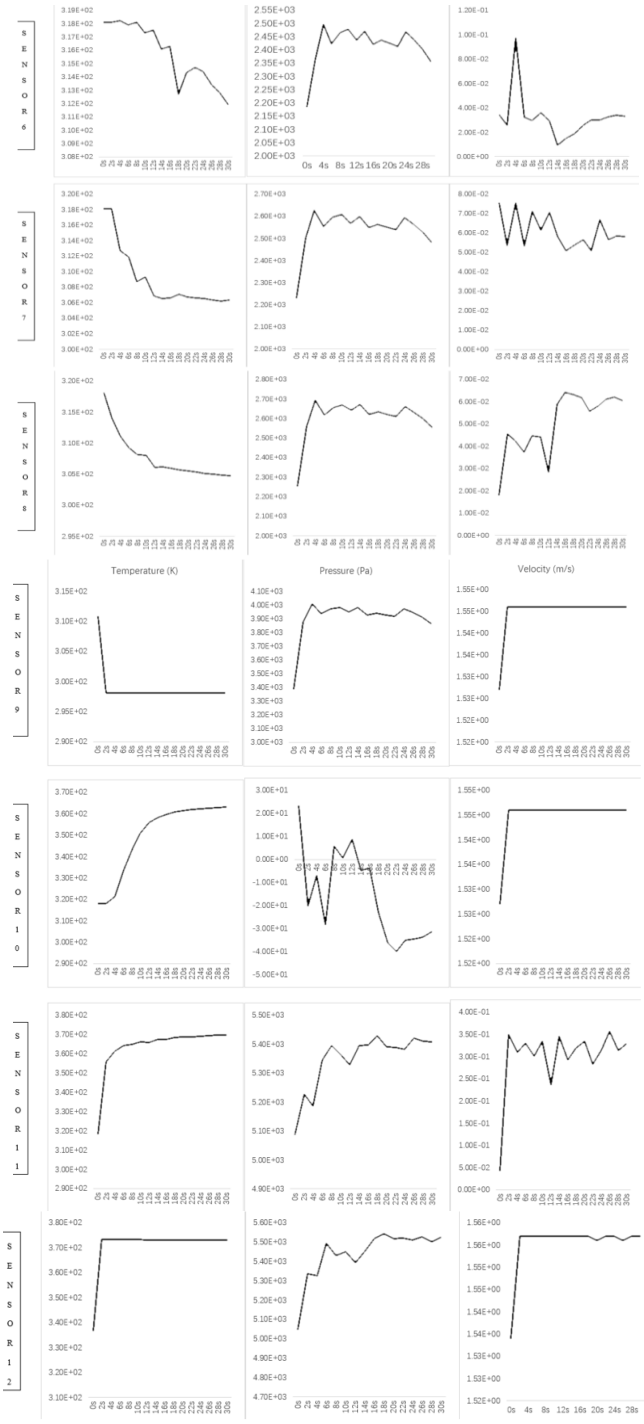

Figure 4 History data of temperature, pressure and velocity at 12 locations.

From these transient CFD simulation results, it can be observed that temperature field throughout the calculating time has been behaving mildly. However, in general pressure field has been changing softly except at location 10 where sharp fluctuations were observed in the process. Location 10 was at the tube side outlet and no rugged geometry was able to cause such violent behaviour in pressure, this may be caused by the mesh nonuniformity at the place. Velocities are oscillating in most of the places, indicating the existence of turbulent flow in a relatively large scale.

B. Contour plots

The temperature, velocity and pressure distribution within the shell-and-tube heat exchanger can be observed via side views of the planes set in post process in ANSYS. The contour plots of temperature and pressure are shown in Fig. 5.

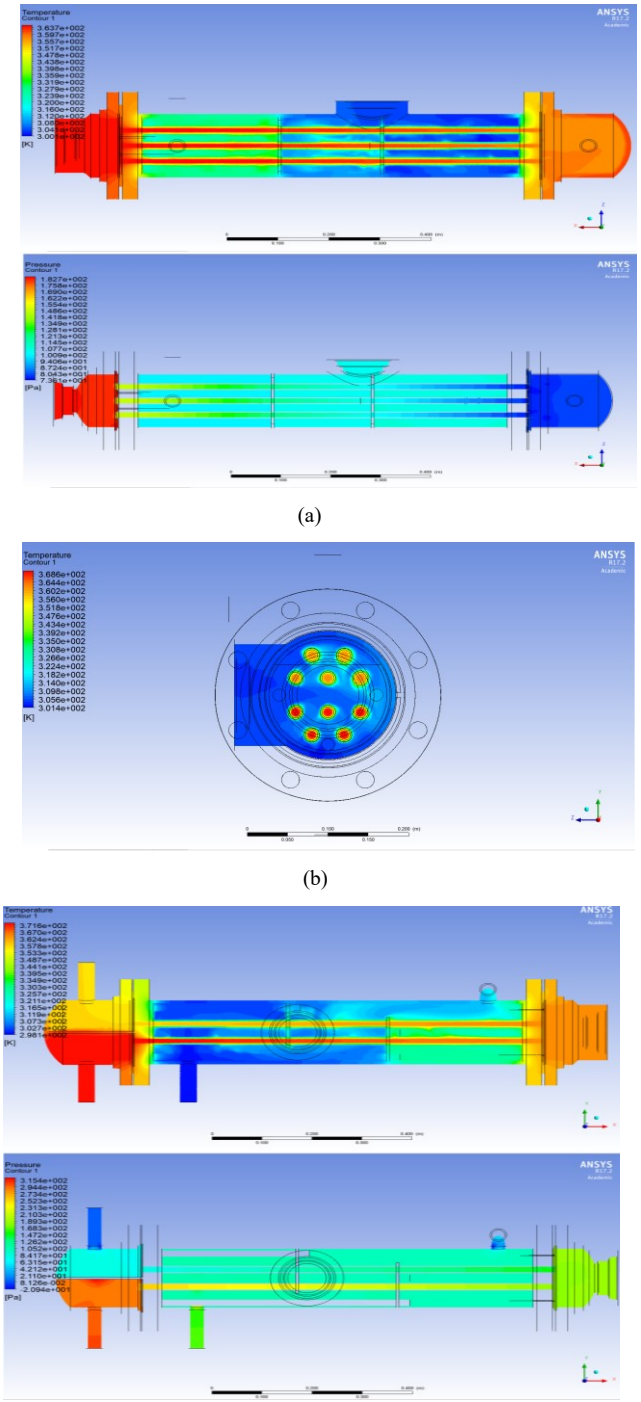

Figure 5 Contour plots of temperature and pressure distribution: (a) symmetry plane y-direction, (b) plane x-direction cut through middle of the observation window, and (c) symmetry plane z-direction.

Temperature distributions clearly show that after the first baffle, the temperature profile becomes evenly from flowing towards shell side outlet, which is attributed by the heat exchanging mainly happening at the inlet side. Differently, according to pressure contour plots, overall the pressures were well distributed throughout the heat exchanger. In Fig. 5(b), it can be seen that the temperature difference between shell side fluid and tube side fluid is already at a considerable

magnitude even lowest of which reaches up to 7% of the hot fluid inlet temperature.

C. *Streamline plots*

Streamline plot is highly suitable for expressing velocity as it shows both direction and magnitude. It also highlights the paths of turbulent flows, explicitly revealing the state of flow field within heat exchanger. From Fig. 6(a), large voids of flows are identified right below shell side outlet, while most of the energy would appear to have formed turbulence flows before the first baffle, above shell side inlet. Such distributions clearly indicates a design weakness of this two-baffle shell-and-tube heat exchanger, which can be improved by increasing baffle cut or adjusting baffle location along the shell. Current design obviously created a dead zone of energy interchange. This can also be seen in Fig. 6(b), it is apparent that the kinetic energies of turbulent flows are mostly dissipated within the shell side to where the inlet is located.

IV. CONCLUSIONS

A CFD model of the L&A's STHes was developed on both shell side and tube side to carry out a series of detailed simulations. The flow, temperature and pressure fields of the STHes were obtained to capture the fluid flows' behaviours. Distinct temperature maldistribution due to the consequence of a design error, flow bypassing baffles was identified from the CFD simulation results. Evidence of the heat maldistribution were observed from multiple angles of temperature results and were consistent with flow velocity streamline plots. Inefficiency of heat exchange and insufficient usage of shell side room were thus concluded in this specific design of shell-and-tube heat exchanger though, several simple approaches for improvement could be proposed. Firstly, baffle cut less than 30% is too low to allow enough flow through to the space around outlet, thus should be increased. Secondly, the space between two baffles is too small that it almost makes fluid flow impossible to reach the place between then, directing fluid flows nearly straight to the outlet without dispersing, hence, the gap of two baffles should be widened. Thirdly, by increasing the shell diameter could better this design as well as it provides bigger room for fluid flows to swirl around within the shell side.

The shell-and-tube heat exchanger was also put into CFD transient simulation to obtain time-step results at designated locations. Observations at a scale of 30 seconds on the heat exchanger enabled the analysis of turbulence flow pattern by time, and chronological temperature distribution variation, the study of which could provide a higher angle of view to examine the flow and temperature fields of shell-and-tube heat exchanger. On the basis of transient simulation results, predictions on the temperature and pressure fields could be analytically made in similar heat exchangers.

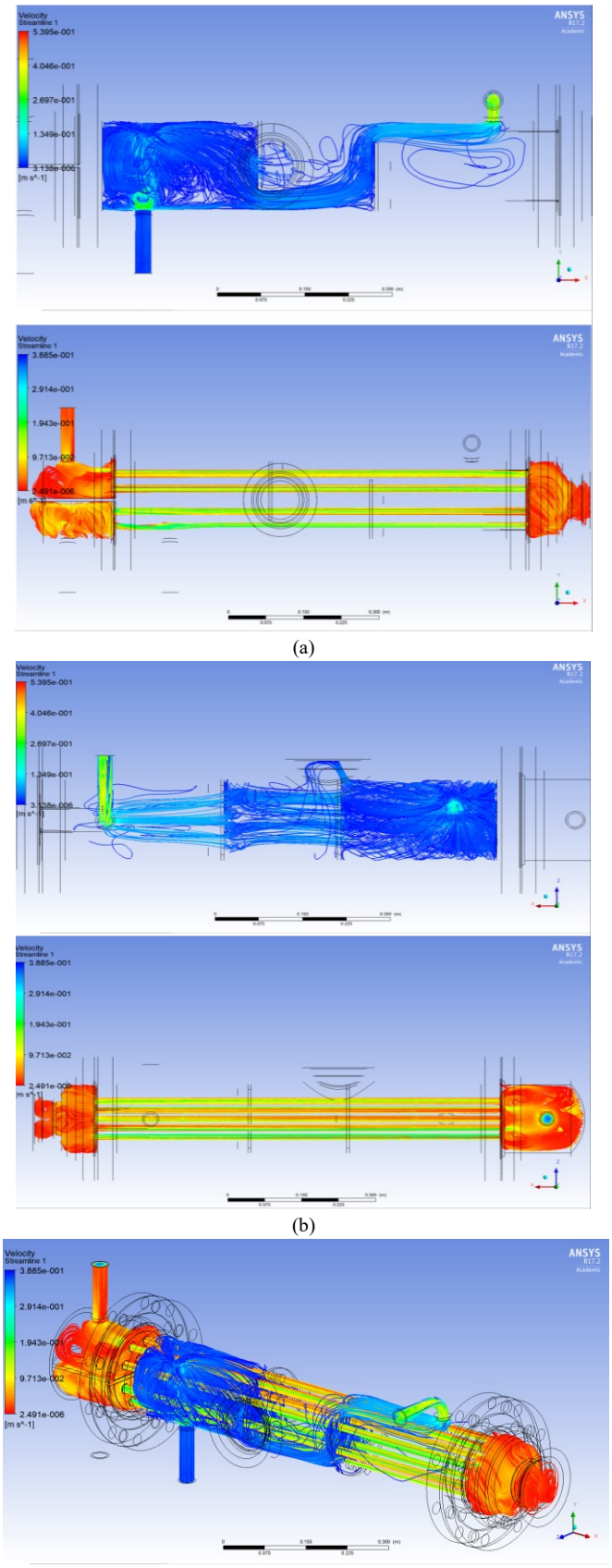

Figure 6 Velocity streamline plots: (a) symmetry plane z-direction, (b) symmetry plane y-direction, (c) isometric view showing both velocity streamline plots at shell side and tube side.

AKNOWLEGEMENT

The authors would like to show their gratitude to the LaunchPad, Western Sydney University and the Department of Industry, NSW State Government for their financial supports through the TechVouchers NSW Funding Program.

REFERENCES

[1] Thirumarimurugan M, Kannadasan T and Ramasamy E 2008, Performance Analysis of Shell and Tube Heat Exchanger Using Miscible System, American Journal of Applied Sciences 5 (5): 548-552.

[2] Fesanghary M, Damangir E, Soleimani I 2009, Design optimization of shell-and-tube heat exchangers using global sensitivity analysis and harmony search algorithm. Applied Thermal Engineering 29, pp.1026-1031.

[3] Selbas R, Kizilkan O, Reppich M 2006, A new design approach for shell-and-tube heat exchangers using genetic algorithms from economic point of view, Chemical Engineering and Processing, 45, pp.268-275.

[4] Kara YA, Gurarasa O 2004, A Computer Program For Designing Of Shell-And-Tube Heat Exchangers, Applied Thermal Engineering University Of Ataturk, Turkey.

[5] Rehman UU 2011, Heat Transfer Optimization of Shell-And-Tube Heat Exchanger through CFD Studies, Chalmers University of Technology.

[6] Bhutta MMA, Hayat N, Bashir MH, Khan AK, Ahmad KN, Khan S 2012, CFD Applications in Various Heat Exchangers Design: A Review, Applied Thermal Engineering, Vol 32, Pages 1-12

[7] Zhang JF, He YL, Tao WQ 2010, A Design and Rating Method For Shell-and-tube Heat Exchangers with Helical Baffles, J. Heat Transfer. 132(5): 051802 (8 pages)

[8] Li HD, Kottke V 1998, Visualization and determination of local heat transfer coefficients in shell-and-tube heat exchangers for staggered tube arrangement by mass transfer measurements. Exp Therm Fluid Sci; 17:210–6.

[9] Li HD, Kottke V 1998, Visualization and determination of local heat transfer coefficients in shell-and-tube heat exchangers for in-line tube arrangement by mass transfer measurements. Heat Mass Transfer; 33:371–6.

[10] Karno A, Ajib S 2006, Effect of tube pitch on heat transfer in shell-and-tube heat exchangers – new simulation software. Heat Mass Transfer; 42:263–70.

[11] Ozden E and Tari I 2010, Shell side cfd analysis of a small shell-and-tube heat exchanger, Energy Conversion and Management, vol. 51, no. 5, pp. 1004 – 1014.

[12] Gaddis ES, Gnielinski V 1997, Pressure drop on the shell side of shell-and-tube heat exchangers with segmental baffles, Chem Eng Process, vol. 36, pp. 149–59.

[13] Gay B, Mackley NV, Jenkins JD 1976, Shell-side heat transfer in baffled cylindrical shell and tube exchangers – an electrochemical mass transfer modelling technique, Int J Heat Mass Transfer, vol. 19, pp. 995–1002.

[14] Kotwal H, Patel DS 2016, CFD Analysis of Shell and Tube Heat Exchanger-A Review, International Journal of Engineering Science and Innovative Technology, Vol 2, pp.325-329.

[15] Prithiviraj M, Andrews MJ. (1998) Three-dimensional numerical simulation of shell and-tube heat exchangers, Part 1: foundation and fluid mechanics. Numer Heat Transfer. Part A, Appl;33:799–816.

[16] Sha WT, Yang CI, Kao TT, Cho SM 1982, Multidimensional numerical modeling of heat exchangers, J Heat Transfer;104:417–25.

[17] He YL, Tao WQ, Deng B, Li X, Wu Y, 2005, Numerical simulation and experimental study of flow and heat transfer characteristics of shell side fluid in shell-and tube heat exchangers. In: Proceedings of the fifth international conference on enhanced, compact and ultra-compact heat exchangers, Science, Engineering and Technology, Hoboken, NJ; p. 29–42.

[18] Andersson B, Andersson R, Hakansson L, Mortensen M, Sudiyo R, and Wachem BV 2010, Computational Fluid Dynamics for Chemical Engineers, Sixth Edition, Cambridge University Press, UK.

[19] ANSYS FLUENT 6.3®. User's Guide Manal; 2006.

[20] Launder BE, DB Spalding. (1972) Mathematical Models of Turbulence. Academic Press, London and New York; p. 169.

[21] Versteeg HK and Malalasekera W 2007, An Introduction to Computational Fluid Dynamics: The Finite Volume Method. Pearson Education Limited.

[22] ANSYS Fluent Theory Guide, http://www.ansys.com, 2010.

[23] Ozden E 2007, Detailed design of shell-and-tube heat exchangers using CFD, M.S. thesis, Middle East Technical University, Ankara, Turkey.

[24] Khaled C, Driss N, Nouredine S 2015, CFD Simulation of Turbulent Flow and Heat Transfer Over Rough Surfaces. Energy Procedia, 74(C), 909-918.

[25] Arendt K, Krzaczek M 2014, Co-simulation strategy of transient CFD and heat transfer in building thermal envelope based on calibrated heat transfer coefficients. International Journal of Thermal Sciences, vol. 85, pp. 1-11.

Engineering of Materials Through the Mapping of Parameter Space. Example of Magnetron Sputtered TiNbN Coatings

Leigh Sheppard
School of Computing, Engineering & Mathematics
Western Sydney University
Penrith, Australia
L.Sheppard@westernsydney.edu.au

Richard Wuhrer
Advanced Materials Characterisation Facility, Division of the Deputy Vice-Chancellor Research & Development
Western Sydney University
Penrith, Australia
Richard.Wuhrer@westernsydney.edu.au

***Abstract*—In order to engineer novel and advanced materials for specific applications it is essential to acquire the technical capabilities to control the imposition of desired functional properties. Using magnetron sputtered TiNbN as an example of an advanced orthopaedic material, the present investigation demonstrates the importance of mapping the available parameter space in order to determine the range of possible outcomes in terms of composition, structure and deposition rate. In a full study, additional parameters and outcomes should be comprehensively explored in order to achieve the desired imposition of functional properties under the most favorable commercial conditions ie high productivity.**

Keywords—TiNbN, magnetron sputtering, orthopaedic coatings,

I. INTRODUCTION

Magnetron sputtering is a commonly utilised technique for depositing materials onto substrates as either thin or thick films [1,2,3]. The purpose of these films varies greatly. In some instances the objective is to protect the underlying substrate from corrosion [4] or wear [5]. In other instances, the objective is to achieve a layer of material with a specific functional property, such as electrical conductivity, that compliments the properties of the substrate or a subsequent film to be later deposited [6,7].

As schematically illustrated in **Figure 1**, the magnetron sputtering technique provides a method for transferring material which is conveniently available as a solid disk (hence forth referred to as a target) onto a selected substrate in the form of a film of controlled thickness. The use of multiple target materials facilitates the deposition of films consisting of compounds [4], alloys [8] or heterogeneous multi-layered structures [9,10]. The utilisation of a reactive process gas during deposition (in combination with the inert sputtering gas) facilitates an additional dimension of deposition outcomes by enabling chemical reactions either at the target itself or during the transit of sputtered species through the plasma. The deposition of metal oxides or nitrides from the sputtering of pure metal targets in the presence of oxygen or nitrogen are common examples of such reactive magnetron sputtering [11,12,13]. Through the deliberate manipulation of the reactive process gas flow rate a range of conventional and novel material films can be readily achieved.

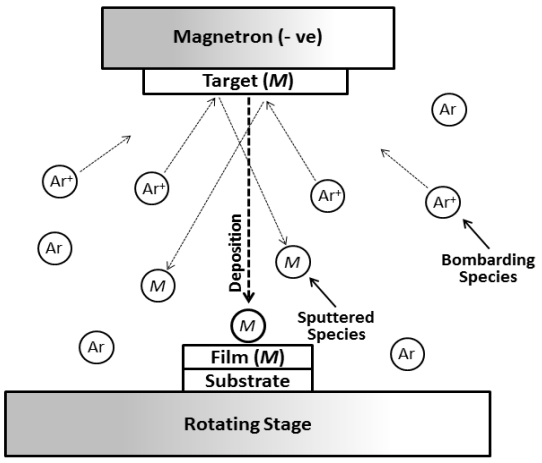

Figure 1. Schematic illustration of magnetron sputtering process.

To a very significant extent, the widespread utilisation of magnetron sputtering for material fabrication is due to the broad ranging scope of material films that can be deposited onto substrates that can be flat or 3-dimensional. The main practical limitation is only the need for the chosen target and substrate materials to be stable under high vacuum. Consequently, the sputtering literature abounds with examples of deposited metals [14], oxides [15], nitrides [16] and carbides [17]. While these are typically crystalline in structure, glasses can also be deposited [18].

The process of sputtering involves several key technical parameters which must be appropriately controlled and manipulated. These are 1) the discharge voltage which is applied to the target material and must be sufficient to establish the sputtering process, and 2) the deposition pressure which is the combined pressure of the inert sputtering gas and the reactive process gas. These parameters combine to achieve the deposition of target material on a substrate. Specifically, the discharge voltage electrostatically attracts and accelerates the ionised fraction of inert gas species (bombarding species) towards the target. Due to the impact of these species, target material is sputtered away from the target as a result (sputtered species). Increasing the discharge voltage has the general effect of increasing both the rate of sputtering and film growth. The quantity of ionised inert species available for bombardment of the target material is related closely to the deposition pressure and so typically an increase in sputter rate results from an increase in deposition pressure. However, if a fraction of the deposition pressure comprises a reactive gas, such as oxygen or nitrogen, then changes in the deposition pressure will be complicated

by the tendency of the target material to become oxidised/nitrided during sputtering. Under these conditions a unique steady-state will be established which has potential to shift markedly in response to any change in either the deposition pressure, process gas flow, or the discharge voltage. The practical significance is that the structural evolution of the deposited film will reflect the specific sputtering conditions that were achieved during deposition. Despite the relative convenience of the sputtering technique, this complexity when dealing with reactive sputtering poses a challenge to achieving broad ranging reproducibility between independent research teams. This complexity also facilitates the means for skilled research teams to achieve new advances in the processing of novel materials.

The aim of the present investigation is to demonstrate the importance of mapping the effects of changes made to key sputtering parameters during deposition. Only through such mapping does it become possible to make predictions concerning the structural evolution of a deposited film. Moreover, with a view towards the deposition of films or coatings for specific functional or technological applications, mapping the relevant parameter space is essential for the customisation of properties to match the needs of specific applications. It is also helpful for ensuring reproducibility and commercial viability. As an interesting model material system, the deposition and growth of TiNbN films will be the subject of this investigation.

II. Brief Literature Review

TiNbN is gaining research interest as an orthopaedic material for the coating of hip and knee replacement components [19, 20, 21, 22, 23, 24, 25, 26, 27]. It is an alternative coating material to TiN which is well established in applications that required hard surfaces for wear resistance or low friction [28, 29, 30, 31, 32, 33, 34]. TiN has been applied extensively to orthopaedic applications due to its outstanding mechanical properties and high biocompatibility but has demonstrated a tendency for brittleness [21, 35]. This is related to its application in hip and knee replacement implants and the naturally occurring but difficult to predict events such as accidental trips and falls. In these cases, a patient may inadvertently crack the TiN coating during a fall. The joint may otherwise be unaffected but the presence of a crack will lead to the onset of accelerated wear and ultimately the need to replace the implant altogether. This has considerable impacts on the patient's health [21, 35]. In an effort to reduce the brittleness of TiN, researchers have added Nb to improve ductility [21]. This has been successful and indications exist that TiNbN could be the successor of TiN in orthopaedic applications [21, 22, 23].

While TiNbN is very promising as an orthopaedic material the challenge lies in the ability to deposit this material in ways that optimise its properties. Underpinning this challenge is control over the composition of TiNbN. Specifically, TiN and NbN share the same structure, *fcc,* and space group (Fm-3m) [19]. Additionally, the lattice spacing of TiN (a = 0.4241 nm [36]) is comparable to that of NbN (a = 0.441 nm [37]). The consequence is that TiN and NbN are completely miscible and form a solid solution whenever mixed [19]. Hence, while TiNbN may be referred to as the phase applied to the orthopaedic application, a more accurate representation is $Ti_xNb_{1-x}N$. An additional complication relates to the tendency for variable uptake of nitrogen which further refines the identity of this material to $Ti_xNb_{1-x}N_y$.

The result of this material complexity is that the properties demonstrated by TiNbN films and coatings are highly variable. This is demonstrated in **Table 1** where all properties exhibit a broad range of reported values. This can be largely attributed to the compositional variability of the material as supported by the first principle investigation undertaken by Arockiasamy *et al* [21]. However, variability in functional properties can also be attributed to specific influences that stem from the applied processing technique. For example, the generation of residual stresses during the deposition of TiNbN films via magnetron sputtering is one identified source of variability in applied performance [25]. In order to fully achieve the potential of TiNbN as an effective and durable orthopaedic coating material, it is essential that this material can be deposited with reliable and predictable material properties.

Table 1. Summary of reported properties of TiNbN

Property	Reported Value
Hardness (GPa)	29.0 [27] 19.8 – 29.1 [21]
Young's Modulus, E (GPa)	452 [27] 375 – 441 [21]
Poisson Ratio, v	0.25 – 0.29 [21] 0.22 [27]
Roughness, Ra (nm)	43.6 [27] 8 [24] 0.5 – 2 [25] 1.5 ± 0.25[31]

III. Experimental Method

A. Specimen preparation and deposition procedure

Small *p*-Si (100) single crystal wafers (University Wafer, www.universitywafer.com) of approximately 15 mm x 15 mm in size were used as substrates for the growth of $Ti_xNb_yN_z$ coatings in this investigation. $Ti_xNb_yN_z$ coatings were then reactively magnetron sputtered onto the substrates using an Orion 5 sputtering instrument, (AJA International, Scituate MA, USA). The targets (50.8 mm dia) were 99.9% titanium (AJA International, Scituate MA, USA) and 99.9% niobium (AJA International, Scituate MA, USA). These targets were co-sputtered with the discharge power (DC) applied to the titanium target held constant at 150 W in all circumstances, whereas the Niobium target received a discharge power of either 75 W or 150 W. This achieved two types of $Ti_xNb_yN_z$ coatings which have subsequently been identified as T150N75 and T150N150. The deposition pressure was fixed at 3 mTorr as the default condition and consisted of 2.4 mTorr of argon (99.9%; Coregas, Australia) and 0.6 mTorr of nitrogen (99.9%; Coregas, Australia) reactive process gas. Each deposition took nominally 90 minutes and was not initiated until a base pressure of <1 x 10^{-6} Torr had been maintained in the deposition chamber immediately prior. The samples were rotated at ~10 rpm during deposition and no substrate heating or bias was applied.

B. Characterisation procedure

After deposition, all $Ti_xNb_yN_z$ coatings were characterised using standard techniques. Energy Dispersive Spectroscopy (EDS) for composition determination, and Glancing Angle X-ray Diffraction (GA-XRD) for phase assessment. EDS X-ray spectra were acquired using a Zeiss 534VP scanning electron microscope operated at 8kV accelerating voltage with a Moran Scientific Microanalysis system using an Amptek silicon drift detector (SDD) that had a C2 Si_3N_4 window (40 nm). The EDS was calibrated with a CrN light element standard from Eastern Analytical. GA-XRD (Discover D8, Bruker, Germany) was used to obtain the crystallographic structures of all coatings. The glancing incidence diffraction measurements were performed at an incident angle of 2° and used Cu *Kα* radiation of 0.15418 nm wavelength.

IV. Results and Discussion

EDS results have been obtained for the two samples, T150N75 and T150N75. The resulting compositions are summarised in **Table 2**. As seen, the application of equal discharge power to both targets (T150N150) has led to a coating that is substantially rich in Nb. In contrast it is the unequal application of discharge power which has achieved a composition that is almost equimolar Ti to Nb. This result reflects the different abilities of these two metals to be sputtered through the bombardment of argon. This has important practical significance, specifically in relation to the choice of target material.

Table 2. EDS determined composition of deposited $Ti_xNb_yN_z$ coatings.

Element Analysed	Coating	
	T150N75	T150N150
[Ti]	22 at. %	13 at. %
[Nb]	23 at. %	34 at. %
[N]	56 at. %	54 at. %

One of the advantages of sputtering is that often there is a choice concerning the target material used to deposit a film or coating. In the case of TiNbN there are examples in the literature of investigators using TiNb alloys as the target material [26]. This can subsequently deposit a TiNb-nitride if nitrogen is used as a process gas. An assumption is often made that the composition of the deposited film will reflect that of the sputtered target material. However as demonstrated in Table 2 for T150N150, this is not necessarily the case due to the different sputtering abilities of individual atoms being sputtered. This is made further complicated by the presence of a reactive process gas, such as nitrogen, and the relative abilities of the constituent elements, and the target itself, to be nitrided.

Displayed in **Figure 2** below is the effect on discharge voltage of incremental changes in nitrogen partial pressure during deposition. Under conditions of fixed applied discharge power, changes in discharge voltage inversely reflect changes in discharge current which relate to the rate that charged species are ejected from the target due to sputtering. As seen, the two target materials display substantially different responses to the presence of nitrogen

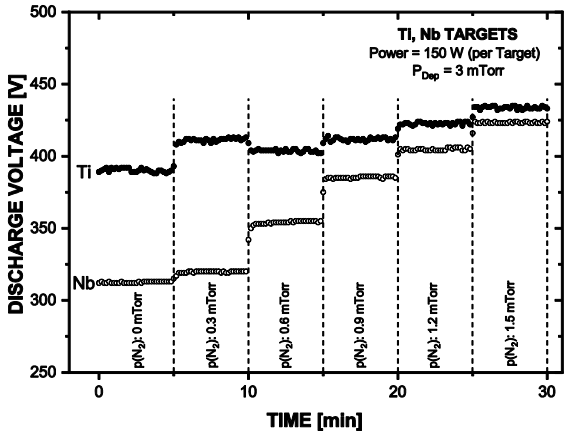

Figure 2. Effect of $p(N_2)$ on the discharge voltage of Ti and Nb targets during deposition.

process gas. When $p(N_2)$ is equal to 0 mTorr, the discharge voltage of Ti and Nb is respectively ~380 V and ~310 V. This indicates that in the absence of nitrogen the sputtering yield of niobium is substantially higher than that of Ti. When the $p(N_2)$ is increased to 0.6 mTorr, which corresponds to the $p(N_2)$ applied during the deposition of the coatings analysed in Table 2 above, the discharge voltage for Ti and Nb have respectively shifted to ~405 V and ~350 V. This indicates that the sputtering yield of the Nb target is still greater than the Ti target but the sputtering yield of both target materials have decreased. This accounts for the compositional variations observed in Table 2 and relates to the tendency of each target material to be nitrided through reaction with the nitrogen process gas during sputtering. Once the surface of the target becomes nitrided the subsequent sputtering yield no longer reflects that of the pure metal but rather a metal nitride. This reduces the sputtering yield due to the general tendency for nitrides to be mechanically harder than metals and therefore the bombarding species require higher kinetic energy in order to achieve sputtering.

What is also observed at $p(N_2)$ equal to 0.6 mTorr is that the Nb target exhibits a proportionately higher change in discharge voltage than the Ti target. Whilst this reflects the underlying tendency for each metal to be nitrided, it also points towards a situation where the sputtering yields of each target material may become equivalent or close to equivalent. From Figure 2 this appears to occur in the vicinity of $p(N_2)$ equal to 1.5 mTorr. Under this condition, achieving an equal loading of Ti and Nb in the resulting nitride film is likely to result from the application of equal discharge power, unlike the case for other $p(N_2)$ values.

The structure of each coating was assessed using glancing-angle x-ray diffraction (GA-XRD). As seen in **Figure 3** the two coatings display the same phase ($TiNbN_2$; JCPDS #89-5134) but substantially differ in the extent of crystallinity as reflected by peak intensity and sharpness. The identification of the $TiNbN_2$ phase indicates that the cation:anion ratio of 1:1 is maintained in consistence with the solid solubility of TiN and NbN [19]. From the obtained EDS results in Table 3, the cation:anion ratio of each coating is 45:56 and 47:54 respectively for T150N75 and T150N150. Combined with the identification of $TiNbN_2$ obtained from GA-XRD, these ratios indicate a tendency for the deposited coatings to be slightly in nitrogen excess. Practically, this indicates that the applied $p(N_2)$ of 0.6 mTorr is too high for achieving a stoichiometric metal nitride and could be

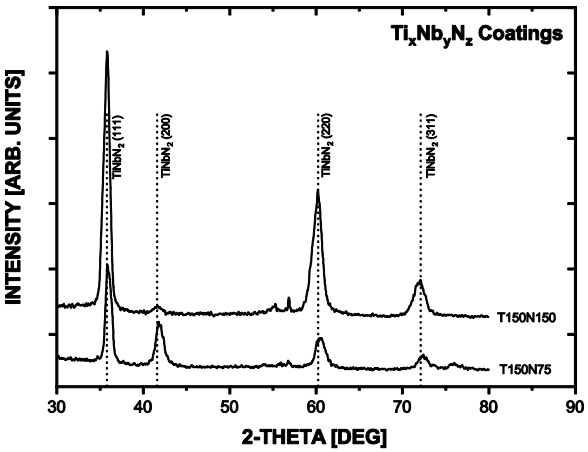

Figure 3. GA-XRD spectra for TixNbyNz. Peaks have been matched to $TiNbN_2$ (JCPDS #89-5134).

reduced. Aside from improving the compositional balance of the coatings, a reduction in the $p(N_2)$ would increase the deposition rate by improving the sputtering yield of each target material. Reducing the time taken to grow a coating is typically a commercial benefit.

The effect of $p(N_2)$ on the deposition of T150N150 coatings is displayed in **Figure 4**. As expected, reducing the $p(N_2)$ from 0.6 mTorr to 0.3 mTorr increases the deposition rate from 8.9 nm/min to 19.0 nm/min. Similarly, increasing $p(N_2)$ to 1.2 mTorr further suppresses the deposition rate to 5.6 nm/min. Hence, the effect of $p(N_2)$ on the rate of coating growth is very strong.

The effect of $p(N_2)$ on composition is also substantial. As displayed in **Table 3**, reducing $p(N_2)$ to 0.3 mTorr has the effect of reducing the [N] to 44 at. % and increasing [Ti] to 24 at.%. [Nb] is only slightly reduced. In this case the cation:anion ratio assumes a value of 56:44 which points towards nitrogen deficiency, however the loading of Ti and Nb are approaching parity unlike at $p(N_2)$ equal to 0.6 mTorr. This result suggests that the optimum $p(N_2)$ would lay in the vicinity 0.45 mTorr but would require some adjustment to the applied discharge power to achieve equimolar Ti and Nb loadings. Increasing $p(N_2)$ to 1.2 mTorr results in only a slight increase in [N]. This points towards the approach of the nitrogen solubility limit in $TiNbN_2$ but would require verification beyond this investigation. The higher $p(N_2)$ also has tended to impact the [Nb] more than the [Ti] which is likely a reflection of the greater impact of $p(N_2)$ on the sputtering yield of Nb as predicted by Figure 2.

Table 3. Effect of $p(N_2)$ on the composition of Ti150N150 coatings.

Element Analysed	$p(N_2)$		
	0.3 mTorr	**0.6 mTorr**	**1.2 mTorr**
[Ti]	24 at. %	13 at. %	18 at. %
[Nb]	32 at. %	34 at. %	26 at. %
[N]	44 at. %	54 at. %	56 at. %

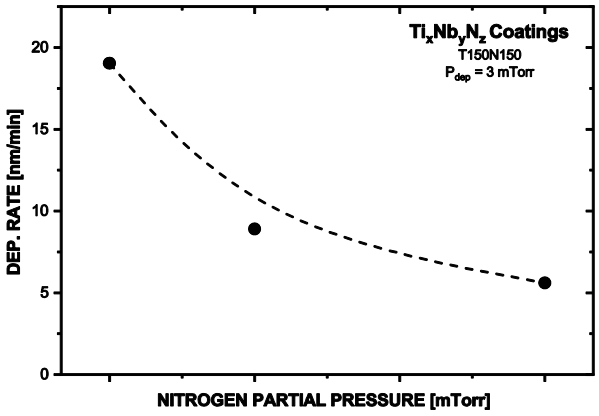

Figure 4. Effect of $p(N_2)$ on the deposition rate of T150N150 coatings.

The choice of deposition pressure also has profound effects on the growth and structural evolution of sputtered films. As seen in **Figure 5**, the deposition rate of T150N150 coatings is greatly influenced by the deposition pressure. Specifically, what is observed is the creation of a maxima in the deposition rate as deposition pressure is increased from 3 mTorr to 24 mTorr. Here the peak deposition rate is observed to be 24.8 nm/min at a deposition pressure of 12 mTorr. The observed trend in deposition rate with deposition pressure reflects the competing effects of increased quantity of bombarding argon species as pressure is increased and the reduced energy of these species due to increased molecular collisions. At 3 mTorr and 298 K, the mean free path of argon molecules is ~16 mm [38]. At 12 mTorr the mean free path is reduced to ~4 mm, and is further reduced to 2 mm when the pressure is increased to 24 mTorr. Despite the increase in the number of bombarding species, each individual species has lost kinetic energy due to having collided frequently with other gaseous species. This reduction in kinetic energy also has an impact on the structural evolution of the growing film. As seen in **Figure 6**, increasing the deposition pressure has a strong tendency to diminish the extent of crystallinity in the deposited coatings. This is indicated by the clear reduction in the peak height and peak sharpness as deposition pressure is increased. This outcome relates to the fundamental mechanism of film growth whereby depositing species encounter the substrate at some time after being sputtered from the target. In the sputtering apparatus used for this investigation the target to substrate distance is approximately 120 mm. Therefore at a deposition pressure of 3 mTorr depositing species encounter a minimum of 8 collisions whereas at 24 mTorr depositing species experience at least 60 collisions. Hence, as the deposition pressure is increased depositing species are reaching the substrate with decreased energy on average. This manifests as poor crystallinity in at least two important ways. Firstly, upon impacting the substrate the kinetic energy of depositing species is transferred to the substrate and the growing film in the form of heat. By reducing the available kinetic energy less heat is transferred to the film therefore the growth of grains and crystal structure is also reduced. Secondly, not all kinetic energy is transferred to the growing film. Some is retained by the depositing species which enables them to diffuse across the surface of the growing film and thereby find orientations and positions that favour crystallinity.

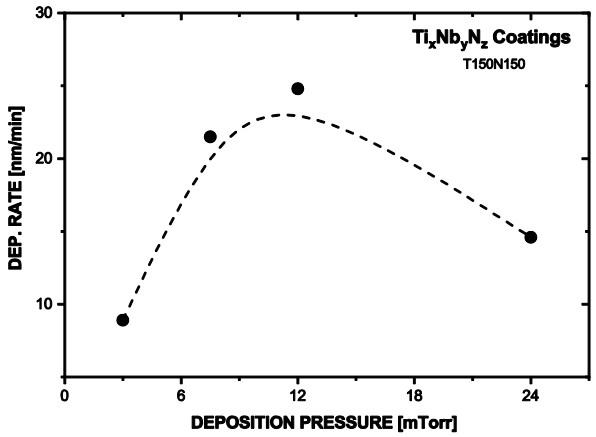

The choice of deposition pressure has important practical significance. From Figure 5 an investigator may elect to deposit TiNbN coatings at 12 mTorr in order to exploit the maxima in deposition rate. However, from Figure 6, this would result in an amorphous or minimally crystalline coating. In an application where hardness needs to be maximised, such as an orthopaedic implant, additional processing such as an annealing would be required. This may be achievable but the direct deposition of a highly crystalline coating without post-treatment would be more favourable in most instances. Hence the selection of a deposition pressure of 3 mTorr is likely to be more appropriate.

V. CONCLUSIONS

Figure 5. Effect of deposition pressure on the deposition rate for T150N150 coatings.

This investigation has demonstrated the importance of mapping the consequences of changes in different parameters during the deposition of TiNbN coatings using reactive magnetron sputtering. As seen repeatedly, each pertinent parameter relating to sputtering has a range of effects on the resulting film composition and structure. The deposition rate is also often affected which is closely linked to practical and commercial significance. For investigators that seek to engineer materials for specific applications, such as TiNbN for improving orthopaedic coatings for hip and knee replacement implants, understanding the full parameter space

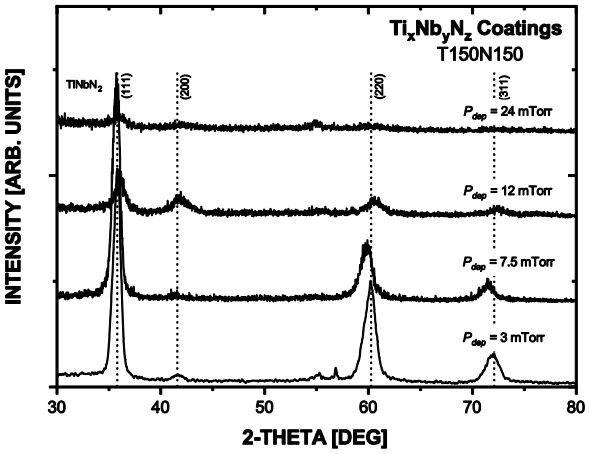

Figure 6. Effect of deposition pressure on the structure of T150N150 coatings (Reproduced from Sheppard *et al* [19])

available to magnetron sputtering is vital for achieving property optimisation. In this investigation it has been shown that the specific composition of a TiNbN film can be varied considerably via the appropriate manipulation of at least two conveniently available parameters; discharge power applied to the target materials, and the reactive proportion of process gas. The choice of deposition pressure is an additional variable that principally relates to the achievement of practically viable deposition rates but can introduce complications relating to the attainment of crystallinity. Additional variables that were not explored as part of this investigation but which are commonly available are the application of substrate heating during deposition, the application of substrate bias during deposition, and the manipulation of the target to substrate distance. In order to thoroughly understand how to engineer the functional properties of magnetron sputtered coatings, a comprehensive mapping of the available parameters is key for achieving successful advanced materials.

ACKNOWLEDGMENT

The authors wish to thank Dr Laurel George, Dr Tim Murphy and Dr Daniel Fanna of the Western Sydney University Advanced Materials Characterisation Facility for their assistance with the collection of data and analysis relating to this investigation. Mr Sam Macartney is also acknowledged for his helpful contributions towards this investigation. Mr David Jaretta and Companhia Brasileira de Metalurgia e Mineração (CBMM) are also warmly acknowledged for their ongoing support of this research project.

REFERENCES

[1] P.J. Kelly, R.D. Arnell, "Magnetron Sputtering: A Review of Recent Developments and Applications", *Vacuum*, **56** (2000) 159

[2] K. Sarakinos, J. Alami, S. Konstantinidis, "High Power Pulsed Magnetron Sputtering: A Review on Scientific and Engineering State of the Art", *Surf. Coat. Tech.*, **204** (2010) 1661

[3] K. Ibrahim, H. Taha, M.M. Rahman, H. Kabir, Z.T. Jiang, "Solar Selective Performance of Metal Nitride/Oxynitride Based Magnetron Sputtered Thin Film Coatings: A Comprehensive Review", *J. Optics*, **20** (2018) 033001

[4] G. Bertrand, H. Mahdjoub, C. Meunier, "A Study of the Corrosion Behaviour and Protective Quality of Sputtered Chromium Nitride Coatings", *Surf. Coat. Tech*., **126** (2000) 199

[5] A. P. Ahiasarian, W-D. Munz, L. Hultman, U. Helmersson, I. Petrov, "High Power Pulsed Magnetron Sputtered CrNx Films", *Surf. Coat. Tech.*, **163-164** (2003) 267

[6] D.R. Sahu, S.Y. Lin, J.L. Huang, "ZnO/Ag/ZnO Multilayer Films for the Application of a Very Low resistance Transparent Electrode", *Appl. Surf. Sci.*, **252** (2006) 7509

[7] J. Fahlteich, M. Fahland, W. Schonberger, N. Schiller, "Permeation Barrier Properties of Thin Oxide Films on Flexible Polymer Substrates", *Thin Solid Films*, **517** (2009) 3075

[8] M. Cahaik, S. Ben Moumen, A. Agdad, C.M. SambaVall, H. El Aakib, H. AitDads, A. Outzourhit, L. Essaleh, "Electrical Impedance Spectroscopy Chartacterisation of ZnTe Thin Film Deposited by R-F Sputtering", *Physica B: Cond. Matter*, **572** (2019) 76

[9] K. Fu, X. An, L. Chang, L. Sheppard, C. yang, H. Wang, L. Ye, "Ultra-High Specific Strength and Deformation Behaviour of Nanostructured Ti/Al Multilayers", *J. Phys. D: Appl. Phys.*, **50** (2017) 365302

[10] K. Fu, L. Chang, C. Yang, L. Sheppard, H. Wang, M. Maandal, L. Ye, "Plastic Behaviour of High Strength Lightweight Al/Ti Multilayer Films", *J. Mater. Sci.*, **52** (2017) 13956

[11] R. Wuhrer, S. Kim, W.Y. Yeung, "Effect of Nitrogen Partial Pressure on the Surface Morphology and Properties of Reactive DC Magnetron Sputtered (Ti,Al)N Coatings", *Scripta Materialia*, **37** (1997) 1163

[12] C.Y.Jeong, Y. Abe, M. Kawamura, K.H. Kim, T. Kiba, "Electrochromic Properties of Rhodium Oxide thin Films Prepared by Reactive Sputtering Under an O2 or H2O Vapor Atmospherte", *Sol. Energy Mats. Sol. Cells*., 200 (2019) 109976

[13] S. Ali, B. Paul, R. Magnusson, E. Ekstrom, C. Pallier, B. Jonson, P. Ekland, J. Birch, "Optical and Mechanical properties of Amorphous Mg-Si-O-N Thin Films Deposited by Reactive Magnetron Sputtering", *Surf. Coat. Tech.*, **372** (2019) 9

[14] R. Alvarez, A. Garcia-Valenzuela, V. Rico, J.M. Garcia-Martin, J. Cotrino, A.R. Gonzalez-Elipe, A. Palmero, "Kinetic Energy-Induced Growth regimes of Nanocolumnar Ti Thin Films Deposited by Evaporation and Magnetron Sputtering", *Nanotechnology*, **30** (2019) 475603

[15] O. Depablos-Rivera, H. Bouyanfif, A. Zeinart, F. Le Marrec, S.E. Rodil, "Synthesis of Bi2SiO5 Thin Films by Confocal Dual Magnetron Sputtering-Annealing Route", *Thin Solid Films*, **688** (2019) 137258

[16] Z.B. Qi, B.B. Wei, J.H. Wang, Y. Yang, Z.C. Wang, "Nanostructured Porous CrN Thin Films by Oblique Angle Magnetron Sputtering for Symmetric Supercapacitors", *J. Alloys and Comps.*, **806** (2019) 953

[17] D.D. Kumar, N. Kumar, S. Kalaiselvam, R. Radhika, A.M. Rabel, R. Jayvel, "Tribo-Mechanical Properties of Reactive Magnetron Sputtered Transition Metal Carbide Coatings", *Tribology Int.*, **114** (2017) 234

[18] H. Maeda, M. Chino, T. Sakai, T. Kasuga, "Enhancing Wettability of Radio Frequency Magnetron-Sputtered Glass Films by Exploiting Structural Defects", *Langmuir*, **35** (2019) 11340

[19] L.R. Sheppard, H. Zhang, R. Liu, S. Macartney, T. Murphy, R. Wuhrer, "Reactive Sputtered TixNbyNz Thin Films. I. Basic processing Relationships", *Mats. Chem. Phys.,* **224** (2019) 308

[20] L.R. Sheppard, H. Zhang, R. Liu, S. Macartney, t. Murphy, P. Wainer, R. Wuhrer, "Reactive Sputtered TixNbyNz Coatings. II. Effect of Common deposition parameters", *Mats. Chem. Phys.*, **224** (2019) 320

[21] M.L.S. Arockiaswamy, M. Sundarewari, M. Rajagopalan, "Ductility Behaviour of Cubic Titanium Niobium Nitride Ternary Alloy: A First Principles Study", *Indian J. Phys.*, **90** (2016) 149

[22] E. Thienpont, "Titanium Niobium nitride Knee Implants Are Not Inferior to Chrome Cobalt Components for Primary Total Knee Arthroplasty", *Arch. Orthop. Trauma. Surg.*, **135** (2015) 1749

[23] L. Lapaj, J. Markuszewski, J. Wendland, A. Mroz, M. Wierusz-Kozlowska, "Massive Failure of TiNbN Coating in Surface Engineered Metal-On-Metal Hip Arthroplasty: Retrieval Analysis", *J. Biomed. Mats. Res. B: Appl. Biomats.*, **104B** (2016) 1043-1049

[24] A.P. Serro, C. Completo, R. Colaco, F. dos Santos, C. Lobato da Silva, J.M.S. Cabral, H. Araujo, E. Pires, B. Saramago, "A Comparative Study of Titanium Nitrides, TiN, TiNbN and TiCN, as Coatings for Biomedical Applications", *Surf. Coat. Tech*., **203** (2009) 3701-3707

[25] T. Matsunaga, H. Maezawa, T. Noguchi, "Characterisation of NbTiN Thin Films Prepared by Reactive DC-Magnetron Sputtering", *IEEE Trans. Appl. Supercond.*, **13** (2003) 3284-3287

[26] L. Yu, R.K. Singh, H. Liu, S.Y. Wu, R. Hu, D. Durand, J. Bulman, J.M. Rowell, N. Newman, "Fabrication of Niobium Titanium Nitride Thin Films with High Superconducting Transition temperatures and Short Penetration Lengths", *IEEE Trans. Appl. Supercond.,* **15** (2005) 44-48

[27] M.P. Gispert, A.P. Serro, R. Colaco, E. Pires, B. Saramago, "Wear of Ceramic Coated Metal-On-Metal Bearings Used for Hip Replacement", *Wear*, **263** (2007) 1060-1065

[28] R.O.E. Vijgen, J.H. Dautzenberg, "Mechanical Measurement of the Residual Stress in Thin PVD Films', *Thin Solid Films*, **270** (1995) 264-269

[29] T. Polcar, T. Kubart, R. Novak, L. Kopecky, P. Siroky, "Comparison of Tribological Behaviour of TiN, TiCN and Cr N at Elevated Temperatures", *Surf. Coat. Tech.*, **193** (2005) 192-199

[30] J.A. Sue, T. P. Chang, "Friction and Wear Behaviour of Titanium Nitride, Zirconium Nitride and Chromium Nitride Coatings at Elevated Temperatures", *Surf. Coat. Tech.*, **76-77** (1995) 61-69

[31] J-E. Sundgren, B-O. Johansson, S-E. Karlsson, H.T.G. Hentzell, "Mechanisms of Reactive Sputtering of Titanium Nitride and Titanium Carbide. II: Morphology and Structure", *Thin Solid Films*, **105** (1983) 367-384

[32] S. Mahieu, P. Ghkiere, G. De Winter, S. Heirwegh, D. Depla, R. De Gryse, O.I. Lebedev, G. Van Tendeloo, "Mechanism of Preferred Orientation in Sputter Deposited Titanium Nitride and Yttria-stabilized Zirconia Layers", *J. Crystal Growth*, **279** (2005) 100-109

[33] R. Machunze, G.C.A.M. Janssen, "Stress and Strain in Titanium Nitride Thin Films", *Thin Solid Films*, **517** (2009) 5888-5893

[34] G. Lemperiere, J.M. Poitevin, "Influence of the Nitrogen Partial Pressure on the Properties of D.C.-Sputtered Titanium and Titanium Nitride Films", *Thin Solid Films*, **111** (1984) 339-349

[35] M.K. Harman, S.A. Banks, W. A. Hodge, "Wear Analysis of a Retrieved Hip Implant with Titanium Nitride Coating", *J. Arthroplasty*, **12** (1997) 938-945

[36] V.I. Ivashchenko, S.N. Dub, P.L. Scrynskii, A.D. Pogrebnjak, O.V. Sobol, G.N. Tolmacheva, V.M. Rogoz, A.K. Sinel'chenko, "Nb-Al-N Thin Films: Structural Transition from Nanocrystalline Solid Solution nc-(Nb,Al)N into Nanocomposite nc-(Nb, Al)N/a-AlN/", *J. Superhard Mats.*, **38** (2016) 103-113

[37] I. Khidirov, T. Khaidarov, "Ultrasonic-Resonance of the Elastic Constants of Titanium Nitride Over its Homogeneity Range", *Inorg. Mater*., **31** (1995) 122-124

[38] https://www.omnicalculator.com/physics/mean-free-path, accessed 11th October 2019.

Advanced Materials Characterisation – Analytical Techniques Aiding a Better Understanding of your Material

Richard Wuhrer
Advanced Materials Characterisation Facility, REDI
Western Sydney University
Parramatta, Australia
Richard.wuhrer@westernsydney.edu.au

Daniel J. Fanna
Advanced Materials Characterisation Facility, REDI
Western Sydney University
Parramatta, Australia
D.Fanna@westernsydney.edu.au

Laurel George
Advanced Materials Characterisation Facility, REDI
Western Sydney University
Parramatta, Australia
L.George@westernsydney.edu.au

Ken Moran
Moran Scientific Pty Ltd
Bungonia, Australia
ken@moranscientific.com.au

***Abstract*— Characterisation techniques are an essential requirement for materials research as well as for quality control in the production of materials. Understanding the distribution of elements and phases in structures is critical to optimising the performance of all materials. There is a wide range of varying characterisation techniques available that can be utilised to obtain a better understanding of your material. Most of the techniques involve electron, x-ray, ion and lasers beams striking your material, followed by analysis of the signal. Over the last 10 years there have been some major improvements in instrumentation, not only from computer technology, but detector improvements and operational changes in the instrument design and capabilities.**

This paper will discuss a number of characterisation techniques that have been installed in the Advanced Characterisation Facility (AMCF) at Western Sydney University's Parramatta South campus, and how they might be utilised to obtain a better understanding of engineering materials.

Keywords*— *Microscopy, Microanalysis, FTIR, X-Ray Diffraction, Thermal analysis, Thermal properties, Material properties, Instrumentation, New materials

I. Introduction

Characterisation of materials frequently involves the determination of variation in composition, structure and microstructure, by the use of a variety of imaging and analysis techniques [1, 2]. The Advanced Material Characterisation Facility (AMCF), located on Western Sydney University's Parramatta South campus, houses a large collection of instruments used for materials analysis. This collection includes, and is not limited to, Scanning Electron Microscopy (SEM), Energy Dispersive Spectroscopy (EDS) also known as microanalysis, X-ray mapping (XRM), Fourier Transform Infra-Red (FTIR) spectroscopy, Raman Spectroscopy and X-ray Diffraction (XRD). Also housed in the AMCF are various thermal analysis techniques such as Thermo-Gravimetric Analysis (TGA), Differential Scanning Calorimetry (DSC) and high temperature XRD.

How each of these techniques work, their benefits as well as current improvements, will be discussed in this paper.

II. Scanning Electron Microscopy

Scanning Electron Microscopy (SEM) analysis is a powerful investigative tool which uses a focused beam of electrons to produce high magnification images of a sample's surface topography [3].

In the past, SEM primary limitations, as a general imaging and analytical technique, were the restrictions it imposed on samples by requiring a high vacuum sample environment. Samples had to be clean, dry and electrically conductive [3]. The mid-eighties saw the development of the variable pressure (VP-SEM) and environmental SEM (ESEM®). Variable Pressure SEM, permits the microscopist to vary the sample environment through a range of pressures, temperatures and even gas environments (water vapour, nitrogen, air) [4-6]. Further to this, these days SEM's are available as desktop instruments with microanalysis packages (Figure 1) that can operate not only in high vacuum mode but also in low vacuum mode (VP mode).

The introduction of gas and innovative electron detectors facilitates SEM imaging and analysis of wet, dry, insulating and conductive specimens in their natural state [6]. Now it is possible to image samples uncoated using back-scattered electron signal (BSE) and gaseous secondary electron detectors (GSED) without any complex sample preparation. It is also possible to perform x-ray microanalysis of samples in their natural state, but care must be taken.

SEM micrographs prepared with the back-scattered electron signal (BSE) can provide direct information on compositional heterogeneity through the mechanism of atomic number contrast and are quite useful for characterising microstructures, but the compositional information that they contain is non-specific. The BSE image contains no information to identify the elements present or the concentration levels [1, 2]. A BSE image EDS or wavelength dispersive spectrometry (WDS) analysis is an established technique for the analysis of the chemical composition of

materials in a SEM. Furthermore, the combination of SEM and EDS through x-ray mapping (XRM) has become an excellent tool for characterising the distribution of elements and phases in material [7-9].

III. Microanalysis

Microanalysis is the chemical identification and quantitative analysis of very small amounts of chemical substances or very small surfaces of material [3]. Traditional microanalysis using EDS involves using higher accelerating voltages [6]. The accelerating voltage of the SEM determines the energy of the electron beam which consequently determines which X-rays are excited during the interaction with the material. The SEM is usually operated at accelerating voltages in the range of 15 kV to 25 kV in order to excite the well-known K-lines in the atomic spectra, however, the use of higher accelerating voltages usually results in larger interaction volumes, which consequently degrades the spatial resolution of the X-ray image and increases the analytical volume (Figure 2) [6].

It is generally not possible to obtain high spatial resolution chemical microanalysis from bulk materials when using high accelerating voltages [10]. However, qualitative X-ray maps can highlight small features on the nanometre level, especially if averaging and filtering techniques are employed to resolve the nano-features [7, 10].

With the development and advancement of silicon drift detectors (SDD's), the sensitivity for X-rays in the low energy part of the spectrum has substantially improved [6]. Manufacturers are now producing SDD's with such large detector areas that greater X-ray collection efficiencies are possible. This, and high count rate throughput, is now allowing the possibility of operating the SEM at much lower accelerating voltages and subsequently reducing the interaction volume of the electron beam with the material as well as achieving higher spatial resolution information (Figure 2). Further to this, full spectrum x-ray maps at high resolution can be performed in a matter of hours instead of tens of hours [7].

IV. X-ray Mapping (XRM)

XRM is the collection of characteristic X-rays as a function of the position of the scanning electron beam on the specimen [1, 2, 6-9]. This analytical technique provides an image related to the distribution and relative abundance of elements within a given specimen. This capability makes XRM particularly useful for: (i) identifying the location of individual elements and (ii) mapping the spatial distribution of specific elements and chemical phases within a sample [7].

Usually X-ray maps are displayed as grey scale images (Figure 3). The use of colour can enhance the visibility of intensity levels in a map because the human eye can

Figure 1: Images of Hitachi (top) and Phenom (bottom) desktops SEM's

distinguish many more shades of colour than grey levels. Pseudo colouring is often referred to as false colour and is used to display different elements. However, pseudo colouring can also be very helpful for locating phases [7, 11, 12].

Pseudo colouring is a simple method for determining elemental associations and is also called "Primary Colour Imaging". This technique is where three elemental maps have been assigned the colours red, green and blue. Because the colours red, green and blue form specific colours when combined on a computer graphics monitor, elemental associations are clearly shown in a single pseudo colour image, Figure 4 [1, 2].

Once an XRM has been collected, a number of analytical software methods can be used to process the data and determine further information about the microstructure and properties of the material. However, much of the quantitative information is extremely complex and as such is enormously difficult to reproduce as a single image.

Through the use of two and three dimensional (2D and 3D) scatter (or correlation) diagrams, the X-ray images can be presented as singular or combinations of elements [2, 4, 5] (phases to be displayed singularly or superimposed over backscattered or secondary electron information). Where, scatter diagrams are pixel frequency versus element concentration profiles plotted against each other in two dimensions for selected elements within the sample, Figures 5 and 6. The rotation of the colours between elements can often reveal further information (and other phases) in the material (elemental association), such as fine precipitates, trace

elements, hairline cracks and small boundary interfaces that would be otherwise missed [1, 2].

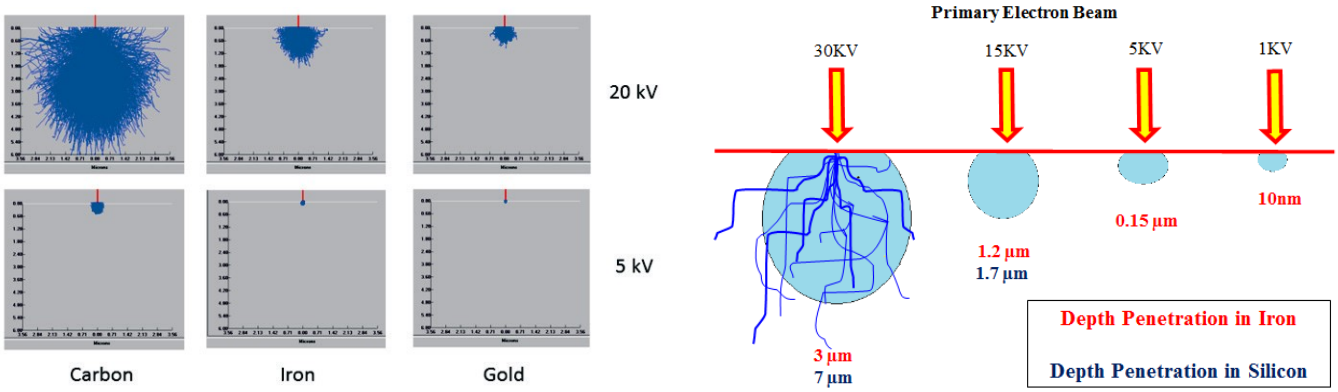

Figure 2: *Left* - Monte Carlo simulations [6]. Electron beam diffusion varies with accelerating voltage and specimen density. All are scaled to the same depth and width [6]. *Right* - Effect of accelerating voltage on interaction volume.

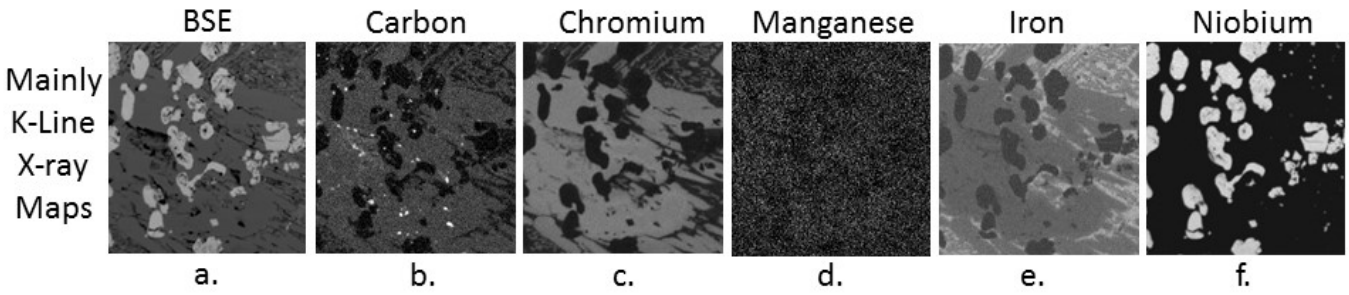

Figure 3: SEM micrograph and X-ray maps of hard-facing material with NbC particles in white cast iron. a) BSE image, b) Carbon K-line, c) Chromium K-line, d) Manganese K-line, e) Iron K-line and f) Niobium L-line [reproduced from reference 6 and 7].

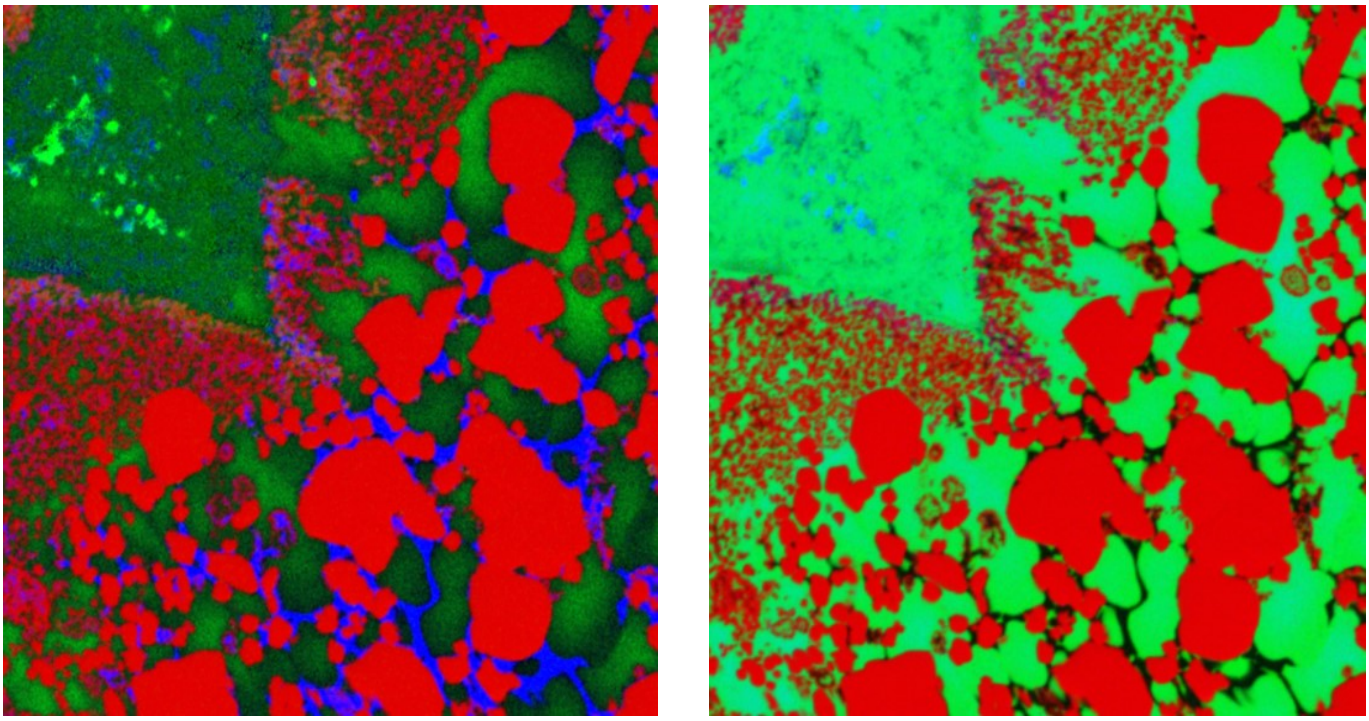

Figure 4: Pseudo-colouring. This technique is where three elemental maps have been assigned the colours red, green and blue. Sample is a hard facing material.

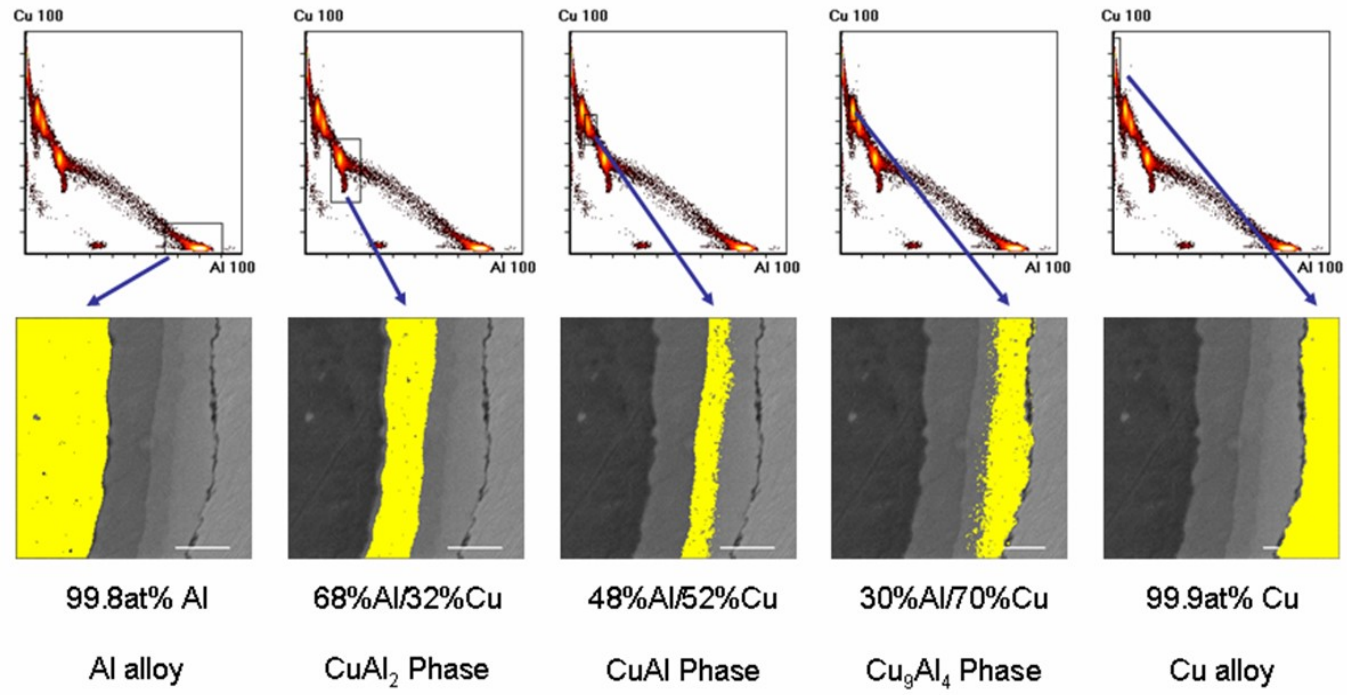

Figure 5: Copper-aluminium scatter diagrams showing different clusters in the interfacial area of the metal laminate after sintering at 450oC for 3 hours. The images below are secondary electron images with phase information determined from the clusters of the scatter diagram superimposed over the image.

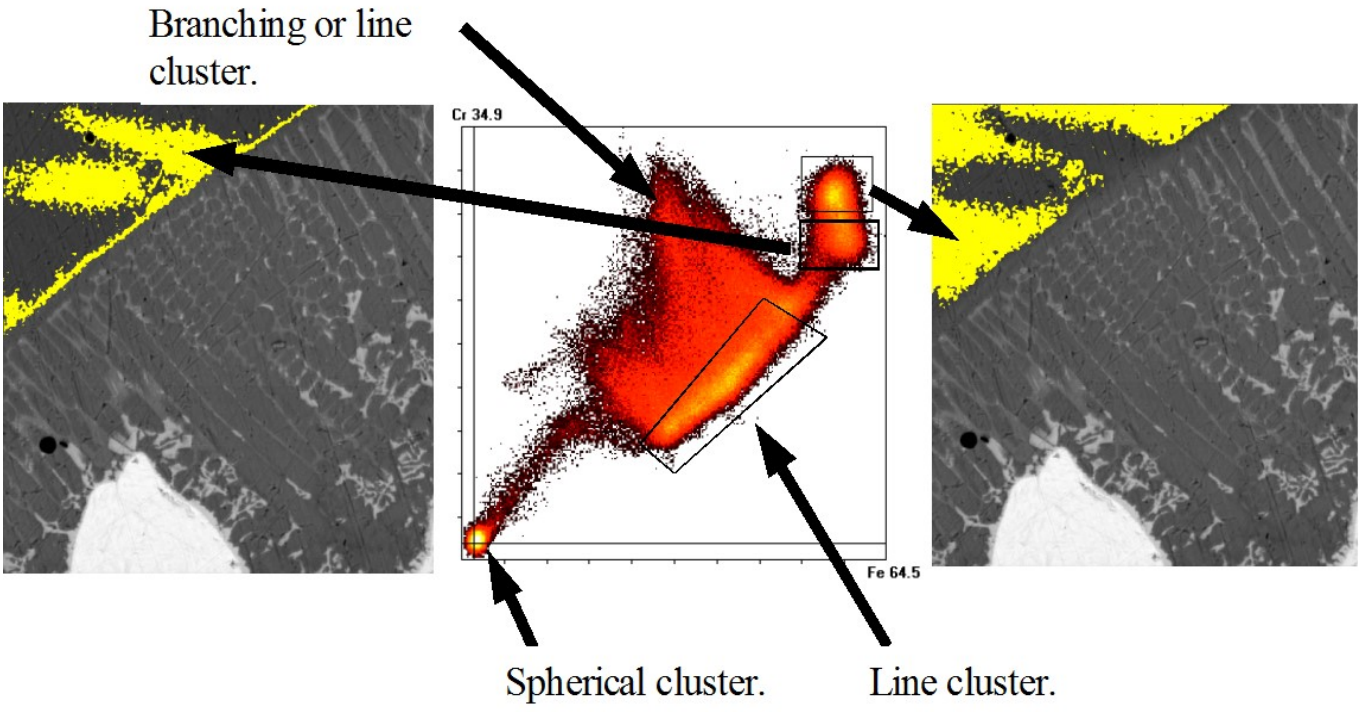

Figure 6: Hard facing material bonded to a steel substrate. BSE image (LHS) with low chrome region superimposed over image (the overlays are on the steel substrate and represent 24 wt% Cr), scatter diagram for chromium and iron showing many of the different cluster types after averaging (middle), BSE image with high chrome region superimposed over image (RHS) and represents 28 wt% Cr [12].

scatter diagrams are pixel frequency versus element concentration profiles plotted against each other in two dimensions for selected elements within the sample, Figures 5 and 6. The rotation of the colours between elements can often reveal further information (and other phases) in the material (elemental association), such as fine precipitates, trace

elements, hairline cracks and small boundary interfaces that would be otherwise missed [1, 2].

V. VIBRATIONAL SPECTROSCOPY

Vibrational spectroscopy is a non-destructive characterisation method used to identify the functional groups present in molecules [13-18]. Each chemical bond has a unique vibrational energy which is related to its molecular characteristics such as the interacting elements, the type of chemical bond (single, double, triple), and also the vibrational movement (stretch, bend, rock, wag, etc.). These vibration energies can be identified by their specific wavenumber absorption (cm-1) and also their relative intensity and characteristics (strong, weak, broad, narrow, etc.). In practice, often samples have many functional groups present, and as such identification of each functional group may be difficult due to the overwhelming number of peaks observed. To counteract this, many materials have had their vibrational spectra measured and deposited into a database. Unknown samples may then be compared to database entries by comparing the peak profile of a sample to standard materials, akin to the way a forensic scientist compares fingerprints [13-18].

As each chemical bond has a unique vibrational energy which is dependent on what other compounds the chemical bond of interest is bound to, each compound will have a unique fingerprint or the output identifying the peak strengths at specific vibrations. This fingerprint can be used to determine the compound structures, identify and characterise compounds, as well as identify impurities [15].

Vibrational spectroscopy is an energy sensitive method. It is based on periodic changes of dipole moments (IR) or polarizabilities (Raman) caused by molecular vibrations of molecules or groups of atoms and combined discrete energy transitions and changes of frequencies during absorption(IR) or scattering (Raman) of electromagnetic radiation [16].

Generally, when considering vibrational spectroscopy as an analytical tool for function group identification, three main techniques come to mind. These are infrared (IR) spectroscopy (more commonly referred to as Fourier transform IR (FTIR)), near-infrared (NIR) spectroscopy and Raman spectroscopy. Currently the AMCF has the capability for FTIR and Raman spectroscopy, with various sample holders to allow for different materials and experimental conditions to be conducted.

A. FTIR spectroscopy

FTIR spectroscopy uses a beam of light within the infrared spectrum (700 nm-1000 nm) to excite chemical bonds and measure the absorption/transmission of light due to the vibrations of these bonds [13-18]. The FTIR spectrum is output by a series of peaks across a wavenumber (cm-1) x-axis with a % absorbance/transmittance shown on the y-axis. This spectrum can then be matched against a database to compare the fingerprint of an unknown sample with those of materials entered into the database.

Historically FTIR involved a relatively complicated sample preparation where a sample was dispersed in KBr and pressed into a transparent pellet [13-18]. The pellet was then mounted in a FTIR spectrometer, and an IR beam passed through the pellet to measure a FTIR spectrum as % transmittance. However, more recently the development of attenuated total reflection (ATR) accessories has allowed the rapid analysis of powders, solids and even liquids easily in their native state. The AMCF currently hosts two types of ATR accessories, a diamond crystal ATR which is suited for routine measurements (Figure 7), and a germanium crystal ATR which is ideal for heavily absorbing samples, ie, black powders. In addition to these, the AMCF also has a variable temperature accessory, in which samples are pressed into KBr pellets allowing samples to be measured from -170 to 250 °C.

When looking at an FTIR spectra fingerprint we can identify certain peaks by considering their wavenumber (x-axis) location and profile, then comparing what is observed to known molecular functions. For example, an alcohol (OH) peak will be wide and within the 3650-3200 cm-1 wavelength wavenumber range. A terminal alkyne will be in a similar wavenumber range (3340-3250 cm-1), but it will be a very narrow peak. These specific functional groups can first be identified in order to begin characterising the compound. This process is useful if we don't already have an FTIR spectrum to which we can compare the compound, for example newly organic molecules.

B. Raman spectroscopy

As with FTIR spectroscopy, Raman spectroscopy is a non-destructive analysis technique that is based upon the interaction of light with the chemical bonds within a material. In FTIR an infrared beam is used to excite the sample, in comparison Raman spectroscopy utilises high powered lasers often in the visible spectrum. Currently the AMCF has four laser options, 532 nm, 633 nm, 785 nm and 1064 nm. The ideal laser for Raman analysis is sample dependent, as some samples will fluoresce upon laser excitation which may make obtaining a good Raman signal challenging, in these instances the selection of a higher wavelength laser may alleviate fluorescence. Both Raman and FTIR each have their pros and cons, and as such they complement each other. As an example of this, some chemical bond vibration modes are IR or Raman inactive, hence utilising both techniques allows for a comprehensive investigation into a materials chemical bonds. A key advantage of Raman is the system operates through an optical microscope, therefore it is possible to visually identify and select specific areas for Raman analysis to be conducted, and sample mapping by Raman is also possible. Shown below in Figure 8 is the Bruker Senterra Raman system currently housed at the AMCF.

Figure 7: A diamond ATR stage mounted in one of two Bruker Vertex 70 FTIR spectrometers housed at the AMCF.

Figure 8: Vibrational spectroscopy instruments housed in the AMCF. A Bruker Senterra Raman spectrometer (right), a Bruker Vertex 70 FTIR coupled to a 1064 nm Ram II FTRaman module (middle-right) and a Hyperion FTIR microscope (left).

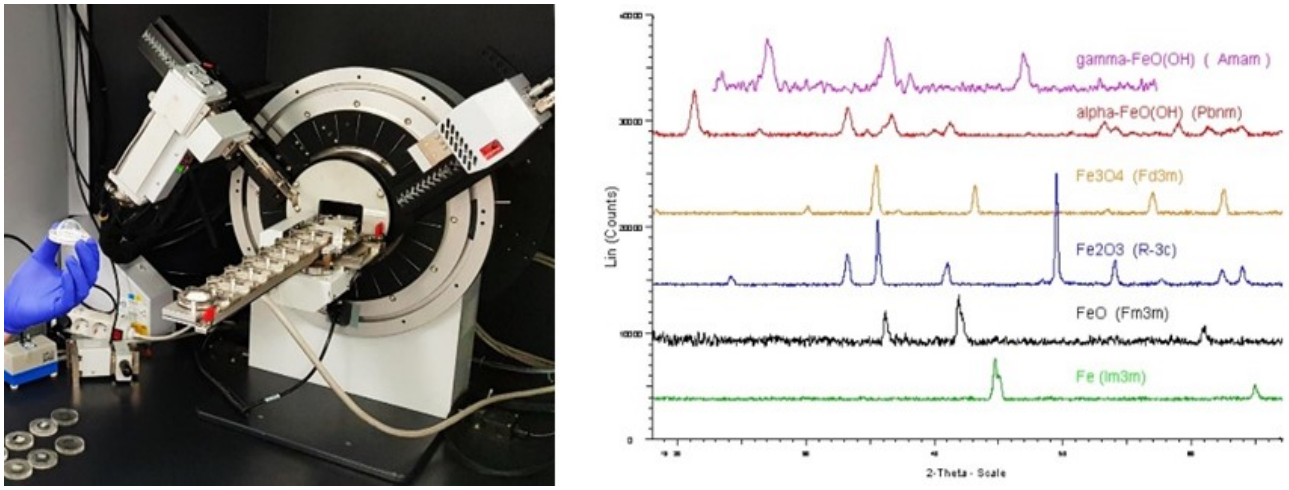

Figure 9: Example: The spectra above show that while a sample may be known to contain iron (Fe) and oxygen (O) (i.e. an iron oxide), the crystal structure that these elements form can be very different. XRD can therefore help identify the crystal structure and therefore phases that are present in a sample [19-23].

VI. X-Ray Diffraction (XRD): Phase Analysis

X-ray diffraction (XRD) is a versatile non-destructive analytical technique in which X-rays are used to investigate the crystalline nature of a material resulting in the identification of crystalline phases present (Figure 9). This technique is commonly applied to powders; however, the analysis of solid samples is also possible. The XRD analysis of a material is also complementary to microanalysis, the two techniques work hand-in-hand to comprehensively probe a materials composition.

In XRD a sample is illuminated by an incident X-ray beam, as this X-ray beam interacts with a sample at the atomic level diffraction peaks are generated which are then measured by the diffractometer across an angular range called 2theta [19-23]. The 2theta position of a diffraction peak relates to the spacing's between repeating atomic units, also referred to as the asymmetric unit, in a materials crystal lattice. From this information, it is possible to determine the phase present in a material by comparing the observed peaks against a database. As the intensity of a diffraction peak is influenced by the relative abundance of a particular phase, it is also possible to use XRD as a means of quantifying the phases present in a sample. However, it must be cautioned that quantification of crystalline phases by XRD may be challenging, and is only suited for ideal samples in which preferred orientation effects are minimal.

It is also possible to probe the substitution of elements into a crystalline sample, as the radius of an atom will influence the spacing between atomic positions. In addition to the above, it is also possible to identify other sample properties from the diffraction peak profile, for example, the width of a diffraction peak is inversely proportional to crystallite size, i.e., the smaller the crystallite, the broader the peak, and vice-versa. Hence XRD may be used for crystallite size determination, a technique that is complemented by measurements using scanning electron microscopy, another analytical tool available at the AMCF.

A limitation to XRD is that it cannot be used for the identification of non-crystalline (amorphous) materials as for diffraction to occur a material must have ordered repeating atomic units. But, although amorphous materials cannot be identified, they can still be observed in XRD as broad regions in the baseline of a spectrum, and as such, it is possible to determine relative percentage of amorphous and crystalline phases in a sample.

From the above techniques, the composition and phases can be determined for the material being investigated. From the information determined from these techniques subsequent thermal analysis can be performed to determine the physical properties of the material.

VII. Thermal Analysis

Thermal Analysis (TA) is a group of techniques that study the properties of materials as they change with temperature. There are many different types of thermal analysis techniques that can be used to monitor and analyse physical and chemical changes under different temperature conditions and even atmospheres and are distinguish by what they measure [24-28]. Physical properties include mass, temperature, enthalpy, dimension, dynamic characteristics and others. For nearly all types of analysis, samples can be heated or cooled at a consistent rate, multiple times if needed to test durability (dynamic temperature), or held at a particular temperature of interest for testing (isothermal temperature). The temperature can also be programmed to include both dynamic and isothermal sequences [27, 28].

The types of thermal analysis include [24-28]:

1. TGA (Thermogravimetric analysis): looking at weight change (Figure 10)
2. DTA (Differential Thermal Analysis): temperature
3. DSC (Differential Scanning Calorimetry): temperature (Figure 10)
4. DIL (Dilatometry): looking at change in length
5. TMA (Thermo Mechanical Analysis): length (with strain)
6. DMA (Dynamic-Mechanical Analysis): length (dynamic)
7. DEA (Dielectric Analysis): conductivity
8. Thermo Microscopy: image
9. Combined methods (evolved gases)

TGA can give information on:

- Thermal decomposition of substances (calcination and heat treatment and polymer stability)
- Corrosion of metals
- Determination of moisture, volatiles, and ash content
- Evaporation rates and sublimation
- Distillation and evaporation of liquids
- Reaction kinetics studies
- Compound identification
- Heats of vaporization and vapour pressure determinations

Samples can be tested at different heating rates, in different atmospheres (e.g. air, nitrogen, argon). A selection of crucibles is available (Figure 9b), and will depend on the temperature range that is to be used, and compatibility with the sample itself. Care also needs to be taken when considering sample size and the reaction of the sample to heat (Figure 9c) [27]. A comparison of properties of each thermal analysis technique can measure is shown in table 1 for TGA, DSC, TMA and FTIR. A typical TGA/DSC schematic diagram form plot is shown in Figure 10.

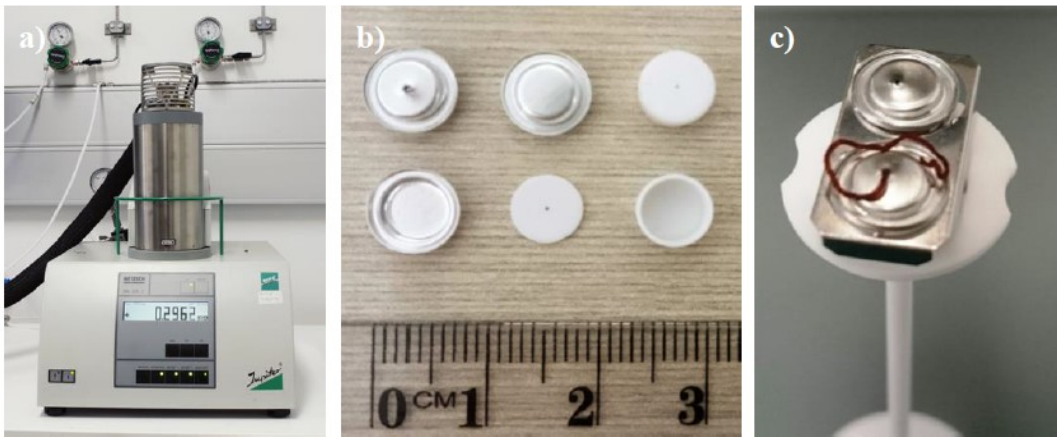

Figure 9: a) TGA setup, b) a selection of crucibles for TGA/DSC analysis (aluminium and alumina), and c) a STA sensor which measures TGA and DSC, with reference crucible (back) and sample crucible (front). Note it is important that sample size is small enough that if it expands, it does not extrude out the top of the crucible as shown above.

Table 1. A comparison of properties each thermal analysis technique can measure [27].

TGA	DSC	TMA
Mass change Decomposition Moisture content Thermal stability Sample composition	Melting/solidification Crystallisation Glass transition Heat of fusion Purity analysis Specific heat Phase transition Curing temperature Sample composition	Expansion/shrinkage Compression/tensile strength Young's Modulus Load deformation Penetration Softening point Sintering temperature Hardness/softness Creep under load Coefficient of thermal expansion
FTIR		
Evolved gas analysis Sample identification		

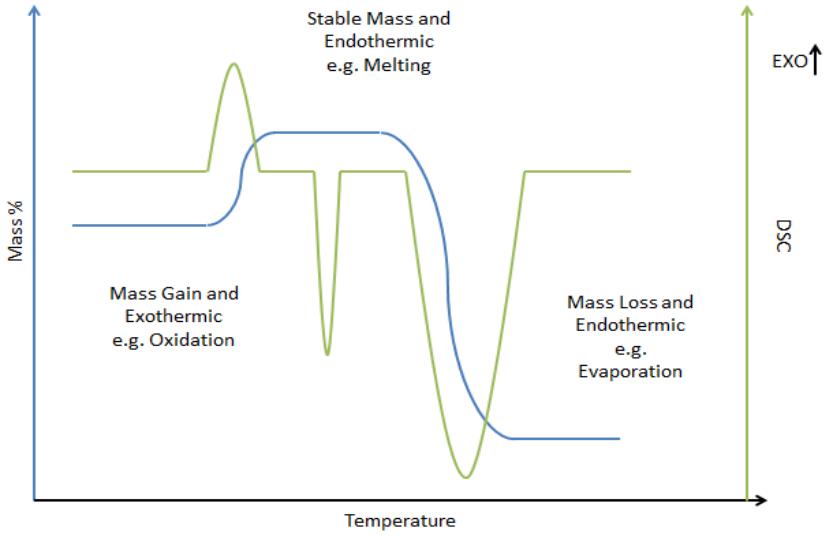

Figure 10: Simultaneous Thermal Analysis (STA- which comprises of TGA and DSC. Figure shows the TGA plot (Green-mass loss) versus temperature and also the DSC (Blue plot – energy) [25, 26].

VIII. Conclusions

There is constantly new material being developed every day that require characterisation as well as process conditions changing that introduce variations in the properties of the material. Quite often only the first technique of microscopy and microanalysis is required to identify a materials microstructure, composition and/or determining the chemical phases present. However, the combination of microscopy, microanalysis and other related techniques like FTIR, Raman spectroscopy and XRD can give further information about the materials being used and phases present [3].

As many new materials are developed, the thermal properties are required in order to fully understand their stability and durability when put into use. This has been recently seen in the building industry where incorrect cladding materials have been used [28].

ACKNOWLEDGEMENTS

The authors would like to acknowledge the support of Western Sydney University (WSU) and the Advanced Materials Characterisation Facility (AMCF), Phenom, Moran Scientific Pty Ltd, Hitachi and Netzsch. We would also like to thank AMCF interns: Edward Huang, Christopher Rhodes, Luke Basso, Denise Duff, Anthony Clark and Sam Macartney.

REFERENCES

[1] R. Wuhrer and K. Moran, "Representation of Microstructures through Rapid X-Ray Mapping", Materials Australia, Volume 38, No 5, September-October (2006) 12-14.

[2] R. Wuhrer, K. Moran and L. Moran, "Characterisation of Materials through X-ray Mapping", Materials Forum, Volume 30, (2006) 63-70.

[3] J.I. Goldstein et al. Scanning Electron Microscopy and X-ray Microanalysis, 3rd ed, Kluwer, Academic Plenum, New York, 2003.

[4] R. Johnson 1996 Environmental Scanning Electron Microscopy-An Introduction to ESEM, Second Edition. (Eindhoven, The Netherlands: Philips Electron Optics)

[5] D. Stokes D 2008 Principles and Practice of Variable Pressure: Environmental Scanning Electron Microscopy (VP-ESEM). (New York: Wiley)

[6] R. Wuhrer and K. Moran, "Low Voltage Imaging and X-Ray Microanalysis in the SEM: Challenges and Opportunities", IOP Conference Series: Materials Science and Engineering Volume 109, Issue 1, (2016).

[7] R. Wuhrer and K. Moran, Quantitative X-ray mapping, scatter diagrams and the generation of correction maps to obtain more information about your material. IOP Conf. Ser.: Mater. Sci. Eng. 55 012021, 2014.

[8] K. Moran and R.Wuhrer, X-ray Mapping and Interpretation of Scatter Diagrams. Mikrochim. Acta 155 209-217, 2006.

[9] K. Moran and R. Wuhrer, So, What Other Information can we Obtain from X-Ray Maps. Microsc. Microanal. 16 (Suppl. 2) 916-917, 2010

[10] J. Liu, High-Resolution and Low Voltage FE-SEM Imaging and Microanalysis in Materials Characterization. Mater. Character. 44 353-363, 2000.

[11] K. Moran and R. Wuhrer, "Quantitative Bulk and Trace Element X-Ray Mapping Using Multiple Detectors", Mikrochimica Acta, Vol. 155, pp. 59-66 (2006).

[12] K. Moran and R. Wuhrer, "X-ray Mapping and Interpretation of Scatter Diagrams", Mikrochimica Vol. 155, pp. 209-217 (2006).

[13] https://en.wikipedia.org/wiki/Fourier-transform_ infrared_ spectroscopy

[14] P. Larkin, Infrared and Raman Spectroscopy-Principles and Spectral Interpretation, Elsevier 2010.

[15] B. C. Smith, Fundamentals of FTIR Spectroscopy, CRC Press, 2011.

[16] https://www.bruker.com/products/infrared-near-infrared-and-raman-spectroscopy/ft-ir-research-spectrometers/vertex-series/vertex-70v/overview.html

[17] P. Griffiths, J. A. de Hasseth, Fourier Transform Infrared Spectrometry (2nd ed.). Wiley-Blackwell, 2007.

[18] https://courses.lumenlearning.com/labmethods/chapter/ftir-methods-attenuated-total-reflection-atr/

[19] B. D. Cullity, Elements of XRD, Addison-Wesley Publishing Copany, 1956.

[20] https://www.bruker.com/products/x-ray-diffraction-and-elemental-analysis/x-ray-diffraction.html

[21] https://en.wikipedia.org/wiki/X-ray_crystallography

[22] S.T. Misture, R.L. Snyder, Encyclopedia of Materials: Science and Technology, 2001

[23] https://serc.carleton.edu/research_education/geochemsheets/techniques/XRD.html

[24] M. E. Brown, Introduction to Thermal Analysis: Techniques and Applications, 2004, Kluwer Academic.

[25] Netzsch Handbook DSC, Differential Scanning Calorimetry, 2015.

[26] Netzsch Handbook, Smart Solutions in Thermal Analysis, 2014.

[27] L. George, J. J. Lee, S. Salek, R. Wuhrer, "Application of Thermal Analysis Techniques (TGA, DSC, TMA and Evolved Gases FTIR) in Understanding New Materials", iCSER2017, 1st International Conference on Structural Engineering Research, 20-22 November 2017, Sydney, Australia, 2017.

[28] L. George and R. Wuhrer, "Characterisation Techniques for the Identification of Composite Cladding Materials", Microsc. Microanal. 25 (Suppl 2), 2019, p744-745.

Characterisation Techniques for the Identification of Composite Cladding Materials and their Thermal Properties

Laurel George
Advanced Materials Characterisation Facility, REDI
Western Sydney University
Parramatta, Australia
L.George@westernsydney.edu.au

Richard Wuhrer
Advanced Materials Characterisation Facility, REDI
Western Sydney University
Parramatta, Australia
Richard.wuhrer@westernsydney.edu.au

Daniel J. Fanna
Advanced Materials Characterisation Facility, REDI
Western Sydney University
Parramatta, Australia
D.Fanna@westernsydney.edu.au

Christopher Rhodes
Advanced Materials Characterisation Facility, REDI
Western Sydney University
Parramatta, Australia
C.Rhodes@westernsydney.edu.au

Qingtao Huang
Advanced Materials Characterisation Facility, REDI
Western Sydney University
Parramatta, Australia
Q.Huang@westernsydney.edu.au

***Abstract*— With many new composite building materials being used in the construction industry, there is a need to identify and verify not only the final composite materials, but also the individual components. This is particularly important as reports highlight the high occurrence of material substitutions and inferior product use in the building industry.**

This paper demonstrates how characterisation techniques such as Scanning Electron Microscopy (SEM), Energy Dispersive Spectroscopy (EDS), Fourier Transform Infra-Red (FTIR) spectroscopy, X-ray Diffraction (XRD) and thermal analysis can be utilised to solve real-world industry based problems, such as verification of building products.

Of particular concern recently in Australia, is the use of Aluminium Composite Panels (ACPs) as cladding on multi-story buildings. After occurrences world-wide of building fires, mostly due to the flammability of the composite's polyethylene core, a ban was imposed on inferior ACP products. This has led to the rating and testing of all buildings to verify what material components are present in the composite material. This paper shows examples as to how materials characterisation techniques can be used to identify components used in composite materials, with ACPs used as an example. These techniques, especially when combined, can help to give an understanding of how individual components in a composite are dispersed, identify the elemental and phase composition of the components and show how a composite behaves in fire conditions.

Keywords*— *Microscopy, Microanalysis, FTIR, X-Ray Diffraction, Thermal analysis, Thermal properties, Material properties, Instrumentation, New materials

I. INTRODUCTION

The characterization of materials is critical for understanding their properties. With many new composite and nanocomposite materials coming into use, particularly in the engineering, construction and medical industries, there is a need to identify and verify not only the final composite materials, but also their individual components and the interfaces between them when combined together. These factors all greatly affect material properties and performance and need to be considered when designing new composites. An understanding of how they perform during the manufacturing process and in their working life is also important. Characterisation of these materials at all stages in the process can be used to solve real-world problems.

In Australia, the decline in manufacturing has seen the rise of imported construction materials. With this there is a risk that the imported materials do not conform to Australian regulations and standards [1]. There are increasing concerns over the number of unreliable, misleading or false material certification documents. There have also been cases of product substitution, where a material has been substituted for an inferior one, most likely to cut manufacturing costs. These concerns were also were also outlined in a 2018 report commissioned by the Building Minister's Forum. In this report it was recommended a compulsory building product certification system be put in place in the industry, particularly for high risk products [2].

In these instances, characterisation techniques such as Scanning Electron Microscopy (SEM), Energy Dispersive Spectroscopy (EDS), Fourier Transform Infra-Red (FTIR) spectroscopy and X-ray Diffraction (XRD), can be used to identify and verify building products, and establish whether certification and product specification documents are correct. Thermal analysis can also be used to understand how these products behave in fire conditions.

A composite material that has attracted a lot of attention recently, not only in Australia but world-wide, is the use of Aluminium Composite Panels (ACPs) as cladding on multi-story buildings. These panels consist of a core material, usually polyethylene (PE) or a polymer/filler composite, which is laminated and sandwiched between two thin aluminium sheets (Figure 1). The panel is then coated in various layers of paint, depending on where the panel is to be used. The commonly used PE core however, is highly flammable and was found to be a contributing factor in fires such as the fatal 2017 Grenfell Tower fire in London and the 2014 Lacrosse building fire in Australia. In both cases the fire spread rapidly up the buildings' external walls where

ACPs had been used. In the case of Lacrosse building fire, the fire travelled the full height of the building (23 levels) in 11 minutes [1].

After an examination of the use of ACPs in the building industry by the NSW Commissioner for Fair Trading in Australia, it was found these panels could pose a safety risk and a ban was imposed in August 2018 on certain types of ACPs [3]. Here, the core material used in ACPs fell into one of three categories:

1. Core materials with close to 100% PE.
2. Core materials with mixtures of PE and mineral fillers.
3. Core materials with less than 3% PE.

The ban specified that ACPs on all buildings greater than 3 storeys high, with a core material containing greater than 30% PE by mass, were banned. This therefore led to the testing of all buildings of at least this height.

As well as the identification of material components, thermal analysis techniques can also be used to understand how different materials behave under high temperature conditions. For example, there is an array of different mineral fillers that can be added to an ACP's core polymer matrix, and each behaves differently in fire conditions. Some of these mineral fillers, such as aluminium hydroxide, will release water when heated above 180°C, delaying ignition of the core. Other mineral fillers do not.

On analysis of over one hundred ACP core samples at the Advanced Materials Characterisation Facility, over fifteen different ACP core composite mixtures have been identified.

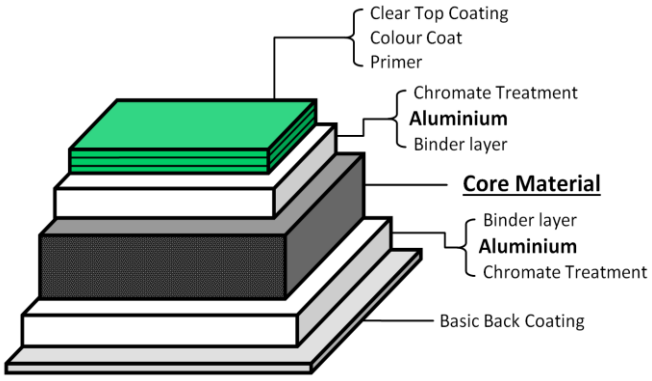

Figure 1: Common layers in an Aluminium Composite Panel (ACP)

II. Characterisation Techniques Used for Identification of Composites

The Advanced Material Characterisation Facility (AMCF), located on Western Sydney University's Parramatta South campus, houses a large collection of instruments used for materials analysis. This collection includes, and is not limited to, Scanning Electron Microscopy (SEM), Energy Dispersive Spectroscopy (EDS), Fourier Transform Infra-Red (FTIR) spectroscopy and X-ray Diffraction (XRD). These techniques, especially when combined, can help to give an understanding of how individual components in a composite are dispersed, and identify the elemental and phase composition of the components and also the interfaces present in a composite [4].

Following is a brief explanation of these techniques and how they apply to composite analysis. For the identification of ACP core materials, these techniques should be carried out in the order given here, as not all techniques are necessary. The results from the first test, will inform the user if the next test is required.

A. Microscopy Imaging

Scanning Electron Microscopy (SEM) equipped with Energy Dispersive Spectroscopy (EDS) microanalysis, is a powerful tool to use to first look at a sample [5].

Firstly an SEM can be used to image the core material from an ACP, and see if any filler material is present. If there is no filler present, then this image alone can be used to prove the core material doesn't comply with the specifications and is banned from use on multistorey buildings.

For imaging, most microscopes have both a secondary electron (SE) and back-scattered electron (BSE) detector which are used for imaging. Secondary electrons are produced when the SEM's electron beam gives atoms from a samples surface enough energy to emit an electron. SE images therefore give good surface detail and information about the morphology of the surface. Backscattered electrons are electrons from the SEM's electron beam that have interacted with a samples material. Heavy elements in the sample cause the trajectory of the electrons to bend more, or backscatter more, than a lighter element. In an image, heavy elements therefore appear brighter and lighter elements appear darker. Because of this, BSE images can give compositional information, and hence an idea of where to use EDS for elemental analysis.

Figure 2 shows SEM-BSE images of different core materials. It can be seen that the sample in Fig. a) has no fillers present, while those in Fig. b) - d) show different amounts of fillers. In Fig. d) the different brightness of fillers in the BSE image, suggests that the elemental composition is different. This can now be checked using EDS microanalysis.

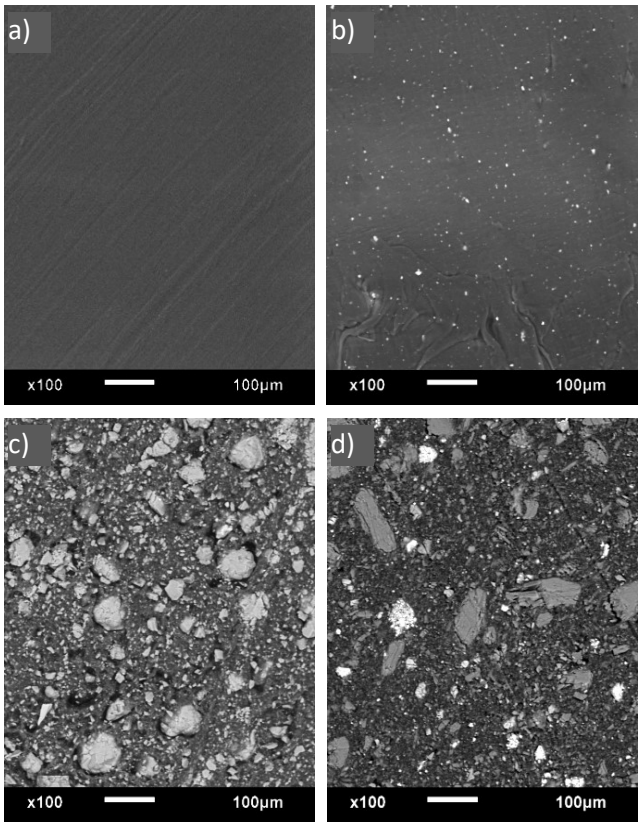

Figure 2: SEM-BSE images of ACP core materials containing; a) PE only, b) PE with a small amount of calcium carbonate filler, c) PE with aluminium trihydrate filler, d) PE with a mixture of different fillers.

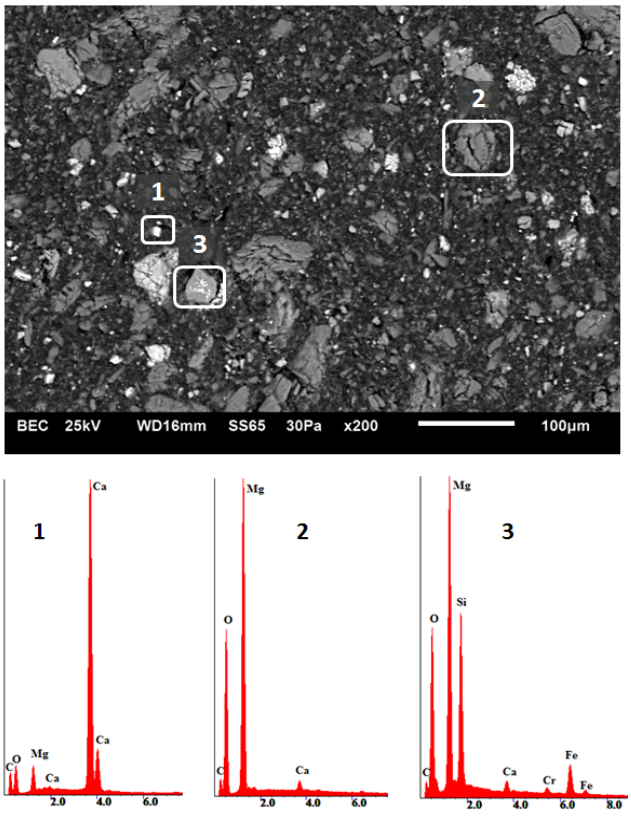

Figure 3: Example of a polyethylene sample with multiple types of fillers present. A SEM-BSE image is shown above, and numbered fillers have been analysed using EDS with the corresponding spectra shown below.

An SEM image should be used with caution to estimate the amount of filler present in a sample. It is important to firstly note that the ban imposed on cladding is for samples with more than 30% PE by *mass*. Using software packages, such as FIJI, to calculate the area of an image taken up by filler, will not give a percentage by mass unless the density of the materials is taken into account. In order to do this, elemental and phase analysis is needed to determine what the sample is actually made of. Caution should also be taken, as the signal collected for the SEM image is coming from an interaction volume in the sample. In other words, depending on the parameters used when imaging, the image that is collected is not just of the very surface. Area calculations can therefore be inaccurate.

B. Elemental Microanalysis

When an electron beam strikes an atom in a sample, an electron can be knocked from its shell, leaving a vacancy. A higher energy electron will then drop down and fill this place, emitting an X-ray as it does. Every element gives off X-rays with a specific energy. They are therefore known as characteristic X-rays. These X-rays can be detected by an Energy Dispersive Spectroscopy (EDS) detector, and a spectrum is created by plotting X-ray energy versus intensity. Peaks can be used to identify what elements are present and hence the elemental composition of a sample. This technique when used under the right conditions can also be quantitative.

For ACP core material analysis, if an SEM image shows fillers are present, EDS can then be used to identify the elements in the fillers, and if the particles are consistent or varied. Figure 3 shows a polyethylene sample with at least three different types of fillers present. This can be seen as the SEM-BSE image shows particles of different brightness, and the EDS spectra confirm there are different elements present. Knowledge of the elements present is also handy when undertaking FTIR and XRD analysis and library matching, and it can help to narrow down search results.

C. FTIR

Fourier Transform Infra-Red (FTIR) spectroscopy is a form of vibration spectroscopy and can be used to identify molecular structures and functional groups present in a sample. It is therefore useful in helping to identify polymers used in ACP core samples and also the fillers present.

A spectrum can be acquired using Attenuated Total Reflection (ATR), which is a method used to collect an infrared spectrum from solids and liquids. An ATR stage uses a crystal with a high refractive index (e.g. diamond or germanium) on which the sample is placed. As an infrared beam passes through the crystal, it is reflected internally many times, in turn creating an evanescent wave that extends beyond the crystal and into the sample placed on top. The sample may then absorb some energy when hit by infrared light, causing molecular bonds in the material to vibrate and bend. This energy absorption thereby attenuates (i.e. changes) the infrared beam as it returns to the detector. This signal is then used to create an FTIR spectrum, where

we can see at what frequency/wavelength energy was absorbed.

The resulting spectrum can then either be matched to library of spectra from known materials, or a correlation chart can be used to help identify peaks in a spectrum. These charts show where common bonds and functional groups fall in on the spectrum. FTIR can also be used in conjunction with SEM/EDS analysis, as the SEM image shows if fillers are expected, and EDS shows which elements are present, helping to narrow down the search for FTIR matches. Spectra obtained from composite materials such as ACP cores, can be harder to match as the spectrum obtained is a composite of the different material spectra added together (Figure 4). Multiple library matches therefore need to be undertaken in order to account for all peaks in a sample's spectrum.

Comparisons of FTIR spectra show how a quick and simple scan can help to differentiate different polymers and fillers, as shown in Figure 5. If of interest, a user can build their own library of spectra to match samples to, rather than rely on what spectra are available in a ready-made library.

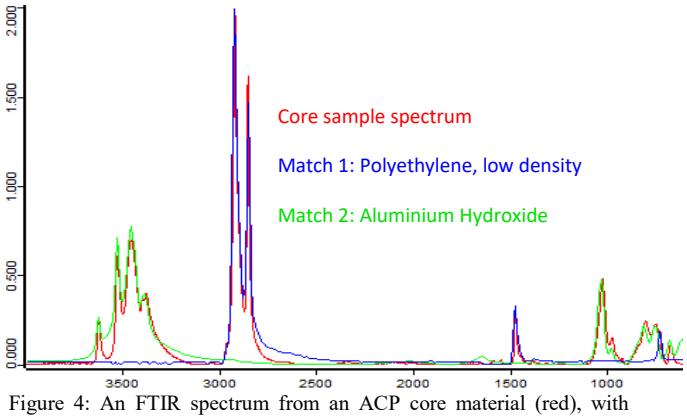

Figure 4: An FTIR spectrum from an ACP core material (red), with library matches to polyethylene (blue) and aluminium trihydrate.

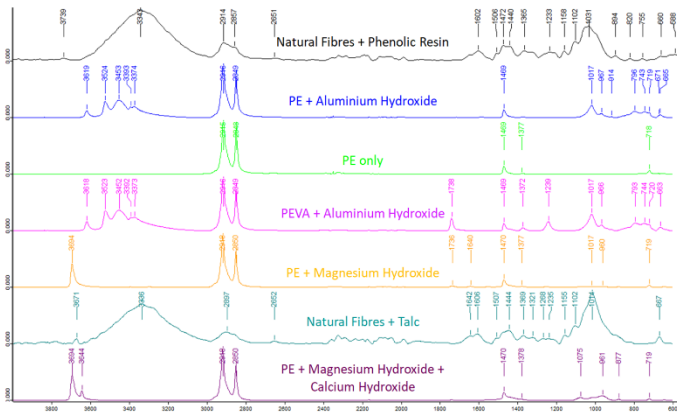

Figure 5: An example of FTIR spectra obtained from some common ACP core composite materials.

D. X-Ray Diffraction

X-Ray Diffraction (XRD) can be used to identify phases present in a sample, and therefore help to verify the fillers present. This analysis is crucial if any percentage mass calculations need to be made, as the exact phase needs to be known for density calculations. If thermal analysis is to be used for mass calculations (as explained in the following section), then XRD also needs to be used to verify the phases left in the samples ash after heating.

XRD involves an X-ray source which is focused onto a sample, and a detector which collects diffracted X-rays and records their intensity. The source and detector are able to move around the sample in order to scan a range of angles, and build up an X-ray spectrum of angle (2Θ) versus intensity. The angle at which a peak is observed depends on the crystal structure, and hence phase, of the material analysed.

Similar to FTIR, XRD spectra can be matched to a library of known materials for identification. By completing EDS prior to XRD analysis, and hence knowing what elements are present, this list can be narrowed down. Again, analysis of composite materials can be difficult due to overlapping peaks and spectra of the different materials present in the one sample. Matching needs to be done so all peaks are accounted for. The ACP core material in Figure 5 matched to aluminium trihydrate (gibbsite). The two peaks unaccounted for were later found to be from polyethylene. This agreed with results from FTIR matching (Figure 4).

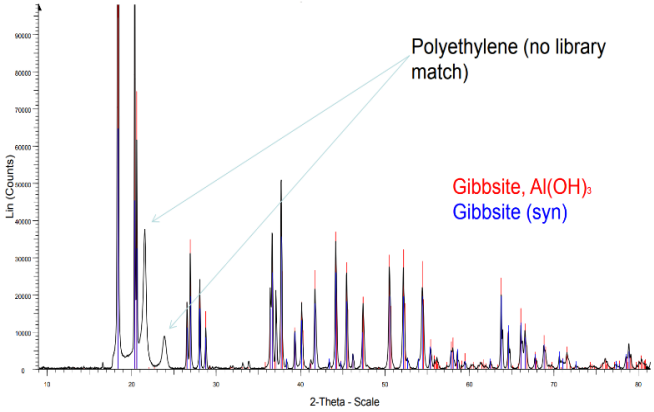

Figure 6: An XRD spectrum from an ACP core material (black line). Library matching showed gibbsite (aluminium trihydrate) was present. The two peaks nots matched are most likely from the PE polymer used in the ACP, which was confirmed with FTIR.

E. Thermal Analysis

Another technique which can be used to help verify ACP polymers, and assist with percentage mass calculations of fillers is Simultaneous Thermal Analysis (STA). This involves the simultaneous running of two or more thermal techniques at the same time on the one sample [6]. Thermal techniques most commonly used are Thermo-Gravimetric Analysis (TGA), and Differential Scanning Calorimeter (DSC).

TGA involves sitting a sample on a sensitive balance, and measuring the change in mass of a sample as it heats up in a furnace. As a sample undergoes a thermal event at a particular temperature, such as decomposition or evaporation, a change in mass is detected and the amount of mass loss measured.

DSC measures the heat going to or from a sample relative to a reference as the sample is heated or cooled. Thermal events which occur are either endothermic, where heat is absorbed by the sample (e.g. melting), or exothermic, where heat is released by the sample (e.g. crystallisation).

The advantage of running TGA and DSC simultaneously is that the results can be directly compared on the same graph, and all test parameters, such as heating rates and gas flow, are identical. Thermal techniques are not always straight forward. If more than one material is present, there may be overlapping thermal events, making it hard to interpret results.

Different polymers and fillers act differently when exposed to heat. In the case of ACP core material analysis, TGA/DSC can be used to identify the polymer's melting point, helping to confirm the polymer that is present. More importantly for ACP core materials with filler present, it can be used to monitor mass loss as the polymer decomposes, leaving a residual mass which consists of the mineral filler. It is important to note, however, that the content left after heating may be a different phase to that at the start of the experiment, i.e. at room temperature. For example, the mineral filler $Al(OH)_3$ (aluminium trihydrate, also known as gibbsite) when heated above 180°C will decompose and release water at three different temperatures as it changes phase (Figure 7). This release of water can help to delay ignition of the core in fire conditions. After being heated to 590°C, all of the $Al(OH)_3$ has been converted Al_2O_3 (amorphous alumina) [7]. This, however, can be checked using XRD and EDS analysis.

Lastly the amount of energy released and the rate at which it is released can be monitored under controlled conditions, giving important information on how a product may behave under fire conditions.

III. Putting It All Together

Once each of these techniques have been completed, the results can be put together to provide a picture of the materials that are being used, and in the case of ACP core materials, if they comply with Australian Standards.

Figure 8 and 9 show results from an example core material from each of the three categories as outlined in the NSW Commissioner for Fair Trading in Australia report and subsequent ban [3]. These materials were found to be:

Category 1: Polyethylene (PE) only.

Category 2: PE with an aluminium trihydrate (ATH) filler.

Category 3: A natural fibre material with talc particles.

It can be seen straight away in the Figure 8 SEM images,

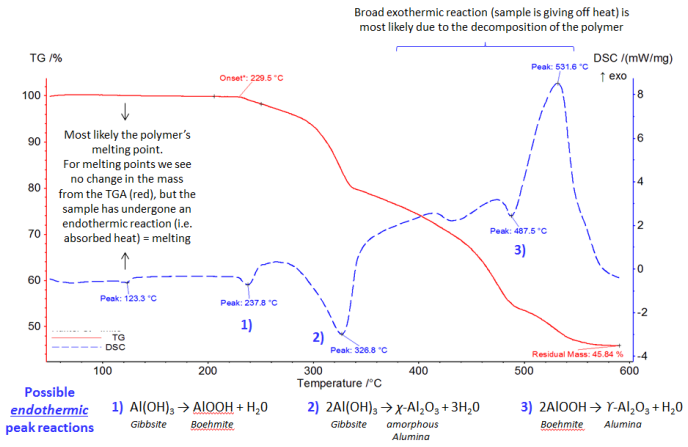

Figure 7: A polyethylene sample with an aluminium trihydrate filler. With each phase change of the original filler, water is released (points 1, 2 and 3). At each of these steps a mass loss can be seen in the TGA curve (red), and a peak in the endothermic direction is observed in the DSC curve (blue).

that the first material (on the left) has no fillers present. With confirmation of the polymer type with FTIR, this is enough information to prove this material falls into category 1 (close to 100% PE), and is hence banned. Further testing with XRD however, confirms no mineral fillers are present. Figure 9 (top) shows the thermal analysis results, showing the melting point (110°C) and onset of decomposition (273°C) of the PE. After heating up to 590°C, there is no sample left, again proving there are no fillers.

The middle SEM image in Figure 8 shows that this sample has particles present. EDS analysis of a particle shows that aluminium and oxygen are present. FTIR results agree with the EDS results and confirm PE and aluminium trihydrate ($Al(OH)_3$) are the best matches with the sample's spectrum. Also in agreement is the XRD spectrum and library match, which also confirms aluminium trihydrate is present. Thermal analysis (Figure 9, middle) shows that upon heating until 590°C, there is a residual mass of 45.9%. XRD of this residual mass confirmed that it was amorphous alumina remaining. This agrees with work completed by Redaoui and coworkers [7] and the endothermic reaction steps shown in Figure 7, where aluminium trihydrate when heated releases water, and in turn changes phase to become amorphous alumina.

Lastly in Figure 8 (right), the SEM image shows a sample that looks more like a fibre than a polymer, with small bright particles. EDS shows the particles have a lot of magnesium, silicon and oxygen present. The FTIR spectrum was a more complicated spectrum which didn't yield the best matches. The SEM image and list of elements present from the EDS analysis however, helped to narrow down possible FTIR library matches to those which made sense. Here the best matches were made with natural fibres, such

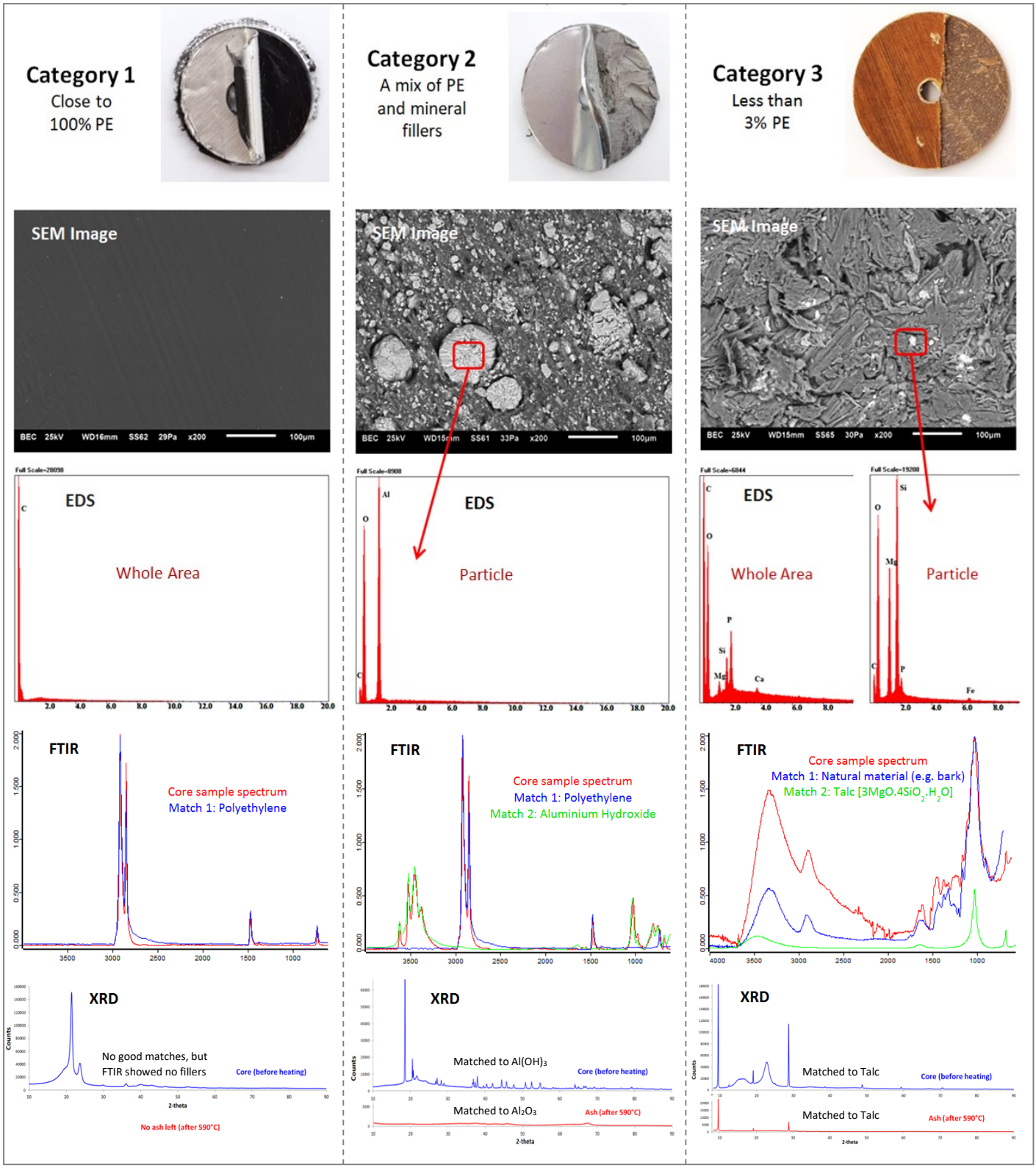

Figure 8: Examples of result sets of ACP core materials from each of the categories stated by the NSW Commissioner for Fair Trading in Australia. Analysis techniques used, (from top to bottom), include optical imaging of the core sample to record the actual colour and appearance, SEM-BSE imaging to reveal if fillers are present, EDS microanalysis to show what elements are present, FTIR to help identify the polymer and fillers, XRD to identify phases present in filler material both before and after heating until 590°C.

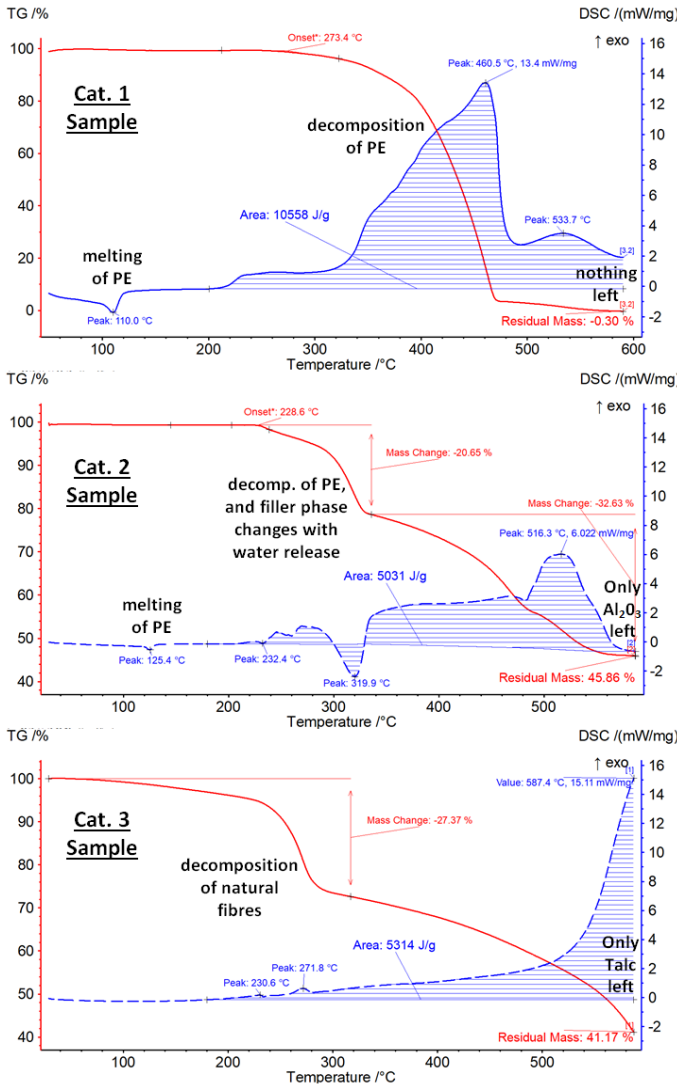

Figure 9: Thermal analysis results (TGA = red line, DSC = blue line) of ACP core materials from each of the categories stated by the NSW Commissioner for Fair Trading in Australia.

as wood/tree materials, phenol resins (not shown) and talc ($3MgO.4SiO_2.H_2O$) which agreed with the EDS results. Talc was also confirmed with XRD, matching the sample spectra both before and after heating. Thermal analysis of this sample (Figure 9, bottom), showed that after heating to 590°C, 41% of the mass remained.

A comparison of samples can also be made with respect to how each sample reacts under heat. The area under the DSC curves in Figure 9 (blue dotted lines), gives the net amount of energy released during heating. The largest area is from the category 1 sample (PE only) which has given off a total of 10,558 J/g of energy. This is the material on the banned list. The category 2 and 3 samples give off 5,031 and 5,314J/g of energy respectively. It can be seen for the Category 2 sample, the aluminium trihydrate releases a lot of water at 320°C, and energy is absorbed rather than released, slowing the burning of the sample. For the Category 3 sample, at 590°C the sample decomposition hasn't finished. It may be that this releases more energy at higher temperatures, whereas the other two samples have pretty much burnt out by 590°C.

IV. Conclusions

With rising incidences of material substitutions and inferior product use in the building industry, coupled with tragedies such as the Lacrosse and Grenfell Tower fires due to use of flammable ACP's, ensuring materials meet Australian quality standards is of the utmost importance.

This paper has shown how complimentary material characterisation techniques, such as SEM, EDS, FTIR, XRD and thermal analysis, provide a powerful toolbox for the identification and verification of traditional and new composite materials. Quite often only an SEM image and FTIR spectrum are required. The combination of these and additional techniques however, can reveal further information about the materials being used.

V. Acknowledgements

The authors would like to acknowledge the support of Western Sydney University (WSU) and the Advanced Materials Characterisation Facility (AMCF) and Netzsch. We would also like to thank, Denise Duff, and Sam Macartney.

VI. References

[1] Non-conforming building products, interim report: aluminium composite cladding, https://www.aph.gov.au/ Parliamentary_Business/ Committees/Senate/Economics/Non-conforming45th/Interim_report_ cladding (accessed Oct 30th 2019).

[2] Shergold, P., Weir, B. (2018). "Building Confidence." Dept. of Industry, Innovation and Science.

[3] Aluminium composite panel ban, www.fairtrading.nsw.gov.au/buying-products-and-services/product -and-service-safety/building-products /aluminium-composite-panel-ban, (accessed Feb 2nd 2019).

[4] George, L., Wuhrer, R. (2019). "Characterisation Techniques for the Identification of Composite Cladding Materials." Micoscopy and Microanalysis 25(2): 744-745

[5] Salek, S., George, L., Wuhrer, R., Samali, B. (2017). "Addressing the Durability Issues of Construction Materials using Microstructural Analysis." Proc. 1st International Conference on Structural Engineering Research, 56-61

[6] George, L., Lee, J.J., Salek, S., Wuhrer, R. (2017). "Application of Thermal Analysis Techniques (TGA, DSC, TMA and Evolved Gases FTIR) in Understanding New Materials." Proc. 1st International Conference on Structural Engineering Research, 247-252

[7] Redaoui, D., Sahnoune, F., Heraiz, M., Raghdi, A. (2017). "Mechanism and Kinetic Parameters of the Thermal Decomposition of Gibbsite Al(OH)3 by Thermogravimetric Analysis." Acta Physica Polonica A 131(3): 562-565

Theoretical Investigation on Mechanical Behaviours of Composite Metal Foams

Phu Thanh Nguyen
School of Computing, Engineering and Mathematics,
Western Sydney University, Penrith, NSW 2751, Australia
18550737@student.westernsydney.edu.au

Chunhui Yang
School of Computing, Engineering and Mathematics,
Western Sydney University, Penrith, NSW 2751, Australia
r.yang@westernsydney.edu.au

***Abstract* - Composite metal foams are a promising type of advanced engineering materials, comprising of a base metal with cellular structure and solid/hollow spheres to form porous spaces. Composite metal foams exhibit superior mechanical properties such as lightweight, high yield strength, high energy absorption capacity, etc. This type of materials show much potential for applications in various industries. It is necessary to fully understand mechanical properties and behaviours of composite metal foams for further design and applications. There were many researches on their behaviours; however, most of those were experimental-based with a few limitations. In this research, a theoretical model and two two-dimensional numerical models of typical composite metal foams were developed to investigate their mechanical behaviours subjected to compressive loadings. The proposed models were validated by comparing the results obtained from analytic and numerical analyses with experimental results from literature review. Parametric studies on the effects of porosity and wall thickness on the mechanical performance and behaviours of composite metal foams were also conducted on the verified models. It is found that composite metal foams behave linearly under compression in elastic region like other types of material and followed by a hardening stage with a level plateau region over a long strain region and ended with densification stage. Parametric studies have also shown that porosity and wall thickness have direct effects on the performance of the materials. Yield strength, plateau stress and density are all enhanced with the increase of wall thickness and the decrease of porosity.**

Keywords–composite metal foams, analytic model, numerical model, finite element analysis, mechanical properties, compression

I. INTRODUCTION

Metal foams are cellular structures developed from metal based materials. This structure has a relatively low density but exhibit excellent properties such as lightweight, high strength, stiffness, energy absorption capacity, soundproofing (Vendra and Rabiei 2007). Metal foams, with these promising characteristics, gained many interests from automotive, aircraft and railway industries (Liu et al. 2018). Various experimental and numerical studies were conducted on this type of foam materials to investigate their mechanical properties and behaviours. Liu et al. (2016) numerically studied the effects of different fundamental parameters on mechanical behaviours of metal foams. It was found that the foam porosity has direct influences on material properties and mechanical behaviours of the material. Further researches on metal foams resulted in the creation of composite metal foams. This type of foams also has a cellular structure but it can be further reinforced by adding solid or hollow metal balls to cells to enhance superior properties of metal foams. Composite metal foams exhibit promising mechanical properties over metal foams made with similar materials (Neville and Rabiei 2008). Potential applications of composite metal foams are anti-intrusion bar in automotive industry, blast and ballistic protection in defence industry or radiation shielding. There were extensive researches on metal foams and composite metal foams in recent years to thoroughly understand their material properties and mechanical behaviours before implementing this type of materials into applications and fully utilising their potentials. However, most of these researches only employed experimental methods to fabricate and characterise such materials. Hence, there are limitations in manipulating degree of porosity, cell size, cell shape, cell wall thickness, etc., which can greatly affect the performance of the composite metal foams (Vendra and Rabiei 2007). With the aids of numerical modelling and simulations, it is essential to build numerical models of composite metal foams to further investigate their mechanical behaviours in a sense of material design. For example, by employing the finite element method, numerical models allow more controls over fundamental parameters, such as porosity, cell size, cell wall thickness, etc. and justify the relationships between these parameters and mechanical performance and behaviours of such materials.

This research focuses on building numerical models of composite metal foams to investigate their material properties and mechanical behaviours subjected to compressive loadings. Firstly, an analytical model of composite metal foams is developed and employed to determine the material properties of aluminium-steel composite metal foams available in literature. Secondly, two two-dimensional finite element models of the aluminium-steel composite metal foams are developed and then finite element analyses are conducted on numerical models to investigate the mechanical behaviours of composite metal foam materials under compression. The developed numerical models are validated by comparing the results with the experimental ones available from literature. Thirdly, parametric studies are carried out to further investigate the effects of wall thickness and porosity on mechanical properties and the stress-strain curve of composite metal foams.

II. ANALYTIC MODELLING OF COMPOSITE METAL FOAMS

A. Analytic Modelling of Composite Metal Foams

The analytic model of Aluminium Alloy – Stainless Steel composite metal foams was developed, which was based on the Aluminium – Stainless Steel composite metal foam specimens from Vendra and Rabiei's work (2007). Fig. 1 shows the cellular structure of the testing sample, which has a phase with matrix material – Aluminium 356 Alloy and an additive phase of steel - 316L Stainless Steel in a hollow spherical form, in which the hollow spheres are of the same size with 3.3 mm inner diameter, 3.7 mm outer diameter and a wall thickness of 0.2 mm. It is worth to note that the distribution of the steel spheres is roughly even.

Figure 1. Cell structure of an aluminium-stainless Steel composite metal foam specimen (Vendra & Rabiei, 2007)

As shown in Table I, these two materials have quite different material properties. As a typical composite metal foam material, the matrix volume fraction is 41% and has small wall porosity of less than 5%.

Table I Main parameters of testing specimen (Vendra and Rabiei, 2007)

Aluminium – Steel composite cast foams		Notes
Matrix material	Aluminium 356 Alloy	
Sphere material	316L Stainless Steel	
Sphere packing density	59%	V_{fs}
Matrix volume fraction	41%	V_{fm}
Sphere outer diameter	3.7 mm	OD
Sphere wall thickness	0.2 mm	t_w
Wall porosity	<5%	V_{fp}
Sphere inner diameter	3.3 mm	ID

The volume fraction of porosities in the wall thickness (V_{fp}) of spheres of the Aluminium Alloy – Stainless Steel composite metal foam specimen in Vendra and Rabiei's work (2007) is slightly less than 5%. However, for an analytic purpose, V_{fp} was assumed to be 5% or 0.05. Physical and mechanical properties of these two materials used in current study are listed in Table II.

For Aluminium 356 Alloy, the physical and mechanical properties data is from commonly-used sources available on the Internet. For stainless steel, all the properties data is provided by Atlas Steels Australia.

Table II Physical and mechanical properties of Aluminium 356 Alloy and Stainless Steel

	Aluminium 356 Alloy	Stainless Steel
Density	2680 kg/m^3	8000 kg/m^3
Yield Strength	124 MPa	170 MPa
Ultimate Yield Strength	172 MPa	485 MPa

Analytic analysis was carried out by using the rule of mixture which was developed for 2-phase composites. Further analytic calculations for theoretical physical and mechanical properties of this composite metal foam material were based on Eq. (1), which is the modified rule of mixture equation used by Rabiei and O'Neill (2005).

$$\rho_{CMF} = \rho_{steel} * \left[1 - \left(\frac{V_{in}}{V_{out}}\right)\right] * V_{fs} * (1 - V_{fp}) + \rho_{Al} * V_{fm} \quad (1)$$

In this equation for three-dimensional problems, the density of Aluminium – Steel composite metal foams (ρ_{CF}) can be estimated according to the densities of steel (ρ_{Steel}) and aluminium (ρ_m), the inner volume (V_{in}) and the outer volume (V_{out}) of a single sphere. In this research, the analytic model of the composite metal foam material is two-dimensional and thus the equations were modified further to be suitable for the two-dimensional analyses. The density, yield strength and relative density of aluminium-steel composite metal foams can be obtained by using Eqs. (2), (3) and (4), respectively, as follows:

$$\rho_{CMF} = \rho_{steel} * \left[1 - \left(\frac{A_{in}}{A_{out}}\right)\right] * V_{fs} * (1 - V_{fp}) + \rho_{Al} * V_{fm} \quad (2)$$

$$\sigma_{y,\,CMF} = \sigma_{y,Steel} * \left[1 - \left(\frac{A_{in}}{A_{out}}\right)\right] * V_{fs} * (1 - V_{fp}) + \sigma_{y,Al} * V_{fm} \quad (3)$$

and

$$\rho_{relative} = \frac{\rho_{CMF} * V_{fs}}{\rho_{Al}} \quad (4)$$

In these modified formulae above, the ratio between the inner and outer volumes of a single sphere was replaced by the ratio between the inner area (A_{in}) and the outer area (A_{out}) of a single sphere.

B. Numerical modelling of composite metal foams

Based on the parameters and calculations in analytic development, two different 2-D models of the composite metal foams were developed by using the commercial finite element analysis software package – ANSYS/Workbench: a) Model A – unit-cell model; and b) Model B – multi-cell model, as shown in Fig. 2. The square plates are the base material or matrix –Aluminium 365 Alloy and the annuli are hollow spheres – Stainless Steel.

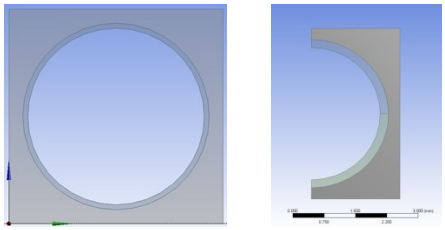

(a) Model A – unit-cell model

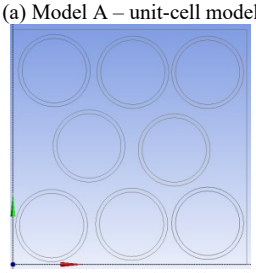

(b) Model B – multi-cell model

Figure 2 2-D Finite Element Models of composite metal foams

It should be noted that Model A is assumed to be an ideal unit-cell model with the sphere in the centre of matrix. Hence, a half model was used to conduct numerical analysis instead to utilise the symmetry condition. For Model B, the spheres were created at random locations. Table III summarises the overall dimensions and parameters of these two composite metal foam models.

Table III Dimensions and parameters of 2-D aluminium-steel composite metal foam models

	Model A (Unit-cell Model)	Model B (Multi-cell Model)
Overall dimension	4.25 mm x 4.25 mm x 0.1 mm	12 mm x 12 mm x 1 mm
Porosity	0.59	0.59
Sphere diameter	3.7 mm	3.7 mm
Wall thickness	0.2 mm	0.2 mm
Overall area	18.0625 mm^2	144 mm^2
Spheres area	10.6569 mm^2	84.96 mm^2
Number of spheres	1	8

Meshes for two models were generated by using the 2D plane element 182. Each element has 4 nodes with 2 degrees of freedom for each node. Mesh convergence studies were conducted on these two composite metal foam models and the appropriate element size for Model A was identified to be 0.025 mm while for Model B it was 0.05 mm.

As the purpose of the research is to investigate full behaviours of composite metal foam materials under compression, non-linear finite element analyses were conducted for the materials at not only elastic region but also plastic region. Non-linear material models with isotropic elasticity and bilinear isotropic hardening for aluminium alloy and stainless steel are shown in Figs. 3(a) and (b), respectively.

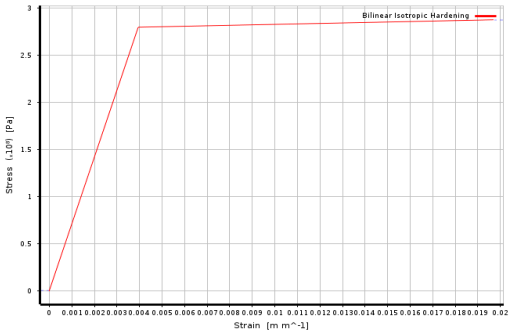

(a)

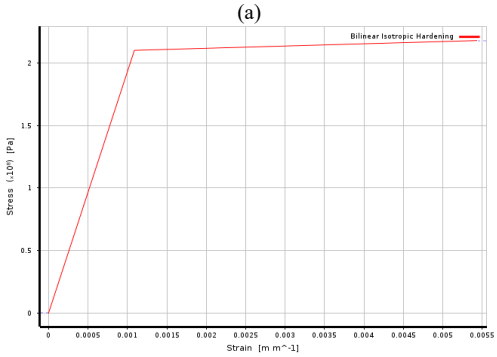

(b)

Figure 3 Stress-strain curves for (a) non-linear aluminium alloy and (b) stainless steel.

Defining contact is extremely important as it constrains the relative movement between defined parts. Bonded contacts were defined at shared edges between the aluminium alloy base and the steel spheres. For simplicity, interfacial interaction between matrix and spheres was disregarded. As self-contact is not available for ANSYS Static Structure, each stainless-steel sphere was divided into upper and lower parts to define the contact surface and avoid self-penetration, as shown in Fig. 4. A frictional contact with the friction coefficient of 0.1 was defined for each pair of inner circular edges.

Other boundary conditions were also defined to constrain the models and simulate a compressive mechanical testing. The bottom edge of the models was constrained by a fixed support while the top edges were subjected to a downward displacement in the vertical direction. For unit-cell model, a zero-displacement boundary condition was applied at the symmetry edge of the model. In addition, linear periodic condition in horizontal direction was employed in Model B to homogenise the mechanical properties of the composite metal foams. Large deflection was activated to conduct non-linear finite element analysis simulations. It is worth to note that non-linear adaptive region was also applied to the spheres. This boundary condition will perform a localised re-mesh at distorted area when a distortion occurs. However, there are some limitations when using this environment condition. For 2-D FEA, the mesh element order and large deflection must be turned on. must be linear. Fig. 4 shows the applied boundary conditions to the 2-D composite metal foams models.

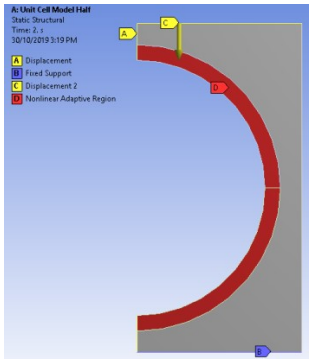

(a) Half unit-cell model

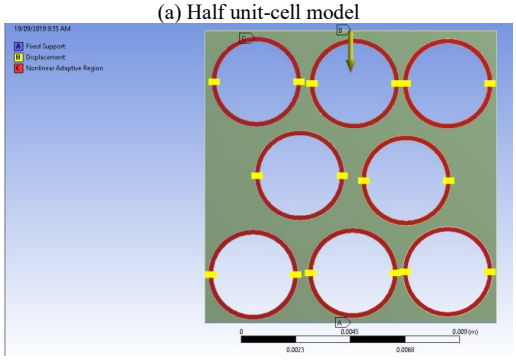

(b) Multi-cell model

Figure 4 Applied boundary conditions

Probe was used to monitor the reaction force at the fixed support when the displacement is applied. Total deformation results were also monitored. Based on the applied downward displacement and the reaction force, stress and strain were calculated by using Eqs. (5) and (6):

$$\sigma = \frac{F_R}{Wt} \quad (5)$$

$$\varepsilon = \frac{\delta}{H} \quad (6)$$

where σ is the stress, F_R is the reaction force at the fixed support, W is the width of the model, t is the thickness of the model, ε is the strain, δ is the applied downward displacement and H is the height of the model.

C. Parametric studies:

For the parametric studies, Model A and B were both further modified to investigate the effects of key parameters, wall thickness and porosity, on the material properties and mechanical behaviours of the composite metal foams.

Three different wall thicknesses - 0.2 mm, 0.275 mm and 0.35 mm were selected to consider the effects on material properties and mechanical behaviours. For a comparison, parametric studies of wall thickness was also conducted by using the analytic model. By modifying the wall thickness parameter only, density and yield strength can be calculated using Eqs. (2) and (3). Similarly, three different values of porosity - 0.341, 0.445 and 0.59 were considered to investigate the influences of the porosity on the on material properties and mechanical behaviours. For both two cases of parametric studies, the stress-strain curves with different wall thickness and porosities were obtained.

III. RESULTS AND DISCUSSION

A. Analytic analysis

An analytic analysis was conducted on the proposed analytic model by using Eq. (2), (3) and (4). It was found that the composite metal foam material model has a density of 2015.9074 kg/m^3 with a relative density of 45.32%. The plateau stress of the material was also estimated to be 70.3285 MPa. Table IV provide the comparisons between the analytic results and experimental ones from Vendra and Rabiei's work (2007).

Table IV Comparisons between analytic and experimental results

	Analytic results	Experimental results (Vendra & Rabiei 2007)	Percentage Error
Density (kg/m^3)	2015.9074	2490	19.04%
Plateau stress (MPa)	70.3285	70	0.47%
Relative density	45.32%	43%	5.40%

It can be clearly seen that values of plateau stress and relative density from both analytic and experimental results are very close with only 0.47% and 5.40% difference. The only notable difference was found on the density which may attributed by .the fundamental difference between 2-D analytical model and 3-D experimental model. There may be slightly different values of density of base materials (Aluminium 356 Alloy and Stainless Steel) used in the theoretical model and specimens

B. Numerical analysis

Model A – Unit-cell Model:

Numerical simulations were conducted on Model A by applying different downward displacement values. Fig. 3.1 below illustrates the deformation of the unit-cell model at different strain values.

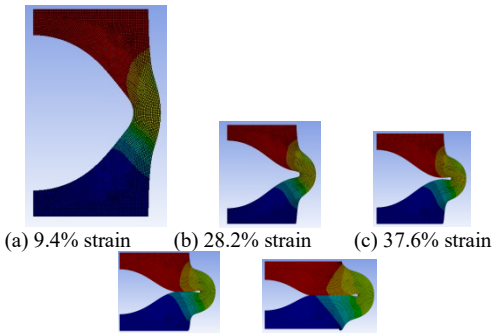

(a) 9.4% strain (b) 28.2% strain (c) 37.6% strain

(d) 47% strain (e) 58.8% strain

Figure 5 Total deformations generated for Model at different strains

As can be seen in Fig. 5, the unit-cell model gradually compressed stage by stage. At the 58.8% strain, the sphere is almost fully compressed with its internal circumference contacting with itself. Deformations occur smoothly and uniformly without any shear bands. This shows good agreement with the deformation mechanism of composite metal foam specimens under compression in Neville and Rabiei's work (2008).

Model B – Multi-cell Model:

Numerical simulations with different values of displacement were conducted on the model. Fig. 6 shows the total deformations of Model B under compression at different displacements applied onto the top edge of the model.

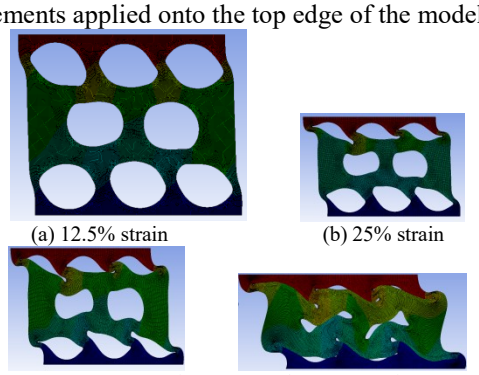

(a) 12.5% strain (b) 25% strain

c) 33.3% strain (d) 58.3% strain

Figure 6 Total deformations generated for Model B at different strains

In Fig. 6, the gradual deformations of this multi-cell model are developed as the applied displacement value increases. When the model was subjected to a downward displacement of 7 mm as shown in Fig. 6(d), some of the spheres in Model B are fully compressed and their internal circular edges touches for self-contact. This is a good illustration for the densification stage of composite metal foams with only little space left within each sphere. It can be also observed that the multi-cell model did not deform uniformly. Shear bands can also be clearly observed with stair shape deformations on two sides of Model B. This is opposite to the deformation mechanism of the composite metal foams shown in Fig. 5. This uneven distribution of displacement is possibly due to the distribution of the spheres as the spheres in Model B were randomly placed.

C. Stress-strain curves

Based on numerical data of calculated stress and strain values for each simulation, the stress – strain curves of Model A and Model B can be plotted. Fig. 7 below shows the plotted stress-strain curves of Model A and Model B as well as the stress-strain curve based on experimental data from literature review (Vendra & Rabiei 2007).

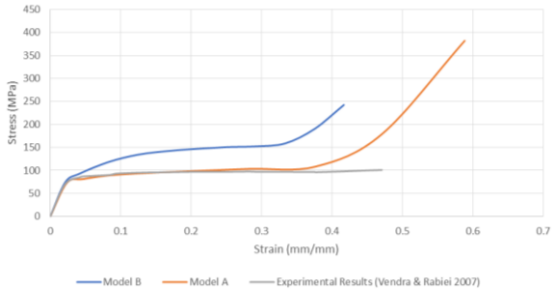

Figure 7 Comparisons on mechanical behaviours of different aluminium-steel composite metal foam models

In Fig. 7, the three stress-strain curves are almost synchronous in the elastic region with slightly higher yield strength from Model B. In plateau region after the yield point, differences between these three stress-strain curves can be seen. The stress-strain curve from the unit-cell model closely follows the curve from literature until approximately 0.35 strain point. For Model B, its stress-strain curve has a higher plateau stress than those from Model A and literature. The differences become noticeable as the strain value increases. Both the curves from Models A and B shows a shorter plateau region (only up to approximately 35% strain) compared with the experimental stress-strain curve from Vendra and Rabiei's work (2007). However, the overall shape of the stress-strain curves from both models are similar to a typical stress-strain curve of composite metal foams with an initial elastic region followed by a level plateau region over a long strain region and ended with a densification stage. Even though there are still differences between the results from the proposed numerical models and the experimental results from literature review, these two numerical models still successfully demonstrate the mechanical behaviours of composite metal foams under compression through three stages: elastic region, plateau region and densification. The developed numerical models of composite metal foams were validated by experimental results from Vendra and Rabiei's research (2007).

D. Parametric studies

Wall thickness effect:

Wall thickness effect was considered using both the theoretical composite metal foam material model and numerical models of Aluminium – Steel composite metal foams. In order to investigate the effect of wall thickness on the mechanical performance of composite metal foams, analyses were conducted on analytic material model estimate the density and yield strength using Eqs. (2) and (3). The calculated values of density and yield strength with three different wall thicknesses are listed in Table V.

Table V Comparisons on the effect of different wall thicknesses on mechanical properties of composite metal foams

Wall thickness (mm)	0.2	0.275	0.35
Density (kg/m^3)	2015.907	2332.801	2634.955
Yield Strength (MPa)	70.329	77.063	83.483

It is clear that as the wall thickness increase from 0.2 mm to 0.275mm (37.5% increase) then 0.35mm (70% increase), the density of composite metal foam material model also increases from 2015.907 kg/m^3 to 2332.801 kg/m^3 (15.72% increase) then 2636.955 kg/m^3 (30.71% increase). Similar with density, with the increase of wall thickness, yield strength value also increases 9.57% with 0.275 mm wall thickness and 18.07% with 0.35 mm wall thickness. It can be concluded that the increase of wall thickness will improve the mechanical properties of composite metal foam materials. Furthermore, the percentage of increase of mechanical properties is in proportion to the increase percentage of wall thickness.

Numerical models were used to investigate the influence of wall thickness on the mechanical behaviours of this type of materials. Figs. 8(a) and (b) show the stress- strain curves obtained from the finite element analyses conducted on the modified versions of Model A and Model B with different values of wall thickness.

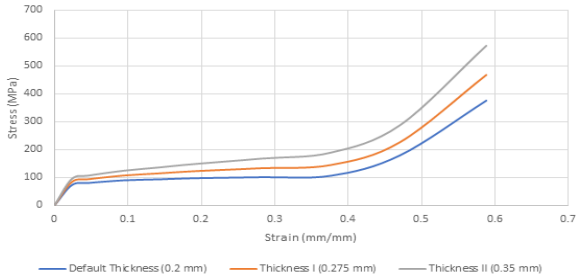

(a) Model A

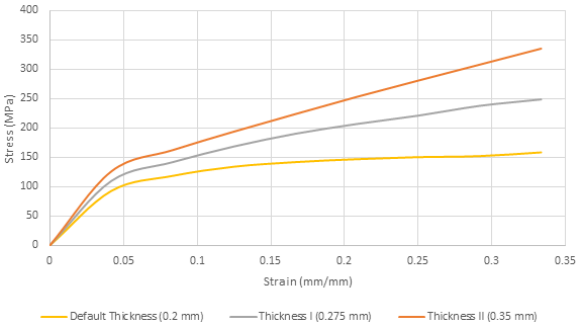

(b) Model B

Figure 8 Comparisons on the effects of different values of wall thickness to mechanical behaviours

It can be concluded that the wall thickness parameter has direct effects on the mechanical behaviours of composite metal foams. With the increase of wall thickness value, the yield strengths and plateau stresses from the stress-strain curves of both models rise significantly. This agrees well with the analytic results of the wall thickness's effects on the analytic model in Table V.

Porosity effects

Parametric studies on the effects of porosity on the mechanical performance and behaviours of composite metal foams were considered using both the analytic material model and numerical models.

Analytic model of aluminium-steel composite metal foams was used to investigate the influence of the porosity on the mechanical properties of this material. The values of density and yield strength computed using Eqs. (2) and (3) with three different porosity values are presented in Table VI

Table VI Comparisons on the effect of different porosity values on mechanical properties of composite metal foams

Porosity	0.59	0.455	0.341
Density (kg/m^3)	2015.907	2167.861	2296.177
Yield Strength (MPa)	70.33	82.61	92.98

With the decrease of porosity, the density and yield strength increase. Density value rises from 2015.907 kg/m^3 (at 59% porosity) to 2296.177 kg/m^3 (at 34.1% porosity). Yield strength value also increases 32.2% (70.33 MPa to 92.98 MPa) when porosity value decreases 42.2%. These prove that mechanical properties of composite metal foam materials are enhanced when the porosity value decreases.

Numerical analyses were conducted on Models A and B. By considering three different values of porosity, the stress-strain curves of Models A and B obtained from numerical analyses are shown in Fig. 9. The results show that the porosity also has an influence on the mechanical performance. The models with lower porosity values show better mechanical behaviours with higher yield strengths and plateau stresses. In addition, similar with wall thickness, at higher strain values the differences between the three stress-strain curves become more significant.

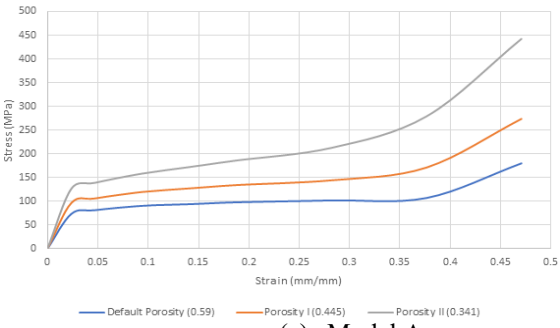

(a) Model A

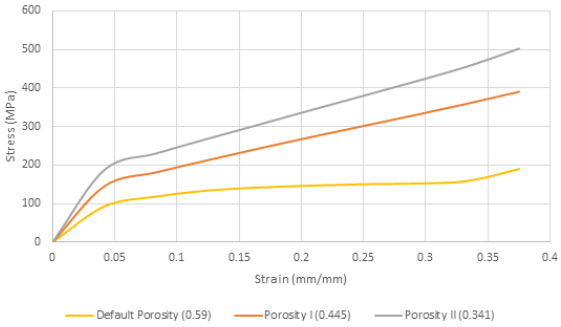

(b) Model B

Figure 9 Comparisons on the effects of porosity to mechanical behaviours

Overall, both porosity and wall thickness show direct effects on the mechanical performance and behaviours of composite metal foam materials. Density, yield strength and plateau stress values increase when wall thickness increases and porosity is reduced. These findings also agree well with the results from numerical studies on the effects of wall thickness and porosity on aluminium foams (Liu et al., 2016). Furthermore, the percentage of increase of mechanical properties is in proportion to the percentage increase of wall thickness and the percentage decrease of porosity.

IV. CONCLUSIONS

In this study, analytic and 2-D numerical models of a composite metal foam material were developed and employed to investigate the mechanical behaviours of composite metal foam materials under compression. Results obtained from analytic and numerical analyses conducted on these models were validated using data from literature review. These theoretical models provide good insights into the mechanical behaviours of composite metal foams under compression through 3 stages, including initial elastic region followed by a level plateau region over a long strain region and ended with densification stage. Parametric studies were conducted on the proposed models to investigate the effects of wall thickness and porosity on mechanical performance and behaviours. Results proved that both wall thickness and

porosity have direct effects on mechanical behaviours. Specifically, wall thickness modification will improve both yield strength and plateau stress while porosity adjustment weakens the mechanical performance.

There are still limitations with the developed model. Firstly, all the developed models of composite metal foams in this study are two-dimensional. Hence, results from these models should only be used as a reference. Secondly, the interfacial interaction between matrix and spheres was not fully considered. This may affect the accuracy and reliability of generated results. As for the future work, further studies on the behaviours of composite metal foams under other types of static and dynamic loadings will be needed. Parametric studies on the effects of other fundamental parameters on composite metal foam materials will also be considered. In addition, 3-D numerical models could be developed for more reliable results.

ACKNOWLEDGEMENT

The authors would like to express their deep appreciation to Western Sydney University for financial and equipment supports for this research.

REFERENCES

Liu J, He S, Zhao H, Li G and Wang M 2018, Experimental Investigation on the Dynamic Behaviour of Metal Foam: From Yield to Densification, *International Journal of Impact Engineering*, vol. 114, pp. 69-77.

Liu C, Zhang YX and Yang C 2016, Numerical Modelling of Mechanical Behaviour of Aluminium Foam Using a Representative Volume Element Method, *International Journal of Mechanical Sciences,* vol. 118, pp. 155-165.

Neville BP and Rabiei A 2008, Composite Metal Foams Processed through Powder Metallurgy, *Materials and Design,* vol. 29, no.2, pp. 388-396.

Rabiei A and O'Neill AT 2005, A study on processing of a composite metal foam, *Materials Science & Engineering A,* vol. 404, no. 1, pp. 159-164.

Vendra LJ & Rabiei A 2007, A Study on Aluminium–steel Composite Metal Foam Processed by Casting, *Materials Science & Engineering A*, vol. 465, no. 1, pp. 59-67.

A High-performance Epoxy Adhesive Reinforced with CNTs for Aerospace Structure Applications

D. T. Mahon
School of Engineering and Information Technology
University of New South Wales, Canberra, Australian Defence Force Academy,
ACT 2600, Australia

Y.X. Zhang
School of Computing, Engineering and Mathematics,
Western Sydney University, Sydney, NSW 2751, Australia

John Wang
Aerospace Division
Defence Science and Technology Group,
Melbourne, Victoria 3207, Australia

Andrew Rider
Aerospace Division
Defence Science and Technology Group,
Melbourne, Victoria 3207, Australia Panta

Panta Jojibabu
School of Engineering and Information Technology
University of New South Wales, Canberra,
Australia Defence Force Academy,
ACT 2600, Australia

Kunkun Fu
School of Engineering and Information Technology
University of New South Wales, Canberra,
Australian Defence Force Academy,
ACT 2600, Australia

***Abstract*—This paper investigates the effect of carbon nanotubes (CNTs) on the lap shear strength of an epoxy adhesive EA9396, which is certified for aircraft repair applications and has high shear strength at both room and elevated temperatures. Single lap shear tests were performed to evaluate the effect of various amounts of CNT reinforcement on the joint shear strength. The highest shear strength was achieved for 1 wt. % CNT with a 60% improvement over the joint shear strength of the pure epoxy.**

Keywords—Adhesive bonding, carbon nanotubes, epoxy, lap shear strength

I. INTRODUCTION

Adhesive bonding has been widely used for producing structural joints and patch repairs in the aircraft because of its advantages compared to traditional joining methods such as mechanical fastening. Bonded joints reduce the stress concentrations inherent with mechanical fasteners. They have a high-strength-to-weight ratio, high fatigue resistance and improved damage tolerance. They also have the benefits of design flexibility and ease of fabrication [1].

Epoxy adhesives have high strengths [2], excellent chemical resistance and relatively low cure temperatures. They are ease of use and of low cost [3]. They adhere well to most fibres [4]. The properties include Young's modulus of 2.9 – 4.0 GPa and a glass transition temperature of 107 – 195°C [4]. Despite these advantages, epoxy has a low fracture toughness and as a result, is vulnerable to crack propagation [5].

The inclusion of reinforcing nanofillers such as carbon nanotubes (CNTs) can enhance the mechanical properties of the epoxy. The reinforcement of epoxy adhesives with CNTs has been broadly studied [6,7]. CNTs have extremely high strength and stiffness and they transfer mechanical load from the resin via the interphase. The interphase is the boundary between the resin and the CNTs and is a region of altered chemistry. The high surface area of the CNTs enables significant changes in bond strength with low weight fractions of 0.5-2 wt. % [6].

In this research work, CNTs are used to reinforce EA9396 to achieve enhanced shear strength for the adhesive material. EA9396 is of particular interest for aircraft applications since on one hand, similar to other paste adhesives certified for aircraft repair applications such as EA9394, or EA9395. The EA 9396 adhesive has high bonding strength both at room temperature and at elevated temperatures (due to its Tetraglycidyl diaminodiphenylmethane (TGDDM) composition which gives it a relatively high glass transition temperature [4]). On the other hand, this adhesive has relatively low viscosity and thus is suitable for wet-layup repair applications.

Wet layup material systems utilising two-part epoxy resin and dry reinforcement fabric has the merits of long shelf life, ease of storage and the ability to be processed using minimal infrastructure and thus has seen wide use in aircraft repair applications [14-16]. Despite these merits, quality control associated with this type of repair is more difficult and thus the resultant repair strength would be lower when compared with typical pre-impregnated composite systems. Thus enhanced bond strength for an adhesive to be applied along the interface between the wet-layup laminate patch and the parent structure would be highly desirable.

Many researchers have been reported on adding nanofiller with low viscosity epoxies, but very few have used a relatively high viscosity epoxy as EA9396 (though the viscosity of EA9396 is significantly lower than other paste adhesives as described above), most likely due to the increased difficulty of achieving a homogeneous dispersion in these viscous materials, which has been a notorious problem for nanocomposite research.

In this paper, a high-performance nanocomposite adhesive material is developed by adding CNT into EA9396. The effect of various amounts of CNTs on the shear strength of the epoxy is investigated by conducting a single lap shear tests. A

suitable mixing method is developed to disperse the CNTs homogeneously in the epoxy matrix.

II. MATERIALS

As mentioned earlier, the epoxy selected for the adhesive bonding was LOCTITE EA 9396 Aero (Aerospace materials, Australia), a two-part TGDDM paste structural adhesive. This epoxy has high lap shear strength at room temperature and retains respectable shear strength at high temperatures. This material also has a high peel strength, which is important for adhesives. The resin has a viscosity of 80 Pa. at room temperature, which is high in terms of achieving a homogeneous dispersion of nanofillers in this material. AA 2024-T3 (Airport materials, Australia) plates were used as substrates to prepare the single lap shear joints. The multi-walled CNTs (Cheap tubes, USA) with an outer diameter of 20 – 30 nm and a length of 10 – 30 μm were used as reinforcement to enhance the strength of the epoxy joints.

III. EXPERIMENTAL PROGRAMS

The CNT/epoxy mixtures were prepared using a combination of manual stirring, shear mixing and ultrasonication at high temperature, to ensure they were suitably processed in the high viscosity resin. Preliminary trials involving the epoxy indicated that the room-temperature viscosity of EA 9396 resin is too high to achieve suitable nanofiller dispersion using the planned mixing procedures. To overcome this, material processing occurred at higher temperatures to reduce the viscosity. The variation in viscosity with temperature is significant and was verified experimentally, resulting in easier processing.

A. Viscosity Test of EA9396

A rheological study was conducted to develop appropriate mixing parameters for the epoxy. A rotational rheometer (Anton Paar MCR302) was used to measure the steady-state viscosity of the EA 9396 at four different temperatures such as 20°C, 40°C, 60°C, and 80°C. The samples were tested using a parallel geometry with 25 mm diameter and a gap size of 1 mm, over a shear rate of 0.1 s^{-1} to 100 s^{-1}. Thermal equilibrium was achieved throughout the material prior to testing. Each test was repeated twice to ensure the reproducibility. The epoxy resin showed Newtonian fluid behaviour and the viscosity of the was decreased significantly as a function of temperature and viscosity. The measured viscosity of the epoxy resin was 125 Pa-s at 20°C and decreased to 0.27 Pa-s at 80°C, as seen in Fig. 1. A reduction in viscosity assists the nanofiller processing and therefore the material was mixed at higher temperatures.

B. Mixing Method

The deagglomeration and uniform dispersion of CNTs in the epoxy matrix are difficult due to their large surface areas [7] which can further increase the resin viscosity. The high viscosity of the resin can inhibit deagglomeration and dispersion or fail to prevent re-agglomeration if it is too low. Mixing procedures must be highly tailored to the application to produce optimal nanofiller dispersion. A commonly used method is stirring, ultrasonication and calendaring.

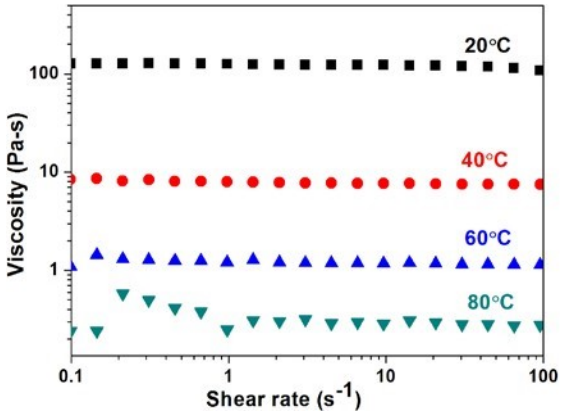

Fig. 1. Effect of temperature on the viscosity of EA9396

Mechanical stirring can achieve a fine dispersion in some applications, but a low-speed mixer will not de-agglomerate the tightly bound particles, while high-speed mixing results in aeration that can be difficult to remove even in a vacuum [9]. Stirring can be supplemented by ultrasonication, which deagglomerates nanofillers through the attenuation of soundwaves at high energy intensities [5] but which can be limited by the maximum power output in bath ultrasonicators. A further method that is traditionally more useful for highly viscous materials is calendaring [6], which generates high shear forces by squeezing the material through thin gaps (5 - 500 μm). The short residence time limits the breakages of the nanofillers [6], but this method can suffer from a low throughput because of the very small gap sizes.

In this study, CNTs were added to a 10-gram sample of EA9396 resin in appropriate quantities measured by weight, then stirred by hand for 2 minutes. The resin was processed using a laboratory shear mixer for 30 minutes at 200 rpm and 60°C, to achieve a coarse pre-mix. After the shear mixing, the material was processed for one hour using a bath-type ultrasonication (Power Sonic 420) at 700W and 40 kHz with a bath temperature of 50°C. After ultrasonication, the material was degassed at 60°C to entrap the air bubbles formed during the mixing process. The hardener was then added stoichiometrically (100: 30 by weight) and carefully mixed in by hand to reduce the aeration of the epoxy. The final mixture was then degassed again at 60°C for a short while (less than 15 minutes) to avoid premature curing.

C. Adhesive joint preparation

An effective surface preparation of substrates by surface roughening is a critical factor for producing a high strength bond. Mechanical roughening treatments often lack the durability of chemical ones. Common chemical treatment is chromic-sulphuric acid etching, which produces a roughened surface of 5 nm fibrils extending 40 nm from the etched

surface. The resulting surface oxide is comparable to the widely used Forest Products Laboratory (FPL) treatment [10].

This method has been demonstrated to be effective for aluminium alloys, particularly the AA-2024 series, because the copper alloying elements react well with chemical treatments, creating a porous oxide layer suitable for bonding [11]. The single-lap shear test is a common method for evaluating bond strength [1] and

In this study, the surfaces of the AA 2024-T3 were first cleaned with acetone to remove oils and other contaminants. The cleaned surfaces were then immersed in chromic- sulphuric acid etch solution for 20 mins at 60°C. The solution was prepared with 68.8% de-ionised water, 6.7% sodium dichromate dihydrate and 24.5% sulfuric acid. After the treatment, the surfaces were rinsed in running water at room temperature followed by drying at 50°C for 15 minutes. Care was taken to prevent contamination of the treated surface.

The single-lap shear joints were prepared as per the ASTM D1002 with a bondline thickness of 0.2 mm. The joints were then cured at 66°C for one hour as per the manufacturer specifications. To provide even pressure to each joint, they were pressed under a 1 kg weight during curing. The schematic and dimensions of the adhesive joint are shown in Fig. 2.

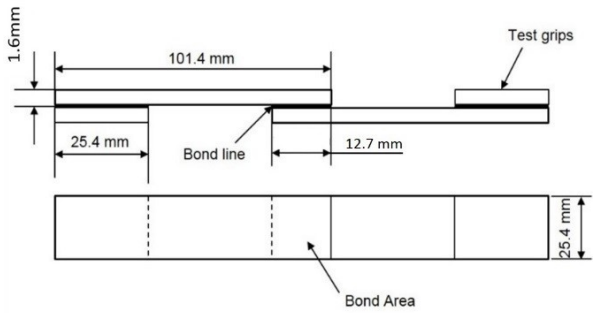

Fig. 2. Lap shear sample as per ASTM D1002

D. Single Lap Shear Test

Single-lap shear tests were performed using a universal testing machine (Shimadzu AG-100kN) with a loading rate of 1.3 mm/minute, as per the ASTM D1002 standard. The bond area was measured prior to testing using a digital micrometre. The dispersion of CNTs in epoxy resin was observed using an optical microscope (ZEISS Axiocam MRc) at a magnification of 200x.

IV. RESULTS and ANALYSES

A. Shear Strength

The results of the mechanical testing are shown in Fig. 3, where the strengths reported are an average and standard deviation of at least three samples. All tested cases achieved a higher strength than the pure epoxy (19.7 ± 2.1 MPa). The highest strength achieved was 31.5 ± 2.1 MPa, a 60% improvement at 1 wt. %.

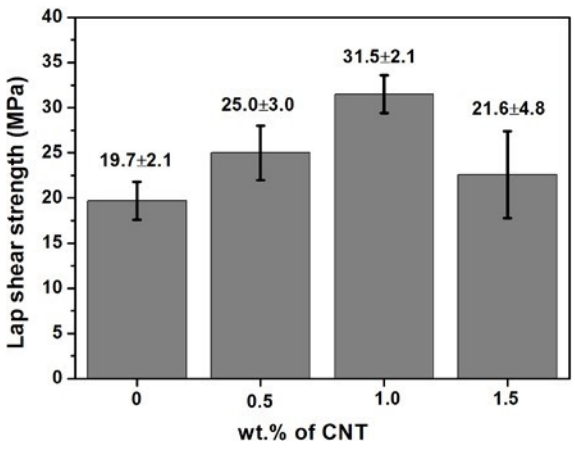

Fig. 3. Lap shear strength of epoxy adhesives with various CNT content

B. Failure Modes

The samples all had mixed adhesive and cohesive failure mode as shown in Fig. 4, where the higher strength joints had a higher extent of cohesive zones and evidence of peel failure. This implies that the adhesive bond strength does not just depend on the surface preparation and epoxy, but also on the nanoparticle agglomeration which has previously been reported in [12]. The surface treatment produced nano-sized structures, so it is expected that the nanofiller-rich epoxy would have achieved good wetting with the nano-roughened surface. In a low strength joint, any agglomerates will act as stress concentrations within the adhesive and limit strength increases possible. The rough fracture surface on some high strength samples indicates that in a more well-dispersed CNT/epoxy composites, the reduced agglomeration has helped to increase joint strength. The fracture surfaces of the strongest joints, 1 wt. % CNT showed mixed interphase and cohesive failure mode.

The interphase failure mode could be eliminated by using an improved surface treatment approach, such as grit blast – epoxy silane surface treatment procedure for metal substrates as reported [17], which will be considered in future work.

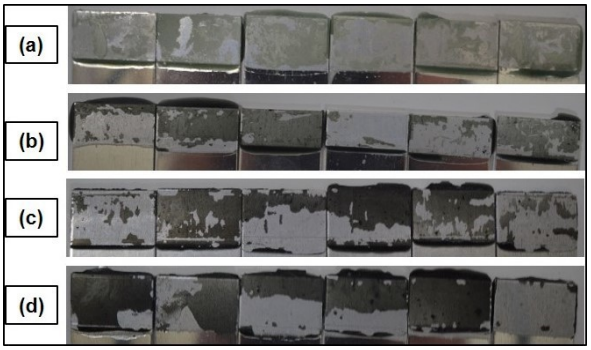

Fig. 4. Failure modes of the adhesive joints a) Pure epoxy, b) 0.5 wt.% CNT/epoxy, c) 1.0 wt.% CNT/epoxy, and d) 1.5 wt.% CNT/epoxy

C. Optical Microscopy

The CNT dispersion in epoxy resin was physically examined with a microscope just prior to adding the hardener. Fig. 5(a) and (b) shows the difference in agglomerate size between the 0.5 wt. % and 1 wt. % cases for CNT. The size of the particles is only slightly larger for the 1 wt. % case, even though there are twice as many CNTs present, which indicates that the agglomeration is only slightly greater for the 1 wt. % case, but the additional strength of the 1 wt. % joint has more than compensated for the slight increase in agglomeration. As noted previously, it was not necessarily the smallest agglomerates which provided the most significant strengthening effect, but those agglomerates which could provide the highest method of energy absorption before failing [13]. It is possible that these slightly larger agglomerates could absorb more energy in their fracture than an equivalent number of individual nanotubes. Fig. 5(c) shows very large agglomerates formed in the 1.5 wt. % CNT joint, indicating the strength decrease, in this case, is related to the agglomerate formation. The dispersion of the 1.0 wt. % CNT nanofillers is quite uniform as seen in Fig. 5(a).

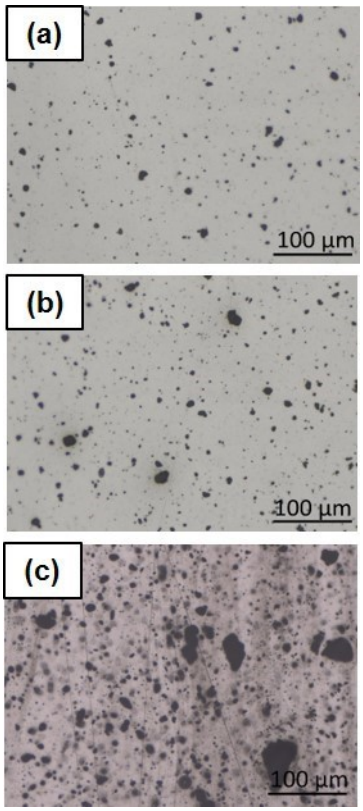

Fig. 5. Optical images of (a) 0.5 wt. % CNT; (b) 1 wt. % CNT; (c) 1.5 wt. % CNT

V. CONCLUSIONS

This work has developed a high strength adhesive joint by mixing CNTs into the EA 9396 epoxy system. The mixing method reduced the viscosity of the material by shear mixing and ultrasonication at high temperature and this was demonstrated to be effective. Strength improvements of 60% were achieved for a CNT joint of 1 wt. %. The developed nanocomposite adhesive material achieves a shear strength of 31.5 MPa. The shear behaviour of the material under elevated temperature will be studied in the future.

ACKNOWLEDGEMENT

Fund support from the Department of Defence and technical support from staff at UNSW Canberra.

REFERENCES

[1] M. D. Banea, and L. F. M. da Silva, (2009), 'Adhesively bonded joints in composite materials: an overview', in *Proceedings of the Institution of Mechanical Engineers, Part L: Journal of Materials: Design and Applications*, 223(1), pp. 1–18.

[2] F. Wang, *et al.* (2015), 'Mechanical properties and thermal conductivity of graphene nanoplatelet / epoxy composites', Journal of Materials Science, 50(3), pp. 1082–1093.

[3] S. Liu, *et al.* (2018), 'A review of extending performance of epoxy resins using carbon nanomaterials', Composites Part B, 136, pp. 197–214.

[4] A. Baker (2004), *Composite Material for Aircraft Structures*. 2nd edn. Reston: American Institute of Aeronautics and Astronautics.

[5] R. Atif, I. Shyha, and F. Inam, (2016), 'Mechanical, thermal, and electrical properties of graphene-epoxy nanocomposites-a review rasheed', Polymers, 8(281). doi: 10.3390/polym8080281.

[6] P. C. Ma, *et al.* (2010), 'Dispersion and functionalization of carbon nanotubes for polymer-based nanocomposites: A review', Composites Part A: Applied Science and Manufacturing. 41(10), pp. 1345–1367.

[7] P. Jojibabu, *et al.* (2016), 'Effect of different carbon nano-fillers on rheological properties and lap shear strength of epoxy adhesive joints', Composites Part A: Applied Science and Manufacturing, 82, pp. 53–64.

[8] J.Tomblin, *et al.* (2002), *Shear Stress-Strain Data for Structural Adhesives*, Wichita State University Department of Aerospace Engineering.

[9] S. Yu, M. Nah, and G. Critchlow (2010), 'Use of carbon nanotubes reinforced epoxy as adhesives to join aluminum plates', Materials and Design, 31, pp. 126–129.

[10] G. W. Critchlow, and D. M. Brewis, (1996), 'Review of surface pretreatments for aluminium alloys', International Journal of Adhesion and adhesives, 16(4), 255-274.

[11] S. G. Prolongo, A. Ureña (2009), 'Effect of surface pre-treatment on the adhesive strength of epoxy-aluminium joints', International Journal of Adhesion and Adhesives, 29(1), pp. 23–31.

[12] A. Al Robaidi, *et al.* (2011), 'The effect of different surface pretreatment methods on nano-adhesive application in high strength steel and aluminum bonding', Journal of Adhesion Science and Technology, 25(14), pp. 1725–1746.

[13] E. T. Thostenson, T. Chou, (2006), Processing-structure-

multi-functional property relationship in carbon nanotube
/ epoxy composites', Carbon, 44, pp. 3022–3029.
[14] R.F. Wegman and T.R. Tullos, *Handbook of Adhesive Bonded Structural Repair*. 1992: Noyes Publications.
[15] [22] J. Wang and A. Baker. Aspects of Battle Damage Repair of Helicopter Structures. *The Aeronautical Journal,* V114 No 1155, Royal Aeronautical Society, UK,
2010.
[16] J. Wang, Z. Zhou, R. Vodicka and W. K. Chiu. Selection of Patch and Adhesive Materials for Helicopter Battle Damage Repair Applications. *Journal of Composite Structures.* V91. 2009. 278–285.
[17] A. Baker and R Jones. Bonded repair of aircraft structure. The Hague: Martinus Nijhoff Publishers; 1988.

Investigation of influence factors on strip crown during cold strip rolling by elastic-plastic FEM

Lianjie Li
School of Mechanical, Materials, Mechatronic and Biomedical Engineering, Faculty of Engineering and Information Sciences
University of Wollongong
Wollongong, Australia
ll940@uowmail.edu.au

Haibo Xie
School of Mechanical, Materials, Mechatronic and Biomedical Engineering, Faculty of Engineering and Information Sciences
University of Wollongong
Wollongong, Australia
xie@uow.edu.au

Xu Liu
Iron & Steel Research Institute
Hesteel Group
Shijiazhuang, China
liuxu@hbisco.com

Tianwu Liu
Iron & Steel Research Institute
Hesteel Group
Shijiazhuang, China
liutianwu@hbisco.com

Enrui Wang
Iron & Steel Research Institute
Hesteel Group
Shijiazhuang, China
wangenrui@hbisco.com

Zhengyi Jiang
School of Mechanical, Materials, Mechatronic and Biomedical Engineering, Faculty of Engineering and Information Sciences
University of Wollongong
Wollongong, Australia
jiang@uow.edu.au

Abstract*—It is common that strip shape problem occurs in practical production. This is because that strip shape including the cross-section profile and flatness is influenced by muti-factors and the interaction relationship is coupled and complex. This paper aims to study the muti-factors on strip crown and reveals their quantitative relationship. In this paper, a three-dimensional (3D) elastic-plastic finite element (FE) model for cold strip rolling Universal Crown Control mill (UCM) was developed and verified experimentally. The influences factors on strip crown including the bending force of work roll (WR) and intermediate roll (IMR), IMR transverse shifting, the diameter of WR, IMR and back-up roll (BR), rolling force, strip width, entry strip crown and exit strip tension were taken into account. The results obtained provide valuable guidelines for the strip shape control in industrial production.*

Keywords—Elastic-plastic FEM, strip crown, cold strip rolling, UCM mill

IX. Introduction

Recent development of manufacturing industry like automobiles and household electrical appliances leads to an increasing of quality requirement of cold rolled strip, especially in strip shape including cross-section profile and flatness. In order to obtain the high quality strip shape, it is vital to obtain the precise mathematical models to calculate the key rolling parameters [1]. However, it is difficult to model and calculate the whole strip tandem rolling accurately as the rolling process is dynamic, nonlinear and muti-factors coupled. Finite element method (FEM) is an effective tool to solve the complicated rolling problem [2].

In the past years, the strip shape problem has been studied by a number of researchers using FEM. Chen et al [3] first urposed a two-dimensional (2D) thickness variable FEM to calculate the roll stack deflection. Zhou et al [4] applied a 2D thickness variable FE model to predict the strip crown under various strip width, WR bending force and shifting values, transverse friction and roll contact. Kim et al [5] developed a 3D FE model to analyse the strip profile under different strip width, WR crown, rolling force and WR crossing. Jiang et al [6] calculated the profile and flatness of thin strip under friction variation taking advantage of the rigid-plastic FEM. Linghu et al [2,7] investigated the strip shape during multi-pass strip rolling under the different IMR transverse shifting and bending force of WR and IMR through a 3D elastic-plastic FE model. Aljabri et al [8] simulated the asymmetrical strip rolling taking WR crossing and WR shifting into accounts by FEM. Wang et al [9,10] studied the effect of IMR transverse shifting and bending force of WR and IMR on strip profile and flatness via a 3D elastic-plastic FE model.

In this paper, a 3D elastic-plastic FE model for the 1740mm UCM tandem cold rolling mill was proposed by integrating the plastic deformation of strip with elastic deformation of rolls together. Then the more comprehensive influence factors on strip crown were analyzed quantitatively using the FE model.

X. FE model of cold strip rolling

A 3D elastic-plastic FE model was developed according to practical parameters of the UCM tandem cold rolling mill. Then the developed FE model was verified by experiment in the light of rolling force.

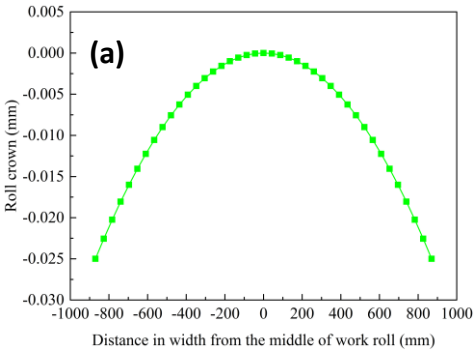

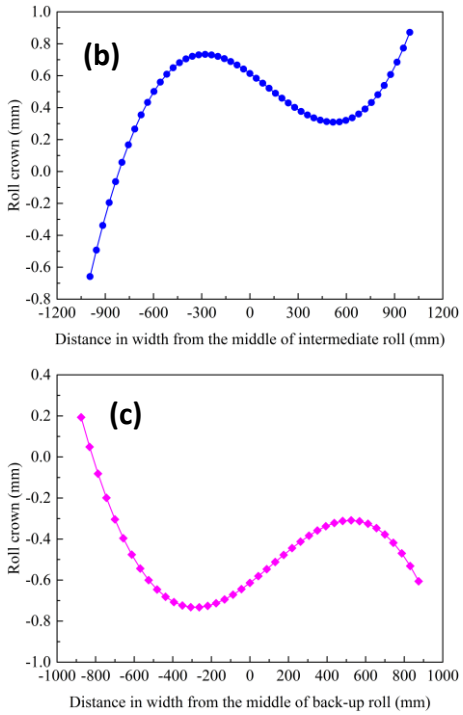

Fig. 1. Roll contour: (a) WR; (b) IMR; (c) BR

A. Roll contour

The roll contour was taken into account in the FE model. For this UCM mill, the initial crown of WR is -50 μm, as shown in Fig. 1 (a); the roll contour of IMR and BR both are SmartCrown developed by VAI [11], and they are antisymmetrical, as shown in Fig. 1 (b) and (c) respectively.

B. Material model

In this FE model, the strip and rolls are considered as elastic-plastic body and elastic bodies, separately. The material of strip is one type of high-strength steel FL590 produced by upstream hot rolling. Fig. 2 presents the true strain-true stress curve, which was obtained by uniaxial tensile test. The Young's modulus of strip and rolls are 211 GPa and 206 Gpa, respectively, and the Poisson ratio of strip and rolls both are 0.3.

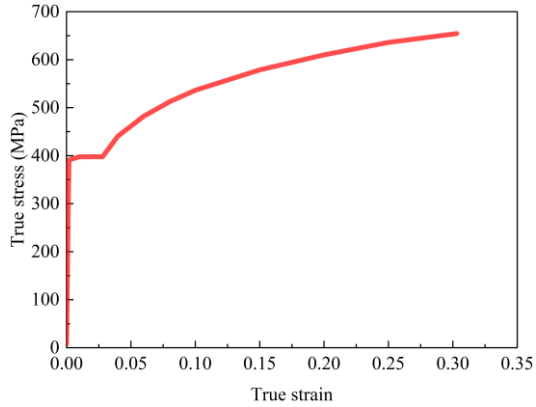

Fig. 2. True strain-true stress curve of FL590

C. Simulation conditions

Table 1 lists the actual geometry parameters and processing parameters collected from the industrial production line.

TABLE 1. SIMULATION CONDITIONS.

Parameters	Value
Diameter of work roll (mm)	445
Barrel length of work roll (mm)	1740
Distance between bearings of work roll (mm)	2900
Diameter of intermediate roll (mm)	520
Barrel length of intermediate roll (mm)	1740
Distance between bearings of intermediate roll (mm)	2900
Diameter of back-up roll (mm)	1400
Barrel length of back-up roll (mm)	1750
Distance between bearings of back-up roll (mm)	2900
Chamfer length of back-up roll (mm)	175
Chamfer height of back-up roll (mm)	0.75
Strip width (mm)	1030
Entry thickness of strip (mm)	2.75
Exit thickness of strip (mm)	2.11
Rolling speed (mm/s)	1850
Shifting value of intermediate roll (mm)	0
Bending force of work roll (kN)	64
Bending force of intermediate roll (kN)	119
Entry tension of strip (mm)	44
Exit tension of strip (mm)	88
Friction coefficient	0.05

D. 3D elastic-platic FE model of UCM mill

A 3D elastic-plastic FE Model of UCM mill was set up using the MSC Marc software, shown in Fig. 3. It can be seen that the contact areas between the strip and rolls are refined, while the other areas are meshed by coarse elements. This not only ensures the calculated accuracy, but also improves the computational efficiency. In this model, the rolling process is assumed as quasi-static without considering the inertia effect [12]. Full Newton-Raphson method is applied to iterative calculation. In addition, the Coulomb bilinear friction model and Von Mises yield criteria are adopted in the model.

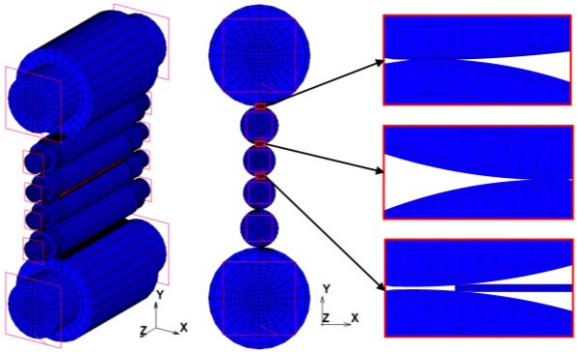

Fig. 3. 3D FE model of 1740 mm UCM mill

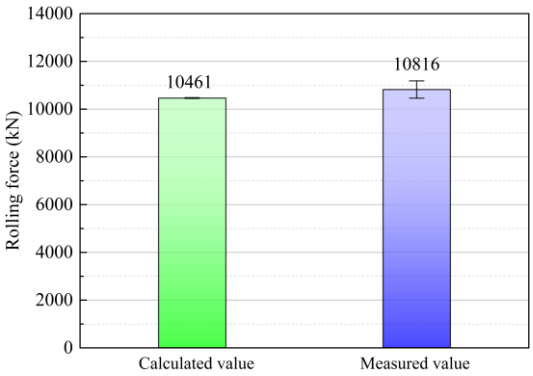

Fig. 4. Compassion between calculated and measured rolling force

E. Experimental verification

In order to verify the accuracy of the established FE model, the rolling experiment was carried out in one cold rolling mill. As the FE model is established on the basis of the first stand, it is difficult to measure the exit strip crown inter-stand. Therefore, the rolling force is utilized to evaluate the FE model. Fig. 4 compares the calculated and measured rolling force, which are 10461 kN and 10816 kN respectively, and the relative error is less than 3.5%. Therefore, the developed FE model is accurate and reliable.

XI. RESULTS AND DISCUSSION

A. Effect of roll bending force on strip crown

In order to study the effect of roll bending force on strip crown, six different bending forces are chosen in the FE model. Fig. 5 shows the strip crown along the strip width under the various WR bending force. It can be seen from Fig. 5 that the strip crown decreases from positive crown to negative crown with the increase of WR bending force. Fig. 6 presents a clear decreasing trend of strip crown C_{w40} and the slope of -0.28543 can be obtained by linear fitting.

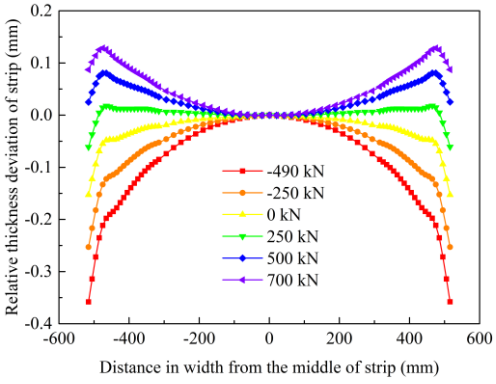

Fig. 5. Strip crown under different WR bending force

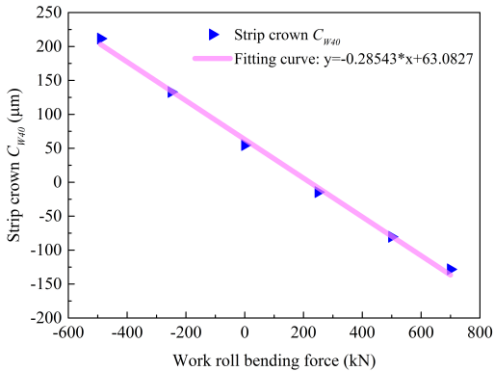

Fig. 6. Effect of WR bending force on strip crown

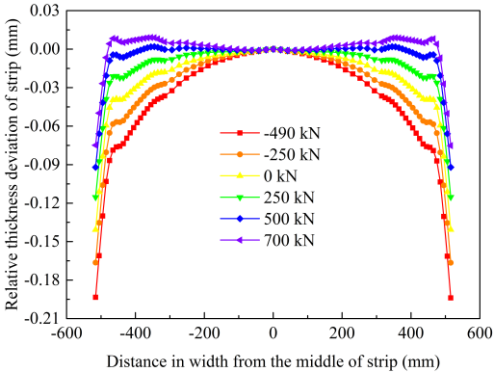

Fig. 7. Strip crown under different IMR bending force

Fig. 7 and Fig. 8 show the strip crown under the various IMR bending force. We can observe from Fig. 7 that the strip crown decreases obviously as the IMR bending force increases. It can be seen in Fig. 8 that there is a linear relationship between C_{w40} and IMR bending force, and its slope is -0.07624, which is about one fourth of that of WR bending force. This means that the effect of WR bending force on strip crown is more significant than IMR bending force.

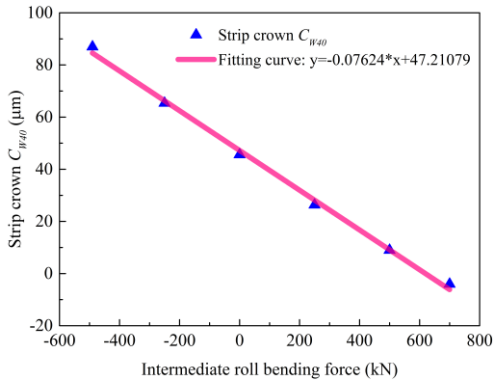

Fig. 8. Effect of IMR bending force on strip crown

B. Effect of intermediate roll transverse shifting on strip crown

Fig. 9 and Fig. 10 show the strip crown under the various IMR transverse shifting. From Fig. 9 and Fig. 10 we can see that the strip crown decreases from positive crown to negative crown with increasing of IMR transverse shifting. The C_{w40} is linear with IMR transverse shifting, and its slope is -0.98875. This is to say, C_{w40} decreases by about 1 μm when IMR transverse shifting increases by 1 mm.

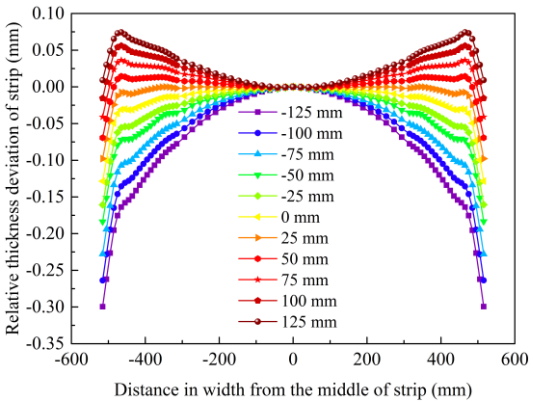

Fig. 9. Strip crown under different IMR transverse shifting

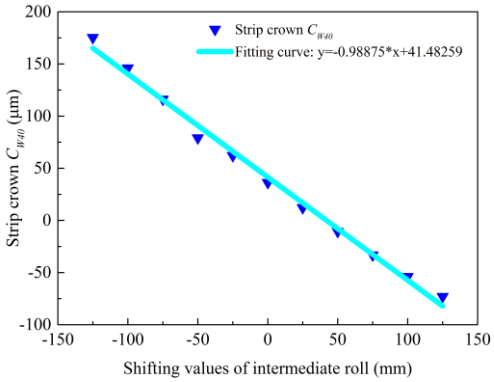

Fig. 10. Effect of IMR transverse shifting on strip crown

C. *Effect of roll diameter on strip crown*

Fig. 11 and Fig. 12 present the strip crown under the different WR diameter. It can be seen from Fig. 11 that the strip crown increases slightly with the decrease of WR diameter. This is because when WR diameter decreases, the strip exit thickness become thinner and thinner. As a result, the strip crown increases with the increment of reduction ratio. We can also see from Fig. 12 that the slope of fitting curve is -0.1052. This suggests that C_{w40} increases by 5 μm while WR diameter decreases from 480 mm to 430 mm.

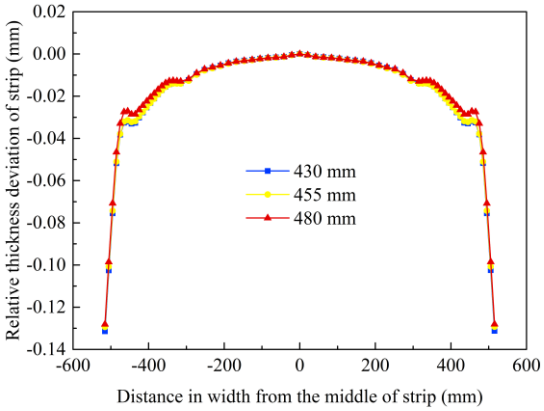

Fig. 11. Strip crown under different WR diameter

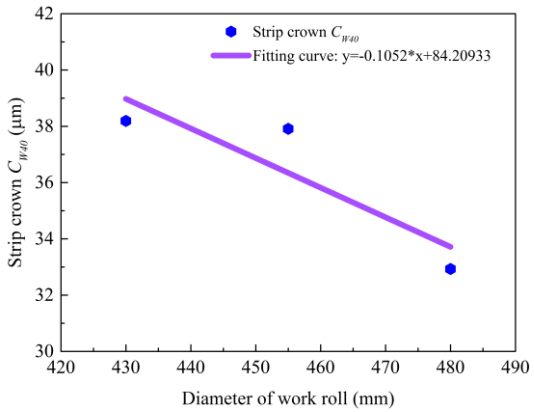

Fig. 12. Effect of WR diameter on strip crown

Fig. 13 and Fig. 14 present the effect of IMR diameter on the strip crown. It is obvious from Fig. 13 that the strip crown remains stable when IMR diameter varies. We can observe from Fig. 14 that the slope of the fitting curve is 0.00213, which means that the IMR diameter has little effect on C_{w40}.

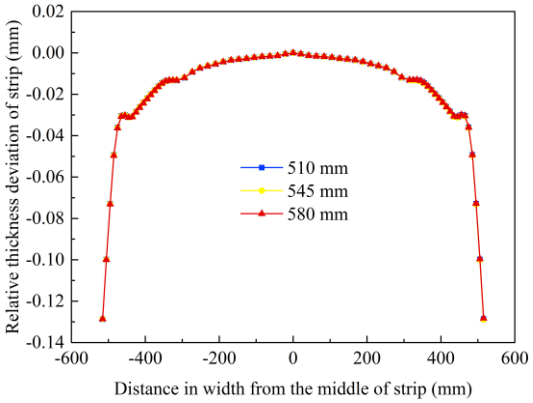

Fig. 13. Strip crown under different IMR diameter

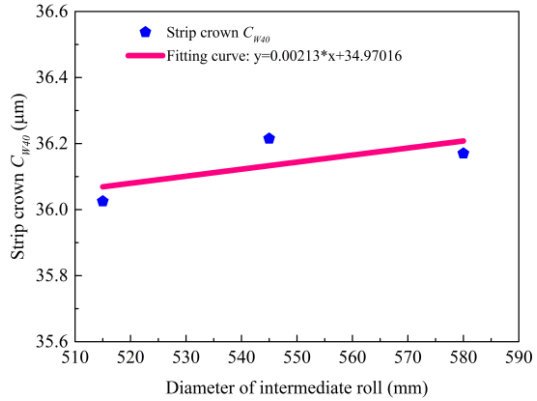

Fig. 14. Effect of IMR diameter on strip crown

Fig. 15 and Fig. 16 show the strip crown under the different BR diameter. We note from Fig. 15 that the strip crown increases significantly with the increment of BR diameter. This is because that the stiffness of roll stack increases with the increase of BR diameter, which leads to the larger reduction, and the strip crown increases. It can be seen from Fig. 16 that there is a linear relationship between C_{w40} and BR diameter, and the slope is 0.01727. This indicates that BR diameter has little effect on C_{w40}.

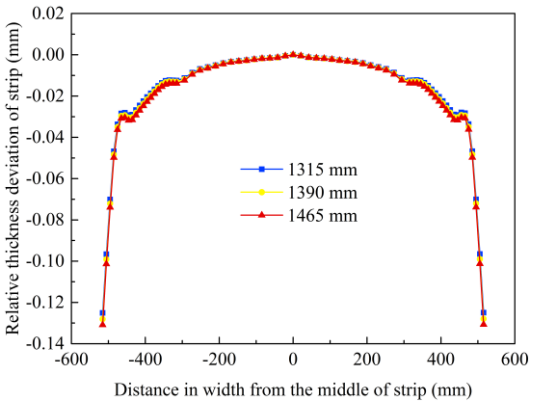

Fig. 15. Strip crown under different BR diameter

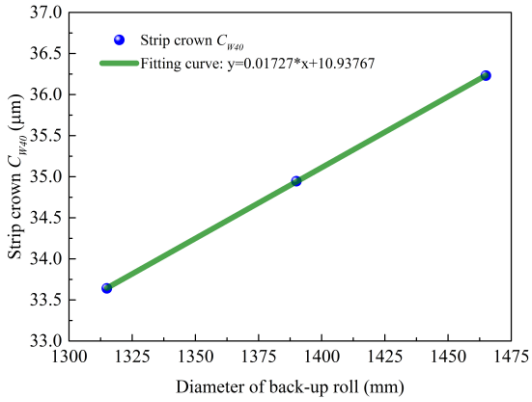

Fig. 16. Effect of BR diameter on strip crown

D. *Effect of rolling force on strip crown*

Fig. 17 and Fig. 18 present the strip crown under the different rolling force. As shown in Fig. 17, the strip crown increases with the increase of rolling force. This can be explained by that: the larger rolling force is, the larger reduction is. This results in the increase of strip crown. From Fig. 18, we can see that C_{w40} increases linearly with rolling force, and its slope is 0.0135.

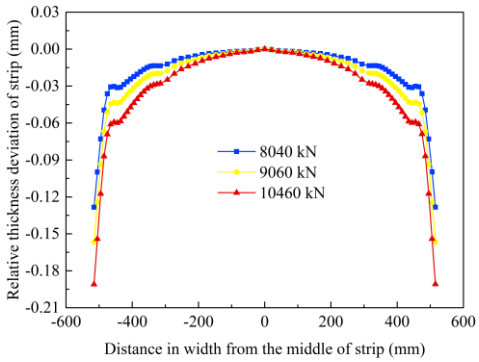

Fig. 17. Strip crown under different rolling force

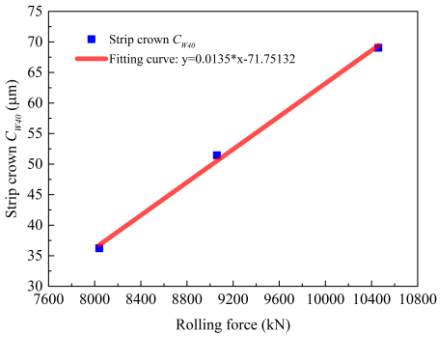

Fig. 18. Effect of rolling force on strip crown

E. *Effect of strip width on strip crown*

Fig. 19 and Fig. 20 show the strip crown under the different strip width. Fig. 19 indicates the strip crown decreases from positive crown to negative crown when strip width increases. It can be found that the slope of the fitting curve is -0.25821.

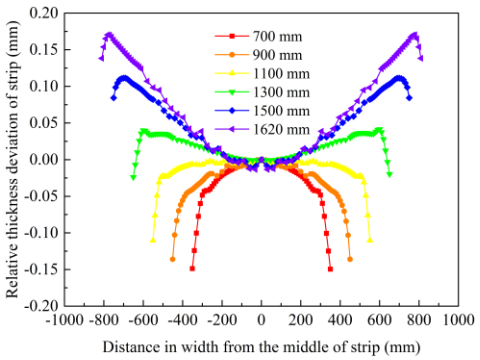

Fig. 19. Strip crown under different strip width

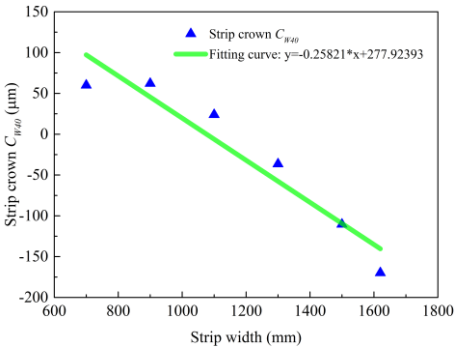

Fig. 20. Effect of strip width on strip crown

F. *Effect of entry strip crown on strip crown*

Fig. 21 and Fig. 22 show the strip crown under the different entry strip crown. We can see from Fig. 21 that the strip crown increases with increasing of entry strip crown. We can also observe that there is a linear relationship between C_{w40} and entry strip crown, and the slope is 0.1689.

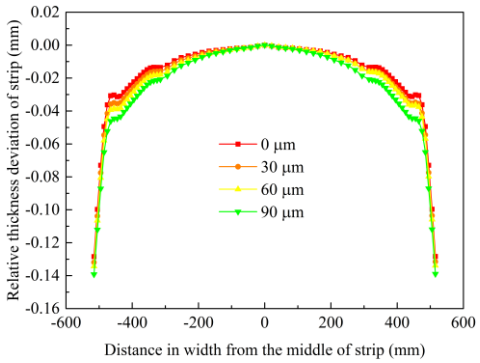

Fig. 21. Strip crown under different entry strip crown

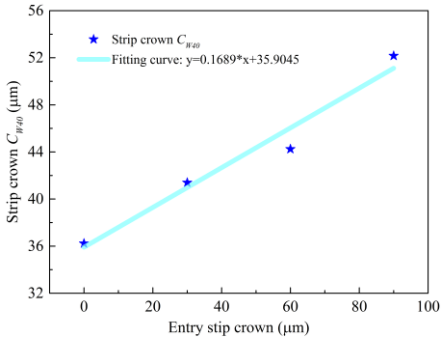

Fig. 22. Effect of strip width on strip crown

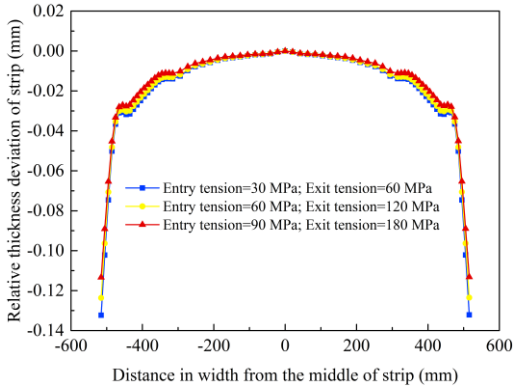

Fig. 23. Strip crown under different exit strip tension

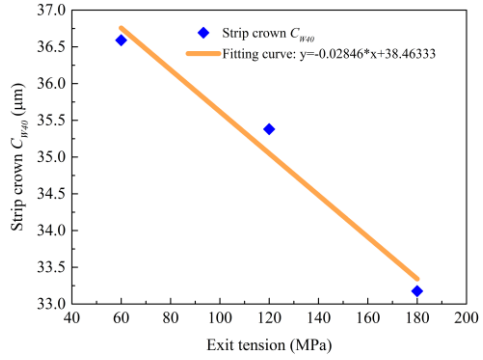

Fig. 24. Effect of strip width on exit strip tension

G. Effect of exit strip tension on strip crown

Fig. 23 and Fig. 24 show the strip crown under the different exit strip tension. It can be seen from Fig. 23 that the strip crown decreases slightly with increasing of entry strip tension. As shown in Fig. 24 that C_{w40} decreases linearly with entry strip tension, and the fitted slope is -0.02846.

XII. Conclusion

In this study, a 3D elastic-plastic FE model for UCM mill was built firstly, and then the FE model was verified by comparing with the calculated and measured rolling force. The quantitative relationships between C_{w40} and influence factors of strip crown are obtained by the developed FE model. The following results can be obtained:

(1) With the increase of WR bending force, IMR bending force and IMR transverse shifting, the strip crown decreases linearly;

(2) The strip crown increases slightly with the increment of WR diameter and BR diameter, while IMR diameter has almost no effect on strip crown.

(3) The strip crown increases with increasing of rolling force, while decreasing with the increase of strip width.

(4) With the increase of entry strip crown, the strip crown increases linearly. By contrast, the strip crown decreases slightly when entry strip tension increases.

Acknowledgment

The authors gratefully acknowledge the financial support from HBIS Group Technology Research Institute, China.

References

[1] X.H. Liu, X. Shi, S.Q. Li, J.Y. Xu and G.D. Wang, "FEM analysis of rolling pressure along strip width in cold rolling process", Journal of Iron and Steel Research International, vol. 14, 2007, pp. 22-26.

[2] K.Z. Linghu, Z.Y. Jiang, J.W. Zhao, F. Li, D.B. Wei, J.Z. Xu, X.M Zhang and X.M. Zhao, "3D FEM analysis of strip shape during multi-pass rolling in a 6-high CVC cold rolling mill", Int J Adv Manuf Technol. Vol. 74, 2014, pp. 1733-1745.

[3] X.L. Chen and J. X. Zou, "A specialized finite element model for investigating controlling factors affecting behavior of rolls and strip flatness", Proceeding of the 4th International Steel Rolling Conference, Deauville, France, 1987, pp. E4.1-E4.7.

[4] S.X. Zhou, C. Plociennik, J. Zhong, Application of 2-dimensional FEM to predict the thickness profile in 4-high mills, Steel Research, 69 (1998): 482-488.

[5] T. H. Kim, W. H. Lee and S. M. Hwang, "An integrated FE process model for the prediction of strip profile in flat rolling", ISIJ International, vol. 43, 2003, pp. 1947-1956.

[6] Z.Y. Jiang, A.K. Tieu, X.M. Zhang, C. Lu and W.H. Sun, "Finite element simulation of cold rolling of thin strip", Journal of Materials Processing Technology, vol. 140, 2003, pp. 542-547.

[7] K.Z. Linghu, Z.Y. Jiang, F. Li, J.W. Zhao, M. Yu and Y.Q. Wang. "FEM analysis of profile control capability during rolling in a 6-high CVC cold rolling mill", Advanced Materials Research Vol. 988, 2014, 257-262.

[8] A. Aljabri, Z.Y. Jiang and D.B. Wei, "Finite element analysis of thin strip profile in asymmetric cold rolling considering work roll crossing and shifting", Advanced Materials Research , vol. 515, 2015, pp. 1061-1062.

[9] Q.L. Wang, J. Sun, Y.M. Liu, P.F. Wang and D.H. Zhang, "Analysis of symmetrical flatness actuator efficiencies for UCM cold rolling mill by 3D elastic–plastic FEM", The International Journal of Advanced Manufacturing Technology, vol. 92, 2017, pp. 1371-1389.

[10] Q.L. Wang, J. Sun, X. Li, Y.M. Liu, P.F. Wang and D.H. Zhang. "Numerical and experimental analysis of strip cross-directional control and flatness prediction for UCM cold rolling mill", Journal of Manufacturing Processes, vol. 34, 2018, pp. 637-649.

[11] A. Seilinger, A. Mayrhofer and A.J. Kainz, "SmartCrown-A new system for improved profile & flatness control in strip mills", Iron & Steel Review, International, 2002, pp. 84-88.

[12] S.Y. Yuan, L.W. Zhang, S.L. Liao, G.D. Jiang, Y.S. Yu and M. Qi, "Simulation of deformation and temperature in multi-pass continuous rolling by three-dimensional FEM", Journal of Materials Processing Technology, vol. 209, 2009, pp. 2760-2766.

Effects of Internal Fillers of Cola Can on Impact Deformation and Energy Absorption

Zhiwei Jiao
School of Computing, Engineering and Mathematics
Western Sydney University
Sydney City Campus, Australia
19053309@student.westernsydney.edu.au

Keqin Xiao
School of Computing, Engineering and Mathematics
Western Sydney University
Sydney City Campus, Australia
k.xiao@city.westernsydney.edu.au

Richard Yang
School of Computing, Engineering and Mathematics
Western Sydney University
Penrith, Australia
R.Yang@westernsydney.edu.au

***Abstract* — This paper aims to understand the impact deformation patterns and energy absorption of filled Cola cans. The can was filled with two different materials, i.e., pearl wool and corrugated paper. Numerical simulation was carried out using Abaqus at an impact speed of 20 m/s. The deformation of an individual hollow can is characterized by the buckling and folding patterns, and the energy absorption capacity of the hollow can is relatively poor. When the Cola can is filled, the can shows a homogeneous plastic deformation characterized by a typical bulging behavior of filled hollow structures. It was also found that the energy absorption capacities of the Cola cans filled with two materials were increased by about 30 times while the pearl wool-filled can shows a slightly larger energy absorption capacity than that of the corrugated paper-filled one. Finally, this study concludes that the recyclable beverage cans can be considered a potential energy absorption member by filling it with low cost materials.**

Keywords — Cola can, impact deformation, energy absorption, pearl wool, corrugated paper

I. INTRODUCTION

Energy absorbers that limit the force transmitted to the key components of structures or users have been used in industries for many decades. The development of new types of low cost and effective energy absorbers has been attracting great attention from researchers and engineers. The recyclable beverage can (Cola can) as a potential energy absorber is being explored recently due to its low cost and easy availability at large quantities. The mechanical properties of a single pop can in the process of falling were investigated by Xiao-Li Song et al [1]. In their work, the stresses of the can bottom were analyzed in different drop ways and under different drop heights using the finite element method. Palanivelu et al. [2] investigated the deformation behavior of the hollow Cola can under explosion using finite element analysis and experimental test. Cola cans were arranged in the form of arrays as the inner core of a sacrificial cladding structure. Numerical simulation results obtained using Abaqus were found to be in good agreement with the experimental results. They concluded that the recyclable beverage cans can be considered as a potential member to protect the civil engineering structures from the air blast load. The impact behaviors of cylindrical shells similar to the Cola can structure were investigated by many researchers in the past. The buckling behavior of axially compressed cylindrical shells was analyzed using Abaqus by O. Ifayefunmi [3]. Based on the Abaqus simulation, Y.S.Taia et al. [4] investigated the axial compression and energy absorption characteristics of high-strength thin-walled cylinders under impact load. The relationships between displacement and load, average load, and energy absorption properties were analyzed.

Previous studies reveal that the impact energy absorption capacity of hollow thin-walled structures can be improved significantly when they are filled with different materials. S. R. Reid [5] reviewed the characteristics of a number of metal components proposed as impact energy absorbers. Progressive buckling, inversion, and splitting were discussed. The buckling of thin-walled square section tubes filled with polyurethane foam was also discussed. Djamaluddin et al. [6] evaluated the energy absorption performance of foam-filled double circular tubes. It was found that optimal foam-filled tube had better crashworthiness than the hollow tube under pure axial loading. Maximizing the energy absorption and minimizing the weight of filled foam was investigated by [7, 8].

While the hollow Cola can was demonstrated to have great potential as an emerging new type of energy absorber, further improvement of the impact crashworthiness of the filled can has not been investigated yet. This work will explore the possibility of enhancing the energy absorption capacity of Cola can by filling it with two cheap materials, i.e., pearl wool and corrugated paper. The impact behavior of the cans will be simulated using Abaqus. Deformation, and the energy absorption under axial impact will be discussed.

II. FINITE ELEMENT MODELING AND SIMULATION

A. Cola can model

Fig. 1. Dimensions of Cola can

The Cola can model was created using the ABAQUS software and the sizes of the can were obtained by measuring the actual cans from the market. The dimensions of the can are shown in Fig. 1. It has two different thickness values. At the top and bottom of the can, the thickness is 0.2 mm. The rest of

the body has a 0.1 mm thickness. The height of the Cola can is 120 mm and the radius of the main body is 33 mm, respectively.

B. Filling materials

The density, Young's modulus, Poisson's ratio, and yield strength for the materials used in this study are given in Table 1. Cola can is usually made of either aluminum or tinplate. In this work, only a tinplate can of steel grade 4340 is analyzed. Pearl wool and corrugated paper are used as filling materials because of their low cost. The material properties in Table I [9] are inputted in the ABAQUS simulation.

C. Johnson-Cook model for tinplate

TABLE I. MATERIAL PROPERTIES FOR COLA CAN AND FILLED MATERIALS

Materials	Density [g/cm^3]	Young's modulus [MPa]	Poisson's ratio	Yield strength [MPa]
Tinplate	7.8	210000	0.3	355
Pearl wool	0.03	70	0.3	3.4
Corrugated paper	0.06	2000	0.3	4.5

Under dynamic impact, the material usually experiences high strain rate, large strain, and elevated temperature. The behavior of the material differs significantly from the quasi-static loading condition. The Johnson Cook model is a popular constitutive material model for metals and widely used in the simulation of impact and penetration related problems. It is extensively integrated into most of the finite element tools to simulate the plastic deformation of the materials. In reliable flow stress and well-constructed models, the Johnson-Cook model is more supporting in a range of strain rates and high temperature resistance performance in terms of effectively predicting the ductility of materials. The Johnson-Cook model is described by Eqs. 1, 2 and 3 where A, B, C, m and n are the material constants, ε_p is the effective plastic strain, $\dot{\varepsilon}_0$ is the reference strain rate and T, T_0, T_m are the working temperature, room temperature, and melting temperature, respectively. The Johnson-Cook parameters for tinplate are given in Table II [10].

$$\sigma_{eq} = \left[A + B{\varepsilon_p}^n\right][1 + Cln(\dot{\varepsilon}^*)][1 - T^{*m}] \quad (1)$$

$$\dot{\varepsilon}^* = \dot{\varepsilon}_p/\dot{\varepsilon}_0 \quad (2)$$

TABLE II. INPUT PARAMETERS FOR THE JOHNSON COOK PLASTICITY MODEL

A (MPa)	B (MPa)	C	m
792	510	0.014	1.03
n	T_m (K)	T_0 (K)	$\dot{\varepsilon}_0$ (1/s)
0.26	1793	293.2	1.0

D. Abaqus general data input

The friction coefficient used in the simulation is 0.1. The simulation is run with an analysis time of 0.005 second and a maximum compression depth of 120 mm, causing an impact speed of 20 m/s. Dynamic explicit analysis was performed using a general contact type, and calculation convergence was achieved.

III. RESULTS AND DISCUSSION

A. Mesh sensitivity analysis

The mesh size in a Finite Element (FE) model has a significant effect on the accuracy of the FE analysis result. Therefore, a detailed mesh sensitivity analysis was performed in this study. Fig. 2 shows the deformation of the hollow Cola can with different mesh sizes and a maximum compression depth of 80 mm. The red areas represent the high stress concentrated areas. The quantitative evaluation of the mesh size effect can be seen in Fig. 3. The control parameters used to perform this mesh analysis are ALLPD and ALLWK. ALLPD is the energy dissipated by both rate-independent and rate-dependent plastic deformation. ALLWK is the total work done by the impact force during high speed compression. As the mesh density increases from mesh 1 to mesh 2, both ALLPD and ALLWK decrease, as shown in Fig. 3. After mesh 2, ALLPD and ALLWK remain almost unchanged. This demonstrates that mesh 2 with an element number of 8041 is good enough to generate a stable and accurate result. However, in this work, mesh 5 with an element number of 21958 is chosen to minimize the possible effect of different impact conditions on the results.

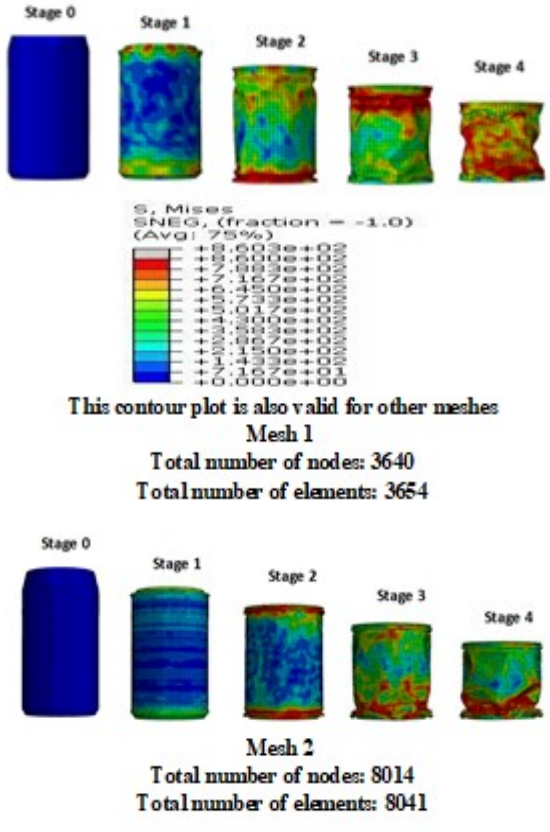

Fig. 2. Continued

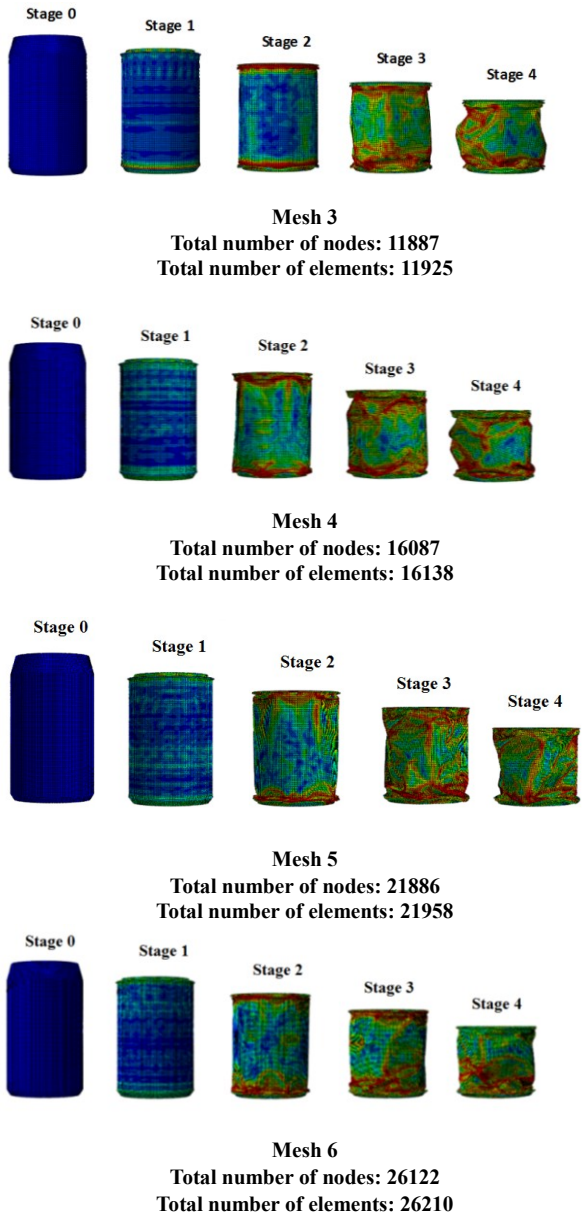

Fig. 2. Deformations of hollow Cola can with different mesh sizes (original height of the can is 120 mm and compression depth 60 mm).

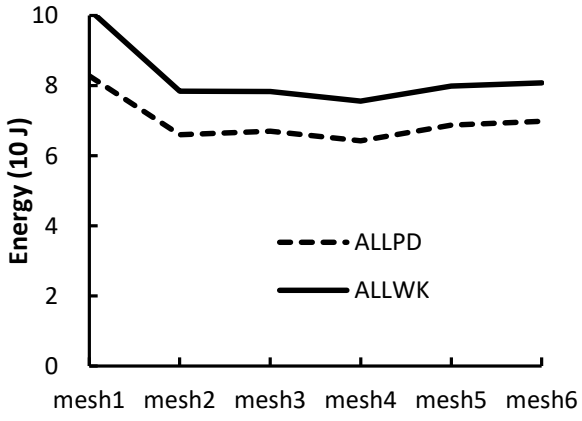

Fig. 3. Energy absorption of hollow Cola can with different mesh sizes.

B. Impact deformation and energy absorption of hollow Cola can

The hollow Cola can is simulated at a maximum compression depth of 100 *mm, i.e., about* five sixth of the can height. Fig. 4 shows the impact deformation of the hollow Cola can at different compression stages. It is clear that the high stress concentration areas start to form at the top and bottom folding edges at stage 3 followed by the appearance of the initial buckling patterns. These buckling and folding patterns look very similar to those found by [1]. The energy absorption of the hollow can during impact can be visualized in Fig. 5. In general, the energy absorbed is proportional to the compressed depth. At the maximum compressed depth of 100 mm, ALLPD and ALLWK reach 98 Joules and 112 Joules, respectively.

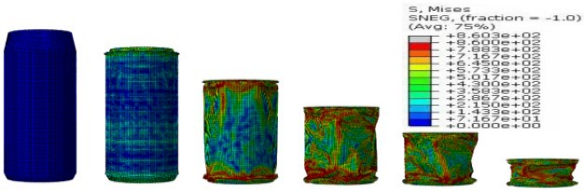

Figure 4. Impact deformation of empty Cola can with mesh 5 at a maximum compression depth of 100 mm.

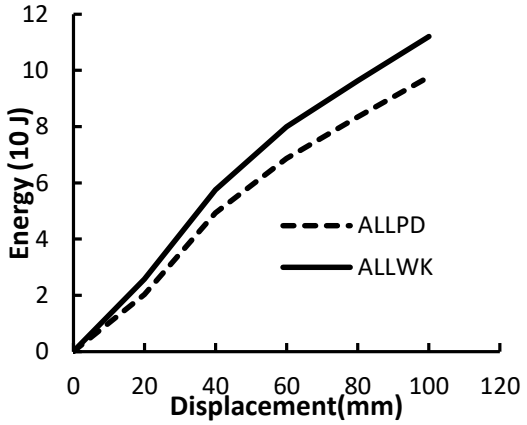

Figure 5. Plastic energy and total impact work of empty Cola can with mesh 5 at a maximum compression depth of 120 mm.

C. Impact deformation and energy absorption of filled Cola can

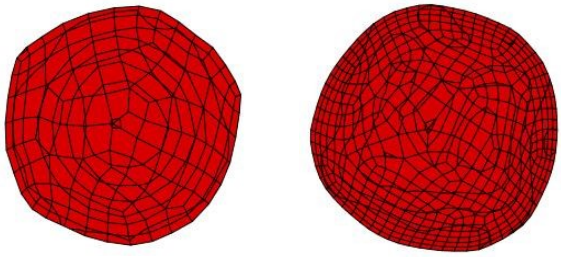

(a) Pearl wool (b) Corrugated paper

Fig.6. Meshed fillers, (a) Pearl wool-filled and (b) Corrugated paper.

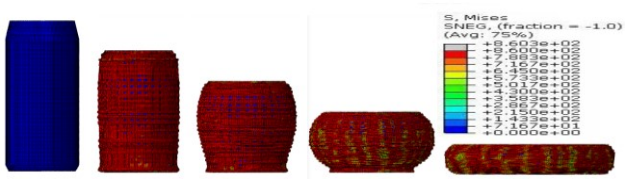

(a) Pearl wool-filled Cola can

(b) Corrugated paper-filled Cola can

Figure 7. Deformation of filled Cola can (a) Pearl wool-filled and (b) Corrugated paper-filled.

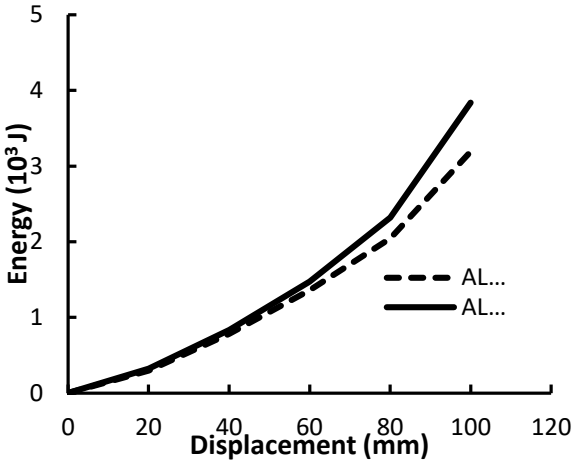

(a) Pearl wool-filled Cola can

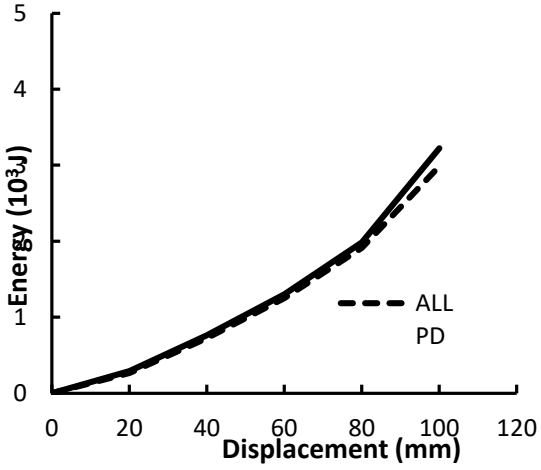

(c) Corrugated paper-filled Cola can

Figure 8. Plastic deformation energy and total work (a) Pearl wool-filled Cola can and (b) Corrugated paper-filled Cola can.

In this section, the results of the deformation and energy absorption of Cola cans filled with pearl wool and corrugated paper are presented and discussed. Fig. 6 displays the morphology of meshed fillers while the deformation characteristics of filled Cola cans at different compression depths is shown in Fig.7. When the deformation patterns of the hollow Cola can were compared, as shown in Fig.4, it was found that filled Cola can demonstrates a homogeneous surface stress distribution with a typical bulging behavior of filled cylindrical hollow structures under axial loading. The buckling and folding patterns of the hollow Cola can are not formed when the can is filled. This is understandable because the filled material supports the thin wall of the can during the compression. As a result, the filled can deforms homogeneously. Fig. 8 displays the energy absorption of filled can as a function of compression depth. It is very clear that the absorbed energy of filled can increases exponentially with increasing compression depth. Maximum von Mises stress, absorbed energy ALLPD due to plastic deformation, and the ratio of ALLPD to the total work ALLWK done by the impact force are presented in Table III. Maximum von Mises stresses during the impact for two filled cans are also the same. Most importantly, the energy absorption capacities for two filled cans show a significant increase by about 30 times. PLLPD for the pear wool-filled can is slightly higher than that of the corrugated paper-filled one. However, the ratio of ALLPD to ALLWK for pear wool-filled can is smaller than that of the corrugated paper-filled one. This indicates that friction-related energy absorption for the pear wool-filled can takes up a larger portion of the total absorbed energy than friction-related energy absorption for a corrugated paper-filled can.

TABLE III. MAXIMUM VON MISES STRESS AND THE RATIO OF ALLPD TO ALLWK FOR THREE COLA CAN MODELS

Can model	Max stress (MPa)	ALLPD (J)	ALLWK (J)	ALLPD/ ALLWK
Hollow	816	98	112	88%
Pearl wool-filled	855	3190	3840	83%
Corrugated paper-filled	858	2990	3220	93%

IV. CONCLUSIONS

In this work, the deformation characteristics and energy absorption of Cola can under high speed compression were simulated using the ABAQUS software. Three cases, i.e., the hollow can and the cans filled with pearl wool and corrugated paper, respectively, were studied. Firstly, the mesh size effect of the Finite Element can model was analyzed and the fine mesh size with an element number of 21958 was chosen to generate accurate simulation results. Based on the simulation results, the following conclusions were drawn:

1. The deformation of the hollow can is characterized by the buckling and folding patterns, and the energy absorption capacity of the hollow can is relatively poor.

2. When the Cola can is filled, the can shows a homogeneous plastic deformation without buckling and folding patterns. On the other hand, typical bugling behavior was observed in the filled cans.

3. The plastic deformation energy of filled cans increases exponentially with increasing compression depth, and the energy absorption capacity of filled can increases by about 30 times.

4. Pearl wool is slightly better than corrugated paper for improving the energy absorption capacity of the filled cans.

5. The results demonstrate that filled Cola cans have a great potential to be used as an effective energy absorption device.

REFERENCES

[1] S. Palanivelu1, W. Van Paepegem1, J. Degrieck1, K. De Wolf, J. Vantomme, D. Kakogiannis , J. Van Ackeren, D. Van Hemelrijck and J. Wastiels, "Study of blast load on recyclable empty metal cans," DYMAT, pp. 709–715, 2009.

[2] Xiao-Li Song, Gai-Mei Zhang, Can Wang, Xue-Ying Sheng and Fan-jun Meng, "Analysis on mechanical properties of pop can in the process of falling based on finite element method," Energy and Mechanical Engineering, pp. 461–468, 2016.

[3] OIfayefunmi, "Buckling behavior of axially compressed cylindrical shells: Comparison of theoretical and experimental data," Thin-Walled Structures, Vol. 98, pp. 558–564, 2016.

[4] Y.S.Taia, M.Y.Huang, H.T.Hu and K. Elissa, "Axial compression and energy absorption characteristics of high-strength thin-walled cylinders under impact load," Theoretical and Applied Fracture Mechanics, Vol. 53, pp. 1–8, 2010.

[5] S. R. Reid, "Plastic deformation mechanisms in axially compressed metal tubes used as impact energy absorbers," Int. J. Mech. Sci. Vol. 35, No. 12, pp. 1035–1052, 1993.

[6] Djamaluddin, S. Abdullah, A.K. Ariffin, Z.M. Nopiah, "Optimization of foam-filled double circular tubes under axial and oblique impact loading conditions," Thin-Walled Structures Vol. 87, pp. 1–11, 2015.

[7] Guo LW, Yu JL. "Dynamic bending response of double cylindrical tubes filled with aluminum foam," Int J Impact Eng, Vol 38, pp. 85–94, 2011.

[8] HR Zarei and Kröger, "Optimization of the foam-filled aluminum tubes for crush box application," Thin-Wall Struct., Vol 46, pp. 214–21, 2008.

[9] Gordon R. Johnson, William H. Cook., "Fracture characteristics of three metals subjected to various strains, strain rates, temperatures and pressures," Engineering fracture mechanics, Vol 21, pp. 31–48, 1985.

[10] Yildiz S, Gezerb F, Yildiz U, "Mechanical and chemical behavior of Spruce wool modified by heat." Build Envirn., Vol. 41, pp. 1762–1766, 2006.

Axial segregation of a rotating drum with an inclined axis of rotation.

P. Widhate, H.P. Zhu, Q.H. Zeng and K.J. Dong
School of Computing, Engineering, and Mathematics, Western Sydney University
Locked bag 1797, Penrith, NSW 2751, Australia

***Abstract*—Different experimental and numerical studies have been carried out to study the effect of input properties on axial segregation patterns in rotating drums in the past, but little effort has been made to investigate the effect of angle of inclination of the rotating drums, though such inclined drums exist in industrial waste management, food processing, power and pharmaceutical industries. To overcome this gap, in this work, the discrete element method was used to study the axial segregation phenomena of a rotating drum with different angles of inclination from 0 to 15 degrees for variable angular velocity of a drum. The axial segregation patterns along the length of the rotating drum were examined. It was found that with an increase of angle of inclination of the drum, which directly affects the inclination of the particle gravitational force acting on particles along the axial direction, which induces axial dispersion of large particles towards the lower end of the drum. As a result, large particles tend to accumulate on the lower end of the rotating drum, which leads towards controlled band formation applications to the industrial process with continues segregation output requirements.**

Keywords*— *axial Segregation, rotating drum, inclined rotating drum.

I. INTRODUCTION

Rotating drum is a common device in the industry for mixing, drying or granulation. Therefore, knowledge of the dynamics of particles in a drum is of high interest in engineering. Axial segregation is one of the complex phenomena the particle flow in rotating drums exhibiting. Over the past few decades, many experimental and numerical efforts have been done to understand the phenomenon.

When a random binary mixture of granular particles is rotated in a drum with a certain velocity, smaller particles tend to accumulate along the axis of the drum while large particles accumulate along the circumference of the drum first, and then axial segregation bands start to form[1]. The axial segregation pattern is complicated. It depends on the various input parameters [2-4] and affected by material properties and system parameters such as the angle of repose of particles, drum fill degree, drum velocity, friction and time of rotation [1, 5-9]. The axial segregation band's location and thickness are not stable but evolves with the time forming fewer and fewer bands as time progressed [3]. This phenomenon was later studied [4] and concluded that coarsening and oscillatory motion of the axial segregation bands was mostly affected by radial segregation as axial bands involved a flow of small particles through the radial core, in particular when the band position or width oscillated. This phenomenon was not observed in the absence of a radial core filled with small particles. The measure of axial segregation was quantified as the segregation index and rate of axial segregation directly proportional to the logarithmic coarsening [5]. All the studies above were concentrated towards rotating drums with the horizontal axis of rotation. Very little emphasis has been given to study the axial segregation on the rotating drum with the inclined axis of rotation though the inclined drum is also a common device in industries related to waste management, food processing, power, and pharmaceutical process. In this study, the discrete element method was used to study the axial segregation of a rotating drum with a variable angle of inclination and rotational speed.

II. SIMULATION METHOD AND CONDITIONS.

The discrete element method (DEM) was used to study the granular flow inside the rotating drum. Particles in the drum have two types of motion: translational and rotational, and are governed by Newton's second law of motion. In the case of macro-sized dry granular particles, the governing equations can be given by

$$m_i \frac{d\boldsymbol{v}_i}{dt} = \sum_{j=1}^{k} \boldsymbol{F}_{c,ij} + m_i \mathbf{g} \qquad (1)$$

$$I_i \frac{d\boldsymbol{\omega}_i}{dt} = \sum_{j=1}^{k} \boldsymbol{M}_{ij} \qquad (2)$$

where $\boldsymbol{v}_i$, $\boldsymbol{\omega}_i$ are, respectively, the translational and angular velocities of particle i with mass m_i and moment of inertia I_i. The forces involved are the gravitational force, m_i g, and contact force $\boldsymbol{F}_{c,ij}$ between particles due to the plastic and elastic deformation resulting from particle collision, sliding and rolling. $\boldsymbol{M}_{ij}$ is the torque acting on particle i by particle j arising from their interaction. Based on given force models, equations (1) and (2) can be solved to determine the position and velocity of each particle. Drum diameter (D_d) of 40 mm and length (L_d) of 100 mm were used for the instigation in this study. In each simulation, a random mixture of solid spherical particles, of size ratio (SR) = 2, with larger (D_l) and smaller particle (D_s) diameter of 2 mm and 1 mm respectively, was generated inside the rotating drum. The drum was partially filled with 40% volumetric filled (f) for each case. The mixture was then simulated until a steady state was achieved. Four inclinations of the drum with respect to the horizontal, i.e., 0^0 (horizontal position), 5^0, 10^0 and 15^0, for constant angular speeds of 30 rpm, 50 and 70 rpm were considered.

The material properties for the particles and drum were the same as those used in the work Elskamp et al. (2017) [10] and are given in Table 1.

MATERIAL PROPERTIES AND PARAMETERS

Properties	Parameter
Fill degree	40%
Drum diameter	40 mm
Proportion of volume of particles	65 % (small particle), 35 % (large)
Particle diameter	1 mm (small), 2 mm (large)
Density of particles	1430 kg/m^3
Coefficient of sliding friction	0.17
Coefficient of rolling friction	0.0000722 (particle-drum), 0.0000594 (particle-particle)
Young's modulus	2.84e+09 (particle), 2.08e+11 (drum)
Poisson's ratio	0.35 (particle, drum)
Coefficient of restitution	0.80 (particle-drum), 0.84 (particle-particle)

III. RESULTS AND DISCUSSION

In order to validate the simulation method model in the work, experimental data obtained by Kawaguchi, Tsutsumi & Tsuji (2009) [11] using an MRI measurement technique were used to compare with the DEM results under the similar conditions, as shown in Fig. 1. For both cases, the drum has an inner diameter of 40 mm and a length of 100 mm and is horizontal. A mixture of 1 mm and 2 mm of particles were used. A slice of 2.7 mm thickness of the cylindrical drum was considered for analysis. Images from the simulation have been binarized into red for small particles and blue for large particles.

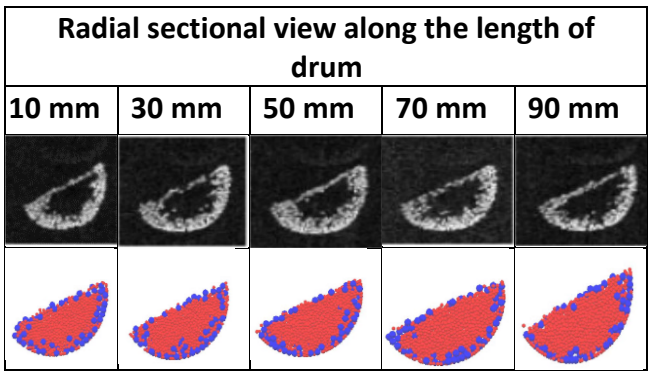

Fig.1. Flow patterns of a mixture of particles in a horizontal rotating drum with an angular speed of 30 rpm: top layer, from an experiment done by [11] and bottom layer, from the DEM simulation.

It can be observed that the experimental and DEM simulation results demonstrate a likely pattern: large particles are located at the surface of the flow and near the wall of the drum, and the number of blue pixels of the large particles remains almost constant along the length of the drum. It should be noted that the ratio of the number of blue pixels points to the cross-sectional area is different in the experiment and

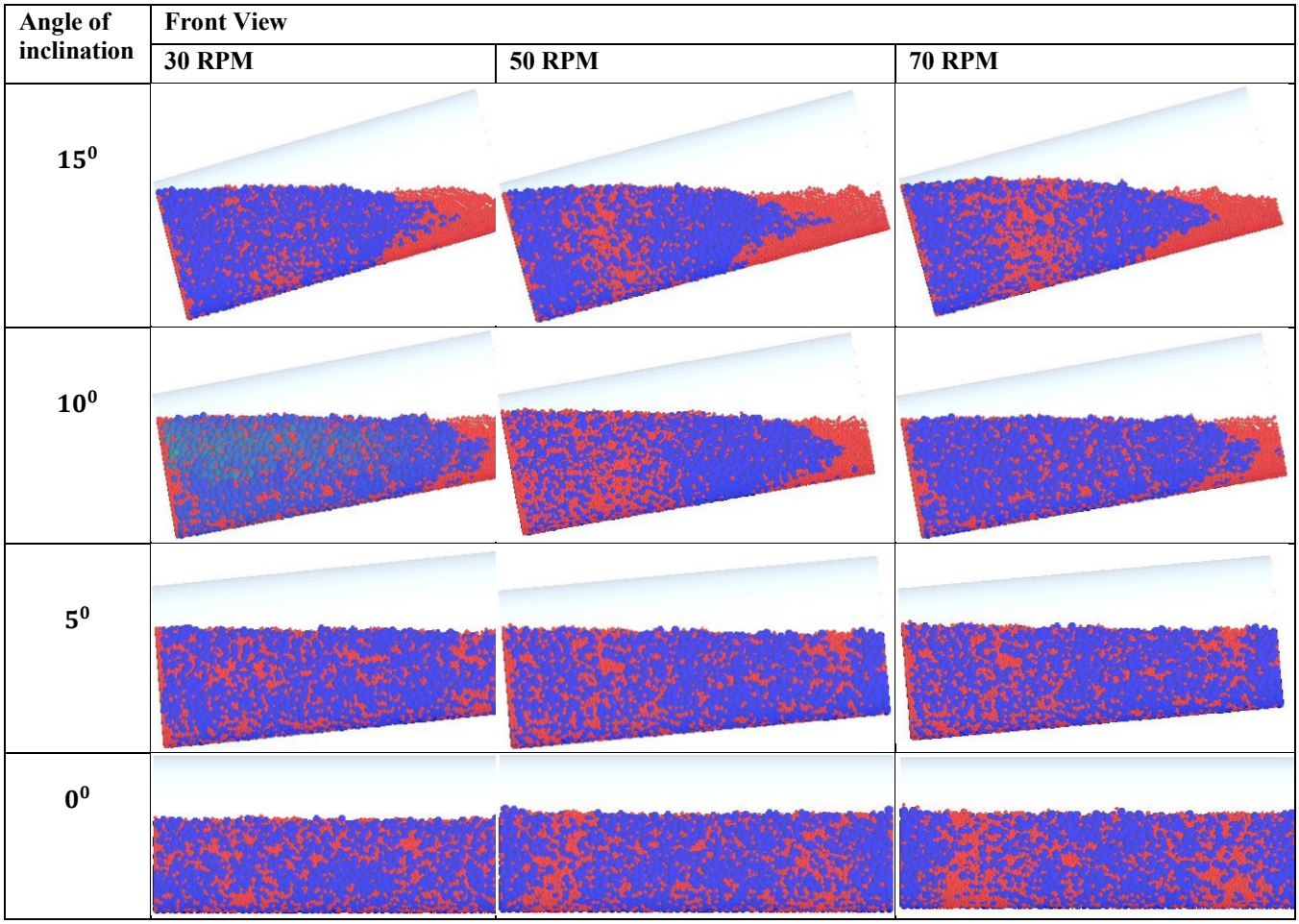

Fig. 2. Front view of rotating drum with different angle of inclination and rotational speed.

simulation. The difference is due to the difference in the volumetric filling level. In the experiment, the volumetric filling fraction is 50% for large particles while in the DEM simulation the volumetric filling fraction for large particles is 35% as shown in Table. 1. Hence there exist a gap of approximately 15% or 0.15 N/mm^2. Anyway, results with the same trend in the DEM simulation and experiment validate the applicability of the DEM simulation model in the present study.

Fig.1 shows the front view of the drum with a different angle of inclination and angular velocity. As the rotation of drum begins, radial segregation patterns developed in the first a few rotations where smaller particles percolated towards the center of the drum while larger particles along the periphery as described by Alizadeh et al. (2006) [12] in an experiment, which happens due to the percolation effect. Thereafter large particle moments start towards the inclination in the inclined rotating drum. Hence larger particles start accumulating towards inclination due to gravity effect except the case for horizontal drum. With an increase of the angle of inclination, larger particles are located at the lower part of the drum.

To show the axial segregation more clearly, half-length (from left-to-right) of the drum has been considered to quantify the axial dispersion of the large particles for a different angle of inclination of the drum and angular velocity. Fig. 3 shows the percentage of the number of the large particles in the first half portion of the rotating drum out of the total number of large particles with respect to the angle of inclination of the rotating drum for different angular velocity.

It can be observed from Fig. 3 that angle of inclination plays a dominant role in the axial dispersion of the particle along the length of the drum as compared to the angular velocity of the drum. Larger particles are in the lower part of the drum for a higher angle of inclination. This is due to the component of the gravitational force in the axial direction depending on the angle of inclination. If the angle is θ, the component would be mg sin θ. With the increase in the angle of inclination, the axial gravitational force component of a particle increases \which resulting in more particles flowing towards the low end of the drum. These hence lead to the formation of two different particle bands along the periphery of the particles in the drum: large particle band on the lower end of the drum, and small particle band on the upper end of the drum.

When the rotational speed is low, the particle motion is slow, steady and stable (rolling or cascading mode). On the other hand, the particle motion becomes vigorous and unstable (cataracting mode) for the higher rotational speed. Therefore, there are different trends for different rotational speeds, as shown in Fig. 3. For a lower angular speed of 30 rpm, the percentage of the large particles grows linearly as the rotational speed. For the case with a higher angular speed of 50 and 70 rpm, there is a peak in the distribution near 6^0. These peaks are results of more flow of large particles initially with an increase in the angle of inclination of a drum, a large number of free space is available for particles in cataracting mode for percolation. Once this space is filled with a sizeable number of large particles, then large particles start moving uniformly towards the bottom end of the drum due to resistance on the motion for large particles by themselves due to their accumulation on the lower end of the drum. Hence the motion of large particles tends to stabilize and almost linear once the initial peak is achieved with an increase in the angle of inclination of a rotating drum.

IV. CONCLUSION

In the present paper, DEM simulation was used to study the axial segregation of binary granular mixture in steadily rotated horizontal and inclined rotating drums. The results are summarized as follows:

1) Experimental and DEM simulation results demonstrate a likely pattern where large particles are located at the surface of the flow and near the wall of the drum resulting in radial segregation. Radial segregation pattern remains almost constant along the length of the drum at a horizontal position, which validated DEM simulation results for binary particles

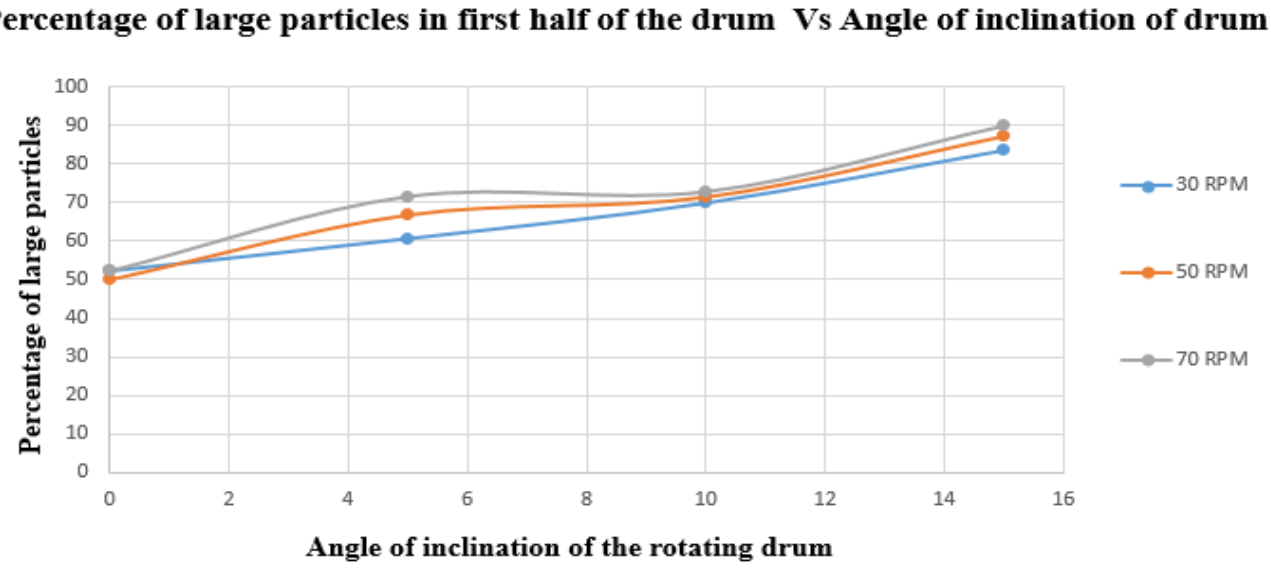

Fig. 3. Percentage of large particles in the first half portion of the rotating drum vs angle of inclination of the drum.

in the rotating drum system leading to further study of axial segregation in an inclined rotating drum.

2) In DEM simulation, with an increase in the angle of inclination of the rotating drum larger particles tend to move towards the bottom end of the rotating drum. Axial band is formed along the periphery of particles, where larger particles forming band towards the bottom end of the drum and small particles towards the upper end of the drum without affecting the radial segregation in that region. This observed band formation phenomenon is different as compared to the horizontal rotating drum where band strips are formed as mentioned by Hill, K, Caprihan, A & Kakakios, J (1997)[3]. Hence this analysis will lead the way to further investigate the effects of various properties such as the angle of repose of particles, drum fill degree, drum velocity, friction and time of rotation, which plays a major role in axial band formation in an inclined rotating drum.
3) In comparison to variable angular velocity, the angle of inclination has more effect on the axial dispersion of the large particles, which leads to the band formation. Hence industries will have greater output with less energy input as there is less deviation due to the angular speed of the drum. Therefore, this research will also help in energy optimization at the time of drum plant design and set up in various industries such as industrial waste management, pharmaceuticals, and food processing were inclined rotating drum is being used currently.

ACKNOWLEDGMENT

The authors are grateful to the Australian Research Council (ARC IH140100035), Jiangsu Industrial Technology Research Institute and Western Sydney University for the financial support of this work.

REFERENCES

[1] T. Elperin and A. Vikhansky, "Mechanism of the onset of axial segregation in a rotating cylindrical drum filled with binary granular mixtures," *Physical Review E,* vol. 60, no. 2, p. 1946, 1999.
[2] T. Finger, A. Voigt, J. Stadler, H. G. Niessen, L. Naji, and R. Stannarius, "Coarsening of axial segregation patterns of slurries in a horizontally rotating drum," *Physical Review E,* vol. 74, no. 3, p. 031312, 2006.
[3] K. Hill, A. Caprihan, and J. Kakalios, "Axial segregation of granular media rotated in a drum mixer: Pattern evolution," *Physical Review E,* vol. 56, no. 4, p. 4386, 1997.
[4] N. Taberlet, M. Newey, P. Richard, and W. Losert, "On axial segregation in a tumbler: an experimental and numerical study," *Journal of Statistical Mechanics: Theory and Experiment,* vol. 2006, no. 07, p. P07013, 2006.
[5] I. Aranson and L. S. Tsimring, "Dynamics of axial separation in long rotating drums," *Physical review letters,* vol. 82, no. 23, p. 4643, 1999.
[6] K. Choo, T. Molteno, and S. W. Morris, "Traveling granular segregation patterns in a long drum mixer," *Physical review letters,* vol. 79, no. 16, p. 2975, 1997.
[7] K. M. Hill, A. Caprihan, and J. Kakalios, "Bulk segregation in rotated granular material measured by magnetic resonance imaging," *Physical Review Letters,* vol. 78, no. 1, p. 50, 1997.
[8] G. Seiden and P. J. Thomas, "Complexity, segregation, and pattern formation in rotating-drum flows," *Reviews of Modern Physics,* vol. 83, no. 4, p. 1323, 2011.
[9] Z. Cui *et al.*, "Transition of axial segregation patterns in a long rotating drum," *Particuology,* vol. 13, pp. 128-133, 2014.
[10] F. Elskamp, H. Kruggel-Emden, M. Hennig, and U. Teipel, "A strategy to determine DEM parameters for spherical and non-spherical particles," *Granular Matter,* vol. 19, no. 3, p. 46, 2017.
[11] T. Kawaguchi, K. Tsutsumi, and Y. Tsuji, "MRI measurement of granular motion in a rotating drum," *Particle & Particle Systems Characterization,* vol. 23, no. 3-4, pp. 266-271, 2006.
[12] E. Alizadeh, O. Dubé, F. Bertrand, and J. Chaouki, "Characterization of mixing and size segregation in a rotating drum by a particle tracking method," *AIChE Journal,* vol. 59, no. 6, pp. 1894-1905, 2013.

Using Numerical Analysis and In-Field Measurement to Study the Dynamic Interaction between Concrete Sleeper and Ballast on the Railway Track

Ralph (Wei) Zhang
School of Computing, Engineering and Mathematics
Western Sydney University
Sydney, Australia
Email address:
17602059@student.westernsydney.edu.au

Helen Wu
School of Computing, Engineering and Mathematics
Western Sydney University
Sydney, Australia
Email address:
Helen.Wu@westernsydney.edu.au

Chunhui Yang
School of Computing, Engineering and Mathematics
Western Sydney University
Sydney, Australia
Email address:
R.Yang@westernsydney.edu.au

***Abstract*— The interaction between the ballast layer and concrete sleeper plays a very important role in track performance and maintenance, i.e., the condition and performance of ballast can significantly impact the functionality and life of concrete sleepers. A new type of heavy duty concrete sleeper is designed to strengthen the Australian railway tracks on the eastern coast. To optimize the design work, the features of concrete sleeper failure under the Australian heavy haul traffic condition have been studied and addressed. To understand the interaction and stress distribution on the concrete sleeper and the surrounding ballast, the 3-dimensional non-linear finite element model is created to undertake the numerical analysis. The detailed stress distribution on the concrete sleepers which are resulted from different ballast conditions are represented within this paper. It is used to give the explanation for the features of the failure of concrete sleepers. The ideal ballast pressure (500 kPa) and the results from the numerical study for heavy haul traffic condition have been presented and compared. In addition, the best practical engineering solution is provided (high resilient rail pad and under sleeper pad). Moreover, the in-filed testing results of the performance of the under sleeper pads have been represented in the paper.**

Keywords*— *Numerical, In-field measurement, Dynamic, Sleeper, Ballast.

I. INTRODUCTION

The concrete sleeper and ballast are the major railway track components. The concrete sleepers distribute the wheel loads from rails to the ballast layer. The ballast is installed and packed between, below, and around the sleepers as a layer to provide a "track bed" to support the sleepers. Concrete sleepers are designed to carry out the functions of supporting rails, spreading wheel loads to ballast, holding rails to gauge and inclination, transmitting lateral and longitudinal forces, and providing a base for rail seats and fastenings. After successful application around the world for over half a century, prestressed concrete sleepers have shown their technical superiority. This is based not only on their greater load-bearing capability, but also, and especially, on their longer life cycles [1]. Their service lives last between 30 and 60 years, depending on the types of loads applied and the condition of the ballast layers beneath.

A type of heavy-duty prestressed concrete sleeper was designed to strengthen the mainline tracks on the east coast of Australia. The design of the sleeper was intended to achieve a balance between performance and cost effectiveness. During the design phase, the current track conditions, outcomes of new innovations of track performance under heavy haul revenue, and new technical design parameters such as dynamic factor of wheel load and sleeper spacings were considered [2].

II. TRAFFIC CONDITION

The most significant feature of railway traffic on the railway networks of eastern Australia is a combination of heavy axle freight trains (25 t on the north-south corridor linking the three largest capital cities of Australia, Brisbane, Sydney, and Melbourne; 30 t on the mineral corridor – Hunter Valley) and semi-high-speed passenger trains (such as the XPT train, with a maximum speed of 140–160 km/h) [2].

III. FEATURES OF THE FAILURE OF CONCRETE SLEEPERS

To optimize the concrete sleeper design and determine the possible reasons for concrete sleeper failure caused by poor ballast conditions, the classic severe damage and failure types of concrete sleeper under heavy haul revenue were studied in detail. The most severe concrete sleeper failure (ineffective condition) types were identified and classified into six types [2] - [4]:

- Bending crack at the rail seat area (cracks initiating from underneath the concrete sleeper and extending through the whole cross section of the sleeper to the rail seat), as shown in Fig. 1;
- Severe worn at the base of the middle section (usually combined with center-bound-type cracks on the top surface of the middle section of the concrete sleeper), as presented in Fig 2;
- Center-bound-type failure (directly caused by poor ballast condition), as illustrated in Fig. 3;

- Longitudinal crack between the two steel shoulders at the rail seat of sleeper;
- Longitudinal split;
- Sleeper end longitudinal crack.

IV. Current Design Practices in Australia

Australian Standard AS 1085.14 – 2012: "Railway track material, Part 14: Prestressed concrete sleepers" is the guideline for concrete sleeper and turnout bearer design in Australia. The basic design principles include the following [5]:

- Sleepers shall be designed as fully prestressed sections.
- The stresses shall be calculated from the design bending moments, and the rail seat load R (which cannot be less than the R_v, the vertical load on the rail seat load) is utilized for the bending moment calculation.
- The standard length is 2.5 m, and the minimum length of the sleeper shall be determined by the bond development requirements of the prestressing reinforcements. The base width shall be not less than that determined by the allowable bearing pressure.
- Design ballast contact pressure: The calculated ballast pressure shall not exceed 750kPa for high-quality, abrasion-resistant ballast. Where lower quality ballast materials are used, consideration shall be given to reducing the allowable ballast pressure.

Determination of the vertical design wheel load involves the following:

- The vertical design wheel load is calculated by static wheel load × dynamic (service) factor; the default value given by AS 1085.14 is 2.5.
- The vertical design rail seat load R_v is calculated by vertical design wheel load × distribution factor (DF). DF is determined by the designed sleeper spacing.
- The beam on elastic foundation method is to be utilized to determine the proportion of the loading applied to individual sleepers.

Although the design principles are the same, there are presently three different basic designs of prestressed concrete sleeper installed on tracks in NSW (the most important state in Australia). The major differences between the three design methods are the dynamic factors used by the railway authorities. For example, the Australian Rail Track Corporation uses 2.04, Sydney Trains uses 2.57, and an earlier State Rail Authority used 2.5.

Fig. 1: Bending crack at the rail seat area (cracks initiating underneath the concrete sleeper and extending through the whole cross section of the sleeper to the rail seat)

Fig. 2: Severe worn at the base of middle section (usually combined with center-bound-type cracks on the top surface of middle section)

Fig. 3: Centre-bound-type failure (directly caused by poor ballast condition)

V. Technical Specification and for New Concrete Sleeper

The medium duty concrete sleepers will be designed and manufactured to provide a minimum service life of 50 years based on annual tonnage of 25 MGT, nominal axle load of 25 t axle load freight train predominated traffic at speed of 80 km/h. Sleepers should be designed to a preferred length of 2.5 m with 667 mm sleeper spacing (1500 sleepers/km). It is suggested that the maximum depth of the concrete sleeper be located at the rail seat area to resist the positive bending moment from the wheel load and the high shear stress introduced by the wheel load. The concrete sleeper is to be designed with an adequate width, which can have a larger contact area with the ballast. Hence, the ballast pressure

beneath the concrete sleeper is to be not higher than 500kPa. This needs to be confirmed by calculation as detailed in AS 1085.14. The width of the rail seat on the top of concrete sleepers is to be not less than 160 mm plus any chamfer or rounding. If any special rail pads or fastening systems are designed for assembly with the concrete sleeper, the greater width can be utilized for design. The sleeper base surface shall be rough cast to lock with the ballast. The top and side surfaces of the concrete sleeper shall be smooth to prevent retention of moisture and foreign material. The new designed sleepers are to be assembled with resilient fastenings and insulators. As described in Section 5.4 of AS 1085.14, Design Parameters, an impact factor of 2.04 is recommended for the design of medium duty concrete sleepers. Hence, the impact (dynamic) factor 2.04 is utilized.

The design wheel load of the medium duty concrete sleeper is dynamic wheel load. It is a combination of static wheel load and relatively dynamic influence. The dynamic wheel load on one rail is calculated as 250 kN. According to the AS 1085.14, for concrete sleeper design the sleeper load DF of approximately 0.55 for 667 mm spacing should be used. Hence, the vertical load is 250 × 0.55 = 137.5 kN. In addition, the horizontal force equals 0.5 times the vertical load, which is 68.95 kN. As the lateral load is carried by the fastening systems, only the vertical load of 137.5 kN was applied to the top surface of the rail seat of the FEA concrete sleeper model. The angle was considered by rotating the coordination system of the nodes at the rail seat. In addition, the 2.86º angle caused by the slope of rail seat was also considered.

VI. Nonlinear Finite Element Model

A. *Three-Dimensional Finite Element Model*

Nonlinear finite element (FE) models were created to undertake the design, parameter study, and critical concrete sleeper failure analysis. Three-dimensional (3-D) physical models were created to simulate a new concrete design work which is fully compliant with the technical specifications. This finite element model includes a 3-D FEA model of the concrete sleeper, the ballast layer underneath the sleeper, as well as the contact elements used to connect the elements of concrete sleeper and ballast and carry out the simulation of friction between them. The widely used FE software for structural analysis, ANSYS, was used.

Four types of elements were used to create the 3-D FE model, which includes the newly designed medium duty concrete sleeper and the underneath ballast layers with variable thicknesses of 200, 250, 300, and 450 mm. The SOLID65 element was used to simulate the concrete sleeper, the SOLID45 3-D 8-node structural solid element was used to simulate the ballast layer, the BEAM4 3-D beam element was used to simulate the prestressed steel tendon in the concrete sleeper, and the 3-D TARGE170 element and the 3-D CONTA174 element were used to simulate the interaction surface between the concrete sleeper and the ballast. The friction between the concrete sleeper and the ballast was simulated by using a friction factor of 0.8 for the contact elements. The physical FE model of the concrete sleeper and ballast layer is created. To make it easier to see the details of every kind of element, a FE mesh with cross section detail is shown in Fig. 4.

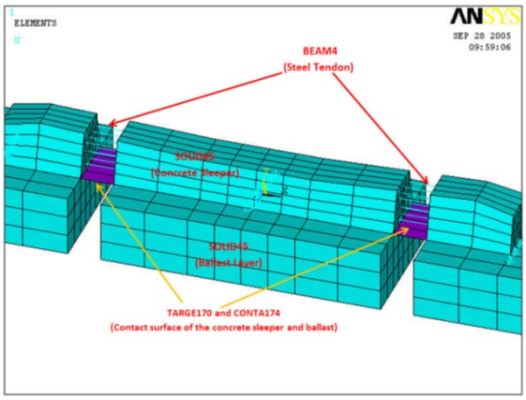

Fig. 4: Finite element types used to create the concrete sleeper (details)

Material Nonlinearities. To accurately represent the situation of a concrete sleeper under the train load, the nonlinearities of the concrete material and steel reinforcement were considered and simulated by means of the material nonlinearities. The nonlinear material properties were input into the ANSYS FEA model via its material nonlinearities function "multi-linear kinematic hardening." The material behaviour is described by a piece-wise linear stress-strain curve, starting at the origin, with positive stress and strain values [6].

Numerical Simulation of Ballast Condition. Ballast profile and condition can significantly affect the performance of concrete sleepers under the train traffic. Hence, within these FEA models the thickness and condition of the ballast was changed to simulate different conditions of ballast support to the sleepers. The ballast conditions were carried out by changing their elastic modulus value, E.

B. *Results from the Numerical Analysis (FE Model)*

When the ballast was in good condition, the concrete sleepers performed well. The FEA results showed that if the ballast layer was 250 mm in thickness and its material properties were uniformly distributed, the maximum compression stress areas were located at the two rail seat areas, with maximum stress value of -13,032 kPa for x-direction and 11,419 kPa for von Mises. Comparing the maximum compression stress with the final permit stresses value, which is at 22,500 kPa, it was found that the maximum compression stress was still 42.1% and 51.1% lower than the material limitation. This ensures that failure will not occur when the sleeper is under the 25 t axial load.

Furthermore, the tension stress value both at the bottom of rail seat and top surface at the centre area were no more than 2,533 kPa, which is 10.5% lower than the permit tensile stress value of 2830 kPa.

Ballast Conditions Impact to the Bending Moment. According to the Australian design standard (AS 1085.14), the maximum positive bending moment should occur at the rail seat for a uniform ballast support condition. The maximum negative bending moment should occur at the centre of the sleeper, under partially or totally centre-bound conditions, producing tensile stress at the top and compressive stress at the underneath of the sleeper. The absolute value for both positive and negative bending moments calculated by the equation offered by AS 1085.14 was 19.22 kN·m.

Based on the experience of concrete sleeper maintenance ([1] & [7]), poor ballast condition was the major reason for development of concrete sleeper damage and failure. The most severe ballast condition included the loosening or void between the sleeper and the ballast below the rail seat when maintenance was neglected, the centre-bounding caused by poor quality or neglected maintenance work, as well as ballast degrading factors such as fouling and pumping action.

From the numerical study, it was found that the maximum positive bending moment (tension on the bottom surface) was located at the rail seat areas in all the ballast situations. Comparing the results, the results of all ballast conditions were very close.

The negative bending moment occurred at the middle of the concrete sleeper, the result of the ballast condition that was "centre bound" combined with loosening ballast (highly deteriorated ballast) in the rail seat area was much higher than the uniform ballast condition. Moreover, studying the three centre-bound ballast conditions, it was found that the ballast condition at the rail seat location can significantly influence the negative bending moment at the middle of the concrete sleeper.

Centre-Bound Damage in Concrete Sleepers. Centre-bound concrete sleeper failure is mainly caused by the poor ballast conditions. This concept has been acknowledged by the track maintenance department for many years. During this numerical study, the relationship between centre-bound damage and ballast condition has been studied by investigating the deformation shape of the concrete sleeper with different ballast conditions. It was found that the vertical displacements were significantly changing with the different ballast conditions. The most significant vertical deformation happened with the centre-bound and loosing or void ballast at the rail seat ballast situation. A lesson learned from this is that centre-bound ballast conditions alone cannot cause very significant and continuously distributed centre-bound concrete sleeper failure. They must be combined with the delay of track tamping work (loosing ballast condition at the sleeper rail seat area).

X-Direction Bending Stress. X-direction (along the length of concrete sleeper) bending stress is the predominant bending stress of the concrete sleeper under the wheel load. The failure types of bending crack at the rail seat area, severe worn at the base of middle section, longitudinal split, and sleeper end longitudinal crack all either result from this stress or are significantly influenced by it. The x-direction stress of the base (bottom) of the concrete sleeper along the longitudinal centre line for three ballast conditions was plotted as shown in Fig. 5.

For the uniform ballast condition, the maximum stress value at the top surface was about 16% higher than at the bottom surface. However, if the ballast was in the centre-bound and rail seat loosening condition, the compressive stress at the centre of the sleeper base could be more than two times higher than the uniform ballast condition. Moreover, when the tensile stress at the top surface of the middle 500 mm area of the concrete sleeper was checked it was found that even in the centre-bound condition the positive x-direction stress value was still very low (σ_{max} = 168 kPa). Hence, the horizontal and mesh cracks on the top surface of the middle area of concrete sleeper could be avoided. However, with the uniform ballast condition, the maximum x-direction tensile stresses of 2528 kPa were found at the bottom surface of the two end areas.

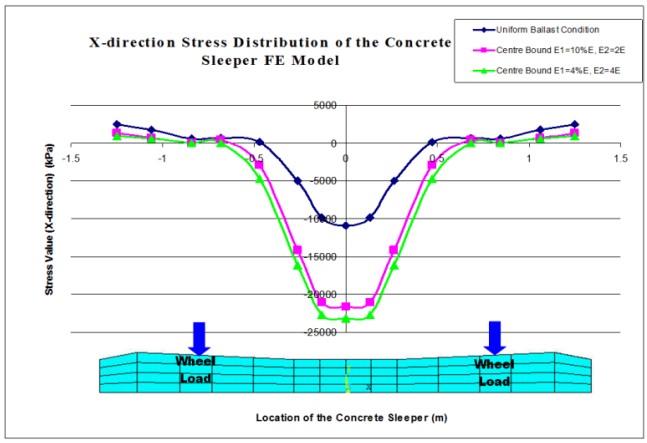

Fig. 5: The nodal stress of the concrete sleeper base (x-direction stress)

Ballast Pressure. Based on the FEA results, the maximum pressure results changed with the ballast conditions. With the uniform ballast condition, the locations of the maximum ballast pressure of these three conditions were all found at the area under the rail seat. The lowest values were located at the middle areas. The maximum ballast pressure for uniform ballast condition (ideal condition and also AS 1085 design condition) is 528 kPa, which is nearly 5.6% higher than the requirement 500 kPa. These results were checked by calculations based on the equation suggested by Australian Standard AS 1085.14, which is given as 474 kPa (the difference is 11.3%).

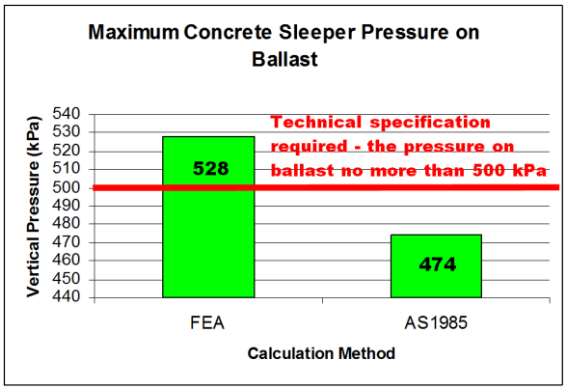

Fig. 6: Concrete sleeper pressure on ballast

VIII. Potential Technical Improvement

Theoretically, there are two effort directions which have the potential to significantly improve the interaction between concrete sleeper and ballast. They are: increase the contact area between concrete sleeper and/or decrease the dynamic vibration by using rail pads and/or under sleeper pads with higher dynamic attenuation.

A. Increase the Contact Area

The simplest way to achieve the lower ballast pressure (≥ 500MPa) is to increase the width of the concrete sleeper. According to the Australian Standard AS 1085.14, to improve the original design, the width of the concrete sleeper should

be increased from the current designed 290 mm to 300–305 mm.

B. High Resilience Rail Pad

If a concrete sleeper introduces pressure on the ballast layer underneath it that is significantly higher than the ideal ballast pressure (≥ 500 kPa), a cost-effective and efficient solution is to replace the HDPE or low-impact attenuation rubber rail pads with pads with high impact attenuation and vertical deflection, such as Pandrol's Hytrel (average deflection: 0.165, impact attenuation: 43.5%) [8] or other type of natural rubber pads.

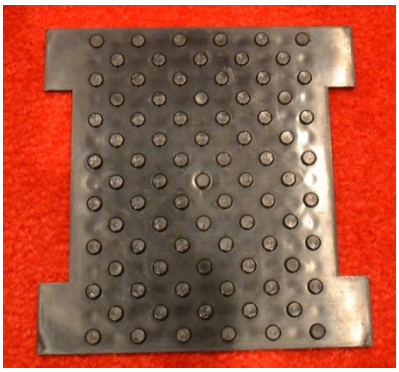

Fig. 7: Hytrel rail pad

C. Under Sleeper Pad

This is the option that introducing specially designed elastic under sleeper pads (USPs) which is glued underneath of the concrete sleepers above the ballast track bed. These products are placed directly underneath the concrete sleeper and increase the vertical elasticity in the track (as shown in Figure 8 and 9).

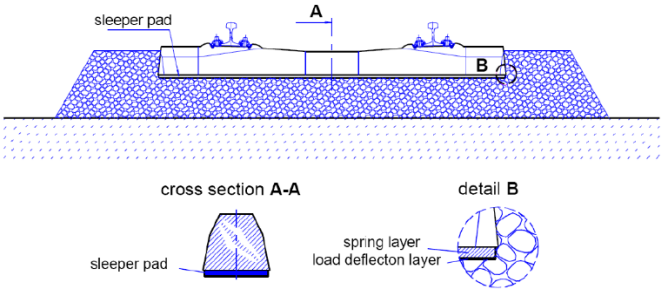

Fig. 8: The under sleeper pad (USP) used on the ballast track

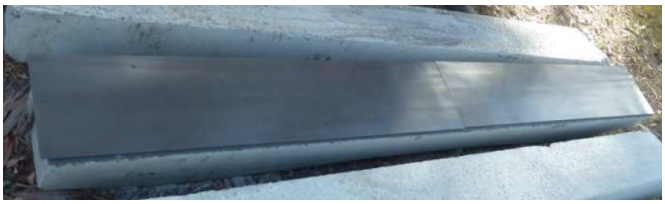

Fig. 9: The under sleeper pads are glued to the sleeper underneath

The benefits that can be obtained from the under sleeper pads included:

- Decrease the dynamic load and vertical vibrations in the ballast layer. The USP reduces the direct dynamic impact load on the ballast layer. Hence, both of the track settlement and ballast broken have been mitigated.
- Distribute the axle load from train wheels to a larger number of sleepers. The elastic properties of the USP increased the bending affected length along the rails, i.e. more amount of concrete sleepers along the track are involved to distribute the load from one wheel. Hence, the ballast pressure under each concrete sleeper will be reduced.
- Increase of the contact area between sleeper and ballast. The USP's unique material properties of the polyurethane can provide an ideal embedding of the ballast with the surface of the USP.

Within Australia, the USPs which are supplied by Getzner GmbH have been installed on a freight and passenger trains mix operated track. The maximum axle load of freight train is 25t and maximum passenger train speed is 140km/h. The track configuration consist of 60kg/m head hardened rails, Pandrol "e" clip fastening system, heavy duty concrete sleepers and clean ballast with adequate profile.

To quantify how the USP can mitigate the vibration to the track, the vibration measurements were carried out by the accelerometer and speed radar. Two locations were investigated: at the interface between USP and ordinary tracks; and at the location where the USP is installed. The vibration results for a freight train are represented in Fig. 10.

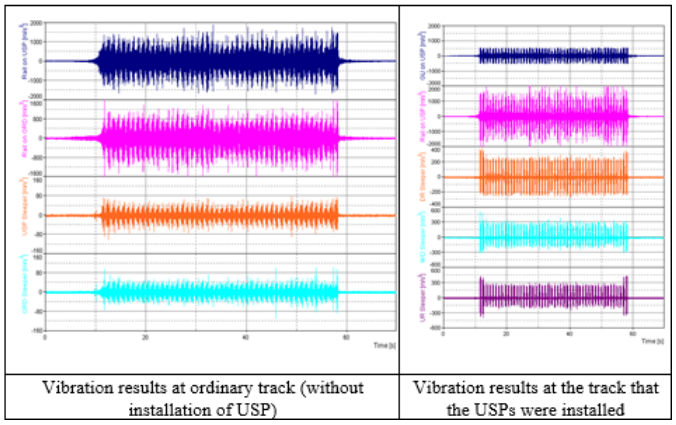

Fig. 10: The vibration results for a freight train

The vibration measurements show that the resiliency of USPs resulted in increased vibrations of both rail and sleeper. It is important to note that the sleepers with USPs tend to have lesser flexures as the phase difference is insignificant, i.e., the sleeper bending strains are lessened by USPs.

The dynamic effect of train speeds on track components is more pronounced than that of axle loads in a broad range of frequencies. However, sleeper vibrations at a low frequency band can be highly influenced by axle loads (pronounced by freight trains).

IX. CONCLUSIONS AND RECOMMENDATIONS

For a concept designed concrete sleeper with the technical features to suit the heavy haul freight and mixed with passenger trains operational conditions, the following findings were obtained from the numerical study and in-field testing:

- When the ballast was in good condition, the concrete sleepers performed well.
- Centre-bound ballast conditions alone cannot cause very significant and continuously distributed centre-bound concrete sleeper failure. They must be combined with the delay of track tamping work (loosing ballast condition at the sleeper rail seat area).
- X-direction bending stress is the predominant bending stress of the concrete sleeper under the wheel load.
- The ballast pressure underneath of the concrete sleeper is not evenly distributed along the length of the sleeper, and the actual maximum ballast pressure is located at the locations where the two "rail seat" areas of a concrete sleeper. And its value is higher than the results which is calculated by the equation that provided by the AS1085.14 design standard.
- To achieve the lower ballast pressure (≥ 500MPa), the simplest way is to increase the width of the concrete sleeper. For example, from the current 290 mm to 300–305 mm.
- A cost-effective and efficient solution to decrease the wheel load on concrete sleeper is using the high impact attenuation and vertical deflection rail pads, such as the Pandrol's Hytrel pads.
- Under sleeper pads (USPs) decreases the dynamic load and vertical vibrations on the ballast layer. The vibration measurement confirms that the sleeper bending strains are lessened by USPs. The dynamic effect of train speeds on track components is more pronounced than that of axle loads in a broad range of frequencies. However, sleeper vibrations at a low frequency band can be highly influenced by axle loads (pronounced by freight trains).

REFERENCES

[1] Kerr A. Fundamentals of Railway Track Engineering. Omaha, NE: Simmons-Boardman Books, 2003.

[2] Zhang R and Wu H. "Optimization of concrete sleeper design for heavy haul operated railway track by non-linear finite element and empirical studies," WIT Transactions on the Built Environment, vol. 181, 2018 [COMPRAIL 2018 – 16th Intl. Conf. Railway Engineering Design & Operation Portugal, 2018].

[3] Vincent G. Modal Analysis and Numerical Modeling of a Concrete Railway Sleeper. Thesis for the degree of licentiate of engineering. Division of concrete structures. Department of structural engineering. Chalmers University of Technology, Goteborg, Sweden, 2001.

[4] Gustavson G. Static and Dynamic Finite Element Analysis of Concrete Sleeper. Thesis for the degree of licentiate of engineering. Division of concrete structures. Department of structural engineering. Chalmers University of Technology, Goteborg, Sweden, 2000.

[5] Australian Standard, Australian Standard: Railway Track Material. Part 14: Prestressed Concrete Sleepers. AS 1085.14. 2012.

[6] Zhang R. The Behavior of Long Span Deep-Corrugated Reinforced Steel Box Culverts. Thesis of Master of Engineering. Faculty of engineering. University of Technology, Sydney, Australia, Sept. 2004, pp. 26–34.

[7] Taherinezhad J, Sofi M, Mendis P, and Ngo T. "A review of behavior of prestressed concrete sleepers," Special Issue: Electronic Journal of Structural Engineering, vol. 13, no. 1, 2013.

[8] Lubout N & Gräbe H. Performance of resilient rail pads used in Tubular modular track under South African service conditions. Civil Engineering, 20-22. May, 2012.

Elliptical Crack Breathing Mechanism in an Unbalanced Rotating Shaft

H.M. Mobarak
School of Computing, Engineering and Mathematics
Western Sydney University
Penrith, Australia
mobarak.hossain@westernsydney.edu.au

Helen Wu
School of Computing, Engineering and Mathematics
Western Sydney University
Penrith, Australia
helen.wu@westernsydney.edu.au

Chunhui Yang
School of Computing, Engineering and Mathematics
Western Sydney University
Penrith, Australia
r.yang@westernsydney.edu.au

***Abstract*—Shaft with elliptical crack simulated using ABAQUS/Standard to analyses the mechanism of crack breathing. Crack breathing at various locations along the shaft length under the impact of unbalance force is studied. It discovered that under the unbalanced force, a crack has more breathing patterns. Besides, when crack located at $0.2L$, where L is the total shaft length, a crack will never open and will never close at $0.8L$. Moreover, crack in unbalanced shaft will act as in a balanced shaft when crack located at $0.3L$ and $0.825L$. However, the cracked unbalanced shaft stiffness relates to the balanced shaft observed in three areas based on the variability in crack-breathing behavior along the length of the shaft. The unbalanced shaft is stiffer when the crack is located between $0.3L$ and $0.825L$ and flexible when located in two side regions for the angular position of an unbalanced force between 90° and 270°. On the other hand, when the angular position of an unbalanced force between 0° and 90° or 270° and 360°, the unbalanced shaft is flexible for the middle crack region and stiffer in two side regions. The present model can be further extended to obtain the cracked shaft stiffness matrix and then study the nonlinear dynamic response with large unbalance force.**

Keywords—crack breathing, crack location, elliptical crack, unbalance force, rotating shaft

I. INTRODUCTION

This template, In rotating machinery, the damage is always caused by the breathing (the crack closes and opens once per revolution) of the fatigue crack, leading to unpredictable and damaging vibration scenarios [1]. Traditional crack detection methods are not very efficient due to the inconvenience of having offline with the loss of manufacturing, such as ultrasonic testing and ultraviolet radiation [2]. More effective online crack monitoring methods such as vibration and eddy current monitoring have been used over the past decades to avoid these costs [3-5]. However, each of these techniques has its benefits and disadvantages [6-8]. Signal and vibration-based assessment [9-11], model-based techniques [12-14] and mixed approaches [15, 16] were also used in cracked rotor literature. The fracture model is adopted as the fundamental component for linearizing mathematical models in analytical research. Many researchers used three dimensional (3D) finite element models to analyse the real crack breathing mechanism [2, 13] considering elastic behaviour material [17], elastic-plastic properties material [18], and contact interaction behaviour [19].

Breathing a crack is the consequence of stress and strain distribution around the cracked region [10, 20] owing to static loads or dynamic loads while torsion effects are negligible [21, 22]. The weight-dominant crack breathing is commonly considered by most research. However, the dynamic loads considerably impacted the lightweight rotors, lightly damped rotors, and vertical machinery crack breathing behaviour. Some studies, however, have regarded the dynamic load impact of analysing the vibration response of the rotor system. Bachschmid et al. [21] investigated the effect of the crack's nonlinear breathing behaviour and discovered that the presence of the unbalances sometimes reinstated the system's strength. Cheng et al. [23] also observed that because of the unbalance, the strength of the rotor system could be returned.

Most of them used simple rotor model and simple crack geometry with a straight front transverse crack at middle [21, 24]. But, localised stiffness decrease is directly related to crack depth, while global stiffness decrease is affected by both crack size and crack location along the shaft [21]. Unfortunately, to simplify the analysis, many researchers disregard the impacts of crack location and mitigate crack geometry impacts. Some studies, however, explored the dynamics of a more realistic cracked rotor system, taking into account a crack at fixed crack locations [25, 26].

There is still no investigation into a shaft's breathing behaviour given the impact of unbalance force and more reasonable elliptical crack. Furthermore, all the above-described studies discovered that crack breathing is independent of the location of the crack, owing to considering the simple support boundary condition. In this paper, to evaluate the crack breathing behaviour, a numerical model is developed considering the effect of more realistic fixed end boundary condition. This model used to visualise the effect of crack location/unbalance configurations to study the nonlinear crack breathing behaviour by analysis the status of crack.

II. SIMULATION MODEL

A. Elliptical Crack Modelling

For analysis, a crack with the elliptical shape a/b (being the elliptical shape axis a and b see Fig. 1a) to the shaft cross-section was considered. In the crack section, the 'Tie constraint' is used to produce the intact part. A surface-to-surface agreement relationship is used in crack faces to prevent interpenetration between them during the closing. The details of the contract interaction at the crack cross-section are shown in Fig. 1b. The upper part refers to the intact part, and the lower part refers to the crack section. In the lower part, normal property, "hard" contact is used to prevent penetration and tangential property, "rough" friction is used to prevent all relative sliding motion between the two contacting surfaces.

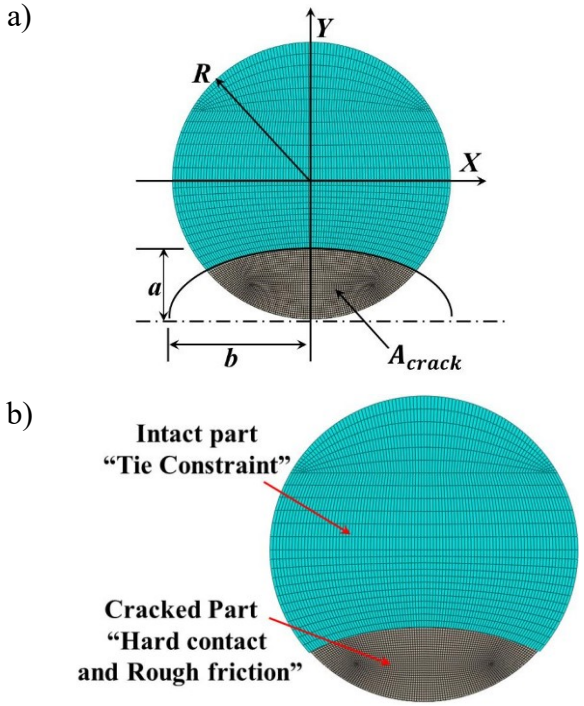

Fig. 1. Schematic diagram of a) the crack cross-section and b) surface to surface contact interaction in crack cross-section.

For analysis, a crack with the elliptical shape a/b (being the elliptical shape axis a and b see Fig. 1a) to the shaft cross-section was considered. In the crack section, the 'Tie constraint' is used to produce the intact part. A surface-to-surface agreement relationship is used in crack faces to prevent interpenetration between them during the closing. The details of the contract interaction at the crack cross-section are shown in Fig. 1b. The upper part refers to the intact part, and the lower part refers to the crack section. In the lower part, normal property, "hard" contact is used to prevent penetration and tangential property, "rough" friction is used to prevent all relative sliding motion between the two contacting surfaces.

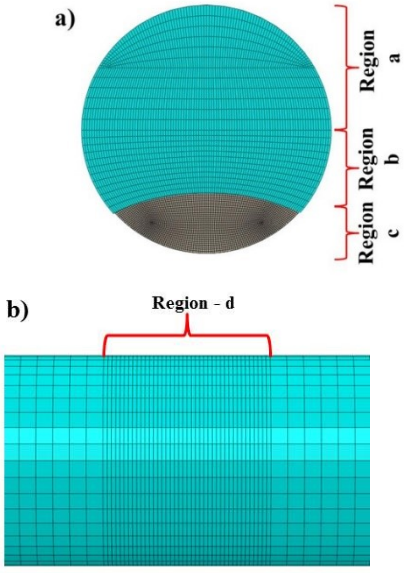

Fig. 2. Mesh around the crack section in the a) longitudinal and b) transversal direction

A full 3D rotor model is simulated. The shaft has meshed with an item of series C3D8R called linear hexahedral components. As illustrated in Fig. 2, the mesh density in both ways is much higher around the crack. The mesh size is acquired through mesh sensitivity analyses after a convergence test of the outcomes. In Fig. 3, the results of the convergence test for the balanced case are presented at crack location $0.5L$ and angular position 90°. The closing percentage is seen to converge after the mesh figures achieve 12, 12, 80 and 24 in four areas (a, b, c and d). The closing percentage will be outlined in-depth, subsequently.

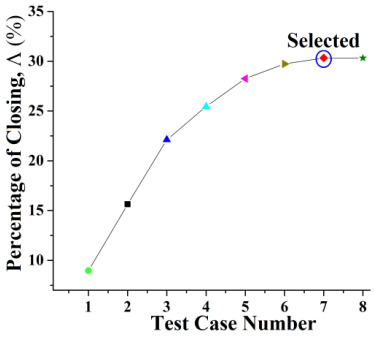

Fig. 3. Mesh sensitivity analyses

The analysis is performed as a succession of static problems considering the following crack configurations:

a) 40 crack locations varying from 0 to L with $0.025L$ increments where L is the shaft length.

b) 24 different angular positions of the crack, θ, varying from 0° and 360° with increments of 15° to the fixed reference axis.

While the actual issue is dynamic, the static one is regarded at the angular position of the crack to understand the impact of the crack angular position. Simulated an elliptical crack with shape $a = 0.5R$ and $b = R$ where R is the radius of the bar.

B. Unbalanced Force Modelling

The unbalance force (F_{un}) due to unbalanced mass (m_u) was considered. The initial location of the unbalance force (F_{un}) is (θ+β). Where θ is the angular position of crack or shaft rotation angle and β is an angular position of unbalance force relative to the crack direction as shown in Fig. 4.

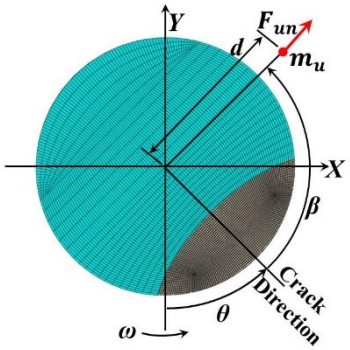

Fig. 4. Relative positions of the unbalance force to the crack direction

It should be noted that there is no unbalanced force on the crack plane, and it is only a projection of unbalanced force on the crack plane. Different unbalance force ratio (ratio of the gravitational force and unbalance force), and angular location of unbalanced force was regarded to distinguish the influence of the angular position of the crack and the unbalance force together. In order to evaluate the crack breathing behaviour simulation has been done consideration:

a) 5 unbalance force ratio, η = 1, 2, 10, 100 and ∞ (balanced)

b) 5 angular position of unbalance force, β= 0°, 45°, 90°, 150° and 180°.

Five angular position of unbalance force within half angular position of unbalance force (0° to 180°) was considered to be symmetrical as the effect of angular position of unbalance force on crack breathing behaviour (first half the same as the second half of angular position of unbalance force, 180° to 360°).

The static force due to the shaft weight and two disks weights have been included in the analysis. In Fig. 5 has been shown the details loading and boundary condition of the simulated model. The model represents a fixed-supported two-disk rotor. The total length of the shaft, L, is 724 mm, whereas 6.35 mm is the radius, R. The material of the shaft is steel with the following mechanical properties: density, ρ=7800 kg/m^3, Poisson ratio, v=0.3 and Young's Modulus, E=210GPa. The shaft weight has been applied as a gravitational force and two disks weights applied as a concentrated force. Unbalance force was implemented as a concentrated force on the X-axis [$F_{un}\cos(\theta+\beta)$] and the Y-axis [$F_{un}\sin(\theta+\beta)$] on right side disk.

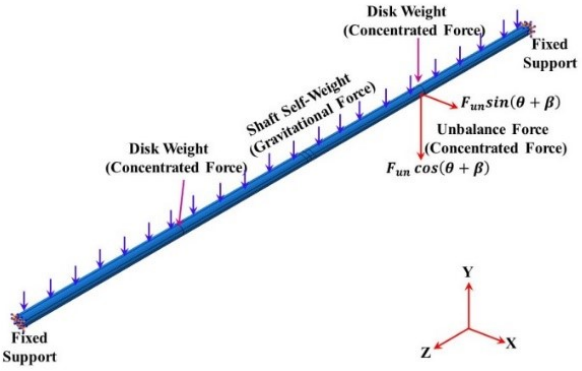

Fig. 5. Details loading and boundary condition of the simulated model

III. Crack Breathing Mechanism Analysis Procedure

The status and percentage of the closing were evaluated for a different crack location along the shaft length. Unbalanced force ratio, the angular position of unbalance force and angular position of crack were considered to distinguish the breathing behaviour of crack. It can relate to the stiffness changes in the cracked shaft and eventually calculate the response of vibration. When a crack status is fully closed, or the percentage of the closing of the crack is 100 per cents, the shaft has the same stiffness as the solid shaft. The crack will never propagate, and there will always be a zero stress intensity factor. Similarly, if a crack status is fully opened or percentage of the closing of the crack zero per cent, the shaft has minimum stiffness. It is likely to propagate, and the percentage of the closing would take positive values and could overcome the critical value called fracture toughness. Also, if a crack status is a partly open/closed, or if the percentage of the closing of the crack is between zero per cent and 100 per cents, the shaft has a minimum to maximum stiffness. The specific modules in fracture mechanics analysis of ABAQUS are used to determine the status of the crack and crack closed area to calculate the percentage of the closing of the crack, as shown in Fig. 6.

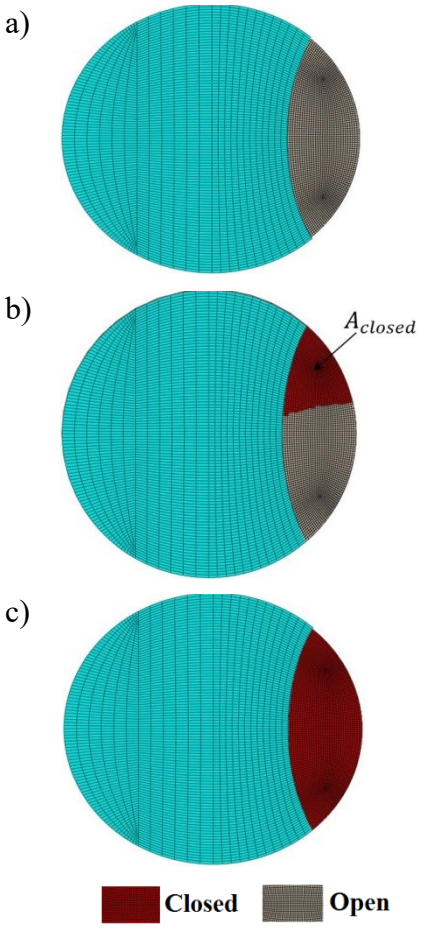

Fig. 6. Status of the crack a) fully opens b) partially open/closed and c) fully closed

The percentage of closing of the crack was calculated using equation (1). Where, A_{crack} is the areas of crack section at the time zero (see Fig. 1a). A_{closed} is the closed portion of the crack segment during the rotation, as shown in Fig. 6b. The A_{crack} and A_{closed} region were discovered as the history output of ABAQUS. The minimum and maximum value of A_{closed} is zero for fully open crack and same as A_{crack} for fully closed crack respectively. The percentage of closing of a crack is equivalent to 0 per cent and 100 per cents, respectively, for a fully open crack and a fully closed crack.

$$\Lambda\,(\%) = \frac{A_{closed}}{A_{crack}} \times 100 \qquad (1)$$

IV. Results and Discussions

The percentage of the closing of a crack along the shaft length for different force ratios is illustrated in Fig. 7. It is constant for balanced shaft, but it has a change at crack locations 0.2L and 0.8L. Therefore, at these crack locations along the shaft length, two different types of crack breathing behaviour of the balanced shaft can be split. One type when a crack located between 0.2L and 0.8L for example at crack location 0.5L and another type when crack located outside this crack region for example at crack location 0.125L (see Figs. 7 and 8).

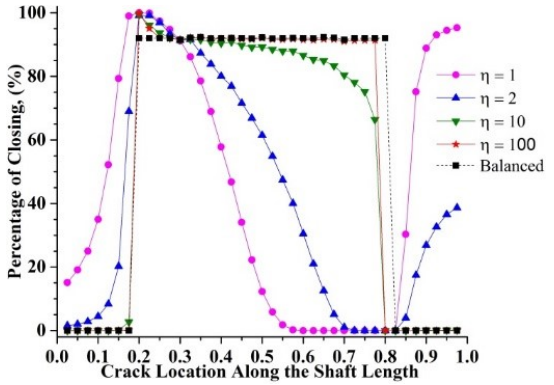

Fig. 7. Percentage of the closing of a crack along the shaft length for different force ratios, η, for β=0° and θ =135°.

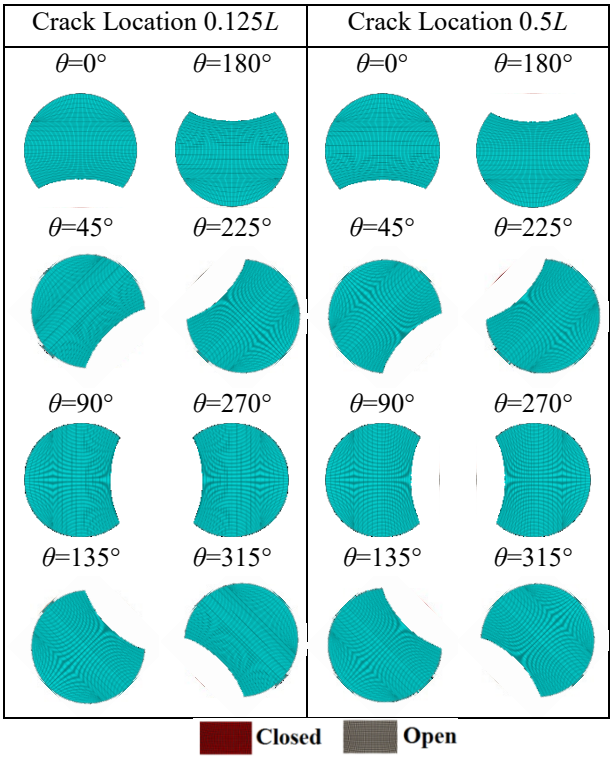

Fig. 8. Statues of the crack of a balanced shaft at crack locations 0.125L and 0.5L

Crack position, however, is symmetrical about the first half and second half of shaft rotation for both crack location regions, but different sequential. When the crack at 0.125L undergoes a continuous change from entirely closed, partly open/closed, wholly opened, partly open/closed, and then completely closed. On the other side, when crack at 0.5L undergoes a continuous change from fully open, partly open/closed, fully closed, partly open/closed, and then completely open (see Figs. 8 and 9). The duration of crack status remains unchanged for both instances (see Fig. 9). Therefore, although balanced shaft status of the cracks depends on the crack location, the stiffness would be independent of crack location along the shaft length.

The percentage of the closing of a crack along the shaft length for the unbalanced shaft is significantly different from the balanced one. However, it is the same as the balanced shaft at 0.3L and0.825L see Fig. 7 also, for complete shaft rotation, see Fig. 10. Thus these two crack locations are autonomous of the unbalance force. However, the crack statue at these two crack location is different in sequence as there are located in different crack regions. At location 0.3L the crack starts with a fully open configuration at θ=0° than partly open/closed, completely closed, partly open/closed and then open again. At crack location 0.825L starting with a fully closed status at θ=0° than partially open/closed, completely opened, partially open/closed and then completely closed again (see Fig. 10). As a result, if crack at these crack locations, the unbalanced shaft crack will breathe as balanced shaft crack. The shaft's stiffness would be the same as the balanced shaft.

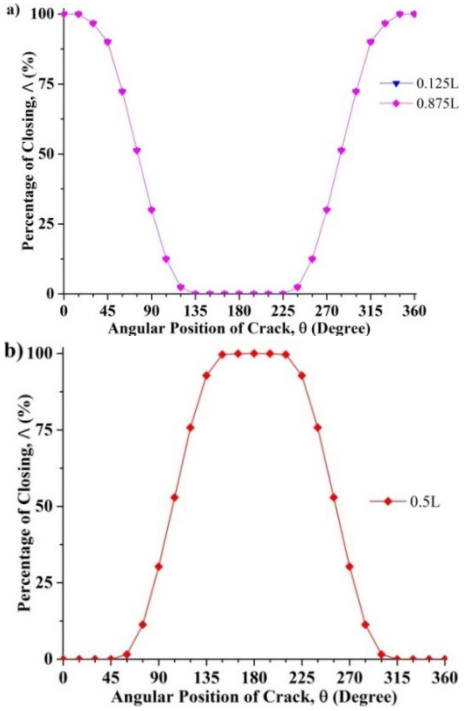

Fig. 9. Percentage of closing of the crack of the balanced shaft at crack locations a) 0.125L & 0.875L and b) 0.5L

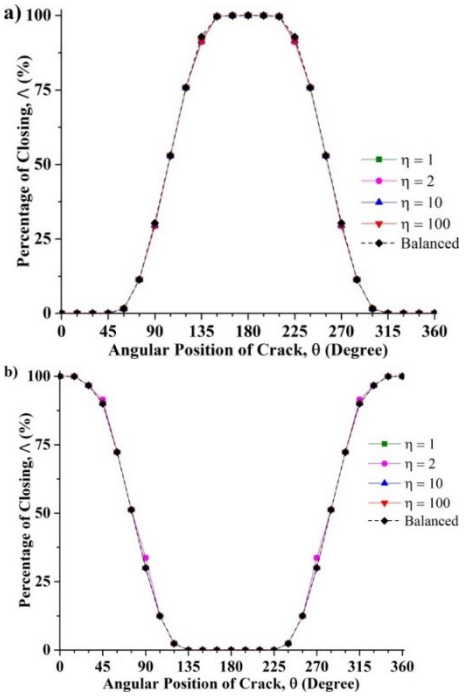

Fig. 10. Percentage of the closing of the crack of different force ratios at crack locations a) 0.3L and b) 0.825L

Another two unique crack places are 0.2L and 0.8L; the percentage of the closing of a crack is the same for all unbalanced force ratios see Fig. 7 also, for complete shaft rotation, see Fig. 11. As a consequence, the unbalanced shaft

crack will breathe independently of the unbalanced force ratios at these locations. In Fig. 12, the crack status of an unbalanced shaft (η=10 & β=0°) was shown for a complete shaft rotation. A crack in an unbalanced shaft is completely closed-never-open during rotation at 0.2L, just like an uncracked shaft. The shaft will have maximum stiffness and become virtually identical to an uncracked shaft. It is entirely open-never-close at 0.8L, just like a notch. The shaft is going to have a minimum stiffness.

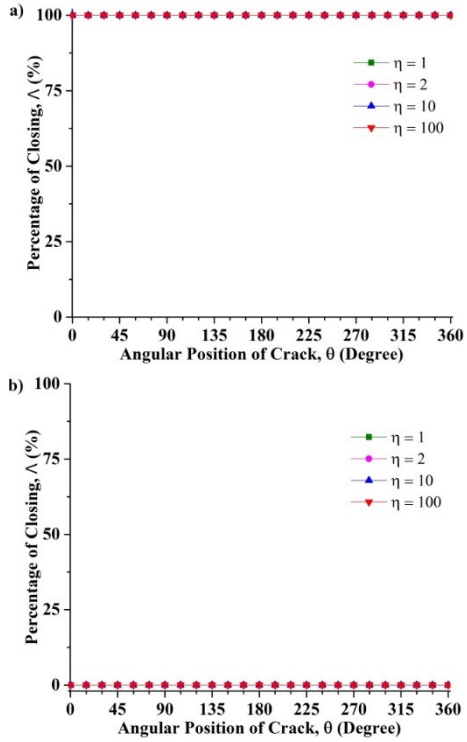

Fig. 11. Percentage of closing of the crack of different force ratios at crack locations a) 0.2L and b) 0.8L

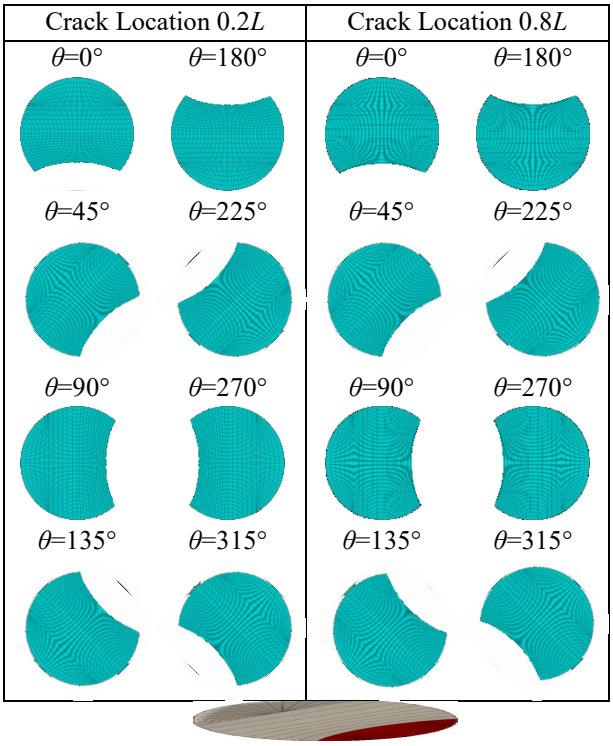

Fig. 12. Status of crack of a unbalanced shaft (η =10 & β = 0°) at crack locations 0.2L and 0.8L

Moreover, as unbalanced force ratio increases (force decreases), percentage of the closing of a crack gradually approach to balanced shaft see Fig. 7 also, Fig. 13. This is indicated that if the unbalanced force ratio is big enough, the unbalanced model would be finally in agreement with a balanced model.

The shaft will usually generally experience two processes during a complete rotation, i.e., a stiffening process corresponding to the increasing in Λ and a softening process corresponding to the decreasing in Λ. These two processes are seen to be symmetrical about θ=180°. The straight portion of the graph is either a completely open range (Λ= 0%) or a completely closed range (Λ= 100%). In detail, when the crack at 0.5L, the closing of the crack for the unbalanced shaft is smaller than for the balanced shaft, indicating that the unbalanced shaft is more flexible than the balanced shaft (see Fig. 13b). However, it is higher than the balanced shaft at 0.125L and 0.875L; the unbalanced shaft becomes stiffer (see Figs. 13a and 13c).

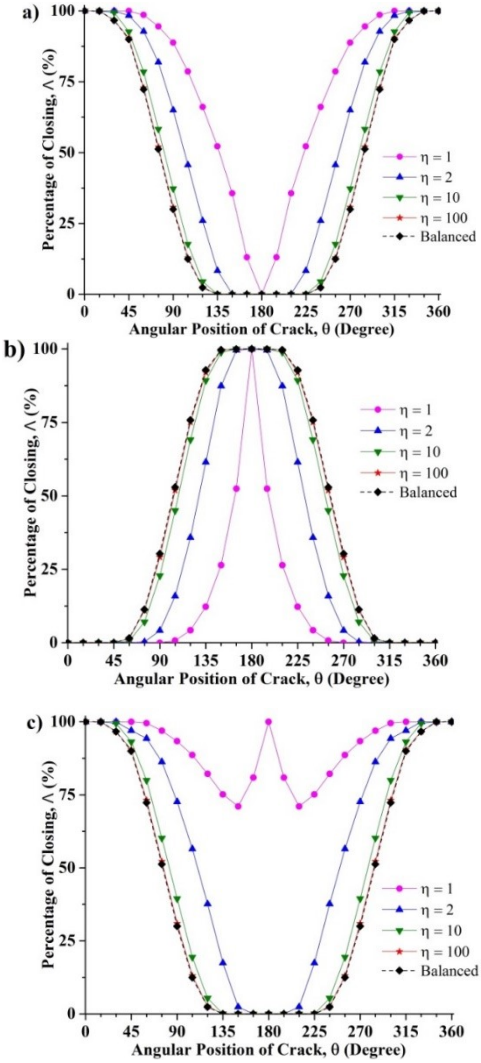

Fig. 13. Percentage of closing of the crack of different force ratios for crack locations a) 0.125L b) 0.5L and c) 0.875L

Fig. 13 represents only a particular case where the angular unbalances force position is β=0°. In Fig. 14 exemplifies percentage of the closing of an unbalanced shaft for the different angular position of unbalance force, β. The unbalanced shaft is generally more flexible than the balanced counterpart when β=0°, and β=45° and the shaft has the lowest

stiffness with β=0° (see Fig. 14b) when the crack located at 0.5L. However, overall, the unbalanced shaft is stiffer than the balanced count when the crack at 0.125L and 0.875L for these two angular positions and the shaft is stiffer with β=0° (see Fig. 14a and 14c). On the other hand, when the angular position of the unbalanced force is β=135° and β=180° the unbalanced shaft is generally stiffer than the balanced shaft. Especially at β=180°, the shaft is stiffest (see Fig. 14b). At 0.125L and 0.875L, the unbalanced shaft is more flexible than the balanced shaft for these two angular positions as a percentage of the closing of the unbalanced shaft is lower than the balanced shaft. The shaft is particularly flexible when β=180° (see Fig. 14a and 14c). Regardless of the location of the crack, however, β=90° is recognised as different orientations see Fig. 14. The percentage of the closing for the unbalanced shaft is sometimes more significant than that of a balanced shaft and sometimes lower during complete rotation. Therefore, the unbalanced shaft stiffness is more or less the same as the balanced shaft. It is also seen that, except for β=0° and β=180°, the stiffening process and the softening process is not symmetry during rotation. The orientation of the unbalance force will have a significant impact on the cracked shaft's vibration, as earlier noted by Cheng et al. [23].

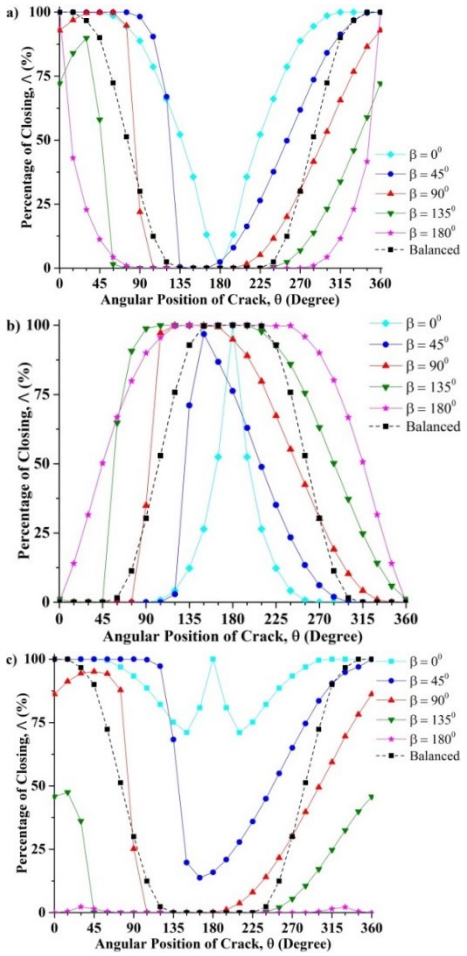

Fig. 14. Effect of unbalance force orientation on crack breathing behaviour at a) 0.125L b) 0.5L and c) 0.875L

V. CONCLUSIONS

A series of analyses were conducted using the ABAQUS simulation. The effect of various variations on the crack breathing behaviour, such as crack location, crack angular position, unbalance force and angular position, was analysed. Compared to the balanced shaft's notably different breathing behaviour of the unbalanced shaft have been recognised. It was found a single status, dual status, symmetrical and unsymmetrical behaviour. A crack stays completely closed at 0.2L and fully opened at 0.8L, which will never occur in a balanced shaft. A crack in the unbalanced shaft, however, behaves like one in the balanced shaft at 0.3L and 0.825L.

Three shaft stiffness variation is found along the length based on a different combination of crack location, and unbalanced force. If the crack in the middle region (0.3L to 0.825L) and β is between 90°<β<270°, the unbalanced shaft is stiffer than the balanced shaft. For two side areas, it is flexible. On the other hand, the unbalanced shaft is flexible for the middle crack region where β is between 0°<β<90° or 270°<β<360° and it is stiffer for two side areas.

The presented model can be further extended to achieve the cracked shaft stiffness matrix and then investigate the nonlinear dynamic behaviour with significant unbalance force.

ACKNOWLEDGMENT

The author is grateful for the financial support provided by the School of Computing, Engineering and Mathematics, Western Sydney University, Penrith NSW 2747.

REFERENCES

[1] Kumar, and C. Rastogi, “A brief review on dynamics of a cracked rotor”, International Journal of Rotating Machinery, pp. 1-6,2009.

[2] P. Saavedra, and L. Cuitino, “Vibration analysis of rotor for crack identification”, Journal of Vibration and Control, vol. 8, pp. 51-67, 2002.

[3] Z. Ren et al., “Crack fault diagnosis of rotor systems using wavelet transforms”, Computers & Electrical Engineering, vol. 45, pp. 33-41, 2015.

[4] M. Silani, S. Ziaei-Rad, and H. Talebi, “Vibration analysis of rotating systems with open and breathing cracks”, Applied Mathematical Modelling, vol. 37, pp. 9907-9921, 2013.

[5] K.S. Wang, D. Guo, and P.S. Heyns, “The application of order tracking for vibration analysis of a varying speed rotor with a propagating transverse crack”, Engineering Failure Analysis, vol. 21, pp. 91-101, 2012.

[6] M. Xu, and R. D. Marangoni, “Vibration Analysis of a Motor-Flexible Coupling-Rotor System Subject to Misalignment And Unbalance”, Journal of Sound and Vibration, vol. 176, pp. 663-679, 1994.

[7] M. Ichimonji, and S. Watanabe, “The Dynamics of a Rotor System with a Shaft Having a Slant Crack: A Qualitative Analysis Using a Simple Rotor Model”, JSME international journal, vol. 31, pp. 712-718, 1998.

[8] I. Mayes, and W. Davies, “Analysis of the response of a multi-rotor bearing system containing a transverse crack in a rotor”, Journal of Vibration, Acoustics, Stress and Reliabilityin Design, vol. 106, pp. 139–145, 1984.

[9] C. Guo et al., “Application of empirical mode decomposition to a Jeffcott rotor with a breathing crack”, Journal of Sound and Vibration, vol. 332, pp. 3881-3892, 2013.

[10] Z. Kulesza, “Dynamic behavior of cracked rotor subjected to multisine excitation”, Journal of Sound and Vibration, vol. 333, pp. 1369-1378, 2014.

[11] Yan et al., “A novel approach to detecting breathing-fatigue cracks based on dynamic characteristics”, Journal of Sound and Vibration, vol. 332, pp. 407-422, 2013.

[12] R.T. Liong, and C. Proppe, “Implementation of a cohesive zone model for the investigation of the dynamic behavior of a rotating shaft with a transverse crack”, Proc. Appl. Math. Mech., vol. 10, pp. 125 – 126, 2010.

[13] L. Rubio, and J. Fernández-Sáez, “A new efficient procedure to solve the nonlinear dynamics of a cracked rotor”, Nonlinear Dynamics, vol. 70, pp. 1731-1745, 2012.

[14] P. Pennacchi, N. Bachschmid, and A. Vania, "A model-based identification method of transverse cracks in rotating shafts suitable for industrial machines", Mechanical Systems and Signal Processing, vol. 20, pp. 2112-2147, 2006.

[15] J. Guo, X. Huang, and Y. Cui, "Design and analysis of robust fault detection filter using LMI tools", Computers & Mathematics with Applications, vol. 57, pp. 1743-1747, 2009.

[16] J. Xiang et al., "Crack detection in a shaft by combination of wavelet-based elements and genetic algorithm", International Journal of Solids and Structures, vol. 45, pp. 4782-4795, 2008.

[17] B. Dirr, and B. Schmalhorst, "Crack depth analysis of a rotating shaft by vibration measurement", Journal of vibration, acoustics, stress, and reliability in design, vol. 110, pp. 158-164, 1988.

[18] W. Ostachowicz, and M. Krawczuk, "Vibration analysis of a cracked beam", Computers & Structures, vol. 36, pp. 245-250, 1990.

[19] L. Rubio et al., "Quasi-static numerical study of the breathing mechanism of an elliptical crack in an unbalanced rotating shaft", Latin American Journal of Solids and Structures, vol. 11, pp. 2333-2350, 2014.

[20] J. Lee et al., "Prognostics and health management design for rotary machinery systems—Reviews, methodology and applications", Mechanical Systems and Signal Processing, vol. 42, pp. 314-334, 2014.

[21] N. Bachschmid, P. Pennacchi, and E. Tanzi, "Cracked rotors: a survey on static and dynamic behaviour including modelling and diagnosis", Springer Science & Business Media, 2010.

[22] M. Mobarak et al., "New crack breathing mechanism under the influence of unbalance force", Archive of Applied Mechanics, pp. 1-32, 2017.

[23] L. Cheng et al., "The influence of crack breathing and imbalance orientation angle on the characteristics of the critical speed of a cracked rotor", Journal of Sound and Vibration, vol, 330, pp. 2031-2048, 2011.

[24] J. J. Sinou, "Effects of a crack on the stability of a non-linear rotor system", International Journal of Non-Linear Mechanics, vol. 42, pp. 959-972, 2007.

[25] Lei et al., "Simulation on the motion of crankshaft with a slant crack in crankpin", Mechanical Systems and Signal Processing, vol. 21, pp. 502-513, 2007.

[26] Teng, "Numerical prediction of slant fracture with continuum damage mechanics", Engineering Fracture Mechanics, vol. 75, pp. 2020-2041, 2008.

Steel Fire Behaviour in Vehicular Bridge Accidents

Hamid Fatemi
Roads and Maritime Services
Transport for NSW
Parramatta, NSW, Australia
hamid.fatemi@rms.nsw.gov.au

Eric Ancich
Visiting Research Fellow
Centre for Infrastructure Engineering
Western Sydney University
Penrith, NSW, Australia
anciche@iprimus.com.au

Richard Yang
School of Computing Engineering and Mathematics
Western Sydney University
Penrith, NSW, Australia
r.yang@westernsydney.edu.au

***Abstract*— After bridge fire events, the main task of engineers would be opening the bridge to traffic as quickly as possible without compromising the structural integrity of the bridge or the safety of road users. The recently published AS 5100.8 provides some guidance for assessment of bridge materials including steel, concrete, masonry and timber. However, the type and extent of required tests depend on the results of the preliminary inspection by specialist engineers and asset owners' strategic decisions considering the criticality of a bridge on the roads network. Therefore, there is a need for an efficient design of testing in order to ensure that the materials properties have not been jeopardised due to the fire within the limited allocated time-frame of bridge traffic closure. This task becomes more complex in cases that the vehicular impact causes a fire as steel losses about half of its strength when the temperature rises to almost half of the melting temperature.**

This paper presents a case study for assessment of possible changes in critical materials properties in the fire event on a bridge. Also, the paper highlights the need for a comprehensive guideline to bridge fire damage assessment and repair, depending upon the bridges' traffic functionality. This in turn may result in improving the bridge design strategies from fire safety perspective.

Keywords—materials inspection and testing, steel bridge, post fire assessment

I. INTRODUCTION

A study of bridge fire damage incidents in United States showed, even though fire damage is rare it is not so uncommon either. The majority of the fire incidents were caused by fuel tanker truck accident. In most cases the bridge did not collapse and only in few cases major structural collapse occurred or the bridge had to be demolished. However, in all cases high costs were sustained due to traffic closure [1]. Another study conducted in the National Cooperative Highway Research Program (NCHRP) and sponsored by the American Association of State Highway and Transportation Officials identified a strong correlation between that the risk of bridge fire and the likelihood of vehicle accidents on or under the bridge. The research compared steel's thermal and mechanical properties changes in high temperatures according to American Society of Civil Engineers and Eurocode prediction models [2]. There are also several studies on fire performance of specific bridge designs. Quiel, Yokoyama, Mueller, Bregman and Marjanishvili studied the effect of fire on a cable-stayed bridge [3]. On the other hand, Braxtan, Whitney, Wang and Koch investigated composite steel box girder bridges in fire and compared weathering steel and structural steel performance. They identified that fire beneath a box girder bridge poses a significant risk to the structural integrity [4]. This paper also presents a case study of in situ steel failure analysis. The paper describes the results of a materials investigation and tests as part of the assessment team, feeding to the asset owner for strategic decisions on the serviceability of the subject bridge. The bridge is located south of Sydney, NSW, Australia. The fire took place when a truck crashed into a safety barrier and was hanging over the side of bridge. Shortly after the crash, the truck was burning until the Rural Fire Service extinguished the fire. The crash closed a major arterial highway in both directions for several hours. A visual inspection of the bridge condition was quickly carried out by a specialist team of engineers from Roads and Maritime Services which was followed by detailed structural assessment and materials testing. As a result, the bridge could be safely open to traffic as early as possible.

Also, the paper highlights the need for a comprehensive guideline to bridge fire damage assessment and repair, depending upon the bridges' traffic functionality. This in turn may result in improving the bridge design strategies from fire safety perspective.

II. AUSTRALIAN STANDARDS PROVISIONS

AS 5100.1 has left fire requirements to the discretion of relevant authorities [5]. AS 5100.2 includes a new fire effect load case in the 2017 revision, but it would still be subjected to the relevant authorities' specifications [6]. Similarly, parts 5 and 6 of the Standard provide some guidelines for structural performance of concrete and steel bridges respectively [7, 8]. They further refer to AS 3600 and AS 4100 for, if deemed necessary [9, 10]. AS 4100 and AS 3600 require fire resistance period for structural adequacy which is not mandatory in bridge design. However, the scenario of World Trade Centre towers proved that it does not cater for extreme cases. Perhaps, the building designers never envisaged impacts from fully laden (and fueled) passenger aircrafts. These buildings were steel framed not reinforced concrete as is more common in Australia. Although the aircraft impacts damaged a number of perimeter steel columns, there was sufficient redundancy to sustain the structure. However, steel columns require fire protection and this is normally achieved using a sprayed coating of Vermiculite and gypsum plaster. The fires raged for several hours before the towers eventually collapsed. This suggests that the fire proofing spray was of insufficient thickness to protect the columns for the duration of the fires that occurred.

III. CASE STUDY

A B-double truck crashed into a bridge in southern region of NSW, Australia. It was hanging over the side of the bridge after hitting the traffic barrier and igniting into flames. Fig. 1 is a photo taken by Australian Broadcasting Corporation (ABC) from the incident [11].

Fig. 1. ABC News phot from the truck crash and fire incident, south of Sydney, NSW [11].

The incident closed an arterial highway for a few hours until bridge engineers successfully completed their assessment. The bridge is a composite structure including steel box girders with concrete deck. This paper only focuses on materials testing of fire affected areas. However, this would be the first step in a post fire assessment which must be supplemented with system testing including speed limit, load rate, composite action, member distortion, bearing and expansion joints, welded and bolted connections as well as serviceability assessment of structure. Moreover, these are to be followed by developing any required repair technique.

Initially inside and outside of the steel box girder as well as concrete deck surface were visually inspected. Then non-destructive testing (NDT) was undertaken on both steel and concrete. NDT included magnetic particle and dye penetrant testing on steel and Schmidt Hammer testing on concrete. Then further detailed assessment of the steel was carried out by in-situ hardness testing and metallographic replication.

NDT did not indicate existence of any cracks in the box girder's steel plate or loss of surface hardness in deck's concrete. Also, in-situ hardness test results on the girder's heat affected areas were converted to equivalent tensile strength using AS 5016 2004 [12] and ASTM E140 [13]. The results indicated that the heat from the fire on and under the bridge had not adversely affected the mechanical properties of steel. This was also verified by microstructure analysis of the steel. The experiments were designed according to the suggested tests in AS 5100.8 [14] by Roads and Maritime Specialist Engineer and were successfully undertaken at the bridge site. The asset owner thanked and acknowledged the team for their prompt and dedicated teamwork in opening the bridge to traffic as quickly as possible without compromising integrity of the bridge or safety of the road users.

IV. DISCUSSION

Historically, fire damage assessment had not considered as a core expertise in Roads and Traffic Authority [15]. However, currently Roads and Maritime has material specialists in steel, concrete and timber who contribute in development and maintenance of bridge related standards too.

The recently developed AS 5100.8 provides general guidance for fire damage assessment as part of strengthening and rehabilitation of steel, concrete, masonry and timber bridges [14]. On the other hand, AS 5100.7 [16] which covers bridge assessment only requires assessment in a fire event without elaborating on the assessment methodology.

Assessing mechanical properties of a bridge element which is subjected to fire requires comparison of the fire event with the specific time-temperature curve. AS 5100.2 provides different approaches for determination of the curve as part of design for fire which could also be adopted for assessment, if deemed acceptable, including [16]:

- Specification of the relevant authority
- Replication of the fire
- Fire modelling
- Taking AS 1530.4 curves (Fig.2) [17]

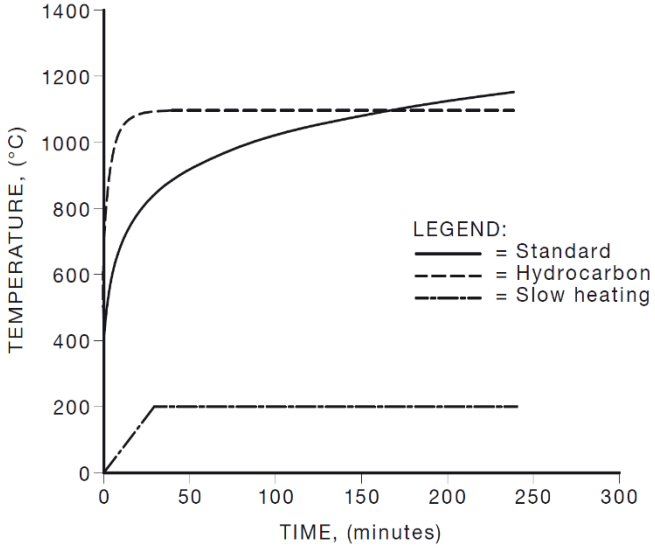

Fig. 2.Time-temperature curves for cellulose materials [17].

- Table 26 of the Standard (Fig.3).

Traffic type	Structural elements	
	Hydrocarbon fire curve	Duration minutes
Road	RWS/HCinc	120
Rail	RABT-ZTV	
Bus	RABT-ZTV	

Fig. 3.Design time-temperature curves for fire [16].

In addition, AS 4100 provides variation of mechanical properties of steel with temperature for determination of limiting steel temperature (Fig. 4).

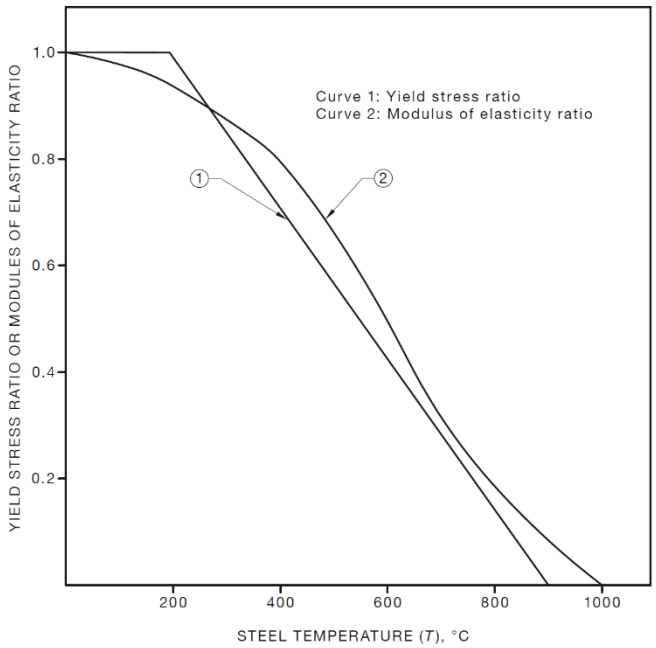

Fig. 4.Variations of mechanical properties of steel with temperature.

Furthermore, comparing the available data in Australia with international fire modelling practices [18] suggests determination of time temperature-curves comes with uncertainties.

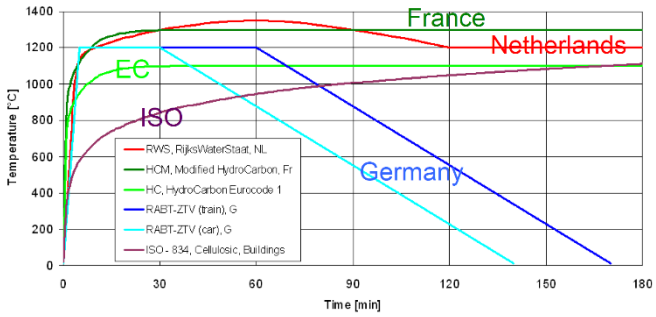

Fig. 5.International fire modeling.

In this regard, authors believe there is a need for development of a comprehensive technical document not only from structural performance perspective, but also from materials point of view. These may in turn change bridge design approaches such as the proposed importance factor by Kodur and Naser [19]. NCHRP in United States published "highway bridge fire hazard assessment" in 2013 which could be benchmarked for development of such a document [2].

V. Conclusion

There is a need for an efficient design of testing after a fire event on a bridge in order to ensure that the materials properties have not been jeopardised. This in turn requires a comprehensive technical procedure and such a document does not currently exist in Australia. The American "highway bridge fire hazard assessment" could be benchmarked for development of such a document.

Acknowledgment

The opinions and conclusions expressed in this paper are those of the authors and do not necessarily reflect the policies of Roads and Maritime.

References

[1] L. Giuliani, C. Crosti and F. Gentili, "Vulnerability of bridges to fire," Bridge Maintenance, Safety, Management, Resilience and Sustainability – Biondini & Frangopol (Eds), pp.1565–1572.

[2] W. Wright, B. Lattimer, M. Woodworth, M. Nahid and E. Sotelino, "Highway Bridge Fire Hazard Assessmen" Virginia Polytechnic Institute and State University, Blacksburg, VA, United States, 2013.

[3] S. Quiel, T. Yokoyama, K. Mueller, L. Bregman and S. Marjanishvili, "Mittigating the effects of a tanker truck fire on a cable-stayed bridge," pp. 1002–1012.

[4] N.L. Braxtan, R. Whitney, Q. Wang and G. Koch, "Preliminary investigation of composite steel box girder bridges in fire," *Bridge Structures*, 11, 1963, pp. 105–114.

[5] AS 5100.1 Bridge design–Part: 1, "Scope and general principles," *Standards Australia, Sydney*, 2017.

[6] AS 5100.2, Bridge design–Part: 2, "Design loads," *Standards Australia, Sydney*, 2017.

[7] AS 5100.5, Bridge design–Part: 5, "Concrete," *Standards Australia, Sydney*, 2017.

[8] AS/NZS 5100.6, Bridge design–Part: 6, "Steel and composite construction," *Standards Australia, Sydney*, 2017.

[9] AS 3600, "Concrete structures," *Standards Australia, Sydney*, 2018.

[10] AS 4100"Steel structures," *Standards Australia, Sydney*, 2016.

[11] ABC News, "https://www.abc.net.au/news/2017-10-11/hume-highway-video-shows-truck-crash-off-bridge/9040164," *Australian Broadcasting Corporation,* 2017.

[12] AS 5016 2004, Metallic materials - Conversion of hardness values, *Standards Australia, Sydney*, 2016

[13] ASTM E140, "Standard Hardness Conversion Tables for Metals Relationship Among Brinell Hardness, Vickers Hardness, Rockwell Hardness, Superficial Hardness, Knoop Hardness, and Scleroscope Hardness," *American Society for Testing and Materials,* 2007.

[14] AS 5100.8, Bridge design–Part:8, "Rehabilitation and Strengthening of existing bridges," *Standards Australia, Sydney*, 2017.

[15] Chirgwin and C. Gibbons, "Fire damage on a concrete bridge," *Austroads Bridge Conference,* 2000, pp. 287–308.

[16] AS 5100.7, Bridge design–Part:7, "Bridge assessment," *Standards Australia, Sydney*, 2017.

[17] AS 1530.4, " Methods for fire tests on building materials, components and structures, fire-resistance tests for elements of construction," *Standards Australia, Sydney*, 2014.

[18] N. Elhami-Khorasani, "Fundamentals of fire engineering for bridges," *University of Buffalo*, 2017

[19] V.K.R. Kodur and M.Z. Naser, "Importance factor for design of bridges against fire hazard," *Engineering Structures,* 54, 2013, pp. 207–220.

An optimization study on kerf, MRR and power consumption in WEDM for Al-Si alloy using taguchi method and OEC

Kaja Sai Suhruth Teja
School of Engineering and Technology
BML Munjal University
Haryana, India
kajasaisuhruthteja@gmail.com

Abstract— **Wire Electrical Discharge Machining (WEDM) is a process that can machine intricate shapes and materials that cannot be machined conventionally. The current experimental investigations aim is to establish a fundamental understanding of the effect of WEDM parameters in machining Aluminum-Silicon alloy. The experimental studies were conducted under varying parameters. The parameters T_{on},W_f, W_t, S_v and S_f are identified and Taguchi's method is used to form 18 experiments from which Kerf width, MRR and Power consumption were determined experimentally. With these results, Overall Evaluation Criteria (OEC) was used and normalized values of operating parameters were obtained. Best possible optimum parameters were determined after performing ANOVA. Results showed that the parameter T_{on} had large impact in machining the material. The optimal results showed in this research were determined through experiments planned, conducted and analyzed using Taguchi's method and OEC. The parameters suggested in this research can be used according to requirements for Al (80%)-Si(20%) alloy.**

Keywords*— *WEDM, Parameters, ANOVA (Analysis of Variance), MRR (Material Removal Rate), Kerf width, Overall Evaluation Criteria (OEC), T_{on} (On time), W_f (Wire Feed), W_t (Wire Tension), S_v(Servo Voltage) and S_f(Servo Feed).

I. INTRODUCTION

With the evolution of mankind, many materials were discovered and invented. Each time a new element was found different properties were observed, some were tougher while some were harder, some were lighter while some were heavier. Using conventional manufacturing methods for these materials entails high tool costs and long process times [1]. So, the technology for cutting/machining these materials has been developing since ages. Non-Traditional machining process is the type of process which removes the excess material using thermal, mechanical, electrical and chemical energy. These types of machining techniques are also used to machine complex and intricate geometries. Such type of techniques provides better surface finish and dimensional tolerances in comparison to the other type of conventional ones. Electrical Discharge Machining (EDM) is a non-contact process which has the capability of machining any conductive hard material. The continuous spark discharge in this process causes electrical erosion of material. The Spark temperature for this process may reach up to 12,000℃ . In this process, the work piece is connected to a positive terminal and the tool is connected to a negative terminal with a potential applied. This entire network is submerged in a dielectric fluid such as deionized water. Depending on the potential applied the height between the tool and the work piece is decided. Since, this is a non-contact process the tool is maintained at a height that enables spark generation. Industrially this technique widely uses graphite materials as electrodes for fabricating molds for die-casting, plastics and more. Since drilling precise small holes is tough, it is usually done with the help of EDM.

Wire Electrical Discharge Machining (WEDM) is one such type of electrical discharge machining which has a brass wire spooling along with dielectric fluid flowing continuously at a defined rate. In this process the wire with a diameter of 0.2 – 0.3 mm is usually used as a tool electrode [2]. A spark is generated in between the brass wire and the work piece which helps in localized heating, melting and vaporization of substrate material, thus removing the material. This machinery is used to create two and three dimensional conductive cavities and complicated shapes. The process is used to machine plastic molds, punching dies, squeezing die etc. WEDM has wide range of applications and is supposed to be a cutting-edge technology. It can be used to machine the bolster plate and other complex shapes and patterns. WEDM is used for manufacturing different mechanical equipment that cannot be machined easily. It is also possible for the machine to manufacture small products but at a slower rate. The process of machining in WEDM is a time-consuming process and requires consumables such as Wire, filters or deionizing resin, but when compared to other methods this machine could deliver efficient results.

Taguchi Method was designed to pick up the best fit combination of parameters. At the very beginning a method proposed by R.A. Fisher known as Factorial Design of Experiments was used to form different combinations of parameters that can be used to run experiments. Meaningful results from the wide variety of experiments conducted were contingent on selection of parameters. That led Taguchi to define a set of rules which would enable convenient selection of such parameters. Overall Evaluation Criteria (OEC) is a method that is used when there are more than one response parameters the process is expected to satisfy. Each of the response parameters are analyzed if the requirement is to

reduce, increase or normalize their values. Weightage for each response is also estimated according to the requirement and normalized values obtained for all the experiments are used to calculate ANOVA to find optimized parameters. The formula for OEC is

$$OEC = \left(\frac{X-X_{min}}{X_{max}-X_{min}}\right) W_x + \left(1 + \frac{Y-Y_{min}}{Y_{max}-Y_{min}}\right) W_y \quad (1)$$

ANOVA test is done to understand significance level of each parameter. It is a statistical test method used to understand the differences of group means in a sample and also its statistical significance.

Many studies have evidenced experimental research in Advanced Manufacturing to widen the scope of the process. J.P Misra et al [3] used combustor material (Waspalloy) and observed the effects of wire related input parameters and servo feed on Material Removal Rate (MRR) and Wire Wear Rate (WWR). They used One Factor At-A-Time Approach (OFAT) and decided the optimum parameters. Results from their study showed that a feed rate 4M/Min, Wire Tension of 11 machine units, and servo feed of 2050 mm/min provided highest results of MRR. Surface Quality of the products machined is a big matter of concern for all the engineers. Maintaining the quality of the surface of the product improves fatigue strength, Corrosion resistance and wear resistance. Mohammed Yeakub Ali et al [4] worked on stainless steel. They used different parameters and found out the effects on surface roughness. Parameters such as voltage open, wire speed, wire tension, voltage gap, and off time were used. The results showed that off time had the most impact on the surface roughness and the optimum parameters decided were 10 V open voltage, 2.84 µs off time, 12 m/min wire speed, 6.3 N wire tension, and 54.91 V voltage gap. Jinkai Xu et al [5] worked on the influence of recast layer formed while machining Aluminium 7075 alloy on mechanical physical properties through WEDM. Results showed that the thermal power density decreases, surface roughness increases, micro/nano pits increase with increase of current and voltage. Omkar Kulkarni and Shalaka Kulkarni [6] worked on carbon high chromium steel. They used the optimization technique of Grey Wolf Optimizer (GWO) which mimics the hunting mechanisms and hierarchical leadership qualities of grey wolfs. They studied the process input parameters such as pulse on time, pulse off time, wire feed, wire tension, upper flush and lower flush for thinning in automotive sealing cover. Their results showed that pulse time on is the most influencing parameter for MRR from which the optimum parameters were decided. A. Conde et al [7] studied the influence of wire deformation on the part geometry. Their results showed an increase in wire deformation as much as 45% for cutting a circular geometry of 0.8mm than that of a straight line with similar thickness. Also, as the radius increases the percent of discharge without the ionization time increases and decreasing that which has an ionization time above 10µs.

A.V.S Ram Prasad et al [8] worked on proper selection of parameters to optimize MRR and Roughness for machining a titanium alloy. ANOVA was applied and the most significant parameters among peak current, pulse on time, pulse off time and servo voltage were selected. Results showed that the most significant parameters were peak current and pulse on time. Linshuai Zhang et al [9] generated reaction films on Ti–6Al–4V with the help of high speed wire electrical discharge machining for the improvement of micro-hardness and corrosion resistance. The thickness of the film increased micro-hardness and corrosion resistances of alloys processed were also superior whereas the corrosion current densities would decrease with thicker films. Their studies showed important insights of surface modifications of the alloy.

The advancement of technology, high quality products with precise tolerances can be manufactured but productivity remains biggest concern for all the industries. The detailed literature survey uncovers a fact that there is a gap to establish the detailed understanding of the WEDM process parameters influence in machining a Al-Si alloy. Hence, an objective has been set to establish the WEDM characteristics of Al-Si alloy. Industrially the optimized parameters determined can be used in piston manufacturing and rim manufacturing industries for reduced power consumption, increased MRR and decreased kerf width. Taguchi design of experiments methodology has been used to optimize the selected parameters and understand the influence of these parameters on MRR, Kerf Width and Power Consumption.

II. MATERIAL AND METHOD OF EXPERIMENTS

The experiments were conducted on Electronica, Wire-cut Electric Discharge Machine, which has the capability of holding the specimen up to a height of 250 mm. The electrode wire used in the experimentation is made up of Brass having tensile strength more than 50 Kgf/mm^2. The material of the wire should be electrically conductive, suitable for clamping and Non-combustible. The diameter of wire used is 0.02mm, where the tension and dielectric fluid flushing force are kept constant for all the experiments. The machine zone is in contact with the dielectric fluid, which is continuously flushed through the nozzle on both sides of the work piece. The power supply unit has Electric pulse generator, motor drive units for X, Y, U, V axes and CNC controller which is kept constant. The figure shows the machine that was used for experimental purposes.

Figure 1: Machine used for experiments

For this experimentation, for an aluminum silicon alloy spectroscopy is conducted to identify its composition (Table 1). It is apparent from Table 1 that there is about 79% of Aluminium with silicon of about 20%, and rest of the other elements in very small quantities. Then the experiments were conducted on the work pieces according to the set parameters.

Table 1: Composition of the workpiece material used

Element	Si	P	Cu	Al	Ni	Ti	Nb	Co	W	B
Value %	20.5	0.004	0.009	79.5	0.007	0.004	0.005	0.007	0.008	0.011

A set of 18 experiments are conducted and all the required readings are taken. The machining time for each set of parameters varied from 0.58 minutes to 3 minutes according to the rate of the cut. The collected data of weights is used to calculate the experimental MRR. T_{off} is calculated by assuming the duty factor as 0.69. The cuts are marked according to the experiment number for indication. Since T_{off} is calculated on the basis of T_{on}, it wasn't considered in the Design of Experiments of Taguchi's method.

The cuts are made on the work pieces according to the set parameters to calculate the Material removal rate, Kerf width, Power consumption and time taken to cut until the desired depth. An optical microscope is used to take the readings for the Kerf's width while the MRR was calculated by measuring the weight of the samples before and after the process and applying it in the formula 2. Power consumption is determined for an experiment using an electrometer attached to the machine. Table 2, shows the complete array of input parameters and their respective response parameter values after the experimentation and further characterization.

$$\text{MRR}= \frac{Initial\ weight - Final\ Weight}{Time\ taken\ for\ machining} \quad (2)$$

Table 2: Taguchi L-18 arrays with process parameters and MRR, Kerf Width and Power.

S.no	T_{on} (µs)	T_{off} (µs)	W_f (m/min)	W_t (Kgf)	S_v (V)	S_f (mm/min)	MRR (mg/min)	K_w (mm)	Power (Watt)
1	100	43	5	4	20	1100	0.011	0.27	86.76
2	100	43	8	8	40	1400	0.005	0.28	84.24
3	100	43	10	12	60	1600	0.391	0.28	86.49
4	110	48	5	4	40	1400	0.013	0.31	86.95
5	110	48	8	8	60	1600	0.01	0.31	87.02
6	110	48	10	12	20	1100	0.016	0.31	88.2
7	120	53	5	8	20	1600	0.046	0.33	38.7
8	120	53	8	12	40	1100	0.038	0.34	35.69
9	120	53	10	4	60	1400	0.0305	0.34	29.1
10	100	43	5	12	60	1400	0.00424	0.28	86.49
11	100	43	8	4	20	1600	0.0053	0.28	86.43
12	100	43	10	8	40	1100	0.00422	0.28	87.02
13	110	48	5	8	60	1100	0.011	0.31	84.85
14	110	48	8	12	20	1400	0.0166	0.31	87.53
15	110	48	10	4	40	1600	0.015	0.32	87.36
16	120	53	5	12	40	1600	0.0431	0.32	29.66
17	120	53	8	4	60	1100	0.022	0.30	28.89
18	120	53	10	8	20	1400	0.066	0.31	30.34

III. Results and Discussion

It can be observed that the control parameters are different for higher MRR, nominal Kerf width and lower power consumption. So there is a need to use multi-objective optimization considering MRR, Kerf width and Power consumption which will give the best condition among all the experiments conducted. OEC is used as an optimization method to optimize the values according to the requirement. The relative weight percentage of individual criterion for evaluation considered for these responses is shown in the table 3. Power consumption is an important factor which was given the highest weightage of about 50% and is required to be less in quantity. Kerf Width is expected to be nominal with 30% weightage. Since, in WEDM the material is removed with the process of vaporization of substrate material, the MRR is given least weightage of 20%.

Table 3: Parameters with weight percentage for OEC

Parameter	Worst Value	Best Value	Condition	Weightage
MRR	0.00422	0.391	B>>	20
Kerf Width	0.34	0.27	<<N>>	30
Power	88.2	29.1	<<L	50

For OEC the different standards with quality characteristics are normalized and weighed with bigger is the best. After calculating OEC for each experiment the average effects of response parameters to the input parameters is determined and graphically represented.

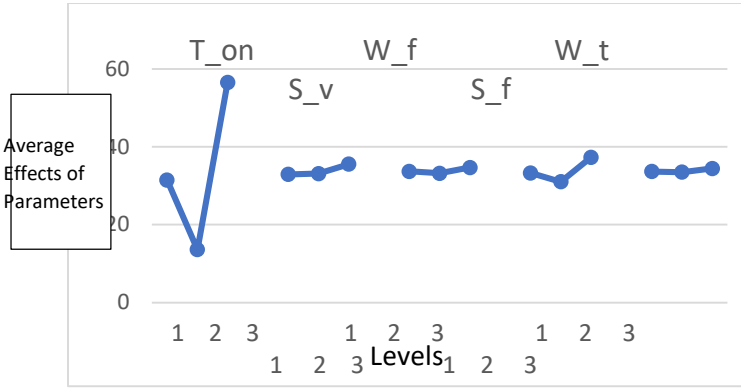

Figure 2: Average Effects of Response Parameters on input Parameters

The results reveal that the Average Effect of the parameters on T_{on} apparently decreases from first level to second and increases for third. The higher $T_{on}$is, higher is its impact in reducing power consumption and increasing MRR.

Interestingly, the figure for W_f is steadily increasing whereas, the graph for W_t and S_f is almost linear throughout indicating that the different levels of these parameters have similar effects on the response parameters.

S_v or Servo Voltage firstly down-surges and later increases until the 3rd level. The most influential parameter of all is T_{on} = 120 µs. Since machining in WEDM occurs in successive intervals. Pulse time on (T_{on})and Pulse time Off (T_{off}) determines the time in micro seconds for repeated to and fro action of the wire for material removal. As T_{on} increases MRR increases and Kerf Width increases. Similarly, Power consumption also depends on T_{on}. As the pulse time on increases power consumption is decreased.

Normalized values obtained for all the 18 experiments were used to perform ANOVA to understand the percentage contribution of each input parameter for the decided output. The results of ANOVA are shown in the Table 4.

Table 4: ANOVA Results(change)

Factor	DOF (f)	Sum Of Sqrs (S)	Variance (V)	F-Ratio (F)	Pure Sum (S')	Percent P(%)
T_{on}	2	5567.824	2779.863	32.765	5397.894	85.404
W_f	2	25.603	12.801	0.15	0	0
W_t	2	6.687	3.343	0.039	0	0
S_v	2	122.546	61.273	0.721	0	0
S_f	2	2.974	1.487	0.017	0	0
Other Error	7	594.755	84.965			14.596
Total	17	6320.392				100.00%

From the above table we can infer that T_{on} is contributing about 85% and that it is the only efficient influencing parameter. The effects of the parameters with that of the response parameters are shown in the figure 1. An approximate 15 percent of other error is shown, which occurs due to the other input parameters that were not considered. If the rest of the parameters are used, then it can decrease from 15% to a lesser quantity. Lastly, the optimum parameters found out were T_{on} = 120µs, $W_f = 10\text{m/min}$, W_t = 12Kgf, S_v= 60V and $S_f = 1600\text{mm/min}$.

IV. CONCLUSIONS

In this paper an investigation on optimization and effect of the chosen machining parameters on Kerf width, MRR and Power Consumption in WEDM was done.

1)It was found out that T_{on} was the only influential parameter on the response parameters for machining an Al (80%) Si(20%) alloy. For OEC, different measure with quality characteristics are normalized and weighted with smaller is the best, bigger is the best and nominal is the best as per the requirement. ANOVA, calculations were done to identify the most influential parameter and the optimum parameters.

2) Input parameters used in this study do not include many other possible parameters. If the parameters that were not considered are considered for the experiments the error percentage obtained in the table 4 could be reduced.

3) The Optimized parameters as from the observations above are T_{on} = 120µs,$W_f = 10\text{m/min}$,$W_t = 12\text{Kgf}$, S_v= 60V and $S_f = 1600\text{mm/min}$.

4) Since the most influential parameter is T_{on} then it can be said that it has higher ability to reduce Power consumption, increase MRR and nominalize Kerf. W_f and S_v make a linear graph individually explaining that all of the level of each input parameter indicates similar effects on the response parameters.

REFERENCES:

[1] Krämer A, Lung D, Klocke F. 2012, High Performance Cutting of Aerospace Materials. Adv Mater Res 2012; 498:127 –32.

[2] K.H. Ho, S.T. Newman, S. Rahimifard, R.D. Allen,2004,State of the art in wire electrical discharge machining (WEDM), Int.

J. Mach. Tools Manuf 44 (12) (2004) 12471259.

[3] J. P Misra, M Danish, Prateek, A Singh, M F Ullah, 2018, IOP Conf. Series: Materials Science and Engineering 402 (2018) 012165 doi:10.1088/1757-899X/402/1/012165.

[4] Mohammad Yeakub Ali, Asfana Banu1 , Mazilah Abu Bakar ,2018, IOP Conf. Series: Materials Science and Engineering 290 (2018) 012019 doi:10.1088/1757-899X/290/1/012019

[5] Xu, J., Qiu, R., Lian, Z., Yu, Z., Yu, P., Ren, W., & Yu, H. (2018). Wear and corrosion resistance of electroforming layer after WEDM for 7075 aluminum alloy. Materials Research Express, 5(6), 066502. doi:10.1088/2053-1591/aac636.

[6] Kulkarni, O., & Kulkarni, S. (2018). Process Parameter Optimization in WEDM by Grey Wolf Optimizer. Materials Today: Proceedings, 5(2), 4402–4412. doi:10.1016/j.matpr.2017.12.008.

[7] Conde, A., Sanchez, J. A., Plaza, S., Ostolaza, M., de la Puerta, I., & Li, Z. (2018). Experimental Measurement of Wire-lag Effect and Its Relation with Signal Classification on Wire EDM. Procedia CIRP, 68, 132–137. doi:10.1016/j.procir.2017.12.035.

[8] Prasad, A. V. S. R., Ramji, K., & Datta, G. L. (2014). An Experimental Study of Wire EDM on Ti-6Al-4V Alloy. Procedia Materials Science, 5, 2567–2576. doi:10.1016/j.mspro.2014.07.517

[9] Zhang, L., Xu, J., Chen, B., Yu, H., & Lian, Z. (2017). Microhardness and corrosion resistance behaviour of Ti–6Al–4V alloy-coloured surface under WEDM-HS process. Micro & Nano Letters, 12(9), 618–623. doi:10.1049/mnl.2017.0037.

Studying the Behaviour of Long Span Deep-Corrugated Reinforced Steel Box Culverts by In-Field Measurement and Numerical Analysis

Ralph (Wei) Zhang
School of Computing, Engineering and Mathematics
Western Sydney University
Sydney, Australia
Email address:
17602059@student.westernsydney.edu.au

Helen Wu
School of Computing, Engineering and Mathematics
Western Sydney University
Sydney, Australia
Email address:
Helen.Wu@westernsydney.edu.au

Chunhui Yang
School of Computing, Engineering and Mathematics
Western Sydney University
Sydney, Australia
Email address:
R.Yang@westernsydney.edu.au

***Abstract*—The structural behaviour of buried long-span deep-corrugated reinforced steel box culverts is investigated using the finite element method (FEM). A parametric study was conducted using two- and three-dimensional finite element analyses. Key parameters included poor/well compacted soil, effectiveness of rib-stiffeners, connection and the interaction with surrounding soil. The ANSYS FEA program was used for the numerical analysis, which included material nonlinearities of the backfill soil, geometric nonlinearities in the steel arch and soil-steel interface. In addition, the orthotropic material properties of the deep corrugated steel plates were accounted for in the 3D models. The FE results were compared with the results from in-field testing and published papers. Research has found that the use of corrugated-stiffeners as a kind of reinforcement for large span buried structures can improve the structural behaviour of a buried structure. Research also suggests that the material nonlinearities of backfill soil need to be simulated in FE modelling. A suitable material nonlinear model should be chosen (e.g., Duncan and Chang nonlinear model). The relative slippage of the corrugated steel plates caused by the slotted bolt-hole connections influenced the accuracy of the FE results. Some special FE strategies should be investigated to solve this problem.**

***Keywords*—Behaviour, long-span, steel box culvert, in-field measurement, numerical.**

I. INTRODUCTION

Corrugated reinforced steel box culverts have been used extensively as economic alternatives to traditional medium- or short-span concrete girder bridges. These culverts generally have an elliptical arch cross section and soil cover that is small relative to the span, as shown in Figure 1.

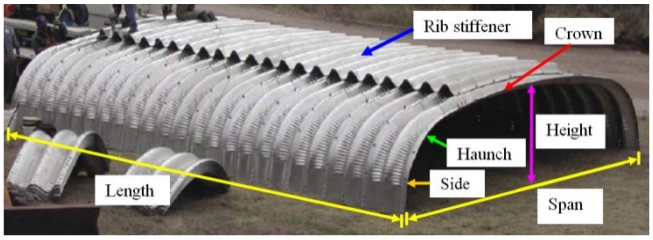

Fig. 1: A long span deep corrugated reinforced steel box culvert

There are many aspects that can greatly influence the quality and stability of the buried steel culvert, such as the quality of the backfill soil, elastic modulus of soil, construction organisation, and compaction during the backfill procedure. Figure 2 shows a collapsed roof of a long span steel culvert structure during its construction. This collapse occurred when the contractor, working without supervision over a weekend, graded the fill over the top of the culvert so that it sloped from one side to the other. The culvert was unable to sustain the unsymmetrical load imposed by the sloping fill, and it collapsed.

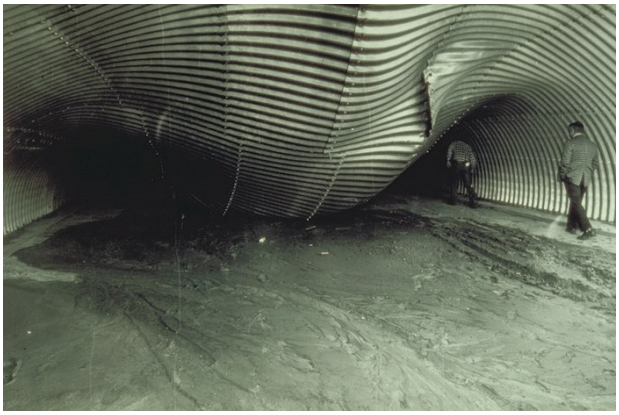

Fig. 2: Collapsed roof of a steel culvert structure, USA, 1979.

The structural performance of long span tunnels can be improved by using stronger materials or by incorporating rib stiffeners. One example is long-span deep-corrugated reinforced steel box culverts (also known as Super-Cor®), developed by Ingal Civil Products and some other companies.

Present code recommendations and design practices do not provide any procedures or guidelines to assist with the design of the deep-corrugated reinforced steel box culverts. Currently, researchers are interested in trying to evaluate the composite effects of the continuous reinforcement, deep-corrugated reinforced steel plates and the fastening system of the structures (bolts, shear studs and holes).

Despite all of these studies, the behaviour of culvert structures is still not well understood. One of the reasons is that there are many kinds of this type of structure and they are usually quite different in size, span, material, rib-stiffener and back fill soil condition. In addition, with the increase in span, problems arise during construction. Problems could also be caused by the large deformation of steel shell conduit, and the

effect of dead and live loading because of the low buckling strength of the shell. Moreover, the structural behaviour of the steel culvert can be significantly affected by the use of rib-stiffeners.

II. INFIELD MEASUREMENT

Experimental Study

In 2002, an experimental study of two long-span deep-corrugated reinforced steel box culverts were completed by Ingal Civil Company (Fig. 3). This study was the first of its type in Australia, and aimed to repeat the North American research for three different size structures subject to Australian vehicle live load and backfilling conditions. The results of this study will be used as additional validation of overseas design and installation methodologies. These results are focused on Australian conditions, and will be important in the development of future State and National road design specification and design standards. The research is of particular interest to the Australian Standards Committee CE25 which is charged with the current corrugated metal structures standards AS1762, AS/NZS2041 and AS3703.

Fig. 3: A long span deep-corrugated reinforced steel box culvert under testing by Ingal Civil Products, Queensland, Australia, 2002.

The study of the behaviour of culverts, composed of rib-stiffened corrugated structural plates, under the action of dead and live loads (Fig. 4). Finite element modelling techniques were applied to identify and analyse and reveal the most important aspects of the structural response of the culvert to loads applied during the soil backfill operation and the loads imposed by a test truck load driven over the culvert. The aim of the case studies was to model the behaviour of the two buried culverts tested by Ingal Civil Products using nonlinear finite element techniques. The modelling was carried out using the finite element package known as ANSYS and predicted several important characteristics of the culvert's performance, including the distribution of stresses and bending moments. One component of this research was to provide a validation of the FE models developed by comparing the numerical predictions with the in-field testing data supplied by Ingal Civil Products. In this comparison, two engineering examples of the deep corrugated reinforced steel culvert projects, the culvert 2H (large span, 10.5m) and the culvert 2G (medium span, 5.9m), have been used to identify important aspects of the structural behaviour of the stiffened steel culvert structures and their structural interaction with the surrounding soil.

Live Load

The live load effects constitute a fairly large proportion of the total load effects with relatively large spans and shallow depth of cover for the buried structure.

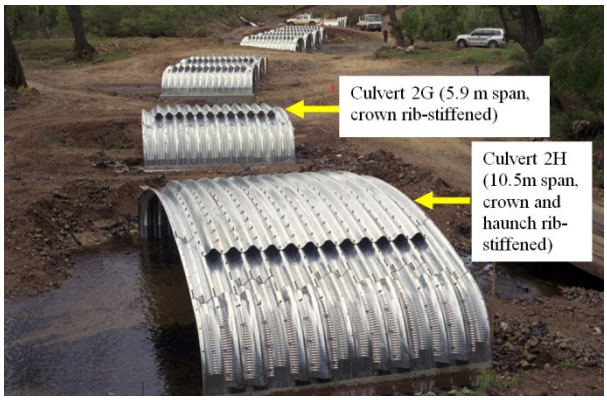

Fig. 4: The Mandalee Super-Cor rib reinforced corrugated steel box culvert structures, Queensland, Australia, 2002 (Ingal Civil Products)

III. STRUCTURAL ELEMENT OF SOIL-BURIED SHELL CULVERTS

The structural response of a soil buried shell culvert depends on the properties of its individual components as well as on the way in which these components interact. Because these components will form the primary building blocks of the finite element models. The material characteristics of soil are nonlinear, inelastic and highly dependent on the magnitudes of the stresses in the soil.

Nonlinearities of the Soil Material

The stress-strain characteristics of soil are nonlinear and inelastic. A soil model that is widely used is Duncan and Chang's nonlinear elastic (hyperbolic) model. This model has been applied in this study, and is described below.

The stress-strain diagram of Duncan and Chang's nonlinear elastic (Hyperbolic) model is shown in Fig. 5. According to Duncan and Chang's theory (Zhang, 2004) the stress-strain behaviour of soil becomes non-linear, particularly as failure conditions are approached. The soil modulus is a function of the confining stress and the shear stress that a soil is experiencing. This non-linear material model is attractive since it requires soil properties which can be obtained quite readily from tri-axial tests.

Duncan and Chang's non-linear stress-strain curve is a hyperbola in the deviatoric stress, $(\sigma_1 - \sigma_3)$, versus axial strain space ε. Depending on the stress state and stress path, three soil moduli are required; namely, the initial modulus, E_i the tangential modulus, E_t, and the unloading-reloading modulus, E_{ur} (Fig. 5).

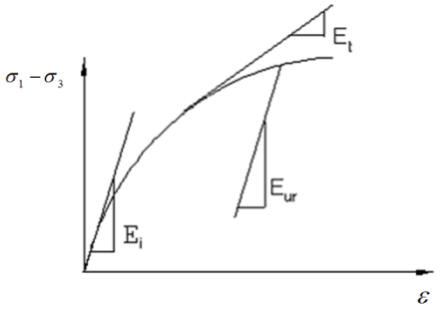

Fig.5: The non-linear stress-strain behaviour of Duncan and Chang's nonlinear elastic (hyperbolic) model

Duncan and Chang (1970) used Equation (1) to express the relationship between $(\sigma_1 - \sigma_3)$ and ε.

$$\sigma_1 - \sigma_3 = \frac{\varepsilon}{\frac{1}{E_i} + \frac{R_f \varepsilon}{(\sigma_1 - \sigma_3)_f}} \quad (1)$$

Where:

ε - Axial strain;

R_f - Failure ratio;

σ_1 - Major principal stress (kPa);

σ_3 - Minor principal stress (kPa);

E_i - Initial modulus (kPa).

Where R_f is the failure ratio, and generally $0.75<R_f<1.0$

$$R_f = \frac{(\sigma_1 - \sigma_3)_f}{(\sigma_1 - \sigma_3)_{ult}} \quad (2)$$

The initial modulus E_i varies with σ_3.

$$E_i = K P_{atm} \left(\frac{\sigma_3}{P_{atm}}\right)^n \quad (3)$$

Where:

P_{atm} - Pressure of 1 standard atmosphere (kN/m^2);

K - Dimensionless "modulus number".

According to the Mohr Colomb failure criterion,

$$(\sigma_1 - \sigma_3)_f = \frac{2c \cos \emptyset + 2\sigma_3 \sin \emptyset}{1 - sin\emptyset} \quad (4)$$

Where:

$\emptyset$ - Friction angle at a confining pressure of 1 atmosphere;

c - Cohesion intercept.

From Duncan and Chang's non-linear theory, the tangent modulus E_t can be calculated by:

$$E_t = \left[1 - \frac{R_f(1 - \sin \emptyset(\sigma_1 - \sigma_3))}{2(c \cos \emptyset + \sigma_3 \sin \emptyset)}\right]^2 K P_{atm} \left(\frac{\sigma_3}{P_{atm}}\right)^n \quad (5)$$

When forces act on a point in the soil, the resistance to squashing from the soil around the point is called the confining pressure (shown as in equation 1). For a given constant value of confining pressure, the value of the elastic modulus is a function of the percent of mobilised strength of the soil, or the stress level. In the FE analysis, the confining pressure is computed iteratively as part of the nonlinear solution.

For soils which are relevant to this research, numerical values of the parameters used in equation 1 are given in Table 1.

Table 1: Numerical values of soil parameters

Soil type	R_f	$\emptyset$	C	K
85% Standard proctor sand	0.9	33	0	200
95% Standard proctor sand	0.7	40	0	3000

Steel Arch

A typical steel arch is shown in Fig. 4 and 6. The steel culvert structure is assembled from corrugated steel plates. On its own, the steel arch is relatively flexible and hence large deformation can take place when the steel culvert structure is subjected to soil load and truck load. Therefore, geometric nonlinearities must be accounted for in the analysis of such flexible culvert structures. The corrugated steel plates give the arch greater strength in the longitudinal direction than in the transverse direction, therefore, it is orthotropic in nature and it exhibits different stiffness in two different orthogonal directions. Furthermore, if the length of the culvert is relatively short, for example, less than 10 m, the restraining effect of the concrete head walls must also be taken into account. In such narrow culverts, the results obtained from a two dimensional model are questionable, and a three dimensional FE model should be used.

Construction Sequence

During the construction procedure, the backfill soil is placed and compacted in layers. Hence the stress distribution of the soil may depend on the loading history. For this research, the construction sequence was accounted for in the finite element analysis.

Fig. 6: Compaction of the backfill soil

Soil-Steel Interaction

Relative movement occurs between the soil and the steel walls of the culvert during the construction procedure and under live load. Moreover, the friction between soil and steel may influence the structural behaviour of the culvert. In this thesis, the significance of soil-steel interaction was studied by comparing the results of two-dimensional analyses incorporating various soil-steel interaction parameters.

Orthotropic Material Properties of the Corrugated Steel Plate

Orthotropic materials exhibit different stiffness in three orthogonal directions. In the case of corrugated steel plates, the geometry of the wall provides greater stiffness in the longitudinal direction than in the transverse direction, as indicted in Fig. 7. If corrugated steel plates are to be simplified as plate finite elements, this difference in stiffness should be taken into account.

Corrugated steel plates and steel ribs can be modelled as an equivalent orthotropic plate. To utilise this method, the "real" axial and transverse bending stiffness of the corrugated steel plate was acquired from 2D and 3D FE models, as shown in Fig. 7.

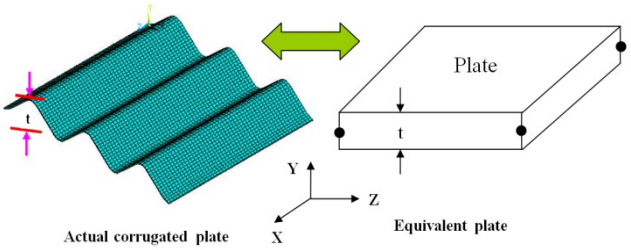

Fig. 7: The corrugated steel plate is simplified as a plate finite element

The approach involved applying a number of unit load cases causing axial and flexural deformation in the FE model of Fig. 8. The deformations obtained were then used to compute the equivalent bending stiffness components required.

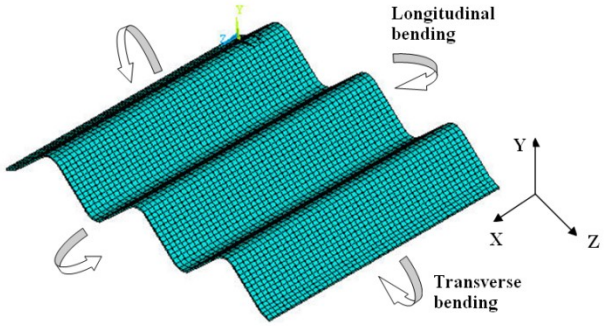

Fig. 8: Longitudinal bending and transverse bending direction

FINITE ELEMENT METHOD

The Plane Finite Element Model

In many instances 2 -dimensional finite element models have been used to idealise 3D structures because the computing requirements are reduced considerably. If the response of the structure in one of the three dimensions is insignificant or does not influence the response of the other two dimensions, then a plane analysis can be considered as a viable idealisation of the structure. Most finite element software packages include specially formulated plane elements for this purpose.

Finite Element Modelling of the Nonlinear Soil Material

The Duncan and Chang stress-strain law of soil is idealised in ANSYS using the multi-linear kinematic hardening model which approximates a curve as a series of short tangential lines. The stress-strain diagram adopted in the finite element analysis is shown as Fig. 5. The multi-linear kinematic hardening model, also called the sub-layer or overlay model, is used to characterise the material behaviour. The material behaviour is assumed to be composed of various portions, all subjected to the same total strain, but each sub-volume has a different yield strength. Each sub-volume has a simple stress-strain response but when combined the model can represent a complex behaviour. This allows a multi-linear stress-strain curve to exhibit the kinematic hardening effect.

The E_{Tk} in Fig. 9 is the slope of the kth segment of the stress-strain curve and is calculated as the tangential modulus Et of the Duncan and Chang's model.

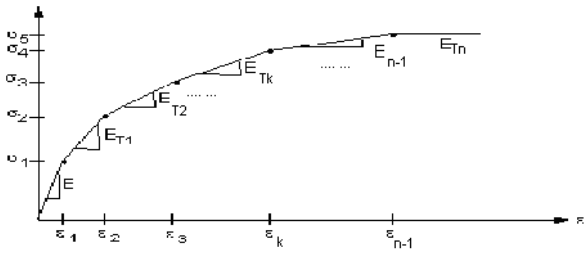

Fig. 9: Uniaxial behaviour for multi-linear kinematic hardening

IV. FIELD MEASUREMENT

Culvert Geometry

The tested culverts, comprise of a 5.9 m bottom span (2G) and a 10.5 m bottom span (2H) steel-soil bridge culverts assembled from curved corrugated plates on the work-site.

A total of 66 strain gauges were installed on the culverts, 36 on the large culvert (2H) and 30 on the medium size culvert (2G). The typical rib and barrel configuration of gauge installation are shown in Fig. 10 and 11 respectively.

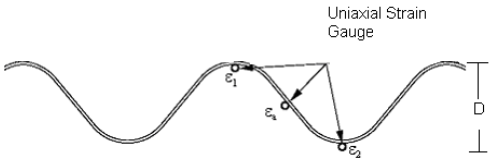

Fig. 10: Typical barrel strain gauge location (Ingal Civil Products)

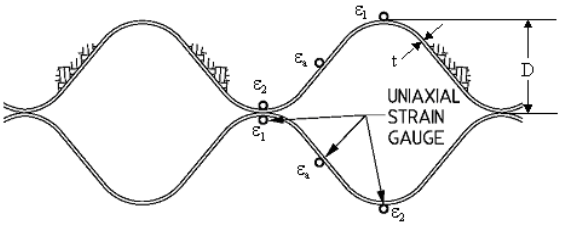

Fig. 11: Typical rib and barrel strain gauge location (Ingal Civil Products)

Three strain gauges were placed on the corrugated steel plate or corrugated steel rib at each testing location. These gauges were located at the neutral axis, outside crest and inside crest as shown in Fig. 10, 11, 12 and 13. The gauges were configured to measure the axial and bending strains. The neutral axis gauges were used to measure the axial strain. The outside and inside crest gauges were used to measure the bending strain. The strain values were then converted to the stress values.

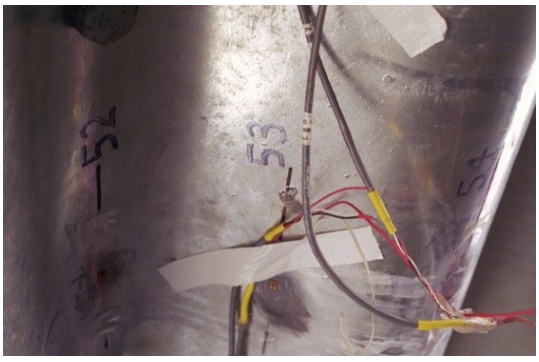

Fig. 12: Installation of strain gauges on barrel

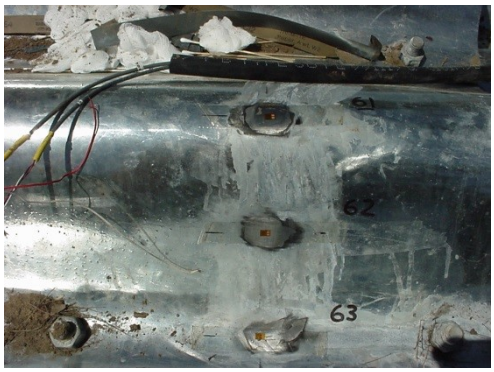

Fig. 13: Installation of strain gauges on a rib stiffener

Field Tests

Strains of the large and medium culverts that occurred during the backfill procedure testing were measured over several months. The measurement configuration resulted in a total of 12 axial and 12 bending strain channels on the large culvert 2H (Fig. 14), and 10 axial and 10 bending strain channels on the medium culvert 2G. All data was recorded on a Data-taker and a data logger, and were subsequently downloaded into MS Excel spreadsheets for data reduction purposes.

Backfilling Test

Backfilling operations were undertaken over the period 25th September – 19th November 2001. All channels were measured every 15 minutes from 25th September to 27th October for the large culvert (2H) and from 25th September to 17th October for the medium culvert (2G). Equipment limitations prevented data logging for the complete duration of backfill operations. Final strains were recorded on the 19th November prior to the loaded truck test and are included in the results.

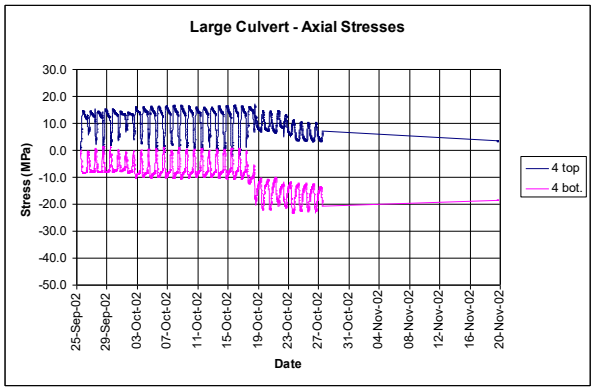

Fig. 14: Rib and barrel axial stress at Station 4 of culvert 2H (dead load only)

Static Truck Test – (Live load)

The culvert structures were tested statically under the loads imposed by a 45.2t truck (Fig. 15).

All channels were measured every second while a loaded truck passed slowly over the structures. The truck stopped as each axle was over the centreline of each culvert (an example is shown in Fig. 16).

Fig.15: Live load testing on the buried culverts

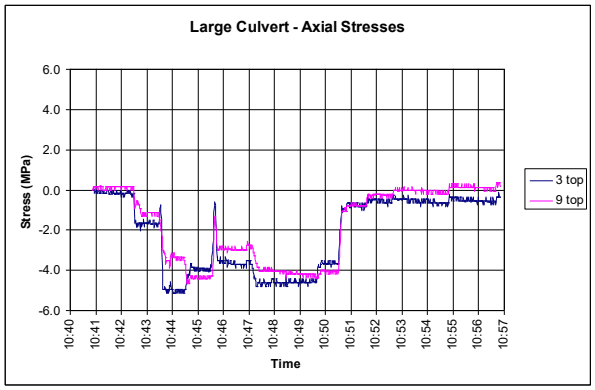

Fig. 16: Axial Stress of Large Arch (2H)

V. 2D FE Modelling and Analysis of Tested Culverts

Material Properties of the Backfill Soil

Backfill consisted of A-1 material (Deco gravel). The density was specified as a 90% standard density (before compaction).

Properties required for the FEA are listed in Table 2

Table 2: The soil properties of the Deco gravel backfill material (The density was specified as a 90% standard density) (Ingal Civil Products, 2002)

Soil Property	γ (t/m^3)	K	N	R_f	K_o	Ø
	2.0387	3000	0.93	0.7	0.5	40

After compaction the density of the back fill soil was specified as 95% standard density, equal to: 2.152t/m^3.

Poisson's Ratio ν was calculated from the at rest earth pressure coefficient K_o

$$K_o = \frac{v}{1-v} \qquad (6)$$

The value of $K_o = 0.5$, in Table 2 leads to $\nu = 1/3 = 0.3333$.

The tangent modulus E_t was calculated from Duncan and Chang's nonlinear theory by equation 5.

2D Finite Element Model

Soil buried culvert/pipe structures are often modelled using a 2D plane-strain finite element model. 2D models have the advantage of reducing the computing requirements considerably by eliminating one dimension from consideration. Two-dimensional models were developed to

simulate the behaviour of culverts 2G and 2H at a section approximately through the centreline of the road.

Finite Element Modelling of Steel Culverts

Steel culverts are assembled from corrugated steel plates. For this study these plates were modelled using standard beam finite elements. Since the culvert was strengthened near the crown with rib stiffeners, additional beam elements with "offset" capability were used to represent the stiffeners. The offset capability accounts for the eccentricity between the centre axes of the culvert and the stiffener elements.

Furthermore, the majority of rib-stiffener elements were rigidly connected to the steel culvert elements in the radial direction only. However, the first and last rib-stiffener elements were rigidly connected to the steel culvert elements in all directions. This was done to reflect the actual design at those locations. To account for the transfer of friction forces between the culvert and stiffener elements, special surface-to-surface contact elements were included in the FE model. A steel-to-steel friction coefficient of 0.7 was used.

FE Modelling of Bolt Connections

The connection between the plates near the crown and the two haunches (Fig. 17) is a slotted bolt connection which allows the plates to slide relative to each other along their axis (Fig. 18). Based on published research, this type of connection has the advantage of reducing the axial thrust in the culvert and hence improves its load carrying capacity (Abdel-Sayed, 1993).

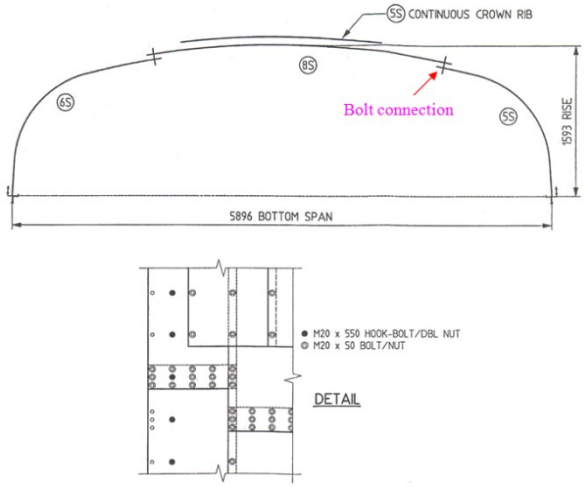

Fig. 17: The cross-section of steel plates and connection details of the culvert 2G

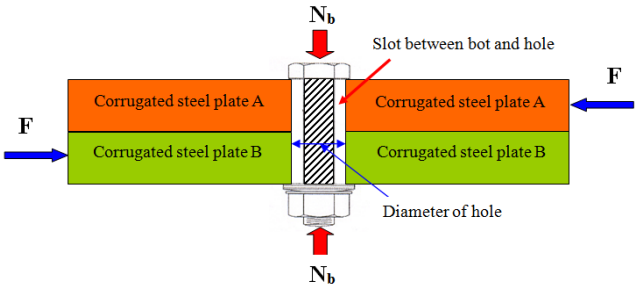

Fig. 18: The slotted bolt connection

The slotted bolt connection was modelled using the arrangement depicted schematically in Fig. 19. Two adjoining beam elements were linked at the connection point with a gap between their end nodes. The gap length was either 1.5mm or 2.5mm depending on the length of the slot. The nodes were coupled rigidly but were released to move relative to each other in the axial direction only. A node-to-node contact element was inserted to connect the two nodes in such a way that they transfer the full axial force in the two beams once the gap (contact length) has been closed. A non-linear axial link or beam (pin-ended bar) was inserted between the nodes to prevent initial instability in the axial direction during the finite element solution. The non-linear load-deflection relationship of the link/beam as modelled in ANSYS is depicted in Fig. 19. Its material nonlinear stress-strain relationship is shown in Fig. 20. The load deflection behaviour of the entire connection for axial action is shown in Fig. 21. It can be seen that while the real connection would experience a relative deformation along ODBC, the modelled connection would deform along path OABC. It is assumed that the difference will have no significant bearing on the end result.

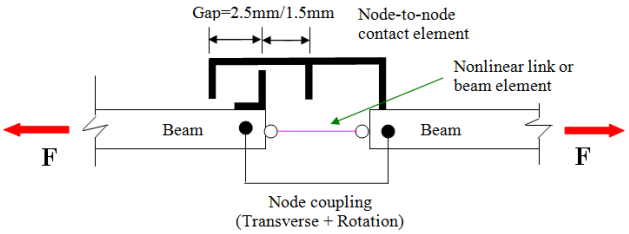

Fig. 19: The FEA simulation of the slotted bolt connection

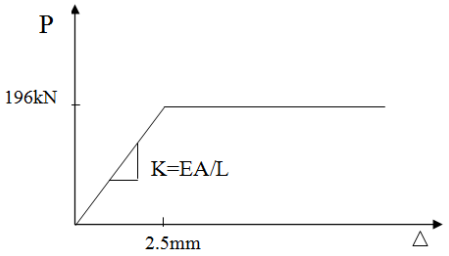

Fig.20: The non-linear load-deflection relationship of the link/beam element

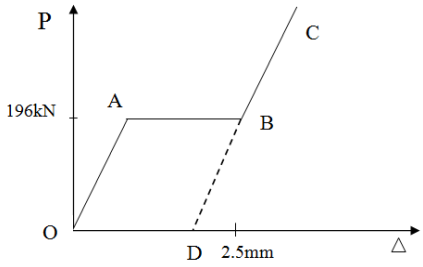

Fig, 21: The load deflection behaviour of the entire connection for axial action

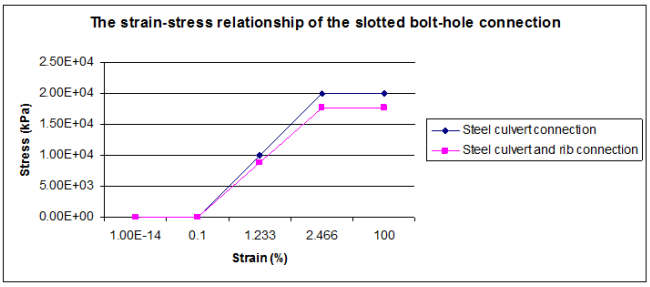

Fig. 22: The strain-stress diagram of the slotted bolt-hole connection (based on the Elastic-perfectly plastic model)

FE Modelling of Backfill Soil and Pavement

The Deco Gravel backfill soil material has been idealised using the Duncan and Chang nonlinear model. For the finite element model the backfill was represented by 8-noded plane strain elements, with the density of backfill soil, $\rho = 2.0387$ t/m^3 and elastic modulus $E_{soil} = 20{,}000$kN/m^2. The pavement material was also idealised by 8-noded plane strain elements but with linear elastic material. The following properties were adopted: density of pavement, $\rho = 2.445$t/m^3 and elastic modulus, $E_{pavement} = 1000{,}000$kN/m^2. The mesh of the finite element models of culverts 2H is shown in Fig. 23.

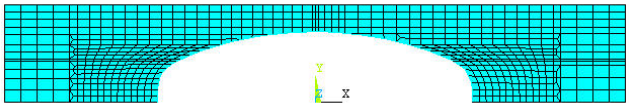

Fig. 23: The mesh of the finite element model of culvert 2H

Soil-Steel Interface

The interface between steel culvert and backfill soil was modelled using surface-to-surface contact elements with a friction coefficient of 0.36. These contact elements allow compression between the two surfaces to be transferred but do not transfer any tension.

VI. Solution of the 2D FEA Model and Comparison with Field Measurements

To validate the 2D FE models used later for parametric studies and to establish the accuracy of FE results, a comparison with in-field testing undertaken by Ingal was made.

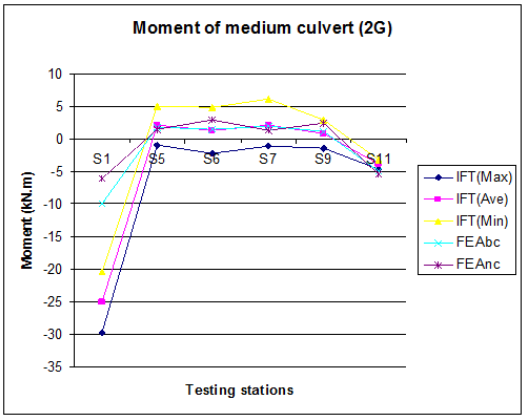

Fig. 24: Moment of medium culvert 2G (dead load only)

The results of analysis of the two 2D FEA models, FEA_{bc} and FEA_{nc}, for the self-weight of soil were in reasonable agreement with the averaged results of the in-field testing. The results of the FEAbc model (with bolt connections) were better than the results of FEAnc (without bolt connections), particularly near the ends of the culvert (stations S1-S3 and S9-S11). The results of axial force and bending moment of the two FEA models at each station were close to the average value of the in-field testing. They also fell between the maximum and minimum results of the in-field testing. Hence, the 2D FEA results of the self-weight of soil from ANSYS nonlinear analysis are acceptable.

The 2D FEA model in this investigation successfully simulated the bolt connection with slot and slippage using a node-to-node contact element and a nonlinear link or beam element, as shown in Fig. 19. This is proven by the computed results of FEA1 at station 3 and station 5 which are close to the measured results IFT (Ave). In the research work done by Byrne, Srithar, Kern (1990) and McCavour (1998) it was found that the predicted thrust value of the 2D FE model did not fall within the result from field measurement when the backfill height exceeded 10m from the footing or 3m above the crown. Any further increase in the depth of soil does not significantly increase the stresses for the real situation, whereas the predicted stress in the 2D FE model continues to increase significantly. Byrne, et al (1990) hypothesised that the sudden drop in the measured build-up of thrust is due to the slippage at the bolted connections causing a drop in the effective stiffness of the arch. This slippage was accounted for in analysis by reducing the axial stiffness of the structural members while maintaining their bending stiffness. In their work, a 50 fold reduction in the elastic modulus value of the steel plate was used to calculate the steel culvert's thrust for the bolt-hole slippage. Although they obtained better results by reducing the elastic modulus value, their modelling was still unable to simulate the higher thrust stresses at the locations of the bolt connections.

In this research, the effect of bolt connection slot was successfully modelled using the mechanism explained previously and by using beam elements with nonlinear material property. The hoop thrust results were in reasonable agreement with the results of the in-field testing. However, some of the in-field testing stations were located very close to the bolt connection at the barrel or the rib stiffeners, causing some measured data to differ greatly from the FEA prediction.

Solution using the 2D FEA Model under Truck Load

In recent years, many researchers have found that the solution under live load in the 2D FEA model does not agree with the results of in-field measurements, especially for small longitudinal breadth culverts (e.g. McGrath, 2002). The primary reason for this is that 2D plane strain FE models ignore the influence of the boundary condition of the third dimension. The third dimension's boundary condition can greatly influence the results of a FE model, especially for small longitudinal breadth culverts. In this section, the live load results of the 2D FEA model were used to confirm the inadequacy of 2D analysis for truck load conditions.

The static live load of the truck was applied to the soil buried culvert structure more than one month after the backfill procedure finished. Furthermore, a thickness of 200 mm asphalt concrete pavement of the road was laid on the top of the backfill layers. The data loggers were reset to zero before the truck load testing, hence, results from the in-field testing only indicate the live load.

The 2D FEA model was used to simulate the response of the culvert when subjected to the truck load. Comparing the results from the in-field measurement and FEA, it is concluded that:

The results of the truck load in the 2-D finite element analysis do not agree with the results of the in-field measurement in terms of its axial force diagrams. The results at each station are very different. The absolute values of FEA at most of the stations were bigger than the values of in-field testing. The results of the bending moment of the truck load in the 2D FEA model have different diagram shapes to the in-field measurement. For example, the value at the crown of the 2D FEA was more than 3 times than the results of the in-field measurement. This situation was also be found by American researchers (McGrath, 2000), who believed that this feature

was caused by the live load which exhibits three-dimensional behaviour. Hence, the 2D FEA method is not suitable to analyse the bending moment of large span culverts. It is also observed that the experimental results are symmetric, which is inconsistent with the truck load being applied non-symmetrically. The reason for this discrepancy could not be established from the available experimental records.

VII. 3D FE Modelling and Analysis of Tested Culvert

The live load testing of 2D FEA models showed anomalies between the 2D FEA results and the in-field measurements. The 2D FE models were used to idealise the 3D structure. However, all real structures are three dimensional. Although eliminating one dimension has the advantages of reducing the computing requirements, it may lower the accuracy by not considering the boundary conditions in the out-of-plane dimension. Usually, there are two kinds of boundary condition in the out-of-plane direction: one with the two edges of the culvert fixed by concrete headwalls, as shown in Fig. 25 and 26, (rigid or semi-rigid edge boundary condition); the other with free end boundary conditions.

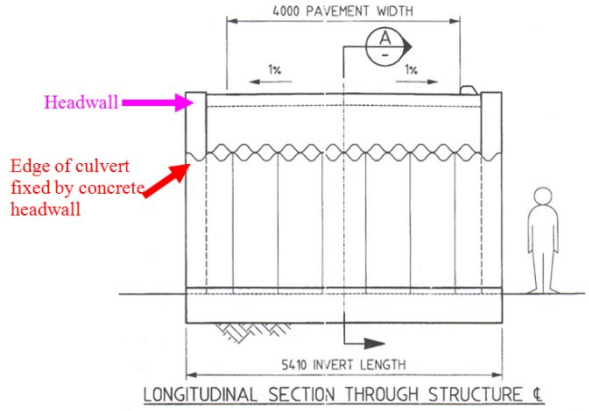

Fig. 25: Longitudinal section through culvert 2H (Ingal Civil Products, 2002)

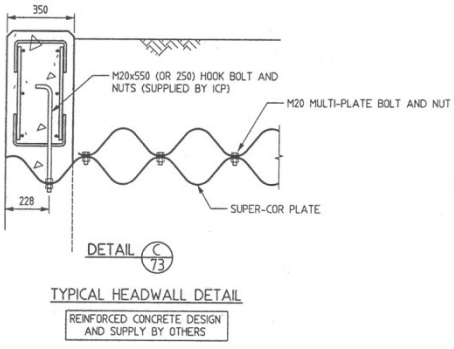

Fig. 26: Typical headwall detail - Edge of culvert fixed by concrete headwall (Ingal Civil Products, 2002)

Influence of Boundary Conditions

To study the influence of boundary conditions in the out-of-plane dimension, a 3D FEA model of the medium span culvert 2G was created and studied. The 3D FE model was created using 3D shell elements.

Two sets of boundary conditions in the z-direction were applied to the finite element model. In the first set, only the z-direction displacement was constrained, simulating a 2D out-of-plane boundary condition. In the second set, all degrees of freedom were fixed, reflecting the capability of 3D modelling. The second set represents the same boundary conditions as the real culverts, in which the two edges of the corrugated steel plate forming the culvert are connected to the two side walls.

From the FEA results it can be seen that the boundary conditions of case 2 produced a lower vertical displacement and a higher stress under the live load compared to case 1. Hence, the results in the 3D FEA model more closely represent the real situation than the 2D FEA model. These results demonstrate that the boundary conditions at the edges of the culvert do influence the accuracy of the model. Boundary condition case 2 (fixed) is representative of the restraint in culvert 2G and 2H and was therefore adopted for analysis of live loads. 2D models do not have the capacity to model these boundary conditions, and therefore a 3D FEA model is more accurate.

Modelling the Corrugated Steel Plate as an Orthotropic Shell

The material properties of the corrugated steel plate are different in transverse and longitudinal direction (orthotropic material). In addition, there are two types of stiffness in two-orthogonal directions. They are the membrane and bending stiffness. The corrugated steel plate can be modelled using shell elements with equivalent material properties which are the same as the corrugated steel plate. Therefore, both the equivalent membrane and bending elastic modulus of the shell element need to be determined. The procedure used to determine the equivalent orthotropic properties for corrugated sheets are described as follows (Zhang 2004):

- Create a small-scale finite element model of the corrugated sheet, including explicit modelling of the corrugations.
- Apply unit forces and obtain the corresponding displacements.
- Calculate the stiffness as: Stiffness = force / displacement.
- Calculate the equivalent material properties for the flat orthotropic shell element.
- Check the equivalent material properties by creating a small-scale finite element model of the corrugated sheet using flat orthotropic shell elements. The applied forces should give the same displacements, or very similar as for the explicit model.
- The equivalent material properties and flat orthotropic shell elements can then be used in a large-scale model to simplify the geometry/mesh and the analysis.

- Calculating the corrugated steel plate bending properties

To establish the corrugated steel plate bending properties, both hand calculations and finite element analysis was required. The longitudinal bending properties were relatively simple to determine from formulas. The transverse bending properties were calculated based on a three point static load test simulated by 2D finite element models. The FEA models of the three point bending test of 7mm thickness steel plate, 6mm thickness steel plate with a 4mm thickness steel rib.

From the 2D FEA models (an example is shown in Fig. 27, the displacement of a 3-wave plate length was obtained and used to calculate the longitudinal elastic bending modulus.

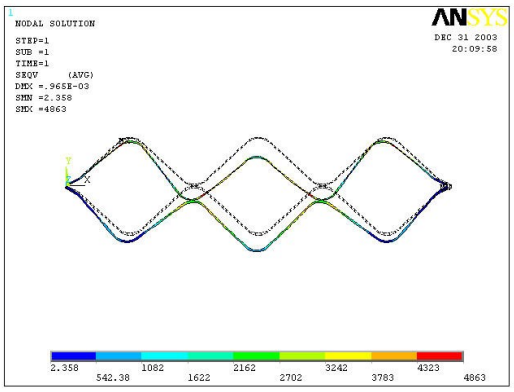

Fig. 27: The stress and deformation diagram of the three point bending test FEA model (the 6mm steel plate + 4mm steel rib)

- Calculating the corrugated steel plate membrane properties

To calculate the corrugated steel plate membrane properties, once again both hand calculations and finite element modelling were required. The longitudinal membrane properties were calculated based on formulas and combined with finite element modelling. The transverse membrane properties were calculated based on the results of the finite element models.

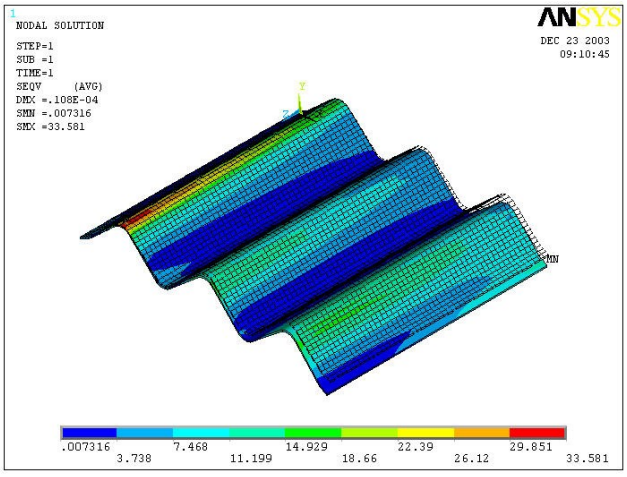

Fig. 28: The stress and deformation diagram of the transverse membrane strength test model (3-D finite element)

- Equivalent material properties of the shell element

The material properties of the shell element are summarised in Table 3.

Table 3: The equivalent material properties of the shell element

	Membrane characteristics (kPa)			Bending characteristics (kPa)		
	E_X	E_Z	G_{XZ}	E_X	E_Z	G_{XZ}
7mm steel plate	1.335E7	1.41E3	5,14E6	4.8E7	6.68E3	5.7E5
6mm steel plate+4mm steel rib	1.005E7	1.64E3	4,16E6	9.3E7	1.39E3	1.13E5
7mm steel plate+7mm steel rib	1.335E7	4.71E3	5,14E6	1.2E7	4.22E3	2.25E5
7mm steel plate+6mm steel rib	1.265E7	3.70E3	4.87E6	1.2E7	3.3E3	1.95E5

Shell Modelling of Corrugated Steel Plate

The corrugated steel plate was modelled using shell elements. After study of the orthotropic properties of the corrugated steel plate, a shell model using the calculated orthotropic properties was then created, and the results compared with that of a solid model. However, ANSYS elements do not support orthotropic properties that are different in bending and membrane elastic modulus. ANSYS requires a combined bending and membrane stiffness to be entered as a single set of modulus of elasticity values. To overcome this problem, it was decided to overlay two SHELL63 elements, one with bending stiffness only, the other with membrane stiffness only.

The SHELL63 element is capable of incorporating either the bending or membrane stiffness separately, or both the bending and membrane stiffness combined. This was done by merging the nodes of the two overlaying shell elements. To ensure both overlayed elements shared common nodes, any applied load to the elements was evenly distributed. The only limitation found was that a true stress could not be plotted, as the culvert was simulated by two different layers of shell elements. One layer carried only membrane forces and the other layer carried bending moment. In the stiffened sections, the steel barrel and the ribs were connected by SHELL63 elements with equivalent properties.

Validating the Calculated Corrugated Steel Plate Properties

To validate the calculated orthotropic properties of the corrugated steel plate, a series of analyses were carried out using ANSYS. The validation process was to essentially simulate laboratory testing using the FEA model and compare the hand calculated deflection with the deflection returned by the FEA model.

By comparing the deflection of the shell model to the calculated results, the effectiveness of the shell model could be gauged. The solid model was first analysed to ensure that the constraint method used was suitable and returned consistent results. Details of the results of the solid model of the corrugated steel plate are presented below.

Creating the 3-D Finite Element Model

Four types of finite elements were used to create the 3-D model for the culvert 2G. These were the SHELL63 elastic shell element to simulate the corrugated steel plate described earlier, the SOLID95 3-D 20-Node structural solid element for the backfill soil, the 3D TARGE170 element and the 3D CONTA174 element to simulate the interaction surface between the steel plate and backfill soil. The friction between soil and steel was simulated using a friction factor of 0.36 for the contact elements.

- 3D Soil Elements

Similar to that of the 2D FEA model the soil material in the 3D FEA model was idealised as nonlinear material, as proposed in the Duncan and Chang model. This was represented in the finite element model by the 3D SOLID95 20-node structural element. In addition, the interaction surface of the steel plate and backfill soil was simulated by the TARGE170 element and the CONTA174 element. The friction factor of the contact surface was 0.36. Since the two edges in the out-of-plane direction of the corrugated steel arch were bolt-connected with the two head walls it was necessary to consider the boundary conditions in the FEA model. This was accomplished by fixing all translational degrees of freedom at both ends.

The mesh of the 3D finite element model of the medium span culvert 2G is shown in Fig. 29.

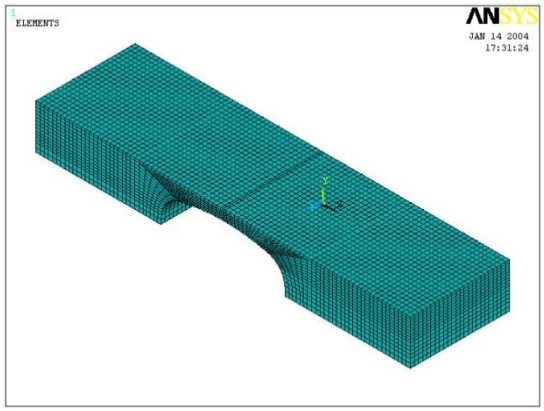

Fig. 29: 3D finite element mesh of culvert 2G

Solution Validation of 3D FEA Model

To validate the FE models both culverts 2G and 2H were analysed under dead and live load conditions.

- Analysis of 3D FEA Model under Self-weight of Soil (Dead Load)

The solutions of self-weight of soil using the FEA model for culvert 2G were compared with in-field test results in Queensland, as shown in Fig. 30.

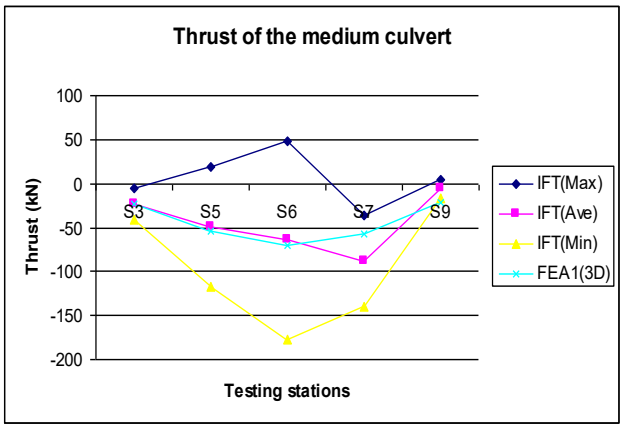

Fig. 30: Thrust of medium culvert 2G (dead load only)

Comparing the results for self-weight of soil for 3D FEA and in-field testing, it is concluded that most results from the 3D FEA for both the axial force and bending moment at each station are very close to the average value of the in-field testing. Anomalies between the in-field testing and 3D FEA results at the edges may be due to bolt slippage and/or inaccuracies in in-field data recording. In addition, almost all the results from the 3D FEA fall between the maximum and minimum values of the in-field testing. As a result, the 3D FEA modelling of the self-weight of soil from ANSYS nonlinear analysis is acceptable.

- Solution of 3D FEA Model under Truck Load (Live Load)

The results of truck load using the FEA model for culvert 2G were compared with the Ingal in-field testing results, as shown in Fig. 31 and 32.

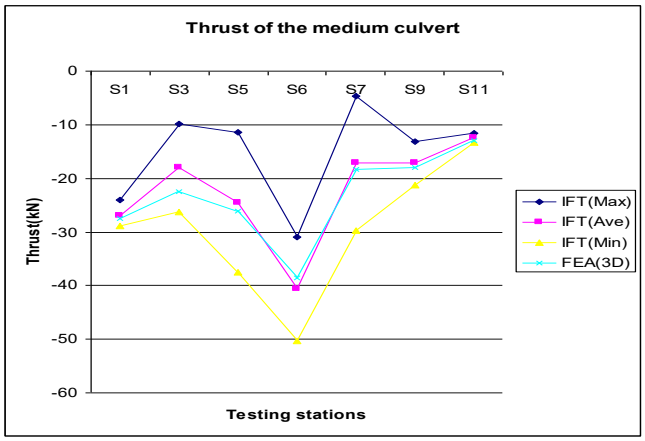

Fig. 31: Thrust of the medium culvert 2G (live load only)

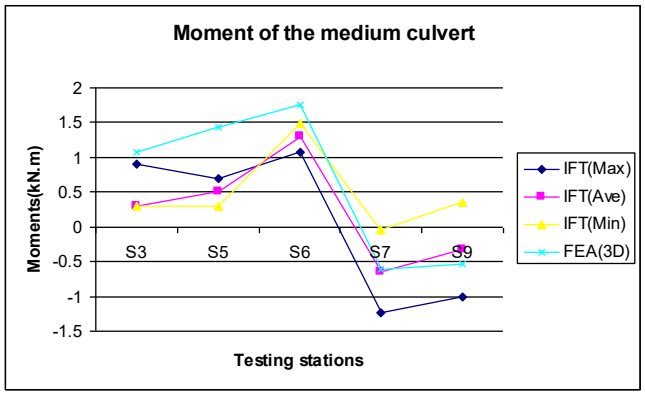

Fig. 32: Moment of the medium culvert 2G (live load only)

Comparing the results from the in-field testing and 3D FEA model leads to the following conclusions:

The results from 3D FEA for both axial force and bending moment at each station are close to the average value of the in-field testing. In addition, all the results of axial force results fall between the maximum and minimum values of the in-field testing. Hence, the 3D FEA modelling of the truck load from ANSYS nonlinear analysis is acceptable. However, some of the in-field testing stations were located very near to the bolt connections at the barrel or the rib stiffeners, which caused some bending moment data to be significantly different from the FEA prediction.

The results of the 3D model under of the self-weight of soil and truck load lead to the following conclusions: The solution of the self-weight of soil and the truck load in the 3D FEA models are in good agreement with the results of in-field testing. Both the axial force and bending moment at each station are very close to the average value of the in-field testing. It is apparent that most results of the 3D FEA fall between the maximum and minimum values of the in-field testing. Hence, the 3D FEA model can be used to simulate the self-weight of soil and truck load for the steel culvert.

VIII. Parametric Study Using Calibrated FE Models

Various studies have been undertaken to examine the performance of buried culverts, and to investigate the ability of numerical models to predict the in-field response.

The results have indicated that the finite element predictions obtained in this study agree reasonably well with solutions reported independently. The predictions also appear to be reasonable when compared to the results of field

measurements. These findings provide confidence in the use of the numerical model to explore different conditions, and to assess the sensitivity of results to different material and structural properties.

Effect of Soil Elastic Modulus and Density

The material characteristics of soil are nonlinear, inelastic and highly dependent on the magnitudes of the stresses in the soil. The two main properties of backfill soil that can influence the behaviour of a culvert are the elastic modulus, E, and the soil density, ρ. Both these values are dependant on the quality of soil compaction. The E value of backfill soil has a wider range, between 200,000 to 20,000 kPa for sand and gravel material. The density is less variable, ranging from 1.867 t/m^3 (for very loose soil) to 2.152 t/m^3 (for well compacted soil).

Four FEA models were considered with different E values of backfill soil to perform the parametric study (dead load only), as shown in Fig. 4. The corresponding densities are presented in Table 4. In general, E values ranged from an upper bound for well compacted soil zones to a lower bound for poor compaction. For the special case of very loose soil in the ring zone around the arch an E value of 2,000 kPa was used. The FEA1 model was used to simulate the condition of a very good compaction procedure. In FEA2, as shown in Fig. 33b, the lower bound E value of backfill soil at zone 2 (the middle of the structure) was 20,000kPa, which was used to simulate a lower quality Deco gravel soil compaction procedure. In FEA3 (Fig. 33c), the E value of backfill soil at zone 3 (ring zone around the arch with a thickness from 50mm to 200mm) was 2,000kPa. This simulates the soil in a very loose condition. The E value at all other locations was the same as FEA2. The very loose soil condition was chosen because the backfill soil surrounding the arch is often poorly compacted as it is difficult to achieve good compaction by machine or hand in that area. In FEA4, the E value for the lower bound of value 20,000kPa was used in all zones.

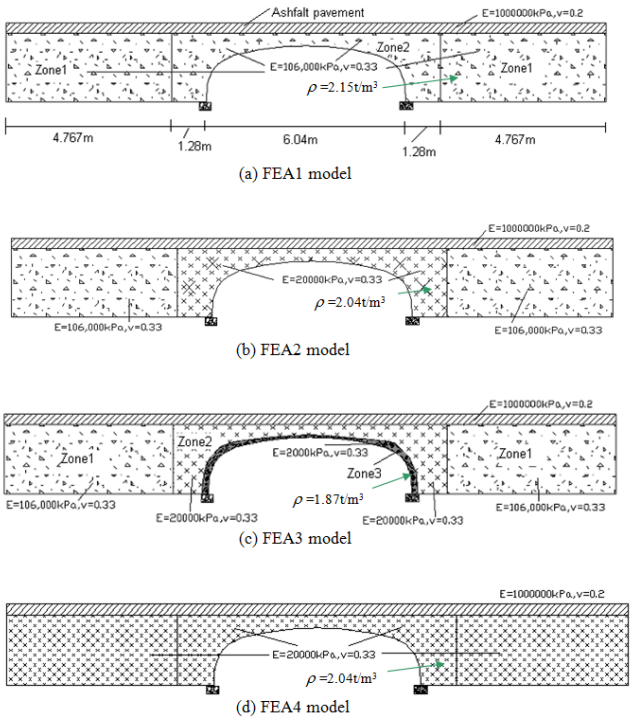

(a) FEA1 model

(b) FEA2 model

(c) FEA3 model

(d) FEA4 model

Fig. 33: Four FEA models with different initial elastic modulus value E

The density of soil and their relative E values are shown in Table 4.

Table 4: Elastic modulus and density values for different soil compaction

	Elastic Modulus, E (kPa)	Soil Density, ρ (t/m^3)
Upper bound (good compaction)	106,000	2.152
Lower bound (poor compaction)	20,000	2.0387
Special (very loose)	2,000	1.867

- Predictions of culvert axial force

Fig. 34 shows the hoop thrust distributions predicted by FEA1, FEA2, FEA3 and FEA4.

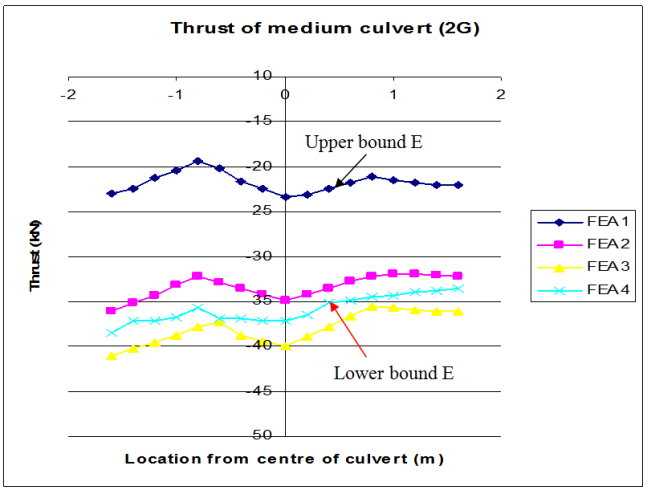

Fig. 34: Hoop thrust of medium culvert 2G (self-weight of soil)

In each model, the maximum hoop thrust forces were located at the crown part and the minimum values were located at the haunch. The maximum value from the upper bound E was 37% less than the lower bound, and the minimum value from the upper bound E was 39% less than the lower bound. It is apparent that good compaction of the backfill soil (upper bound E value and higher density ρ) caused a significantly lower circumferential axial force than the lower bound E value. In addition, the hoop thrust forces from the FEA3 model were the highest, and it was 6.8% higher than the lower bound. It is apparent that the lower E value and density of the backfill soil in the thin ring zone around the culvert has a slight effect on the overall axial force distribution on the culvert. This is due to two main reasons: firstly, the thinness of the ring zone (50 to 200mm) which means that the influence of the varied density is minimal; and secondly, the density change in these two models was small (less than 10% change). Since, from the FEA results, the maximum hoop thrust force was located at the crown part, it is hypothesized that a rib-stiffener added to the crown would decrease the circumferential axial stress.

- Predictions of Culvert Bending Moments

The bending moment distributions predicted by the FEA models are shown in Figure 35.

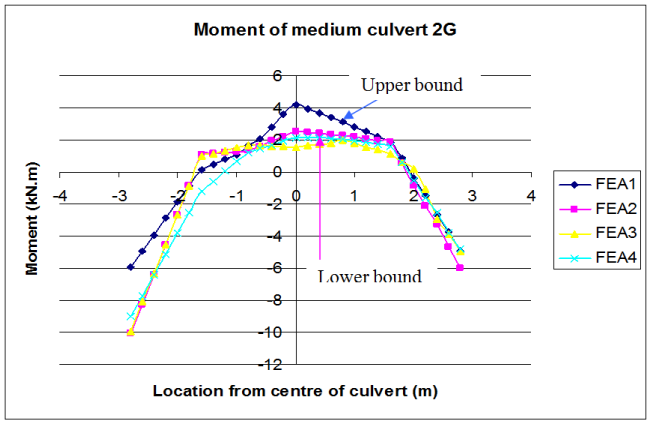

Fig.35: Bending moment of medium culvert 2G (self-weight of soil)

For both the lower bound and upper bound cases, the maximum positive bending moments were located at the crown and the maximum negative values were located at the sides. However, the maximum positive value from the upper bound E was approximately two times higher than the lower bound, whereas, the maximum negative value from the upper bound E was approximately 30% lower than the lower bound value. It is apparent that good compaction of the backfill soil (upper bound E value) caused a higher positive bending moment at the crown. This result seems to be counter intuitive and would require further investigation to confirm or explain the cause, which maybe attributed to the relatively higher soil density above the crown area. It is hypothesised that a rib stiffener added to the crown would decrease the bending moment. It is also observed that the results are non-symmetric although the soil loading itself is symmetric. This non-symmetry is attributed to the inclusion of bolt hole connections which are located non-symmetrically.

- Predictions of Culvert Deformation

Table 5 shows horizontal (x) and vertical (y) displacement of the medium culvert 2G for analysis corresponding to FEA1, FEA2, FEA3 and FEA4.

Station	Direction	Displacement (mm)			
		FEA1	FEA2	FEA3	FEA4
1	x	-0.016	0.06	-0.28	0.06
3	y	-1.3	-2.1	-2.6	-2.2
5	y	-1.9	-0.25	-9.8	-0.21
6	y	-2.4	-3.6	-9.3	-3.7
7	y	-3.1	-5.2	-8.8	-5.3
9	y	-1.5	-2.6	-7.8	-2.7
11	x	-0.06	-0.13	0.52	-0.13

Note: x- horizontal displacement, y-vertical displacement.

Table 5: The comparison of the displacement for the medium culvert structure 2G

The comparison of displacement for the four FEA models leads to the following two primary conclusions: The lower E value used in FEA2 and FEA4 in zone 2 has caused up to 68% larger horizontal and vertical displacements. This suggests that for medium span culverts displacement is sensitive to changes in E value. FEA3 which models inadequate backfill compaction in the area surrounding the culvert shows that both the vertical and horizontal displacements are three times higher than the results from the FEA1 and FEA2 models. Evidently, the input of a very loose soil condition has a significant effect on the behaviour of the model, which can be attributed to the higher flexibility of the surrounding ring of soil. Due to the lack of experimental data it was not possible to calibrate or validate the model for displacement, and this effect should be the subject of future research.

Effects of the Slotted Bolt-Hole Connections

The steel plates and connection details of the steel culvert structure are shown in Fig. 36. In recent years, various researchers (e.g. Zhang, 2004) have found that the thrust stress in terms of the ring compression in deep embankment fill reduces if there is a larger gap between the bolt and hole in the corrugated metal culvert.

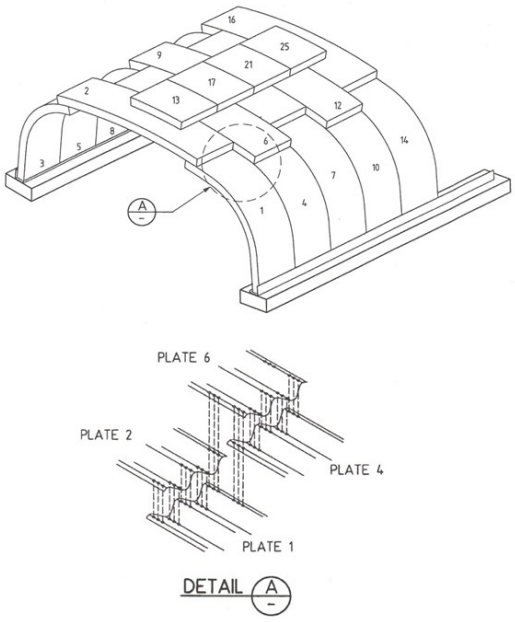

Fig. 36: Steel plates and connection details of the steel culvert structure (Ingal Civil Products)

FEA models with and without simulated bolt connections were used to study the influence of the connections on the hoop thrust and bending moment. A finite element model (denoted FEA_{bc}) was used to simulate the influence of bolt connections, while model FEA_{nc} was used for simulations without bolt connections. The comparison of results between FEA_{bc} and FEA_{nc} are shown in Fig. 37 and 38.

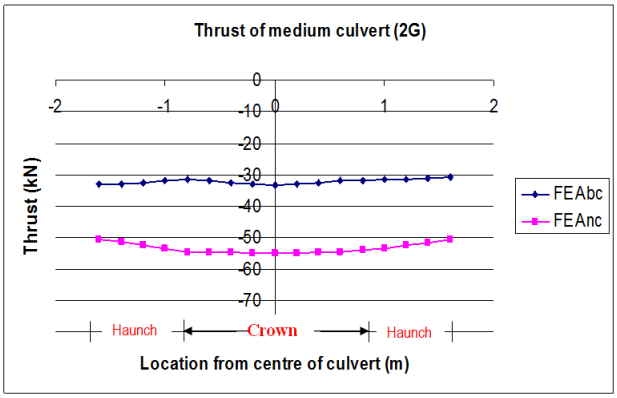

FEAbc ---- with slotted bolt connections
FEAnc ---- without slotted bolt connection

Fig. 37: Hoop thrust of medium culvert 2G (Soil load)

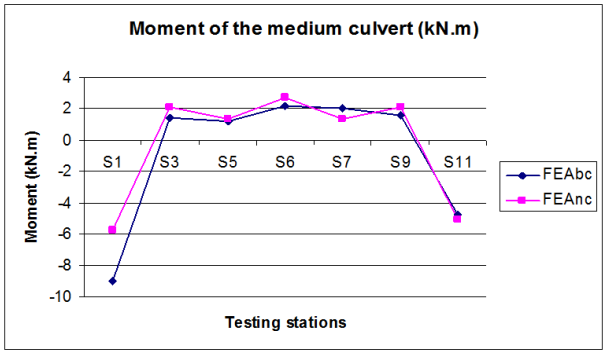

FEAbc ---- with slotted bolt connections
FEAnc ---- without slotted bolt connections
Fig. 38: Bending moment of medium culvert 2G (Soil load)

Fig. 37 show the average hoop thrust value of the model without simulation of bolt connections was higher than the model with the simulation of bolt connections at all testing stations. The slotted bolt connections reduced the effective hoop thrust by approximately 40% compared with results of non-slotted bolt connection. However, the effect of slot and slippage in the connections in terms of its bending moment was very small (Fig. 38) with the two moment diagrams for FEA_{bc} and FEA_{nc} closely matched. It is obvious that the bolt connections have a significant effect on the hoop thrust distribution of the structure.

Effects of Rib-Stiffeners

Recently, structural designers specified the use of rib-stiffeners for several sections of culverts to enhance load-carrying capacity and to reduce tunnel deformations. Zhang (2004) reported that rib-stiffeners affected the structural behaviour of the culvert/pipe, as indicated by the circumferential strain, bending stress and hoop stress.

The sensitivity of the culvert performance to the use of rib stiffeners is of significant interest. Predictions of the circumferential stresses and bending stress of the structure have been made for culvert structures without rib-stiffeners under the backfill soil load and truck load by 2D and 3D FEA models. These results were used to perform a comparison with the culvert 2G with a 4 mm thick rib stiffener. The results are shown in Fig. 39 to 9.14. FEAr denotes the model with rib stiffeners, while FEAnr represents models without rib stiffeners.

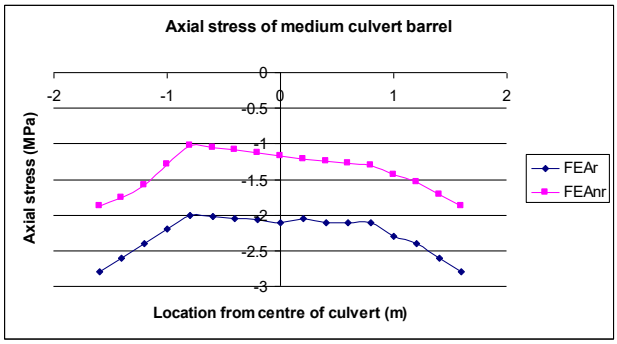

FEAr ---- with rib-stiffeners
FEAnr ---- without rib-stiffeners
Fig. 39: Hoop stress of medium culvert barrel 2G (self-weight of soil)

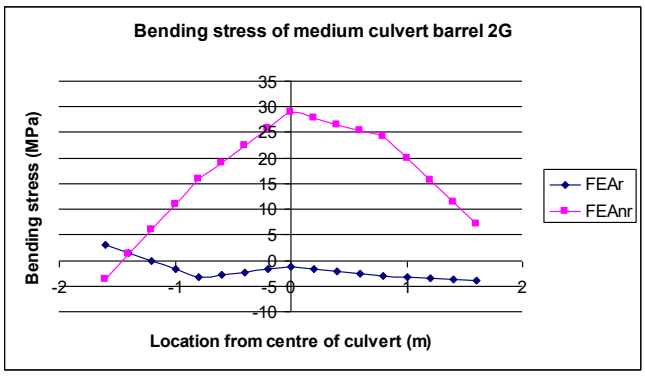

FEAr ---- with rib-stiffeners
FEAnr ---- without rib-stiffeners
Fig. 40: Bending stress of medium culvert barrel 2G (self-weight of soil)

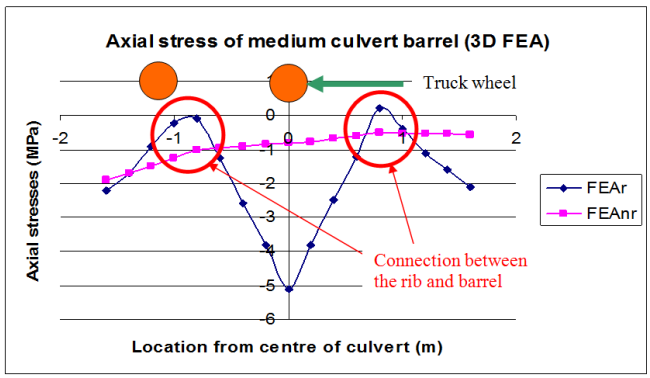

FEAr ---- with rib-stiffeners
FEAnr ---- without rib-stiffeners
Fig. 41: Hoop stress of medium culvert barrel 2G (Truck load)

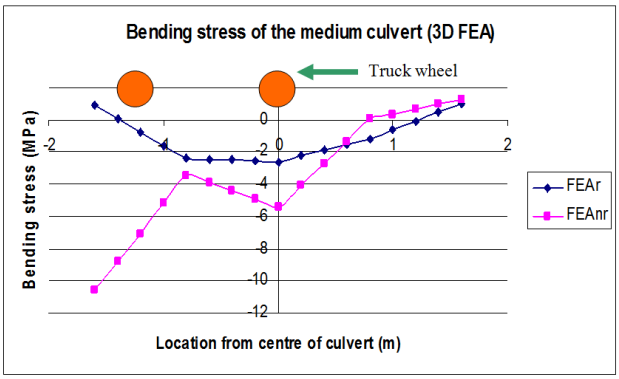

FEAr ---- with rib-stiffeners
FEAnr ---- without rib-stiffeners
Fig. 42: Bending stress of medium culvert barrel (Truck load)

Fig. 39 shows that for dead load conditions (self-weight of soil) the axial stress of the barrel of the culvert actually increased (by a factor of two) when rib stiffeners were included. Fig. 40 show that the inclusion of rib stiffeners dramatically decreased bending stress in the barrel of the culvert for dead load conditions. It should be noted that the bending stress is significantly larger than the axial stress in culverts, and that rib stiffeners are a very effective means of reducing these bending stresses.

Fig. 41 shows that the inclusion of rib stiffeners significantly increased the compressive axial stress in the barrel of the culvert under the truck wheels. (Truck load is approximately uniformly distributed on the culvert). The connections between the rib and barrel provide some extension, which accounts for the two bumps in the graph at

approximately one metre each side of the centre of the culvert. Fig. 42 shows that the inclusion of rib stiffeners decreases the bending stress of the culvert barrel under the truck wheels.

Fig. 43 to 45 show the combined stresses (axial + bending) for culverts with and without rib stiffeners. Dead load, live load and combined dead + live loads have been considered.

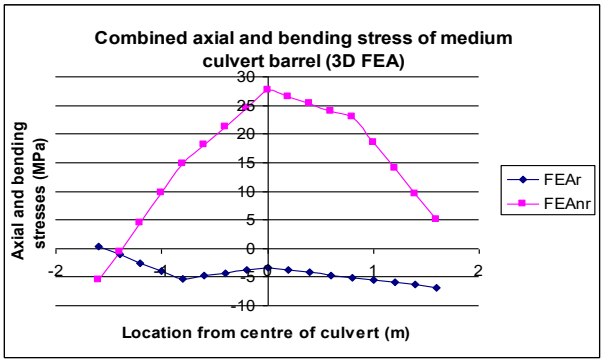

FEA_r ---- with rib-stiffeners
FEA_{nr} ---- without rib-stiffeners
Fig. 43: Hoop and bending stress of medium culvert barrel 2G (self-weight of soil)

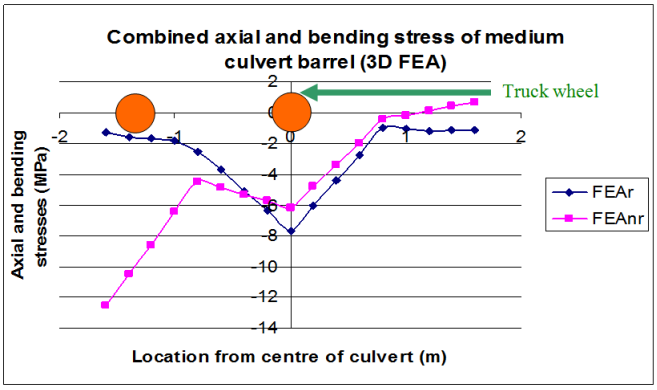

FEA_r ---- with rib-stiffeners
FEA_{nr} ---- without rib-stiffeners
Fig. 44: Hoop and bending stress of medium culvert barrel 2G (Truck load)

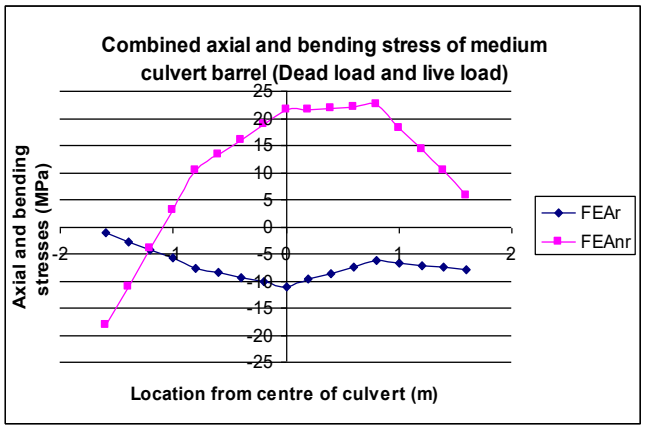

FEAr ---- with rib-stiffeners
FEAnr ---- without rib-stiffeners
Fig. 45: Hoop and bending stress of medium culvert barrel 2G (dead + live load)

Fig. 43 shows that the inclusion of rib stiffeners dramatically decreased the combined stresses in the crown and haunch areas of the culvert under dead load conditions. Fig. 44 show that the inclusion of rib stiffeners significantly decreased the combined stresses for the haunch beneath the truck wheels (live load conditions). Fig. 45 represent a combination of Fig. 43 and 44 and shows that the dead load has a much greater influence than the live load on the overall stresses in the culvert. These graphs clearly show the benefits of rib stiffeners in reducing stresses in the culvert barrel.

Truck Load Distribution along the Z Direction

To consider the loading distribution from the truck on the culvert, the FEA results from different locations were assessed. One set of results were taken directly below the wheels (FEA_w). The other set of results were taken on the culvert directly below the centreline of the road (FEA_{cl}). Results were determined at 200 mm spacings. Fig. 46 show the culvert configurations and loading locations. These models were utilised to investigate the out-of-plane truck load distribution with respect to its thrust and bending moment. The results are shown in Fig. 47 and 48.

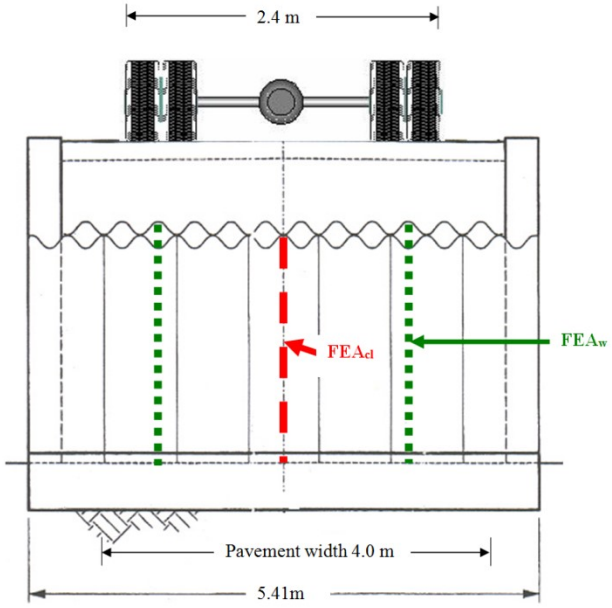

Fig.46: Truck load projection onto culvert

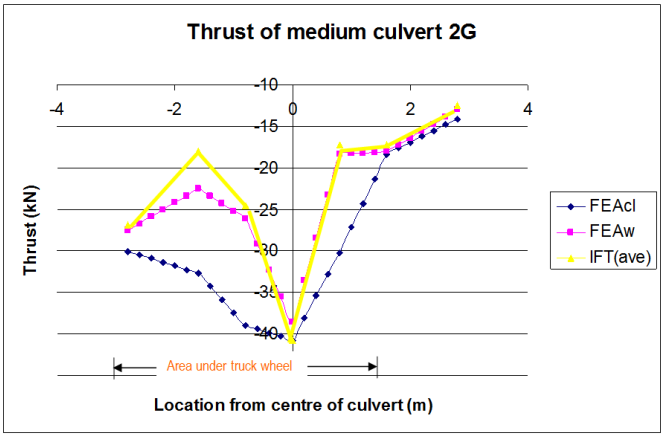

Fig. 47: Hoop thrust of the medium culvert 2G (Truck load)

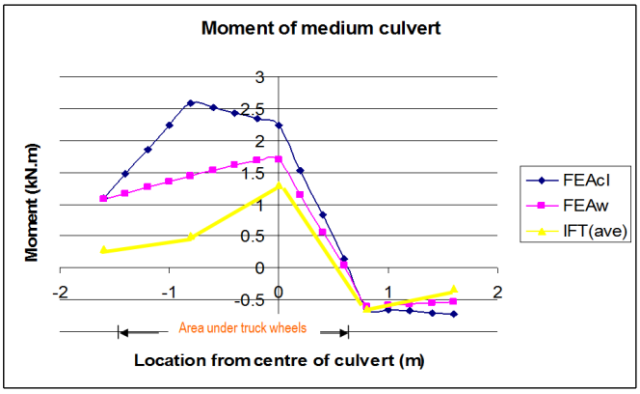

Fig. 48: Bending moment of the medium culvert 2G (Truck load)

From the FEA results, it can be seen that when the truck load was applied on the culvert structure, the maximum displacement, hoop thrust and bending moment occurred at the centre line between the truck wheels.

Fig. 47 and 48 show that the FEA_w results more closely match the average in-field test results (IFT_{ave}). This is expected because the in-field test results were recorded in the region directly below the truck wheels (as simulated by FEA_w). The results of FEA_{cl}, however, reveal that the maximum stresses are higher below the centreline of the road than below the wheels (Fig. 48). In the area not under the truck wheels the results for in-field testing, FEA_{cl} and FEA_w are closely matched, because there is no truck load effect.

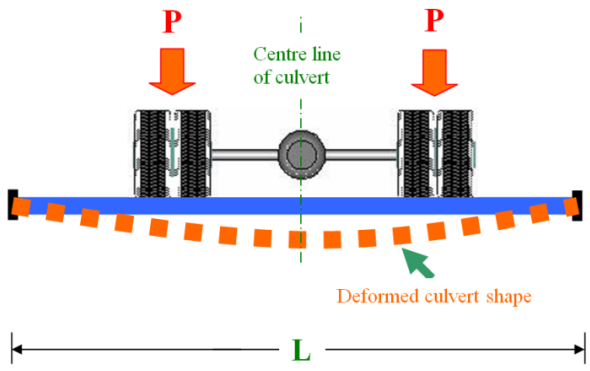

Fig. 49: Truck load and deformation of culvert along culvert length

It can be seen that as the culvert length (L in Fig. 49) changes the bending moment and axial stresses will change also. These stresses will be dependant on the location of the truck wheels and the distribution factor employed to project the loads onto the culvert structure, as well as the boundary conditions of the structure. These aspects should be the focus of future research.

Based on the FEA model case studies and their solution validation, some basic parametric studies were done using the calibrated FE models. It is concluded that a very loose soil surrounding the ring of the culvert causes both the vertical and horizontal displacements to be higher than the well compacted culvert. It is also confirmed from the FEA results that the circumferentially slotted bolt connections, with a larger gap between the bolt and hole for the corrugated metal culverts, effectively reduces thrust stress or ring compression in deep embankment installations. The rib-stiffener was also shown to have good capability to decrease the deformation and bending moment for culverts under soil load (dead load) as well as truck load (live load). It was found that when a truck load was applied on the culvert structure, the maximum displacement, hoop thrust and bending moment occurred at the centre line between the truck wheels.

IX. Conclusions & Recommendations

The structural behaviour of long span deep corrugated reinforced steel box culverts with rib stiffeners, under the influence of backfill soil and truck loads, has been examined using nonlinear finite element analysis. The finite element calculations have been conducted using the finite element package, ANSYS. Nonlinearities accounted for were material nonlinearities and geometric nonlinearities including contact nonlinearities at the soil-steel interface.

A long term systematic in-field testing program was done prior to the numerical study by Ingal Civil Products. Data from two culverts (2G and 2H) in northern Queensland were recorded during the backfill procedure and under truck load conditions.

Two FE case studies were conducted to assess the behaviour of culvert structures with rib-stiffeners. The two case studies were the simulations of the two gauged steel culverts, 2G (medium) and 2H (large), in northern Queensland. 2D and 3D FEA models were used for the numerical simulation for this study. The results predicted by FEA were compared with the results of in-field measurements for culverts 2G and 2H, as supplied by Ingal Civil Products.

From the FE studies the outcomes and conclusions were:

- The 2D FEA model considering the slippage of the bolt connection was used to accurately simulate the dead load conditions (self-weight of soil) of the culvert. The 2D FEA program successfully modelled the bolt connection with slot and slippage by simulating the connection as a “short beam”, consisting of a contact element and a link/beam element. Its results were in agreement with the results of the in-field testing. For the 2D model which did not consider the slippage of the bolt connection, the results for axial force under dead load conditions did not agree with the in-field testing results. The bending moment comparison, however, was better, especially for the larger span culvert (2H). Therefore, the 2D FEA model is not suitable to analyse the axial force solution of the self-weight of soil, but is possible to study its bending moment.
- Neither axial force or bending moment results for live load conditions (truck load) for the 2D FEA model agreed with the results of in-field measurements. Hence, the 2D FEA model is not suitable to analyse live load conditions. The truck live load on the culvert structure could not be simulated by the 2D FEA model because the 2D model does not consider the out-of-plane boundary conditions. This finding led to the development of the 3D FEA models.
- The solution for dead load (self-weight of soil) and live load conditions (truck load) in the 3D FEA models were in good agreement with the results of in-field testing. Both the axial force and bending moment at each station were very close to the results of the in-field testing. Hence, the 3D FEA model can be used to simulate both dead load and live load acting on the steel culvert.

The validated FEA models were then used to undertake a parametric study. The effects of soil elastic modulus and soil density, connection behaviour, rib-stiffeners and truck loading location were considered. Key findings are presented below:

- The effect of soil elastic modulus and density was assessed by comparing the results from four FEA models with different elastic modulus E and density ρ. It was found that in all cases the maximum hoop thrust forces were located at the crown and the minimum values were located at the haunch. It was found that good compaction of the backfill soil (higher E, higher soil density ρ) caused a significantly lower circumferential axial force.
- For both lower bound E and upper bound E cases, the maximum positive bending moments values were located at the crown and the maximum negative values were located at the sides. It was found that good compaction of the backfill soil caused a significantly higher positive bending moment at the crown and a moderately reduced maximum negative bending moment at the sides. This result was unexpected and will require further investigation in the future.
- The comparison of displacement for the four FEA models leads to the following two primary conclusions: for medium span culverts displacement is sensitive to changes in E value of soil. Lower E value could cause higher horizontal and vertical displacements. The input of very loose soil condition has a significant effect on the behaviour of the model, which can be attributed to the higher flexibility of the surrounding ring of soil.
- The effect of slotted bolt hole connections was assessed by comparing the results from FEA models both with and without simulation of bolt connections. It was found that slotted bolt connections significantly reduced the effective hoop thrust of the culvert. The effect of slot and slippage in the connections in terms of its bending moment was very small.
- The effect of rib stiffeners was assessed by comparing the results from FEA models both with and without the simulation of rib stiffeners, under both dead load and live load conditions. For dead load conditions (self-weight of soil) the axial stress of the barrel of the culvert increased and the bending stress dramatically decreased when rib stiffeners were included. It was noted that the bending stress is significantly larger than the axial stress in culverts, and that rib stiffeners are a very effective means of reducing these bending stresses. For live load conditions (truck load), rib stiffeners significantly increased the compressive axial stress, and decreased the bending stress in the barrel of the culvert under the truck wheels. The inclusion of rib stiffeners dramatically decreased the combined axial and bending stresses in the crown and haunch areas of the culvert under dead load conditions (which has a much greater influence on the overall stresses in the culvert than live load conditions).
- The effect of the location of the projected truck load on the culvert was considered by comparing results from FEA models simulating load directly under the truck wheels and load directly under the centre line of the road. It was found that when the truck load was applied on the culvert structure, the maximum displacement, hoop thrust and bending moment occurred at the centre line between the truck wheels. It was observed that as the culvert length changes the bending moment and axial stresses change also. These stresses will be dependent on the location of the truck wheels and the distribution factor employed to project the loads onto the culvert structure, as well as the boundary conditions of the structure.

X. Recommendations for Further Study

A number of key outcomes were obtained from this research. In some cases, these findings have revealed various other factors worthy of further investigation, but which were outside the scope of this thesis. The following aspects should be the subject of further research:

- In the truck load analysis, the effect of distribution of the live load along the length direction has not been studied. It may be possible to develop a modification factor for the 2D FEA model of truck live load, with different backfill depth, structural width and span.
- Both in-field testing and numerical studies (3D FE modelling) are recommended to study the effect of lower compaction quality backfill soil in the area surrounding the ring of the culvert (thickness of 50mm to 200mm). This phenomenon is common in construction practice because it is difficult to obtain good compaction by a machine or manual work in that area.
- The contribution of the circumferentially slotted bolt connections in reducing the thrust stress (ring compression) is still not very clear. The slippage of these connections has also not been measured or systematically investigated by special in-field testing or laboratory testing. In addition, it is recommended to develop a 3D FE model to simulate this condition, which may lead to more accurate results.

REFERENCES

R. Zhang. The behavior of long span deep-corrugated reinforced steel box culverts. Thesis of Master of Engineering. Faculty of engineering. University of Technology, Sydney. September, 2004. P26-34. Sydney. Australia. 2004.

A. Campbell. Three-dimensional finite element modelling of corroded corrugated metal pipe culverts. Thesis of Master Degree of Engineering. Dalhousie University, Halifax, Nova Scotia. April, 2018.

T. Elshimi. Three-dimensional nonlinear analysis of deep-corrugation steel culverts. PhD Thesis. Department of civil engineer. Queen's University. Kingston, Ontario, Canada. April, 2011.

G. Abdel-Sayed, B. Bakht and L. Jaeger (1993). Soil-steel bridges. McGraw-Hill, Inc. New York.

G. Abdel-Sayed and S Salib. "Minimum depth of soil cover above soil-steel bridges". Journal of geotechnical and geoenvironmental engineering. August, 2002.

Australian Standard. Long-span corrugated steel structures. Part 1: Materials and manufacture. AS3703.1-1989.

Australian Standard. Long-span corrugated steel structures. Part 2: Design and installation. AS 3703.2-1989.

Australian/New Zealand Standard. Buried corrugated metal structures. AS/NZS 2041:1998.

J. Duncan. Long-span metal culverts. University of California. College of engineering. USA. 2002.

K. El-Sawy. "Three-dimensional modeling of soil-steel culverts under the effect of truckloads". Thin-walled structures. 41 (2003) 747-768. January, 2003.

T. McGrath, I. Moore, E. Selig, M. Webb and B. Taleb. Design examples for large-span culverts. Supporting material for NCHRP report 473. National research council. 2002.

P. Byrne, T. Srithar and C. Kern (1990). Field measurements and analysis of a large diameter flexible culvert. Structural performance of flexible pipes. A.A.Balkema Publishers. Rotterdam. P27-38.

T. McCavour, T. Morrison and M. Winters (2000). Long span reinforced deep corrugated structural plate arch. Transportation research board 79th annual meeting. January 9-13, 2000. Washington, DC.

Railway Bridge Transition Defects and Maintenance on Australian Heavy Haul Operated Tracks

Ralph (Wei) Zhang
School of Computing, Engineering and Mathematics
Western Sydney University
Sydney, Australia
Email address:
17602059@student.westernsydney.edu.au

Helen Wu
School of Computing, Engineering and Mathematics
Western Sydney University
Sydney, Australia
Email address:
Helen.Wu@westernsydney.edu.au

Chunhui Yang
School of Computing, Engineering and Mathematics
Western Sydney University
Sydney, Australia
Email address:
R.Yang@westernsydney.edu.au

***Abstract*—Poor track conditions at the bridge / track transition area, especially for the non-ballast steel bridges has been acknowledged by the railway companies and authorities for decades. The defects have included: Significant loss of top and long twist at the bridge transitions and across the ballast top under-bridge, track slack present at the transition from the embankment formation to the ballast top formation at the bridge abutments, and highly fouled ballast. These defects are resulted from transition problem and soft soil track formation. Within this paper, the classic bridge transition defects are presented. Based on the technical analysis for the reasons which results for the different types of transition defects, some long term and short team remedial actions are provided.**

Keywords—railway bridge, transition, defects, maintenance, heavy haul

I. INTRODUCTION

Bridge/track transition condition problems, especially for the non-ballast steel bridges has been acknowledged by the heavy haul revenue railway companies and authorities for decades and some specified remedial actions have been developed to relieve it [1]. However, in recent year, on ballasted concrete bridges, track deterioration and high frequent track maintenance have also been reported at the track-bridge transition area. The defects have included: Significant loss of top and long twist at the bridge transitions and across the ballast top underbridge, track slack present at the transition from the embankment formation to the ballast top formation at the bridge abutments, and highly fouled ballast. To find out the best remedial actions, the reasons that lead to this type of defects are investigated based on the information from in-field studies.

II. TRACK DEFECTS AT THE TRANSITION AREA

Rail track transition points occur in substructures between embankments, bridges and tunnels. From the track maintenance point of view, the transition areas in the railway networks are the locations where with significant changes in the vertical rail support, i.e. the stiffness variation existed.

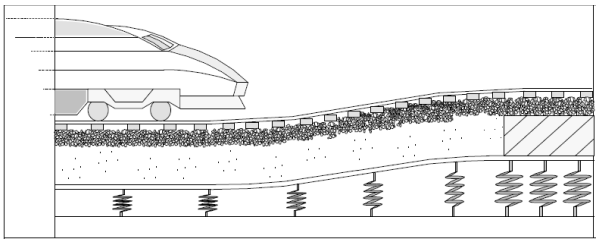

Fig. 1 Principle of train response at a transition

The significant stiffness variations at these transition areas (as illustrated in Fig. 1) will generate high dynamic loads, and in turn the high dynamic load will result the deterioration of the track components.

A. Track Geometry Issues

Significant track geometry defects, especially the track geometry defects of top, alignment and long twist, are widely existed at the transition area between the steel bridges and their adjacent tracks, as shown in Figure 2.

Fig.2 Transition between embankment and steel girder bridge

Figure 3 shows a defective track transition from a high embankment onto a bridge [2]. At this location, the problems are arisen from the rapid change in track support stiffness between a relatively soft embankment which suffered track drainage problems (bog-hole defects) and the steel bridge with high track stiffness. In addition, the "pumping action (vertical dynamic movement)" can be observed, when trains pass through this transition area (significantly less than the 5 mm or so on the approach).

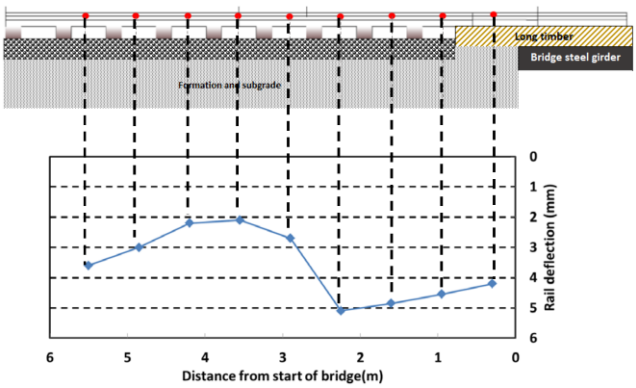

Fig. 3 General arrangement and maximum dynamic displacement at the approach to an overbridge

Moreover, the repeat wet track beds and voids below sleepers were developed as the embankment settled relative to the bridge. The continuing differential settlement required high frequently track maintenance work (track resurfacing - lifting and packing) to enable safe operation and temporary or permanent speed restrictions were set up at these locations.

B. Track Settlement and Subgrade Issues

Similarly to the transition issues that happened at the bridge approach zones between tracks and steel bridges, the "track settlement and subgrade issues" also existed at the bridge approach sections. However, for the practices of track maintenance, this type of issues are usually used to emphasize the issues that happen between the plane track and a concrete ballast top bridge, which has much less track stiffness difference compare with the plane track and steel bridge.

Regarding to the plane track to concrete ballast top bridge transition zone issues, there is a pronounced track slack present at the transition from the embankment formation to the ballast top formation at the bridge abutments. The track slack at the bridge transitions is likely to be due to settlement of the poor quality fill under train loading and the presence of a significant and abrupt change in track modulus from a low modulus track formation to a ballast top structure.

Regarding to track geometry and maintenance at this location, the track geometry inspection car's records has indicated: On both of the Up and Down line - significant loss of top on Up and Down rails at the city and country bridge transitions (within 5m of bridge) and across the ballast top underbridge. Significant (Maximum exceedance 4) long twist is present at the approach to the underbridge and occurs in the centre of the underbridge. Visual assessment of track condition along the up and down lines confirmed the inspection car results with a pronounced track slack present at the transition from the embankment formation to the ballast top formation at the bridge abutments. The significant track slack on the up coal at both the city and country abutments is shown in Fig. 4. Survey measurements along the up line up rail at the city transition noted a drop in rail level of 37mm from the transition over a distance of 3m to the city (1 in 80 slack) compared to the 1 in 220 grade across the bridge. Selected site photographs showing site conditions are presented below.

Fig. 4 Track shows dip in track at bridge transition.

C. Short Spot Track Dynamic Response (Pumping Actions from Impact Load)

The short spot track dynamic response issues is used to describe the significant dynamic vertical impact action between the wheel and track that happened in a very short distance (usually no longer than 2m along the railway track).

On Australian heavy haul operated tracks, these short spot track dynamic response issues are happened at the concrete support logs of the non-ballast steel girder bridge ends. For many of the non-ballast steel bridges, the distance between the last concrete sleeper on the plain track and the first timber transom on the steel bridge is significantly longer than the standard sleeper spacing. When the trains pass these locations, the poor support from the larger sleeper-transom spacing is to be combined with the significant differential track stiffness and results high vertical dynamic impact action. As a result, track settlement, bog-hole, track formation failure and severe ballast deterioration are generated at this area.

One of the technical solution from design is the Delkor ALT1 pads are needed to be installed on the ballast logs on both city and country ends of the steel girder bridges to control the additional vertical load from larger sleeper spacings.

Fig. 5 Delkor ALT1 pads are needed to be installed on the ballast logs of the steel girder bridges

D. Deterioration of Ballast & Drainage

The dynamic impact load and differential track stiffness generated high ballast pressure underneath the concrete sleeper and pumping action, increasing the deterioration of the ballast material and the failure of track formation. At the plain

track and bridge transition areas, the geotechnical investigation through the excavation of test pits (to depths ranging between 0.65m to 1.8m below top of rail level). Dynamic Cone Penetrometer testing (DCP) is utilised to assess soil strength at subgrade level.

The ground profile encountered in the test pits is summarised based on geotechnical units as presented in table and shown on sections in Fig. 6. Photographs showing the typical subsurface profiles are shown on test pit logs.

The profile encountered in test pits excavated at the bridge transition (back fill behind bridge abutment) comprised highly fouled ballast to 0.85m to 0.9m below top of rail over general fill comprising a mixture of ripped sandstone rock fragments up to 300mm in size, clay and alluvial sand. The material was visually assessed as poorly compacted and comprising a variable and poor quality fill for use in construction of a bridge transition.

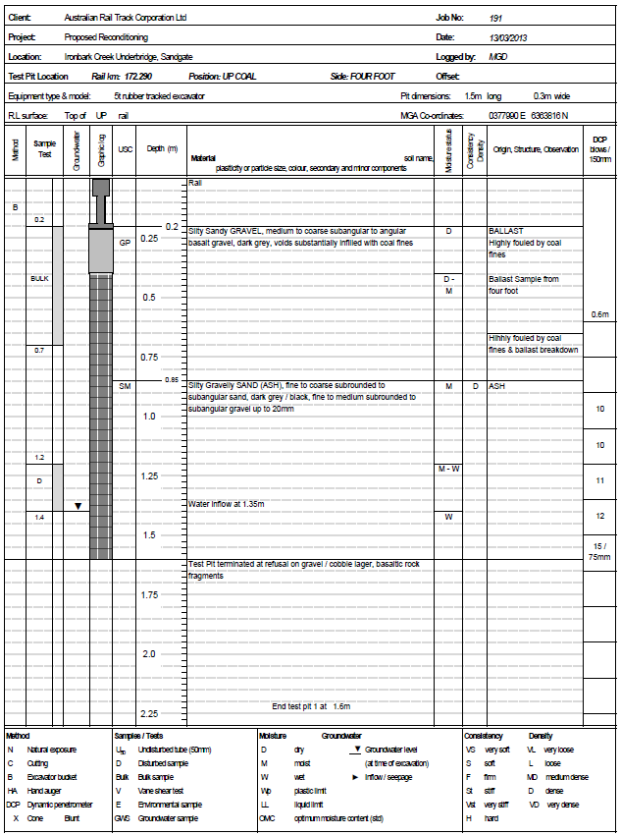

Fig. 6 Geotechnical log – test pit

The profile encountered across the bridge deck comprised highly to very highly fouled ballast to 0.65m to 0.8m below top of rail over a 15mm rubber shock mat over the concrete bridge deck. The depth of ballast at the city end of the bridge is less than the country end indicating that the bridge deck was installed level and the ballast depth adjusted to accommodate a 1 in 220 fall to the city at rail level.

Perched water was observed at 1.35m to 1.45m below rail level in the ash and in the structural fill layer in test pits. This groundwater level is well above the embankment toe level and suggests the presence of perched water most likely trapped in a dished ash and structural fill profile beneath the coal lines.

Fig. 7 Ballast highly fouled by fines and perched water in ash

PRACTICES OF THE NEW DEVELOPED REMEDIAL METHODS

Dynamic interactions between train and track are influenced significantly by track stiffness variations and can be improved by adjustments in the track stiffness.

Track stiffness (k) is the resistance to deflection (y, right underneath the load) when subjected to a vertical load (P). Its generalised measure (force per unit length of rail per unit deflection) is "track modulus" with a unit, MPa. Track modulus (u) could be expressed in the MPa unit of Newton force required to cause a 1 mm length of track to deflect 1 mm.

The relationships between track stiffness and track modulus are as follows:

$$k = P/y$$

$$u = k^{4/3} / (64EI)^{1/3}$$

Where:

k - The track stiffness (global track resistance);
E - The rail modulus of elasticity; and
I - The rail moment of inertia.

To optimise the track stiffness, the first step is to obtain the required stiffness of the track. It is generally predominated by a requirement of the maximum deflection of the rail. For the heavy haul freight predominated railway tracks, the value in North America is no more than 5mm. It is variable based on the different track revenue conditions:

- Higher axle loads and/or speed needs a stiffer track, due to higher dynamic forces;
- A stiff track structure leads to a higher load at each fastening point and on the rail;
- A soft track distributes the load over more fastening points but is less stable.

Theoretically, the aim is to reduce the stiffness on the stiffer track structure and foremost to build a smooth transition zone to the track with lower stiffness.

The most widely used concepts/techniques to deal with this problem is to smooth the stiffness/modulus step change at the interface by gradually increasing stiffness on the lower stiffness side of the transition [2], see Fig. 8.

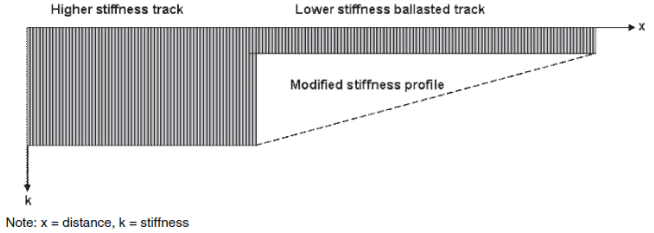

Note: x = distance, k = stiffness

Fig. 8 Transition remedy in which the stiffness step change is modified with a gradual increase in stiffness

E. Full Depth Track Reconditioning

The characteristics of track whose support is too stiff, too flexible or too variable (including at a transition onto or off a hard substructure) symptom nearly always include a rapid or persistent loss of track geometry that is difficult to address using normal maintenance methods.

Track reconditioning work is required as the remedial action for the track formation failure at the transition zone, especially at a steel girder bridge ends. Usually the reconstruction work needs to be conducted during a 72 hour possession. For the heavy haul operated railway tracks in Australia, the site specific scope of the bridge end track reconditioning work involves:

- Removal of ballast, capping and subgrade materials to achieve design excavation levels;
- The installation of a strengthened transition zone to both the city and country ends of the steel underbridge as per Fig. 9 below.
- Geogrids to be Tensar SS20 (Terragrid TG3030) or equivalent, Geofabric to be Bidim A34 or equivalent. The agricultural drain shall comprise 225mm class four pipe (225mm slotted ADS N-12 ST IB Pipe), wrapped with geofabric and graded at 1V:30H to a suitable of the shelf headwall which freely discharges;
- As illustrated within Figure , formation outside the bridge approach is to be installed at a standard depth of 1.4m BTOR, unless directed otherwise by railway authorities' Geotechnical Representative;
- Capping quality material shall be used for all bridge approach formation;
- Refer to earthwork guidelines near structures on railway network;
- The track resurfacing work is must to be occurred after the new transoms on the steel girder bridge have been installed and secured down, and the resurfacing work on the plain track must to suit the transom design alignment over the steel girder bridge and is to be started away from the bridge abutments on the two ends of the bridge.

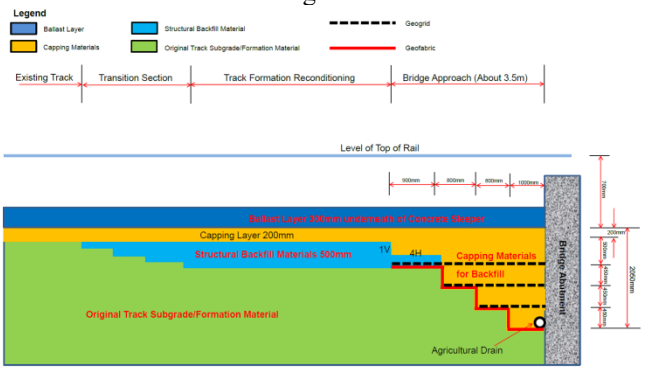

Fig. 9 Typical bridge approach crossing section (not to scale)

F. Additional Fastening System on the Concrete Log

The short spot track dynamic response which is caused by the large distance between the last concrete sleeper on the plain track and the first timber transom on the steel bridge can be mitigated by install the Delkor pad lift on the concrete support logs of the non-ballast steel girder bridge ends.

Fig. 10 The ALT.1 Delkor plate is installed on the abutment / ballast log

The ALT.1 Delkor plates on the abutment / ballast log is required to better allow rail support under train loading (as shown in Fig. 10). This is to be done using an appropriate HDPE packer, to be placed between the ballast log and the ALT.1 plate. A gap of 4 ± 1 mm between the plate and the foot of rail is to be achieved.

Undercutting/Cleaning Ballast Profile + New Geo-Synthetic

The remedial actions include undercutting/cleaning the ballast profile and strengthen the track transition area by using a special type newly developed geo-synthetic - Tracktex. It has been created to address the track and ballast deterioration problem caused by "Erosion Pumping Failure".

This method is designed to address the transition problems where site is located on a broad flat low lying area associated with the floodplain of the river, where are the sensitive wetland swampy areas [5].

To deal with the poor ballast condition on the concrete bridge, bridge transition, and adjacent track the full cross-section undercutting (300mm below the underneath of sleeper) is to be applied instead of the excavation that can reduce the risk of encountering groundwater in excavation to design subgrade level (Fig. 12) [5].

Fig. 11 Hi-rail based undercutting machine is carrying out the track bed undercutting work

For the pumping at the bridge transition, the remedial actions include undercutting/cleaning the ballast layer and strengthen the bridge transition area by using a special type newly developed geosynthetic - Tracktex. When installed at the ballast formation interface it prevents rain water penetrating through to the underlying deposits whilst under load, allowing a controlled upward movement of water through capillary action and also filtering and retaining any fine soil particles.

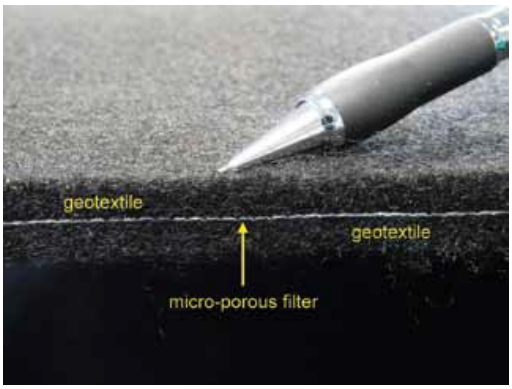

Fig. 12: The concept of Tracktex Geosynthetics

Fig. 13: The details of the cross-section of Tracktex Geosynthetics

Tracktex is featured as a composite material consisting of a unique micro-porous filter, sandwiched between two high strength protection geotextiles, as shown in Fig. 12 and 13. Its features and benefits including:

- Pore-water is relieved upwards through the composite under the cyclic loading;
- Rainfall cannot penetrate the micro-porous filter and is drained laterally to the sides of the track;
- Any residual slurry becomes dried as any pore water is dissipated;
- Conforms to surface depressions in the formation layer preventing the creation of slurry pockets.

Furthermore, to prevent the ballast damage the Tracktex, the Tensar SS40 geogrid is to be installed above Tracktex (Fig. 14).

In addition, track damping is an important consideration for ride quality and track component life.

To decrease the damping action to bridge transition area, Tracktex together with Tensar SS40 geogrid that installed at the undercut bridge transition is used to provide acceptably smooth bridge approaches. This ramp can provide a smoother transition from bridge to open track.

Stopping differential settlement is not practical at most track transitions. Thus, a method of accommodating differential settlement's effects on track performance is required. Having a ramp is certainly an acceptable alternative to a large track surface change over a short distance. By spreading the elevation change evenly across a longer segment of track, the effects on train operations are minimized. This can be done by varying the strength of materials, varying the unit loading on the ballast and subgrade or by doing both. Strengthening the ballast and/or subgrade layer is also possible with the use of geogrid tensile reinforcement. Varying the number of layers used or the proper ties of the grid can produce the desired ramp effect. Basic on this concept for this location, at the undercut open track the Tensar SS40 geogrid is installed on the subgrade.

Fig. 14 Tracktex combined with Tensar SS40 geofabric at the concrete bridge transition area

G. Ballast Glue

Ballast glue/bond at the bridge/track transition area has shown its capacity to improve the performance and effectiveness at the bridge end area.

End of the bridge was instrumented with accelerometers to measure vibration responses. The bridge is a transom-top on the steel girders. The track configuration consists of 60kg rails, standard guard rails, Pandrol fastening system (fast-clip type), low profile medium duty concrete sleepers, ballast bed and formation. Both ends of the steel girder bridge were resurfaced by tamping machine.

During a 40 hours' possession, the bridge ends were lifted and adjusted to the alignment by the tamping machine. Then, the ballast glue/bond material was applied to both bridge ends. The MC-ballastbond 70 was used. In addition, from the technical specification it is stated that the ballast-bond material has a structural design life of 50 years.

The stiffness ramping, which defines the area to glue the ballast, was designed as shown in Fig. 15.

Fig. 15 Area for ballast glue at the bridge end

The ballast glue was sprayed over the full shoulder for 6 sleeper-spacings' distance, and then only half shoulder for the next adjacent 6 sleeper-spacings, next to this only area of the sleeper length (2.5m in width of track) to be ballast glued along the track for 6 sleeper-spacings, and the work finished by the last 6 sleeper-spacings by only glue the track area of ½ sleeper length.

Post the inspection the vibration measurements were performed to examine the track condition after ballast gluing. It was observed that the glue did not seepage much through the voids of ballast aggregates, even though the ballast had recently been lifted and tamped.

The glue is varied about 250-300mm deep from the top surface of ballast, resulting in about 70 - 100mm underneath the sleeper soffit (250-180 = 70mm).

Vibration measurements were carried out at two stages, initial condition (pre-ballast glue), and after condition (post ballast glue). The tests will allow benchmarking the dynamic performance of the bridge ends and evaluation of the effectiveness of the ballast glue method.

The comparison of averaging peak vibration magnitudes at the bridge end shown that the ballast glue changes the dynamic track characteristics [6]. The maximum amplitude of vibration of rail at the bridge end tends to significantly increase due to ballast adhesion, whilst the vibration amplitude of sleeper at the bridge end surprisingly remains at the same level. It is noted that the rail vibration levels at the bridge end are in a similar range with those over the bridge. This shows that the track stiffness at the bridge end increases significantly, which consequently increases the wheel-rail dynamic interaction.

It is noticeable that the sleeper is damped by the ballast cohesion. The vibration suppression level is very high as the dynamic effect of larger lumped mass attached to sleeper is pronounced. Also, the duration of sleeper's vibration spectra is shortened due to ballast glue (Fig. 16).

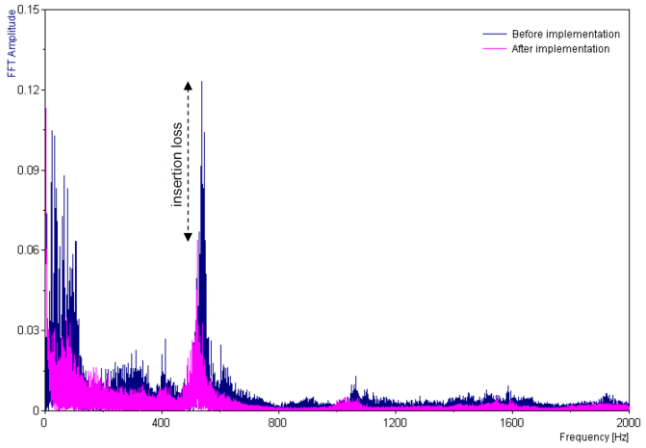

Fig. 16 Comparative frequency responses of bridge end - Sleeper's peak vibration at bridge end

Based on the vibration test measurements, it is evident that the ballast glue can help suppress the vibration of sleepers and ballast at the bridge approaches in a short term. Track inspection vehicle data shows that the dynamic rail deflection deviation is improved by about 30% in a short term. The linear regression prediction of track settlements shows that the ballast glue will strengthen the bridge ends and reduce the level of track settlement overtime.

III. CONCLUSION

The transition from ballasted track forms to non-ballasted track forms often causes a high rate of track deterioration due to the dynamic impact excitation by the abrupt change of track stiffness. This results in accelerated rates of track geometry and component degradation, high maintenance need, poor ride comfort, and high fatigue stress threshold for passing rolling stocks.

These issues represented as the bridge transition defects are including: poor track geometry, significant track settlement and formation/subgrade failure, deterioration of ballast and drainage, and short spot track dynamic response (pumping actions from impact load), etc.

From the point of view of structural mechanics, the significant dynamic and impact loads are caused by the high differential of track stiffness at these track/bridge transition areas. A criterion for the stiffness transition is to smooth the stiffness interface between the dissimilar track types.

Feasible options are to design the transition to:

Option 1: Equalise the stiffness and rail deflection of the ballasted and non-ballasted tracks, by controlling the resilience of the rail on the non-ballasted track;

Option 2: Provide a gradual increase in the stiffness of the ballasted track to match that of the non-ballasted track.

Regarding to the option 2, within Australian some successful and effective methodologies and maintenance practices have been developed and introduced. These including: specially designed full depth track reconditioning, install the Delkor pad on the concrete support logs of the non-ballast steel girder bridge ends, undercutting/cleaning ballast profile plus the installation of new geo-synthetic, and ballast glue at bridge end. All of these methods have shown its effectiveness and/or portantial to mitigate the problem.

REFERENCES

[1] International Heavy Haul Association, Guidelines to Best Practices for Heavy Haul Railway Operations – Infrastructure Construction and Maintenance Issues. Chapter 3.9. 2009. USA.

[2] W. Powrie, L. Le Pen, A Guide to Track Stiffness. The Cross Industry Track Stiffness Working Group. August, 2016.

[3] R. Zhang, H. Wu, Strengthening the Track Bridge Transition Area ON Heavy Haul Line by New Generation Geosynthetic. Railway Engineering 2019: 3-4 July 2019, Edinburgh, UK.

[4] Selig, J. Waters, Track Geotechnology and Substructure Management, Thomas Telford, London. 1994.

[5] Ionescu, Evaluation of the Engineering Behaviour of Railway Ballast. PhD thesis from University of Wollongong, Faculty of Engineering Civil Mining and Environmental Engineering. 2004.

[6] S Kaewunruen, "Impact damage mechanism and mitigation by ballast bonding at railway bridge ends", International Journal of Railway Technology, Volume 3, Issue 4, P1-22.

Review on Lane Marking Detection Based on Deep Learning

Nima Zarbakht, Ju Jia Zou, Gu Fang

School of Computing, Engineering and Mathematics
Western Sydney University
Sydney, Australia
{N.Zarbakht, J.Zou, G.Fang} @westernsydney.edu.au

***Abstract*—Lane detection plays a vital role in an Advanced Driver Assistance System (ADAS). The accuracy and robustness of lane detection are essential measures. Therefore, many researchers have proposed different methods to achieve fast and robust lane detections. Nowadays, most lane detection algorithms are based on deep learning, particularly through the utilisation of the Convolutional Neural Network (CNN) because of the high accuracy and low computational time of CNN when they are compared with classical methods. In this paper, recent lane detection methods based on CNN are reviewed. The primary motivation of this survey is to analyse the methodology and accuracy of these methods. This survey highlights different architectures in CNN, as well as their performances in different illumination and weather conditions. however, at this stage there is no comprehensive data-set available for lane mark detection in varying conditions. As a final point, a discussion is presented on the achievements and limitations of current lane detection methods based on CNN.**

***Index Terms*—Lane Detection, CNN, Deep learning.**

I. INTRODUCTION

The Advanced Driver Assistance System (ADAS) is one of the most advanced systems in modern cars. ADAS seems to become one of the highly demanded options for vehicles, as it helps drivers to drive safely and effortless. ADAS can consist of sensors such as cameras in order to scan and detect the surrounding obstacles. Furthermore, in order for ADAS to perform well, each subsystem should be able to compute in real-time and in diverse conditions. One of the essential subsystems in ADAS is lane marking detection, which assists the driver in maintaining between the lane markings on the roads. Most of the lane detection systems utilise camera and machine vision framework to compute and detect lane markings. Since lane marking detection assists drivers to avoid sudden, or unintentional lane changes, a high accuracy and a robust system is essential.

Lane marking detections introduce many challenges to researchers in the field of machine vision and image processing, as they are required to process each image instantaneously and accurately. Researchers have developed numerous techniques to address these challenges, such as real-time detection or diverse illumination conditions. Among these developed techniques, the Convolutional Neural Network (CNN) which is based on deep learning has become a dominating approach in machine vision [1]. CNN has proven its capability in many image processing applications, and lane detection is not an exception among them [2]. Since CNN is able to overcome many challenges in image processing that classical methods were unable to solve, or they were computationally demanding to solve, most lane detections are performed on CNN [3].

Since CNN is one of the state-of-the-art techniques and has been widely applied in lane detection frameworks, a review on this technique and recent advances in the lane detection area is necessary. To the best of our knowledge, a survey on recent advances and progress on using CNN on lane detection is unavailable from the literature. Therefore, a survey from previous methods can be an aid to highlight the recent advances and progress this field and to point out future directions for further research.

II. LANE DETECTION BASED ON DEEP LEARNING

Digital image processing has been a growing field. Therefore, it has attracted many researchers' attention to develop robust and low computational time techniques. After almost three decades, researches are still battling with this state-of-the-art technology to keep it emerging and introducing better techniques compared to previous methods [4].
A camera is like no other sensor as it can capture a large amount of information such as colour, objects, distance, and different geometries. Now with this amount of information, the challenge has become how to extract it without sacrificing any crucial data and computational time, especially in many lane marking detection applications which require high accuracy and real-time response since they are demanding, both algorithmically and computationally [5].

A. Classical methods

In classical approaches in lane detection, edge detection is commonly carried out by the Canny edge operator and lane detection with the Hough Transform [6]. In order to improve lane detection algorithms, a combination of gradient cue, colour cue and line clustering was applied to detect

the lane markings [7]. However, in order to achieve a low computational time, active Region of Interest (ROI) extraction was applied to generate good results [8]. Alternatively, geometric constraints are applied, to avoid false detection [9]. These lane detection methods are based on classical image processing techniques and they are overshadowed by new techniques, such as deep learning.
Lane detection can also be achieved by stereo or dual cameras to gain more accurate reading of the road scene [10]. Many scholars focus on the use of a single camera and a classical method for lane detection. The results reported show improvements in terms of accuracy and computational time. However, there are drawbacks in other conditions, such as different asphalt colours which can be detected as the lane marking [11].

By using a framework based on unsupervised feature learning, it is possible to achieve lane marking detection as well as road sign marking detection [12]. The unsupervised learning is a fast approach for unlabelled data-sets, in contrast with supervised learning, as supervised learning is demanding in computing time.

Spatio-temporal incremental clustering demonstrates good results in low illumination conditions, showing a robust outcome in diverse conditions [13]. Furthermore, another innovation in this method is detecting the lane markings as well as road sign markings, such as arrows and speed limits which could be very useful for ADAS, but a drawback of the proposed method is the false detection for some lane markings which are close to each other.

B. Combined CNN and Classical method

Though lane marking detection may appear simple, the developed method must perform accurately under diverse conditions and have a low computational time. Since classical lane marking detection techniques have reached their limits in terms of computational time, most researchers tend to employ deep learning. Nowadays, the Convolutional Neural Network (CNN) is one of the most remarkable developments in the field of deep learning. It is used for many image processing procedures, such as lane detection, due to its proven capability in machine vision [14]. Furthermore, it has superior performance in other tasks such as object detection, when compared to classical methods [15].

Combining a classical method of lane marking detection and CNN is another useful method [16]. The method has utilised stereo cameras and a combination of a classical method and CNN to detect lane markings and distance. The algorithm begins with the extraction of an ROI and then converts it to grey-scale. For a lane detection, a self-adaptive Hough space and a constraint for the maximum line angle are applied to extract the lane markings. Once the lane marking is extracted, the grey-scale image will be fed to a shallow CNN to extract the lane marking types. Furthermore, by using an electronic map or a Geographic Information System (GIS), the authors have achieved a robust outcome in the proposed method. As this method uses two different cameras for lane detection, it can also detect the distance for the front vehicle to aid drivers in well-structured highways. Since this method is mainly implemented in classical frameworks, a long computational time has an impact on the performance in real-time applications. However, the proposed method depends on well-structured highways which are not always available in many cases.

A spiking neural network for edge extraction is introduced by Li et al. [17], and the extracted lane markings are based on the Hough transform. The idea of the proposed method is inspired from the human neuron system, wherein the presence of edges in the image network will produce a dense pulse signal, while the flat input makes the system to generate a sparse pulse signal. In this method, once the ROI is extracted, the image is fed to the spiking neuron network. At the first layer of this architecture, each pixel corresponds to a receiver as the first layer is a photonic receptor's layer. The second layer consists of four parallel arrays of neurons, and each neuron-set in the middle section will detect different edges and combine them with appropriate weights in the last layers. Once the edges are extracted, the Hough transform is applied to extract lane markings.

In most image pre-processing frameworks, an image with noise can cause a CNN to produce a false output. To overcome this issue, Kim et al. [18] applied a combination of RANSAC and CNN. The CNN, with three convolution layers, is used to remove image noise which is interfering the lane marking detection, but if the output of this layer is still contaminated by noise, the image will be fed to the input in another CNN layer for further noise reduction. However, if the pooling result shows that the input image is not noisy, the RANSAC will be directly applied to the edges to fit a lane model.

C. Different CNN Architecture

CNN can be varying in their architectures such as depth of the network. Moreover, CNN can be paralleled by a different variant of neural networks, such as Recurrent Neural Network (RNN) [19].
The proposed method starts by providing CNN with an extracted ROI image, in order to have two different outputs. The first output is a discrete classification and represents the existence of the lane markings. The output will send a 'visible signal' if the lane markings appear in the image. If the output is categorised as a lane marking, subsequently the second output will be the evaluation of the lane orientation and position. However, in order to find the global lane position in a series of videos as an alternative of local lane position in the individual image, RNN was applied for locating the lane structure in the sequence of data which was already provided. The proposed method is using images from three cameras to train its network based on a combined scene from front,

left, and rear areas. Results show that the RNN can help to recognise connected lane markings even if they are occluded by other cars or obstacles.

Moreover, to achieve high accuracy and low computational time in lane marking detection, a laser scanner can be also a solution [20]. In this method, the laser scanner is used to generate a point cloud map. Also, in order to improve robustness and to reduce the computational time, a steady up-sampling is applied. The computational time was claimed to be 28.8 seconds on average for each frame and the method can be used off-line for high-accuracy map construction.

Another method to reduce noise in imagery is the use of two different views from a single camera, namely, one view from the top and the other from the front. On the front view, all the false detections such as curbs, moving objects and barriers are rejected. For the top view, however, the extra road markings such as arrows and road signs are excluded. Once the unnecessary data is removed from the image, a 'weighted hat-like' filter is used to extract possible lane markings. This filter can also reduce the disturbance which is caused by gradual textures [21]. They fed the pre-trained CNN with two images from different views simultaneously. The main network contains two sub-CNN, in order to process two images at the same time but separately. An optimal global strategy is used to scan the lane width, length, and orientation to create a threshold for final lane markings. Once the lane candidates are extracted from the top view image, they are remapped to the extracted lane marking detected by the front view. After remapping, the lane-markings will be marked as the final output. This method produces a good result with robust noise reduction in most illumination conditions. However, the computational time is excessive. Therefore, it is not ideal for real-time applications as ADAS demands real-time processing.

Another state-of-the-art architecture in deep learning uses the Regions-Convolutional Neuron Network (R-CNN) [22]. R-CNN decomposes the whole detection issue into the problem of detecting an object location in a category- uncertain fashion by utilising low level signals such as texture and colour. Then the CNN classifier is applied to categorise object varieties at those locations. Such an architecture in deep learning, which applies a two-stage approach, increases the accuracy in image classifications.

Another way that can help to reduce the computational time is to extract the Region of Interest (ROI), by using adoptive soft voting in the image area [23].
By introducing a multi-task learning network to predict the vanishing point, lane detection can be achieved accurately under diverse conditions. Furthermore, the computational time can also be reduced [24]. The proposed method has applied an end-to-end trainable CNN, which can handle lane markings that are provided by the vanishing point under diverse conditions. This method was inspired by the architecture from Huval et al. [25], which consists of seven convolution layers and two branches to perform regression tasks as well as classification. However, this method modifies the architecture into four modules in order to fulfil their aim. By taking the advantage that lane marking converges, they were able to detect the vanishing point regardless of weather conditions. Detecting the vanishing point also helps to define a global geometric context in the image, which is also crucial for locating a lane marking. The CNN architecture was trained with 20,000 images, which were taken under different illumination conditions and weather conditions.

Since this training depends on a vanishing point, they divide the architecture into two different phases. In the first phase, the main focus of training is vanishing Points detection. Therefore, other parameters in the neural networks are set to zero to avoid a high computational time. By doing so, the global context of the image can be learned as well. In the second phase, the rest of the networks is trained with the kernels from the first phase to detect the lane marking and sign markings. The method presented achieves a cutting-edge result in vanishing point detection and lane making detection under adverse conditions. Another method to estimate vanishing points is by using Gabor filters and using the dominant orientation pixels [26]. Unfortunately, some of these methods such as the Gobor filter and using various voting to find a vanishing point do not have a satisfactory outcome in particular situations such as night time or foggy weather. By using probability voting, it would have a better outcome to estimate the vanishing point [27].

Simonyan and Zisserman [28] used very small convolution filters to achieve good image classification. Their research contributes to the relation of depth of the CNN compared to its accuracy. By applying a (3×3) convolutional filter on 19 weighted layers of CNN, the accuracy has been improved remarkably. This method uses the generic form of CNN, which is fed with an image to calculate the training set by subtracting the mean RGB value. The method reports that the depth of network can be beneficial for accurate image classification.

Since a deep CNN is challenging to train, Deep Residual Learning can be helpful for ease of training [29]. This method uses a stacked of weight layers directly to fit a residual mapping. This method can help to avoid the degradation problem, which is caused by deeper networks. As they become deeper, the accuracy gets saturated, and their performance degrades continuously.

Furthermore, to address the degradation problem, Huang et al. [30] proposed a Dense Connected Convolutional Network. The proposed method helps to reduce the length of the network to the output layers in a feed-forward manner. Each layer in this method is directly connected to the input and the output, unlike classical networks where one layer is connected to the next layers. In the dense network, not only each block

of CNN is connected to the input and output, but also the previous block is connected to all other following blocks. The benefits of such an architecture include strengthening feature propagation and substantially reducing the number of parameters. The method demonstrates its efficiency on several benchmark data-sets.

Another method which has proven a successful result is Aerial LaneNet detection where images are taken from the air and are fed to a CNN to extract the lane marking and achieve lane classification [31].

Song et al. [32] have performed object detection by using the stereo camera. The proposed method has classified images to accomplish a forward collision system and lane marking detection. The proposed method has reported a successful outcome, but it suffers from false detection in the night time and close to pedestrian lines. This is due to using the CNN to classify the lane markings but not for lane markings extraction.

D. CNN Trained on Artificial Imagery

Lane detection can be achieved by training a deep CNN with synthesised images as well as real images. Chen et al. [33] introduced lane detection with CNN trained with both synthetic and real images. For high accuracy of lane detection, side facing stereo cameras were used. Their network identifies the sideline position with the use of an end-to-end detection process.

In another proposed method with a good outcome by using laterally mounted camera, the lane marking position is estimated directly using a CNN [34]. The CNN was trained by diverse semi-artificial images. The proposed method can detect lane marking existence in the frame as well as its position with an accuracy of fewer than centimetres in 100 frames/s. Since some of the lane markings have low representation on the edge compared to the middle section, the histogram is dominated by the middle point rather than edges. In order to overcome this issue during the CNN training, they apply synthesised images. Another advantage of this proposed method is that the artificial images are generated with the same camera and from real driving scenes.

Moreover, by training CNN on pure artificial data, Murali et al. [35] could successfully detect signs in real-world images. In terms of training, the CNN on artificial images for autonomous driving applications is another good example, but this method is mostly applied on a video game called The Open Racing Car Simulator (TORCS) [36]. It cannot be compared in a real-world situation especially in adverse weather conditions.

III. DISCUSSION

In this section, we highlight the current advances and limitations of the state-of-the-art lane marking detection frameworks based on CNN.

After reviewing the most recent publications on lane detection based on deep learning, it can be observed that lane detection is a growing field. Although it is mature enough to be implemented in real-world applications, there are some areas which can be improved, especially in diverse weather conditions. Most classical methods for lane marking detection perform well on good weather conditions. Their performance will degrade in adverse weather conditions Similarly, lane marking detentions based on CNN suffer from the same issue. Recently, researchers have tried to overcome this issue by developing new architectures base on CNN and deep learning. Although they prove good performance in available benchmarks and in real-world applications, they are reported to still suffer under adverse weather conditions.

The various weather conditions on the road scene can lead to a false lane marking detection. This is due to sudden illumination changes on the roads. Most of the developed methods fail to compensate for these changes.

The lack of date-sets in varied weather conditions is another challenge for many researchers who are trying to address issues in lane detection. For instance, the Caltech data-set [37] only contains 1225 images from different places. Another data-set called Road Marking Data-set [38] includes 1400 labelled images with eleven different lane markings.

Furthermore, artificial imagery is an alternative solution for supervised neuron network training. Because all the labels can be generated automatically on artificial imagery, the training may become effortless. A major drawback is that adverse weather conditions are not addressed in artificial data sets. However, all these mentioned data-sets are captured in excellent and clear weather conditions. Therefore, there is a need for a data-set which is captured under adverse conditions and different lane markings.

There are challenges, such as rainy conditions, which are left unsolved for existing lane marking detection frameworks. They should be dealt with in future research. During the night time, there are lots distortions such as, glare which occurs due to many light sources and other cars which may lead a false lane detection. Furthermore, data-sets can be established to test and evaluate the current and future deep learning based lane detections. The established data-sets must cover all diverse conditions as well as a variety of lane markings.

IV. CONCLUSION

While the deep learning-based lane detection frameworks have been extensively investigated in the past years, it is difficult to declare this investigation has been mature. Moreover, there are still many crucial studies that are essential to be conducted, such as effective system incorporation, the validation architecture design and especially the construction of deep learning data-sets. Furthermore, an expanding number of innovative object detection architectures and techniques have been established to enhance lane detection systems. The continuous research and applications of these approaches will further advance the ADAS and autonomous driving industry.

Lane detection approaches based on CNN offer the significant potential for future accomplishment under diverse conditions.

REFERENCES

[1] J. Redmon and A. Farhadi, "Yolo9000: Better, faster, stronger," in *2017 IEEE Conference on Computer Vision and Pattern Recognition (CVPR)*, July 2017, pp. 6517–6525.

[2] Y. Jia, E. Shelhamer, J. Donahue, S. Karayev, J. Long, R. Girshick,

[3] S. Guadarrama, and T. Darrell, "Caffe: Convolutional architecture for fast feature embedding," in *Proceedings of the 22nd ACM international conference on Multimedia*. ACM, 2014, pp. 675–678.

[4] H. Bei, A. Rui, Y. Yang, and L. Xianpeng, "Lane marking detection based on convolution neural network from point clouds," in *2016 IEEE 19th International Conference on Intelligent Transportation Systems (ITSC)*, 2016, pp. 2475–2480.

[5] K. Bengler, K. Dietmayer, B. Farber, M. Maurer, C. Stiller, and

[6] H. Winner, "Three decades of driver assistance systems: Review and future perspectives," *IEEE Intelligent Transportation Systems Magazine*, vol. 6, no. 4, pp. 6–22, winter 2014.

[7] B. Ranft and C. Stiller, "The role of machine vision for intelligent vehicles," *IEEE Transactions on Intelligent Vehicles*, vol. 1, no. 1, pp. 8–19, March 2016.

[8] V. Gaikwad and S. Lokhande, "Lane departure identification for advanced driver assistance," *IEEE Transactions on Intelligent Transporta- tion Systems*, vol. 16, no. 2, pp. 910–918, 2014.

[9] R. Danescu and S. Nedevschi, "Probabilistic lane tracking in difficult road scenarios using stereovision," *IEEE Transactions on Intelligent Transportation Systems*, vol. 10, no. 2, pp. 272–282, June 2009.

[10] E. Pollard, D. Gruyer, J.-P. Tarel, S.-S. Ieng, and A. Cord, "Lane marking extraction with combination strategy and comparative evaluation on syn- thetic and camera images," in *2011 14th International IEEE Conference on Intelligent Transportation Systems (ITSC)*. IEEE, 2011, pp. 1741– 1746.

[11] C. Lee and J. Moon, "Robust lane detection and tracking for real-time applications," *IEEE Transactions on Intelligent Transportation Systems*, vol. 19, no. 12, pp. 4043–4048, Dec 2018.

[12] V. Gaikwad and S. Lokhande, "Lane departure identification for advanced driver assistance," *IEEE Transactions on Intelligent Transporta- tion Systems*, vol. 16, no. 2, pp. 910–918, April 2015.

[13] D. C. Andrade, F. Bueno, F. R. Franco, R. A. Silva, J. H. Z. Neme, E. Margraf, W. T. Omoto, F. A. Farinelli, A. M. Tusset, S. Okida, M. M. D. Santos, A. Ventura, S. Carvalho, and R. d. S. Amaral, "A novel strategy for road lane detection and tracking based on a vehicle's forward monocular camera," *IEEE Transactions on Intelligent Transportation Systems*, vol. 20, no. 4, pp. 1497–1507, April 2019.

[14] A. Gupta and A. Choudhary, "A framework for camera-based real-time lane and road surface marking detection and recognition," *IEEE Transactions on Intelligent Vehicles*, vol. 3, no. 4, pp. 476–485, Dec 2018.

[15] Y. Shen, T. Xiao, H. Li, S. Yi, and X. Wang, "Learning deep neural networks for vehicle re-id with visual-spatio-temporal path proposals," in *Proceedings of the IEEE International Conference on Computer Vision*, 2017, pp. 1900–1909.

[16] Y. LeCun, Y. Bengio, and G. Hinton, "Deep learning," *Nature*, vol. 521, p. 436, 2015. [Online]. Available: https://doi.org/10.1038/nature14539

[17] Krizhevsky, I. Sutskever, and G. E. Hinton, "Imagenet classification with deep convolutional neural networks," in *Advances in Neural Infor- mation Processing Systems 25*, F. Pereira, C. J. C. Burges, L. Bottou, and K. Q. Weinberger, Eds. Curran Associates, Inc., 2012, pp. 1097–1105.

[18] WSong, Y. Yang, M. Fu, Y. Li, and M. Wang, "Lane detection and classification for forward collision warning system based on stereo vision," *IEEE Sensors Journal*, vol. 18, no. 12, pp. 5151–5163, 2018.

[19] X. Li, Q. Wu, Y. Kou, L. Hou, and H. Yang, "Lane detection based on spiking neural network and hough transform," in *2015 8th International Congress on Image and Signal Processing (CISP)*, Oct 2015, pp. 626– 630.

[20] J. Kim, J. Kim, G.-J. Jang, and M. Lee, "Fast learning method for convolutional neural networks using extreme learning machine and its application to lane detection," *Neural Networks*, vol. 87, pp. 109–121, 2017.

[21] J. Li, X. Mei, D. Prokhorov, and D. Tao, "Deep neural network for structural prediction and lane detection in traffic scene," *IEEE transactions on neural networks and learning systems*, vol. 28, no. 3, pp. 690–703, 2016.

[22] B. He, R. Ai, Y. Yan, and X. Lang, "Lane marking detection based on convolution neural network from point clouds," in *2016 IEEE 19th International Conference on Intelligent Transportation Systems (ITSC)*. IEEE, 2016, pp. 2475–2480.

[23] Bei He, Rui Ai, Yang Yan, and Xianpeng Lang, "Accurate and robust lane detection based on dual-view convolutional neutral network," in *2016 IEEE Intelligent Vehicles Symposium (IV)*, June 2016, pp. 1041– 1046.

[24] R. Girshick, J. Donahue, T. Darrell, and J. Malik, "Rich feature hierarchies for accurate object detection and semantic segmentation," in *Proceedings of the IEEE conference on computer vision and pattern recognition*, 2014, pp. 580–587.

[25] H. Kong, J. Audibert, and J. Ponce, "General road detection from a single image," *IEEE Transactions on Image Processing*, vol. 19, no. 8, pp. 2211–2220, Aug 2010.

[26] S. Lee, J. Kim, J. Shin Yoon, S. Shin, O. Bailo, N. Kim, T.-H. Lee, H. Seok Hong, S.-H. Han, and I. So Kweon, "Vpgnet: Vanishing point guided network for lane and road marking detection and recognition," in *Proceedings of the IEEE International Conference on Computer Vision*, 2017, pp. 1947–1955.

[27] B. Huval, T. Wang, S. Tandon, J. Kiske, W. Song, J. Pazhayampallil, M. Andriluka, P. Rajpurkar, T. Migimatsu, R. Cheng-Yue *et al.*, "An em- pirical evaluation of deep learning on highway driving," *arXiv preprint arXiv:1504.01716*, 2015.

[28] P. Moghadam and J. F. Dong, "Road direction detection based on vanishing-point tracking," in *2012 IEEE/RSJ International Conference on Intelligent Robots and Systems*, Oct 2012, pp. 1553–1560.

[29] J. H. Yoo, S. Lee, S. Park, and D. H. Kim, "A robust lane detection method based on vanishing point estimation using the relevance of line segments," *IEEE Transactions on Intelligent Transportation Systems*, vol. 18, no. 12, pp. 3254–3266, Dec 2017.

[30] K. Simonyan and A. Zisserman, "Very deep convolutional networks for large-scale image recognition," *arXiv preprint arXiv:1409.1556*, 2014.

[31] K. He, X. Zhang, S. Ren, and J. Sun, "Deep residual learning for image recognition," in *2016 IEEE Conference on Computer Vision and Pattern Recognition (CVPR)*, June 2016, pp. 770–778.

[32] G. Huang, Z. Liu, L. v. d. Maaten, and K. Q. Weinberger, "Densely con- nected convolutional networks," in *2017 IEEE Conference on Computer Vision and Pattern Recognition (CVPR)*, July 2017, pp. 2261–2269.

[33] S. M. Azimi, P. Fischer, M. Körner, and P. Reinartz, "Aerial lanenet: Lane-marking semantic segmentation in aerial imagery using wavelet- enhanced cost-sensitive symmetric fully convolutional neural networks," *IEEE Transactions on Geoscience and Remote Sensing*, vol. 57, no. 5, pp. 2920–2938, May 2019.

[34] W. Song, Y. Yang, M. Fu, Y. Li, and M. Wang, "Lane detection and classification for forward collision warning system based on stereo vision," *IEEE Sensors Journal*, vol. 18, no. 12, pp. 5151–5163, June 2018.

[35] C. Chen, A. Seff, A. Kornhauser, and J. Xiao, "Deepdriving: Learning affordance for direct perception in autonomous driving," in *2015 IEEE International Conference on Computer Vision (ICCV)*, Dec 2015, pp. 2722–2730.

[36] A. Gurghian, T. Koduri, S. V. Bailur, K. J. Carey, and V. N. Murali, "Deeplanes: End-to-end lane position estimation using deep neural networks," in *2016 IEEE Conference on Computer Vision and*

Pattern Recognition Workshops (CVPRW), June 2016, pp. 38–45.

[37] V. N. Murali, A. Micks, M. J. Goh, and D. Liu, "Generation and usage of virtual data for the development of perception algorithms using vision," SAE Technical Paper, Tech. Rep., 2016.

[38] B. Wymann, E. Espié, C. Guionneau, C. Dimitrakakis, R. Coulom, and A. Sumner, "Torcs, the open racing car simulator," *Software available at http://torcs. sourceforge. net*, vol. 4, no. 6, 2000.

[39] M. Aly. (2008) Caltech lanes datase. [Online]. Available: http://www.mohamedaly.info/datasets/caltech-lanes

[40] T. Wu and A. Ranganathan, "A practical system for road marking detection and recognition," in *2012 IEEE Intelligent Vehicles Symposium*, 2012, pp. 25–30.

Evaluation of LidarSLAM and Cartographer

Huajie Chen
Center for Autonomous Systems (CAS)
University of Technology Sydney (UTS)
Sydney, Australia
huajie.chen@uts.edu.au

Ayan Shrestha
Center for Autonomous Systems (CAS)
University of Technology Sydney (UTS)
Sydney, Australia
ayan.shrestha@student.uts.edu.au

***Abstract*—This paper compares two of the open-source codes for SLAM using 2D Lidar data, namely LidarSLAM in MATLAB and Google Cartographer. The comparisons using the data collected from the Fetch robot in both the Gazebo simulation environment and real indoor experiment demonstrate that both algorithms can work reasonably well for small environments. However, the robot trajectory and mapping error in LidarSLAM is significantly larger than that of Google Cartographer for bigger environment. One reason for the inferior performance of LidarSLAM is that the submaps do not overlap with one another, in contrast to Cartographer where every two consecutive submaps have about 50% overlap.**

Keywords— SLAM, laser scan, 2D Lidar, cartographer, MATLAB, LidarSLAM, trajectory comparison, simulation

I. INTRODUCTION

One of the prominent topics of discussion in the autonomous system, especially in mobile robotics is localisation which consists of estimating the robot's pose (its position and orientation) while navigating in an environment with a known map. Furthermore, when the robot is moving in an unknown and complex environment, and the exact position of the robot on the map is not identified, the robot navigation problem becomes more difficult. In addition to it, the error in estimation due to inaccurate sensor measurement increases the difficulty of the associated navigation problem. Simultaneous Localization and Mapping, well known as SLAM, is used to deal with this problem of mapping an unknown environment while keeping track of the robot's pose in the environment [1]–[3]. Earlier SLAM methods introduced the use of the Extended Kalman Filter (EKF) (EKF-SLAM) [4] and particle filter (FastSLAM) [5]. Many SLAM methods were developed over the last decade using optimisation based algorithm with each iteration giving us more accurate result. [1]–[3], [6] provides a brief introduction to the SLAM methods. Nowadays various sensors such as LIDAR, SONAR, RGB camera, RGB-D Kinect depth sensor, or stereo camera can be used depending upon the algorithm used to perform SLAM [7] and choosing the best available algorithm along with the sensor for a specific case is a problem on its own.

For the autonomy of an Unmanned Ground Vehicle (UGV), the sensor used plays a vital role. Most of the mobile robot uses Internal Measurement Unit (IMU) consisting of an accelerometer, gyroscope, and magnetometer to measures the orientation, angular velocity and the acceleration of the robot. However, just using the IMU for SLAM methods accumulates error over time, causing navigation error [8] and the final result has a large deviation with respect to map and robot's pose. Thus, a secondary sensor is required to increase the accuracy of the estimations. One of such sensors for robot navigation is LIDAR which is quite expensive but has comparatively more sensor accuracy than other sensors [9]. Various open-source packages can be found for 2D lidar SLAM systems such as GMapping [10], Hector SLAM [11], Google Cartographer [12] and MATLAB LidarSLAM.

Correct evaluation of the SLAM results after the construction of the final map is necessary for precise evaluation of the SLAM methods. One cannot decide that one SLAM method is better than other articulately without a basis for evaluation. Various papers have been published where different approaches have been taken to quantify a "ground truth" or basis for evaluation. For example, [13] uses lidar-based Hector SLAM scans as the ground truth to evaluate the performance of five ROS-compatible stereo visual SLAM methods. Furthermore, [9] and [14] evaluates various SLAM methods with visual and laser sensor based on lidar SLAM trajectories as the ground truth. Instead of using result from other SLAM methods as the ground truth, [15] proposes using precise ground truth obtained by FARO laser tracker. The paper compares three lidar-based SLAM techniques (GMapping, Hector SLAM and Cartographer). A TUM RGB-D benchmark is used in [16] to evaluate some of the new visual SLAM methods such as OpenRatSLAM, LSD-SLAM, L-SLAM and ORB-SLAM.

Another topic within SLAM evaluation is the method or metrics used to compare the final map. [17] outlines a basis for quantitative evaluation of the quality of various 2D laser SLAM algorithms. Various metrics based on capture characteristics of the final map is used to compare ROS-based SLAM methods such as GMapping, Cartographer, Hector SLAM, tinySLAM and vinySLAM. In addition to it, [18] compares the map built through various laser-based 2D SLAM algorithms using metrics based on k-nearest neighbours. A new metrics for comparison was proposed by [19] wherein CMSE (Corner Mean Square Error) and SDS (Summation of the Differences for the map's side length) was used to compare the quality of three 2D SLAM techniques. A similar approach was taken by [15] to compare the maps using ADNN (Average Distance to the Nearest Neighbours) metrics.

This paper focuses on the comparison and evaluation of the MATLAB LidarSLAM and Google Cartographer within a simulated environment created in Gazebo simulator under different circumstances (various loop closure and map area). The simulated world has its advantages like precise ground truth, trajectory, a static and robust environment without any interference. In addition to it, these algorithms were applied to a real indoor environment as well. For the experiment, the system on comparison only uses the laser range data for mapping and localisation without the IMU data. For quantitative comparison, this paper focuses on computing the differences in various distance feature in the result and ground truth map. Also, the euclidean distance between the real

trajectory and SLAM trajectory is used for trajectory comparison.

II. Brief Review of the SLAM algorithm

A. Cartographer

Developed by Google, Cartographer is an open-source library that can provide online 2D or 3D SLAM. Having integrated with ROS, Cartographer can work on multiple mobile robots with various sensor and system configurations. To achieve real-time SLAM on a moderate hardware platform, Cartographer applies pose estimation instead of particle filter to optimise the error accumulation problem for long trajectory. [12] has details about the local 2D SLAM process. Several consecutive scans are used to represent a small chunk of the environment which called submap. The submap is constructed in terms of probability grid map and all the points inside a grid are represented as a square pixel in local map. Each new scan is matched with recent submap constructed using a scan matcher. Ceres scans matching is used to find the optimised pose of the robot which maximises the submap probabilities, and a new scan is inserted into the local map. All scan points are marked as hit and all points between the robot and those scan points are marked as miss. The probability value of each grid is updated accordingly. Similar to scan matching in local process, each completed submap and new scans are matched to detect any loop closure. Branch-and-bound is applied to speed up this process. If a loop closure is detected, a pose graph optimisation is performed on all the robot's poses to optimise the accumulated error. Finally, global map is constructed by populating all the scans with the optimised poses of the mobile platform.

B. MATLAB LidarSLAM

The *LidarSLAM* is one of many open-source implementations that can generate SLAM results for multiple sensor configurations for 2D cases as long as the input argument is in a specific format (i.e. *lidarscans*). All the scans from the LIDAR are stored in a cell variable as *lidarscans* which has a specific property of *Range, Angles, Cartesian* and *Count.* The *Ranges* and *Angles* consist of all the range and angular values if the laser scan in meters and radians, respectively. The *Cartesian* consists of the matrix of the cartesian coordinates with forward and left coordinates, and the *Count* is the number of ranges and angles in the scan. *The Ranges, Angles* and *Cartesian* are associated with the same index.

Submaps are initialised which contains a certain number of scans, and incremental scan matching is performed between two consecutive scans to get a pose estimate of the robot. Firstly, a grid-based approach is used to match the laser scan pairs where the scans are converted into probability grid, and the matching is done through the correlation of the grid. To improve the computational efficiency of the matching over a large discretised search window, a branch and bound strategy is used. The same laser scans pairs are again matched with each other using Normal Distribution Transform (NDT) scan matching wherein the pose estimate is used to provide a refined pose estimate of the mobile platform. Output also consists of a '*score*' that represents the performance of the NDT scan matching (higher the score, better the scans are matched) and a '*hessian*', which is a 3-by-3 matrix representing the uncertainty associated with the pose estimate. If the difference between the pose estimate (from grid scan matching) and the refined pose estimate (from NDT scan matching) is higher than a certain value, the pose estimated in updated. The estimated pose from scan matching is compared to a '*Movement Threshold*' to determine if the robot has moved far enough or not which helps to discard scans that do not provide enough movement of the robot and saves computational time.

If the robot's pose (and scan) is accepted, it searches for loop closure. Based on the current scan and robot's pose, it searches for all the nearby submaps excluding the most recent submap. Then, the scan is matched with all the nearby submaps using a grid-based approach, and then the NDT scan-matching is used to update and refine the robot's pose. The robot poses are updated every time to construct a 2D pose graph iteratively. If the *score* of the match between the current scan and the submap is more than the threshold value (*loopClosureThresholdValue)*, a loop closure is found and the pose graph is updated using a built-in trust-region optimization wherein the node poses in the 2D pose graph is adjusted so that they comply with the underlying edge constraints as much as possible.

The process is repeated for all the scans to create the final map of the robot's movement.

C. Significant Difference

The overall process and how both algorithms work is similar. However, there is some difference in how the scan matching is performed, how the submap is created and pose graph optimisation. Different scan matcher is used for as described above (one uses grid-based and NDT while the other uses Ceres). The submap created on MATLAB LidarSLAM does not have any overlaps while the submaps on Cartographer overlap each other with some scans. Additionally, the pose graph optimiser in MATLAB uses trust-region optimisation whereas in Cartographer Sparse Pose Adjustment is used. As the Cartographer is a real-time SLAM technique, the computational time is far less than that of the MATLAB LidarSLAM.

III. Hardware and software

A. Robot System Configuration

The mobile robot used for all our experiments is called 'Fetch Robot' as shown in Fig. 1 below. The mobile platform is equipped with Intel i5 Haswell Processor, 16GB RAM, 120GB SSD and various sensors such as 2D Laser Scanner (25m Range, 220-degree angle), 3D RGB-D Primesense Carmine 1.09 in head and two IMU wheel encoders on base and gripper to calculate the wheel odometry. It uses Ubuntu Linux 16.04 installed along with ROS Kinetic.

Fig. 1. Fetch Robot used to acquire the data

*Further information on the system overview can be found on Fetch website. (https://fetchrobotics.com/robotics-platforms/fetch-mobile-manipulator/)

B. *Computer Configuration*

As the data were processed offline, we used the ground laptop to run both SLAM algorithms on the dataset obtained through the 2D LIDAR sensor. The ground station has Intel i7 8th generation processor, 16GB RAM and 2GB Nvidia Graphic.

The software used is Gazebo (for map simulation) and ROS melodic in Ubuntu Linux 18.04 for Cartographer SLAM and "MATLAB 2019a" in Windows 10 Home for LidarSLAM.

IV. Experimental Environment and Implementation

A. *Experimental environment*

For our experimental purpose, the data were first collected in a simulated indoor environment. The robot used was 'Fetch Robot' and the environment was organized as shown in Fig. 2 to create loop closure for the SLAM algorithm. Moreover, the algorithms were tested on two ROS bag collected by real fetch robot from 'UTS: Tech Lab' as well.

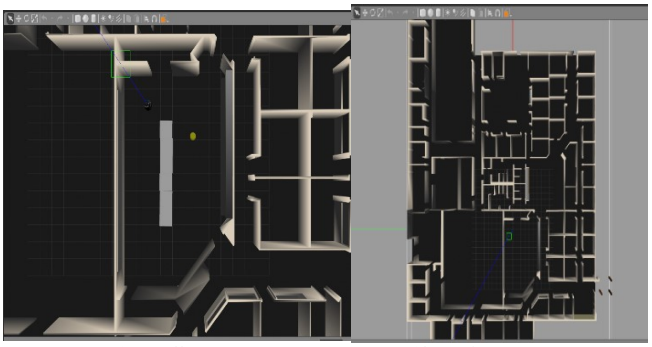

(a) Small map (b) Big map

Fig. 2. Small and big map simulated in Gazebo Simulator

The experiment was conducted with different scenarios for the mobile robot trajectory in the simulated world. A small map corresponding to a small portion of a bigger map was used to compute the efficiency of the SLAM methods. The robot was simulated to move around both small and big map with two different trajectory (one returining back to its initial position) to test the result with loop closure result.

B. *Ground Truth Map*

To compare the different result from both methods, we acquired a precise ground truth map of the simulated environment and generated a 2D occupancy grid map based on it as shown in Fig. 3. This grid map is used against the results obtained from both the Cartographer and MATLAB algorithm to evaluate their performance.

C. *Data Analysis and Map Construction*

To get a fair comparison between the two methods and analyze them under the same condition, the experimental data were collected through the fetch robot and stored as ROS bag files as these bag files will not have any difference to the data collected in real-time and are compatible with MATLAB as well. These ROS bag files consist various ROS topics corresponding to the sensor used to record the data with appropriate time sampling. These bag files were used offline in the SLAM algorithm to obtain an occupancy grid maps as shown in Fig. 4. The occupancy grid is a 2D representation of a map in space, which is a grid; each cell is a state in each space location. A cell can take one of three states: occupied, free and unknown.

In ROS Cartographer, the maps obtained in occupancy form are saved in pgm format using *map_saver* node from *map_server* package. In MATLAB, these bag files are read using built-in *'rosbag'*, *'select'* and *'readMessage'* commands to get the lidar scans. Furthermore, after the SLAM algorithm is applied to these scans, occupancy grid maps are created using the built-in *'buildMap'* function, which uses the lidar scans and the optimised poses obtained through the SLAM algorithm. The map is saved in fig format.

Various methods are available to quantify differences between SLAM result and its ground truth. In this experiment, two quantitative methods are used to evaluate two algorithms in comparison. One of the methods is distance feature measurement, wherein various distance measurements are taken from the ground truth map and compared with the measurements from the resultant map. Though this method is simple, it provides a robust comparison on different SLAM algorithms. Five manual measurements (L_1, L_2, L_3, L_4 and L_5) were taken from the ground truth map as shown Fig 3. As these measurements were taken from the Gazebo simulator itself, it can be considered precise. The measurement are taken from map obtained from Cartographer and MATLAB LidarSLAM as well and compared with the true measurement. The first two measurements are used to compare the results for small map while the last three are used for the big map.

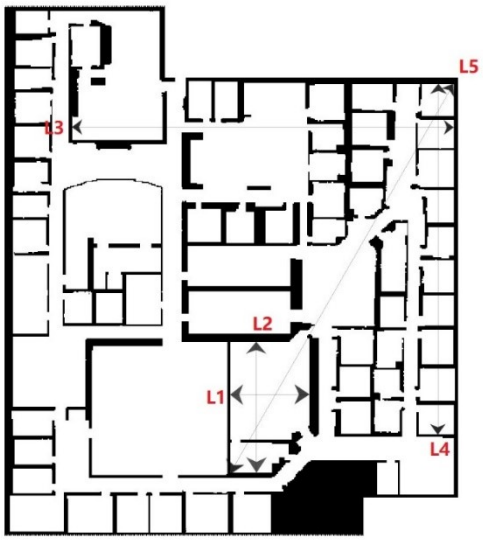

Fig. 3. Ground truth map with manual distance measurements

The second is trajectory comparison, where the Euclidean distance between corresponding points is selected to show the differences. If A and B are two trajectories with size N and M respectively, then the Euclidean distance between two trajectories is given by [20]

$$D(A,B) = \frac{1}{N}\sum_{n=1}^{N}[(a_n^x - b_n^x)^2 + (a_n^y - b_n^y)^2]^{\frac{1}{2}} \qquad (1)$$

V. Result and Discussion

The test result after the Cartographer and LidarSLAM algorithms have been applied for the different map is shown below. It can be seen from comparing the result from Cartographer and LidarSLAM for the small simulated map, there is not much difference, and the resultant map aligns with our world simulated in Gazebo. However, on the big map, there is some discrepancy between the two maps, although they look similar. a_n

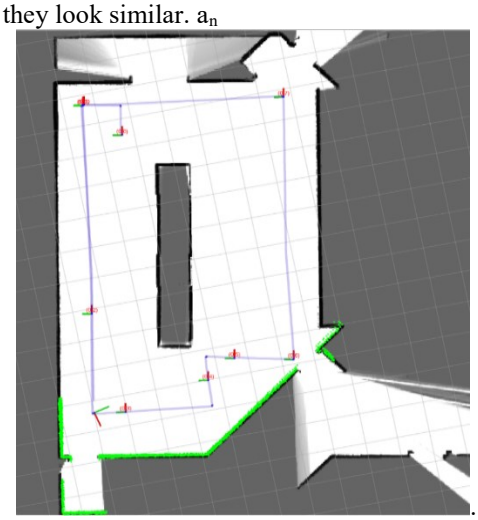
Fig. 4. Cartographer using simulated data (small map)

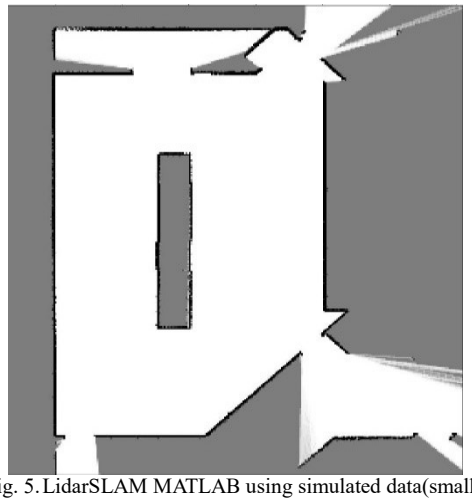
Fig. 5. LidarSLAM MATLAB using simulated data(small map)

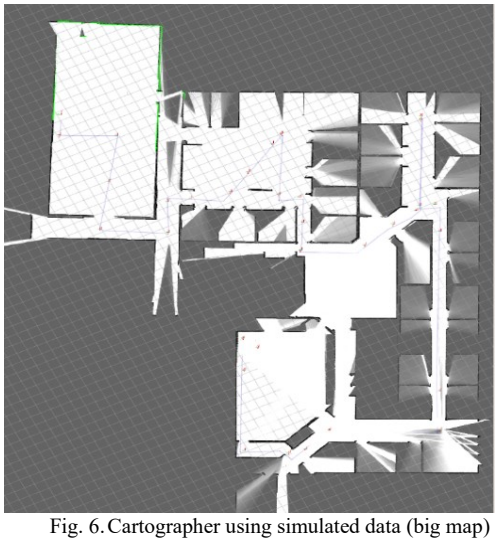
Fig. 6. Cartographer using simulated data (big map)

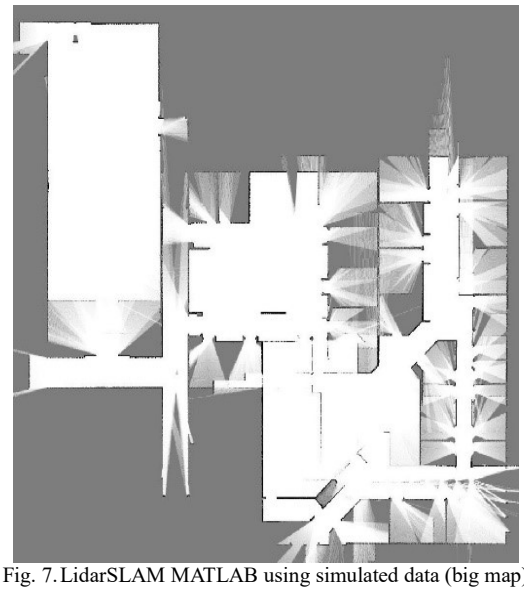
Fig. 7. LidarSLAM MATLAB using simulated data (big map)

From these maps, we acquired the distance measurements L_1, L_2, L_3, L_4 and L_5 as per the ground truth map. The differences in these measurements are shown in Table I.

DISTANCE MEASUREMENT COMPARISON IN PERCENTAGE

Lengths	Percentage Difference			
	Cartographer		*LidarSLAM*	
	Closed-loop	Open-loop	Closed-loop	Open-loop
L_1	0.126%	0.252%	0.390%	0.642%
L_2	0.405%	0.728%	0.566%	0.712%
L_3	0.104%	1.143%	0.156%	0.447%
L_4	0.190%	1.440%	5.041%	16.736%
L_5	0.086%	1.179%	3.718%	11.492%

As we can see from table 1, the measurements of L_1 and L_2 (to check the performance for the small environment) indicates that their difference from the ground truth is less than 0.8% for both the algorithms. Therefore, it can be said that Cartographer and MATLAB LidarSLAM performs well for small environment. The explanation for this is that within smaller environment (with distances less than maximum lidar range), the lidar can detect the whole environment in one scan which results in less accumulated error over the trajectory of the robot.

For the bigger environment, the measurements L_3, L_4 and L_5 indicate that Cartographer still performs well. However, the results from MATLAB LidarSLAM is poor for the bigger environment. Though the distance L_3 is somehow comparable, L_4 and L_5 measurements are very poor. One possible explanation can be that as the map features along L_4 is a long corridor with similar rooms; the MATLAB mistakenly assumes that different rooms along this corridor are same and finds the loop closures along its trajectory (as shown in Fig. 9). This results in the shrinking of the map and ultimately lowering the distance of the corridor.

In addition to it, from Table 1, it can be seen that both the algorithms have better result when the robot's trajectory is closed as opposed to open, especially in the case of MATLAB LidarSLAM, the accuracy of L_4 and L_5 increases about three times. In overall, the result from Cartographer was always better than that of MATLAB LidarSLAM.

The trajectory from Cartographer and MATLAB LidarSLAM along with the true trajectory of the robot for the small and big map is shown in Fig. 8 and Fig. 9, respectively. The black line represents the true trajectory whereas the red and blue line represents the trajectory from Cartographer and LidarSLAM respectively. While Fig. 8 portrays that both the method produces trajectories comparable to ground truth for small map, Fig. 9 shows that the trajectory from LidarSLAM deviates largely over the long corridor (along length L_4).

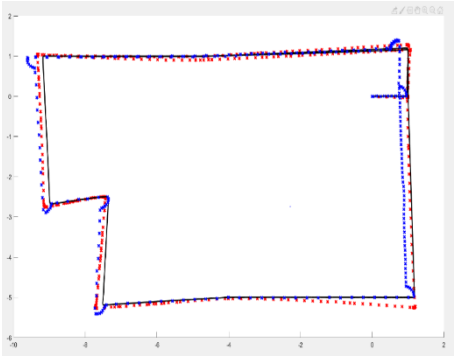

Fig. 8. Trajectory Comparison (small map)

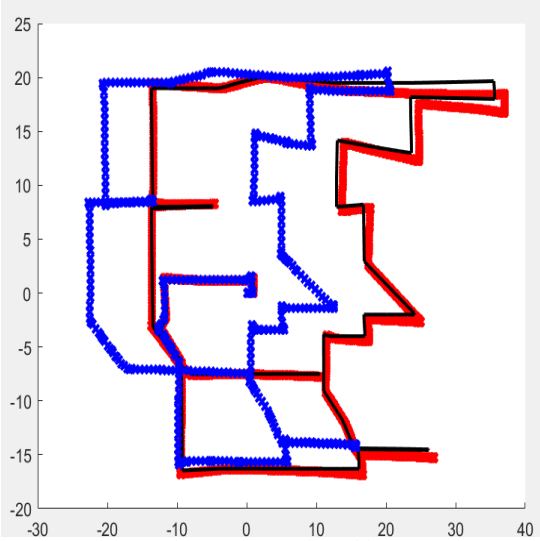

Fig. 9. Trajectory Comparison (big map)

TRAJECTORY COMPARISON

Map	Euclidean Distance in meters			
	Cartographer		*LidarSLAM*	
	Closed-loop	Open-loop	Closed-loop	Open-loop
Small map	0.099	0.112	0.108	0.135
Big map	0.381	0.389	1.318	2.736

The Euclidean distance of the trajectories from Cartographer and LidarSLAM with respect to the true trajectories is tabulated in Table II. The trajectory comparison draws a similar conclusion as distance measurement. Cartographer has superior accuracy than MATLAB LidarSLAM for bigger environment while both the algorithms have similar results for smaller environment.

The above comparison indicates that both LidarSLAM and Cartographer can do accurate SLAM on the small environment. However, LidarSLAM generates poor results on bigger environment. One possible explanation is that for LidarSLAM there is no overlap between submaps. Therefore, LidarSLAM performance poorly on finding the globally optimised poses since it has less constraint between nodes. As for Cartographer, each submap has 50% of scan in common which means that the environment overlaps between each submap.

Furthermore, occupancy grid maps produced using real dataset for LidarSLAM is shown in Fig. 10. We are in the process of conducting more practical experiments for further

comparison between LidarSLAM and Cartographer using the floor plan as the reference.

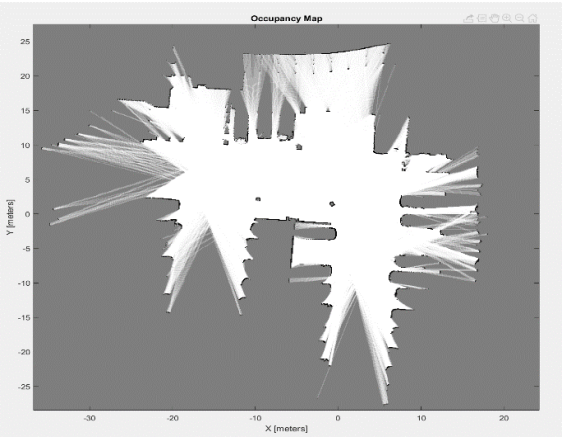

Fig. 10. Occupancy Grid Map with trajectory of real data using MATLAB LidarSLAM

VI. Conclusion and Future Work

This paper outlines the basic algorithm and working principles of google Cartographer and MATLAB LidarSLAM. Through the experiment, it was evident that Cartographer produced maps that were more precise than from LidarSLAM. Although the map generated by LidarSLAM in MATLAB was competent for smaller maps and smaller trajectory, there was some level of discrepancy in the map for a larger robot trajectory and bigger maps. Since the computation time of LidarSLAM is also significantly longer, this work suggests that LidarSLAM could be useful for understanding the modern SLAM algorithms, while Cartographer is much better for practical SLAM applications especially for large environments.

Acknowledgment

Foremost, we would like to express our sincere gratitude to our supervisor A/Prof. Shoudong Huang in Centre for Autonomous Systems, University of Technology Sydney. Along this whole project, A/Prof. Huang always offered sound suggestions and continuous support to us. This paper could not be completed without his support. Furthermore, special thanks to two postdoctoral researchers Dr Yongbo Chen and Dr Felix Kong in Centre for Autonomous Systems, University of Technology Sydney. Although occupied with their own industrial projects, they still spare no effort in helping us with this paper.

It was a great experience to work with the people mentioned above, as they not only taught us the way to do research works and paper writing but also told me the attitude you should have to face all the difficulties in your future life. These things we learnt from this project should benefit us for the rest of our life.

References

[1] T. Bailey and H. Durrant-Whyte, "Simultaneous localization and mapping (SLAM): Part II," *IEEE Robot. Autom. Mag.*, vol. 13, no. 3, pp. 108–117, 2006.

[2] *Springer handbook of robotics*, vol. 46, no. 06. 2009.

[3] C. Cadena *et al.*, "Past, present, and future of simultaneous localization and mapping: Toward the robust-perception age," *IEEE Trans. Robot.*, vol. 32, no. 6, pp. 1309–1332, 2016.

[4] T. Bailey, J. Nieto, J. Guivant, M. Stevens, and E. Nebot, "Consistency of the EKF-SLAM algorithm," *IEEE Int. Conf. Intell. Robot. Syst.*, no. 1, pp. 3562–3568, 2006.

[5] D. Rodriguez-Losada, P. San Segundo, F. Matia, R. Galan, A. Jiménez, and L. Pedraza, "Dual of the factored solution to the simultaneous localization and mapping problem," *IFAC Proc. Vol.*, vol. 6, no. PART 1, pp. 542–547, 2007.

[6] J. Aulinas, Y. Petillot, J. Salvi, and X. Lladó, "The SLAM problem: A survey," *Front. Artif. Intell. Appl.*, vol. 184, no. 1, pp. 363–371, 2008.

[7] T. J. Chong, X. J. Tang, C. H. Leng, M. Yogeswaran, O. E. Ng, and Y. Z. Chong, "Sensor Technologies and Simultaneous Localization and Mapping (SLAM)," *Procedia Comput. Sci.*, vol. 76, no. Iris, pp. 174–179, 2015.

[8] B. Barshan and H. F. Durrant-Whyte, "Inertial Navigation Systems for Mobile Robots," *IEEE Trans. Robot. Autom.*, vol. 11, no. 3, pp. 328–342, 1995.

[9] Ilmir Z. Ibragimov and Ilya M. Afanasyev, "Comparsion of ROS-based Visual SLAM methods in homogenous indoor enviroment," *2017 14th Work. Positioning, Navig. Commun. WPNC 2017*, 2017.

[10] G. Grisetti, C. Stachniss, and W. Burgard, "Improved techniques for grid mapping with Rao-Blackwellized particle filters," *IEEE Trans. Robot.*, vol. 23, no. 1, pp. 34–46, 2007.

[11] S. Kohlbrecher, O. Von Stryk, J. Meyer, and U. Klingauf, "A flexible and scalable SLAM system with full 3D motion estimation," *9th IEEE Int. Symp. Safety, Secur. Rescue Robot. SSRR 2011*, pp. 155–160, 2011.

[12] W. Hess, D. Kohler, H. Rapp, and D. Andor, "Real-time loop closure in 2D LIDAR SLAM," *Proc. - IEEE Int. Conf. Robot. Autom.*, vol. 2016-June, pp. 1271–1278, 2016.

[13] R. Giubilato, S. Chiodini, M. Pertile, and S. Debei, "An experimental comparison of ROS-compatible stereo visual SLAM methods for planetary rovers," *5th IEEE Int. Work. Metrol. AeroSpace, Metroaerosp. 2018 - Proc.*, pp. 386–391, 2018.

[14] M. Filipenko and I. Afanasyev, "Comparison of Various SLAM Systems for Mobile Robot in an Indoor Environment," *9th Int. Conf. Intell. Syst. 2018 Theory, Res. Innov. Appl. IS 2018 - Proc.*, pp. 400–407, 2019.

[15] R. Yagfarov, M. Ivanou, and I. Afanasyev, "Map Comparison of Lidar-based 2D SLAM Algorithms Using Precise Ground Truth," *2018 15th Int. Conf. Control. Autom. Robot. Vision, ICARCV 2018*, pp. 1979–1983, 2018.

[16] A. Huletski, D. Kartashov, and K. Krinkin, "Evaluation of the modern visual SLAM methods," *Proc. Artif. Intell. Nat. Lang. Inf. Extr. Soc. Media Web Search Fruct Conf. AINL-ISMW Fruct 2015*, vol. 7, pp. 19–25, 2016.

[17] A. Filatov, A. Filatov, K. Krinkin, B. Chen, and D. Molodan, "2D SLAM quality evaluation methods," *Conf. Open Innov. Assoc. Fruct*, pp. 120–126, 2018.

[18] J. M. Santos, D. Portugal, and R. P. Rocha, "An evaluation of 2D SLAM techniques available in Robot Operating System," *2013 IEEE Int. Symp. Safety, Secur. Rescue Robot. SSRR 2013*, 2013.

[19] M. Rojas-Fernandez, D. Mujica-Vargas, M. Matuz-Cruz, and D. Lopez-Borreguero, "Performance comparison of 2D SLAM techniques available in ROS using a differential drive robot," *2018 28th Int. Conf. Electron. Commun. Comput. CONIELECOMP 2018*, vol. 2018-Janua, pp. 50–58, 2018.

[20] Z. Zhang, K. Huang, and T. Tan, "Comparison of similarity measures for trajectory clustering in outdoor surveillance scenes," *Proc. - Int. Conf. Pattern Recognit.*, vol. 3, pp. 1135–1138, 2006.

Prioritisation of the Re-Railing Plan based on the "Systematic Factors Weighted Method" and Big-Data

Ralph (Wei) Zhang
School of Computing, Engineering and Mathematics
Western Sydney University
Sydney, Australia
Email address:
17602059@student.westernsydney.edu.au

Helen Wu
School of Computing, Engineering and Mathematics
Western Sydney University
Sydney, Australia
Email address:
Helen.Wu@westernsydney.edu.au

Chunhui Yang
School of Computing, Engineering and Mathematics
Western Sydney University
Sydney, Australia
Email address:
R.Yang@westernsydney.edu.au

***Abstract*—The rails are the most important component in the railroad system. The rails that installed on the track usually are the most costly asset in all of the railroad companies/authorities' financial accounts. Re-railing work has the highest priority for railway companies' annual work plan for both safely and financially. To better and effectively manage the annual re-railing work plan, a "systematic factors weighted method" has been developed to undertake this work. To ensure the accuracy of the planning work, significant amounts of information and data are required for rail and track condition evaluation, risk assessment of track components failure. In contrast to two decades ago, vast amounts of track data have become available in recent years to track engineers and maintenance planners. However, the effective collection, processing, analyzing, and utilization of this "big data" for decision-making in track maintenance works and the creation of accurate maintenance plans is a challenge for the department of track maintenance. To effectively undertake the risk assessment and maintenance prioritization of the re-railing locations on the railway network, the specified analysis model is developed to carry out this work using the "big data."**

Keywords*—*Re-Railing, plan, systematic factors weighted method, big data

I. INTRODUCTION

The economic value of the installed rails in the network is usually the most costly asset for any railway authorities. To better and effectively manage the annual re-railing work for a new financial year, the rail sections listed in an Annual Work Plan (AWP) are prioritised based on the ranking of the importance in the railway network and the potential risks from its worn, fatigue and traffic conditions.

The prioritisation work is started from the development of a specified analysis method (algorithm model), data process and provide the recommendations for the remedial actions.

The rail condition related data/information from track defect database and meter-length based rail condition data from the inspection cars, rail asset management data base - Rail Head Profile Analysis – Residual Life, track characteristic and revenue information such as track speeds and gradient diagrams from the "Drivers Route Knowledge Diagram" and "Track Pages" of curvature and gradient are all used as the information/data resources to undertake the prioritisation work.

II. BIG DATA

Concept of Big Data

In general, big data is a term that describes the large volume of data, both structured and unstructured, that inundates a business on a day-to-day basis.

Big Data usually has a multi-dimensional structure and can be characterized by the 5V's:

- Volume - algorithms or analysis models are required to undertake the processing, analysis and story of the huge amount of data.
- Velocity - how to analyse and process the type of real-time data.
- Variety - how to deal the data with different types of structures.
- Veracity - the indication of integrity of the data.
- Value - the worth of the information/data.

Application in Railway Track

Big data represents a challenge and an opportunity to the railroad industry. One of the major reasons that the railroad industry is so interested in leveraging big data is that a potential for incredible value-added for relatively little expenditure.

Nowadays, in the current "big data" era, the track engineers need to undertake further deep data analysis from extant data but not only focus on collecting new data from new sources.

In recent years, the railroads industry has started to make extensive use of its big data. It is focus on to optimize its capital infrastructure and safely manage its operations while keeping costs under control.

Level of Data Analysis and Big Challenges

The level of "big data" analysis can be divided into 5:

- Level 1: This is the lowest level. For this level, only basic threshold analyses are to be performed. It is used to determine if the data exceed a predefined

threshold which is used to represent the maintenance and safety thresholds.

- Level 2: Big data is used to undertake historical monitoring, trend analysis and basic forecasting.
- Level 3: Big data is used for the statistical analyses to develop higher order forecasting and trend analysis.
- Level 4: Forecasting models are to be combined with maintenance planning to support the advanced decision making.
- Level 5: The highest level. The economic analyses model is introduced into the forecasting model.

This innovation work for level crossing management is in the level 3 to 4.

During the practice of data application, many of the railway authorities have already realized that the integrating multiple data sets and making sure data cross references is a big challenge.

III. Algorithm for Analysis

For the prioritisation work, all the factors/reasons which can cause to the rail replacement are considered. These including: side wear, vertical wear, type of traffic, rail type and rail condition to failure (how far out of standard). In addition, the current rail conditions and its deterioration ratio such as existing rail surface defects, rail internal defects and wear rate are need to be included into the risk/condition assessment. Moreover, the support type (type of sleepers), traffic speed, track curvature (cant deficiency) and gradient are also played as important factors to the safety of the usage of rails.

Technical Requirement

To better and more effectively manage the risks from rail broken which are initiated from the defective rails, the prioritisation analysis of the re-railing work is to be undertaken, including the development of a specified analysis methodology (algorithm model), data process and providing the recommendations/suggestions for the short, medium and long term remedial actions.

Methodology for Data Processing

Based on the concept of always "managing track as an integrated structural system and not individual components," all the causal factors that can lead to the development of rail broken (failure) were considered in the prioritization work.

As the start point of this analysis work, defective rail data collection and validation were undertaken. The data resources collected for use in this prioritization work included: information about the defective rail condition from the track defect database; track patrol reports and findings; rail defect data from walk inspections and the track geometry inspection car; track characteristics and revenue information such as track speeds and gradient diagrams; curvature and gradient data; features of track structures such as bridge transition area, level crossings, turnouts, and tunnels; track classification (main line, branch line, and sidings/loops); level of track equipment (rail type, type of sleeper, and fastening systems); and rail conditions from the meter-length based rail condition data from the inspection cars, Rail Head Profile Analysis – Residual Life.

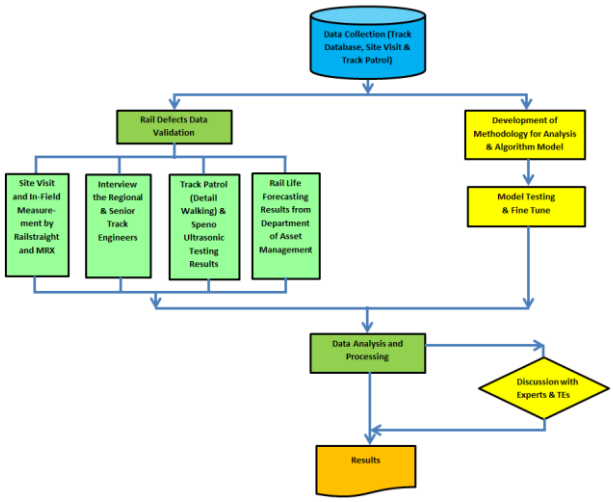

Fig. 1 Flow chart of defective rail replacement prioritisation analysis and data processing

To ensure the accuracy of the rail defect data, validation works were done by means of site visits, interviews with Territory engineers, and comparison of the inspection car data with images from the recording car. A flow chart of the bog hole prioritization analysis and data processing work is shown in the Fig. 1.

Algorithm Development: General Concepts

A specified analysis model was required to carry out the highly complex prioritization work by using "big data," as mentioned previously. For the algorithm development, knowledge of theories and practices of track maintenance were utilized. The analysis model adopts the concept of a "Systematic Factors Weighted Method." Similar ideas were used in a joint development project between the Association of American Railroads and the famous American company Zeta-Tech Associates in the early 2000s for allocating track maintenance costs on shared rail facilities. The outcome of this project—a "weighted system average cost" model—has been programed as specific software, "Trackshare." This analysis model and the Trackshare software have been widely acknowledged and used in North American railway companies as effective tools for rail maintenance management [4].

Regarding the specially designed analysis model for defective rail prioritization work, all the factors affecting the generation of bog holes were categorized into two parts: the "system average damage factors" and "engineering adjustment modifier."

A mathematical formula to represent the above general concept is:

$$S_{risk} = \sum_{i=3}^{3} S_{Rail} \times \left(1 + \sum_{n=4}^{4} F_{RMn}\right) + \sum_{m=2}^{2} S_{Tm} + \sum_{0=2}^{2} S_{DO} + S_{wear}$$

Where:

S_{risk} - The overall score of risk ranking for the re-railing sections, based on the rail condition;

S_{Raili} - Score of risk ranking based on the condition of rail worn, which is including the vertical worn (low rail), side worn (high rail), and the rail types (60kg/m HH, SC, 53kg/m, 50kg/m, etc.);

F_{RM} - Engineering modification factors from curvature (impact from the additional vertical load), gradient (slope of track), support type (track stiffness) and capacity with vertical load (capacity lost caused by vertical wear);

S_T - Score of risk ranking based on the traffic condition, which is including speed (dynamic factors) and type of revenue (passenger only or passenger mixed with freight);

S_D - Score of risk ranking based on the existing rail defects, which is including two categories: the rail surface defects and internal defects;

S_{Wear} - Score of risk ranking base on the wear rate (how many days the rail will reached to the condemned condition based on the current traffic condition and location in the track).

Additional wheel load will apply on the rails by the track design features of curvature (impact from the additional vertical load), gradient (slope of track) and support type (track stiffness). In addition, the additional rail broken risk is raised up from the lost capacity caused by the vertical wear of rail head.

The design features and track conditions of individual track sections were used as the "engineering adjustment factors" to modify the risk ranking scores of these four major reasons.

IV. Thresholds for Risk Ranking

Scores Used to Represent the Rail Conditions

Rail type. The risk ranking for the different type of rails is given in Table 1.

TABLE 1: RISK RANKING FOR DIFFERENT RAIL TYPES

Risk Rank (Score)	*Rail Type*
1	60kg/m Head Hardened
2	60kg/m Standard Carbon
3	53kg/m Head Hardened
4	53kg/m (107LB) Standard Carbon
5	50kg/m Standard Carbon
6	47kg/m Standard Carbon

Vertical worn (low rail), side worn (high rail). The risk of rail broken is highly dependent on the condition of rails. The scores of risk ranking are represented in Table 1.

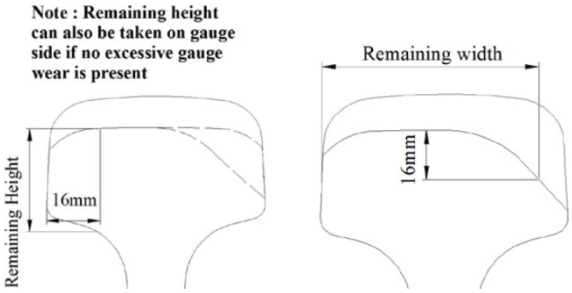

Fig. 2 Rail wear measurement - loss of width and loss of height measurement

Engineering Modification Factors for Rail Condition

For the risk ranking based on the rail condition, the scores need to be adjusted by the engineering modification factors for the rail strengthen capacity (vertical load that can cause the rail broken), structural features of the track which including: the curvature, gradient and support type (track stiffness). The modification factors are developed to represent the impacts from them.

Curvature. Additional wheel load which is caused by cant deficiency only be considered where the radius of curve is equal or less than 400m.

Wheel load due to cant deficiency. This load is produced by the centrifugal acceleration exerted on the wheels of a vehicle that is running in a curve with cant deficiency. It is not, however, a dynamic load in the sense of the load referred to in the previous sections. Therefore, it is often considered to be a semi-static load, and it can be calculated as the following equation:

$$R_{Cant} = \frac{2 \times D \times h_{CG}}{{L_g}^2} \times R_V$$

Where:

R_{cant}- Additional wheel load caused by the cant deficiency, kN;

D - Cant deficiency, mm;

h_{CG} - The height of the centre of gravity of the vehicle from the rail head, m;

R_V - The wheel load, kN;

L_g- The track gauge, m.

For this analysis, the h_{CG} = 2m is used for both of the freight and passenger vehicles.

TABLE 3: MODIFICATION FACTORS FOR THE CURVATURE OF TRACK

Modifier	*Curvature*	*Traffic Type*
0.21	Radius of curve R ≤ 400m	Passenger Main Line and Mixed Passenger Freight Main Line (XPT)
0.15		Light Passenger
0.10	Radius of curve R ≤ 600m & > 400m	Passenger Main Line and Mixed Passenger Freight Main Line (XPT)
0.08		Light Passenger
0	Radius of curve > 600m	All traffic types

Gradient. When locomotives operate on the steep gradient tracks, additional tractive load is required, this will increase the bending stress in the rail and increase the vertical and side wear of rail.

TABLE 4: MODIFICATION FACTORS FOR THE GRADIENT OF TRACK

Modifier	*Gradient*	
0.025	Gradient (1/50 to 1/30)	1:40
0.014	Gradient (1/100 to 1/50)	1:70
0.008	Gradient (1/150 to 1/100)	1:120
0.005	Gradient (1/200 to 1/150)	1:175

Support type (Track stiffness). The track support type will significantly impact to the bending stress of the rails. The track load calculation for modern railway track design is based the "Quasi-static principle". The maximum bending moment is calculated based on the "beam on elastic foundation" model. Using the calculated the design wheel load, the rail bending stress can be worked out:

$$M_{max} = \frac{1}{4k} \sum P\varphi_n$$

Where:

M_{max} - Maximum bending moment of rail;

P - Wheel load (vertical) on the rail head;

k – Factor of proportion between the stiffness of track foundation and rail;

φ_n - 1.1488

$$u = \frac{D}{L_{sleeper}}$$

Where:

u - Modulus of track elasticity, kN/cm/cm;

D - Stiffness of track support, kN/cm, as shown in Table 5;

$L_{Sleeper}$ ---- Sleeper spacing (centre to centre), cm.

TABLE 4: STIFFNESS OF TRACK SUPPORT

Track Condition	*Stiffness of Track Support – D (kN/cm)*	*Modulus of Track Elasticity - u*	*Remarks*
60kg/m rail concrete sleeper track and sleeper spacing is 600mm	300	5.00	
53kg/m rail concrete sleeper track and sleeper spacing is 600mm	220	3.67	
60kg/m rail timber sleeper track and sleeper spacing is 600mm	170	2.83	Average value
53kg/m rail timber sleeper track and sleeper spacing is 600mm	135	2.25	Average value
53kg/m rail timber sleeper track and sleeper spacing is 720mm	100	1.39	Average value
47kg/m rail timber sleeper track and sleeper spacing is 720mm	80	1.11	Average value

$$k = \sqrt[4]{\frac{u}{4EJ}}$$

Where:

u - Modulus of track elasticity, kN/cm/cm;

E - Elastic Modulus of Rail steel E = 2.1×10^5, (MPa);

J - Second moment of area (cm^4).

TABLE 6: FACTOR OF PROPORTION BETWEEN THE STIFFNESS OF TRACK FOUNDATION AND RAIL

Track Condition	*k*	*Modulus of Track Elasticity - u*	*Elastic Modulus of Rail Steel (MPa)*	*Second Moment of Area (cm^4)*
60kg/m rail concrete sleeper track and sleeper spacing is 600mm	0.01194	5.00	2.1×10^5	2930
53kg/m rail concrete sleeper track and sleeper spacing is 600mm	0.01176	3.67	2.1×10^5	2280
60kg/m rail timber sleeper track and sleeper spacing is 600mm	0.01036	2.83	2.1×10^5	2930
53kg/m rail timber sleeper track and sleeper spacing is 600mm	0.01041	2.25	2.1×10^5	2280
53kg/m rail timber sleeper track and sleeper spacing is 720mm	0.00923	1.39	2.1×10^5	2280
47kg/m rail timber sleeper track and sleeper spacing is 720mm	0.00913	1.11	2.1×10^5	1900*

* Estimated value

$$M_{max} = \frac{1}{4k}\sum P\varphi_n$$

For the dynamic load, this is calculated by the static load multiply by the factor of 2.57.

$$M_{max} = \frac{1}{4k}\sum P\varphi_n = \frac{1}{4k}P_{dynamic}$$

TABLE 7: MAXIMUM BENDING MOMENT OF RAIL

Track Condition	*M_{max} (kN.cm)*	*$P_{dynamic}$*	*K*
60kg/m rail concrete sleeper track and sleeper spacing is 600mm	3364.91	160.69	0.01194
53kg/m rail concrete sleeper track and sleeper spacing is 600mm	3415.19	160.69	0.01176
60kg/m rail timber sleeper track and sleeper spacing is 600mm	3878.30	160.69	0.01036
53kg/m rail timber sleeper track and sleeper spacing is 600mm	3858.66	160.69	0.01041
53kg/m rail timber sleeper track and sleeper spacing is 720mm	4967.97	183.38	0.00923
47kg/m rail timber sleeper track and sleeper spacing is 720mm	5018.93	183.38	0.00913

TABLE 8: MODIFICATION FACTORS FOR THE SUPPORT TYPE OF TRACK

Modification Factor	*Track Type*		
	Rail Type	*Sleepers*	*Sleeper Spacing*
0	60kg/m rail	concrete sleeper	600mm
0.015	53kg/m rail	concrete sleeper	600mm
0.153	60kg/m rail	timber sleeper	600mm
0.147	53kg/m rail	timber sleeper	600mm
0.476	53kg/m rail	timber sleeper	720mm
0.492	47kg/m rail	timber sleeper	720mm

Modification factor of rail strengthen capacity (vertical load that can cause the rail broken). The infrastructure modifier of rail conditions is mainly considering the impact from the rail wear. In the case of wear in terms of head-height loss, only the vertical component of the longitudinal bending stress is considered. The calculation is mainly based on the knowledge of material mechanics and the method of calculation of rail wear limits on rail strength, which is recommended by the US Department of Transportation and Federal Railroad Administration. The US method is firstly developed by Jeong, Tang and Orringer in 1996. The details of the mathematical model and numerical study process are represented in the Appendix A: Worn Rail Strength Analysis [7].

The infrastructure modifier of different levels of rail conditions is tabulated in Table 9.

TABLE 9: MODIFICATION FACTOR OF CAPACITY WITH VERTICAL LOAD

Rail Type and Condition of Wear	*Modification Factor*
60kg/m Head Hardened Rail or Standard Carbon Rail at the vertical wear condition of "reportable" level – 17mm	0.2307
60kg/m Head Hardened Rail or Standard Carbon Rail at the vertical wear condition of "Heavy Worn" level – 20mm	0.2640
60kg/m Head Hardened Rail or Standard Carbon Rail at the vertical wear condition of "condemned" level – 23mm	0.2919

Worn rail strength analysis: In the case of wear in terms of head-height loss, only the vertical component of the longitudinal bending stress is considered. The calculation is mainly based on the knowledge of material mechanics and the method of calculation of rail wear limits on rail strength, which is recommended by the US Department of Transportation and Federal Railroad Administration. The US method is firstly developed by Jeong, Tang and Orringer in 1996 [7].

Approximation of worn rail section properties: In this analysis, wear is assumed to occur from uniform loss of material from the rail head. The amount of wear is quantified by the thickness of metal losing from the top of rail head and then a percentage of the rail head area, which can be related to head-height loss.

These equations were derived from idealizing the actual rail cross-section as three rectangular sections representing the head, web, and base of the rail.

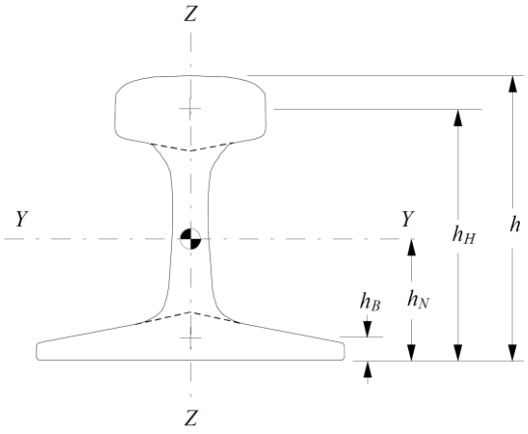

Fig. 3: Dimensions for a generic rail section

According to the method suggested by US Department of Transportation, the following equations are applied to determine section properties for rail affected by wear in terms of head-height loss. The loss of rail-head height and the equivalent rail-head height are related by:

$$\Delta h = \left(\frac{X}{100}\right)\cdot h_{eq}$$

Where:

Δh - The loss of rail head height;

X - The percentage of worn rail-head area;

For the case of 10 mm vertical worn rails: Δh =10 mm, and X ≈ (10×70)/2960 = 23.65%. Input into the above equation:

$$\Delta h = \left(\frac{X}{100}\right)\cdot h_{eq}$$

$$h_{eq} = 42.28 \text{ mm}$$

$h_N(X)$ is the distance from the bottom of the rail to the centroid of the worn rail, which is calculated from:

$$h_N(X) = \frac{A_R \cdot h_N(0) - A_H \cdot h_H(0) + \left[\left(1-\frac{X}{100}\right)\cdot A_H\right]\cdot h_H(X)}{A_B + A_W + \left[\left(1-\frac{X}{100}\right)\cdot A_H\right]}$$

Where:

A_R - Cross-sectional area of the entire rail, AS60kg rail = 7770 mm^2;

$h_N(0)$ - The distance from the bottom of the rail to the centroid of the new or unworn rail, AS60kg rail = 79.1 mm;

A_H - Cross-sectional area for the rail head only;

h_H - Distance from the bottom of the rail to the centroid of the rail head;

A_B - Cross-sectional area for the rail base only;

A_w - Cross-sectional area for the rail web only;

$h_H(X)$ - The distance from the bottom of the rail to the centroid for the rail head only in a worn rail;

$h_H(0)$- The distance from the bottom of the rail to the centroid for the rail head only in a new or unworn rail.

$h_H(0)$ calculated by hand calculation which is equal the centroid of rail head area only add the distance of from bottom of rail head to the bottom of rail base which is: 121 mm + 25.718 mm = 146.718 mm.

For the details of h_H calculation, the y axis is placed along the axis of symmetry so that $\bar{x} = 0$. To obtain $\bar{y}$, we establish the x axis (reference axis) through the base of the area. The whole area of rail head is segmented into one Trapezoidal area and one Triangular area and subtract two Parabolic areas. The centroid location $\bar{y}$ for each area is established, then applying equation:

$$\bar{y} = \frac{\sum \bar{y}A}{\sum A} = 25.718 \text{ mm}$$

$h_H(X)$ is calculated from:

$$h_H(X) = h - \frac{1}{2}\cdot \Delta h$$

Where:

h - The total height of the rail

For the case of 10 mm vertical worn rails: Δh = 10 mm,

$$h_H(X) = h - \frac{1}{2}\cdot \Delta h = 165 \text{ mm}$$

For the AS60 kg/m rail, as shown in Fig. 3, when the vertical worn is 10 mm, applying equation:

$$h_N(X) = \frac{A_R \cdot h_N(0) - A_H \cdot h_H(0) + \left[\left(1-\frac{X}{100}\right)\cdot A_H\right]\cdot h_H(X)}{A_B + A_W + \left[\left(1-\frac{X}{100}\right)\cdot A_H\right]}$$

$$= 78.248691 \text{ mm} \approx 78.25 \text{ mm}$$

Strength analysis for vertical worn rails. Two conditions of vertical worn rails are calculated for this analysis - 10 mm and 15 mm vertical worn from the top of rail head and presume the metal is lost uniformly.

The parallel-axis theorem, however, must be applied to determine the vertical bending inertia because the neutral axis of the entire rail shifts from the loss of material. This concept is shown schematically in Fig. 4.

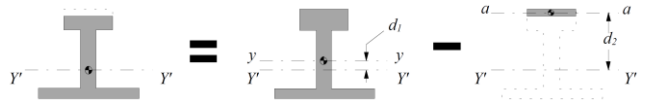

Fig. 4 Schematic for vertical bending inertia calculation for rail head height loss

Referring to this figure, the second area moment of inertia about the horizontal axis through the centroid of the rail with head-height loss is equal to:

$$I_{YY'} = \left[I_{yy} + A_R d_1^2\right] - \left[I_{aa} + A_{aa} d_2^{\,2}\right]$$

Where:

$I_{YY'}$ - Moment of inertia about horizontal axis for a top worn rail

I_{yy} - The vertical bending inertia for the unworn new rail, for the AS 60kg/m rail, using 29.4 × 10^6 mm^4

A_R - The cross-sectional area of the new or unworn rail, for the AS 60kg/m rail, using 7770 mm^2

d_1 - The distance between the centroids of the worn and unworn rails, for the 10 mm vertical worn rail using (79.1-78.25) = 0.85 mm, for the 15 mm vertical worn rail using (79.1-73.0215) = 6.0785 mm.

I_{aa} - The vertical bending inertia for the worn area

A_{aa} - The amount of worn area

d_2 - The distance between the centroid of the entire worn rail to the centroid of the worn-away area. For the 10 mm vertical worn rail using 86.75 mm, for the 15 mm vertical worn rail using 89.4785 mm.

For the 10 mm vertical worn condition:

$$I_{YY'} = \left[I_{yy} + A_R d_1^2\right] - \left[I_{aa} + A_{aa} d_2^{\,2}\right]$$

$$\approx 24.132 \times 10^6 \ (mm^4)$$

Maximum of elastic vertical load:

$$V_e = \frac{\sigma_{YLD}}{\left(\frac{h - h_N}{4\lambda_V I_{yy}}\right)}$$

Where:

h - Height of rail;

I_{yy} - The vertical bending inertia for the unworn new rail, for the AS 60kg/m rail, using 29.4 × 10^6 mm^4;

σ_{YLD} - The proof stress at 0.2%, using 420 MPa for 60kg/m plain carbon rail and 780 MPa for 60kg/m head harden rail.

The "slow bending machine" is designed to carry out the laboratory testing of "Three-points bending". The rail at rail head up direction, and load applied as a point load and the distance between two supporters is 1 m.

For the condition of 10 mm vertical worn, using σ_V = 780 MPa,

$$\sigma_V = \frac{M_V \cdot c}{I_{YY'}}$$

P = 962.2 kN

For the condition of 10 mm vertical worn, using σ_V = 750 MPa, similarly:

P = 925.2 kN

Calculation for the 15 mm vertical worn condition, for the case of 15 mm vertical worn rails: Δh = 15 mm, and X ≈ (15×70)/2960 = 35.47%.

$h_H(X)$ for the condition of 15 mm vertical worn:

$$h_H(X) = h - \frac{1}{2} \cdot \Delta h = 170\text{-}15/2 = 162.5 \text{ mm}$$

$h_N(X)$ is the distance from the bottom of the rail to the centroid of the 15 mm vertical worn rail:

$$h_N(X) = \frac{A_R \cdot h_N(0) - A_H \cdot h_H(0) + \left[\left(1 - \frac{X}{100}\right) \cdot A_H\right] \cdot h_H(X)}{A_B + A_W + \left[\left(1 - \frac{X}{100}\right) \cdot A_H\right]}$$

$$= 73.0215 \text{ mm} \approx 73.0215 \text{ mm}$$

For the 15 mm vertical worn condition:

$$I_{YY'} = \left[I_{yy} + A_R d_1^2\right] - \left[I_{aa} + A_{aa} d_2^{\,2}\right]$$

$$\approx 21.26 \times 10^6 \ (mm^4)$$

For the condition of 15 mm vertical worn, using σ_V = 780 MPa,

$$\sigma_V = \frac{M_V \cdot c}{I_{YY'}}$$

$$0.0182553 \text{ P} = 780 \times 21.260679$$

P = 908.41 kN

For the condition of 15 mm vertical worn, using σ_V = 750 MPa, similarly:

P = 873.47 kN

Similarly, the rail broken load for different level of rail vertical worn can be calculated. Then, by using the "scaled up & take an integer" manner, the modification factors for different vertical worn can be calculated, some widely used factor data are tabulated in the Table 9.

Risk Ranking Score for Traffic Condition

From the practice of rail track maintenance, the track engineers have realised many years ago for that if the annual gross tonnage of traffic is same, the railway traffic which revenue for higher axle load needs more ballast related (tamping, ballast cleaning etc.) track maintenance work. Hence, for the prioritisation work the type of traffic, i.e. the maximum axle load of freight train is to be considered and logically ranked by hierarchized scores.

The risk ranking score for traffic type and axle load is based on the wheel load will apply to the track components (sleepers, fastening system, rail pad/ rail plate, and ballast/sleeper base contact area), as the railway track is designed on the theory of "Beam of Elastic Foundation (BOEF)".

According to the "Australian Standards 1085.14 Railway track material – Part 14: Prestressed Concrete Sleeper" and "1085.19 Railway track material – Part19: Resilient fastening assemblies", the following equation is to be used for the of wheel load calculation:

$$R_V = \frac{P_{dV} \times DF}{100}$$

Where:

R_v - The vertical design rail seat load (kN);

P_{dV} - Vertical design wheel load (i.e. the static wheel load), which is calculated by half of the axle load (kN); for 15t, 25t and 30t axle load, the PdV is 73.6kN, 122.6kN and 147.2kN respectively.

DF - Load distribution factor (i.e., Axle load carried by single sleeper). From the Australian Standard AS1085.14, for the sleeper spacing is 600mm, the DF is 51.

For the axle load is 15t, 25t, and 30t, the vertical design rail seat load Rv is 37.5kN, 62.5kN and 75.1kN.

The actual wheel load applied on the top of rail is the dynamic load, which is calculated by static load R_v multiplied by the dynamic factor, the suggested dynamic factor which is obtained by long-term in-field measurement by Sydney Trains (originally RailCorp), the design value is 2.57. (ARTC is using the dynamic factor of 2.04 for design).

Hence, the value of dynamic load is:

- 96.46kN for 15TAL;
- 160.69kN for 25TAL;
- 192.94kN for 30TAL.

From the Australian Standards AS1085.14 & AS1085.19, the wheel load applied on the rail seat of each sleeper is combination of vertical load and lateral load, the lateral load is calculated by 50% of the vertical dynamic load, hence, the wheel load is to be obtained by combine the vertical and lateral load as:

$$R_{wheel} = \sqrt[2]{(R_V)^2 + (R_L)^2}$$

The wheel load is applied to the rail head and also the rail seat of sleeper with a 26.5° to the vertical direction, as shown in Fig. 5. And the value of wheel load is:

- 107.9kN for 15TAL;
- 179.7kN for 25TAL;
- 215.7kN for 30TAL.

For the risk ranking, the score is obtained by using the 15TAL static vertical wheel load 37.5kN as the reference and scale up by wheel load divide the reference load and take an integer. The risk ranking value is tabulated in the Table 10.

TABLE 10: RISK RANKING SCORES OF TRAFFIC TYPES OF TRACK

Risk Ranking Score	***Wheel load (Combination of vertical and lateral loads) divided reference load 37.5kN***	***Traffic Type & Axle Load***
6	5.75	30TAL & XPT
5	4.79	25TAL & XPT
5	4.79	25TAL & Low Speed Passenger Train
3	2.88	Low speed passenger train only (15TAL)

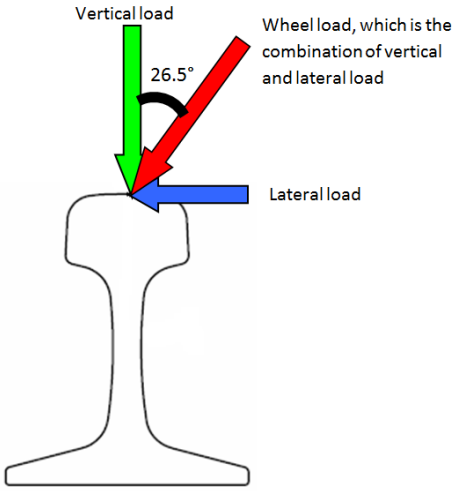

Fig. 5 Wheel loading for concrete sleeper design

Modification Factors for Speed

The additional wheel load that purely results from the speed increasing is not very significant. For example, if the rail surface and track geometry condition is relatively good, when the train speed increased from 60km/h to 120km/h, the additional vertical wheel load is only increased for about 16%.

Irregularities and non-uniformities in the track and the wheel and rail profile: The threshold of the risk ranking is determined by convert the research results that obtained from long team in-field testing of the impact load caused by the shorter wavelength irregularities (wavelength is 60mm and depth is 3mm) in later of 1980s by the Railway Transportation Academy of former Soviet Union. The conversion is in a "scaled up & take an integer" manner, the baseline (reference value) value 1 is represented the wheel riding on even rail surface with the speed of 10km/h, and the dynamic impact load factor is obtained by the average load value in deferent speed divided by the reference load value.

The dynamic factor for concrete sleeper design of RailCrop is utilised 2.57, Australian Rail Track Corporation (ARTC) is used 2.04, and the suggested dynamic factor from Australian Standard AS1089.14 is 2.5.

TABLE 11: RISK RANKING SCORES OF TRAIN SPEED (PASSENGER TRAIN)

Risk Ranking (Score)	Train Speed	Description (Dynamic Factor)
6	≥ 120km/h	NA
5	≥ 100km/h & < 120km/h	3.59
4	≥ 70km/h & < 100km/h	3.23
3	≥ 40km/h & < 70km/h	2.13
2	≥ 10km/h & < 40km/h	1.43

Risk Ranking Scores of Existing Rail Defects

Existing rail defects which including two categories – rail surface defects and internal defects.

Rail surface defects. The risk ranking scores for the rail surface defects is tabulated in Table 12.

TABLE 12: THE RISK RANKING SCORES FOR THE RAIL SURFACE

Risk Rank (Score)	*Type & Details of Rail Surface Defects*	*Remarks & Details*
15	More than one P2 rail surface defects existing	
8	One P2 surface defects existing	Including long wavelength corrugation defects
5	More than one P3 rail surface defect existing	Including medium wavelength corrugation defects
2	P3 rail surface defect existing	Including medium wavelength corrugation defects
1	Corrugation defect existing	Short wavelength or roaring rail corrugation defects

Rail internal defects. The risk ranking scores for the rail internal defects is tabulated in Table 13. For the risk assessment that caused by the rail internal defects, there is no doubt for that the different types and size of the defects should have the different "analysis weight" for the risk assessment. So, the numbers of critical defects among the defects that have been found in the history by ultrasonic test are risk ranked as shown in Table 13.

Regarding to the threshold of the critical defects for this analysis, according to the risk based theory used for scheduling ultrasonic test frequencies which is developed by the US Department of Transportation (DOT), the number of "0.1 'Service' (i.e. Critical) defects/mile" is acknowledged as the allowable baseline for US freight line. And, the risk value for "US Freight Average" and "Low Speed Passenger Service" are 0.1 and 0.03 respectively, i.e., the risk ranking weight of "Low Speed Passenger Service" is 3.33 times higher than the track which is predominated by freight traffic. Hence, the threshold value is set by: $(0.1 / 1.6) / 3.33 = 0.0188 \approx 0.02$ critical defects/km.

TABLE 13: RISK RANKING BASED ON CRITICAL RAIL DEFECTS THAT HAVE BEEN FOUND IN THE HISTORY

Risk Rank (Score)	*Type of Internal Defects*
30	More than 1 critical defects existing
10*	1 critical defects existing
7	Small transverse defect existing
5	Other small size non-critical internal defects existing

Note: The "step" of risk ranking for the situation of below and above the threshold value of critical defects is not linearly changed, which is used to represent the risk to rail broken/failure during the traffic revenue.

Risk Ranking Scores of the Wear Rate

The rate of rail head wear is to determine the expected life of the rail under particular operating conditions. The risk ranking scores for the wear rate is tabulated in Table 14.

TABLE 14: RISK RANKING BASED ON WEAR RATE

Risk Ranking (Score)	*Days Surpass (+) or Reach to (-) the Condition Level of Condemn** (Day)*
5	≥ 1000
4	< 1000 & ≥ 365
3	< 365 & ≥ 180
2	< 180 & ≥ 0
1	< 0 & ≥ -365
0	< -365

* Rail Head Profile Analysis – Residual Life.
** Based on all parameters worst case scenario.

Table 15 represents the risk ranking scores of "How far out of standard".

IV. CONCLUSIONS AND RECOMMENDATIONS

There is cutting-edge research going on globally of big data application in track maintenance in the last decade. The current use has only scratched the surface of deep data analysis. As a practice of big data approach, the "Systematic Factors Weighted Method" model has been utilized to undertaken the prioritization work of the re-railing plan. It has been shown that this is an accurate and effective method to systematically study, assess and prioritize the condition of the planned re-railing locations.

REFERENCES

[1] Zarembski, "Big data in railroad maintenance planning: 2016," Interface – The Journal of Wheel/Rail Interaction. October, 2016.

[2] L. Luo, G. Zhang, W. Wu and X. Chai, The Control of the Situation of Track Irregularities in the Wheel Rail System. P51, Chinese Railway Publishing House, 2006, Beijing. China (in Chinese).

[3] X. Chen, W. Wang, Railway Track Engineering. China Architecture & Building Press, 2006, Beijing. China (in Chinese).

[4] K. Giannakos, Damage of Railway Sleepers Under Dynamic Loads: A Case History from the Greek Railway Network. 6th International Conference on Case Histories in Geotechnical Engineering, August 11-16, 2008. Arlington, VA, USA.

[5] D. Uzarski, Introduction to Railroad Track Structural Design. BCR2A'09 Railroad Track Design Imcluding Asphalt Trackbeds Pre-Conference Workshop. Illinois University Railroad Engineering Program, 2009, USA.

[6] R. Resor, P. Patel, "Allocating Track Maintenance Costs on Shared Rail Facilities". "Transportation Research Record 1785". Paper No. 02-3812. January, 2002.

[7] D.Jeong, Y. Tang, O. Orringer, Estimation of rail wear limits based on rail strength investigation, US Department of Transportation and Federal Railroad Administration. Washington, DC, 1996.

[8] Kerr, Fundamentals of railway track engineering. Simmons-Boardman Books, Inc. Omaha, NE. USA. 2003.

Fusion Bonding and Consolidation of 3D Printed Continuous Carbon Fibre Reinforced Polyamide Composites

Qinghao He, Hongjian Wang, Binghong Yin and Lin Ye* (**Plenary Speaker**)

Centre for Advanced Materials Technology

School of Aerospace, Mechanical and Mechatronic Engineering

the University of Sydney, NSW 2006, Australia

lin.ye@sydney.edu.au

***Abstract* — A major issue of 3D printed fibre reinforced polymer composites is poor fusion between individual filaments and inadequate consolidation in the composites, which results in microscopic voids, as a result, weakened mechanical properties of the composites. In this study, comprehensive characterisations are conducted to evaluate the intralaminar and interlaminar fusion bonding and consolidation of 3D printed continuous carbon fibre reinforced polyamide (CF/PA6) composites with a fibre volume fraction of 35%. Examination of microstructures reveals that the voids result from both raw CF/PA6 filaments and poor fusion between filaments and inadequate consolidation during the printing process contribute to low mechanical performance of the composites. Mode I intralaminar and interlaminar fracture toughness tests are conducted using DCB specimens of printed CF/PA6 composite laminates. It suggests that existence of voids and poor fusion within the 3D printed CF/PA6 composites play a key role in lowering the fracture toughness of the composites significantly, indicating much weaker resistance to initiation of delamination.**

Fusion Bonding and Consolidation of 3D Printed Continuous Carbon Fibre Reinforced Polyamide Composites

Zhengyi Jiang* (**Keynote Speaker**)

School of Mechanical, Materials, Mechatronic and Biomedical Engineering

University of Wollongong

Wollongong NSW 2522, Australia

jiang@uow.edu.au

***Abstract* — Cemented tungsten carbide (WC-10Co) and high strength (AISI 4340) steel were successfully bonded by hot compaction diffusion bonding at a low temperature. The effects of holding time on microstructure and mechanical properties of the sintered carbides and bonding strengths of the bimetallic composites were examined, and a transitional layer was found at the interface as a result of elemental interdiffusion. The optimal bonding parameters were determined to achieve the maximum bonding strength of 204 MPa of the WC-10Co/4340 steel joints. Microforming is introduced to produce lighter and more energy effective products. In this study, Magnesium-Lithium (Mg-Li) alloy a new material in microscale, is chosen to superior formed micro-cup due to its ultralight weight with outstanding ductility. The dry and oil lubrication conditions are chosen as benchmarks to investigate effects of water-based nano-lubricant in microforming of Mg-Li alloy. Finite Element (FE) modelling was conducted and the simulated results of rolling forces are in good agreement with the experimental results. The formed cup quality regarding the surface roughness has been extensively evaluated by consideration of various parameters and the quality improvement is substantial.**

Nonlinear behaviors of wave-induced fluid oscillations in the gap between two fixed barges

Lin Lu* (**Keynote Speaker**)

State Key Laboratory of Coastal and Offshore Engineering,

Dalian University of Technology, Dalian, 116024, China

lulin@dlut.edu.cn

***Abstract* — Extremely large amplitude of resonant wave oscillation is often encountered in the narrow gap between two floating bodies. Nonlinear behavior of the resonant response is numerically investigated based on a fully nonlinear potential flow model in time domain, rather than the linear one in frequency domain. Nonlinear harden spring behavior of the piston-mode wave oscillation in gap is found and confirmed to be resulted from the second order effect with a rise of the mean water level in the narrow gap. The nonlinear solutions demonstrate multiple response components. Their roles in the dynamic response are clarified. Super-harmonic resonance is identified with the nonlinear model, including the second order and third order resonance, and the combined harmonic resonance.**

New devising in diagnosis of knee osteoarthritis based on acoustic emission imaging

Tawhidul Islam Khan* (**Keynote Speaker**)

Intelligent Machines, Department of Mechanical Engineering,

Saga University, Saga 840-8502, Japan

khan@me.saga-u.ac.jp

***Abstract* — Acoustic emission (AE) technique has been applied in devising an adaptive imaging tool for evaluating the integrity of knee joint, which involves a detail study of several anatomical parts of knee joint like bones, cartilage, tendons etc. Any internal damage of these anatomical parts of knee joint causes painful disease like osteoarthritis (OA). The major concern of this disease is the incurability at its matured stage. However, early detection for adopting appropriate measures can reduce the risk of this disease. The present discussion will focus on the characterization of this new devising technique in dynamical behavioral analysis of AE signals from knee joint for easy diagnosis of knee problems in aging as well as other causes. Cases will be discussed based on data from OA participants as well as healthy people.**

Keywords— Integrity of Knee Joint, Osteoarthritis, Acoustic Emission, Biomarker.

New Active Control Method to Improve the Dynamic Stability of High-speed Trains

Chunwei Zhang* (**Keynote Speaker**), Hao Wang, Yang Xu, Shuai Xu

School of Civil Engineering, Qingdao University of Technology, 266033, P.R. China

zhangchunwei@qut.edu.cn

***Abstract* — The dynamic behaviours of high-speed trains are very complex. Two types of adverse dynamic behaviours of high-speed trains are defined in this paper, i.e. the dynamics corresponding to translational vibrations (lateral sway, floating, back -and-forth) and to rotational vibrations (yawing, pitching, rolling). To suppress the adverse dynamic behaviour of high-speed trains, many traditional methods are investigated, e.g. various forms of suspension systems. However, it has been ignored that the traditional and all existing methods are completely invalid for the control of dynamic behaviours corresponding to rotational vibrations. The reasons shall be discussed in details in this talk. Therefore, the innovative control method for adverse dynamic behaviour control of high-speed trains are proposed, namely the Active Rotary Inertia Driver (ARID) system. Firstly, the dynamic mathematical model of high-speed train is established. The active controller is designed based on the mathematical model and the LQR (linear quadratic regulator) algorithm. Next, the numerical analyses are carried out using Simulink to study the effectiveness of the control method. The numerical analyses of the dynamic model subjected to harmonic excitations, sweep excitations and track irregularity excitation are also carried out. Lastly, the parametric analyses are carried out and the control effectiveness are further verified. Furthermore, the dynamic characteristics of the adverse dynamic behaviours of high-speed trains are studied, and the effectiveness and feasibility of the proposed method are well demonstrated and verified.**

Keywords— high-speed train, active control, Active Rotary Inertia Driver, moment control method

Development and application of Fiber Bragg Grating strain sensors using Additive Manufacturing Technology

Li Sun* (**Keynote Speaker**), Tianqi Liang, Chuang Li, Chunyang Zhu, Zhongxin Su, Zihao Zhao

School of Civil Engineering, Shenyang Jianzhu University, Shenyang 110168, P.R. China

sunli@sjzu.edu.cn

Chunwei Zhang

School of Civil Engineering, Qingdao University of Technology, 266033, P.R. China

zhangchunwei@qut.edu.cn

***Abstract* — In the field of civil engineering structural health monitoring, Fiber Bragg Grating (FBG) is a sensing element with excellent performance and wide-range application prospects. With the progress and development of manufacturing technology, the profile of modern civil structure is becoming more and more complex and complicated. Therefore, health monitoring systems should be constantly improved and upgraded correspondingly. New sensors are needed to meet the demand of engineering practice. To improve the efficiency of FBG sensors, this paper investigates a new encapsulation method of FBG sensor based on 3D printing technology. Consumables of Acrylonitrile Butadiene Styrene (ABS) and Polylactic Acid (PLA) are used to manufacture so called clamping type FBG sensors. Cyclic tensile calibrating tests were carried out to study the effect of design parameters on the performance of the FBG sensors. The testing results revealed that for the sensor with ABS-5mm, PLA-5mm and ABS-3mm, the sensitivity coefficients are 0.3 pm/με, 0.2 pm/με, and 0.4 pm/με, respectively. The relative accuracy are 98.733%, 97.904% and 98.829%, respectively. The test results show that the 3D printing using PLA and ABS can be used to fabricate the FBG strain sensor in a compact and efficient way, at the same time with guaranteed high precision, anti-electromagnetic interference property etc., and can be arranged in series distribution to satisfy the needs of various engineering practices.**

Keywords*— *Additive manufacturing; Fiber Bragg Grating; Strain sensor

Engineering Phosphorene by Kirigami

May Gamil
School of Computing, Engineering & Mathematics
Western Sydney University
Penrith, Australia
M.Gamil@westernsydney.edu.au

Yingyan Zhang
School of Computing, Engineering & Mathematics
Western Sydney University
Penrith, Australia
Yingyan.Zhang@westernsydney.edu.au

***Abstract* — Two-dimensional (2D) materials offer excellent electrical, mechanical, and physical characteristics compared to their bulk counterparts' materials. Recently, a newly discovered 2D material known as phosphorene was thoroughly investigated as an alternative material for 2D graphene, and molybdenum disulphide (MoS2) given that it possesses distinctive features. However, the mechanical properties of phosphorene, especially its flexibility, necessitate additional support to prevent early failure under deformations, when subjected to different loadings. In this context, the ancient art of paper cutting, kirigami, will be implemented to enhance the mechanical response of phosphorene under shear, tensile, and impact loadings under a two-phase research project. This report discusses the first stage which investigates the flexibility of perfect phosphorene under tensile, and shear loadings. By using molecular dynamics simulations based on the Stillinger-Weber (SW) potential, we ascertained that monolayer phosphorene exhibits an anisotropic mechanical response along its directions. Under tensile loading, phosphorene can sustain tensile strain up to 5% along the zigzag edge (ZZ), compared to 11% in the armchair edge (AC). Moreover, Young's modulus demonstrates a higher value in the zigzag direction than the armchair one, meaning that the AC edge has greater flexibility than the ZZ edge. Subsequently, the second phase of this research studies the impact of applying the kirigami method on the mechanical performance of phosphorene by comparing the findings with that of the phosphorene-perfect model derived from the first phase. Improving the flexibility of phosphorene might support the current development in the direction of wearable and stretchable nano-applications.**

Graphene Reinforced Cement Composite: Technical Approach for Ecofriendly Construction

Farid Sartipi
School of Computing, Engineering & Mathematics
Western Sydney University
Penrith, Australia
f.sartipi@westernsydney.edu.au

May Gamil
School of Computing, Engineering & Mathematics
Western Sydney University
Penrith, Australia
M.Gamil@westernsydney.edu.au

***Abstract* — Graphene as an emerging material compromising outstanding properties shows great potential for commercial applications in many industries including construction. The current paper seeks to review the advancements in the area of building and construction by focusing on the composition of graphene reinforced cement paste as a suitable material for eco-friendly high-performance construction purposes. Moreover, we focus on the environmental impact of graphene reinforced cement compared to conventional cement. In this review, a bibliometric analysis had been run by using the VOS viewer software based on the data collected from the Web of Science Core Collection database. We found that the potential areas enhancing the performance of conventional cement mortar by graphene had been identified and investigated with a practical perspective based on the existing advancements. However, a proper commercial synthesis method emerges for reducing the unit price of graphene is not covered in the literature yet. Following this result, the Australian market capital has undergone financial research where the graphene was subject as the commodity.**

A Hybrid Deep-Learning Model for Fault Diagnosis of Rolling Bearings

Yang Xu
School of Engineering, Ocean University of China, Tsingdao 266100, China
xuyang@stu.ouc.edu.cn

Zhixiong Li*
School of Engineering, Ocean University of China, Tsingdao 266100, China,
School of Mechanical, Materials, Mechatronic and Biomedical Engineering, University of Wollongong, Wollongong, NSW 2522, Australia
zhixiong_li@uow.edu.au

Zhengjun Ma
School of Engineering, Ocean University of China, Tsingdao 266100, China
zhenjun@uow.edu.au

Weihua Li
School of Mechanical, Materials, Mechatronic and Biomedical Engineering, University of Wollongong, Wollongong, NSW 2522, Australia
weihuali@uow.edu.au

***Abstract* — Detection accuracy of bearing faults is crucial in saving economic loss for industrial applications. Deep learning is capable of producing high accuracy for bearing fault diagnosis; however, in most of existing deep-learning models such as a convolutional neural network (CNN) model or a deep forest (gcForest) model, the fault feature extraction is ignored. In order to address this issue, this study develops a hybrid deep-learning model based on CNN and gcForest. In this new method, bearing vibration signals were converted into time-frequency images using the continuous wavelet transform (CWT). Then, CNN the images were used to extract intrinsic fault features and feed them into the gcForest model. Experimental data provided by CWRU were used to evaluate the performance of the proposed method. The analysis results demonstrated that this proposed hybrid model can achieve higher detection accuracy than CNN and gcForest because of the feature extraction.**

Keywords— Fault diagnosis; Prognostics and health management (PHM); Deep learning

END of Proceeding Book